Agronomy Research

Established in 2003 by the Faculty of Agronomy, Estonian Agricultural University

Aims and Scope:
Agronomy Research is a peer-reviewed international Journal intended for publication of broad-spectrum original articles, reviews and short communications on actual problems of modern biosystems engineering incl. crop and animal science, genetics, economics, farm- and production engineering, environmental aspects, agro-ecology, renewable energy and bioenergy etc. in the temperate regions of the world.

Copyright:

Agronomy Research online:
Agronomy Research is available online at: http://agronomy.emu.ee/

Acknowledgement to Referees:
The Editors of *Agronomy Research* would like to thank the many scientists who gave so generously of their time and expertise to referee papers submitted to the Journal.

Abstracted and indexed:
SCOPUS, EBSCO, CABI Full Paper and Thompson Scientific database: (Zoological Records, Biological Abstracts and Biosis Previews, AGRIS, ISPI, CAB Abstracts, AGRICOLA (NAL; USA), VINITI, INIST-PASCAL).

Subscription information:
Institute of Technology, EULS
St. Kreutzwaldi 56, 51014 Tartu, ESTONIA
E-mail: timo.kikas@emu.ee

Journal Policies:
Estonian University of Life Sciences, Latvia University of Life Sciences and Technologies, Vytautas Magnus University Agriculture Academy, Lithuanian Research Centre for Agriculture and Forestry, and Editors of *Agronomy Research* assume no responsibility for views, statements and opinions expressed by contributors. Any reference to a pesticide, fertiliser, cultivar or other commercial or proprietary product does not constitute a recommendation or an endorsement of its use by the author(s), their institution or any person connected with preparation, publication or distribution of this Journal.

CONTENTS

Polymer acrylic hydrogels with protein filler: Synthesis and characterization

M. Baidakova[*], V. Sitnikova, M. Uspenskaya, R. Olekhnovich and
M. Kremenevskaya

International Research Center for Bioengineering, ITMO University, 49 Kronverksky ave.,
RU197101 St. Petersburg, Russia
[*]Correspondence: mvbaidakova@yandex.ru

Abstract. The water-retention hydrogel composites were synthesized by the free-radical polymerization depending on the order of addition filler of the protein hydrolysate. As the filler was used protein hydrolysate, 'Biostim', obtained by processing cattle hides. The influence of gelation time on the synthesis parameters of hydrogel compositions was investigated. It is found that the gelation time of the sample without filler is 2–2.5 times longer than filled of hydrogel compositions. The structural characteristics of polymer composition by TGA, DSC and atomic force microscopy were determined. FTIR spectra found decrease in the intensity of vibrations of (-COO-) groups, indicating about additional ionic interactions. Decrease the beginning evaporation temperature of polymer composites with increase concentration of protein filler, indicating the destruction of the ordered structure of the polymer material revealed by thermogravimetric analysis (TGA). The influence of various media, such as distilled water, saline solution, and buffer solutions at differents pH on the swelling behavior of hydrogels was also assessed. Maximum swelling capacity showed sample prepared with order of addition filler at the end of synthesis (Scheme I). The kinetics of the release protein hydrolysate from the polymer matrix was measurement by spectrophotometric method. The synthesized hydrogel composites with protein hydrolysate and improved physicochemical properties are of practical interest as water-retaining materials for increasing of crop the yield in agricultural.

Key words: hydrogel, radical polymerization, filler, protein hydrolysate.

INTRODUCTION

Maintaining a constant physical, chemical, metabolic and biological processes occurring in the soil environment, leads to the provision of high soil fertility and increased productivity of agricultural crops. The required conditions for this are: an increase in the moisture capacity of the soil, a decrease in denitrification, and the use of fertilizers (Olekhnovich et al., 2016).

The development of hydrophilic moisture-retaining polymeric materials, which are called hydrogels, allows to solve the problem of not only improving the soil structure, but also storing soil moisture (Jhurry, 1997; Omidian et al., 2005; Mohanty et al., 2013). The content in the composition of such materials macroelements of nitrogen and potassium, contributes not only to increase crop yields, but also their resistance to

adverse environmental factors (Askari, 1993; Dessougi, 2002; Liu et al., 2006; Mahdavinia et al., 2009; Senna & Botaro, 2017).

The wide interest in creating water-holding materials are crosslinked polymers based on acrylic derivatives or their composites (Pereira et al., 2012; Olekhnovich et al., 2015). Acrylamide hydrogels are most common, however, the question of their toxicity remains open.

Therefore, the search for other nitrogen sources when creating hydrogels for agriculture is quite important. In recent decades, much attention has been paid to the use of biologically active substances containing products of the hydrolysis of collagen-containing animal waste. (Maksimova, 2006). Treatment with such substance, having in its composition free amino acids, has a positive effect on crop yields (Kutsakova et al., 1997).

Therefore, the obtaining and study of the properties of hydrogels on the base of acrylic polymer containing as a filler protein hydrolyzate produced by processing secondary raw materials is important.

MATERIALS AND METHODS

Materials

Purified acrylic acid (AA) stored in the refrigerating chamber at a temperature of 3–5 °C. For neutralization of acrylic acid using potassium hydroxide (8 n KOH). Potassium hydroxide is a white, nearly transparent crystals, and stored in sealed standard containers. AA, ammonium persulfate (APS) analytical grade, potassium hydroxide, were purchased from Vekton (Russia).

N,N,N',N'-tetramethylethylenediamine catalyzer, N,N-methylenebisacrylamide cross-linking agent, were all of analytical grade, and purchased from Sigma-Aldrich (USA).

The filler used protein hydrolysate 'Biostim', derived from by-products in the processing of slaughter animals by chemical hydrolysis, the main raw material for the production of which is cattle hides beef. The molecular weight of peptides of the protein hydrolyzate is shown in Table 1. In addition to peptides, amino acids make up the bulk of the protein hydrolysate. Glycine is one third of the total number of amino acids.

Table 1. The molecular weight of peptides of the protein hydrolysate

Name of the peptide	Molecular weight (Da)
Dipeptide	215.0
Tripeptide	313.0
Tetrapeptide	412.1
Pentapeptide	510.6
Hexapeptide	609.2
Heptapeptide	707.7
Octapeptide	806.2
Nanopeptide	904.7
Decapeptide	1,003.3

Preparation hydrogel composite with filler 'Biostim'

Samples were prepared hydrogel composites based on acrylate potassium, with degree of filler 'Biostim' 5wt.%. The synthesis was carried out by free-radical copolymerization of the neutralized acrylic acid and crosslinking agent (MBA) with 0.1wt.%. As the initiator was used redox system: ammonium persulfate (PSA) –

N,N,N',N'-tetramethylethylenediamine (TEMED). The concentration of monomers in the initial aqueous solution was 30 wt.%.

First, the protein hydrolysate 'Biostim' was homogenized by stirring on a magnetic stirrer with the spin rate (1,200 rpm) for 45 minutes. The hydrogel compositions based on potassium polyacrylate and protein hydrolysate were synthesized by free radical polymerization in an aqueous medium, depending on the sequence of adding the filler. Then, AA was partially neutralized with potassium hydroxide (degree of neutralization of 0.9) and in the mixture was added redox system. After this, according to Scheme I, a cross-linking agent was first added and the filler added last (sampl No.1). According to Scheme II, a filler was first added, and then – a cross-linker MBA (sampl No.2). The obtained samples of acrylic hydrogel with and without filler were thermostated at the polymerization temperature 35 °C for 24 hours. Further, the structural differences in the samples obtained by Scheme I and Scheme II will be investigated by IR spectroscopy and thermal methods.

Characteristics of hydrogel compositions

Structural characteristics of acrylic hydrogels with protein filler 'Biostim' were recorded on the console FTIR (frustrated total internal reflection) with a ZnSe crystal at a resolution of 2 cm^{-1}, accumulating 32 scans on the spectrometer TENSOR37 'Bruker' and were measured between 500 and 4,000 cm^{-1}.

Photos of the microstructure of polymer samples were obtained on a measuring microscope STM6 Olympus.

Thermal analysis of the samples was performed on a differential scanning calorimeter DSC 204 F1 Phoenix 'Netzsch' in the range from 25 °C to 350 °C with a heating rate of 10 °C min^{-1} in a nitrogen atmosphere.

Thermogravimetric analysis was performed on a TG 209 F1 Libra 'Netzsch' in the range from 25 °C to 900 °C with a heating rate of 10 °C min^{-1} in a nitrogen atmosphere of 40 mL min^{-1}.

The start time of gelation and the sorption characteristics of acrylic hydrogel composites were determined according to the procedures described in (Uspenskaya, et al., 2006).

Studied sorption characteristics of acrylic composite materials in distilled water, salt solution and buffer solutions with pH = 4.1 and pH = 9.01 at a temperature of 25 °C.

DISCUSSION OF RESULTS

FTIR spectra analysis

In order to better understand the structural characteristics of the composite hydrogels obtained by the method of free-radical polymerization solution-casting method, the samples analyzed by ATR–FTIR (Fig. 1).

The broad peaks at 3,200–3,600 cm^{-1} are attributed to the stretching vibrations of free and bound hydroxyl OH-groups. In addition, the overlapping double peaks at 3,343 cm^{-1}, and 3,280 cm^{-1} indicating the presence of protein bands (or amino acid residues), in particular the valence vibrations of N-H groups take place due to the introduction of a protein filler in the polymer material.

The shift of peaks from 1,640 cm^{-1} to 1,650 cm^{-1} relative to the unfilled material, characteristic of the protein bands–amide I peptide group also occurs due to the presence of protein hydrolyzate in the composite. As you can see from Fig. 1 the intensity of the absorption band at 1,545 cm^{-1} shows the quantitative ratio of carboxylate and carboxyl groups in the hydrogel. Reducing the intensity of vibrations (- COO -) groups in the sample prepared by (Scheme II) because of additional cross-linking protein hydrolyzate with functional groups of the polymer matrix (Sitnikova et al., 2018).
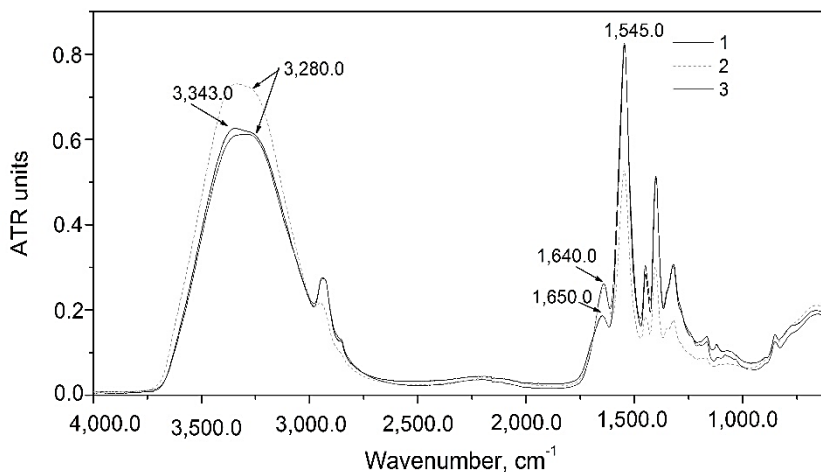
Figure 1. TR–FTIR spectra of the hydrogel samples filled with the protein hydrolysate prepared at different schemes: 1 – Scheme I; 2 – Scheme II; 3 – hydrogel without filler.

Thermal characterization

Thermal behavior of the hydrogel samples filled with protein hydrolysate and without filler were detected on DSC curves (Fig. 2).

As can be seen from Fig. 2, an intensive peak is observed on the DSC curves in the temperature range under study, which is characteristic of the evaporation of free and bound water. The maximum evaporation temperature for all samples is quite close. However, the evaporation temperature of the filled samples prepared according to different schemes differ. The sample prepared according to the Scheme II had a higher evaporation temperature of water (148 °C) by obtaining a more cross-linked hydrogel sample (Kopp et al., 1989).
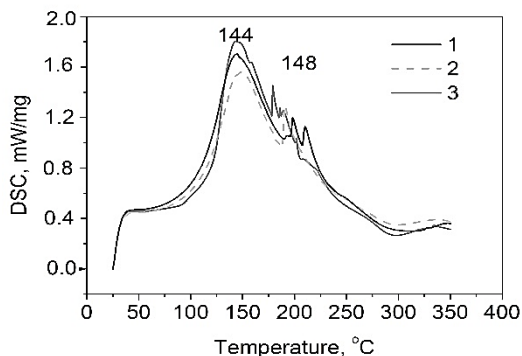
Figure 2. DSC curves of the hydrogel samples filled with the protein hydrolysate prepared at different schemes: 1 – Scheme I; 2 – Scheme II; 3 – hydrogel without filler.

The lowest value of the activation energy of I stage is possessed by hydrogel composites obtained according to Scheme I.

The thermal stability of hydrogel materials was studied by TGA and results were shown in Fig. 3 and Table 2. As shown in Fig. 3, the curves of composite hydrogels are characterized by three stages of mass loss corresponding to the evaporation of water, the destruction of the branches and functional groups of the protein filler and the polymer matrix, and the destruction of the main polymer chain of the hydrogel (Gharekhani et al., 2017).
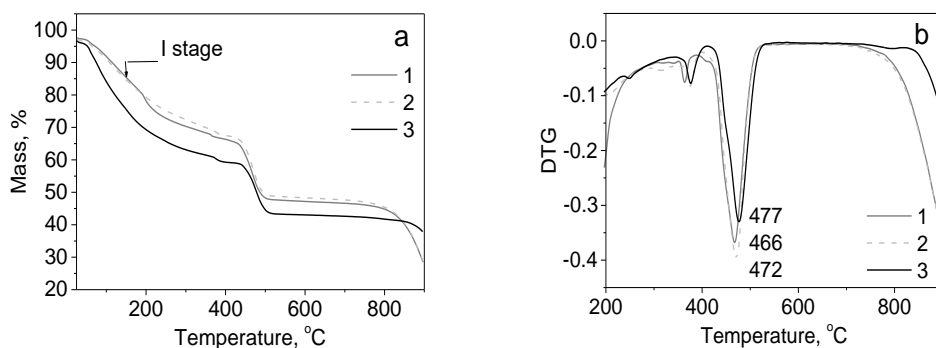
Figure 3. TGA (a), DTG (b) curves of the hydrogel samples filled with hydrogel prepared at different schemes: 1 – Scheme I; 2 – Scheme II; 3 – hydrogel without filler.

Table 2. Thermal characteristics of the hydrogel samples filled with the protein hydrolysate

No.	Moisture content, %	Temperature of evaporation, °C	Temperature degradation, °C	Activation energy of I stage, E_a, kJ
1	29.0	144.0	466.2	18
2	26.6	148.0	472.6	23
3	29.5	144.0	477.0	32

For a filled polymer hydrogel sample prepared according to Scheme I, the degradation temperature was 10 °C lower compared to the unfilled sample and was 466 °C. This phenomenon is primarily due to the formation of a more defective polymer network when embedding the peptide chains of the filler in the polymer matrix of an acrylic hydrogel. Thus the addition of the filler into hydrogel leads to a decrease in thermal stability and the formation of a more amorphous structure of the polymer matrix (Fathima et al., 2010).

This was also confirmed by photo of the surface of the obtained polymer samples shown in Fig. 4. The morphological investigation of the hydrogel composites with protein hydrolysate and without filler was conducted by optical microscope, as seen in Fig. 4. Hydrogel samples without filling have a less rough surface.

As can be seen from Fig. 4 (b, e) the synthesis of acrylic hydrogel composite according to Scheme I leads to a decrease in the size of protein agglomerates and the formation of a more homogeneous structure of the material compared with samples obtained according to Scheme II (Fig. 4, c, f) (Yang, et al., 2009).
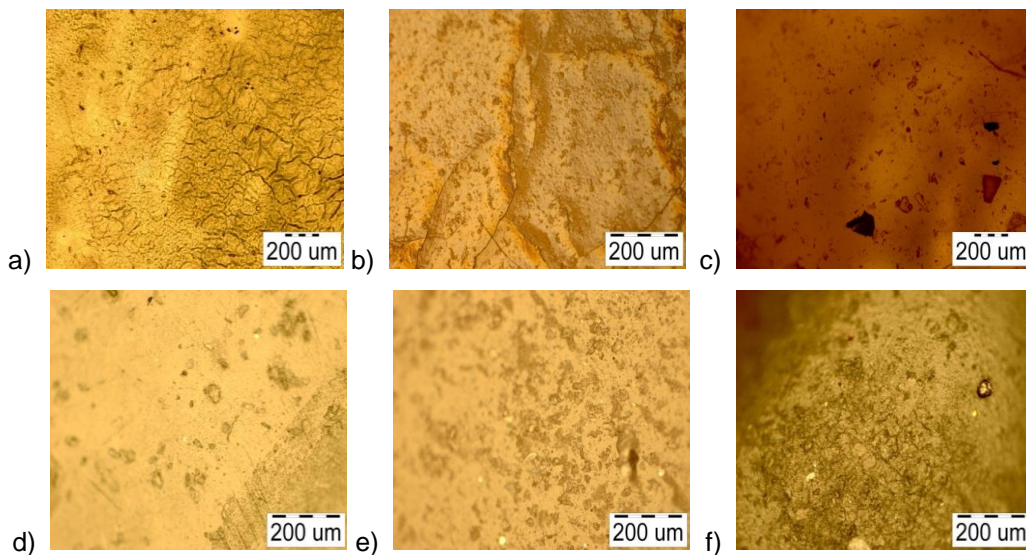
Figure 4. Photo of hydrogel samples in transmitted light and their surfaces: (a, d) without filler, (b, e) Scheme I, (c, f) Scheme II.

Swelling and Release

The sorption characteristics of hydrogels with protein hydrolysate and without filler in various aqueous media were studied in this work. The kinetic sorption curves for hydrogel samples of composites with and without filling in distilled water, physiological and buffer solutions are shown in Fig. 5.

It is well known that one of the basic properties of a guide is the equilibrium degree of swelling, which depends both on the characteristics of the reacting substances, which include: pK of the ionogenic group, degree of ionization, concentration and ratio of monomer units in the network, etc., and from external conditions of synthesis: pH, temperature, ionic strength of the environment, etc. (Kabakova, et al., 2003)

As can be seen from Fig. 5, the values of the equilibrium degree of swelling for filled hydrogel samples are 2.5–3 times larger than for unfilled ones. This may be due, on the one hand, to the formation of a looser structure, on the other hand, by an increase in the content of hydrophilic functional groups, due to the presence of a filler (Ottenbrite, 2010).

The presence of amino groups of the protein hydrolyzate in the composition of the hydrogel composite contributes to the absorption of more distilled water than the polymer matrix, consisting only of acrylic acid units (Zhao et al., 2013).
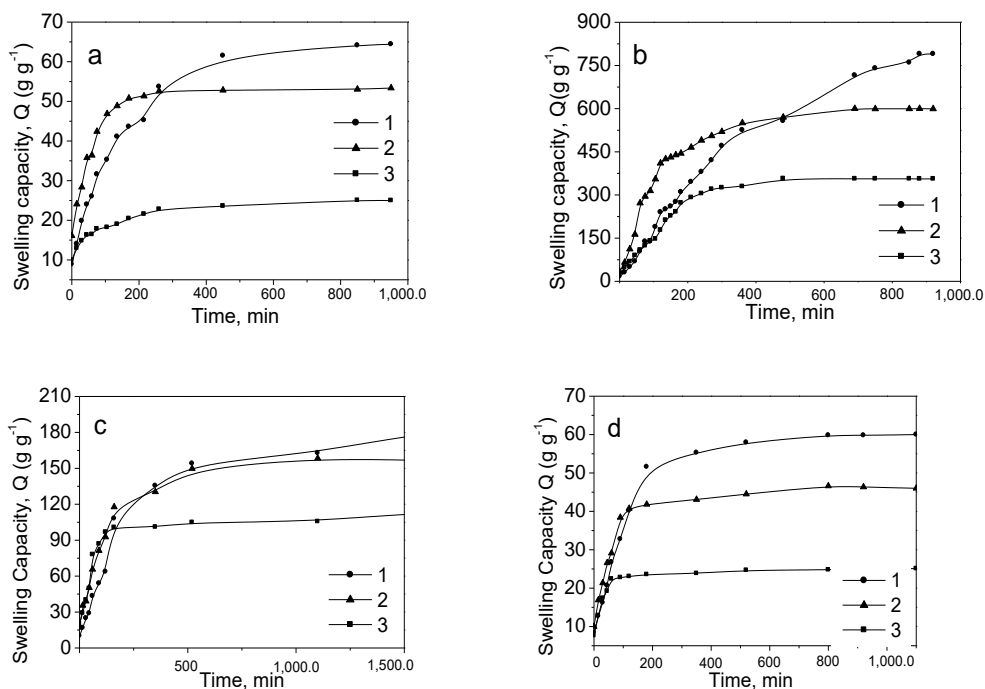
Figure 5. Kinetic sorption curves of composite hydrogels prepared at: 1 – Scheme I; 2 – Scheme II; 3 –without filler: (a) saline solution (b) distilled water (c) pH = 9.01 (d) pH = 4.1.

The values of the equilibrium degree of swelling of filled and unfilled hydrogel composites in various aqueous solutions were demonstrated in Table 3.

Table 3. Sorption characteristics of hydrogels filled with protein hydrolysate and without filling

No.	Moisture content (%)	Gelation time (m)	Maximum swelling degree, Q (g/g)			
			distilled water	saline solution	pH = 9.01	pH = 4.1
1	29.0	17	800.0	65.5	200.0	55.5
2	26.6	30	550.5	50.0	160.5	40.0
3	29.5	50	300.0	20.2	80.0	20.0

It is known (Omidian, et al., 2005) that acrylic anionic hydrogels are highly sensitive to changes in the pH of the external solution. The presence of acid groups in the polymer chain makes it possible to swell with acrylic hydrogels in an alkaline medium and collapse in an acidic medium.

As can be seen from Table 3 and Fig. 5 The swelling of filled and unfilled acrylic composites in a buffer solution pH = 9.01 varies between 80 and 200 g g^{-1}. In a buffer solution pH = 4.1, the maximum values of the degree of swelling are significantly lower and take the value of 55 g g^{-1} for samples prepared according to Scheme I. For practical use of acrylic hydrogel composites in agriculture, it must be remembered that at pH < 5 the swelling is significantly reduced many times with the release of water structured in it from the hydrated gel.

From Table 3 it can be seen that with an increase in the onset time of gelation, the swelling capacity of hydrogels naturally decreased and the smallest value of the equilibrium degree of swelling, regardless of the nature of the external solvent under investigation, had an acrylic hydrogel without filler. The decrease in the degree of swelling of composite hydrogels prepared according to Scheme II is probably associated with the formation of more durable structures (Uspenskaya et al., 1998).

To determine the release of protein hydrolysate from the acrylic matrix, samples obtained according to Scheme I and Scheme II were measured using a UV-visible spectrophotometer UNICO.

Fig. 6 shows the release of protein hydrolyzate at different time intervals in saline solution. The maximum degree of swelling reached the sample prepared according to the Scheme I. However the greatest release of protein hydrolysate from the polymer matrix was observed for the samples obtained according to Scheme II, and was 0.13 mg mL^{-1} after 72 hours.
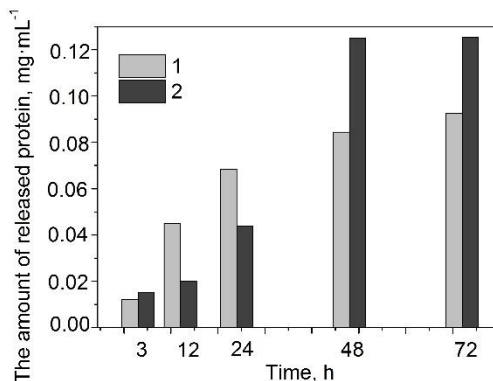
Figure 6. Release of protein filler from hydrogel composites prepared at different schemes: 1 – Scheme I; 2 – Scheme II at different times.

On the basis of the achieved results, such as high adsorption properties and homogeneity of the structure for the hydrogel composite synthesized according to the Scheme I, it is necessary to conduct further studies of desorption properties in different pH media.

CONCLUSIONS

In the present work, acrylic composites filled with 'Biostim' protein hydrolyzate were obtained and studied by radical polymerization in an aqueous medium, depending on the sequence of addition of the filler. Protein filler 'Biostim', having in its composition a set of amino acids and peptides, was obtained by processing secondary animal waste. The best sorption characteristics in various aqueous media were demonstrated by an acrylic polymer sample obtained according to Scheme 1. It was shown that the thermal stability of the filled materials naturally decreased due to the introduction of protein particles into the polymer matrix. The study of the laws governing the isolation of protein hydrolysate from the polymer matrix demonstrated the promise of using the obtained materials as soil conditioners and plant growth regulators in agriculture and horticulture.

REFERENCES

Askari, F., Nafisi, S., Omidian H. & Hashemi, S.A. 1993. Synthesis and characterization of acrylic-based superabsorbents. *J Appl Polym Sci.* **50**, 1851–1855.

Dessougi, H., Claassen, N. & Steingrobe, B. 2002. Potassium efficiency mechanisms of wheat, barley, and sugar beet grown on a K fixing soil under controlled conditions. *J Plant Nutr Soil Sci.* **165**, 732–7.

Fathima, N., Baias, M., Blumichc, B. & Ramasami, T. 2010. Structure and dynamics of water in native and tanned collagen fibers: Effect of crosslinking. *International Journal of Biological Macromolecules* **47**, 590–596.

Gharekhani, H., Olad, A., Mirmohseni, A. & Bybordi, A. 2017. Superabsorbent hydrogel made of NaAlg-g-poly(AA-co-AAm) and rice husk ash: Synthesis, characterization, and swelling kinetic studies. *Carbohydrate Polymers* **168**, 1–13.

Jhurry, D.1997. *Agricultural polymers.* AMAS. Food and Agricultural Research Council, Réduit, Mauritius, pp.109–113.

Kabakova, M.M., Uspenskaya, M.V., Sirotinkin, N.V. & Sanatin, E.V. 2003. Behavior of cross-linked copolymers of acrylic acid and 5-vinyltetrazole in aqueous media. *Russian Journal of Applied Chemistry* **76**(7), 1176–1178.

Kopp, J., Bonnet, M. & Renou, J.P. 1989. Effect of collagen crosslinking on collagen-water interactions (a DSC investigation), *Matrix* **9**, 443–450.

Kutsakova, V.E., Chechetkin, P.I., Zdenek, P., Utkin, Yu.E., Burov & Kononov, A.N. 1997. *A method of stimulating the growth and development of potatoes of early, middle and late varieties and winter and spring crops.* Patent RF No. 2096957.

Liu, M., Liang, R., Zhan, F., Liu, Z. & Niu, A. 2006. Synthesis of a slow-release and superabsorbent nitrogen fertilizer and its properties. *Polymers for Advanced Technologies* **17**, 430–438.

Mahdavinia, G.R., Mousavi, S.B., Karimi, F., Marandi, G.B., Garabaghi, H. & Shahabvand, S. 2009. Synthesis of porous poly(acrylamide) hydrogels using calcium carbonate and its application for slow release of potassium nitrate. *Exp. Polimer Letters* **3**(5), 279–285.

Maksimova, E.M. 2006. Development of technology for recycling of protein waste by enzymatic hydrolysis. *Herald of MGTU* **9**(5), 875–879 (in Russian).

Mohanty, M., Sinha, N.K., Reddy, K.S., Chaudhary, R.S., Rao, A.S., Dalal, R.C. & Menzies, N.W. 2013. How important is the quality of organic amendments in relation to mineral availability in soils? *Agricultural Research* **2**, 99–110.

Olekhnovich, R.O., Baidakova, M.V, Uspenskii, A.B, Slobodov, A.A. & Uspenskaya, M.V. 2016 Phosphorus-containing hydrogel for use in agriculture, *16th International Multidisciplinary Scientific Geoconference*, SGEM **3**(2), 249–256.

Olekhnovich, R.O., Glazacheva, E.N., Uspenskii, A.B., Slobodov, A.A. & Uspenskaia, M.V. 2015. Investigation of hydrogel on the base the phosphorus-containing acrylic copolymer for use in agriculture, *15th International Multidisciplinary Scientific GeoConference, SGEM* **3**(2), 207–214.

Omidian, H., Rocca, J.R. & Park, K. 2005. Advances in superporous hydrogels. *J. Control Release* **102**, 3–12.

Ottenbrite, R.M. 2010. *Biomedical Applications of Hydrogels Handbook. Springe Science+Business Media, USA,* pp 423.

Pereira, E.I., Minussi, F.B., da Cruz, C.C.T., Bernardi, A.C.C., Ribeiro, C. 2012. Urea montmorillonite-extruded nanocomposites: a novel slow-release material. *J. Agric. Food Chem.* **60**, 5267−5272.

Senna, A.M. & Botaro, V.R. 2017. Biodegradable hydrogel derived from cellulose acetate and EDTA as a reduction substrate of leaching NPK compound fertilizer and water retention in soil. *J. Control Release* **260**, 194–201.

Sitnikova, V., Baidakova, M., Olekhnovich, R. & Uspenskaya, M. 2018. Infrared spectroscopic study of dynamics and complexation mechanism in chemosorption of ions of metals by acrylate hydrogels. *Scientific and Technical Journal of Information Technologies, Mechanics and Optics* **18**(4), 614–622 (in Russian).

Uspenskaya, M.V., Sirotinkin, N.V., Gorskii, V.A. & Goloshchapov, Yu.G. 2006. Composites of acrylate copolymers and fullerene. *Russian Journal of Applied Chemistry* **78**(5), 830–833.

Uspenskaya, M.V., Yankovskii, S.A. & Bobasheva, A.S. 1998. Swelling of hydrogels formed by copolymers of acrylic and 3-chloro-1,3-butadiene-2-phosphinic acids. *Russian Journal of Applied Chemistry* **71**(3), 521–523.

Yang, Y., Leone, L.M. & Kaufman, L.J. 2009. Elastic Moduli of Collagen Gels Can Be Predicted from Two-Dimensional Confocal Microscopy. *Biophysical Journal* **97**, 2051–2060.

Zhao, C., Zhao, J., Li, X., Wu, J., Chen, S., Chen, Q., Wang, Q., Gong, X., Li, L. & Zheng, J. 2013. Probing structure antifouling activity relationships of polyacrylamides and polyacrylates. *Biomaterials* **34**, 4714–4724.

Measure of thermal transmittance of two different infill wall built with bamboo cultivated in Tuscany

G. Bambi[1], P.F.P Ferraz[2], G.A.S. Ferraz[2], P. Pellegrini[1] and H. Di Giovannantonio[1]

[1]University of Florence, Department of Agriculture, Food, Environment and Forestry, Via San Bonaventura 13, IT50145 Firenze, Italy
[2]University Federal of Lavras, Department of Engineering, Federal University of Lavras, BR37200-000 Lavras -Minas Gerais, Brasil
*Correspondence: gianluca.bambi@unifi.it

Abstract. Bamboo is used in different scenarios of application, its physical and mechanical characteristics guarantee a high flexibility of use especially in the buildings constructions. The experience gained in civil constructions demonstrates that bamboo can be considered a sustainable material able to replace wood in many constructive elements with structural functions. The applications of bamboo aimed at carrying out structural functions are thoroughly studied. For this reason the present research focuses on the thermal insulation performance. To ensure an approach focused on the sustainability of potential exploitation, the research examined only local material coming from three bamboo fields located in the Tuscany region (Italy). The material harvested and suitably treated was utilized for the realization of two different kind of wall, undergone later to experimental tests in compliance with the ISO 9869 standard for the calculation of the transmittance values. The measure of transmittance enabled to know the characteristics of thermal conduction of bamboo walls. The first wall was made of cut throw longitudinal axis bamboo culms; the second one was made of cut throw longitudinal axis bamboo culms coated in internal face with a sustainable mortar. The test was carried out using insulating thermal box with internal temperature under control.
The calculation of the transmittance in place was compared with the images captured by thermal camera. Thermal imagine allowed to highlight the behaviour of the material subjected to a thermal stress induced by the experimental test.

Key words: bamboo, thermal transmittance, thermal conductivity, sustainable building material.

INTRODUCTION

Europe has spearheaded global efforts to fight climate change, has been a driving force in developing renewables, and leads the world in energy-efficiency solutions for industry, transport, buildings. In order to build a major step in implementing the energy-efficiency-first principle for Europe, the main strategy consists the decarbonisation of the EU's stock in some sector such as building industry (EU, 2018). In addition, the transport system poses enormous potential to cut carbon dioxide emissions, but to do so it requires smart solutions and the approach of zero-km is cornerstone to reach these goals.

The growing human population on our planet in combination with an increase of consumption per capita is putting more and more pressure on global resources, which results in materials depletion, ecosystem deterioration and human health problems (Vogtländer et al., 2010).

The introduction of the concept of 'sustainability' in the building sector gradually led to the production of insulation products made of natural or recycled material. Some of them are already present in the market while others are still at an early stage of production or study. The actual sustainability of the considered insulation materials is linked to their availability. They should be used preferably where they are harvested, produced or manufactured (Asdrubali et al., 2015a).

In order to achieve this sustainable goal it is important to export this result also in developing countries. In rural areas, especially in less economically developed countries (LEDCs), it is very difficult to access to data on building materials, to properly design the buildings (Barbari et al., 2014a; Barbari et al., 2014b).

The engineering design of rural and civil buildings must take the availability of the local materials into account, encouraging wherever possible the use of natural materials such as wood, raw earth, straw and other natural resources that can be regenerated, like bamboo.

The low thermal conductivity and fibrous character of the majority of organic materials contribute to a significant improvement of the thermal-insulation properties after incorporation in the structure of the exterior building envelope (Korjenic et al., 2011).

A great advantage of the insulation based on natural fibres is not only a low value of thermal conductivity but also the natural character of input fibres. Another advantage is that it is a renewable material, which does not place any significant strain on the environment (Zach et al., 2013).

The culm of the bamboo plant is used in rural and civil buildings in various parts of the world and is recognised as a material suitable for meeting various construction needs. Bamboo can be a valid alternative to classical wood construction material. Bamboos encompass 1,250 species within 75 genera, most of which are relatively fast-growing, attaining stand maturity within five years (Scurlock et al., 2000). The morphological, physical and mechanical characteristics make it a resistant and easily workable material. Bamboo is exploited according to the local culture and traditions, however its use as a building material with structural functions is restricted by local regulations that often undermine its effective use.

This work does not represent a survey on the mechanical characteristics of bamboo for which there is already substantial scientific literature, instead, it focuses on the study of the behaviour of bamboo as a material to be used in the building sector, favouring the function of thermal insulation in the creation of infill walls.

This research, after having identified a construction technique that is easy to perform, compares the thermal performances of two types of infill walls. In order to respect the sustainability criteria, the experimental tests have analysed bamboo coming from bamboo plantations found in the Tuscany Region, in the hope of being able to exploit this local material. The bamboo harvested has undergone a preservation treatment without intervening on the fibre structure. In order to take into consideration also the aesthetic aspect of the wall, a constructive system has been adopted that is able to preserve the natural appearance of the bamboo.

MATERIALS AND METHODS

Material

The chemical composition of bamboo is similar to that of hardwood, but it is characterised by the presence of alkaline layers. The mechanical strength is conferred by the presence of silica and cellulose, which perform a reinforcement function in the plant structure like that of steel inside reinforced concrete.

The thermal performance of raw bamboo and engineered bamboo composites materials was also investigated (Wang et al., 2018). All these studies demonstrated that:

− the thermal conductivity of bamboo increases with increase in density (Kiran et al., 2012),

− the specific heat capacity of raw bamboo increases with the temperature (Huang et al., 2016),

− the thermal conductivity and thermal diffusivity of raw bamboo is not constant along the radial direction (Huang et al., 2014).

Given the advantages compared to wood, it should be emphasised that one of the limits of bamboo concerns its natural durability which, compared to wood, may be more vulnerable to deterioration due to the absence of protective chemical elements, in addition to the presence of a hollow section that favours the colonisation of different pathogens capable of deteriorating the structure of the bamboo. To ensure greater durability it is essential to treat bamboo culms with preservatives and the effectiveness of these treatments depends above all on the penetration of the chemical products into the fabric of the culm. The outer part of the culms, moreover, which contains a high percentage of silica, forms a barrier for both insects and preservatives; the inner part is covered by a thin waxy layer, which is also waterproof.

The first phase of the research work identified 3 production sites located in the Tuscany region. These three bamboo plantations cultivate the same species, *Phyllostachys viridiglaucescens*, which is very rustic and able to adapt to the Tuscan territory. Three farms with a different aerial of cultivation in terms of altimetry and field slope were selected.

The samplings were carried out in October 2016 (Farm A), November 2016 (Farm C) and finally in February 2017 (Farm B) (Table 1).

Table 1. Description of sampling Tuscany farms

Farm	A	B	C
Coordinate (WGS84)	N 43.685131	N 43.635049	N 43.934574°
	E 11.205717	E 11.172538	E 10.266368°
Area (ha)	0.3	0,19	1
Ground level (a.s.l.)	205	121	35
Slope (%)	15	0	1

The culms taken from the plants were selected respecting the dimensional requirement to collect material with a diameter of about 7 cm at a height of 150 cm, the dimensional deviations have considered a tolerance of 1 cm.

All the material collected was free from pathologies, consequently the culms were subjected to a treatment with a 10% solution of borax ($Na_2B_4O_7 \cdot 10H_2O$) and boric acid (H_3BO_3) in a 1:1 ratio. The treatment of bamboo is not compatible with appropriate

environment sustainability, but treatment agents are usable for several cycles. This treatment lasted 20 days and was necessary to eliminate the starch present in the stem (Mitch et al., 2009).

The culm of the plant can be divided into three sections that differ one from the other in the diameter and thickness of the stem. The apical section and the basal section are characterised by a morphological deformity that does not make them suitable for the selected construction technique. In fact, it is well-known that in the basal section there is a greater wall thickness (Fig. 1) and a slightly lesser external diameter than the central part.
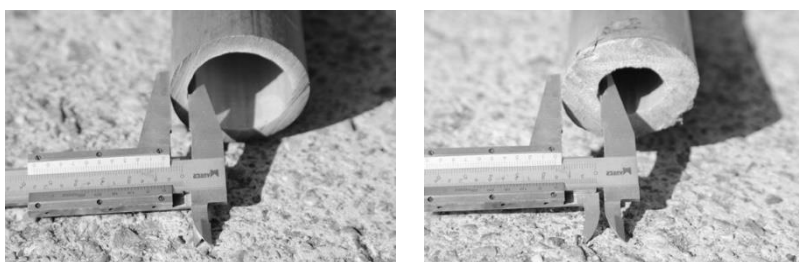
Figure 1. Wall thickness bamboo.

In order to obtain a homogeneous material, the culms were divided into three parts: a basal section of about 50–100 cm, a central section of 400–500 cm and an apical section of about 150–200 cm. At the end of the treatment period the culms were left to dry until achieving the characteristic brownish colour.

The construction technique chosen for the construction of the infill wall is similar to the one commonly adopted for the construction of bamboo roofs. This choice was based on two criteria. The first criterion is not altering the bamboo's natural condition to make it a construction material suitable for use in compliance with Design for Deconstruction (DfD). This is a concept in building science, which has the potential to improve the management of construction waste and thus contributes reducing the environmental impact of a building (Leso et al., 2018). The second criterion is adopting a construction technique capable of preserving the aesthetic features.

The selected and dried culms were cut along their longitudinal axis. This type of cut produced two elements from each individual culm characterised by a natural morphological deformity due to the nature of the plant. The half culms had their nodal diaphragms removed in order to allow for the coupling in the concave part as illustrated in Fig. 2.

Figure 2. Technique construction of bamboo roofs.

The second phase of the research identified the system for detecting the thermal performance. The thermal resistance measurements were made according to the guidelines of the UNI EN 1934:2000 and ISO 9869:1994 standards; the UNI EN 1934 standard thermal performance of buildings. Determination of thermal resistance by means of the hot chamber method with a thermal flow meter does not univocally specify the experimental apparatus to be used, leaving room for the operator to make any changes deemed necessary from time to time (Buratti & Moretti, 2008). For this purpose a metering chamber was constructed, adopting the design criteria indicated by Conti et al. (2017). The Metering chamber was equipped with heaters and ventilation systems in order to produce high temperatures. The internal dimensions of the chamber were 178 cm in length by 112 in width and 40 cm in height.

The metering chamber consisted of a central body, a removable rear wall and a specimen wrapper on the front. The connections between the walls were glued and assembled with a labyrinth shape, in order to avoid heat leakage. The specimen wrapper, designed to contain the specimen, protruded from the front wall. The heating system was installed inside the metering chamber and contained inside a box that acts as an infrared radiation trap which prevented the infrared radiation from directly hitting the specimen or the metering chamber walls. The internal box had an inlet and an outlet for proper air ventilation in order to transfer the heat outside the box and inside the metering chamber. The walls of the metering chamber and the specimen wrapper were made of polystyrene panels (BASF Styrodur) with a nominal thickness of 50 mm. The panels were coupled by means of vinyl adhesive along the entire contact surface to form a 100 mm nominal thickness wall. Polystyrene BASF Styrodur 50 mm thick panels have a 28 kg m^{-3} density. The Thermal Conductivity (λ) declared by the manufacturer is $\lambda = 0.034$ Wm^{-1}k^{1} (at the mean temperature of 10 °C, for panels with a 20–70 mm thickness).

The experimental wall was configured as a separating element between the metering chamber and the external environment (room with a controlled temperature). The wall was created directly on the front of the chamber using 7 bamboo culms from the longitudinal cut of which we obtained 14 medium bamboo culms with a width of between 6.5 cm and 7.5 cm, and an average thickness of 0.5 cm. At the end of the execution the wall had the following dimensions: width 111.9 cm, height 39.9 cm and average thickness 6 cm. In Fig. 3 it is possible to see external face and inner face of the sample wall covered with bio plaster. In the external face two contact probes PT 100 were applied, in the inner face a heat flow plate and one contact probe PT 100 were placed.

Figure 3. Experimental wall**.**

A thermal insulation paste was applied between the edge of the outside of the bamboo wall and the inner edge of the chamber in order to create a frame capable of preventing any heat loss. For the applicability of the method a temperature gradient was respected between the hot room and the environment that exceeded 20 °C.

Instrumentation

Currently, there are two common measurement techniques to evaluate the thermal resistance in existing buildings: direct measurement of the heat-flux, non-destructive method (Zarr, 2001; Cabeza et al., 2010), or direct survey of the fabric layers with direct measure of their thickness, destructive method (Asdrubali et al., 2014b). The non-destructive method requires the use of a heat flow meter that has to be operated according to the standard ISO 9869:1994.

Adopting the design criteria indicated by Evangelisti et al., (2015), the samples were previously monitored with thermographic surveys in order to asses the correct application of the sensors.

A preliminary thermographic analysis was carried out with the support of a FLIR TAU2 thermal imaging camera, which was used to capture the images of the two tests in order to highlight the critical points of the wall. The study of the images captured with thermal camera was conducted with the TermoViewer software.

The instrumental detection system for the survey was a Babuc A/M datalogger to which 3 contact temperature probes and a thermal flow meter probe were connected. On the inside wall of the sample a contact temperature probe BSR 124 and a BSR 240 heat flow plate were installed while the two other contact probes BSR 124 (PT100) were applied on the external wall (Table 2).

Table 2. Probe parameters

	Probe BSR 124	Probe BSR 240
Measuring Range	-50–70 °C	-50–50 Wm^{-2}
Accuracy	0.15°C	
Sensitive element	Pt100 DIN-IEC (EN6075)	Thermopile
Mechanics	Phosphorous Bronze flat probe	
Response time	10 s	
Cable	PVC flat (-15–75 °C)	
Operative temperature		-30–70 °C
Sensitivity (nominal)		0.050 mV W^{-1}m^{-2}
Resistance (nominal)		2 Ω
Temperature dependence		< 0.1% °C^{-1}

The internal temperature of the metering chamber was taken up to a temperature of about 50 °C and after a stabilisation period of 48 hours, the datalogger started recording the values of thermal flux and the temperature. The stabilisation period was monitored with PT 100 temperature probes placed inside the chamber and externally near the outer wall surface. The datalogger recorded the internal and external surface temperature of the wall and the flux-thermal value with a recording interval of 10 minutes. In order to compare the two types of wall, two tests were conducted, each of which had a duration of 210 hours equivalent to 1,260 measurements.

The values recorded by the datalogger were revised using InfoFlux developed by ANIT (National Association of Thermal and Acoustic Insulation) software which allows for calculating the thermal conductance, from which the transmittance value is derived. The experimental tests were performed so as not to have any significant thermal variations. This assumption allowed us to choose the progressive average method as the calculation method.

Once the opaque wall's stratigraphy and material properties are known, the U-value can be determined by the following equations:

$$R_{tot} = R_{si} + \sum_i \frac{d_i}{\lambda_i} + R_{se} \qquad (1)$$

$$U_{design} = \frac{1}{R_{tot}} \qquad (2)$$

where, U_{design} represents the thermal transmittance value evaluated by the calculation method (W m⁻²K⁻¹); d_i the thickness of the i-th layer (m); λ_i its thermal conductivity (W m⁻¹K⁻¹); R_{tot} the total wall thermal resistance (m²K W⁻¹); and R_{si} and R_{se} the interior and exterior surface resistances (K), respectively.

It is important to underline that the calculation method cannot be applied when the thickness and conductivity of each wall layer are not known (Choi & Jin Ko, 2017).

The progressive average method assumes that the U-value can be obtained by dividing the mean density of the heat flow rate by the mean temperature difference, with the average being taken over a sufficiently long period of time that allows a good estimation of equivalent steady-state behaviour (Fokaides & Kalogirou, 2011; Simões et al., 2014). An estimate of the U_{PAM} Progressive Average Method can be obtained as:

$$U_{PAM} = \frac{\sum_{j=1}^{n} q_j}{\sum_{j=1}^{n}(T_{i,j} - T_{e,j})} \qquad (3)$$

where, U_{PAM} represents the thermal transmittance value evaluated by the progressive average method (W m⁻²K⁻¹); n the number of measurement data; q_{ij} the density of heat flow rate (W m⁻²K⁻¹); and $T_{i,j}$ and $T_{e,j}$ the interior and exterior ambient temperatures (m²K W⁻¹), respectively (Choi & Jin Ko, 2017).

The first test was conducted by examining the wall without plaster; the second experimental test entailed the application of a bio plaster on the inner face of the previously analysed wall. Two sheets of untreated natural jute were applied to promote the sealing of the mortar and the overall thickness of the coating was 1.5 cm. Biocalce® Intonaco Kerakoll mortar was used to make the plaster, the test was carried out after respecting the drying times of mortar.

The calculations of the thermal performance took into account the provisions of the ISO 9869 standard that describes the heat flowmeter method for the measurement of measuring the thermal transmission properties (thermal resistance and thermal conductance from surface to surface, total thermal resistance and transmittance from environment to environment) of building components, primarily consisting of opaque layers perpendicular to the heat flow and having no significant lateral heat flow.

RESULTS AND DISCUSSION

The resulting graphs are collected in Fig. 4. They illustrate the behaviour of the wall during the conducting of experimental Test no. 1 which refers to the measurement of the average flow, average internal and external temperature and average conductance of the bamboo wall without plaster, and test no. 2. which refers to the same bamboo wall tested previously, but instead covered with plaster. Table 3 gives a summary of the results of the thermal analysis carried out by means of the progressive averages method.

Average flow

Bamboo wall without plaster

Bamboo wall with plaster

Average temperature

Bamboo wall without plaster

Bamboo wall with plaster

Average Conductance

Bamboo wall without plaster

Bamboo wall with plaster
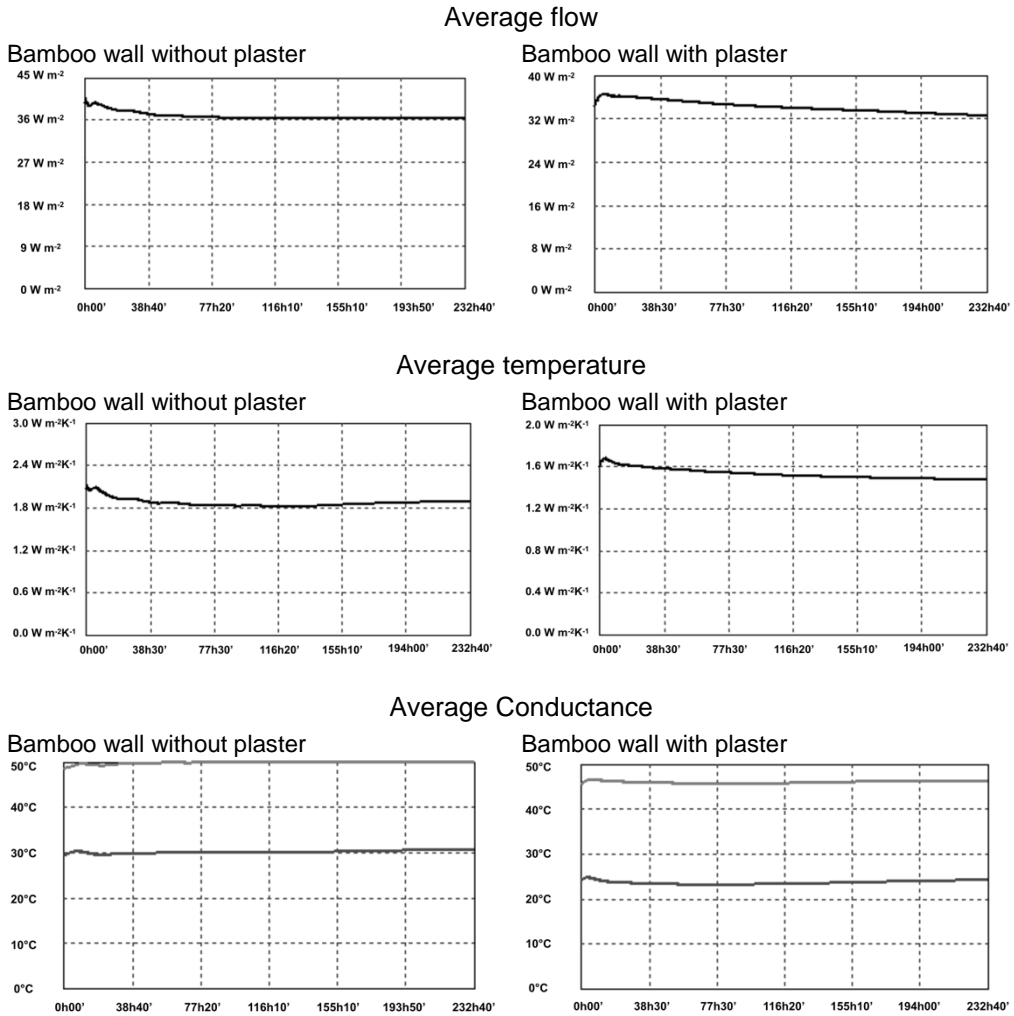
Figure 4. Resulting graphs test no. 1 without plaster, test no. 2 with plaster.

The comparison of the results obtained highlights the result in terms of different thermal insulation capacity between the two wall models tested. The plaster-coated wall recorded a better thermal insulation performance than the wall built with bamboo alone.

Experimental heat flux densities demonstrate that the heat transfer has been higher in the bamboo wall without plaster. More precisely, the heat transfer has been higher by a value of 0.4177 W m^{-2}K^{-1} for conductance and 0.2528 W m^{-2}K^{-1} for transmittance in the wall not covered.

The transmittance values of the bamboo wall covered with plaster was 1.178 W m^{-2}K^{-1}. This value does not deviate from the values of other natural materials such as clay wall thickness 6 cm, with U-value 1.56 W m^{-2}K^{-1} (Goodhew & Griffiths, 2005), or light straw clay, that is a mixture of straw and clay, thickness 12 cm, with U-value 0.55 W m^{-2}K^{-1} (Holzhueter & Itonaga, 2016). The thermal performances of bamboo are different from other natural materials such as straw. Shea et al. (2013) in a test for prefabricated straw bale panel measured a thermal transmittance of 0.190 ± 0.015 W m^{-2}K^{-1}.

Table 3. Results test no. 1 without plaster, test no. 2 with plaster

Test	1	2	
Measurements	1,260	1,260	Nr
Time step	10	10	min
Thermal flow	36.3912	32.5338	W m^{-2}
Inner wall temperature	49.8261	46.2919	°C
Outer wall temperature	30.5866	24.2171	°C
Conductance	1.8915	1.4738	W m^{-2}K^{-1}
Transmittance	1.4313	1.1785	W m^{-2}K^{-1}

Thermal resistance measurements can be wrong if structural abnormalities are found in the measuring points. For this reason, a preliminary thermographic analysis is required (Evangelisti et al., 2015).

The analysis made it possible to carry out a thermal mapping of the wall that allowed measuring the surface temperature through the pixels of the captured image. The images recorded in the two tests are illustrated in Fig. 5, the image on the left refers to test no. 1 and the one on the right to test no. 2.
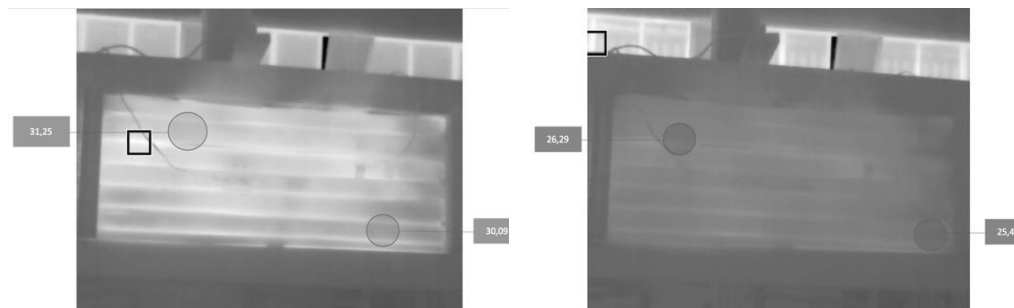
Figure 5. Thermal images of tested wall.

The chromium plating of the two images shown above also appears to be very different. On the whole, they show that the temperature of test no. 1 is higher than that of test no. 2, thus confirming a poorer insulating capacity. At the same time highlighting the presence of some heat dispersion point in the sample wall, it is possible to provide some information to detect the correct position of the probe in the wall.

CONCLUSIONS

Bamboo is a natural material which, due to its morphological characteristics can be used not only in constructions as a structural element, but that it can also have an insulating function as emerged from the tests carried out. Due to its easy of use and processing it can be configured as a material suitable for deconstruction, in addition to which the pronounced rusticity and speed of growth of bamboo allows its cultivation in numerous production areas.

The collection of the experimental material for the samples of bamboo wall, harvested in the same area of cultivation, did not reveal advantages or disadvantages due to altimetric variations between 0 to 205 a.s.l. and slopes of the cultivation fields between 0% and 15%. The culms collected were uniform for morphological, dimensional and sanitary conditions.

Like all natural materials, the performance linked to the insulating capacity of bamboo is influenced by several factors. Although in our study the coupling with a bio plaster (Biocalce®) was examined, the use of other natural materials is not excluded, such as raw earth.

Thermal images permitted to assess the correct application of the sensors and to give an empiric evaluation of thermal performance of the samples.

Moreover, with thermal images the critical points that favour heat dispersion were easily identifiable. These points can be recognised in the coupling lines between one culm and the next. As conclusion, heat dispersion was not due to the nature of the bamboo, but to the construction technique adopted.

Taking into account that the thermal performance of the wall with the plaster improved and considering a different construction technique able to limit heat dispersions, it is possible to hypothesize a further improvement in term of thermal performance of the insulating walls manufactured with bamboo.

Thanks to the speed of bamboo growth and marked adaptability to cultivation in different pedoclimatic scenarios, bamboo is configured as a material with a high potential for exploitation. Having this material at zero km encourages the diffusion and use even at non-industrial levels, promoting the creation of short supply chains and the reduction of the use of synthetic insulating materials, without doing away with technically and aesthetically appreciable solutions.

REFERENCES

Asdrubali, F., Baldinelli, G., Bianchi, F. & Sambuco, S. 2015a. A comparison between environmental sustainability rating systems LEED and ITACA for residential buildings. *Build. Environ*. **86**, 98–108.

Asdrubali, F., D'Alessandro, F. & Schiavoni, S. 2015b. A review of unconventional sustainable building insulation materials. *Sustainable Materials and Technologies* **4**, 1–17.

Barbari, M., Monti, M., Rossi, G., Simonini, S. & Sorbetti Guerri, F. 2014a. Simple methods and tools to determine the mechanical strength of adobe in rural areas. *Journal of Food, Agriculture and Environment* **12**(2), 904–909.

Barbari, M., Monti, M., Rossi, G., Simonini, S. & Sorbetti Guerri, F.S., 2014. Proposal for a simple method of structural calculation for ordinary earthen buildings in rural areas. *Journal of Food, Agriculture and Environment* **12** (2), 897-903.

Buratti, C. & Moretti, E. 2008. Measurement of the thermal resistance of a masonry sample. *In 63 National ATI Congress 'Energy for Sustainable Development',* Palermo, pp. 107–114.

Cabeza, L.F., Castell, A., Medrano, M., Martorell, I., Pérez, G. & Fernández, I. 2010. Experimental study on the performance of insulation materials in Mediterranean construction. *Energy Build*. **42**, 630–636.

Choi, D.S. & Jin Ko, M. 2017. Comparison of Various Analysis Methods Based on Heat Flowmeters and Infrared Thermography Measurements for the Evaluation of the In Situ Thermal Transmittance of Opaque Exterior Walls. *Energies* **10**, 1019.

Conti, L., Goli, G., Monti, M., Pellegrini, P., Rossi, G. & Barbari, M. 2017. Simplified Method for the Characterization of Rectangular Straw Bales (RSB) Thermal Conductivity In: IOP Conference Series: *Materials Science and Engineering* **245**, 052035.

European Commission. 2018. Final Report of the High-Level Panel of the European Decarbonisation Pathways Initiative European Commission. Publications Office of the European Union, Luxembourg.

European Union. 2010. Directive 2010/31/EU of the European Parliament and of the Council of 19 May 2010 on the energy performance of building.

European Union. 2010. Directive 2012/27/EU of the European Parliament and of the Council of 25 October 2012 on energy efficiency, amending Directives 2009/125/EC and 2010/30/EU and repealing Directives 2004/8/EC and 2006/32/EC Text with EEA relevance.

Huang, P., Chang, W.S., Shea, A., Ansell, M.P. & Lawrence, M. 2014. Non-homogeneous Thermal Properties of Bamboo. Aicher, S., Reinhardt, H.W., Garrecht, H. (eds) *Materials and Joints in Timber Structures*. RILEM Bookseries, **9**, 657–664.

Huang, P., Zeidler, A., Chang, W.-S., Ansell, M., Chew, Y. & Shea, A. 2016. Specific heat capacity measurement of Phyllostachys edulis (Moso bamboo) by differential scanning calorimetry. *Construction and Building Materials* **125**, 821–831.

Evangelisti, L., Guattari, C., Gori, P. & De Lieto Vollaro, R. 2015. In Situ Thermal Transmittance Measurements for Investigating Differences between Wall Models and Actual Building Performance. *Sustainability* **7**, 10388–10398.

Fokaides, P.A. & Kalogirou, S.A. 2011. Application of infrared thermography for the determination of the overall heat transfer coefficient (U-Value) in building envelopes. *Appl. Energy* **88**, 4358–4365.

Goodhew, S., Griffiths, R. 2005. Sustainable earth wall to meet the building regulations. *Energy and Buildings*, ENB **1845**, 1–9.

Holzhueter, K. & Itonaga, K. 2016. The Potential for Light Straw Clay Construction in Japan: An Examination of the Building Method and Thermal Performance. *JAABE* **16**(1), 209–213.

ISO 6946:2007, Building components and building elements - Thermal resistance and thermal transmittance - Calculation method.

ISO 9869:1994, Thermal insulation - Building elements - In-situ measurement of thermal resistance and thermal transmittance.

Kiran, M., Nandanwar A., Naidu, M. & Rajulu, K. 2012. Effect of density on thermal conductivity of bamboo mat board. *International Journal of Agriculture and Forestry* **2**(5), 257–261.

Korjenic, A, Petránek, V., Zach, J. & Hroudová, J. 2011. Development and performance evaluation of natural thermal-insulation materials composed of renewable resources. *Energy and Buildings* **43** 2518–2523.

Leso, L., Conti, L., Rossi, G. & Barbari, M. 2018. Criteria of design for deconstruction applied to dairy cows housing: a case study in Italy. *Agronomy Research* **16**(3), 794–805.

Mitch, D.R. 2009. Splitting Capacity Characterization of Bamboo Culms. Undergraduate Thesis, University of Pittsburgh. *http://d-scholarship.pitt.edu/6704/1/Derek_Mitch_Thesis_March_2009.pdf.* Accessed 22/11/18.

Scurlock, J., Dayton, D. & Hames, B. 2000. Bamboo: an overlooked biomass resource?. *Biomass Bioenergy* **19**(4) 229–244.

Shea, A., Wall, K. & Walker, P. 2013. Evaluation of the thermal performance of an innovative prefabricated natural plant fibre building system. *Building Service Engineering* **34**(4) 369–380.

Simões, I., Simões, N., Tadeu, A. & Riachos, J. 2014. Laboratory assessment of thermal transmittance of homogeneous building elements using infrared thermography. *In Proceedings of the 12th International Conference on Quantitative InfraRed Thermography*, Bordeaux, France, 7–12 July, 1–10.

UNI EN 1934:2000 Thermal Performance Of Buildings - Determination Of Thermal Resistance By Hot Box Method Using Heat Flow Meter.

Vogtländer, J., Van der Lugt, P. & Brezet, H. 2010. The sustainability of bamboo products for local and Western European applications. LCAs and land-use. *Journal of Cleaner Production* **18**, 1260–1269.

Wang, J.S., Demartino C., Xiao, Y. & Li, Y.Y. 2018. Thermal insulation performance of bamboo and wood-based shear walls in light-frame buildings. *Energy & Buildings* **168**, 167–179.

Zach, J., Hroudová, J., Brožovský, J., Krejza, Z. & Gailius, A. 2013, Development of Thermal Insulating Materials on Natural Base for Thermal Insulation Systems. In: *11th International Conference on Modern Building Materials, Structures and Techniques*, Procedia Engineering **57**, 1288–1294.

Zarr, R.R. 2001. A history of testing heat insulators at the national institute of standards and technology. *ASHRAE Trans.***107**, 661–671.

Possibilities to identify defective electric automobile batteries

D. Berjoza[1], V. Pirs[1] and I. Jurgena[2]

[1]Latvia University of Life Sciences and Technologies, Faculty of Engineering, Motor Vehicle Institute, J. Cakstes 5, LV–3001 Jelgava, Latvia
[2]Latvia University of Life Sciences and Technologies, Faculty of Economics and Social Development, Institute of Business and Management Science, Svetes street 18, LV–3001 Jelgava, Latvia
*Correspondence: dainis.berjoza@llu.lv; inara.jurgena@llu.lv

Abstract. A pack of batteries is one of the most important and expensive assemblies for an electric vehicle. A pack of batteries is comprised of several batteries connected in series. The number of the batteries connected depends on the operating voltage of the vehicle's on-board system as well as on the individual characteristics of the batteries used, e.g. the operating voltage of a single cell. One or several cells of a pack of batteries could be damaged if improperly exploiting an electric vehicle– excessively discharging the batteries or overloading the electric vehicle. If a self-converted vehicle does not use an intellectual BMS (battery management system) that can identify and register voltage drop for any individual cell in the high-load regime, e.g. when accelerating, it is difficult to identify and change the cells damaged. In case a cell does not demonstrate a complete failure, it is almost impossible to identify a defect in any regime other than the load regime.

The research developed and compared three different methods for identifying defective battery cells. The methods were approbated on a converted Renault Clio. The experiment involved making voltage measurements in road tests, running the electric vehicle on a roll test bench and making voltage measurements of maximally discharged batteries in the no-load regime. A comparison of the measurement results revealed that the measurements made in the road tests were the most accurate and useful. After the experiment, the defective battery cells were replaced, thereby restoring the performance of the battery pack.

Key words: electric vehicle, battery pack, battery voltage, test.

INTRODUCTION

Electric vehicles are known for more than 100 years. A century ago, vehicles with noisy and difficult to start internal combustion engines triumphed over electric vehicles, as it was a period when intercity road infrastructure began developing and a longer driving range per charge was needed. Relatively short ranges per charge are a problem of many modern electric vehicles. Electric vehicles have become more popular over the last decade, as they appeared in the assortment of models of almost any large auto manufacturer. The main field of application of vehicles is still cities where daily distances covered by the electric vehicles are insignificant. The popularity of electric vehicles is hindered by their relatively high prices.

In 2018 in Latvia, an electric vehicle mobility project was implemented, and 75 new fast-charging stations along trunk roads were opened (A network of …, 2018). This gives a possibility to travel by electric vehicle almost across the entire Latvia. As the electric vehicle fleet becomes older, the performance of battery packs decreases, which, in its turn, reduces the range of electric vehicles. Since a battery pack consists of a number of cells connected in series, even one damaged cell can considerably impact the performance of the entire pack. Unfortunately, it is difficult to identify the damaged cell by simple no−load testing methods. For this reason, the present research analyses a number of practically approbated methods of testing for damaged battery cells.

Scientists place a large focus on how to test the batteries of electric vehicles for defective cells, addressing this problem in their research papers. Electric vehicles use lithium batteries, as such batteries are considered a progressive source of accumulated energy. A BMS system, which the base models of serial electric vehicles are equipped with, has to control the charge and discharge of batteries, collect data on each individual cell, provide thermal control and control the technical condition of the batteries. The key reasons of battery defects are overcharge, over discharge, high or low temperatures and a large number of cycles. There are model based and non-model based methods for diagnosing a battery. It is stressed that batteries connected in series make a complicated system with different electrical parameters in each individual cell. Therefore, it is possible to use diagnostics systems based on signals, e.g. voltage or current, yet such systems do not always produce fast and correct results. Using a BMS system, there is one more risk in diagnosing a battery, as the BMS itself might be damaged and inaccurate. Knowledge- and experience-based testing for a defective battery or the expert method is also regarded as a useful method (Wu et al., 2015).

In simulation, Kalman filters that modify a signal allowing identifying the performance of a particular battery are frequently used to test the battery for defective cells. Error scenarios and various measurement methods for testing a battery for defects based on simulation results have been developed as well (Singh et al., 2013).

A test of the performance of a battery pack could be performed in accordance with the USABC (United States Advanced Battery Consortium) Electric Vehicle Battery Test Procedure Manual. Such a test involves the discharge of a battery within three hours at a current of a third of the capacity of the battery. The test produces a voltage-capacity curve (BEV battery, 2012). For example, a 100 Ah battery has to be discharged at a current of 33.3 A. This method is useful for identifying the performance parameters of a battery pack, but not for testing individual cells for defects.

Research studies on BMS enhancement are done as well. A BMS includes an algorithm for measuring each battery cell, and the readings are compared with marginal parameters indicating a potential defect. Research studies analyse a number of logical diagnostics methods, yet no practically useful method is suggested (Marcicki et al., 2010; Lu et al., 2013).

In primary diagnostics of a battery, the most important parameters are as follows: potential power, internal and external temperatures of a cell, charge-discharge time, internal resistance, voltage of the cell and the voltage of the entire battery (Wang et al., 2017; Omariba et al., 2018).

A decrease in the performance of the entire battery pack could be caused by a partial failure of a single cell. Even if battery packs are commented in parallel, the pack with a damaged cell can cause a malfunction of the other packs, which could be identified by

using a mathematical model. Measurements were taken of 504 battery cells with a total capacity of 9 kWh. Tests were done on a power bench in the 3–second advance mode. The results were recorded by means of a standard BMS. The internal resistance of batterie's were calculated based on the experimental results. The experiment performed a 15-minute discharge cycle by running the vehicle on a dynamometric bench. The battery cells were selectively tested also individually (Offer et al., 2012).

The charge of a battery could be tested at various ambient temperatures, e.g. from +5 to +45 °C. Besides, the physical-models approach, the Thevenin model, the runtime-based electrical model, the combined electric model, the data-driven approach, the neural network and fuzzy logic methods are recommended for diagnostics, prognostics and health management of batteries (Rezvanizaniani et al., 2014).

The performance of batteries could be estimated based on the number of battery cycle life, recording the number of charge-discharge cycles as well as battery capacity measurements (Yan et al., 2015). Old batteries could be recycled; however, to protect the environment, a lot of work is done on technologies allowing using old electric vehicle batteries for stationary equipment needing no high current output (Cready et al., 2003).

Most of the methods reviewed in the paper are used for testing a battery pack for defects, yet methods for determining the performance of each individual cell are little analysed in the literature.

The research novelty represents the approbation of a battery pack testing methodology for an electric vehicle through measurement of individual battery cells in the load regime and the no-load regime.

The research aim is to analyse, select and approbate the simplest method of diagnosing the performance of a battery pack in the converted electric vehicle.

MATERIALS AND METHODS

An electric vehicle Renault Clio was converted from an internal combustion vehicle to an electric one. The conversion was done at the Faculty of Engineering, Latvia University of Life Sciences and Technologies. During the conversion process, a number of experiments were carried out as well as system enhancements were made. The battery pack was equipped with a battery management system (BMS) that had to ensure a proper charging process for individual battery cells. During charge, the voltage of an individual cell might not exceed 4.1 V, while in discharge regimes it might not decrease below 2.4 V. At the initial stage of the conversion, the system did no function properly because the BMS was programmed inaccurately, and there were cases where the minimum and maximum voltages were exceeded multi-fold. The key technical parameters of the converted vehicle are presented in Table 1.

After the BMS software had been reprogrammed, the maximum charging voltage was set at 3.8 V and the minimum allowable discharge voltage was set at 2.6 V. However, during road tests when accelerating fast, the BMS often engaged the minimum battery voltage limiter, which indicated that the performance of one or several battery cells decreased. The BMS was capable of identifying voltage drops within 0.015 s, yet it could not determine which particular cell out of 30 ones was faulty. After the voltage drop had been registered, the BMS limited the maximum speed of the electric vehicle, which could be set, for example, at 60 km h^{-1}.

Table 1. Key technical parameters of the electric vehicle Renault Clio

No	Parameter characteristics	Parameter value
1	Vehicle category	M1
2	Motor nominal power	30 kW
3	Gearbox	5−speed manual
4	Used gear	3rd gear
5	Maximum speed	120 km h^{-1}
6	Battery cells	LiFePO4, 30 pcs.
7	Total battery voltage	96 V
8	On-board power	10.5 kWh
9	Nominal voltage of a battery cell	3.2 V
10	Voltages set in the BMS	U_{min} = 2.6 V; U_{max} = 3.8V
11	Range per charge	60 km
12	Minimum BMS response time	0.015 s
13	Battery charging time	3.5 h
14	Battery capacity	100 Ah
15	Maximum discharge current	1,000 A

In previous road tests of the electric vehicle, data were recorded by means of a data logger. When accelerating fast, the data logger registered a voltage drop of battery pack from 98 to 89 V. In each battery cell, the voltage dropped, on average, from 3.27 to 2.97 V. Since the BMS engaged the limiter, such a voltage drop was due to the battery's inability to supply a high current, as the current could exceed 400 A in this regime (Berjoza et al., 2018).

In accordance with the instructions for serial electric vehicles, the entire battery pack is changed after a standard maintenance operation or repair, while the old one is recycled. In the case of a self-converted electric vehicle, only the damaged battery cells could be changed, thereby reducing repair cost even 30-fold (in case only one cell has to be replaced).

The potential ways of diagnosing lithium-ion batteries are as follows:
1) by means of the BMS if it is possible to specify an address for each cell;
2) measuring the voltage of an individual cell by means of multichannel loggers;
3) taking measurements of an individual cell during different driving regimes;
4) taking measurements of an individual cell under no load in a stationary vehicle;
5) visually examining the battery (a considerably damaged battery might have changed its geometrical dimensions, e.g. it could be swollen).

For a battery that does not supply enough power, the very last way of diagnostics is not useful.

The first experimental stage was performed with the battery discharged to the minimum allowable level. The battery was discharge by road testing the electric vehicle. During the road tests, the electric vehicle's average range per charge decreased from 65 to 55 km. It was easy to access the battery pack in the converted electric vehicle. It was required to only remove the cover over the battery pack to take measurements. The measurements were made by a digital multimeter Fluke 87. The device's resolution was 0.01 V.

The electric vehicle was road tested for a distance of 55 ± 1 km under similar conditions. The road tests were done in September at an average ambient temperature of +15 ± 2 °C. To record the data, a data logging protocol for a pack of 30 batteries and

their position addresses was prepared. Right after the vehicle was stooped, the voltage measurements of all the battery cells were made, logging the data in the protocol. The test was replicated three times.

The second experimental stage involved a roll test bench Mustang 1700. The key parameters of the bench were as follows: maximum power – 1,700 hp, maximum speed – 300 km h^{-1}; the brake mechanism was powered by electromagnetic eddy currents. The experiment was done at the Alternative Fuels Research Laboratory, at an ambient temperature of +16 ± 1 °C. Before the experiment, the electric vehicle was fully charged and left inside the laboratory for at least 5 h. The electric vehicle was fastened to the bench and its batteries were warmed up by running it idle at a speed of 50 km h^{-1} for three minutes. After the warm–up, the electric vehicle was run at a speed of 80 km h^{-1} and the wheels were subject to a load of 30 kw. One of the experimental operators simulated the driving of the electric vehicle, while the other one made measurements of individual cells of the batteries. Each cell was measured for on average 5–8 seconds. The data were manually recorded in accordance with the methodology described above. To make the measurements faster, the data were recorded by the operator who simulated the driving. The test was replicated three times. Since a significant decrease in voltage was observed after the second replication, the first two replications were taken into account; the batteries were fully charged and then the third replication was performed.

A sequential scheme of the experiment is shown in Fig. 1.
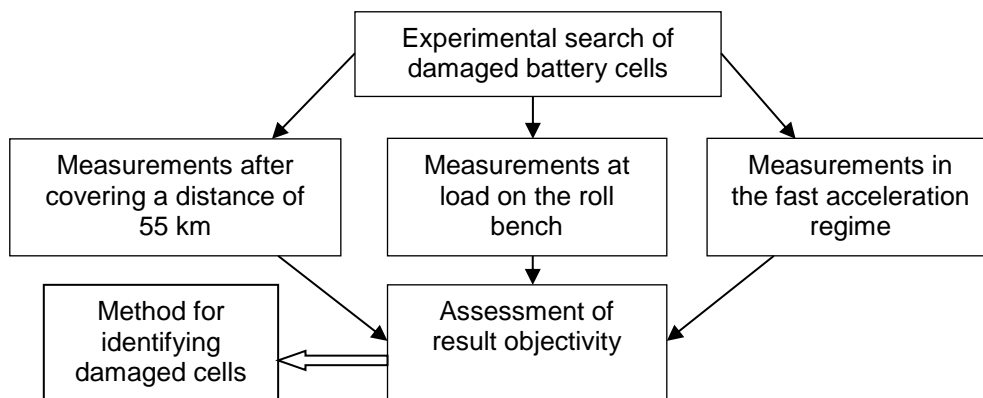
Figure 1. Sequential scheme of the experiment.

The third experimental stage involved road tests. One operator drove the electric vehicle, while the other one made measurements. The measurements were consecutively taken for all the 30 cells. The measurements were made at an ambient temperature of +15±2 °C. The electric vehicle was road tested in non-urban driving at an average speed of 50 km h^{-1}. The measurement operator gave a command at a moment when he was ready to take readings and had connected the multimeter to a particular cell. The electric vehicle was accelerated to a speed of 80 km h^{-1}, and the measurement operator took the lowest voltage reading for each cell and recorded that in the protocol. The acceleration was repeated 30 times for each road test replication and for each series of measurements. Totally, there were three replications.

At all the experimental stages, the batteries were assigned numbers from 1 to 30 according to a scheme presented in Fig. 2.
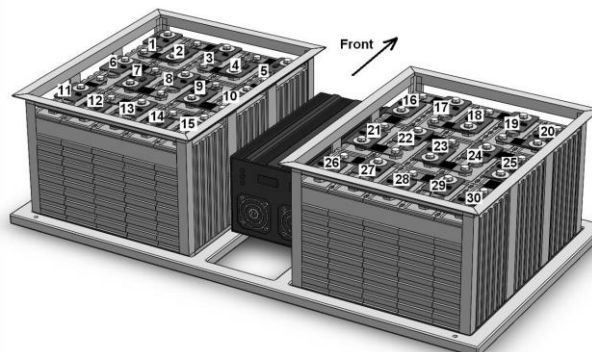
Figure 2. Numbers and positions of the batteries.

The data were aggregated and analysed after each series of tests. Based on the experimental data, the batteries were tested for defects and replaced.

RESULTS AND DISCUSSION

First of all, the experimental data on the measurements taken after the vehicle had covered a distance of 55 km were processed. The average readings of the mentioned measurements are presented in Fig. 3. The measurement results shown in the graphs have a confidence level of 95%, i.e. a confidence interval falling within two standard errors (Figs 3–5).
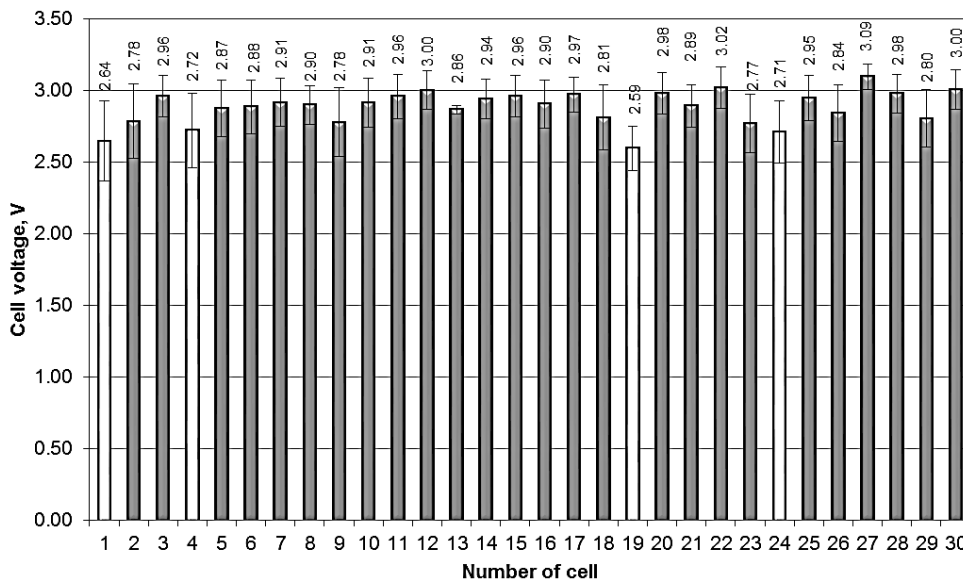
Figure 3. Average readings of the voltage measurements taken after the electric vehicle had covered a distance of 55 km.

According to the readings, the average voltage of battery 19 was the lowest at 2.59 V, which was 10.1% lower than the average for all the batteries (2.88 V). Battery 1 demonstrated the second lowest voltage – 2.64 V, which was 8.3% lower than the average. Batteries 24 (2.71 V) and 4 (2.72 V) also had low voltages, 5.9% and 5.6%, respectively, lower than the average.

The best performers were batteries 12, 22, 27 and 30, the voltages of which were in the range of 3.00–3.09 V – 4.2–7.3% higher than the average.

The experimental data on the measurements taken on the roll bench are presented in Fig. 4.
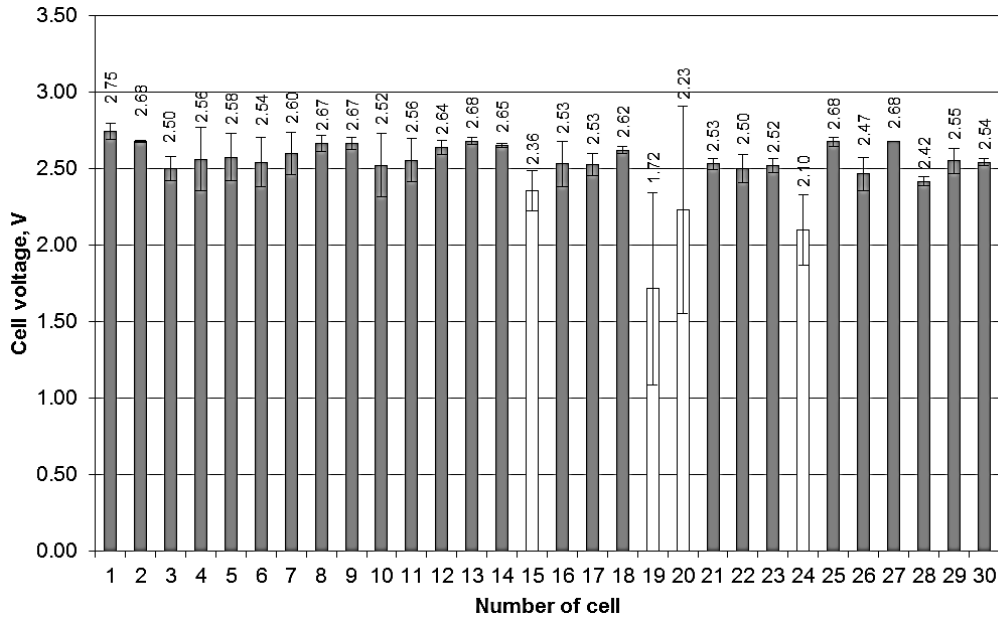
Figure 4. Average readings of the voltage measurements taken on the roll bench.

The lowest average voltage (1.72 V) was demonstrated by battery 19, which was 31.7% lower than the average for all the batteries (2.52 V). The second lowest voltage was observed for battery 24 (2.10 V), which was 16.7% lower than the average. The voltage of battery 20 was 2.23 V, which was 11.5% lower than the average. Battery 15 demonstrated a voltage of 2.36 V, which was 6.3% lower than the average. The voltages of the analysed batteries were lower the allowable voltage of 2.4 V, and the batteries were not capable of operating in such a regime for a long time, otherwise the batteries might get irreversibly damaged.

The best results acquired on the roll bench were demonstrated by batteries 1 with 2.75 V (9.1% higher than the average) and 2, 13, 25 and 28, the voltages of which were equal to 2.68 V (6.3% above the average).

The data acquired in the road tests, accelerating the electric vehicle from 50 to 80 km h^{-1}, are presented in Fig. 5.
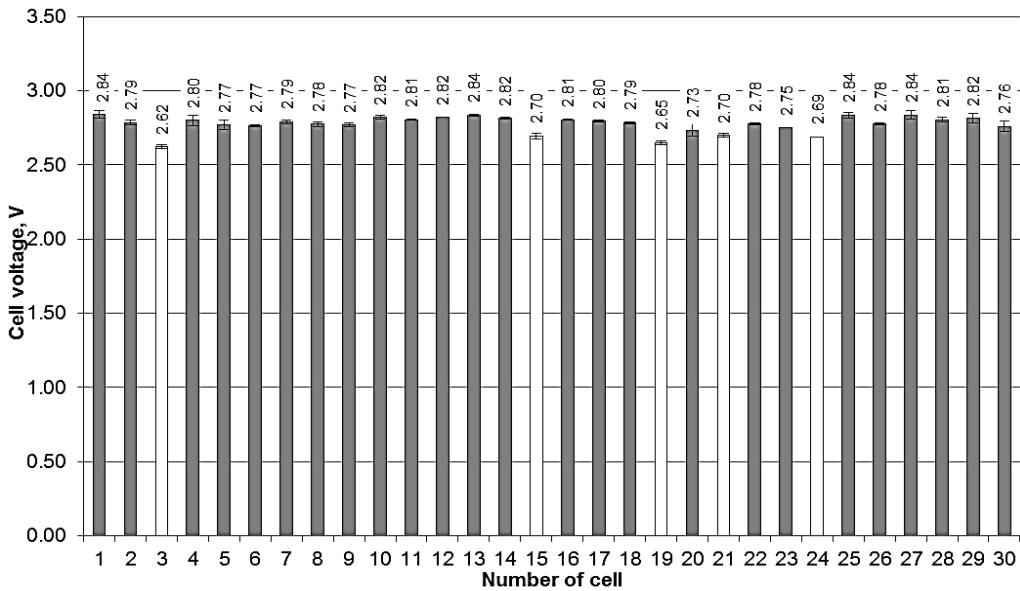
Figure 5. Average readings of the voltage measurements taken in the acceleration regime.

The lowest average voltage recorded when accelerating the electric vehicle was observed for battery 3 at 2.62 V, which was 5.4% lower than the average for all the batteries. The voltage of battery 19 was equal to 2.65 V, which was 4.3% lower than the average. The voltage of battery 24 was 2.69 V, while that of batteries 15 and 21 was 2.70 V, which differed from the average by 2.9% and 2.5%, respectively.

In the acceleration regime, the highest average readings of voltage were demonstrated by batteries 1, 13, 25 and 27 at 2.84 V, which was 2.5% higher than the average for all the batteries.

To accurately diagnose the batteries, out of the three series of tests only the tests on the batteries under load were taken into account. The data were processed to identify the average voltages of the batteries; the data are presented in Fig. 6.

According to the average readings of the voltage measurements taken in two series of tests of the electric vehicle – on the roll bench and when accelerating – the lowest voltages were demonstrated by batteries 3, 15, 19 and 24. The average voltage ranged for 2.18 to 2.56 V. The research compared the results on defective batteries shown in Figure 6 with the results shown in Figs 4 and 5. In view of the fact that the results shown in Figures 6 and 5 had greater consistency, the research assumed that the voltage measurements taken in the acceleration regime were the most accurate and this method would have to be employed in the future.

Taking measurements according to the above-analysed methods requires free access to the batteries measured while driving the vehicle, otherwise another method has to be chosen. A more accurate but more expensive method is the application of a multichannel data logger that accurately takes measurements in different regimes. However, the cost of using a multichannel data logger with at least 30 channels is high, and the connection of the logger to the battery pack to be measured is very labour intensive.
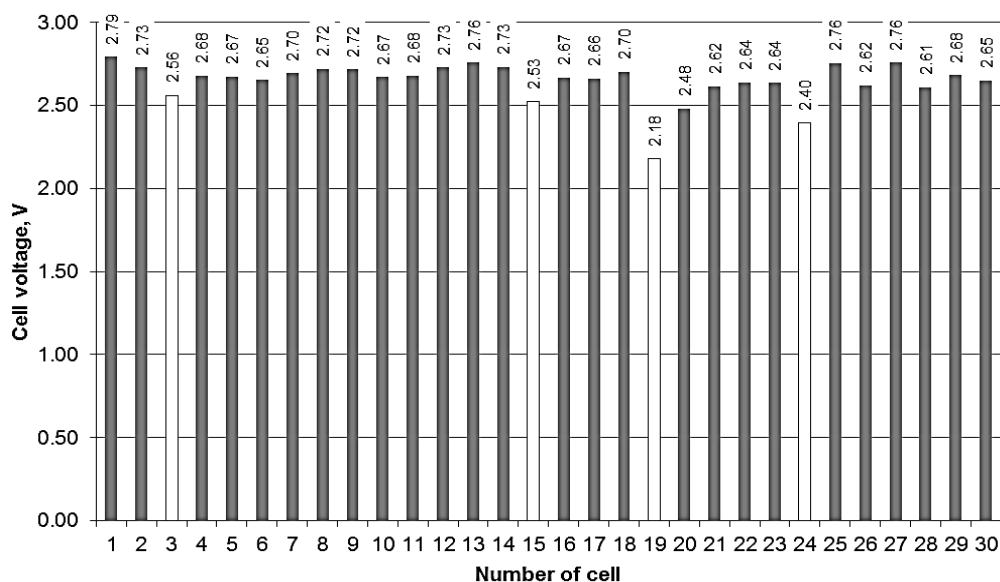
Figure 6. Average readings of the voltage measurements of the batteries under load.

After the experiment, four defective batteries were changed, thereby restoring the initial driving range of the electric vehicle (60 km).

CONCLUSIONS

1. For serial electric vehicles, regular testing for defective batteries involves identifying and changing the entire battery pack, which is an expensive and environmentally unfriendly way.

2. No simple method for identifying a defective battery cell, which could restore the normal performance of the entire battery pack, is available. Expensive data loggers could be used to identify a defective cell, or simple measurements by means of a multimeter could be taken. A defective cell could be accurately identified by also modern BMS systems having the address of each particular cell.

3. The research developed three different methods for testing batteries for defective cells. The first one was the least reliable, as it involved testing a battery after the vehicle had covered a distance of 55 km and did not represent a load regime for the battery.

4. The second method involved testing of the electric vehicle on the roll bench at a constant load. The choice of a proper loading regime on the roll bench could take a lot of time, and the regime could be very different from real operational conditions. The voltage measurements of battery cells taken in a regime different from the real operational conditions might lead to inaccurate results on the actual technical condition of the cells.

5. The defective cells identified in each series of tests were not the same, yet cells 19 and 24, the lifespan of which was undoubtedly about to end, were identified as defective.

6. The measurement readings taken while accelerating the electric vehicle were more reliable and consistent with the real voltage drop during the operation of the

943

vehicle. In this driving regime, the largest voltage drop in the range of 2.62–2.70 V was observed for five batteries.

7. An analysis of the average readings of the voltage measurements taken when accelerating the electric vehicle and on the roll bench revealed that the highest correlation was observed for the road tests in particular. For this reason, this method is recommended as the main method for testing the Renault Clio Electric and analogues for defective battery cells that provide direct access to their battery cells.

8. Since the batteries were connected in series, the damaged cells affected the performance of the entire battery pack and their internal resistance hindered the proper operation of the entire battery pack.

9. Four defective batteries were changed in the experimental electric vehicle, thereby restoring the performance of the battery pack and increasing the driving range of the vehicle by 20%.

REFERENCES

Berjoza, D., Pirs, V. & Jurgena, I. 2018. Investigation into the performance characteristics of electric automobiles by means of a data logger. *Agronomy Research* **16**(S 1) 958−967.

BEV battery testing results 2012. Mitsubishi iMiev − VIN 3178. Advanced Vehicle Testing Activity. Idaho National Laboratory.

Cready, E., Lippert, J., Pihl, J., Weinstock, I., Symons, P. & Jungst, R.G. 2003. *Technical and economic feasibility of applying used EV batteries in stationary applications*. A Study for the DOE Energy Storage Systems Program. Final Report. Sandia National Laboratories, Albuque, New Mexico and Livermore, California, 130 pp.

A network of fast charging stations for electric vehicles is started to work. 2018. CSDD: http://www.e-transports.org (in Latvian) Accessed 10.01.2019.

Lu, L., Han, X., Li, J., Hua, J. & Ouyang, M. 2013. A review on the key issues for lithium−ion battery management in electric vehicles. *Journal of Power Sources* **226**, 272–288.

Marcicki, J., Onori, S. & Rizzoni, G. 2010. Nonlinear fault detection and isolation for a lithium-ion battery management system. In *Proceedings of the ASME 2010 Dynamic Systems and Control Conference*. Cambridge, Massachusetts, USA, pp. 607−614.

Offer, G.J., Yufit, V., David. A. Howey, D.A., Wu, B. & Brandon, N.P. 2012. Module design and fault diagnosis in electric vehicle batteries. *Journal of Power Sources* **206**, 383−392.

Omariba, Z.B., Zhang, L. & Sun, D. 2018. Review on health management system for lithium-ion batteries of electric vehicles. *Electronics* 2018, 7, 72.

Rezvanizaniani, S.M., Liu, Z., Chen, Y. & Lee, J. 2014. Review and recent advances in battery health monitoring and prognostics technologies for electric vehicle (EV) safety and mobility. *Journal of Power Sources* **256**, 110−124.

Singh, A., Izadian, A. & Anwar, S. 2013. Fault diagnosis of li−ion batteries using multiple−model adaptive estimation. In *Proceedings of IEEE Industrial Electronics Conference*, IECON, Viena, Austria, pp. 3522−3527.

Wang, D., Yang, F., Zhao, Y. & Tsui, K.L. 2017. Battery remaining useful life prediction at different discharge rates. *Microelectronics Reliability* **78**, 212–219.

Wu, C., Zhu, C., Ge, Y. & Zhao, Y. 2015. A review on fault mechanism and diagnosis approach for li−ion batteries. *Journal of Nanomaterials* **2015**

Yan, W., Dou, W., Liu, D., Peng, Y. & Zhang, B. 2015. Parameters adaption of lebesgue sampling−based diagnosis and prognosis for li−ion batteries. In *Annual Conference of the Prognostics and Health Management Society*, Coronado, California, US, pp. 173−181.

An analysis of influences of blinds and solar radiation on microclimate in office rooms during summer days: a pilot study

D.V. Cao[*] and P. Kic

Czech University of Life Sciences Prague, Faculty of Engineering, Department of Technological Equipment of Buildings, Kamýcká 129, CZ165 21, Czech Republic
[*]Correspondence: caodoan2006@gmail.com

Abstract. Windows are the only part of a building that can directly penetrate the solar radiation into the occupied space and thus the shading devices are needed to control the solar penetration. In the office buildings, they usually use external blinds and internal blinds to reduce heat gains during summer caused by sunlight as well as solar radiation. Therefore, these blinds are main part to maintain thermal comfort for office workers. The aim of this paper is to present results of measurements in four big office rooms in different situations of blinds application. Then, the influence of the internal and external blinds on the internal microclimate conditions inside the large offices during the hot summer days with high solar radiation will be evaluate. The offices floor area is from 43.3 m^2 to 59.5 m^2 and height 2.8 m. The experiments in this research were focused on measurement and evaluation of globe temperature, indoor air temperature and relative humidity at level of working place during several hot summer days. Comparison of the results of short-term measurements in a room with open blinds and closed blinds has shown the influence of the blinds on the reduction of indoor temperature. More significant was the effect of external aluminium blinds. Solar energies passing through the windows into the interior were 3,476 W without blind and 305 W in case of aluminium venetian external blinds. When the maximum outside temperature was 29.9 °C and office workers used blinds with natural ventilation, the maximum air temperatures in four rooms were from 27.2 °C to 28.5 °C, which exceeded maximum recommended temperature (28 °C). The external aluminium venetian blinds and internal fabric vertical blinds did not maintain thermal comfort inside the offices during all summer days, but it can help in reduction of energy consumption for air-conditioning.

Key words: air-temperature, glazed window, globe temperature, measurement.

INTRODUCTION

Building energy consumption is closely related to the lighting environment, according to daylighting. Daylighting is an important factor in determining indoor visual comfort, and affects user satisfaction and productivity (Edmonds & Greenup, 2006; Hirning et al., 2014). In addition, daylighting from windows can bring both positive and negative experience: access to view and daylight, but also glare and thermal discomfort (Boubekri & Boyer, 1992; Leather et al., 1998; Aries et al., 2010).

Glazed windows are the critical component of building envelope that influences highly on the building energy demand. In the summer when skylight is voluminous and the sun transverses in all directions, windows with properly designed shading introduce

effectively exterior daylight to illuminate an interior space jointly with light from electric lamps including protecting building occupants from glare situation (Hirning et al., 2014).

People nowadays expect good natural lighting in workplaces especially as glazed facades have become more popular. However, among all components of the building envelope, these surfaces demonstrate the weakest thermal performance (Al Touma et al., 2016), at least five times weaker than the walls according to conservative building codes (The Saudi Building Code, Energy Conservation, 2007). In hot climates, their thermo-physical properties increase the space loads significantly, which outweighs its benefits even during cold seasons, and raise the occupants' sensation of thermal and visual discomforts and radiation asymmetry due to the exposure.

Some researchers have been conducted to study the impact of large surfaces that is useful for using natural lighting on the workshops (Cao & Kic, 2018). Those surfaces have a great influences to indoor temperature in the summer also to the heat balance in the winter.

The effects of adding shading devices, such as blinds, screens and shutters, to glazed surfaces and implementing control strategies have been widely studied. For instance, the effect of roller shutter placement on windows along with the implementation of shading and lighting control strategies were investigated (Gosselin & Chen, 2008).

The distribution of solar radiation as a function of the wavelength is called the solar spectrum, which consists of a continuous emission with some superimposed line structures. The Sun's total radiation output is approximately equivalent to that of a blackbody at 5,776 K. The solar spectrum is usually divided into three main parts: ultraviolet sunlight (2% of total solar radiation), visible solar radiation (47% of total solar radiation) and infrared solar radiation (51% of solar radiation).

When this total sunlight impact on the glazed window, it is divided according to the technical parameters of the windows, namely: reflection, absorption and transmission (Qiang, 2006; Mishchensko et al., 2015).
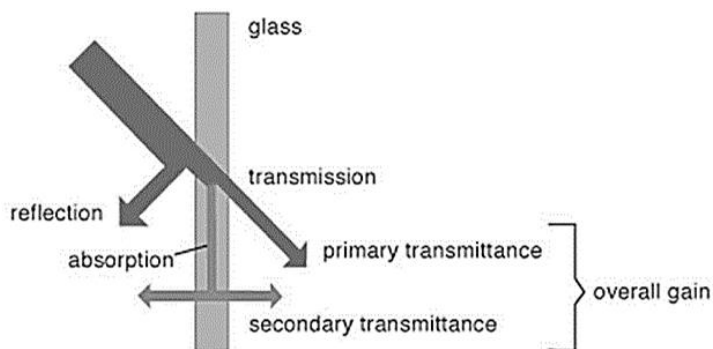
Figure 1. Sunlight impact on the glazed window (Alwetaishi, 2019).

The influence of the sunlight impact on the glazed window is indicated on the Fig. 1. The shine reflected by the window (reflection) is returned to the external area and it does not effect on the heating. The radiation that is absorbed by the window (absorption) increases its temperature. The radiation that is transmitted through window

into an interior (transmission) heats up surface behind it. The proportion between all three components is determined by the angle of incidence and by the type of glazing.

According to the position in a building, the sun shading device can be classified as one of three types: internal, external and inter-pane (Fig. 2).

Internal sun shading devices (curtains, venetian blinds, vertical louvre blinds, roller blind etc.) have only a limited effect on reducing the heat load. They are usually adjustable and allow to the occupants in the rooms to regulate the amount of direct light entering their space. This type has mostly the form of horizontal or vertical blinds attached above the windows.
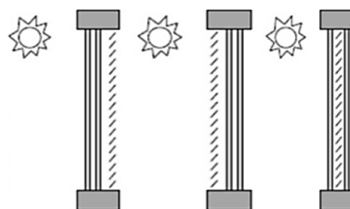
Figure 2. Sun shading devices: inside (left), outside (centre) and mid-pane (right).

External sun shading devices (vertical, horizontal and egg-crate) are considered better than internal. This type is more thermally efficient as it controls the amount of radiation entering the building externally (Kumar, 2016).

Internal and external blinds are used in different type of buildings and rooms, e.g. family houses, shops, offices, restaurants etc. where is necessary to reduce the summer heat load and cerate the suitable microclimate for people. The use of blinds is one of the form of so called passive system of air-conditioning, which could reduce the consumption of energy for cooling of the air.

The main objective of this study is to evaluate the influence of the internal and external blinds on the internal microclimate conditions inside the large offices during the hot summer days with high solar radiation.

Table 1. Work class according to the average total energy output of people (M)

Work class	Work type	M, W m^{-2}
I	Seated work with minimal whole body movement activity, office administrative work, control activity in control rooms, work with PC, laboratory work, compilation or sorting small light object etc.	≤ 80

The suitable conditions which are recommended for office workers with computer in the office rooms are presented in the Government decree no. 361/2007 Coll. (data summarized in the Table 1). The recommended temperature should be from 20°C to 28°C and recommended relative humidity should be from 30% to 70% (data summarized in the Table 2).

Table 2. Microclimate requirement (operating temperature t, relative humidity RH and airflow velocity v_a) according to work classes and total energy output of people (M)

Work class	M W.m^{-2}	t_{min} °C	t_{max} °C	v_a m.s^{-1}	RH %
I	≤ 80	20	28	0.1 to 0.2	30 to 70

The results of this research will show and evaluate the thermal comfort for office workers in four big office rooms in different situations of blinds application.

MATERIALS AND METHODS

For this research has been selected a building, which has large windows equipped with internal and external blinds. This allows to study the effect of blinds on reducing the heat load in the summer. Four large rooms on the top floor of the building were selected for the measurements (Fig. 3), as the windows are not shaded by trees or other structures. Six office workers with personal computers work in each room. No room is equipped with air conditioning. General related construction information of four rooms are shown in the Table 3.

Table 3. Main construction parameters of the four measured rooms

Rooms	Floor area	Glazed area	Type of blind
-	m^2	m^2	-
R1	59.5	19.1	External
R2	43.3	6.8	External
R3	58.8	18.9	Internal
R4	54.2	7.1	Internal

The suitable period for this research and measurements was since June 25th to July 04th 2018, during the hot summer days.
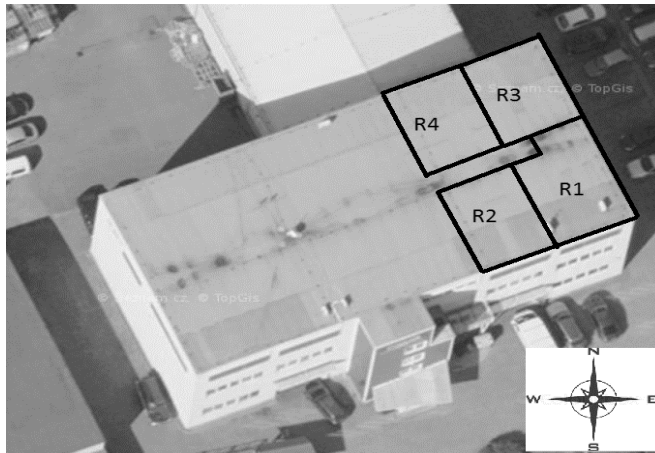
Figure 3. Orientation of the relative position of the building and four rooms (R1, R2, R3, R4), where N is the north; S is the south; W is west; E is east.

Room 1 (R1) and room 3 (R3) have two walls with glazed windows, room 2 (R2) and room 4 (R4) have only one wall with glazed windows. Four rooms have the same height (2.8 m) but have different internal area. R1 and R2 have aluminium venetian blinds which are installed externally, R1 and R2 have fabric vertical blinds which are installed internally. This room layout allows to measure one room on the same side of the building with shaded windows and the other room unshaded with the same intensity of external sunshine. This enables to assess the effect of blinds on internal conditions.

The first measurements (long-time measurements) were carried out continuously during the working days (from Monday to Friday, working hours since 7 a.m. till 5 p.m.). The indoor conditions were influenced by the opening the windows and regulation of

blinds by the persons inside the offices. This arrangement of measurement enable to evaluate the effect of blinds in the real office operation.

The second (short-time measurements) were carried out during the daytime of the weekend (since 8 a.m. till 5 p.m.) when the rooms were empty without persons and without ventilation (closed windows). It enables to measure more directly and exactly the influence of the blinds on the indoor conditions.

The information about the measuring conditions of four rooms are in Table 4.

Table 4. Measuring conditions during the long-time and short-time measurements

Rooms	Instruments	Period	Type of blinds	Use of blinds
Long-time measurements				
R1, R2	Comet System ZTH65	Continuously Monday to Friday	External	Individual by people
R3, R4	Comet System ZTH65	Continuously Monday to Friday	Internal	Individual by people
Short-time measurements				
R1	Almemo 2690	Saturday	External	Opened
R2	Almemo 2590	Saturday	External	Closed
R3	Almemo 2690	Sunday	Internal	Opened
R4	Almemo 2590	Sunday	Internal	Closed

During the working days, office workers used blinds and natural ventilation. Air temperatures and relative humidity were measured by data loggers Comet System ZTH65 inside the offices with registration at intervals of 15 minutes during one week (long-time measurement). Parameters of ZTH65 are: temperature operative range –30 to + 70 °C with accuracy ± 0.4 °C and operative range of relative humidity 5–95% with accuracy ± 2.5%.

At the weekend, R1 and R2 were continuously measured on Saturday, R3 and R4 were measured on Sunday by globe temperature which includes the combined effect of radiation, air temperature and air velocity (measured by globe thermometer FPA 805 GTS with operative range from –50 to +200 °C with accuracy ± 0.1 °C and diameter of 0.15 m) together with temperature and humidity of surrounding air measured by sensor FHA 646–21 including temperature sensor NTC type N with operative range from –30 to +100 °C with accuracy ± 0.1 °C, and air humidity by capacitive sensor with operative range from 5 to 98% with accuracy ± 2%. All these data were stored at intervals of one minute to measuring instrument ALMEMO 2590 and ALMEMO 2690 during approximately nine hours (short-time measurement).

Effect of combinations of temperature and relative humidity is included in the THI (Sleger & Neuberger, 2006; Vladut, 2011). According to (Zejdova et al., 2014) the THI is determined by the equation (1). Calculation of the BGHI is based on the results from short-time measurements with the use of black globe temperature instead off dry bulb temperature, according to the Eq. (2).

$$THI = 0.8 \cdot t_i + \frac{(t_i - 14.4) \cdot RH_i}{100} + 46.4 \qquad (1)$$

where THI – temperature-humidity index, -; t_i – internal temperature of air, °C; RH_i – internal relative humidity of air, %.

$$BGHI \ = \ 0.8 \cdot t_g + \frac{(t_i \ - \ 14.4) \cdot RH_i}{100} \ + \ 46.4 \qquad (2)$$

where *BGHI* – black globe-humidity index, -; t_g – globe temperature, °C.

For evaluation of THI are usually used the following limit values. If THI ≤ 65 it means comfort state; if THI is from 66 to 79 it means alert state, prolonged exposure occurs fatigue; and if THI ≥ 80 it means discomfort, if THI ≥ 84 it is dangerous, heat stress is highly probable if the activity continues. BGHI is widely used index to describe the heat stress, and it is also a key indicator of the environmental conditions of stress, as it includes not only air temperature, but also the influence of radiation measured by globe thermometer.

There was also measured and evaluated illumination in the four rooms by using daylight factor. The different translucent area of windows resulted in different daylight factors, which were measured by lux meter TECPEL 536. The daylight factor is visual and light condition in interior. It shows the quantitative criterion of luminous state of the environment. The daylight can be calculated according to the Eq. (3).

$$e \ = \frac{E_m}{E_H} \cdot 100 \qquad (3)$$

where *e* – daylight factor, %; E_m – illumination of the given plane in the interior, lx; E_H – simultaneous unshadowed external horizontal illuminance, lx.

Total solar energy transmittance with protection against sunlight is calculated according to the equation:

$$g_{total} = F_c \cdot g \qquad (4)$$

where g_{total} – total solar energy transmittance with protection against sunlight; F_c – reduction factor (according to DIN 4108). The value of this coefficient is between 0 and 1 (the value is 1 when is not protection against sunlight); *g* – solar energy transmission factor of window that is determined by the manufacturer of window.

The obtained results of air temperature and relative humidity as well as the daylight measurements were processed by Excel software and verified by statistical software Statistica 12 *(ANOVA* and *TUKEY HSD Test)* to recognise if the differences are significant. Different superscript letters (*a, b, c*) in common are significantly different from each other in the columns of the tables *(ANOVA; Tukey HSD Test; P ≤ 0.05)*, e.g. if there are the same superscript letters in the columns (office R1, R2, R3 and R4) it means the differences between the values in rooms are not statistically significant at the significance level of *0.05*.

RESULTS AND DISCUSSION

The main objective of this article is a presentation of measured results of main microclimate parameters in office rooms and comparison of obtained results with values recommended in relevant standards. Based on the measurement results the influence of blinds to the main microclimate is evaluated.

The results of long-time measurement of temperature and relative humidity of the air in four office rooms are presented in Table 5.

Table 5. Average values and standard deviation of the air temperature t, relative humidity RH and temperature-humidity index THI in four office rooms and outside in meteorological station during the long-time measurements. Different letters (*a, b, c*) in the superscript are the sign of high significant difference (*ANOVA; Tukey HSD Test*; *P≤ 0.05*) between the conditions in the rooms

Place of measurement	t	RH	THI
-	°C ± SD	% ± SD	-
External	18.9 ± 3.3	69.6 ± 14.2	64.1 ± 4.3
R1	24.8 ± 1.1[a]	45.5 ± 5.1[a]	70.9 ± 1.2[a]
R2	25.0 ± 0.9[a, b]	45.2 ± 4,8[a]	71.2 ± 1.0[a, b]
R3	25.4 ± 1.1[c]	44.2 ± 5.4[a]	71.5 ± 1.2[b]
R4	25.2 ± 1.0[b, c]	44.3 ± 5.3[a]	71.3 ± 1.0[b]

SD – Standard deviation.

Working hours in days are usually from 7 a.m. till 5 p.m., which is the time when the microclimate was evaluated. This period includes maximum air temperatures and minimum relative humidity. According to the Government decree no. 361/2007 Coll. for work with computer in the office room, the recommended temperature is from 20 °C to 28 °C and recommended relative humidity is from 30% to 70%. The indoor conditions are influenced by the activity of people inside (different position of blinds, different ventilation etc.), therefore, the comparison and statistical evaluation of microclimate common for all four rooms.

The best conditions were in room R1, but there were not significantly different air temperatures in rooms R1 and R2 with external blinds, which were lower than in the rooms with internal blinds R3 and R4. The difference between the temperatures in rooms R3 and R4 was not significant. There was even not significant difference between the temperatures in rooms R2 and R4. It can be explain by different activity of people inside.

Internal relative humidity of air was in the recommended range, significantly lower than external as the internal temperature was higher. There were not significant differences between the rooms. The measured results show that the relative humidity is in the range of recommended values, however, the air temperatures are sometimes higher than recommendation. It means that this way do not maintain thermal comfort inside the rooms for all office workers during their work in the office, they need to use air conditioning to reduce air temperature.

Regarding the influences of using blinds, maximum air temperature in the room R1 (28.0 °C) and R2 (27.2 °C) were not exceed maximal recommended temperature but and in the room R3 (28.5 °C) and R4 (28.3 °C) were exceed maximal recommended temperature. The results show that, the use of external venetian blinds was useful in this building, it contributed to reduce air temperature.

The temperature-humidity index THI is from 70.9 to 71.3, it means alert state, prolonged exposure occurs fatigue. There were better conditions inside the rooms with external blinds (R1 and R2), the difference of THI in comparison to rooms with internal blinds was not big, nevertheless significant between room R1 and others.

The course for representative of the air temperature and relative humidity of air in four office rooms and outside during 24 hours (from Monday morning to Tuesday morning) of working day is in the Figs 4 and 5.
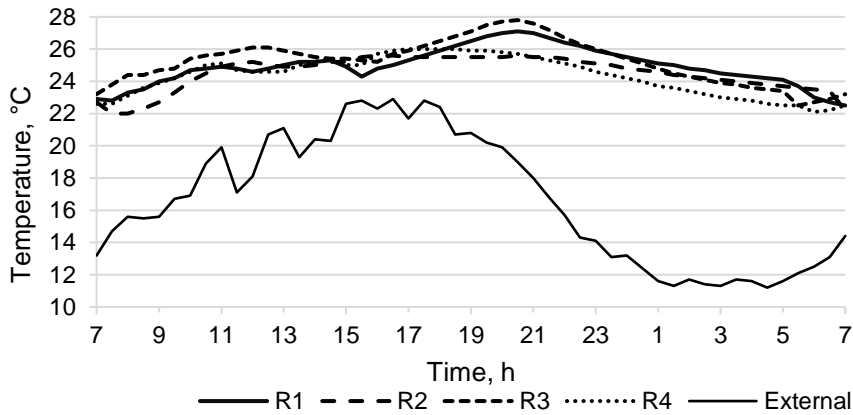
Figure 4. The course for representative of the air temperature outside and inside the rooms R1, R2, R3 and R4 during 24 hours of working day (on Monday).
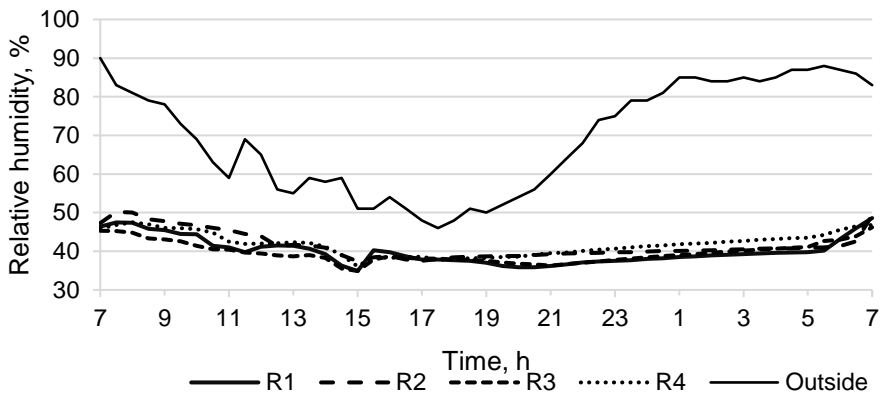
Figure 5. The course for representative of the air relative humidity outside and inside the rooms R1, R2, R3 and R4 during 24 hours of working day (on Monday).

The courses of air temperature and relative humidity in four rooms during day were repeated similarly every day from Monday to Friday. It show that the temperature in room R3 was almost the highest during day, the temperature in room R2 was the lowest. However the difference was not high in comparison with others. It means that the external venetian blinds decrease air temperature more than using fabric vertical blinds, but the difference and efficiency was not much during working periods when the natural ventilation is used. The highest temperature in four rooms was in period time from 7 p.m. to 9 p.m. The reason is thermal accumulation in the building walls during the sun radiation, and as these rooms were not ventilated because of the closed windows. Recommended maximum relative humidity 70% was not exceeded in all rooms.

In the short-time measurements, air temperature and relative humidity were measured to evaluate influences of radiation when rooms were empty, closed and ventilation was not active. The blinds of room R1 and R3 were opened to receive natural light. Average values and standard deviation of the external air temperature, globe temperature, internal air temperature, relative humidity, temperature-humidity index and

black globe-humidity index during the short-time measurements are presented in Table 6. The statistics is used for separated comparison of indoor conditions of rooms equipped by the same type of blinds (external or internal) which are opened in one room and closed in the second one.

Table 6. Average values and standard deviation of globe temperature t_g, air temperature t, relative humidity RH, temperature-humidity index THI and black globe-humidity index BGHI in four office rooms and outside in meteorological station during the short-time measurements on Saturday and on Sunday with corresponding situation of blinds. Different letters (*a, b*) in the superscript are the sign of high significant difference (*ANOVA; Tukey HSD Test*; *P≤ 0.05*) between the conditions in the rooms

Place of measurement	Situation of blinds	t_g °C ± SD	t °C ± SD	RH % ± SD	THI % ± SD	BGHI % ± SD
Saturday	External	-	19.8 ± 1.6	43.1 ± 5.4	64.4 ± 1.8	-
R1	Opened	28.5 ± 1.0[a]	28.2 ± 0.6[a]	35.4 ± 1.4[a]	73.8 ± 0.7[a]	74.1 ± 1.2[a]
R2	Closed	26.0 ± 0.4[b]	25.8 ±0.4[b]	48.1 ±1.2[b]	72.5 ± 0.3[b]	72.7 ± 0.4[b]
Sunday	External	-	19.1 ± 1.6	40.9 ± 4.1	63.5 ± 1.7	-
R3	Opened	27.4 ± 0.6[a]	27.3 ± 0.6[a]	35.5 ± 1.0[a]	72.8 ± 0.6[a]	72.9 ± 0.6[a]
R4	Closed	26.0 ± 0.7[b]	25.8 ±0.7[b]	41.6 ±1.0[b]	71.7 ± 0.7[b]	71.9 ± 0.7[a]

SD – Standard deviation.

Window view with external aluminium venetian blind when the room R1 was opened (in left photo) and the room R2 was closed (in right photo) is shown in Fig. 6. Similarly, Fig. 7 is a photograph of the internal fabric vertical blind when the room R3 was opened (in the left photo) and the room R4 was closed (in the right photo).

Figure 6. Situation of external aluminium venetian blind when the room R1 was opened (in left photo) and the room R2 was closed (in right photo).

Figure 7. Situation of internal fabric vertical blind when the room R3 was opened (in left photo) and the room R4 was closed (in right photo).

The short time measurements give better idea about the influence of blinds. From the measured results it is evident the negative effect of radiation, which increased the globe temperatures in all rooms. When the external blinds were not used, air temperature in room was higher (about 2.5 °C) in comparison with using blinds. Moreover, maximum air temperature in this case exceed maximum recommended temperature (28 °C) and this negative effect makes thermal discomfort for office workers. We can use this results to calculate power or energy for air conditioning to maintain better thermal comfort inside the room. The differences between the air temperature, globe temperature, relative humidity, THI and BGHI in rooms with opened and closed blinds are in all cases statistically significant (Table 6).

The higher air temperatures resulted in higher THI, which was from 71.7 to 73.8, it means alert state, prolonged exposure occurs fatigue and this effect of solar radiation is even more obvious from the BGHI which was from 71.9 to 74.1.

The use of external or internal blinds contributes to reduce the impact of solar radiation on the indoor thermal comfort and reduces the inside temperature. However, the artificial lighting must be used. The comparison of average measured illuminance and daylight factors in the office rooms R1 and R3 are presented in Table 7.

Table 7. Results of measurement of the illuminance and calculated daylight factor e in two office rooms R1, R3 during the short time with the area of glazed windows. The same letter (*a*) in the superscript is the sign that there is not high significant difference (*ANOVA; Tukey HSD Test; P≤ 0.05*) between the daylight factors in the rooms

Place of measurement	Area ofwindows	Average measured illuminance	Daylight factor e
	m^2	lx ± SD	% ± SD
R1	19.1	3,188 ± 3,684	9.67 ± 11.16[a]
R3	18.9	1,632 ± 1,590	4.53 ± 4.41[a]

The average daylight factor e = 9.67% in the room R1 was bigger than e = 4.53% in the R3. The difference between the daylight factors was evaluated statistically and surprisingly the difference was not significant at the significance level of 0.05. It can be explained by the large standard deviations of the measured values of illuminance. According to the visual activity class IV in both office rooms minimum demanded daylight factor is 1.5%. The room R1 has average daylight factor e bigger which is caused by the orientation of this room (see the Fig. 3).

We calculated solar energy through the window into the interior in period time of short measurement following equation (2). We also used values global solar radiation, reduction factor F_c of blinds and solar energy transmission factor of glass (g = 0.65). All values and obtained results are showed in Table 8.

Table 8. Solar energy through the window into four rooms in time period of short measurement.

Room	Type of blinds	F_c	g$_{total}$	Global radiation	Solar energy through into the interior
		-	-	W m^{-2}	W
R1	Without blind	1.0	0.65	280	3,476
R2	Aluminium venetian external	0.25	0.16	280	304
R3	Without blind	1.0	0.65	235	2,887
R4	Fabric vertical internal	0.5	0.33	235	550

When the room was not covered by blinds, the solar energy through the window into the interior was very high (in room R1 and R3) in comparison to room that was covered by blinds (room R2 and R4). This solar energy makes increase air temperature in the rooms. Therefore, the temperature in the room R1 and R3 is higher than in the room R2 and R4. The use of aluminium venetian external is more effective than fabric vertical internal. Therefore it can be said once more that the use of blinds for glazed windows helps to improve indoor thermal comfort of the internal microclimate.

CONCLUSIONS

During working days, relative humidity in all measured rooms were in the range of recommended value. When index THI was used to evaluate effect of combinations of temperature and relative humidity, internal climate conditions in four rooms were not in comfort state but in alert state, prolonged exposure can occur fatigue. The reduction of inside air temperature is needed.

The external aluminium venetian blinds maintained thermal comfort inside the rooms (R1 and R2) for office workers during their work in the office in summer, but internal fabric vertical blinds did not, air conditioning is needed to reduce the air temperature.

Concerning the influences of blinds during the working periods, the use of external venetian blinds only slightly contributes to reduce air temperature in comparison with internal blinds. Without ventilation and without external blinds the air temperature was higher (about 2.5 °C) in room in comparison with the use of blinds. Obtained results of measurement inside the tested rooms can be useful for calculation of power for air conditioning to maintain better thermal comfort inside the room.

The position and orientation of building and rooms are important as they influence the radiation and light from the sunlight and thus effect indoor microclimatic conditions. Blinds can help to reduce slightly the inside air temperature and reduce the consumption of energy for cooling, but there is reduced also natural daylight therefore it is necessary to use the artificial illumination.

REFERENCES

Alwetaishi, M. 2019. Impact of glazing to wall ratio in various climatic regions: A case study. *Journal of King Saud University - Engineering Sciences* **31**(1), 6–18.

Al Touma, A., Ghali, K., Ghaddar, N. & Ismail, N. 2016. Solar chimney integrated with passive evaporative cooler applied on glazing surfaces. *Energy* **115**, 169–179.

Aries, M. B. C., Veitch, J.A. & Newsham, G.R. 2010. Windows, view, and office characteristics predict physical and psychological discomfort. *Journal of Environmental Psychology* **30**, 533–541.

Boubekri, M. & Boyer, L.L. 1992. Effect of window size and sunlight presence on glare. *Lighting Research and Technology* **24**(2), 69–74.

Cao, V.D. & Kic, P. 2018. Analysis of indoor temperature in the workshop building during the summer: a pilot study. *Agronomy Research* **16**(4), 1614–1621.

DIN 4108. Thermal protection and energy economy in building. *German Institute for Standardisation*. 1969.

Edmonds, I.R & Greenup, P.J. 2002. Daylighting in the tropics. *Solar Energy* **73**, 111–121.

Gosselin, J.R. & Chen, Q. 2008. A dual airflow window for indoor air quality improvement and energy conservation in buildings. *HVAC&R Res.* **14**(3), 359–372.

Government decree no. 361/2007 Coll. Conditions of health protection at work. (in Czech).

Hirning, M.B., Isoardi, G.L. & Cowling, I. 2014. Discomfort glare in open plan green buildings. *Energy and Buildings* **70**, 427–440.

Kumar, R. 2016. Presentation: Shading devices. *MBS School of Planning and Architecture. https://www.slideshare.net/RohitKumar79/7-shading-devices.* Accessed 1.3.2019.

Leather, P., Pyrgas, M., Beale, D. & Lawrence, C. 1998. Windows in the workplace: sunlight, view, and occupational stress. *Environment and Behavior* **30**(6), 739–762.

Mishchensko, M., Travis, L. & Lacis, A. 2015. Radiation tranfer in the atmosphere. *Encyclopedia of Atmospheric Sciences,* 27–36.

Sleger, V. & Neuberger, P. 2006. Using meteorological data to determine the risk of heat stress. *Research in Agricultural Engineering* **52**(2), 39–47.

Qiang, F. 2006. Radiative Transfer. *Atmospheric Science,* 113–152.

The Saudi Building Code (SBC), Energy Conservation, 2007 (Section 601).

Vladut, A. 2011. Temperature – Humidity Index (THI) within the Oltenia plain between 2000 and 2009. Forum geografix. Studi si cercetari de geografie si protectia mediukui, vol. **10**(1), pp. 149–156.

Zejdova, P., Chladek, G. & Falta, D. 2014. *Influence of stable environment on behaviour and milk production of dairy cows*. Mendel University, Brno, 26 pp. (in Czech).

Combustion characteristics of compression ignition engine operating on rapeseed oil-diesel fuel blends

J. Čedík[1,*], M. Pexa[1], D. Mader[1] and R. Pražan[2]

[1]Czech University of Life Sciences Prague, Faculty of Engineering, Department for Quality and Dependability of Machines, Kamýcká 129, CZ165 21 Prague 6, Czech Republic
[2]Research Institute of Agriculture Engineering, Drnovská 507, CZ161 01 Prague 6, Czech Republic
*Correspondence: cedikj@tf.czu.cz

Abstract. The effect of biofuels on the operational parameters of the combustion engines, such as performance parameters or emission production, are monitored often. These changes are, however, based on the effect of biofuels on the course of combustion pressure inside the combustion chamber. The contribution deals with the effect of rapeseed oil-diesel fuel blends on the combustion characteristics of turbocharged compression ignition engine. The course of cylinder pressure was monitored and analysed and heat release rate was calculated. The brake specific fuel consumption, indicated and brake thermal efficiency were calculated and evaluated, in-cylinder temperature and ignition delay were also evaluated. As a test fuels a 5% and 20% concentrations of rapeseed oil in diesel fuel were selected while 100% diesel fuel was used as a reference. Turbocharged CI engine Zetor 1204 located in the tractor Zetor Forterra 8642 was used for measurement. During measurement the rotation speed of the engine was kept constant at approx. 1,950 min^{-1} and the load of the engine was selected at approx. 20, 60, 80 and 100%. The results showed decreased cylinder peak pressure, decreased intensity of heat release rate and earlier end of combustion in all tested loads for both tested fuel blends in comparison with diesel fuel, while the lowest peak cylinder pressure was reached using fuel with 5% rapeseed oil. Fuel with 5% rapeseed oil also showed highest indicated efficiency. Ignition delay was found shorter with both of the blended fuels in comparison with diesel fuel.

Key words: biofuels, cylinder pressure, heat release rate, engine efficiency.

INTRODUCTION

The energy consumption, greenhouse gas emissions and fossil fuel consumption by agriculture sector is on the increase in present time (Garnier et al., 2019; Zhang et al., 2019). In agriculture sector the compression ignition engine is the most common source of the energy for machinery in the field conditions. For a diesel engine the liquid biofuels, based on vegetable oils are one of the most widely utilized alternatives to the fossil diesel fuel (Jindra et al., 2016; Babu et al., 2017; How et al., 2018; Mat et al., 2018a).

The vegetable oils have different properties in comparison with diesel fuel. The different origin of vegetable oils, edible or non-edible, means also different physical and

chemical properties. However, some properties are similar for vegetable oils in general in comparison with diesel fuel e.g. higher viscosity, density, surface tension, flash point and oxygen content and lower cetane number, calorific value and carbon content (Franco & Nguyen, 2011; Esteban et al., 2012; Sirviö et al., 2018). Preheat or modification of the fuel, such as hydrotreatment or transesterification, is necessary in order to utilize the neat vegetable oils as a fuel in diesel engines (Birzietis et al., 2017; Gad et al., 2018; Hsiao et al., 2018; Kim et al., 2018; Zahan & Kano, 2018). Alternatively, it is possible to blend the vegetable oils with diesel fuel or alcohols, such as butanol or methanol (Masjuki et al., 2001; Elango & Senthilkumar, 2011; Yilmaz & Morton, 2011; Pexa et al. 2014; Patel et al., 2016; Pexa et al. 2016; Gad et al., 2018; Mat et al., 2018a). The most of authors used vegetable oil-diesel fuel blends in concentration up to 20% of vegetable oil in the diesel fuel. According to Dabi & Saha (2019) blending vegetable oils in concentration up to 20% of vegetable oil makes a comparable performance with diesel fuel.

From the viewpoint of combustion characteristics vegetable oils and its blends in diesel fuel were found to decrease the peak cylinder pressure and maximum of heat release rate (HRR) (Nwafor et al. 2003; Devan & Mahalakshmi, 2008; Pradhan et al. 2014; Patel et al., 2016; Mat et al., 2018b; Sanli, 2018). Ignition delay (ID) was found shorter when using vegetable oil and its blends in comparison with diesel fuel (Devan & Mahalakshmi, 2008; Pradhan et al., 2014; Koder et al., 2018). However, some authors (Shah & Ganesh, 2016; Shah et al., 2018) state increased ignition delay and increased peak cylinder pressure when using neat karanj oil and sunflower oil in comparison with diesel fuel.

Vegetable oils and its blends in diesel fuel were found to decrease the brake thermal efficiency (BTE) of the engine while increasing the brake specific fuel consumption (BSFC) with increasing proportion of vegetable oil in the fuel blend (De Almeida et al., 2002; Devan & Mahalakshmi, 2008; Gad et al., 2018; Sanli, 2018; Dabi & Saha, 2019). However, other authors (Rakopoulos et al., 2006; Agarwal & Rajamanoharan, 2008; Bajpai et al., 2008; Rakopoulos et al., 2011) reported increased brake thermal efficiency in various of blending ratios from 10% to 75% of vegetable oil in the fuel blend. Rakopoulos et al. (2011) also found lower BSFC with 10% and 20% blends of sunflower and with 10% blend of corn oil in comparison with diesel fuel.

Higher exhaust gas temperature was found by many authors when using vegetable oil-diesel fuel blends or neat vegetable oils from different origin in comparison with diesel fuel (Pramanik, 2003; Hebbal et al., 2006; Agarwal & Kumar, 2007; Agarwal & Rajamanoharan, 2008; Devan & Mahalakshmi, 2008; Gad et al. 2018).

The aim of the paper is to experimentally verify the influence of rapeseed oil-diesel fuel blends, in concentrations of 5% and 20% of rapeseed oil, on the combustion characteristics, specific fuel consumption, thermal and indicated efficiency of the turbocharged compression ignition engine in comparison with diesel fuel.

MATERIALS AND METHODS

For the measurement the turbocharged compression ignition engine Zetor 1204, mounted in the Tractor Zetor Forterra 8641 (Fig. 1), was used. The basic specification of the engine used for measurement are listed in the Table 1. The engine did not exceed 150 hours of operation time and it is unmodified. Start of injection (SOI) is given by

manufacturer and the injection pressure was checked before the measurement using manual testing device.

Figure 1. Tractor Zetor 8641, used for measurement (left), mobile dynamometer MAHA ZW 500 (right).

Table 1. Basic engine specification (*according to Deutsche Landwirtschafts-Gesellschaft)

Parameter	Specification
Manufacturer and type	Zetor 1204
No. and arrangement of cylinders	4, in-line
Air fill	Turbocharged
Rated speed	2,200 min^{-1}
Rated power	60 kW (53.4 kW on PTO*)
Maximum torque	351 Nm (312 Nm on PTO*)
Engine displacement volume	4.156 l
Cylinder bore X stroke	105 X 120 mm
Compression ratio	17
Fuel supply	Mechanical in-line injection pump
Injection type	Direct injection
Start of injection (SOI)	12° before top dead center
Injection pressure	22 MPa
Valve mechanism	OHV
Valves per cylinder	2

The engine was loaded via tractor PTO (Power Take Off) using mobile dynamometer MAHA ZW 500 (Fig. 1). Specification of the dynamometer can be seen in Table 2. A data acquisition unit, provided by manufacturer, was used to store the data from the dynamometer to the hard drive of the PC with the frequency of 10 Hz.

Table 2. Basic dynamometer specification

Parameter	Specification
Manufacturer and type	MAHA ZW 500
Max. power	500 kW
Max. torque	6,600 Nm
Max. speed	2,500 min^{-1}
Torque inaccuracy	< 1% over the full speed range

The cylinder pressure was measured by means of pressure sensor Optrand C322-GPA (measuring range = 0–20.7 MPa, accuracy = 1%), mounted instead of the glow plug. The cylinder pressure was measured with a resolution of 1°CA (crankshaft angle), since the incremental sensor SICK DKS with 360 pulses per revolution was used as a trigger for cylinder pressure record. Therefore the frequency of cylinder pressure measurement is dependent on the engine speed.

The fuel consumption was measured by means of standard precision scale VIBRA AJ 6200 (range = 0–6200 g, accuracy = 0.1 g, readability = 0.01 g), where an external fuel tank was placed. Fuel consumption was measured with the frequency of 1 Hz.

The mass air flow through the engine was measured by means of mass air flow sensor Sierra FastFlo 620S (accuracy ± 1% of full scale, repeatability ± 0.2% of full scale). The data from the sensor were recorded to the hard drive of PC using A/D converter LabJack U6 with frequency of 10 Hz.

During the measurement the fuel temperature, exhaust gas temperature and ambient conditions, e.g. temperature, humidity and atmospheric pressure were monitored. Exhaust gas and fuel temperature were monitored by means thermocouples type K, the fuel temperature was monitored at the input of the injection pump and the exhaust gas temperature was measured in the muffler.

As a test fuels a mixtures of rapeseed oil and fossil diesel fuel were used. The rapeseed oil-diesel fuel bends were used in concentrations of 5% (R5D95) and 20% (R20D80) of rapeseed oil. As a reference the diesel fuel with no bio-components was used (D100). The basic fuel properties are listed in Table 3. Values of density and viscosity of the fuels were measured using Stabinger Viscometer SVM 3000 made by Anton Paar GmbH (measuring accuracy < 1%, repeatability 0.1%). The values of calorific value of the fuels were reached by means of isoperibol calorimeter LECO AC600 (measuring range 23.1–57.5 MJ kg^{-1} for a 0.35 g sample, accuracy 0.1% RSD) according to ČSN DIN 51900-1 and ČSN DIN 51900-2.

Table 3. Fuel parameters (*EN 590, 2013; **Cisek & Szlachta, 2001)

Fuel	Temperature °C	Kinematic Viscosity mm^2 s^{-1}	Dynamic Viscosity mPa s	Density kg m^{-3}	Calorific value MJ kg^{-1}	Cetane number -
D100	15	2.843	2.329	819.1	43.15	50*
	40	1.801	1.444	801.65		
R5D95	15	3.224	2.65	821.9	42.72	-
	40	2.022	1.627	804.4		
R20D80	15	5.042	4.216	836.1	41.74	-
	40	2.984	2.443	818.75		
Rapeseed oil	15	97.655	89.962	921.2	37.1	39.6–44**
	40	35.697	32.326	905.33		

The measurement was carried out in stabilized conditions at constant rotation speed of approx. 1,950 min^{-1}. The engine rotation speed of 1,950 min^{-1} was chosen because at this point the PTO shaft reaches rotation speed of 1,000 min^{-1}, which is necessary for proper function of connected agricultural equipment, so it could be assumed that the engine spends most of its working time at this rotation speed. Load of the engine was selected 20, 60, 80 and 100%. The loads of the engine were calculated from maximum

torque at 1,950 rpm for each fuel. At each measurement point the monitored parameters were stabilized. After stabilization the monitored parameters were recorded for approx. 80 s. The mechanical losses in gearbox have no influence on comparative measurement and therefore they were not taken into account. The MS Excel was used for evaluation of the measured data.

Heat release rate (HRR) is one of the most effective ways to obtain information about the combustion process in internal combustion engines. HRR was calculated according to the first law of thermodynamics and Eq. (1). The calculation does not take into account the heat losses during the process. According to Ozsezen et al. (2008), temperature gradients, pressure waves, non-equilibrium conditions, fuel vaporization, and mixing can be ignored. In order to eliminate noise effects, the Savitzky-Golay smoothing filter was used on the recorded pressure data for HRR calculation.

$$\frac{dQ}{d\theta} = \frac{\gamma}{\gamma - 1} p \frac{dV}{d\theta} + \frac{1}{\gamma - 1} V \frac{dp}{d\theta} \quad (1)$$

where $dQ/d\theta$ – heat release rate (J/°CA); V – instantaneous cylinder volume (m^3); p – instantaneous cylinder pressure (Pa); θ – crankshaft angle (°CA); γ – ratio of specific heats at constant pressure and volume (considered constant at 1.35 (Heywood, 1988; Imtenan et al., 2015)).

Cumulative heat release was calculated as integral from HRR as can be seen in Eq. (2). Relative cumulative heat release (RCHR) was calculated from cumulative heat release and it is expressed in percentage.

$$Q_{CHR} = \int_{EOC}^{SOC} \frac{dQ}{d\theta} d\theta \quad (2)$$

where Q_{CHR} – cumulative heat release (J); SOC – start of combustion (°CA); EOC – end of combustion (°CA).

Indicated work was calculated according to (Heywood, 1988) as an area inside the p-V diagram according to Eq. (3). For the calculation of indicated work only compression and expansion strokes were used in order to exclude the gas exchange from the result, as described Gailis et al. (2017).

$$W_i = \int_{180}^{-180} p \, dV \quad (3)$$

From the measured and calculated data the indicated efficiency, brake specific fuel consumption (BSFC) and brake thermal efficiency (BTE) were calculated. Indicated efficiency is ratio between indicated work and chemical energy, delivered into cylinder in the fuel. Brake thermal efficiency is ratio between effective power and chemical energy delivered into the engine in the fuel.

For comparison of conditions in the cylinder before start of combustion (SOC) the temperature of charge at SOI was calculated according to the ideal gas law. The calculation was performed according to Eq. (4).

$$T_{SOI} = \frac{p_{SOI}\, V_{SOI}}{m\, R_i} \qquad (4)$$

where T_{SOI} – temperature of charge at SOI (K); V_{SOI} – instantaneous cylinder volume (m^3); m – mass air flow per cycle (kg); R_i – specific gas constant of air (J kg^{-1} K^{-1}).

The ignition delay (ID) was also determined from the data. ID is the period between SOI and SOC, stated in time or crankshaft angle. The SOI is kept constant at -12°CA (crankshaft angle). SOC can be determined by various methods, including HRR profile (Aldhaidhawi et al., 2017). According to some sources (Heywood, 1988; Aldhaidhawi et al., 2017), change of slope in the HRR profile defines the SOC, other authors (Imtenan et al., 2015) state that SOC occurs once the HRR becomes positive. The moment when HRR becomes positive was considered as SOC. The moment when HRR becomes negative was considered as the end of combustion (EOC).

RESULTS AND DISCUSSION

In Fig. 2 the cylinder pressure profile, measured at 20% engine load for all tested fuels can be seen. It is evident that at lower loads the SOC appears after the top dead center. Also, from the figure, it is evident that the cylinder pressure was lower for both of the tested fuel blends in comparison with D100. In the case of R5D95 the decrease of peak cylinder pressure was 7.13% and in the case of R20D80 approx. 2.25%. Also lower cylinder pressure during compression stroke can be seen when using both of the blended fuels in comparison with D100.
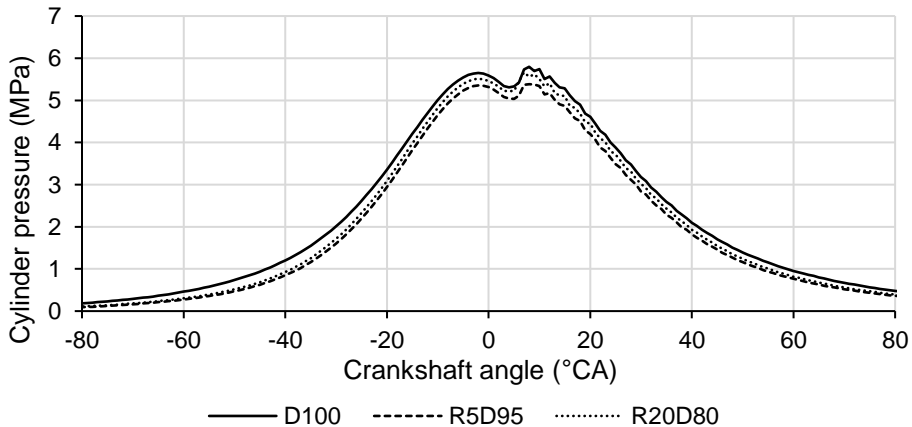
Figure 2. Course of the cylinder pressure in dependance on crankshaft angle at 20% load.

Fig. 3 shows the results of HRR and RCHR at 20% engine load for all tested fuels. It can be seen that premixed combustion phase (the first peak on HRR profile after the start of combustion) takes the significant part of the heat, released during combustion (approx. 30–35%). Also, the premixed combustion phase is stronger for D100 fuel than for both of the tested fuel blends. Lower intensity of premixed combustion may be caused by worse atomization of the fuel blends with higher viscosity in combination with poor evaporating ability of rapeseed oil in the fuel blends. Diffusion and late combustion

phases showed shorter duration and lower intensity in comparison with D100. Combustion duration was shorter when using R5D95 blend by 9.68% (3.5°CA) and R20D80 by 8.12% (2.93°CA).
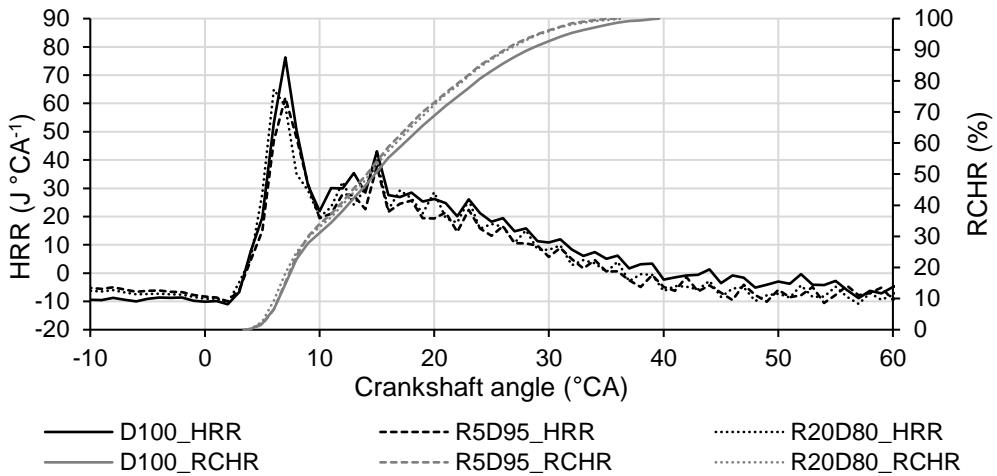
Figure 3. Course of HRR and RCHR in dependance on crankshaft angle at 20% load.

ID for all tested fuels at all tested engine loads can be seen in Fig. 10. At 20% engine load the differences are under 1% (by 0.67% longer for R5D95 and by 0.51% shorter for R20D80).

Fig. 4 shows the cylinder pressure profile for all tested fuel at 60% engine load. It can be seen that peak cylinder pressure is considerably lower for both of tested fuel blends in comparison with diesel fuel at this engine load (by 6.52% for R5D95 and by 5.05% for R20D80). Also, lower cylinder pressure can be seen during both compression and expansion strokes. This may be caused by lower calorific value of the blended fuels and by different energy of exhaust gas and thus different intake air pressure.
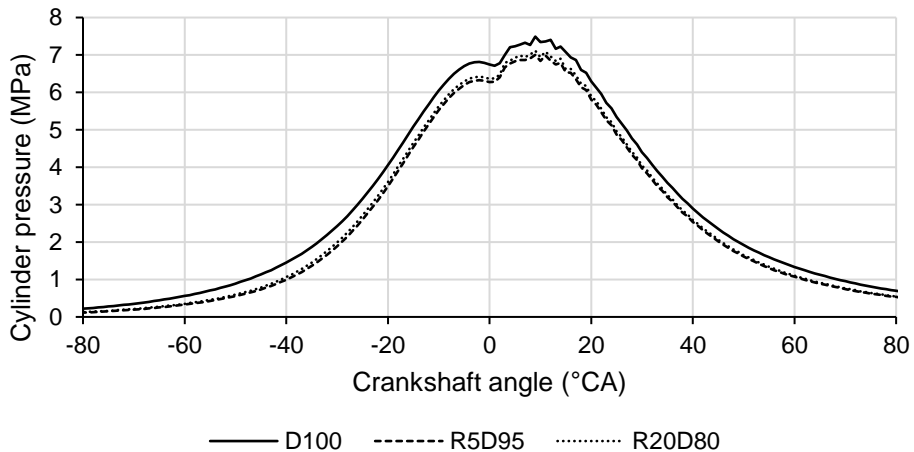
Figure 4. Course of the cylinder pressure in dependance on crankshaft angle at 60% load.

HRR and RCHR for 60% engine load are shown in Fig. 5. It is evident that with increasing engine load the higher proportion of fuel is burned during diffusion combustion phase. Both of the blended fuels reached higher RCHR during premixed combustion in comparison with D100 (R5D95 – 14.4%, R20D80 – 14.3%, D100 – 12%). In absolute values the fuel blends also released higher heat, released during the premixed combustion phase (by 2.97% using R5D95 and by 4.54% using R20D80). This may be caused by shorter ID and longer duration of the premixed combustion phase. Also higher oxygen content in the fuel contributes to premixed combustion. The diffusion and late combustion phases showed shorted duration in comparison with D100, since the EOC occurred earlier, the combustion duration was shorter by 9.97% (3.88°CA) for R5D95 and by 10.01% (3.9°CA) for R20D80. Also, the intensity of diffusion combustion phase was lower for both of blended fuels.

ID at 60% engine load, as can be seen in Fig. 10, was shorter for both blended fuels in comparison with D100. Fuel blend R5D95 showed by 2.85% (0.37°CA) and R20D80 by 1.56
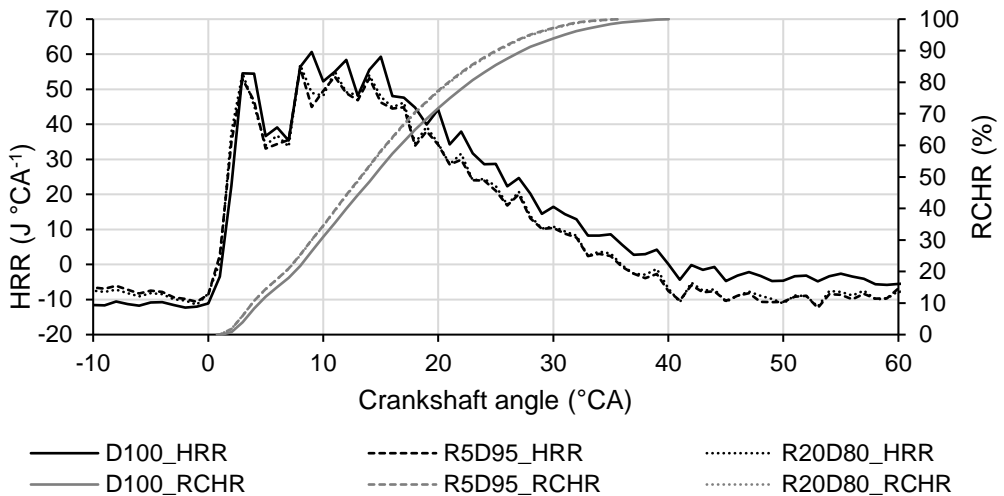
Figure 5. Course of HRR and RCHR in dependance on crankshaft angle at 60% load.

Fig. 6 shows the cylinder pressure profile for all tested fuels at 80% engine load. In comparison with D100 the peak cylinder pressure was lower by 4.75% using R5D95 and by 2.18% using R20D80 fuel blend. Similarly to 60% engine load the lower cylinder pressure can be seen during compression and expansion strokes for both of the tested fuels.

In Fig. 7 HRR and RCHR at 80% engine load for all tested fuels are shown. From the figure it can be seen that at this engine load the peak of the premixed combustion appears earlier for both of the blended fuels in comparison with D100. This is connected with the ignition delay which was shorter for both of the blended fuels in comparison with D100 and with oxygen content in the blended fuels. However, the duration and RCHR of the premixed combustion phase in the case of R20D80 fuel blend was lower than in case of D100 (RCHR for D100 – 8.36%, RCHR for R20D80 – 7.48%, premixed combustion shorter by 1°CA). It is evident that at higher engine load the 20% proportion

of rapeseed oil in the fuel significantly affects the ability of the fuel to evaporate and lowers the intensity of premixed combustion. When using R5D95 fuel blend the RCHR during premixed combustion was higher by 10.11% than in the case of D100. This may be the result of shorter ID and thus longer premixed combustion phase while the peak value remains lower than in case of D100. The EOC also occurred earlier for both of the blended fuels, combustion duration was shorter by 9.17% (3.67°CA) when using R5D95 and by 8.65% (3.48°CA) when using R20D80.
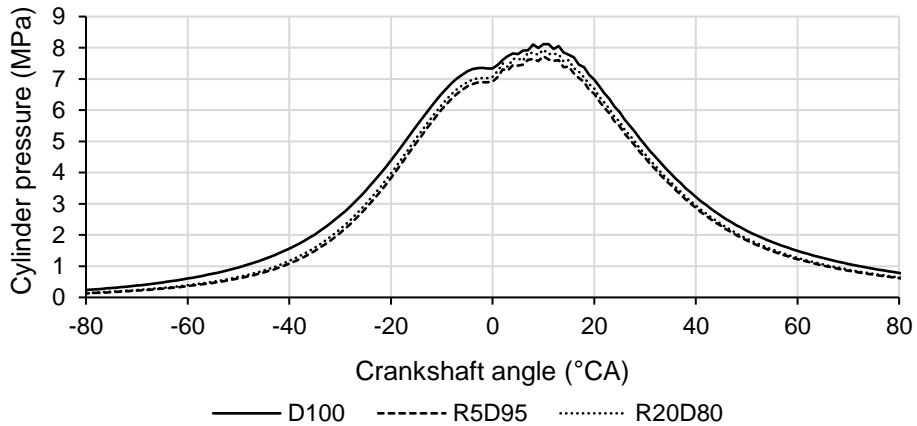
Figure 6. Course of the cylinder pressure in dependance on crankshaft angle at 80% load.

Figure 7. Course of HRR and RCHR in dependance on crankshaft angle at 80% load.

ID at 80% load was shorter for both blended fuels in comparison with D100. When the engine was running on the fuel blend R5D95 ID decreased by 1.93% (0.23°CA), during operation on the fuel blend R20D80 ID decreased by 3.95% (0.48°CA).

In Fig. 8 the pressure profile in dependence on crankshaft position for all tested fuels at full engine load is shown. It is evident that peak cylinder pressure is also lower

for both of the tested fuel blends in comparison with D100, but the difference is lower in than in previous measured engine loads. Especially when using R20D80 where the difference in peak cylinder pressure was close to the sensor accuracy (1.44%), when using R5D95 fuel blend the peak cylinder pressure at this engine load was lower by 4.17%. However, lower cylinder pressure during compression stroke can be seen, similarly to previous measured engine loads.
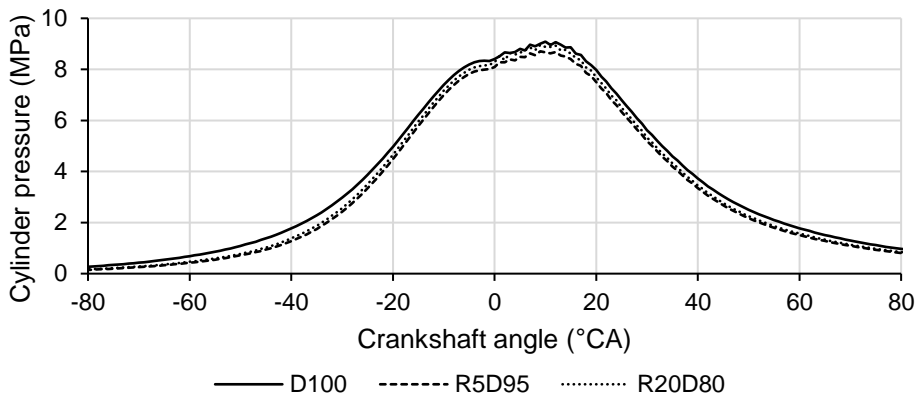
Figure 8. Course of the cylinder pressure in dependance on crankshaft angle at 100% load.

HRR and RCHR for 100% engine load are shown in Fig. 9. SOC and premixed combustion phase, similarly to 80% engine load, appears earlier with blended fuels in comparison with D100. When using R20D80 the duration of the premixed combustion is also considerably shorter (by 2°CA). RCHR at the end of premixed combustion phase was 5.42% for R5D95, 2.06% for R20D80 and 4.49% for D100. The combustion duration was shorter when using R5D95 fuel blend by 8.2% (3.32°CA) and when using fuel blend R20D80 by 7.53% (3.05°CA) in comparison with D100.

Figure 9. Course of HRR and RCHR in dependance on crankshaft angle at 100% load.

The shorter ID at full engine load was found when using both of the blended fuels in comparison with D100. When the engine was running on the fuel blend R5D95 ID decreased by 2.75% (0.32°CA), during operation on the fuel blend R20D80 ID decreased by 3.34% (0.37°CA).
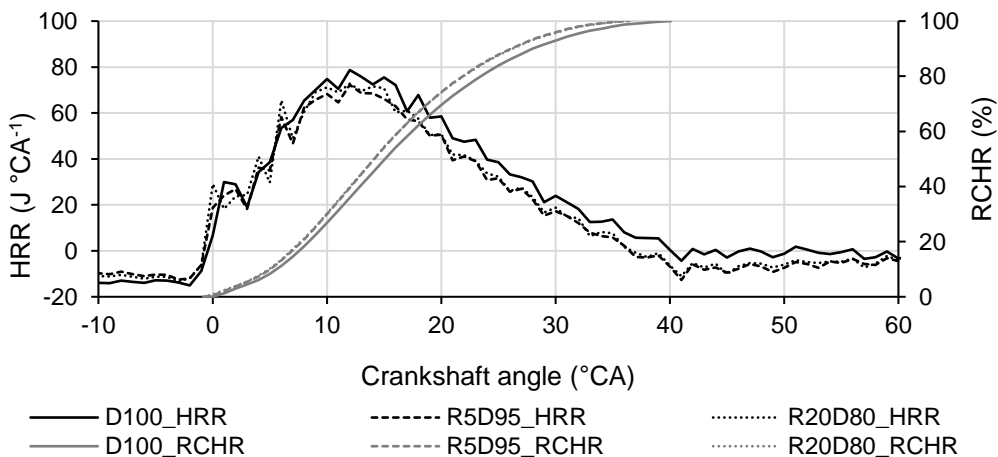
At all of the measured engine loads the statistically significant difference in peak cylinder pressure was found between all fuels. In Table 4. the analysis of variance (ANOVA), complemented with Tukey HSD post-hoc test for peak cylinder pressure at full engine load can be seen.

Table 4. ANOVA with Tukey HSD post-hoc test for peak cylinder pressure at full engine load

ANOVA				
$\alpha = 0.05$	Sum of squares	Degrees of freedom	Variance	F
Between groups	73.5574	2	36.7787	7,743.04
Within groups	16.9429	3,567	0.0047	
Total	90.5003	3,569		
Tukey HSD Post-hoc Test				
D100 vs R5D95: Diff = -0.3788, 95%CI = -0.3862 to -0.3714, $p = 0.0000$				
D100 vs R20D80: Diff = -0.1311, 95%CI = -0.1378 to -0.1243, $p = 0.0000$				
R5D95 vs R20D80: Diff = 0.2477, 95%CI = 0.2413 to 0.2541, $p = 0.0000$				

The lower RCHR and duration of premixed combustion phase when using R20D80 fuel blend at higher engine loads (80% and 100%) may be a result of poor evaporating ability of the rapeseed oil in the fuel mixture. Also, shorter ID causes lesser amount of fuel is being injected into the combustion chamber before the combustion begins.

ID and temperature of charge at SOI for all tested fuels at all measurement points are shown in Fig. 10. It is evident that differences in ID between individual tested fuels are increasing with the engine load. It can be seen that in 3 out of 4 measurement points the fuel blend R20D80 showed the shortest ID. Similar results of ID was reached by Devan & Mahalakshmi (2008) with 20% blend of poon oil who also found shorter ID in comparison with mineral diesel fuel. Koder et al. (2018) with neat jatropha and soybean oils also reported shorter ID when using vegetable oils in all measured engine modes.
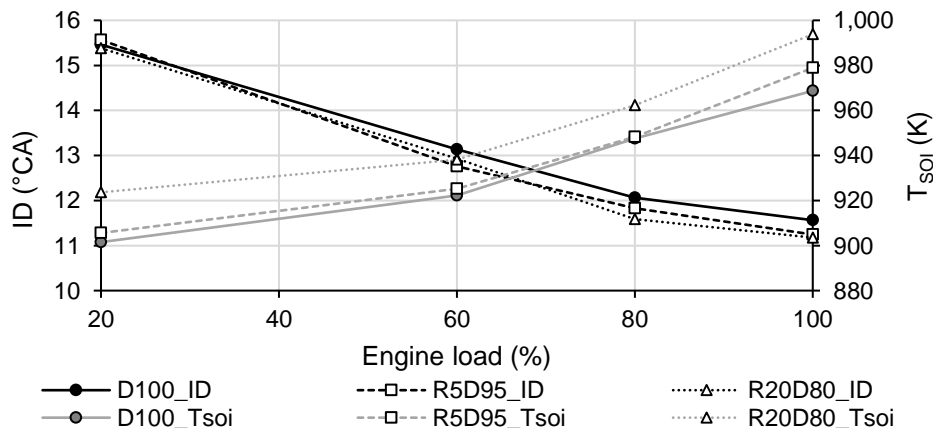
Figure 10. Ignition delay and temperature of charge at SOI for all tested fuels at all measured points.

Shorter ID may be result of the temperature of charge at SOI which was highest at all measurement points when using fuel blend R20D80. Also, increased value of compressibility of vegetable oil may cause a slightly earlier injection of the fuel blends into the cylinder (Varde, 1984; Rakopoulos et al., 2005). From the results it can be stated that when using the tested fuel blends in comparison with D100, the temperature of charge at SOI in combination with physical and chemical properties of rapeseed oil shortened the ID despite the cetane number, which was lower for both of the tested fuel blends. However, the differences in temperature of charge between individual fuels are on the border of measurement accuracy (especially the sensor of mass air flow) and the calculation does not take into account the heat losses during the compression.

The temperature of charge is to a large extent affected by speed of turbocharger and its temperature. The speed of the turbocharger depends on kinetic energy of exhaust gas. The kinetic energy of exhaust gas could be affected by the earlier EOC that occurs when using both of the tested fuel blends in comparison with D100. Temperature of the exhaust gas (Fig. 11), that affects the temperature of the turbocharger, was higher when using both of the blended fuels at all measured engine loads in comparison with D100. This can be explained by higher oxygen content for both of blended fuels, especially for R20D80. Gad et al. (2018) also found higher exhaust gas temperature when using 20% blend of palm oil in diesel fuel caused by poor combustion characteristics of the blend. Lower speed and higher temperature of the turbocharger means less mass of air in the cylinder with higher temperature. Also, temperature of the intake air and other ambient conditions affects to some extent the temperature of charge in the cylinder. The ambient temperature variations between individual measurement points were very small, the ambient temperature for D100 was approx. 24.03 °C, for R5D95 approx. 25.58 °C and for R20D80 approx. 26.64 °C.
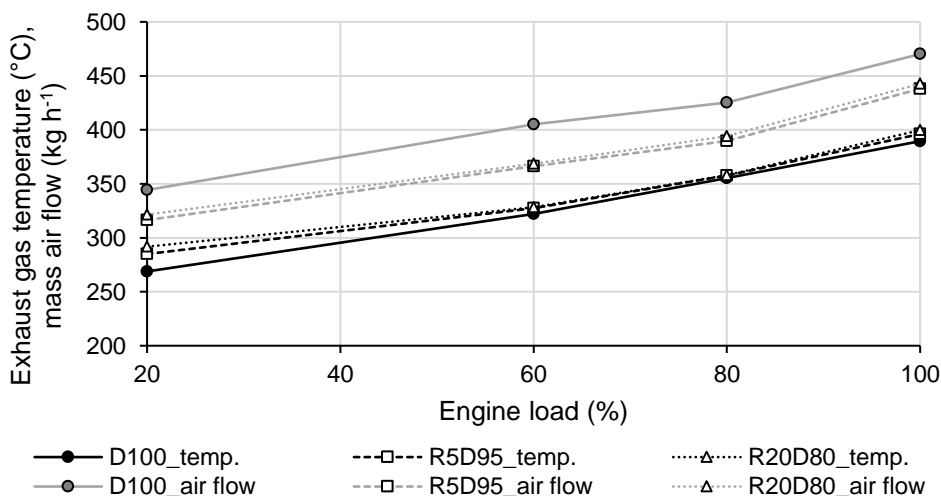
Figure 11. Ignition delay and temperature of charge at SOI for all tested fuels at all measured points.

In Figs 2, 4, 6 and 8 the lower pressure during compression stroke (approx. from -80°CA to -20°CA) can be seen. This may be caused by different kinetic energy of exhaust gas. The lower kinetic energy of exhaust gas causes the lower speed of turbocharger and lower mass of charge. This is confirmed by the mass air flow (Fig. 11), which was lower when using both the blended fuels in comparison with D100 at all measured points. Also, from the Figs 3, 5, 7 and 9 it is evident, that during the combustion the R5D95 and R20D80 released lower amount heat than D100 at all measurement points. However, lower amount of intake air takes lower energy during the compression stroke, so that during the whole cycle, the engine produced similar amount of indicated work, as can be seen in Fig. 12. In the case of R5D95 the maximum difference of indicated work in comparison with D100 was 1.27%, in the case of R20D80 the maximum difference was 4.46%.
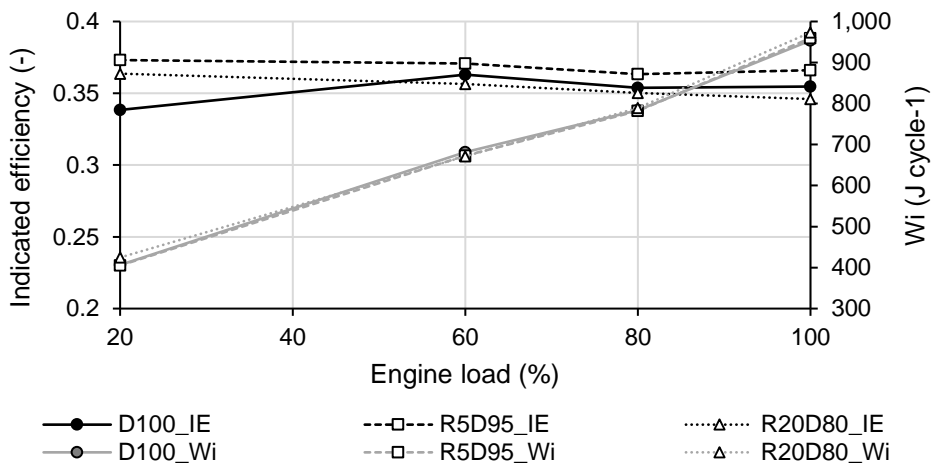
Figure 12. Indicated efficiency and indicatd work per cycle for all tested fuels at all measured points.
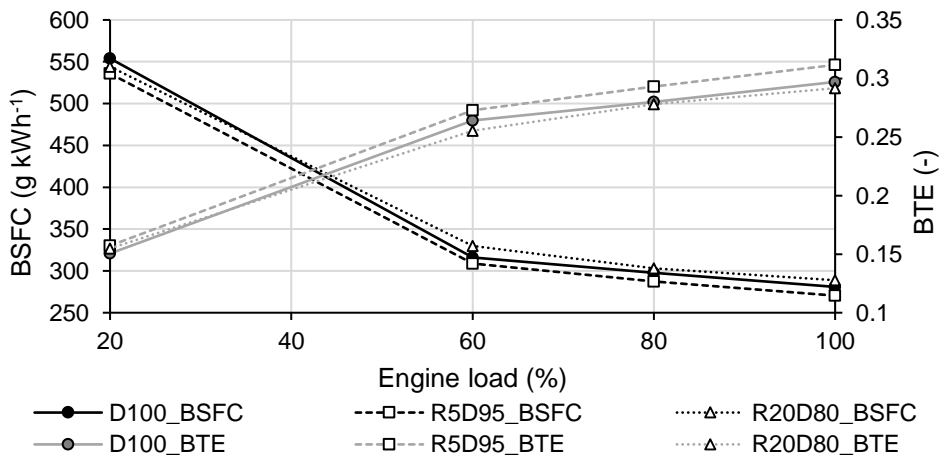
Figure 13. Barke specific fuel consumpton and brake thermal efficiency for all tested fuels at all measured points.

Indicated efficiency of the engine at all measurement points for all tested fuels is shown in Fig. 12, BTE and BSFC are shown in Fig. 13. It is evident that fuel blend R5D95 showed the highest indicated efficiency and BTE and the lowest BSFC. R5D95 fuel blend reached the best results in terms of utilization of chemical energy, given in the fuel. This may be caused by increased oxygen content in the fuel in comparison with D100 in combination with fuel properties closer to diesel fuel than in case of R20D80. Rakopoulos et al. (2011) also found increased BTE and even decreased BSFC when using sunflower oil-diesel fuel and corn oil-diesel fuel blends in comparison with diesel fuel.

CONCLUSIONS

The article is focused on comparison of combustion characteristics and engine efficiency of CI engine, operated on rapeseed oil-diesel fuel blends in comparison with neat diesel fuel. From the results of the measurement following results were made:

- Lower cylinder pressure during compression and expansion stroke was found for both of tested fuel blends in comparison with diesel fuel. Statistically significant decrease of peak cylinder pressure was found at all loads for both of the fuel blends. This may be caused by lower calorific value in combination with lower mass air flow.

- Earlier EOC was found and combustion duration was decreased for both of tested fuel blends in comparison with diesel fuel. As a result, lower heat was released during combustion.

- Despite the lower heat, released during combustion, indicated work was comparable in all measurement points for all fuels. This is a result of lower mass air flow, which may be caused by different kinetic energy and temperature of exhaust gas, which affects the turbocharger. Lower mass of air in the cylinder then consume less energy during compression stroke.

- Ignition delay was shorter using the blended fuels in all measured loads in comparison with the diesel fuel. The fuel, containing 20% rapeseed oil reached the shortest ID in 3 out of 4 measured loads. The cause may be higher temperature of charge when using biofuels in combination with physical and chemical properties of rapeseed oil.

- In comparison with diesel fuel the indicated efficiency and BTE was considerably increased while BSFC was slightly decreased using fuel blend with 5% of rapeseed oil. On the contrary, 20% blend of rapeseed oil caused increase of BSFC and slight decrease of BTE and indicated efficiency.

From the obtained results it is evident that from the viewpoint of combustion characteristics and engine efficiency, the fuel with 5% rapeseed oil showed the best results from the tested fuels since the fuel blend and its combustion are closer to the diesel fuel than blend with 20% rapeseed oil, while higher amount of oxygen contributes to higher engine efficiency in comparison with diesel.

Research in the field of biofuels is still very important. In present time the large development of electric mobility is reflected only in some areas. In many areas the utilization of current electric drive technologies is absolutely impossible. Agriculture is one of these important areas. In agriculture it is very interesting to explore the

possibilities of using various products of plant and livestock production as a fuel to power machinery and equipment. Even a few percent of biofuel in the diesel fuel could significantly contribute to cleaner environment and fulfilment of internationally binding agreements.

REFERENCES

Agarwal, D. & Kumar Agarwal, A. 2007. Performance and emissions characteristics of Jatropha oil (preheated and blends) in a direct injection compression ignition engine. *Applied Thermal Engineering* **27**, 2314–2323.

Agarwal, A.K. & Rajamanoharan, K. 2008. Experimental investigations of performance and emissions of Karanja oil and its blends in a single cylinder agricultural diesel engine. *Fuel* **86**, 106–112.

Aldhaidhawi, M., Chiriac, R. & Badescu, V. 2017. Ignition delay, combustion and emission characteristics of Diesel engine fueled with rapeseed biodiesel – A literature review. *Renewable and Sustainable Energy Reviews* **73**, 178–186.

Babu, V., Murthy, M. & Rao, A.P. 2017. Butanol and pentanol: The promising biofuels for CI engines – A review. *Renewable and Sustainable Energy Reviews* **78**, 1068–1088.

Bajpai, S., Sahoo, P.K. & Das, L.M. 2008. Feasibility of blending karanja vegetable oil in petro-diesel and utilization in a direct injection diesel engine. *Fuel* **88**, 705–711.

Birzietis, G., Pirs, V., Dukulis, I. & Gailis, M. 2017. Effect of commercial diesel fuel and hydrotreated vegetable oil blend on automobile performance. *Agronomy Research* **15**(S1), 964–970

Cisek, J. & Szlachta, Z. 2001. Correlation between autoignition delay and cetane number of rape fuels at varied diesel engine work conditions. *Journal of Kones. Combustion Engines* **8**(1–2), 110–115.

ČSN DIN 51900-1. Testing of solid and liquid fuels - Determination of the gross calorific value by the bomb calorimeter and calculation of the net calorific value - Part 1: General information, basic equipment and method. 2014.

ČSN DIN 51900-2. Testing of solid and liquid fuels - Determination of the gross calorific value by the bomb calorimeter and calculation of the net calorific value - Part 2: Method using isoperibol or static jacket calorimeter. 2014.

Dabi, M. & Saha, U.K. 2019. Application potential of vegetable oils as alternative to diesel fuels in compression ignition engines: A review. *Journal of the Energy Institute*. Article in press

De Almeida, S.C.A., Rodrigues Belchior, C., Nascimento, M.V.G., Dos, L., Vieira, S.R. & Fleury, G. 2002. Performance of a diesel generator fuelled with palm oil. *Fuel* **81**, 2097–2102.

Devan, P. K. & Mahalakshmi, N.V 2008. Performance, emission and combustion characteristics of poon oil and its diesel blends in a DI diesel engine. *Fuel* **88**, 861–867.

Elango, T. & Senthilkumar, T. 2011. Performance and emission characteristics of CI engine fuelled with non edible vegetable oil and diesel blends. *Journal of Engineering Science and Technology* **6**(2), 252–262.

EN 590 Automotive fuels. Diesel. Requirements and test methods. 2013

Esteban, B., Riba, J.-R., Baquero, G., Rius, A. & Puig, R. 2012. Temperature dependence of density and viscosity of vegetable oils. *Biomass and Bioenergy* **42**, 164–171.

Franco, Z. & Nguyen, Q.D. 2011. Flow properties of vegetable oil-diesel fuel blends. *Fuel* **90**, 838–843.

Gad, M.S., El-Araby, R., Abed, K.A., El-Ibiari, N.N., El Morsi, A.K. & El-Diwani, G.I. 2018. Performance and emissions characteristics of C.I. engine fueled with palm oil/palm oil methyl ester blended with diesel fuel. *Egyptian Journal of Petroleum* **27**, 215–219.

Gailis, M., Rudzitis, J., Kreicbergs, J. & Zalcmanis, G. 2017. Experimental analysis of hydrotreated vegetable oil (HVO) and commercial diesel fuel blend characteristics using modified CFR engine, *Agronomy Research* **15**(4), pp. 1582–1601.

Garnier, J., Le Noë, J., Marescaux, A., Sanz-Cobena, A., Lassaletta, L., Silvestre, M., Thieu, V. & Billen, G. 2019. Long-term changes in greenhouse gas emissions from French agriculture and livestock (1852-2014): From traditional agriculture to conventional intensive systems. *Science of the Total Environment* **660**, 1486–1501.

Hebbal, O.D., Reddy, K.V., Rajagopal, C.A. Assistant, K. & Doddappa, P. 2006. Performance characteristics of a diesel engine with deccan hemp oil. *Fuel* **85**, 2187–2194.

Heywood, J.B. 1988. Internal Combustion Engine Fundamentals. McGraw-Hill, London, 930 pp. ISBN 0-07-028637-X.

How, H.G., Masjuki, H.H., Kalam, M.A. & Teoh, Y.H. 2018. Influence of injection timing and split injection strategies on performance, emissions, and combustion characteristics of diesel engine fueled with biodiesel blended fuels. *Fuel* **213**, 106–114.

Hsiao, M.-C., Hou, S.-S., Kuo, J.-Y. & Hsieh, P.-H. 2018. Optimized Conversion of Waste Cooking Oil to Biodiesel Using Calcium Methoxide as Catalyst under Homogenizer System Conditions. *Energies* **11**(10), art. no. 2622.

Imtenan, S., Masjuki, H., Varman, M., Rizwanul Fattah, I., Sajjad, H. & Arbab, M. 2015. Effect of n-butanol and diethyl ether as oxygenated additives on combustion-emission-performance characteristics of a multiple cylinder diesel engine fuelled with diesel-jatropha biodiesel blend. *Energy Conversion and Management* **94**, 84–94.

Jindra, P., Kotek, M., Mařík, J. & Vojtíšek, M. 2016. Effect of different biofuels to particulate matters production. *Agronomy Research* **14**(3), 783–789.

Kim, J.-K., Jeon, C.-H., Lee, H. W., Park, Y.-K., Min, K.-I., Hwang, I.-H. & Kim, Y.-M. 2018 'Effect of Accelerated High Temperature on Oxidation and Polymerization of Biodiesel from Vegetable Oils. *Energies* **11**(12), art. no. 3514.

Koder, A., Schwanzer, P., Zacherl, F., Rabl, H.-P., Mayer, W., Gruber, G. & Dotzer, T. 2018. Combustion and emission characteristics of a 2.2L common-rail diesel engine fueled with jatropha oil, soybean oil, and diesel fuel at various EGR-rates. *Fuel* **228**, 23–29.

Masjuki, H.H., Kalam, M.A., Maleque, M.A., Kubo, A. & Nonaka, T. 2001. Performance, emissions and wear characteristics of an indirect injection diesel engine using coconut oil blended fuel. In: *Proceedings of the Institution of Mechanical Engineers, Part D: Journal of Automobile Engineering* **215**(3), 393–404.

Mat, S.C., Idroas, M. Y., Hamid, M.F. & Zainal, Z.A. 2018a. Performance and emissions of straight vegetable oils and its blends as a fuel in diesel engine: A review. *Renewable and Sustainable Energy Reviews* **82**, 808–823.

Mat, S.C., Idroas, M.Y., Teoh, Y.H. & Hamid, M.F. 2018b. Physicochemical, Performance, Combustion and Emission Characteristics of Melaleuca Cajuputi Oil-Refined Palm Oil Hybrid Biofuel Blend. *Energies* **11**(11), art. no. 3146.

Nwafor, O.M.I. 2003. The effect of elevated fuel inlet temperature on performance of diesel engine running on neat vegetable oil at constant speed conditions. *Renewable Energy* **28**, 171–181.

Ozsezen, A.N., Canakci, M. & Sayin, C. 2008. Effects of Biodiesel from Used Frying Palm Oil on the Performance, Injection, and Combustion Characteristics of an Indirect Injection Diesel Engine. *Energy & Fuels*, **22**(2), 1297–1305.

Patel, C., Lee, S., Tiwari, N., Kumar Agarwal, A., Lee, C.S. & Park, S. 2016. Spray characterization, combustion, noise and vibrations investigations of Jatropha biodiesel fuelled genset engine. *Fuel* **185**, 410–420.

Pexa, M., Čedík, J. & Pražan, R. 2016. Smoke and NOx emissions of combustion engine using biofuels. *Agronomy Research* **14**(2), 547–555.

Pexa, M., Mařík, J., Čedík, J., Aleš, Z. & Valášek, P. 2014. Mixture of oil and diesel as fuel for internal combustion engine. In: *2nd International Conference on Materials, Transportation and Environmental Engineering*. CMTEE, Kunming, pp. 1197–1200.

Pradhan, P., Raheman, H. & Padhee, D. 2014. Combustion and performance of a diesel engine with preheated Jatropha curcas oil using waste heat from exhaust gas. *Fuel* **115**, 527–533.

Pramanik, K. 2003. Properties and use of jatropha curcas oil and diesel fuel blends in compression ignition engine. *Renewable Energy* **28**, 239–248.

Rakopoulos, C.D., Antonopoulos, K.A. & Rakopoulos, D.C. 2005. Multi-zone modeling of Diesel engine fuel spray development with vegetable oil, bio-diesel or Diesel fuels. *Energy Conversion and Management* **47**, 1550–1573

Rakopoulos, C.D., Antonopoulos, K.A., Rakopoulos, D.C., Hountalas, D.T. & Giakoumis, E.G. 2006. Comparative performance and emissions study of a direct injection Diesel engine using blends of Diesel fuel with vegetable oils or bio-diesels of various origins. *Energy conversion and management* **47**, 3272–3287.

Rakopoulos, D.C., Rakopoulos, C.D., Giakoumis, E.G., Dimaratos, A.M. & Founti, M.A. 2011. Comparative environmental behavior of bus engine operating on blends of diesel fuel with four straight vegetable oils of Greek origin: Sunflower, cottonseed, corn and olive. *Fuel* **90**, 3439–3446.

Sanli, H. 2018. An experimental investigation on the usage of waste frying oil-diesel fuel blends with low viscosity in a Common Rail DI-diesel engine. *Fuel* **222**, 434–443.

Sirviö, K., Niemi, S., Help, R., Heikkilä, S. & Hiltunen, E. 2018. Kinematic viscosity studies for medium-speed CI engine fuel blends. *Agronomy Research* **16**(S1), 1247–1256.

Shah, P.R. & Ganesh, A. 2016. A comparative study on influence of fuel additives with edible and non-edible vegetable oil based on fuel characterization and engine characteristics of diesel engine. *Applied Thermal Engineering* **102**, 800–812.

Shah, P.R., Gaitonde, U.N. & Ganesh, A. 2018. Influence of soy-lecithin as bio-additive with straight vegetable oil on CI engine characteristics. *Renewable Energy* **115**, 685–696

Varde, K.S. 1984. Bulk modulus of vegetable oil-diesel fuel blends. *Fuel* **63**(5), 713–715.

Yilmaz, N. & Morton, B. 2011. Effects of preheating vegetable oils on performance and emission characteristics of two diesel engines. *Biomass and Bioenergy* **35**(5), 2028–2033.

Zahan, K.A. & Kano, M. 2018. Biodiesel Production from Palm Oil, Its By-Products, and Mill Effluent: A Review. *Energies* **11**(8), art. no. 2132.

Zhang, L., Pang, J., Chen, X., Lu, Z. & Gan, J. 2019. Carbon emissions, energy consumption and economic growth: Evidence from the agricultural sector of China's main grain-producing areas. *Science of the Total Environment* **665**, 1017–1025.

Selenium in nanosized form as an alternative to microfertilizers

O. Chernikova[1], Yu. Mazhayskiy[1] and L. Ampleeva[2]

[1]Academy of law management of the federal penal service of Russia, Sennaya street 1, RU390036 Ryazan, Russia
[2]Ryazan State Agrotechnological University named after P.A. Kostychev, Kostycheva street 1, RU390044 Ryazan, Russia
*Correspondence: chernikova_olga@inbox.ru

Annotation. Nowadays, it is an obvious fact that it is necessary to look for new approaches to agriculture, which would ensure the maximum reduction in the dependence of the volumes and quality of the crop on external factors. The use of nanopreparations in crop production is the most promising. The development of new technologies and techniques using nanomaterials, which would ensure high yields and quality of potato products, is relevant and has great practical importance. The research in recent years has established the important role of selenium in the regulation of plant activity.The purpose of this work was to research the effect of selenium nanoparticles and selenium in the form of micronutrient fertilizers on early-maturing varieties of potatoes for table use: adaptive capacity and nutritional value. Selenium nanopowder in the form of a solution contained the optimum nanoselenium concentration applied–0.13 g per hectare seeding rate. The potato tubers were soaked in distilled water 30 minutes before seeding. The treatment of potato tubers with selenium micronutrient, the dose of which amounted to 400 g per 1 hectare, was also carried out before planting. The soil preparation and agrotechnology cultivation generally accepted in the Ryazan region.The research results showed that presowing treatment of potato tubers with selenium nanopreparation had the most favorable effect on the adaptive capacity of plants (heat resistance, water-holding properties), as well as on yield increase, than treatment of tubers with selenium in the form of microfertilizer. The use of Se nanoparticles leads to an increase in the protein and vitamin C content. The Udacha potato variety showed great responsiveness to the entering of various forms of selenium in comparison with others. The use of selenium in the form of microfertilizer leads to an increase in the accumulation of starch and dry matter. These figures were the highest in potato tubers of the Zhukovskiy Ranniy variety.

Key words: selenium, nanoparticles, microfertilizer, potatoes, water-holding capacity, heat resistance, yield, starch, dry matter, protein, vitamin C.

INTRODUCTION

The volume of modern food production is constantly increasing, and therefore, the development of agriculture should be based on the achievements of modern science, that ensures the population's need for environmentally friendly and safe food, the main objectives of which are aimed at: protection of human life and health, preventing actions that mislead acquirers (consumers), environmental protection.

However, the quality of the products obtained depends not only on the feedstock, but also on the production conditions. For this, it is necessary to apply environmentally friendly methods, without using the hormones, antibiotics, genetically modified ingredients and other heterogenous agents (Pavlov, 2002).

A promising activity direction in crop production is the search and development of techniques that could increase the yield of cultivated plants without increasing the rates of fertilizer application, and also improve the quality of agricultural products. One of these directions is the transition to technologies that contribute to optimizing the plant nutrition with microelements and stimulants of their growth and development in accordance with the biological requirements of crops, to the strategy of integrated and differentiated use of genetic, soil, climatic and technological factors. Adaptive intensification of agriculture requires the widespread use of methods of biological correction, which includes the foliar nutrition with growth stimulants.

Microelements, which are part of a number of hormones, enzymes and vitamins, are directly involved in metabolic processes. An acute deficiency or excess of microelements leads to the appearance of many plant diseases (Mishin, 1991).

Recently, an interest has recently increased in the most important microelement - selenium, which, as vitamins A, C and E, is a part of the antioxidant-antiradical body defense system.

Most regions of Russia, as well as neighboring countries, are characterized by a low content of selenium in the environment.

Products of plant origin, in which selenium is contained in the most accessible form of selenmethionine, are the main ways of selenium entering the body.

It is established that selenium belongs to conditionally necessary microelements of nutrition of plants, however, it participates in their metabolic processes. Due to the proximity of ionic radii, selenium is capable of replacing sulfur in sulfides, and seleno-organic compounds are similar to sulfur. In case of excessive content in soil, selenium can have a toxic effect on plants (Gromova, 2004).

The use of inorganic forms of selenium (selenite- and selenite- ions) can cause negative phenomena associated with their high toxicity. That predetermines the search for other selenium derivatives.

The nanosized selenium in contrast to ionic forms is less toxic, and also has an increased bioavailability, it not only prevents, but also stops the development of malignant tumors. It is shown that selenium is involved in the chlorophyll production, the synthesis of tricarboxylic acids, as well as in the metabolism of high molecular weight fatty acids. It is a part of a number of redox enzymes alone or together with iron and molybdenum as a cofactor (Vapirov et al., 2000).

Thus, nanoparticles, in contrast to ionic forms, have a prolonged effect and are less toxic. These properties help to increase the absorption of mineral substance, carbohydrate metabolism, cell respiration and photosynthesis.

The production of environmentally friendly products and healthy food has recently become one of the priorities of the industry. The high-quality raw materials are the basis in this process.

One of the most important crops of versatile use is potatoes. The tubers of this plant contain on average 25% of dry matter, including 14–22% of starch and about 2% of protein. The particular importance in human nutrition is also due to the content of the most important components: vitamins and minerals. The potatoes, having also a fairly

high potential of the content of ascorbic acid and especially valuable substances - antioxidants (carotenoids, anthocyanins), can have an important role in the prevention of a number of diseases. As a result, it is one of the most valuable products in the healthy human diet (Anisimov, 2006). All listed above, as well as high taste qualities, determine the high feed and nutritional value of potatoes.

The purpose of this work was to research the effect of various forms of selenium on early-maturing varieties of potatoes for table use: its adaptive capacity, yield and nutritional value.

MATERIALS AND METHODS

The following varieties of potatoes were chosen as objects of the research: Bryanskiy ranniy, Zhukovskiy ranniy, Udacha. This choice was due to the fact that all of the above listed varieties are early-maturing, for table use, with good taste, the tolerance region is Central, with a marketable average yield of 400 c ha^{-1}.

The Bryanskiy ranniy variety is a light-beige tuber, oval-rounded, the flesh is white. The eyeholes are small. The corolla is red-purple. The commodity yield is of 300–470 c ha^{-1}. The marketability is 90–93%. The weight of the grocery-ware tuber is 84–108 g.

The Zhukovskiy ranniy variety is a plant of medium height, semi-spreading. The leaf is small, green, glossy. The flowering is long, with medium intensity. The corolla is red-purple. The tubers are pink, the flesh is white. The eyeholes are small and red. The marketability is 90–92%. The commodity yield is of 400–450 c ha^{-1}. The weight of the grocery-ware tuber is 100–120 g.

The Udacha variety is a plant of medium height, semi-spreading. The leaves are dark green, with large lobes. The corolla is white. The tuber is light-beige. The eyeholes are small. The flesh is white. The commodity yield is of 300–500 c ha^{-1}. The marketability is 96%. The weight of the grocery-ware tuber is 120–250 g (Potato variety ..., 2013) (Fig. 1).

Figure 1. Potato varieties: 1. Bryanskiy ranniy; 2. Zhukovskiy ranniy; 3. Udacha.

The research was conducted in soil culture in 3–time replication in 2017. The parameters of agrochemical indicators of sod–podzolic soil are the following: humus – 1.47%; pH – 5.8; N_{total} – 0.100%; P_2O_5 – 18.7 mg per 100 g; K_2O – 9.8 mg per 100 g.

In the experiments, selenium was used in nanoform, as well as sodium selenite in the form of Voshchenko No. 3 microfertilizer (composition: zeolite 99%, sodium selenite 1%). Nanoparticles produced at the Moscow Institute of Steel and Alloys, the size of selenium nanoparticles was in the range of 4–8 nm. Selenium nanopowder (NP Se) in the form of a solution contained the optimal concentration of nanoselenium– 0.13 g per hectare seeding rate. The tubers of potatoes were soaked in distilled water 30 minutes before sowing (Ampleeva & Chernikova, 2018). The treatment with selenium

microfertilizer, a dose of which was 400 g per 1 hectare, of potato tubers was also carried out before planting. (Table 1). The soil preparation and agrotechnology cultivation generally accepted in the Ryazan region (Dospekhov, 1985).

Table 1. The layout of the experiment

No.	Variant names, selenium doses	Abbreviations in tables
1	Control – without the use of selenium	Control
2	Voshchenko No.3 – selenium dose 400 g ha^{-1}	V No.3/400
3	Selenium nanopreparation – dose of 0.13 g ha^{-1}	NP–Se/0.13

The water–holding capacity, which characterizes the ability of colloids to retain water, was determined by the amount of water loss in the time interval of 20–40–60 minutes and expressed in % of the initial wet weight.

The heat resistance was estimated by the lethal temperature of the leaves kept in a water bath at different temperatures (Viktorov, 1983).

The protein content in potatoes was determined using biuret reagent and photoelectric colorimeter. The biuret method is based on the ability of protein solutions to give a violet color when interacting with a copper sulfate solution in an alkaline condition. The intensity of the color is proportional to the protein concentration in the solution.

The determination of starch content in potato tubers was carried out by the polarimetric method by its hydrolysis with a hydrochloric acid solution (Novokshanova, 2009).

The amount of ascorbic acid was determined by the 'Murri' method. The method is based on the transfer of ascorbic acid into a solution and on the ability to reduce it in an acidic environment 2.6–dichlorophenolindophenol sodium–to leucoform, while ascorbic acid is oxidized to dehydroascorbic acid. The reaction is due to the ascorbate oxidase enzyme. It should be noted that the higher the ascorbic acid content, the higher the activity of the ascorbate oxidase enzyme.

RESULTS AND DISCUSSION

The research conducted over past decades shows that biotic and abiotic factors causing excessive oxidative loads on plants limit the attainment of high stable yields of good quality.

One of the most important components of plant activity is water metabolism. The maintenance of a certain level of water balance in cells and tissues is a prerequisite not only for normal growth and development of plants, but also their resistance to environmental factors.

Under the conditions of increasing man-made load on the soil and periodically occurring droughts, it is of undoubted scientific and practical interest to study the effect of microelements on adaptive capacity and increasing the plant resistance.

The main function of selenium in plants is to participate in the construction of glutathione peroxidase–an enzyme of antioxidant protection of the plant organism from the action of free radicals produced from oxidative stress (Vikhreva et al., 2012).

The role of selenium in the implementation of the adaptation capacity of plants in case of insufficient water supply is associated with an increase in the resistance of the photosynthetic apparatus of agricultural plants. Selenium increases the leaf life,

improving the efficiency of the leaf apparatus, and also contributes to better supply of maturing grains with nutrients. This reduces the specific surface density of the leaves, that indicates a more economical use of assimilates on the formation of the leaf surface and a decrease in the negative effect of drought (Seregina, 2011). In addition, a partial replacement of sulfur by selenium in ferrodoxils of chloroplasts was revealed, so that it can be assumed that selenium is involved in chlorophyll formation.

The results show that the use of various forms of selenium reduced water loss, that increased the water-holding capacity of plants (Table 2). In this case, the greatest effect was observed when using NP Se. Compared to the control, the water loss decreased by 6% in the Bryanskiy ranniy and Udacha potato varieties, and by 7% in Zhukovskiy ranniy.

As a rule, the water content of the leaves increases by 2–6% during using selenium, that leads to an increase in the plants resistance during a short–term soil drought through an increase in the water-absorbing function of the root.

Table 2. The effect of Se various forms on the water–holding capacity of potato leaves

Water loss, % of the initial weight	Control	V No. 3/400	NP-Se / 0.13
Bryanskiy ranniy	9	5	3
Zhukovskiy ranniy	9	4	2
Udacha	8	4	2

An important characteristic of the adaptation capacity of plants is heat resistance. The heat resistance is one of the indicators of drought resistance, reflecting the ability of plants to withstand high air and soil temperatures. The temperature above 40 °C is unfavorable for most plants in the temperate zone and cause the plant to die in case of prolonged exposure (Arestova, 2000). The higher plants do not tolerate positive temperatures above 51 °C for 10 minutes (Scherbakov, 1962).

The degree of heat resistance of leaves can be judged by the time at which pheophytin stains appear, and also by the degree of leaves turning brown, i.e. destruction of chlorophyll. If the leaf is exposed to high temperature and then immersed in a diluted solution of hydrochloric acid, so the damaged and dead cells turn brown due to the free penetration of acid, which will cause the conversion of chlorophyll to pheophytin, while the intact cells remain green, into cells.

The adaptive properties of selenium appeared when it was applied as a microfertilizer, and when it was used as a nanoform (Table 3).

However, NP Se had a much better impact on this indicator. Thus, the number of

Table 3. The heat resistance of potato leaves

Heat resistance, the number of pheophytin stains	Control	V No. 3/400	NP-Se / 0.13
Bryanskiy ranniy	12	10	5
Zhukovskiy ranniy	12	10	5
Udacha	11	9	4

pheophytin stains on potato leaves decreased by 7 in comparison with the control. In the variant where Voshchenko No. 3 microfertilizer was used on the leaves of the Bryanskiy ranniy and Zhukovskiy ranniy varieties –by 5, on the leaves of the Udacha variety–by 2.

Puzina & Tsukanova (2008) have shown that the weight of potato tubers increased by 15–17% with using the selenium. The obtained data may be due to the antioxidant effect of selenium on plants, the mechanism of which is due to the functioning of proteins which active center contains 'selenium amino acids'.
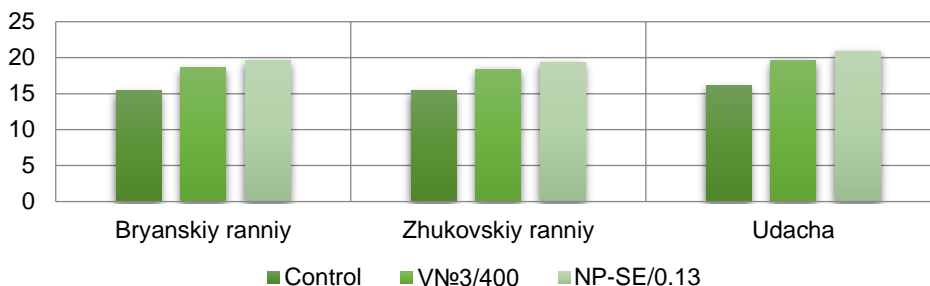
The presowing treatment of potato tubers with selenium microfertilizer and NP Se had a different effect on the potatoes yield (Table 4). It should be noted that, in

comparison with the control variant, the use of selenium made it possible to increase this indicator in two other variants.

Table 4. The effect of Se on the yield of potatoes

No.	Yield (t ha^{-1})	Control	V No. 3/400	NP-Se / 0.13
1	Bryanskiy ranniy	15.4	18.6	19.6
2	Zhukovskiy ranniy	15.4	18.4	19.4
3	Udacha	16.1	19.6	20.9

The analysis of the obtained data showed that the maximum yield increase was observed in variant with the use of NP Se (Fig. 2). Thus, the yield of Bryanskiy ranniy variety increased by 27%, Zhukovskiy ranniy variety–by 26%, Udacha–by 30%.

Figure 2. The effect of presowing treatment of potato seeds with various forms of selenium on the yield (t ha^{-1}).

Biochemical characteristics of tubers depend mainly on the genotype of the variety, however, the conditions of cultivation, the ratio and doses of fertilizers, the use of various preparations can significantly change their content, which affects not only the taste of tubers, but also the quality of the processed products.

The potato protein is highly nutritious and is superior to many other crops, contains almost all the essential amino acids and is equal to animal proteins, approximately to casein. It is contained more in the early varieties than in the late ones. The potato protein has genetic information and biological activity. The potato varieties that contain an increased amount of protein are the most viable, due to the fact that they are more resistant to pathogens (Shanina & Dubinin, 2015).

From the data in Table 5 it can be noted that the use of NP Se and selenium in the form of microfertilizer led to an increase in the protein content in all variants of the experiment. However, the largest increase in

Table 5. The protein content in the wet weight of potato tubers

Protein, %	Control	VNo.3/400	NP-Se / 0.13
Bryanskiy ranniy	2.85	3.2	4.4
Zhukovskiy ranniy	2.77	2.95	4.2
Udacha	2.98	3.08	5

this component was due to the use of selenium in the form of nanoparticles. Thus, the protein content in potato tubers of the Bryanskiy ranniy variety increased by 35.2%, in Zhukovskiy ranniy by – 34.0%, and in Udacha by – 40.4%, compared with the control.

The starch is the main component of potatoes and widely used in the food industry as a thickener. At the same time, the structure and the taste of potatoes depends on its

quantity. The starch consists of digestible and indigestible components. The last one, resistant starch is an important element for the intestinal microflora (Anisimov, 2006). The resistant starch inhibits carcinogenesis like other ballast substances, especially in the rectum.

Se nanoparticles and selenium in the form of microfertilizers had a positive effect on starch accumulation and dry matter content in all variants of the experiment (Table 6). It should be noted that the use of the Voshchenko No. 3 preparation increased these figures more than the use of NP Se. There is an inverse relationship between the protein and starch content in plants. The higher the protein content, the lower the starch content. Probably, when using selenium in nanoscale form and in the form of Voshchenko No. 3 microfertilizer, this tendency appeared.

Table 6. The content of starch and dry matter, %

Experiment variant	Bryanskiy ranniy		Zhukovskiy ranniy		Udacha	
	Starch	Dry matter	Starch	Dry matter	Starch	Dry matter
Control	14.5	23.1	14.1	22.5	16.0	23.4
VNo.3/400	20.1	24.3	22.0	26.2	21.7	25.6
NP-Se /0.13	18.3	24.1	17.9	24.8	16.6	23.8

Thus, in potato tubers of the Bryanskiy ranniy variety, the starch content increased by 27.86%, and the dry matter content–by 4.94%; of the Zhukovskiy ranniy variety–by 35.90% and 14.12%; of the Udacha variety–by 26.27% and 8.59%, respectively, compared with the control variant of the experiment.

The potatoes contain a whole range of vitamins that are good for humans, especially water-soluble ones, but their amount in tubers is a subject to large fluctuations. The relatively high content of vitamin C, as a natural source of ascorbic acid, has the particular importance.

Table 7. The content of vitamin C in the wet weight of potato tubers

Vitamin C mg, %	Control	VNo.3/400	NP–Se / 0.13
Bryanskiy ranniy	12.3	15.2	37.2
Zhukovskiy ranniy	12.8	15.9	39.4
Udacha	14.0	16.3	50.1

The use of selenium in the form of microfertilizers and in the form of nanoparticles led to an increase in the content of this substance in potato tubers of all varieties compared with the control variant of the experiment (Table 7). However, the greatest effect occurred during using NP Se.

Thus, the amount of vitamin C in the Bryanskiy ranniy variety increased by 66.9%, in the Zhukovskiy ranniy–by 67.5%, and in Udacha variety tubers–by 72.0%, in relation to the control.

If we compare the increase in this figure with selenium microfertilizer, then the increase occurred in the variety Bryanskiy ranniy by 59.1%, Zhukovskiy ranniy–by 59.6%, Udacha–by 67.5%, in comparison with the use of NP Se.

CONCLUSIONS

The obtained data allow concluding that the presowing treatment of potato tubers with selenium nanopreparation has the most favorable effect on the adaptation

properties: heat resistance, water–holding capacity, and also yield increase, than the treatment of tubers with Voschenko No.3 microfertilizer. The Udacha potato variety showed great responsiveness to the application of various forms of selenium in comparison with the Bryanskiy ranniy and Zhukovskiy ranniy varieties.

A comparative analysis of various forms of selenium revealed that the use of Se nanoparticles led to an increase in protein and vitamin C, and in this case Udacha variety was the most responsive. The use of selenium in the form of micronutrients led to an increase in the accumulation of starch and dry matter. These figures were the highest in potato tubers of the Zhukovskiy ranniy variety.

REFERENCES

Ampleeva, L.E. & Chernikova, O.V. 2018. The influence of various forms of selenium on the yield and quality of early varieties of potatoes. *Innovative scientific and educational support of the agro-industrial complex: materials of the 69th International Scientific and Practical Conference*. Publishing House of RSATU named after P.A. Kostychev. Ryazan, pp. 9–13 (in Russian).

Anisimov, B.V. 2006. The nutritional value of potatoes and its role in human healthy diet. *Potatoes and vegetables* **4**, 9–10 (in Russian).

Arestova, E.A. 2000. The enrichment of dendroflora of arid regions of the south-east by entering the introducents of the Sorbus L genus and Aronia L genus (on the example of the Saratov region). *PhD Thesis*, MarSTU, Yoshkar-Ola, 199 pp. (in Russian).

Dospekhov, B.A. 1985. *Methods of field experience (with the basics of statistical processing of the research results)*. Kolos, Moscow, 351 pp. (in Russian).

Gromova, O.A. 2004. Caution – Selenium! *The sustenance* **7**, pp. 15 (in Russian).

Mishin, P.Ya. 1991. *Microelements in the soil of the Orenburg region and the effectiveness of microfertilizers.* South–Ural publishing house, Chelyabinsk, 92 pp. (in Russian).

Novokshanova, A.L. 2009. *Laboratory workshop on organic, biological, physical and colloidal chemistry: a learning guide*. GIORD, St. Petersburg, 224 pp. (in Russian).

Pavlov, G.V. 2002. The use of ultra-dispersive powders in agriculture *Achievement of science and technology in the agro-industrial complex* **3**, 3–8 (in Russian).

Potato varieties cultivated in Russia. 2013. Reference book. Agrospas, Moscow, 144 pp. (in Russian).

Puzina, T.I. & Tsukanova, M.A. 2008. The effect of soil drought on the hormonal and antioxidant Solanum tuberosum system, depending on the treatment with selenite. *The scientific notes of Oryol State University* **2**, 51–56 (in Russian).

Seregina, I.I. 2011. The influence of the nitrogen nutrition conditions, water availability and the use of selenium on the photosynthetic activity of plants of different varieties of spring wheat. *Agrochemistry* **7**, 17–25 (in Russian).

Shanina, E.P. & Dubinin, S.V. 2015. The nutritional value of potato protein. *Potatoes and vegetables* **3**, 29–31 (in Russian).

Shcherbakov, B.I. 1962. On the issue of the heat resistance of plants. Materials on the introduction and acclimatization of plants. *Proceedings of the Institute of Botany of the Academy of Sciences of the KazSSR* **14**, 191–213 (in Russian).

Vapirov, V.V., Shubina, M.E. & Vapirova, N.V. 2000. Selenium. *Some aspects of chemistry, ecology and participation in the development of pathology* (*review)*. Petrozavodsk, 68 pp. (in Russian).

Vikhreva, V.A., Blinokhvatov, A.A. & Kleimenova, T.V. 2012. *Selenium in plant life*. RIO PGSHA, Penza, 222 pp. (in Russian).

Viktorov, D.P. 1983. *A small workshop on plant physiology*. High school., Moscow, 136 pp. (in Russian).

Autonomous photovoltaic system for night-time lighting in the stable

M-Q. Dang, J. Šafránková[*], M. Libra, V. Poulek, P. Kouřím and J. Sedláček

Czech University of Life Sciences Prague, Kamycka 129, CZ16521 Prague, Czech Republic
[*]Correspondence: janicka.safrankova@gmail.com

Abstract: Autonomous photovoltaic (PV) systems are suitable, for example, for powering various appliances or scientific instruments in the field, for automatic data collection, for signaling, etc. At the Czech University of Life Sciences Prague, we have designed an experimental autonomous PV system designed for night-time lighting for orientating in a stable for horses. The article describes the construction of a PV system with a PV panel rated at 170 Wp, with a lead-acid accumulator and a 1.5 W LED light source. The data collection was automated. The data evaluation shows that during the whole year, the PV system has been recharged and there was no lighting failure. The paper also presents important measured characteristics.

Key words: photovoltaics, off-grid PV system, LED.

INTRODUCTION

Autonomous photovoltaic (PV) systems are typically built in places where they are far away from the grid and the cost of networking would be higher than the cost of energy storage. Autonomous PV systems can also be designed because we require their independence from the grid. They are suitable, for example, for powering various appliances or scientific instruments in the field, for automatic data collection, signaling, etc. (see Bakos & Soursos, 2002; Axaopoulos & Theodoridis, 2009; Ghafoor & Munir, 2015; Wang et al., 2017). Their use is extended in settlements or camps without an electrical grid connection. We have dealt with the construction of autonomous PV systems and their inclusion in the automation structure earlier, see eg Kouřím et al., 2015.

Previously, it was used to power a classic light bulb. However, these have little energy conversion efficiency to visible radiation (about n = 3%), and therefore the batteries have been discharged very quickly. Halogen lamps or discharge lamps have been more efficient, but today the most economical and therefore the most commonly used are light emitting diode (LED) semiconductor sources. They work on the principle of the radiative electron passage between energy levels in the band pattern of energy levels in the semiconductor. For yellow LEDs, the efficiency reaches up to n = 40%. For white light emitting diodes, the efficiency is no more than n = 30%, because the white light is achieved by the fact that the semiconductor chip gives light in the blue area of the spectrum, and by means of the luminophores, part of the photons are convertedinto

photons with less energy in other areas of the visible spectrum. The resulting radiation color is then white. In addition, the LED light source has a lifetime of about 50,000 hours, but the classic bulb has a lifetime of only about 1,000 hours. The serial production of LED light sources has also lowered their cost, which has also been positively influenced by their expansion, see, for example (Sastry et al., 2010; Das et al., 2015).

Lately, we have seen more and more autonomous PV systems designed for illumination. E.g. Fig. 1 shows an autonomous PV system designed for street illumination in Shanghai. As a light sources, low-pressure sodium discharge lamps were used there. In this article we will describe the design and results of testing our experimental autonomous PV system for night-time illumination in a horse stable. A larger PV system for street lighting has been described, for example, in the work (Liu, 2014).

Figure 1. Autonomous PV system for street illumination in Shanghai.

A comparison of European sites in terms of the amount of energy produced in PV panels was given, for example, in works (Libra et al., 2016; Olšan et al., 2018) and data monitoring from PV systems was concerned with work (Beránek et al., 2018).

MATERIALS AND METHODS

At the Czech University of life Sciences in Prague, we designed an experimental autonomous PV system designed for night-time lighting in the horse stable. This PV system was then installed in a stable in Panenske Brezany near Prague. The position is approximately 50.2° north latitude and 14.4° east longitude. The outside of the PV system consists of a monocrystalline silicon PV panel with nominal power Pmax = 170 W, see Fig. 2. Inside the building there is s a lead-acid battery Tesla (12 V, 45 Ah) and MPPT solar charge controller) (see Fig. 3). The Solar charge controller itself controls the lighting of the light source at dusk and at dawn. When the battery is fully charged, it gives the

Figure 2. Outer part of the PV system - PV panel.

open circui voltage about Ue = 14 V and can accumulate about Wmax = 0.5 kWh of energy. The LED light source is shown in Fig. 4, it takes power of about $P = 1.5$ W (12 V, 165 lm, 120°) and is located in a waterproof housing. Automatic data storage is provided by microcontroller ARDUINO UNO programmable platform, data is stored on the SD card. The block diagram of the PV system is in Fig. 5.

Figure 3. Lead acid accumulator with charge regulator with MPPT.
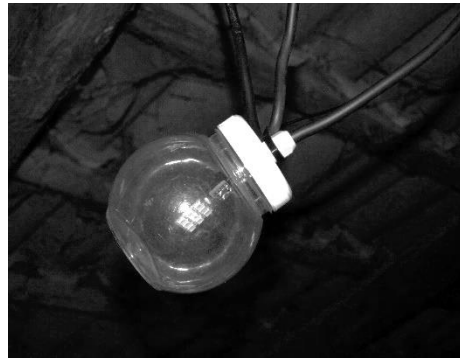
Figure 4. LED light source in the watertight case.
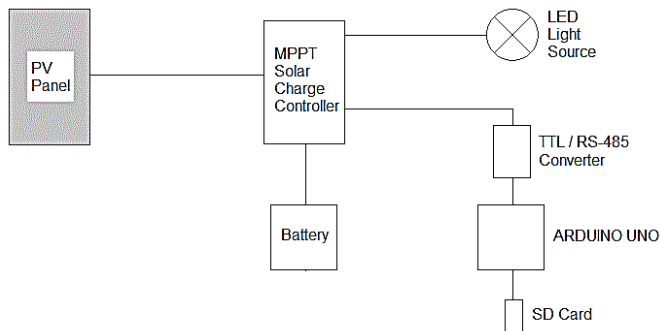
Figure 5. Block diagram of the PV system.

RESULTS AND DISCUSSION

Our PV system was put into operation in the spring of 2017 and the data storrage was started too. Based on our previous measurements and the internationally-used software of the expected amount of produced electricity in a specific PVGIS site (http://re.jrc.ec.europa.eu/pvgis/apps4/pvest.php#), we made the following estimation. Throughout the year, the PV panel is able to deliver more than $W_d > 160$ kWh of electricity. If the light is switched on for 10 hours per day, it consumes an energy of about $W_s \approx 6.5$ kWh per year. Theoretically, the PV system should be self-sufficient even if some energy losses are accounted for, mainly due to lower lead acid efficiency (efficiency about 0.4). However, it is to be expected that the winter days will be much shorter, the sun will be below the horizon, and therefore the PV panel will deliver less energy than in the summer. If the battery is fully charged, the extra energy cannot accumulate, and the charging unit further charges the battery only with a maintenance current which compensates self-discharge. Therefore, it has to be verified whether the PV system is sufficient to recharge the battery during the entire winter time. The system is optimised for good performance in December. During December the electric energy production is approximately 5 kWh (PVGIS 2018) and the system's energy consumption is approximately 0.8 kWh (efficiency about 0.4). Long-term data monitoring has shown that our autonomous PV system is truly self-sufficient throughout the year.
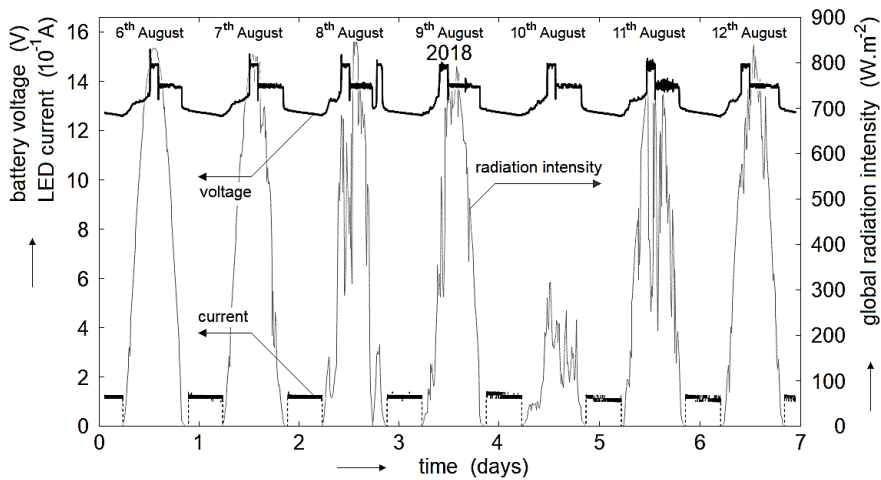
Figure 6. Time dependence of the battery voltage, LED current and global radiation intensity during the selected summer days.

In Fig. 6, battery voltage, light source current, and global radiation intensity (on a horizontal surface) over time are selected over several selected summer sunny days. It can be seen that every day in the afternoon, the battery is fully recharged and recharged only by the maintenance current, which corresponds to a constant value of the open circuit voltage of approx. U = 14 V. In the evening when the light source is switched on, the voltage dropped slightly, according to Kirchhoff laws and slowly discharge during lightning.
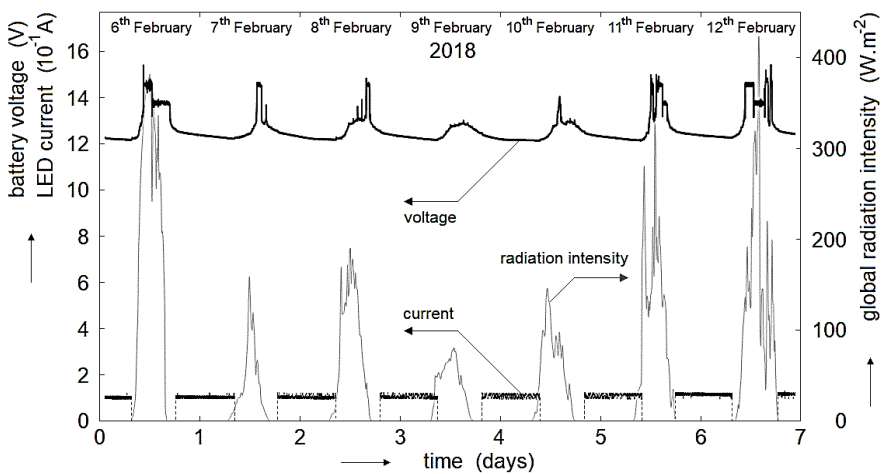
Figure 7. Time dependence of the battery voltage, LED current and global radiation intensity during the selected winter days.

Fig. 7 shows similar dependence for several selected winter days. Days with cloudy weather were selected. It can be seen that even if there were shorter days in winter and low radiation intensity, there was no failure in the function of the device. Even though the battery was not fully charged in some days, it still worked reliably.

CONCLUSION

We have designed the autonomous PV system for lighting. The installation was completed in the summer of 2017 and immediately began its testing and data collection. The evaluation of the annual traffic data showed that the PV system was self-sufficient all year round. It was even able to recharge the battery in the winter at the shortest days and several consecutive days with low global radiation intensity.

Our PV system has proven itself well for night-time lighting in the stable. The low light intensity of the light source does not interfere with the night's peace, but it allows orientation of people in the stable.

We will collect and evaluate the data further and we will monitor whether the parameters will change over a longer period of operation. We assume that due to the aging of the lead-acid battery, it may show a decrease in its capacity over several years.

The system is not very economical if it is very close to the electric grid (less than 100 m). The main advantage is the independence on the electric grid. On the other hand, the system is economical when it is located more than 1000 m from the electric grid.

REFERENCES

Axaopoulos, P.J. & Theodoridis, M.P., 2009. Design and experimental performance of a PV Ice-maker without battery. *Solar Energy* **83**, 1360–1369.

Bakos, G.C. & Soursos, M. 2002. Techno-economic assessment of a stand-alone PV/hybrid installation for low-cost electrification of a tourist resort in Greece. *Applied Energy* **73**, 183–193.

Beránek, V., Olšan, T., Libra, M., Poulek, V., Sedláček, J., Dang, M.Q. & Tyukhov, I.I. 2018. New Monitoring System for Photovoltaic Power Plants' Management. *Energies* **11**, article ID 2495.

Das, N., Pal, N. & Pradip, S.K. 2015. Economic cost analysis of LED over HPS flood lights for an efficient exterior lighting design using solar PV. *Building and Environment* **89**, 380–392.

Ghafoor, A. & Munir, A. 2015. Design and economics analysis of an off-grid PVsystem for household electrification. *Renewable and Sustainable Energy Reviews* **42**, 496–502.

Kouřím, P., Libra, M. & Poulek, V. 2015. Off-grid photovoltaic system for illumination. *Research in Agricultural Engineering* **61**(3), 106–110.

Libra, M., Olšan, T., Avramov, V. & Poulek, V. 2016. Low degradation of a-Si solar panels of the building integrated PV power plant in Prague historical area. *Agronomy Research* **14**(4), 1386–1394.

Liu, G. 2014. Sustainable feasibility of solar photovoltaic powered street lighting systems. *Electrical Power and Energy Systems* **56**, 168–174.

Olšan, T., Soucase, B.M. & Libra, M. 2018. Comparison of predicted and real parameters of PV systems in the Czech Republic and Spain. *Agronomy Research* **16**(S1), 1150–1158.

PVGIS. Photovoltaic Geographical Information System-Interactive Maps. Available online: http://re.jrc.ec.europa.eu/pvgis/apps4/pvest.php# (accessed on 4 November 2018).

Sastry, O.S., Kamala Devi, V., Pant, P.C., Prasad, G. & Rajesh Kumar, Bibek Bandyopadhyay. 2010. Development of white LED based PV lighting systems. *Solar Energy Materials & Solar Cells* **94**, 1430–1433.

Wang, D., Hu, L., Liu, Y. & Liu, J. 2017. Performance of off-grid photovoltaic cooling system with two-stage energy storage combining battery and cold water tank. *Energy Procedia* **132**, 574–579.

Suitability of 2.4 GHz and 5 GHz wireless communications in production processes

J. Hart[*] and J. Bradna

Czech University of Life Sciences Prague, Faculty of Engineering, Department of Technological Equipment of Buildings, Kamýcká 129, CZ165 00 Prague, Czech Republic
[*]Correspondence: janhart77@gmail.com

Abstract. Today, it is increasingly modern to use wireless transmissions in production. It is possible to send information messages, control messages and it is often possible to access the technologies as IoT (the Internet of Things). The aim of this work was to find out which of the selected Wi-Fi frequencies is more suitable for use in syrup processing equipment. The evaluation was performed on the basis of attenuation and download speed at each frequency (2.4 GHz and 5 GHz bandwidth). These frequencies have been chosen due to their massive deployment for wi-fi networks that currently dominate wireless communications. Measurements were made downloading files on different frequency bands. Mean and maximum data throughput and signal strengths were also measured. By measuring, it has been found that when using 2.4 GHz wireless Wi-Fi technology, you can very often encounter strong interference effects. Despite the theoretically worse 5 GHz frequency spread, you can achieve up to 30% better data throughput on average. The results show the suitability of 2.4 and 5 GHz Wi-Fi technology. The main finding is that, despite the worse frequency spread of 5 GHz, it is more appropriate. Not only due to speed but also in the future due to better transmission capacities and future channel expansion.

Key words: wireless communication, wi-fi, production processes, IoT, frequency, data.

INTRODUCTION

Today, it is increasingly modern to use wireless transmissions in production. Many companies are switching to wireless systems with the expectation of helping them save money by eliminating cabling costs. These are companies that have frequent changes in interiors. They may also be companies with flexible workstation locations. As a rule, these are large shops with furniture, warehouses, factories, etc. The most common non-license radio bands are 433, 450, 869, 2,400 and 5,000 MHz (these bands are called ISM). However, ensuring secure and reliable wireless transmission in industrial objects is very complex at these frequencies. (Kamerman & Aben, 2000; Kuchta et al., 2009; Lee, 2017; Zheng et al., 2018)

ISM bands (industrial, scientific and medical) are radio broadcasting bands. They are free, which means that licensed (approved) devices are allowed to operate without license fees, but without any guarantee of interference. These frequencies may collide with another broadcast, so the sent message may not be complete. Another issue is their

real impact and the speed of data transmission in the rugged space (Huang et al., 2005; Kuchta et al., 2009; Lee, 2017; Cena et al., 2018; Zheng et al., 2018).

Wi-fi technologies are currently massively deployed to create LAN networks. These LAN networks serve both industrial and domestic applications. For this reason, the tests focused on the 2.4 GHz and 5 GHz bands. These frequencies were chosen for the applicability of results in the syrup processing facility (Kamerman & Aben, 2000; Hart & Hartová, 2017; Ismaiel et al., 2018; Marčev & Kotek, 2018).

The aim of this work was to find out which of the selected wi-fi frequencies is more suitable for use in syrup processing equipment. The evaluation was performed on the basis of attenuation and download speed at each frequency. Measurements were made at the user's direct request.

MATERIALS AND METHODS

Tests which were performed accurately determined strength of the wireless signal and download speed of wi-fi in production facilities. The equipment used in these tests is as follows:

Testing devices
− **Edimax BR-6288ACL** (Rev. A Firmware 1.12)
  - wi-fi router
  - has technology for transmission at 2.4 and 5 GHz
  - has a 100Mbit transmission rate
  - easy-to-use 2-way wireless router with iQ Setup
  - 5in1 (Router, Access Point, Range Extender, Wi-Fi Bridge and WISP)
  - 802.11ac support, 2.4 or 5 GHz frequency bands
  - 1x 10/100 Mbps WAN / LAN combined port (RJ-45)
− **Lenovo Y700-15ISK (80NV00BKCK)**
  - portable computer
  - has technology for transmission at 2.4 and 5 GHz

Software
− **Scilab 5.5.2**
  - an application for sorting measured data from logs
− **LAN Speed Test 3.5.0**
  - wireless data transfer measurement software
  - measuring tool for output data when measuring data transmissions
− **Wi-fi Analyzer 3.10.5-L**
  - an auxiliary application for measuring the signal strength
− **Plotly**
  - additional data processing
  - creation of heat maps
− **Autodesk Homestyler**
  - Creating a floor plan.

For measuring was syrup processing facility has been selected. This object is owned by Produkty-Vladimír s.r.o. and so far, it has no Ethernet and only 1x WAN cable is

tightened. This is the production facility of the company. A request was made for the possibilities of wi-fi technology with the possibility of its implementation in this production facility. There was a requirement to determine which of the frequencies (2.4 or 5 GHz) would be more suitable for use. Fig. 1 shows the layout of the object where the tests were performed. Measured points were displayed in this object, which were subsequently numbered for clarity.

On this plan the graphical data of measured signal strength and data throughput in the form of a heat map will be shown. All signal strength values are measured in dBm units and data rate values are measured in Mbps. At each selected point, measurement was cyclically repeated 20 times for all types of tests.

The Edimax BR-6288ACL was placed at point 20 for its maximum possible effect (in this case, point 15 could also be used). The router was built on a prepared shelf at a height of 170 cm. Devices to use the new wi-fi network are located at points 28 and 10. The inner walls of the building are made of burnt bricks with a thickness of 10 cm. The door was closed during the measurement, as is the case with the full operation of the syrup processing facility. The height of the measuring instruments from the floor was equal to 120 cm throughout the

Figure 1. Methodical location of measured points.

measurement. It was also measured at 120 cm at points 21 and 22, but below the wooden staircase. The syrup processing facility is 100 meters from the nearest building and no other Wi-Fi network interference has occurred. In the tests, the wi-fi device was used only for tests. She didn't use other devices during wi-fi tests.

RESULTS AND DISCUSSION

Fig. 2 shows the heat map of the signal strength for 2.4 GHz and 5 GHz. By comparison, it is clear that 5 GHz has a stronger signal strength at smaller distances, but 2.4 GHz has better signal propagation in the object.

Fig. 3 shows a heat map of the average download speed for 2.4 GHz and 5 GHz. Compared with the heat map of the signal strength, it is clear that even though 2.4 GHz has overall better signal coverage than 5 GHz, average data downloads do not achieve such good results. The speed / signal ratio is better for 5 GHz (Cena et al., 2018; Kamerman & Aben, 2000).
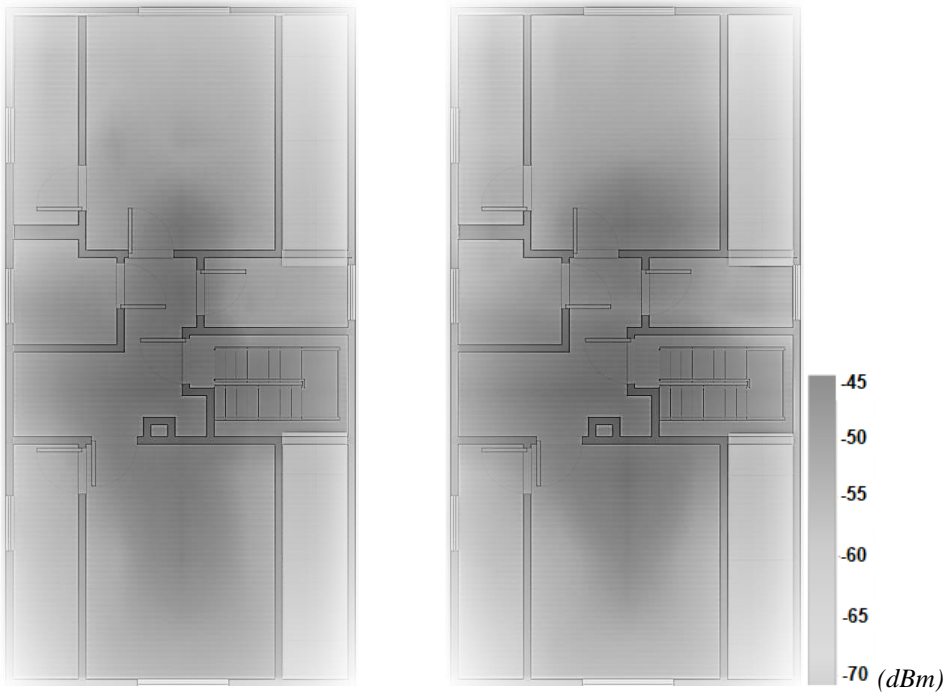
Figure 2. Wireless signal strength at frequencies of 2.4 GHz (left) and 5 GHz (right).
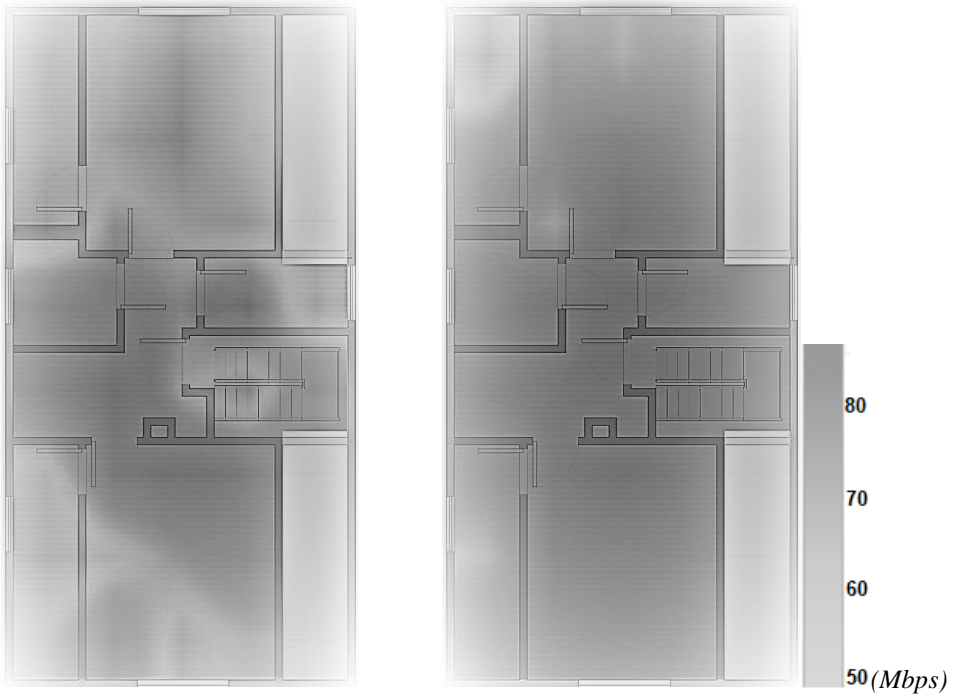
Figure 3. Data download speed on wi-fi 2.4 GHz (left) and 5 GHz (right).

Although it is quite clear at first sight that the 2.4 GHz technology has better signal propagation, this difference is on average only about 1.3 dBm better. However, it is good to say that 2.4GHz technology is at its maximum, and the channel overlay concept is not at all suitable for use in locations where there are multiple wi-fi networks. Based on these results, better 5GHz technology is therefore more appropriate and, thanks to other features, is more suitable. It can be read from the data that 5 GHz technology has an average of about 30% better speed (Kamerman & Aben, 2000; Hart & Hartová, 2018; Cena et al., 2018)

CONCLUSIONS

As is clear from the measurement results, it is more convenient to use 5 GHz technology for normal use in production areas, provided it is used in a small unobstructed space. It is also advisable to use 5 GHz if the areas in the wi-fi area are 2.4 GHz. The 5 GHz wi-fi has a higher speed, but also greater attenuation. Thus, when the connection fails, there may be a larger distance. Although 5 GHz is limited by its reach, it is much more promising in the future, with an average throughput of up to 30 % better than 2.4 GHz, even in larger areas. Recommendations for larger spaces are the use of repeaters that can distribute the signal across the entire building.

For specific use in the syrup processing facility, it is advisable to select the location of the router at centralized (points 20 or 15), which is the center of the building. In this case, it is appropriate to use the 5 GHz band, because its range from this point is sufficient. Because the wi-fi router is centrally located, it is not necessary to use a repeater. It often happens that it is necessary to download the current configuration into the wi-fi devices and to interrupt the current production. This process needs to be implemented as quickly as possible. Although data is not large (hundreds of MB), it is necessary to download it quickly. For these reasons it is better to use the 5 GHz band in this case.

REFERENCES

Cena, G., Scanzio, S. & Valenzano, A. 2018. Improving Effectiveness of Seamless Redundancy in Real Industrial Wi-Fi Networks, In: *IEEE TRANSACTIONS ON INDUSTRIAL INFORMATICS*, pp. 2095–2107.

Hart, J. & Hartová, V. 2017. QUALITY OF TRANSMISSION FOR WIFI CAMERAS NETATMO NSC01-EU, D-LINK DCS-5222L AND EDIMAX IC-7113W, In: *16th International Scientific Conference on Engineering for Rural Development*, pp. 1012–1017

Huang, C.W.P., Vaillancourt, W., Parolin, A. & Zelley, C. 2005. Low power consumption 2.4 GHz WLAN front-end module for a multiple radio handset. In: 2005 IEEE Radio Frequency Integrated Circuits (RFIC) Symposium, Digest of Papers, pp. 193–196.

Ismaiel, B., Abolhasan, M., Ni, W., Smith, D., Franklin, D. & Jamalipour, A. 2018. Analysis of Effective Capacity and Throughput of Polling-Based Device-To-Device Networks, In: *IEEE TRANSACTIONS ON VEHICULAR TECHNOLOGY*, pp. 8656–8666.

Kamerman, A. & Aben, G. 2000. Throughput performance of wireless LANs operating at 2.4 and 5 GHz, In: PIMRC 2000: *11TH IEEE INTERNATIONAL SYMPOSIUM ON PERSONAL, INDOOR AND MOBILE RADIO COMMUNICATIONS, VOLS 1 AND 2, PROCEEDINGS*, pp. 190–195.

Kuchta, R., Vrba, R. & Sulc, V. 2009. IQRF Smart Wireless Platform for Home Automation: A Case Study, In: *5th International Conference on Wireless and Mobile Communications*, Cannes, France, pp. 168–173.

Lee, I.G. 2017. Digital Pre-Distortion of Carrier Frequency Offset for Reliable Wi-Fi Enabled IoTs, In: *FUTURE INTERNET*, Art. Num. UNSP 46.

Marčev, D. & Kotek, M. 2018. Influence of the road profile in different geographical areas of the Czech Republic to the operational parameters of the electric vehicle. *Agronomy Research* **16**(S1), 1025–1031.

Zheng, Z., Cui, W.P., Qiao, L. & Guo, J.H. 2018. Performance and Power Consumption Analysis of IEEE802.11ah for Smart Grid, In: *WIRELESS COMMUNICATIONS & MOBILE COMPUTING*, Art. Num. 5286560.

Reliability of parking assistants depending on the material of detected obstacles

V. Hartová[1], M. Kotek[1], J. Hart[2] and Š. Pícha[1]

[1]Czech University of Life Sciences Prague, Faculty of Engineering, Department of Vehicles and Ground Transport, Kamýcká 129, CZ165 00 Prague, Czech Republic
[2]Czech University of Life Sciences Prague, Faculty of Engineering, Department of Technological Equipment of Buildings, Kamýcká 129, CZ165 00 Prague, Czech Republic
*Correspondence: nidlova@tf.czu.cz

Abstract. Today's modern vehicles are equipped with a range of assistance systems to enhance road safety. The standard equipment of most cars are parking assistants. It turns out that not always sensors can reliably detect the obstacle on the travel path of the vehicle. The aim of the paper is to determine the reliability of the parking sensors depending on the material of the obstacle detected. The original parking assistants of Škoda Rapid, Škoda Octavia II, and Škoda Superb have been tested in laboratory conditions using obstacles made of various materials (glass, mirror, plastic, metal, cardboard ...) located at distance of 100 cm from the vehicle. Distance values of the original sets of parking assistants were measured during the measurement from on-board diagnostic vehicle using diagnostic kit VAG-COM. The real distance was checked using a calibrated gauge. The results of the research show, that original sets of parking assistants achieve significantly more accurate results with a wider coverage of the space being scanned. Material composition of obstacles has a great influence on the reliability of parking systems. Not every material can respond properly to parking sensors.

Key words: parking sensors, assistance systems, reliability, materials.

INTRODUCTION

Assistance technologies in the automotive industry are becoming an integral part of mass-produced cars. The main reason for this is to increase the driving comfort and safety of car traffic. In particular, the second motive - safety - is an important incentive for the development of vehicle driver assistance systems. Minor accidents are most often due to driver inattention and during difficult parking situations. These types of accidents usually occur at relatively low driving speeds, but despite this, minor injuries to the crew can occur, such as whiplash injuries. However, pedestrians are much more at risk and, unfortunately, most are children who may not be registered by a parking driver due to their low body height. Although the damage and severity are usually low, these accidents represent a significant proportion of all road complications.

Different systems - laser, radar and others - can be used for assisted parking. However, sensors based on ultrasonic (US) waves are most commonly used Kidd & McCartt, 2016. The reason is their relative reliability, low cost and technical robustness.

The rear parking sensor system works by automatically switching on when the reverse gear is engaged, thus guarding the space behind them. The active part of the device sends a US signal that bounces off the obstacle and travels back to the sensor receiving area, which evaluates the quality and latency of the response. The result is returned as the distance of the car from the obstacle.

The quality and intensity of the received signal - US echo - is significantly influenced by the distance the US wave must travel from emitter to sensor. This part of the detection system is very well tested by the manufacturer, and its calibration is reliable and accurate. Virtually the only possible artificial intervention that may interfere with the result is the mechanical contamination of the sensor itself. Depending on the quality level of the system, the measuring apparatus can be equipped with back-up control systems for correct operation. The second component of the system is the reflection point for US, hence the obstacle itself. In this case, the reliability of the measurement cannot by its very nature be ensured by standard conditions, as this element is subject to changes depending on the operation of the motor vehicle (Filatov & Serykh, 2016). The detection system should therefore be primarily designed to capture as many types or qualitative variations of surfaces as possible that serve as a reflective surface for US. It can be assumed that surfaces that are homogeneous, smooth and reflect US well will be detected well. The problem, however, is obstacles whose surface is differently porous or otherwise inhomogeneous. At such a moment the US signal can pass through the obstacle, be reflected in different directions, or it can be absorbed. No signal response is returned to the target detector, which the system incorrectly evaluates as an absence of an obstacle and an accident may occur (Mazzae et al., 2008).

For this reason, it is important to also pay attention to parking sensors in terms of their reliability depending on the material of the relevant obstacle. Nowadays, these systems are assembled in most vehicles in the basic equipment, and it is therefore appropriate to verify their reliability for detection of obstacles from different types of material.

This issue can be resolved, for example, by changing the measurement method principle used to detect obstacles, such as automatic emergency braking systems that operate with radar technology in combination with a laser. However, it should be borne in mind that ultrasonic parking sensors are most often used in transport, even for parking assistants. For this reason, it is necessary to know their reliability.

MATERIALS AND METHODS

The research was carried out in the laboratory of the Department of Vehicles and Ground Transport, Faculty of Engineering, Czech University of Life Sciences Prague. Testing took place under the following laboratory conditions: 21 °C, 49% humidity and 493 lx light intensity. Three vehicles from VW group were selected for testing:
- Škoda Superb combi (model year 2018)
- Škoda Rapid (model year 2016)
- Škoda Octavia combi (model year 2004).

The distances of the individual obstacles were detected using the OBD of the VAG-COM Diagnostic System, where the immediate distance values of the obstacles from individual sensors were read by means of serial communication with the control unit of

the parking system. The actual obstacle distance was determined via a calibrated distance gauge.

Test distance of the obstacle from the vehicle of 100 cm was determined for measurement repeatability and accuracy.

The choice of material was adapted to the physical properties of US waves so that obstacles from good, moderate and minimally reflective materials are represented, and which are realistic in normal operation.

- Sheet metal (without corrosion), thickness 2 mm, manufacturer unknown
- OSB, thickness 18 mm; Egger Holzwerkstoffe Wismar GmbH & Co. KG Am Haffeld 1 23970, Wismar Deutschland
- MDF laminated particleboard (mdf), white, smooth (also laminate board); Kronospan CR, spol. s.r.o, Company ID No. 62417690 Registered office: Jihlava, Na Hranici 6
- Carton - plain smooth packaging paper cardboard
- Polystyrene - extruded polystyrene Isover EPS 100; (Divize ISOVER, Saint-Gobain Construction Products CZ a.s., Prague)
- Straight foam rubber, smooth, thickness 30 mm, manufacturer unknown
- Glass wool - Basalt wool Isover N (Divize ISOVER, Saint-Gobain Construction Products CZ a.s., Prague) (https://www.isover.cz/produkty/isover-n)
- Mirror
- Wire glass, thickness 6 mm, size ok wire mesh 10 x 10 mm
- Transparent glass thickness 3 mm, smooth
- Glass with thin wire mesh (thin wire) – window size 2 x 2 mm, wire strength 2 mm
- Glass with thick wire mesh (thick wire) – window size 30 x 30 mm; wire strength 3 mm
- Facade fabric, window size 4 x 4 mm, Vertex R 117, fibre thickness 2 mm; Saint-Gobain Construction Products CZ, Prague

The test materials were always 100 x 100 cm in size. Individual tests were performed cyclically using them. These tests were repeated 10 times for each sensor. The measurements were carried out on rear parking sensors. The test surface was placed at a constant distance from the vehicle and the distance detected by the parking assist control unit was checked against the real distance determined by the certified length gauge.

The statistical method ANOVA and Tukey's HSD test were used for statistical evaluation.

RESULTS AND DISCUSSION

As expected, problems occurred with some of the test materials in that the sensors were not able to detect them. These materials are summarized in Table 1.

These materials probably cause poor reflection of ultrasonic waves. In this case these materials was used as an obstacle in form of standing solid

Table 1. Undetected materials

Materials	Superb	Rapid	Octavia
mirror	+	-	-
straight foam rubber	+	+	+
glass wool	+	+	+

+ means undetected materials; - means detected materials.

object but some materials can be used as a clothing material. Especially glass wool can have a similar properties as many winter clothing materials. There is a possibility that it could lead to bad detect a moving person in winter clothes.

Fig. 1 show the average detected distance of individual obstacles measured on the Škoda Superb at distances of 100 cm. Parking sensors showed lower distance values than the real obstacle distance. The parking sensors had different results depending on the obstacle. The worst values were achieved by the obstacle of glass with thick wire mesh, where the sensor has detected an obstacle with a wider variance of distance and close to the nominal value of 100 cm.
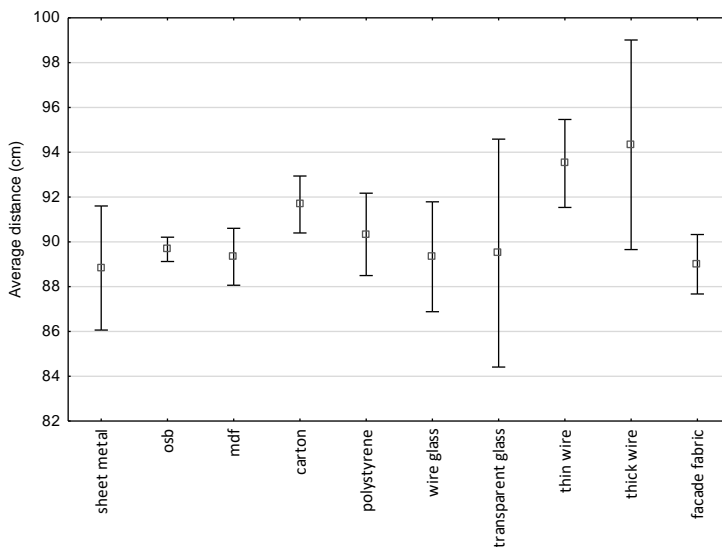
Figure 1. Measurement results for the parking sensors of the Škoda Superb vehicle at a distance of 100 cm.

Table 1 summarizes the results of distance of Skoda Superb for individual obstacles with marked out homogeneous groups calculated by Tukey's HSD test. There is evident that statistically significant difference can be seen at the obstacle of glass with thick wire mesh. Statistical analysis confirmed 2 homogeneous groups of materials with statistically significant different properties.

Fig. 2 shows the average values of distance measured on the Skoda Rapid at distances of 100 cm. The largest variance of distance were obtained at OSB obstacle. Approximately half of the obstacles

Table 1. Average distance of the obstacle and marked out homogeneous groups (*Tukey's HSD test*) on Skoda Superb

Material	Avg. distance (cm)	Homogeneous groups[1]	
sheet metal	88.83	****	
facade fabric	89.00	****	
mdf	89.33	****	
wire glass	89.33	****	
transparent glass	89.50	****	****
osb	89.67	****	****
polystyrene	90.33	****	****
carton	91.67	****	****
thin wire	93.50	****	****
thick wire	94.33		****

[1] homogeneous group symbolize the group of materials with similar properties with no statistical significant difference in measured parameter.

were detected at a distance of less than 100 cm. As a wrong detectable material can be identified the obstacle in form of wire glass, where the average detected distance exceeded the real distance by 5 cm.
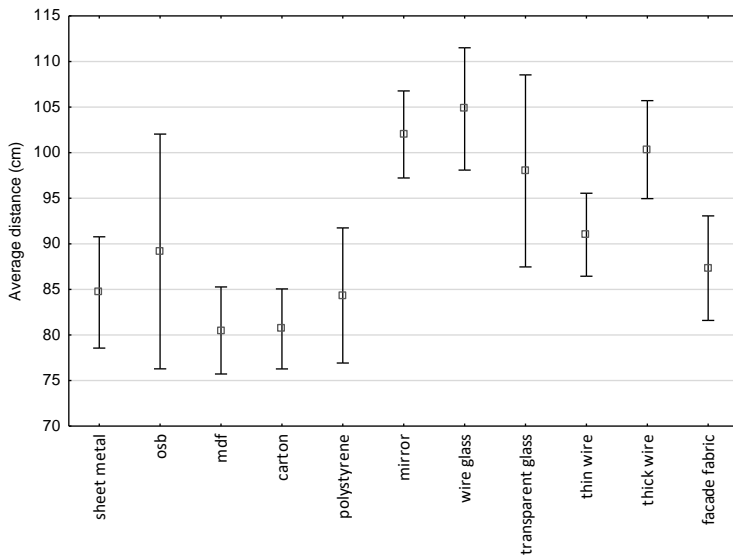
Figure 2. Measurement results for the parking sensors of the Škoda Rapid vehicle at a distance of 100 cm.

Table 2 summarizes the results of distance of Skoda Rapid for individual obstacles with marked out homogeneous groups calculated by Tukey's HSD test. There are 4 homogeneous groups of materials with statistically significant difference in dependence of detected distance.

Table 2. Average distance of the obstacle and marked out homogeneous groups (*Tukey's HSD test*) on Skoda Rapid

Material	Avg. distance (cm)	Homogeneous groups[1]			
mdf	80.50	****			
carton	80.67	****			
polystyrene	84.33	****			
sheet metal	84.67	****			
facade fabric	87.33	****	****		
osb	89.17	****	****		
thin wire	91.00	****	****	****	
transparent glass	98.00		****	****	****
thick wire	100.33		****	****	****
mirror	102.00			****	****
wire glass	104.80				****

[1] homogeneous group symbolize the group of materials with similar properties with no statistical significant difference in measured parameter.

Fig. 3 shows the average values of distance measured on the Skoda Octavia at distances of 100 cm. Compared to previously tested vehicles, in case of Skoda Octavia,

obstacles were detected predominantly in distance above 100 cm. Out of measurements it is therefore evident that the detected distance may not affected only by the material of obstacles, but also by basic settings of the parking system sensitivity. The largest variance of distance were obtained at obtacle from glass with thin wire mesh.

Figure 3. Measurement results for the parking sensors of the Škoda Octavia vehicle at a distance of 100 cm.

Table 3 summarizes the results of distance of Skoda Octavia for individual obstacles with marked out homogeneous groups calculated by Tukey's HSD test. There are 3 homogeneous groups of materials with statistically significant difference in dependence of detected distance.
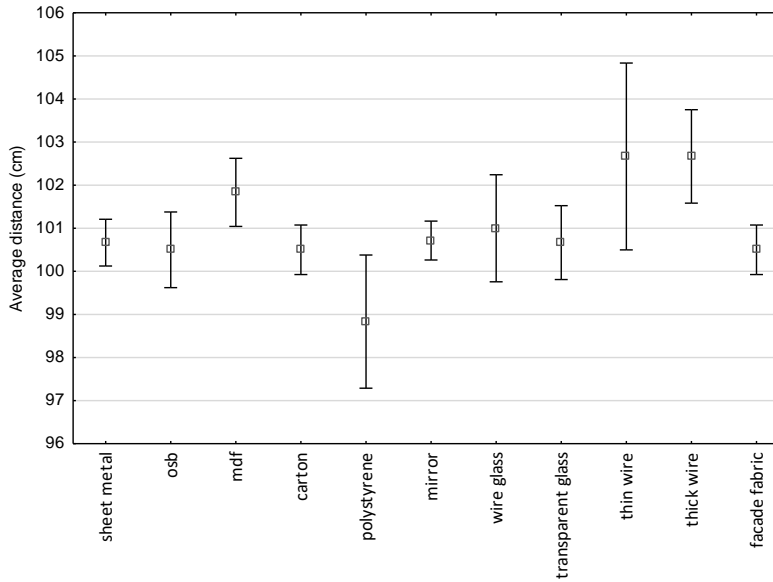
The experiments carried out shows that the most problematic in terms of detection are materials that poorly reflects ultrasound waves. In most cases, glass-containing materials have proved problematic, while homegene materials have been detected predominantly reliably.

(Cicchino, 2019) focuses on a similar problem. Cicchino deals with the evaluation of the effects of rear

Table 3. Average distance of the obstacle and marked out homogeneous groups (*Tukey's HSD test)* on Skoda Octavia

Material	Avg. distance (cm)	Homogeneous groups[1]		
polystyrene	98.83		****	
osb	100.50	****	****	
carton	100.50	****	****	
facade fabric	100.50	****	****	
transparent glass	100.67	****	****	
sheet metal	100.67	****	****	
mirror	100.71	****	****	
wire glass	101.00	****		****
mdf	101.83	****		****
thick wire	102.67			****
thin wire	102.67			****

[1] homogeneous group symbolize the group of materials with similar properties with no statistical significant difference in measured parameter.

cameras, rear parking sensors and rear automatic braking systems during accidents. Cicchino assesses the suitability of these systems compared situations where these systems are absent. On the other hand, (Nascimento et al., 2018) deals with the improvement of the reliability of parking sensors using a Bayesian Filter, but this technology has been found to be somewhat costly.

(Mazzae et al., 2008) reported that some owners turned sensor systems off because they were not reliable. Drivers who reverse too fast may also exceed the functional capabilities of sensor systems (Llaneras et al., 2011). Finally, one study found that sensor systems had difficulty detecting pedestrians, especially moving children (Mazzae et al., 2008). Kidd et al. (2015) reported the problem of preventing a collision with an unexpected stationary or moving object in the backing path.

Lee & Chang (2014) in their article Development of A Verification Method on Ultrasonic-based Perpendicular Parking Assist System it discusses that, an accurate verification method is required to develop the parking assist system because this system has a risk of crashing into other vehicles while parking. Thus, the standard test specification and parameters of the verification method are proposed to prove the system accurately. Especially, it considers the mechanism of the parking system and risk points of sensors on the system sufficiently.

Authors (Cui et al., 2013) talk about ultrasonic array based obstacle detection in automatic parking. An ultrasonic array for automatic parking is designed and accomplished in this paper. The details of software and hardware of the system were presented in the article, and the system was validated in a refitted vehicle by automatic parking. The detection result of the ultrasonic array was contrast with that of LADAR. The system showed the advantages in the robust, economy, environments irrespective, and easy to widely application.

Another paper (Park et al, 2008) deals with parking space detection by using ultrasonic sensor. Using the multiple echo function, the accuracy of edge detection was increased. It can scan parking space more accurately in real parking environment. It was propose the diagonal sensor to get information about the side of parking space.

The results of our measurements can help to improve the system developed by the team (Hosur et al, 2016), which focused on to locate objects in the vicinity of moving and/or stationary vehicles using ultrasonic sensors. The around view system proposed here is based on distance calculation between the object and the vehicle. It is a supporting technology that assists drivers in parking and driving the vehicle more easily by giving a better understanding of the environment around vehicle. The proposed system, makes use of twelve ultrasonic sensors to cover 360 degrees of the vehicle. That means three ultrasonic sensor are used to cover one side of the vehicle with 180 degrees.

CONCLUSIONS

It is clear from the measured values that not every material is detectable by this technology, which uses ultrasonic waves to detect obstacles. Ultrasound waves are reflected from an obstacle, and if this obstacle is made from non-homogeneous material or material unable to repel ultrasound waves, this obstacle detection technology may be very unreliable. If we neglect the consequences of a minor accident in the form of damage to a vehicle or public space, this weakness may be very significant in the detection of pedestrians, especially children. Especially glass wool can have a similar

properties as many winter clothing materials and therefore there is potential danger that some materials covering human body can led to poor detection of pedestrians.

The most problematic materials were foam, mirror, thin wire, glass wool and reinforcement mesh, which were not detected at all. With regard to glossy materials, there was poor reflection and distortion of the retransmission of the transmitted signal.

Out of measurements it is also evident that the detected distance may not affected only by the material of obstacles, but also by basic settings of the parking system.

REFERENCES

Cicchino, J.B. 2019. Real-world effects of rear automatic braking and other backing assistance systems, *Journal of Safety Research* **68**, pp. 41–47.

Cui, H.H., Song, J.Z. & Liu, D.X. 2013, Ultrasonic Array Based Obstacle Detection in Automatic Parking. In: *Proceedings of 2013 Chinese Intelligent Automation Conference*, Yangzhou, China, pp.129–140.

Filatov, D.M. & Serykh, E.V. 2016. Intellegence autonomous parking control system of four-wheeled vehicle. In: *19th International Conference on Soft Computing and Measurements*, Saint Petersburg Electrotechnical University, pp. 102–107.

Hosur, P., Shettar, R.B. & Potdar, M. 2016. Environmental Awareness Around Vehicle Using Ultrasonic Sensors. In: *International Conference on Advances in Computing, Communications and Informatics*. ICACCI, Jaipur, India, pp. 1154–1159.

Kidd, D.B., Hagoski, B.K., Tucker, T.G. & Chiang, D.P. 2015, Effects of a rearview camera, parking sensor system, and the technologies combined on preventing a collision with an unexpected stationary or moving object, *Hum. Factors* **57**(4), pp. 1–26.

Kidd, D.G. & McCartt, A.T. 2016. Differences in glance behavior between drivers using a rearview camera, parking sensor system, both technologies, or no technology during low-speed parking maneuvers. *Accident Analysis & Prevention* **87**, pp. 92–101.

Lee, Y. & Chang, S. 2014. Development of a verification method on ultrasonic-based perpendicular parking assist system. In: *18th IEEE International Symposium on Consumer Electronics*, ISCE, South Korea, pp. 1–3.

Llaneras, R.E., Neurauter, M.L. & Green, C.A. 2011. Factors moderating the effectiveness of rear vision systems: what performance-shaping factors contribute to drivers' detection and response to unexpected in-path obstacles when backing. In*: SAE 2011 World Congress & Exhibition* (Paper No. 2011-01-0549), Society of Automotive Engineers, Warrendale, pp. 689–700.

Lubecke, B.O. 2016. *Doppler Radar Physiological Sensing*, 1. US: John Wiley & Sons Inc., ISBN 9781119078418.

Mazzae, E.N., Barickman, F., Baldwin, G.H.S. & Ranney, T. 2008. On-road Study of Drivers' Use of Rearview Video Systems, National Highway Traffic Safety Administration, Washington DC, pp. 1–140.

Nascimento, A.M., Cugnasca, P.S., Vismari, L.F., Junior, J.B. & De Almeida, J.R. 2018, Enhancing the Accuracy of Parking Assistant Sensors with Bayesian Filter, In: *IEEE International Conference on Vehicular Electronics and Safety*, Madrid; Spain, pp. 1–6.

Park, WJ., Kim, B.S., Seo, D.E., Kim, D.S. & Lee, K.H. 2008, Parking Space Detection Using Ultrasonic Sensor in Parking Assistance System. In: *IEEE Intelligent Vehicles Symposium*, Eindhoven, Netherlands, pp. 1039–1044.

Effect of long-term operation of combustion engine running on n-butanol – rapeseed oil – diesel fuel blend

M. Holúbek[*], M. Pexa, J. Čedík and D. Mader

Czech University of Life Sciences Prague, Faculty of Engineering, Department for Quality and Dependability of Machines, Kamýcká 129, CZ165 21, Prague 6, Czech Republic
[*]Correspondence: holubekm@tf.czu.cz

Abstract. The short time use of biofuels in compression ignition engines is being studied by many authors. However, in many cases the real long–term operation of the engine on biofuels may cause problems. The article deals with the operation parameters of the combustion engine, fuelled by n-butanol – rapeseed oil – diesel fuel blend, during 70 hours operation in total. Two brand new diesel power generators Kipor KDE 6500 with output power of 4.6 kW were used for certain testing. The first generator was operated on 100% diesel fuel and it was used as a reference and the second generator was operated on experimental fuel containing 10% n-butanol – 20% rapeseed oil – 70% diesel fuel blend. The generators were equipped with single cylinder compression ignition engine Kipor KM 186 with the rated power of 5.7 kW. For the first 10 operating hours approx. 40% load was applied. Then, the generators worked for another 60 operating hours with approx. 70% load. The harmful emissions, smoke, fuel consumption and the amount of produced particles were also measured after 10 hours run-in period and then after another 60 hours of operation. Consequently, the results were compared. Measurements were carried out at gradually increasing electric power output, approx. 14%, 28%, 42%, 56%, 68%, 82% and 95% (in results can be found in Watts). Emission analyser and opacimeter BrainBee and Engine Exhaust Particle Sizer TSI were used for the measurements. The results showed increased production of emission of the engine running on fuel blend after 70 hours of operation. On the other hand, engine which operated on standard diesel reached lower fuel consumption. After 70 hours the blended fuel tended to produce more particles in comparison with diesel fuel.

Key words: emissions, fuel consumption, biofuels, power generator, particles, opacimeter.

INTRODUCTION

In order to reduce the use of diesel and its negative impact on the environment, renewable energy sources have been receiving much attention in recent years (Saadabadi et al., 2019). Utilisation of biofuel for internal combustion engines is gaining importance in the global energy policy, on the way to reduction of our dependency on fossil fuels. The most harmful products of diesel combustion engines are particles, smoke emissions and nitrogen oxides (Doğan, 2011; Pexa et al., 2016). The biomass based fuels can offer a feasible solution to the world's dependence on petroleum–based fuels and can provide advantages, such as environmental protection

and sustainability. Biofuels are almost free from sulphur, continually produced from vegetable matter and have low toxicity (Atmanli et al., 2015; Killol et al., 2019).

N-butanol is a promising next generation alternative fuel for stabilizing diesel fuel–vegetable oil blends at low temperatures. N-butanol represents a better alternative fuel than ethanol and methanol (lower alcohols). N-butanol is also a bio-origin renewable fuel that can be produced by alcoholic fermentation of biomass (Jin et al., 2011).

In comparison with other biofuels, butanol has a lower auto–ignition temperature, it is less evaporative and releases more energy per unit of mass. It also has a higher cetane number, higher energy content and better lubricating ability than ethanol and methanol. Butanol is less corrosive and better miscible with vegetable oils, diesel, etc. (Szwaja & Naber, 2010; Hönig et al., 2014; Peterka et al., 2016).

Butanol's chemical properties are closer to diesel fuel than to lower alcohols. Lower alcohols cause a longer ignition delay period of combustion because of their higher latent heat of vaporization and low ability to ignite (Mařík et al., 2014). Moreover, n-butanol shows appropriate combustion characteristics in diesel engines. Usage of n-butanol demands neither a cetane enhancing additive nor a solubilizer due to its relatively high cetane number, high solubility and no phase separation in diesel fuel (Siwale et al., 2013; Atmanli et al., 2015).

Vegetable oils, such as rapeseed oil, may be used in several ways while the modification of fuel or the fuel system is mostly required. Raw vegetable oil can be added into the diesel oil in ratio 20% oil and 80% diesel and it can be burned without modification of the engine (Pexa et al., 2015). The main advantage of using purified rapeseed oil is primarily its low price. The extraction and processing of vegetable oils are simple low energy processes that support agricultural production (Altin et al., 2001).

Vegetable oils are also degradable, renewable and they have positive energy balance. However it is necessary to respect the diversity of vegetable oil properties compared to diesel (heat of combustion, cetane number, freezing point, etc.) (Hönig & Hromadko, 2014). Due to their high viscosity and thickening in cold conditions, vegetable oil fuels still have problems with low flowing, atomization and heavy particle emissions. Maximum power and torque decrease due to a lower energy content of triacylglycerols (Kleinová et al., 2011). Vegetable oil blend may reduce unburned hydrocarbon and CO emissions. Effect on emission of NOx and particle matter and fuel consumption is less clear and appears to be dependent on test conditions (Gailis et al., 2017).

Although there are several valuable works concerning n-butanol–gasoline blended fuels in combustion engines, there is limited information of combustion characteristics over a range of blends of *n*-butanol and diesel including vegetable oils.

The aim of this paper was to compare fuel consumption and production of emissions of two generators when operating on blended fuel (containing 10% of n-butanol, 20% of rapeseed oil and 70% of diesel) and standard diesel as a reference in the same type of engine, operated with around 70% of its nominal load. Different effect of fuels on combustion engine was observed. The harmful emissions and fuel consumption were monitored after 10 and 70 hours of operation.

MATERIALS AND METHODS

For the experiment two mobile generators Kipor KDE 6500E were used (Fig. 1). Specifications of the generator are listed in Table 1. One generator was running on fossil diesel fuel with no bio-components and the second generator was running on biofuel blend. For the first 10 operating hours (run-in period) the generators were loaded by 2 kW (40%) according to the recommendation from the manufacturer. Then, the generators were loaded with approx. 3.2 kW (70% of the nominal output power) for 60 operating hours. During the long-term operation the generators were running for 70 operating hours. The rotation speeds of engines of generators were set by the build-in regulator and it should be kept constant at approx. 3,000 rpm. The build-in regulator was not modified.

The short-time measurements were performed after the first 10 operating hours and then after 70 operating hours. The measurements were performed at stable conditions (at least 2 minutes stabilization at each point) with gradually increasing loads, approx. 14%, 28%, 42%, 56%, 68%, 82% and 95%. After engine stabilization the measured parameters were recorded for approx. 1 minute. The engine was loaded using electrical heaters. The heaters have a scale with a step of approx. 650W and does not have specified accuracy of consumed power. The output electrical power (current, voltage and frequency) was measured using the electrometer ZPA ED310 equipped with an RS 485 (accuracy 0.05%).

For the mass fuel consumption measurement was used the standard precision scale Vibra AJ 6200 (accuracy 0.1 g, readability 0.01 g).

Figure 1. Generator Kipor KDE 6500E.

Table 1. Basic specification of generator Kipor KDE 6500E

Electrical parameters	
Parameter	Specification
Manufacturer	Kipor
Type	KDE 6500E
Rated power	4,600 W
Output voltage	220 V
Output frequency	50 Hz
Output current	19.6 A
Engine parameters	
Parameter	Specification
Manufacturer	Kipor
Type	KM 186FAG
Rated power	5.7 kW at 3,000 min^{-1}
Max. torque	18.7 Nm at 2,880 min^{-1}
Engine type	4-stroke, compression ignition
Displacement	418 cm^3
Cooling	Air cooled
Bore X Stroke	86 X 72 mm
Compression ratio	19:1
Valves	2
Valve mechanism	OHV
Lubrication	Combined
Crankshaft orientation	Horizontal
Fuel system	Mechanical injection pump
Start of injection	17° BTDC ± 1°

Data from laboratory scale and electrometer were transmitted to the PC memory using RS482 to RS232 interface and for that purpose developed software application in LabView.

For measurement of harmful gaseous emission components and opacity the emission analyser BrainBee AGS 200 and opacimeter BrainBee OPA 100 (Table 2) was used. The values of opacity were converted into mass concentration using the converting table, given by manufacturer. Engine Exhaust Particle Sizer 3090 (EEPS) made by TSI Inc. was used for analyse of solid particles, produced by engine. Specification of the EEPS is listed in Table 3. Before entering the EEPS the exhaust gas was diluted (dilution ratio = 0.0009702, dilution factor = 1030.8). Data from BrainBee emission analyser and opacimeter and from EEPS were stored via data acquisition units, provided by manufacturers.

Table 2. Basic specification of the BrainBee emission analyser and opacimeter

Component	Resolution	Accuracy
CO	0.01% vol.	0.03% vol. or 5% read value
CO_2	0.1% vol.	0.5% vol. or 5% read value
HC	1 ppm vol.	10 ppm vol. or 5% read value
O_2	0.01% vol.	0.1% vol. or 5% read value
NO	1 ppm	10 ppm vol. or 5% read value
Opacity	0.1%	2%
Temperature	1 °C	2.5 °C

Table 3. Basic specification of the EEPS

Particle Size Range	5.6–560 nm
Particle Size Resolution	16 channels per decade (32 total)
Electrometer Channels	22
Charger Mode of Operation	Unipolar diffusion charger
Inlet Cyclone 50% Cutpoint	1 μm
Time Resolution	10 size distributions (s^{-1})

As a test blended fuel the n-butanol – rapeseed oil – diesel fuel blend was used, containing 10% of n-butanol, 20% of rapeseed oil and 70% of diesel. Diesel fuel with no bio-component was used as a reference. Basic specification of the fuels, used in experiment are shown in Table 4. Stabinger Viscometer SVM 3000 made by Anton Paar GmbH (measuring accuracy < 1%, repeatability 0.1%) was used for measurement of density and viscosity of the fuels. Isoperibol calorimeter LECO AC600 (measuring range 23.1–57.5 MJ kg^{-1} for a 0.35 g sample, accuracy 0.1% RSD) was used for measurement of calorific values of the used fuels according to standards ČSN DIN 51900-1 and ČSN DIN 51900-2. Cetane indexes of the fuels was calculated from distillation curves according to EN ISO 4264.

Table 4. Basic specification of used fuels

Fuel	Density at 15°C kg m^{-3}	Calorific value MJ kg^{-1}	Viscosity at 40 °C mm^2 s^{-1}	Cetane number -	Cetane index -
Diesel 100	819.13	43.15	1.798	50	47.73
70D20R10B (blended fuel)	832.58	40.84	2.850	-	41.6
N-butanol	815.27	33.1	2.266	17	-
Rapeseed oil	924.05	37.1	3.148	39.6–44	-

RESULTS AND DISCUSSION

The data of fuel consumption, smoke amount and emission of particles measured for diesel engine are shown in following tables. In the Table 5 are shown results for the engine which worked on standard diesel as reference, firstly after run-in period (10 hours) at 40% load and secondly, in Table 6 are data after 70 hours of operation at 70% load.

Table 5. Fuel consumption, smoke and emissions production after 10 hours run-in period – standard diesel

Engine speed	Output power	CO	CO_2	HC	NO	Smoke	Fuel consumption
min^{-1}	W	$g\ h^{-1}$	$g\ h^{-1}$	$g\ h^{-1}$	$g\ h^{-1}$	$g\ h^{-1}$	$g\ h^{-1}$
3,122	0	16.79	938.53	0.50	2.70	0.07	456.46
3,114	656	22.82	1,208.96	0.27	4.55	0.08	562.07
3,082	1,308	12.29	1,428.45	0.43	7.04	0.08	675.00
3,052	1,929	9.73	1,682.21	0.40	10.03	0.09	789.91
3,011	2,570	9.60	1,963.60	0.28	13.78	0.12	897.31
2,994	3,143	9.55	2,275.05	0.26	16.68	0.23	1,015.23
2,980	3,702	9.50	2,637.92	0.28	19.52	0.37	1,191.75
2,967	4,339	12.09	3,159.30	0.34	22.97	0.77	1,381.02

Table 6. Fuel consumption, smoke and emissions production after 70 hours of operation – standard diesel

Engine speed	Output power	CO	CO_2	HC	NO	Smoke	Fuel consumption
min^{-1}	W	$g\ h^{-1}$	$g\ h^{-1}$	$g\ h^{-1}$	$g\ h^{-1}$	$g\ h^{-1}$	$g\ h^{-1}$
3,123	0	42.32	977.95	1.13	1.45	0.08	477.05
3,111	638	40.46	1,188.13	0.91	3.04	0.09	568.47
3,093	1,249	36.98	1,397.60	0.75	5.55	0.10	671.40
3,072	1,937	31.84	1,663.45	0.74	9.02	0.13	787.52
3,052	2,579	29.19	1,949.42	0.65	12.38	0.16	913.10
3,015	3,162	25.47	2,228.18	0.70	15.48	0.25	1,045.08
2,934	3,715	25.73	2,499.36	0.64	19.19	0.30	1,174.55
2,914	4,304	30.20	2,973.24	0.63	21.70	0.90	1,357.49

Table 7. Fuel consumption, smoke and emissions production after 10 hours run-in period – blended fuel

| Engine speed	Output power	CO	CO_2	HC	NO	Smoke	Fuel consumption
min^{-1}	W	$g\ h^{-1}$	$g\ h^{-1}$	$g\ h^{-1}$	$g\ h^{-1}$	$g\ h^{-1}$	$g\ h^{-1}$
3,226	0	33.43	1,010.11	0.72	1.99	0.08	516.97
3,211	658	28.15	1,265.14	0.77	3.91	0.09	629.64
3,197	1,299	22.94	1,521.52	0.72	6.59	0.11	740.99
3,179	1,932	19.23	1,792.05	0.70	9.91	0.14	867.78
3,157	2,578	15.10	2,096.07	0.54	13.57	0.09	1,005.14
3,137	3,174	15.00	2,425.10	0.60	17.17	0.17	1,159.69
3,127	3,754	14.96	2,805.45	0.56	20.96	0.22	1,328.63
3,120	4,405	20.81	3,321.34	0.83	23.63	0.48	1,546.09

The same data for the engine operated on blended fuel are given in Table 7 after run-in period (10 hours) at 40% load and in Table 8 after 70 hours at 70% load. Consequently, data are compared and commented.

Data were evaluated separately for the generator which worked on standard diesel fuel and for generator which worked on blended fuel.

Table 8. Fuel consumption, smoke and emissions production after 70 hours of operation – blended fuel

Engine speed	Output power	CO	CO_2	HC	NO	Smoke	Fuel consumption
min^{-1}	W	$g\,h^{-1}$	$g\,h^{-1}$	$g\,h^{-1}$	$g\,h^{-1}$	$g\,h^{-1}$	$g\,h^{-1}$
3,205	0	43.44	1,003.67	1.16	1.48	0.13	544.36
3,199	645	41.60	1,221.81	0.93	3.13	0.16	673.88
3,189	1,264	38.14	1,441.31	0.78	5.72	0.19	766.36
3,177	1,956	32.93	1,720.34	0.77	9.33	0.25	871.85
3,161	2,600	30.24	2,019.40	0.67	12.83	0.30	1,014.27
3,142	3,195	26.53	2,321.63	0.73	16.13	0.45	1,150.39
3,102	3,777	27.20	2,642.23	0.68	20.29	0.58	1,299.85
3,081	4,408	31.92	3,143.43	0.67	22.94	1.25	1,508.15

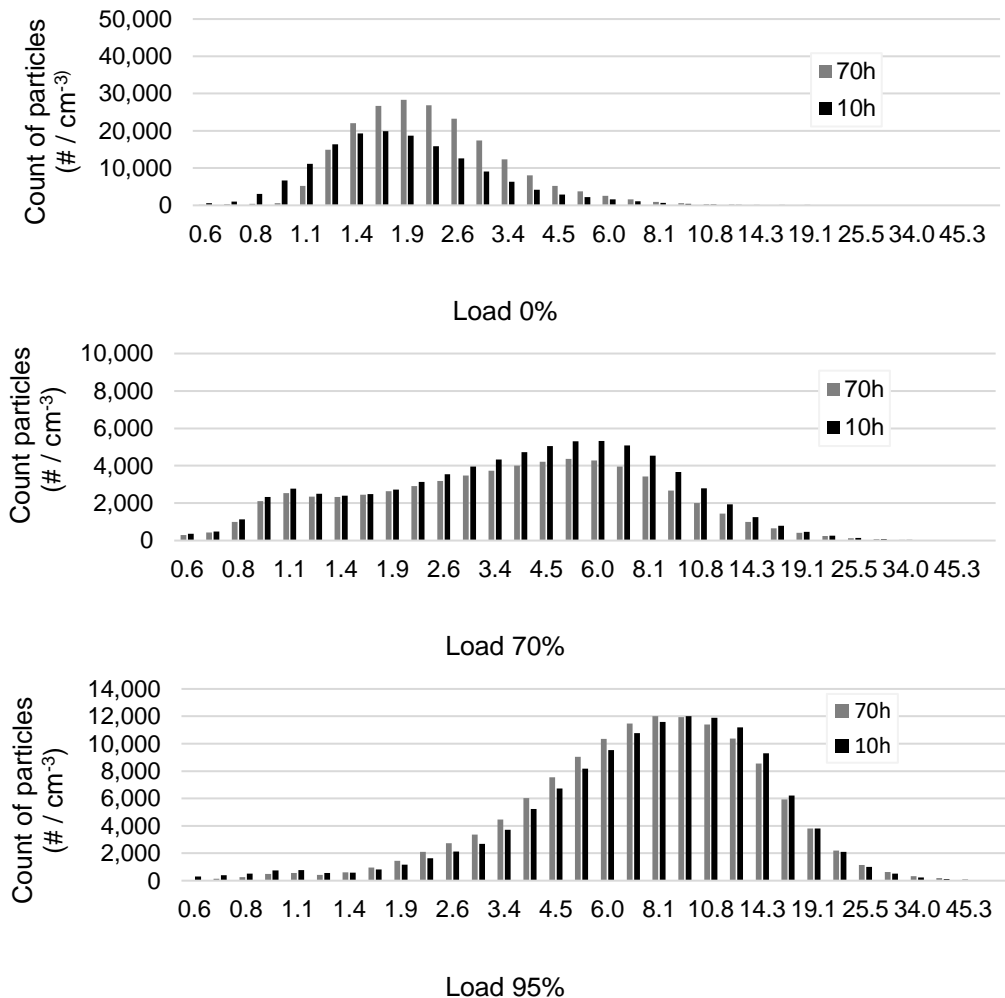**Generator operating on standard diesel fuel**
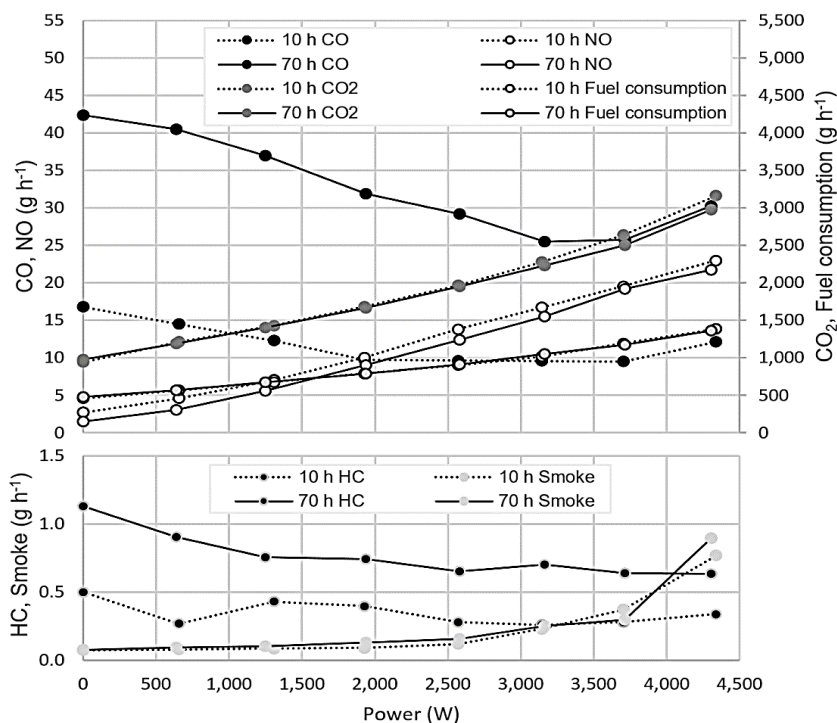
Figure 2. Hourly production - fuel consumption and emissions for the generator operated on standard diesel fuel after 10 and 70 hours of operation.

Considering the fact, that measured points were set with an error of less than 0.05% for revolutions and 0.8% for loads, the operating parameters of the generator were compared in hourly fuel consumption and emissions.

Fig. 2 shows the dependance of fuel consumption and emissions on the power that is taken from the generator as the energy output (used for external heating). Fig. 2 shows the dependance for the engine after run-in period (10 h) and after 70 hours of operation (70 h). It is evident from Fig. 2 that an increasing trend occurs mainly in the production of CO and HC and this progress has a negative effect on environment.

The increase of smoke amount and the production of particles for engine operating on standard diesel, is also confirmed in Fig. 3, where it is seen that the number of particles in the operation of the generator after 70 hours is higher in almost all the components of the spectrum than after 10 hours. Fig. 3 shows the number of particles in three different stages of the engine: the load-free (0%), the long-term load (70%) and the load close to the maximum (95%). The X-axis defines particle size in micrometres.

Load 0%

Load 70%

Load 95%

Figure 3. Exhaust particle distribution by its size (X-axis) – engine operating on standard diesel.

Overall, there has been an increase in production of emissions, especially for the components of CO and HC (those are the components where the measuring instrument is the least sensitive). As a result, the smoke increase is almost 15%. The unchanged fuel consumption is positive result – no significant increasing has been recorded.

The average changes are shown in Fig. 4. Here the average emission values and fuel consumption for the operation of generator are compared after 10 and 70 hours. It is obviocorrus that CO emissions have been increased 2.5 times and that the production of HC emissions has increased 2.3 times. Smoke in 15%. On the other hand, CO_2 emissions have decreased by about 2% and NO emissions by about 17%. Fuel consumption increased by only 1%.
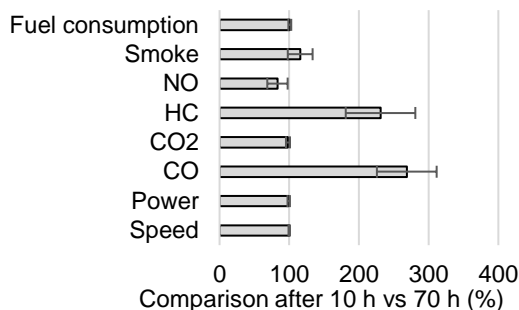
Figure 4. Change in emissions and fuel consumption in percent - 10 vs 70 h (diesel).

**Generator operating on blended fuel**
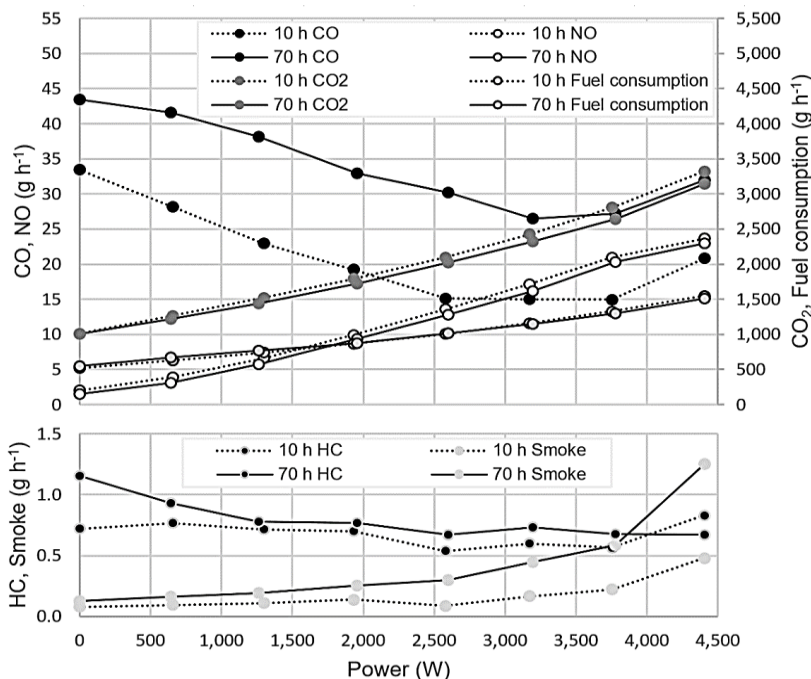
Figure 5. Hourly production - fuel consumption and emissions for the generator operated on blended fuel after 10 and 70 hours of operation.

Considering the fact, that measured points were set with an error of less than 0.4% for revolutions and 0.2% for loads, the operating parameters of the generator were compared in hourly fuel consumption and emissions.

Fig. 5 shows the dependance of fuel consumption and emissions on the power that is taken from the generator as the energy output (used for external heating). Fig. 5 shows the dependence for the engine after run-in period (10 h) and after 70 hours of operation (70 h). From Fig. 5 is significantly visible that an increasing trend occurs mainly in the production of smoke, CO and HC and this progress has negative environmental effect.

The increasing trend of smoke and the production of particles, is also confirmed by Fig. 6, where it is visible that the number of particles in the operation of the generator for 70 hours is mainly in the area of larger particles. Fig. 6 shows the number of particles only for three different states of the engine operated on blended fuel: the load-free motor (0%), the long-term load (70%) and the load close to the maximum (95%). The X-axis defines particle size in micrometres (μm).

Load 0%

Load 70%

Load 95%
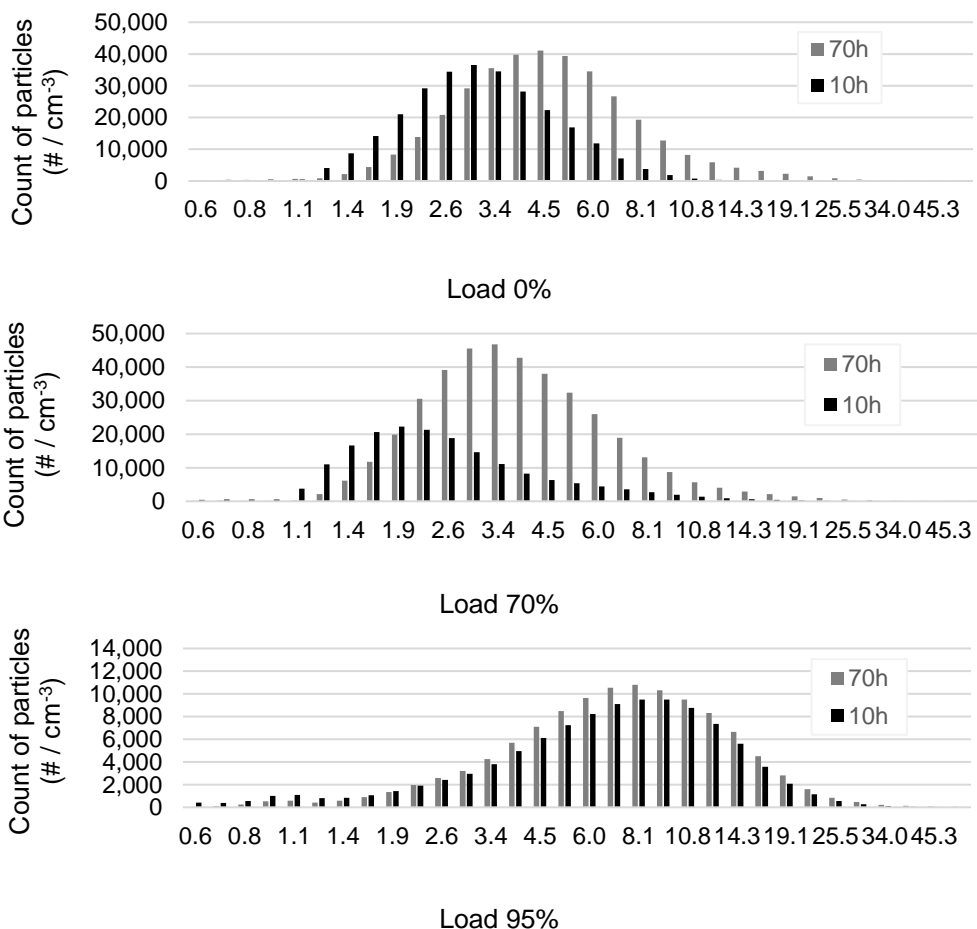
**Figure 6.** Exhaust particle distribution by its size (X-axis) - blended fuel.

As a result of this part of experiment, there has been an increase in production of emissions, especially for the components of CO and HC (those are the components where the measuring instrument is the least sensitive. As a result, the smoke increase is almost 130%. The unchanged fuel consumption is a positive result for this experiment.

On average, the changes for engine operated on blended fuel are shown in Fig. 7.

Here are shown average emission values and fuel consumption for the generator are compared after 10 and 70 hours. It is obvious, that CO emissions have been increased 1.6 times and increased HC emissions by 1.2 times. Smoke increased about 130%. On the other hand, CO_2 emissions have dropped by about 4% and NO emissions decreased about 10%. Fuel consumption increased only by 1%.
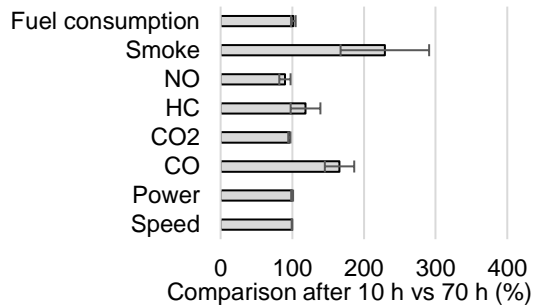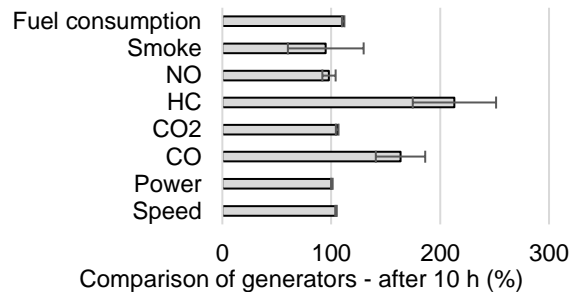

Figure 7. Change in emissions and fuel consumption in percent - 10 vs 70 h (blended fuel).

Comparison of generator operating on standard diesel and generator operating on blended fuel
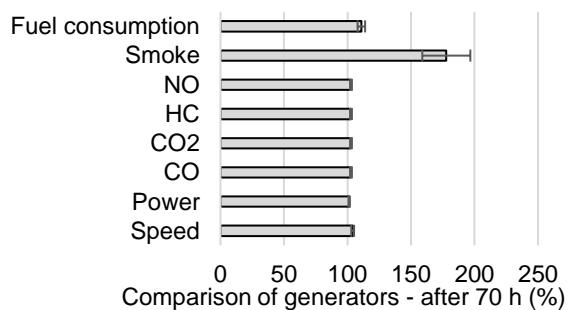
Figs 8 and 9 show a comparison of the generators operated on standard diesel and blended fuel. The comparison is based on specific emissions and fuel consumption. The difference is then expressed as a percentage of all measured points. The displayed standard deviation shows how the components fluctuated at the measuring points.

Fig. 8 shows a run-in comparison of generators after 10 hours. In this graph is shown that the generator with blended fuel has higher CO and HC outputs, and at a higher load points there was a relatively significant smoke reduction of more than 20%. For other operating parameters, the difference is very low.

Figure 8. Comparison of the generator operated on blended fuel with the generator operated on diesel fuel after 10 h.

Fig. 9 shows the comparison of engines after 70 hours. When compared after 70 hours, almost all operating parameters appear to be almost same. The generator operated on blended fuel had slightly higher fuel consumption. Surprisingly, there was a noticeable increasing of smoke production, which was in average 75% worse than in generator operated on standard diesel.

Figure 9. Comparison of the generator with blended fuel and generator with standard diesel - after 70 h.

1010

CONCLUSIONS

During the long-term operation of diesel engines on standard diesel fuel and blended fuel, the generators were loaded with 70% of their nominal power using electric heaters. The operation parameters were measured in short-time measurements after run-in period and after 70 operating hours. The results after 70 operating hours shown that:

- After run-in period of the engines (10 h) it was shown, that blended fuel could have a positive effect on smoke, especially at higher loads (20% difference in results for smoke). After 70 hours, however, the opposite effect occurred. Smoke production of the generator operated on blended fuel increased by 75% in compare with reference diesel engine.

- The fuel consumption of the generator powered with blended fuel showed higher values, but these are caused by a lower calorific value of the blended fuel. Higher fuel consumption was observed both after 10 and 70 hours.

- From the point of view of particle production, it can be stated, that the diesel engine has comparable values after 10 and 70 hours of operation. On the other hand, the blended fuel generator has a significantly increased particle production after 70 hours, especially in higher particle sizes. When comparing these two generators, the production of particulates is clearly lower for the standard diesel-powered generator.

Lower emissions and smoke production using different biofuels and their diesel fuel blends can be achieved in short-time scale. In terms of long-term operation, however, they may cause operating difficulties in engines (cumulation of sediments, effect on oil content, etc.), which degrades engine operating parameters and may potentially result in increasing emissions and smoke production.

These results were achieved with specific composition of blended fuel containing 10% of n-butanol, 20% of rapeseed oil and 70% of diesel. Problems with emissions were most likely caused by vegetable (rapeseed) oil and its mechanical and chemical properties. Different mixtures might prove significantly different burning properties. Testing of various blended fuels will be object of future research projects.

REFERENCES

Altin, R., Çetinkaya, S. & Yücesu, H.S. 2001. Potential of using vegetable oil fuels as fuel for diesel engines. *Energy Conversion and Management* **42**(5), 529–538.

Atmanli, A., Ileri, E. & Yüksel, B. 2015. Effects of higher ratios of n-butanol addition to diesel-vegetable oil blends on performance and exhaust emissions of a diesel engine. *Journal of the Energy Institute* **88**(3), 209–220.

ČSN DIN 51900-1 Testing of solid and liquid fuels - Determination of the gross calorific value by the bomb calorimeter and calculation of the net calorific value - Part 1: General information, basic equipment and method. 2014.

ČSN DIN 51900-2 Testing of solid and liquid fuels - Determination of the gross calorific value by the bomb calorimeter and calculation of the net calorific value - Part 2: Method using isoperibol or static jacket calorimeter. 2014.

Doğan, O. 2011. The influence of n-butanol/diesel fuel blends utilization on a small diesel engine performance and emissions. *Fuel* **90**(7), 2467–2472.

EN ISO 4264 Petroleum products – Calculation of cetane index of middle-distillate fuels by the four variable equation. 2007.

Gailis, M., Rudzitis, J., Kreicbergs, J. & Zalcmanis, G. 2017. Experimental analysis of hydrotreated vegetable oil (HVO) and commercial diesel fuel blend characteristics using modified CFR engine. *Agronomy Research* **15**(4), 1582–1601.

Hönig, V., Kotek, M. & Mařík, J. 2014. Use of butanol as a fuel for internal combustion engines. *Agronomy Research* **12**(2), 333–340.

Hönig, V. & Hromadko, J. 2014. Possibilities of using vegetable oil to power diesel engines as well as their impact on engine oil. *Agronomy Research* **12**(2), 323–332.

Jin, C., Yao, M., Liu, H., Lee, C.F. & Ji, J. 2011. Progress in the production and application of n-butanol as a biofuel. *Renewable and Sustainable Energy Reviews* **15**(8), 4080–4106.

Killol, A., Reddy, N., Paruvada, S. & Murugan, S. 2019. Experimental studies of a diesel engine run on biodiesel n-butanol blends. *Renewable Energy* **135**, 687–700.

Kleinová, A., Vailing, I., Lábaj, J., Mikulec, J. & Cvengroš, J. 2011. Vegetable oils and animal fats as alternative fuels for diesel engines with dual fuel operation. *Fuel Processing Technology* **92**(10), 1980–1986.

Mařík, J., Pexa, M., Kotek, M. & Hönig, V. 2014. Comparison of the effect of gasoline - ethanol E85 - butanol on the performance and emission characteristics of the engine saab 9-5 2.3 l turbo. *Agronomy Research* **12**(2), 359–366.

Pexa, M., Čedík, J., Mařík, J., Hönig, V., Horníčková, Š. & Kubín, K. 2015. Comparison of the operating characteristics of the internal combustion engine using rapeseed oil methyl ester and hydrogenated oil. *Agronomy Research* **13**(2), 613–620.

Pexa, M., Čedík, J. & Pražan, R. 2016. Smoke and NOx Emissions of Combustion Engine using Biofuels. *Agronomy Research* **14**(2), 547–555.

Peterka, B., Pexa, M., Čedík, J. & Aleš, Z. 2016. The Influence of Biobutanol on Performance Parameters of Mobile Generator. *Agronomy Research* **14**(1), 167–173.

Saadabadi, S.A., Thallam Thattai, A., Fan, L., Lindeboom, R.E.F., Spanjers, H. & Aravind, P.V. 2019. Solid oxide fuel cells fuelled with biogas: Potential and constraints. *Renewable Energy,* 194–214.

Siwale, L., Kristóf, L., Adam, T., Bereczky, A., Mbarawa, M., Penninger, A. & Kolesnikov, A. 2013. Combustion and emission characteristics of n-butanol/diesel fuel blend in a turbo-charged compression ignition engine. *Fuel* **107**, 409–418.

Szwaja, S. & Naber, J.D. 2010. Combustion of n-butanol in a spark-ignition IC engine. *Fuel* **89**(7), 1573–1582.

Separation of dust particles in the low-pressure pneumatic conveying system

T. Jehlička[*] and J. Sander

Czech University of Life Sciences Prague, Faculty of Engineering, Department of Technological Equipment of Buildings, Kamýcká 129, CZ165 21 Prague 6 – Suchdol, Czech Republic
[*]Correspondence: jehlickat@tf.czu.cz

Abstract. This paper focuses on the possibility of separation of dust particle created as a by-product of technological processing of composite materials. The aim was to design and verify technology for the separation of dust particles from polydisperse granular mixtures, which are created by physical-mechanical processes of materials processing (crushing, sorting, machining or surface treatment of products such as grinding or polishing the surface). Under experimental conditions, a low-pressure pneumatic conveying system was designed and tested in operation, supplemented by a powerful electrostatic dust particles separation system. The entry requirement was to design a system that would be able to work with high separation efficiency using low-pressure suction. The designed separation conveying device consists of three parts: the conveyance section for the grain material suction and conveying, the coarse grain share cyclone separator and the electrostatic precipitator of the dust particles released from the air flow. Operational capacity of the proposed technology was verified by evaluating the separation efficiency of processing the polydisperse granular mixture resulting from the crushing of laser printer toner cartridges. These contain toner powder residues, which are the source of composite dust particles. The separation efficiency of the system was monitored according to the set pressure of the air in front of the electrostatic separator. Evaluation of the results thus obtained confirmed the operational reliability of the system at low-pressure operation and the high separation efficiency of the electrostatic separator under the set operation conditions.

Key words: dust particles, electrostatic separation, low-pressure pneumatic conveying system.

INTRODUCTION

This paper focuses on the possibility of separation of dust particles created by physical-mechanical processes of materials processing. The dust particles are separated from the air flow used for dust suction and transport. The aim was to design and verify technology for the separation of dust particles from polydisperse granular mixtures with a large dispersion of size and density of particles created by the physical-mechanical process of crushing the material. The technology is designed to achieve a high dust particle separability at low volume air flow and low operating pressure throughout the system (low-pressure suction, pneumatic conveying and separation). Achieving high separability at low pressure is a prerequisite for low-energy operation of the whole technology. In the thesis, the construction solution, verification of the operational

function and evaluation of dust particle separation efficiency of the proposed separation conveying device are elaborated.

Experience from various manufacturing operations shows that the presence of fine dust particles (dispersed in the air in the production environment) is a significant factor affecting the safety of operation, product quality, production economy, as well as the health and safety of workers (Tönshoff et al., 1997; Heederik et al., 2012; Kažimírová & Opáth, 2016). Emissions of dust particles are monitored as an air pollutant. These emissions are monitored at national and international levels and their permissible content is regulated in the form of emission limits for each source of the polluting dust particles (EP and Council, 2010). Industrial technologies using physical-mechanical materials processing techniques are not among the dominant sources of air pollution. On the other hand, it is necessary to address the problem of the impact of dust particles created by physical-mechanical processing of materials, as a technological, safety and hygienic risk factor of the production environment (Balout et al., 2007; Kalliny et al., 2008). Concentration of dust particles in the production environment is monitored in accordance with valid legislation (health and safety of workers) (Council of the European Communities, 1998).

Among the physicochemical properties of dust particles, important are those that affect the hygiene and safety of operation and the efficiency of separation from the environment. Significant physicochemical properties of dust particles are size distribution and particle shape, chemical and mineralogical composition and, potentially, particle resistivity (unit electric resistance) (Aksa et al., 2013). Dust particles are generally irregular in shape and their size cannot be precisely defined. Therefore, an equivalent diameter is used to determine the size. The most important physical property of dust particles observed is the so-called aerodynamic equivalent diameter. It corresponds to the size of the spherical particle of density 1,000 kg m^3 that has the same steady velocity due to the gravitational force in the ambient air as the particle observed (Kulkarni et al., 2011). From the health effect point of view, different size fractions of dust particles are defined where the aerodynamic diameter is given in micrometers (Kim et al., 2015). Particles of PM10 (particles smaller than 10 μm) to PM0.1 (particles smaller than 100 nm) are usually determined.

Processes involving crushing, sorting, machining or surface treatment of products such as grinding or polishing the surface are considered the most important sources of dust particles in the production environment (in the workplace) (Tilmatine et al., 2009). These processes result in mixtures of dust particles of submicroscopic to microscopic size of different physical and chemical properties. The released dust particles subsequently make a polydisperse system together with the air (Al-Salem et al., 2009; Malaťák & Passian, 2011). The high polydispersity of the mixture results from the crushing process. Depending on the nature of the material processed, mixtures of substances with large dispersion of size and density are produced (Vaculík et al., 2016). The size and density dispersion of the resulting particles increases the operational demand for conveyance of the mixture and the separability of the dust particles. In operation, this demand is solved by changing the properties of the conveyed material (reduction of particle size and density dispersion by sorting) or by adjusting the operating parameters of the suction system, i.e. by increasing the air flow volume and the operating pressure (Taylor, 1998).

In a manufacturing environment where physical-mechanical processes of material processing are applied, dust particles are removed by suction. Various suction arms or suction filter tables are used. These devices are then combined with powerful separation systems where the dust particles are separated from the air flow (Cao et al., 2018). The separation efficiency of dust particles at the point of their origin, the energy intensity of the suction system, and the subsequent separation of the dust particles from the carrier medium are important operation indicators of the entire suction system (Burgess et al., 2004). The operational disadvantage of the equipment used is its high energy intensity. This is due to the large operating pressures that are required to convey the exhausted material and the correct operation of the dust particle separators (Goodfellow & Tähti, 2001). Reducing the energy intensity of the operating system can be achieved by shortening the convey routes, by using a separation method with low-pressure drop, or by a combination of several separation methods (use of a multi-stage sorting separators).

Methods of sedimentation (use of gravity, centrifugal, inertial forces), filtration, diffusion or separation using particle electric properties are used to separate dust particles from the air flow (Peukert & Wadenpohl, 2001). By setting comparable conditions, i.e. properties of the dispersed particles (size, shape, mass concentration, electric properties), properties of the dispersion (concentration and fractional composition of the solid phase) and the environment (density, viscosity, power and electric field strength), the lowest pressure drop is achieved at the separation using electric properties of particles (electrostatic precipitators), pressure drop is 50–250 Pa. On the contrary, filtration separation systems (e.g. fabric filters) work with the greatest pressure drop, the pressure drop at 500–2,000 Pa (Burgess et al., 2004; Goodfellow & Tähti, 2001).

MATERIALS AND METHODS

Under experimental conditions, the separation conveying device for suction of crushed material, its pneumatic conveyance and subsequent separation of the dust particles from the air flow was designed and tested. This device was designed to work with a high dust separation with a low volume air flow and a low operating pressure throughout the suction system, pneumatic conveyance and separation. This was assured by the construction of the conveyor section of the device and by the use of the separator with a low-pressure drop. The designed separation conveying device consists of three parts: the conveyance section for the grain material suction and conveying, the coarse grain share cyclone separator and the electrostatic precipitator (hereinafter referred to as 'ESP') of the dust particles released from the air flow.

The operational efficiency of the separation conveying device was verified by assessing the dust particle separability when processing the polydisperse granular mixture resulting from the crushing of electrical waste. In particular, used laser toner cartridges were processed. These contain residues of toner powder that is the source of composite dust particles of submicroscopic size. The separability of released dust particles was monitored as a function of the change of the pressure in the conveying pipeline in front of the ESP.

Design and function of the proposed separation conveying device

Construction of the separation conveying device is shown in Fig. 1. The electrical waste is shredded by knife mill Terier G200/300 (1). From a knife mill, the crushed material is fed into a closed metal conveying pipeline (2) of circular profile diameter of 150 mm and it is conveyed by a combination of pneumatic and mechanical conveyance to a cyclone separator (3) with tangential inlet size of 600 x 1,750 mm. At the bottom, the cyclone separator is closed by a turnstile feeder (4). The cyclone separator separates the crushed material from the air flow. The air from the cyclone separator with dust particle fractions, which are not separated by the cyclone separator, then enters the EPS of the dust particle AEROFOG–E (5). It is a series of (industrially) manufactured EPS of horizontal chamber structure with air flow volume up to 1,800 m^3 hod^{-1}. The interconnection conveying pipeline between the EPS and the cyclone separator and the interconnection conveying pipeline between the EPS and the pressure source is of circular profile diameter of 300 mm. A radial fan URBAN Technik VE–2000 (6) is a pressure source with an air volume flow rate of 1,800 m^3 hod^{-1}, operating pressure of 1,800 Pa and engine speed at 2,800 min^{-1}. During the measurement, a mechanical fabric filter (7) was placed in front of the fan, which prevented any dust particles to be emitted at high operating pressures and thus prevented reduction of the EPS separability. Operating parameters of the separation conveying device were designed based on the calculation of air–conditioning variables (volume flow rates, air flow velocity, operating pressures, pipe dimensions).
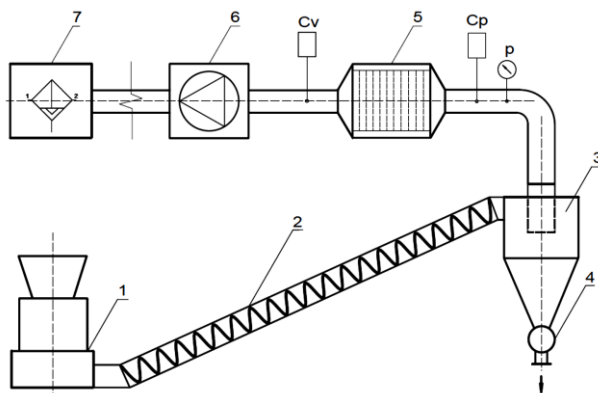
Figure 1. Separation conveying device construction: 1 – knife mill, 2 – combined (pneumatic and mechanical) conveyance, 3 – cyclone separator, 4 – turnstile feeder, 5 – electrostatic precipitator, 6 – fan, 7 – fabric filter, p – pressure sensor, C_p, C_v – dust analyser probes.

The use of low pressure in the entire system of the designed device allows the construction of combined (pneumatic and mechanical) conveyance (2), shown in Fig. 1. The essence of the construction is a low–pressure pneumatic conveying pipeline in combination with a mechanical towing part (Jehlička & Sander, 2015). The combination of both types of conveying is designed in such a way that the towing part in the form of an axis–less helix is inserted into the inner space of the conveying pipeline. In such a defined environment, the material is conveyed due to the dynamic effects of the flowing media and is simultaneously carried by the mechanical movement of the rotating axis–

less helix. Such technical solution allows carrying out both pneumatic and mechanical conveying of particles in a single conveying space (conveying pipeline).

With this construction of the pneumatic conveying pipeline, it is possible to convey the material of a wide spectrum of specific weight of individual particles. Particles with lower density and greater aerodynamic resistance are carried by the air flow mainly through the centre of the pipeline. Particles of larger density are moved by the mechanical energy of the axis–less helix. The described pneumatic pipeline construction can be utilized to handle short distances in the horizontal and oblique plane.

Method of measurement of dust particles separability

Dust particle separability was monitored as a function of the change of the operating air pressure. The operating pressure was set by the frequency control of the fan revs. The fan revs were set by the Movitrac LTE–B + frequency converter within the range of 1,400 min^{-1} to 2,600 min^{-1}, always by 200 min^{-1}. The operating pressure and the mass concentration of the dust particles in the pipeline were measured at each set of the fan revs. The location of the probes is in Fig. 1. A Testo 521–1 device monitored the operating pressure with a pressure sensor located in the conveying pipeline at a distance of 0.7 m from the EPS entrance. The mass concentration of the dust particles was monitored by the optical real–time measurement method using the Testo 380 dust particle analyser. There were two dust analyser probes (C_p and C_v). The first was located in the pipeline about 0.5 m before the entrance to the EPS (C_p) and the other was in the outlet pipeline about 0.6 m behind the EPS (C_v).

The Testo 380 analyser is available on the market in the original user interface, which is optimized to evaluate the dust particle mass concentrations in the flue gas mixture. In order to measure dust particle mass concentrations of pre–defined physicochemical properties in the air flow, it was necessary to recalibrate the supply setting. The recalibrating of the analyser was performed in cooperation with the Testo service representative. Accuracy of dust particle mass concentration measurements after analyser recalibration is burdened with an error corresponding to inaccuracy in the specification of the physicochemical properties of the dust particles into the analyser software application. In order to monitor the changes in the dust particle mass concentrations in relation to the set operating parameters of the separation conveying device and graphically illustrate these changes, the accuracy of the operational measurement is sufficient and within the range of measured values it is above 95%.

The dust particle separability O_c was calculated from the general relationship:

$$O_c = \frac{C_p - C_v}{C_p} \cdot 100\% \qquad (1)$$

where C_p – particle mass concentration on input (mg m^{-3}); C_v – particle mass concentration on output (mg m^{-3}).

With each set of the fan revs, the measurement of the pressure and mass concentrations of the dust particles was repeated five times, always in 5 minute intervals. Mean values were calculated from the values thus measured.

RESULTS AND DISCUSSION

The proposed separation conveying device has three construction parts that are not common in similar dust removal devices in common operation practice. It involves the use of combined (pneumatic and mechanical) conveyance between the dust particle source and the coarse grit separator, the use of a low-pressure drop dust separator and in addition, the inclusion of this separator in front of the fan on the suction line, see Fig. 1. The described construction modification allows energy efficient operation at a low operating pressure of up to 1,000 Pa.

In order to verify the assumption of operational reliability and high dust separability in low-pressure operation (suction of the crushed material, its pneumatic conveyance and subsequent separation of the dust particles from the air flow), dust particle separation was monitored in dependence on changes in operating pressure. Table 1 shows the set fan revs, the mean values of the measured operating pressures and the mean mass concentrations of the measured dust particles on the inlet and outlet of the EPS, which correspond to the set fan revs. Further, in Table 1, the calculated values of dust particle separation of the EPS are given.

Table 1. Operation pressure and concentration of dust particles

Fan revs [min^{-1}]	Pressure [pa]	Particle mass concentration on outlet c_v [mg m^{-3}]	Particle mass concentration on inlet c_p [mg m^{-3}]	Dust particle separability o_c [%]
1,400	450	1.16	58	98
1,600	587	1.5	60	97.5
1,800	743	1.83	61	97
2,000	918	2.27	65	96.5
2,200	1,111	4.87	65	92.5
2,400	1,322	11.22	66	83
2,600	1,552	19.5	65	70

The dependence of the observed factors, i.e. the mass concentration of the dust particles on the outlet of the EPS and the operating pressure, is shown in Fig. 2. The measured values are intersected by the trend line. To illustrate the variation of the mass concentration of the dust particles at the operating pressure, the exponential trend of the trend line is used. It corresponds the most to the actual operational changes of the monitored factors. Correlation reliability is 0.99.

From the measured mass concentrations of dust particles on the outlet of the EPS follows the dependence on the change in the operating pressure in the system. This dependence is exponential. The graphic presentation in Fig. 2 shows, that the increase in mass concentrations up to the pressure of 1,000 Pa is very gradual and does not exceed the mass concentration of 5 mg m^{-3}. For pressures above 1,000 Pa, there is a characteristic steep increase in the mass concentration of dust particles. The increase of the dust particle mass concentration at the operating pressure above 1,000 Pa is related to the changes in other operating factors. The velocities and volumes of the air flow vary in the system and, as shown in Fig. 3, overall separation decreases. The course allows a conclusion that the designed separation conveying device reliably separates the dust particles during low-pressure operation up to 1,000 Pa. Outlet mass concentrations of

dust particles at low values below 5 mg m^{-3} comply with the legal regulations in force in the EU Member States. This applies to both dust emission limits as well as health and safety of workers (EP and Council, 2010; Council of the European Communities, 1998).
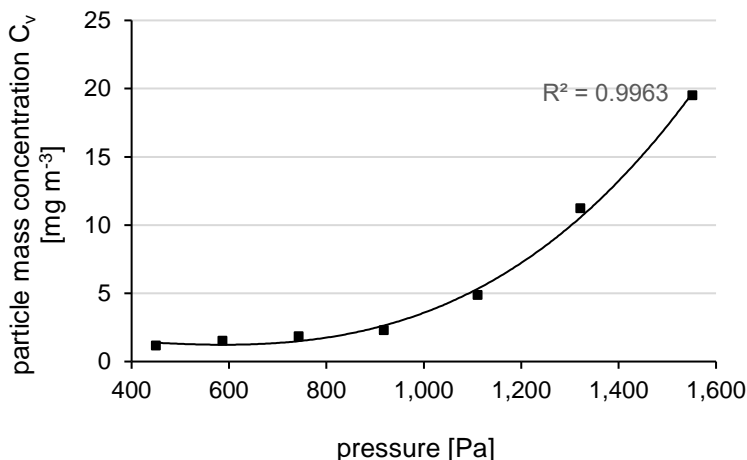
Figure 2. Dependence of mass concentration of dust particles on the outlet of the separator and operating pressure.

The values of the inlet mass concentrations dust particles (C_p) have a balanced value over the entire measuring range. This is given by the uniform properties of the processed material at all measurements. Small changes (in mg m^{-3} units) may be due to sedimentation of particles in the conveying pipeline due to a drop in operating pressure or due to physicochemical reactions that cause the dust particles to bind to the coarse fraction of the grit with which they are subsequently separated in the cyclone separator.
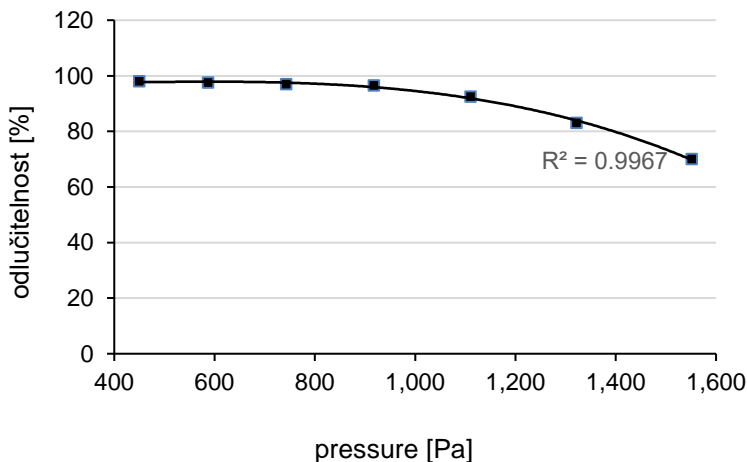
Figure 3. Separability of dust particles in dependence on operating pressure.

The dependence of the outlet mass concentration of the dust particles at the operating pressure and other operating values that are related to the set pressure (volume flow and flow velocity) is affected by the physical properties of the crushed material. When using the EPS, it is primarily particle resistivity and less particle size and shape (Goodfellow & Tähti, 2001).

An objective assessment of dust particle separability in the proposed separation conveying device would be to compare the measured values of the separability of dust particles released during the processing of the toner cartridges with the separability of the dust particles resulting from the processing of materials of different properties, i.e. other pre-sorted electrical waste. The grit from the printer toner cartridge is a mixture of plastic particles (a cassette case) and submicroscopic carbon particles and metal oxides (toner powder) (Pirela et al., 2015). The resulting grit from toner cartridges has optimal resistivity (Mazumder et al., 2006) and hence high separability on the EPS (Matsusaka & Masuda, 2003). On the other hand, the material resulting from the crushing of other pre-sorted electrical waste will show a much wider range of physicochemical properties.

From the operation energy point of view, it would be interesting to compare the method of mechanical separation by air filtration and the method of electrostatic separation with the same total dust particle separability. When using filtration, the overall separation is affected by the size and shape of the particles. Filtration separates the solid particles from the air flow and holds them on the filter element. From the energy point of view, the pressure drop that occurs on the filter element is a problem. Industrial filters can work with a final pressure drop of up to 2,000 Pa (Burgess et al., 2004). By comparing the electrostatic separation method and the mechanical separation method based on air filtration, the energy saving of electrostatic separation would be clearly proved with the proposed mechanical equipment.

CONCLUSIONS

The result of the experiment is the design of a technology for the separation of dust particles, which are created by physical-mechanical processes of materials processing. The proposed technology and its operational verification are focused on the separation of dust particles from polydispersion granular mixtures with large scattering of particle size and density, which are created by the physical-mechanical process of crushing composite materials. The separation conveying device was designed to achieve a high degree of separation with minimal energy consumption for the whole technology operation, which allows conveyance, separation of the grit from the air flow and separation of the dust particles using low operating pressure. The measurements were made by processing a material, which was assumed to have a high content of dust particles of submicroscopic size. The material used were toner cartridges for laser printers containing toner powder residues. The operational efficiency of the separation conveying device at low-pressure operation was verified by assessing the dust particles separability in dependence on the change in air pressure in the conveying pipeline in front of the ESP.

Experimental measurements showed that on the EPS outlet the growth of mass concentrations of dust particles up to a pressure of 1,000 Pa (low-pressure operation) is very gradual and does not exceed 5 mg m^{-3}. For pressures above 1,000 Pa, a steep increase in the mass concentration of unseparated dust particles is characteristic, which

corresponds to the exponential course. It can be concluded from the course that the designed separation conveying device reliably separates the dust particles during low pressure operation up to 1,000 Pa. Outlet mass concentrations of dust particles in low values below 5 mg m^{-3}, comply with the legislation in force in the EU Member States.

According to the proven results, the dust separation technology in low-pressure operation can generally be considered as operationally efficient. The technical design of the proposed technology is structurally simple and demonstrates high technical and technological reliability.

REFERENCES

Aksa, W., Medles, K., Rezoug, M., Boukhoulda, M.F., Bilici, M., Dascalescu, L. 2013. Two stage electrostatic separator for the recycling of plastics from waste electrical and electronic equipment. *Journal of Electrostatics* **71**(4), 681–688.

Al–Salem, S.M., Lettieri, P. & Baeyens, J. 2009. Recycling and recovery routes of plastic solid waste (PSW): A review. *Waste Management* **29**(10), 2625–2643.

Balout, B., Songmene, V. & Masounave, J. 2007. An experimental study of dust generation during dry drilling of pre–cooled and pre–heated workpiece materials. *Journal of Manufacturing Processes* **9**(1), 23–34.

Burgess, W.A., Ellenbecker, MJ. & Treitman, RD. 2004. *Ventilation for Control of the Work Environment: Second Edition*, Wiley & Sons, Inc., Hoboken, New Jersey, 1–424.

Cao, Z., Wang, Y., Zhai, C. & Wang, M. 2018. Performance evaluation of different air distribution systems for removal of concentrated emission contaminants by using vortex flow ventilation system. *Building and Environment* **142**, 211–220.

Council of the European Communities. 1998. Council Directive 98/24/EC of 7 April 1998 on the protection of the health and safety of workers from the risks related to chemical agents at work (fourteenth individual Directive within the meaning of Article 16(1) of Directive 89/391/EEC). *Official Journal L* **131**, 23.

EP and Council. 2010. Directive 2010/75/EU of the European Parliament and of the Council of 24 November 2010 on industrial emissions (integrated pollution prevention and control). *Official Journal of the European Union L* **334**.

Goodfellow, H. & Tähti, E. 2001. *Industrial Ventilation: Design Guidebook*, Academic Press, San Diego, California, 1–1519.

Heederik, D., Henneberger, PK. & Redlich, CA. 2012. Primary prevention: Exposure reduction, skin exposure and respiratory protection. *European Respiratory Review* **21**(124) 112–124.

Jehlička, T. & Sander, J. 2015. Use of combined pneumatic conveying in the processing of granular waste materials. *Agronomy Research* **13**(1), 83–88.

Kalliny, M.I., Brisolara, J.A., Glindmeyer, H. & Rando, R. 2008. A survey of size–fractionated dust levels in the U.S. wood processing industry. *Journal of Occupational and Environmental Hygiene* **5**(8), 501–510.

Kažimírová, V. & Opáth, R. 2016. Biomass combustion emissions. *Research in Agricultural Engineering* **62**, 61–65.

Kim, K–H., Kabir, E. & Kabir, S. 2015. A review on the human health impact of airborne particulate matter. *Environment International* **74**, 136–143.

Kulkarni, P., Baron, P.A. & Willeke, K. 2011. *Aerosol Measurement: Principles, Techniques, and Applications: Third Edition*. Wiley & Sons, Inc., Hoboken, New Jersey, 1–900.

Malaťák, J. & Passian, L. 2011. Heat–emission analysis of small combustion equipments for biomass. *Research in Agricultural Engineering* **57**(2), 37–50.

Matsusaka, S. & Masuda, H. 2003. Electrostatics of particles. *Advanced Powder Technology* **14**(2), 143–166.

Mazumder, M.K., Sims, R.A., Biris, A.S., Srirama, P.K., Saini, D., Yurteri, C.U., Trigwell, S. & Sharma, R. 2006. Twenty–first century research needs in electrostatic processes applied to industry and medicine. *Chemical Engineering Science* **61**(7), 2192–2211.

Peukert, W. & Wadenpohl, C. 2001. Industrial separation of fine particles with difficult dust properties. *Powder Technology* **118**(1–2), 136–148.

Pirela, S.V., Sotiriou, G.A., Bello, D., Shafer, M., Bunker, K.L., Castranova, V., Thomas, T. & Demokritou, P. 2015. Consumer exposures to laser printer–emitted engineered nanoparticles: A case study of life–cycle implications from nano–enabled products. *Nanotoxicology* **9**(6), 760–768.

Taylor, T. 1998. Specific energy consumption and particle attrition in pneumatic conveying. *Powder Technology* **95**(1), 1–6.

Tilmatine, A., Medles, K., Bendimerad, S.–E., Boukholda, F. & Dascalescu, L. 2009. Electrostatic separators of particles: Application to plastic/metal, metal/metal and plastic/plastic mixtures. *Waste Management* **29**(1), 228–232.

Tönshoff, H. K., Karpuschewski, B. & Glatzel, T. 1997. Particle emission and immission in dry grinding, *Annals of the CIRP* **46**(2) 693–695.

Vaculik, P., Chladek, L., Přikryl, M., Smejtková, A. & BrANÝ, P. 2016. The temperature changes of barley malt during its disintegration on a two roller mill. *Agronomy Research* **14**(2), 1488–1497.

Physical-chemical properties and possible applications of clay minerals and humic acid composite materials

M. Jemeljanova[*], R. Ozola and M. Klavins

Department of Environmental Science, University of Latvia, Raina Blvd. 19, LV-1586 Riga, Latvia
[*]Correspondence: marta.jemeljanova@gmail.com

Abstract. Pollution caused by pharmaceuticals has become an increasingly serious issue, therefore innovative and cost – effective methods of pharmaceutical's removal must be studied. Clay – humic acid composite materials can be considered as prospective and low cost sorbents for contaminants. The aim of this study is to develop clay mineral and humic acid composite materials and to characterise their possible applications. For this research, three types of clay minerals (montmorillonite, kaolinite and bentonite) were modified with three types of humic substances: technical humic acid from lignite, humic substances extracted from raised bog peat and technical K humate from lignite. The sorption was characterised according to the chosen clay mineral and humic acid type and concentration. The obtained material was characterised by Fourier Transform Infrared spectroscopy and Scanning Electron microscopy. The composite materials were tested for sorption of pharmaceuticals (chlorpromazine hydrochloride). The obtained results characterise clay mineral and humic acid composite materials' possible applications as sorbents for removal of pharmacologically active substances.

Key words: clay composites, humic acids, sorption, environmentally friendly technologies.

INTRODUCTION

Clay minerals are phyllosilicates and their crystal structure consists of tetrahedral $[SiO_4]^{4-}$ and octahedral $[AlO_3(OH)_3]^{6-}$ sheets in either a 1:1, 2:1 or 2:1:1 proportion. The arrangement and composition of octahedral and tetrahedral sheets mostly determine the physical and chemical properties of clay minerals. Commonly known clay mineral kaolinite's structure consists of a single tetrahedral sheet and a single octahedral sheet with little or no permanent charge. The structure of montmorillonite consists of two tetrahedral sheets with a central octahedral sheet with a charge from 0.5 to 1.2 e/uc per unit cell (Murray, 2007; Lee & Tiwari, 2012). The negative charge is due to isomorphous substitution in octahedral (e.g., Al^{3+} for Mg^{2+}) sheet and it is compensated with exchangeable cations (Na^+, Li^+, Ca^{2+} etc.) present in the interlayer space of the clay mineral. Due to isomorphous substitution, montmorillonite has a higher cation exchange capacity and surface area than kaolinite (Schulze, 2005; Zhu et al., 2016).

Humic substances is a group of naturally occurring organic substances which results from long-term physical, microbial and chemical transformations of organic matter. Humic substances are high-molecular weight polycationites and can be used for

clay modification to obtain a sorbent for the removal of organic and inorganic pollutants (Jin et al., 2016; Wang et al., 2018). Nowadays humic substances from different sources are produced in quantities of tons and can be considered as low cost natural material.

Natural clay minerals have received a lot of attention as potential sorbents, because of high sorption and ion-exchange properties as well as their abundance and low cost (Zhang et al., 2015). Clay minerals can be modified using different approaches to obtain innovative materials for their application as sorbents in the removal of different types of pollutants (Lee & Tiwari, 2012). In the last two decades most studies have concentrated on using organoclays to remove organic and inorganic contaminants from wastewater (Ozola et al., 2018). Organoclays are prepared by intercalating specific organic molecules in the interlayer space of a clay mineral through an ion exchange reaction. The surfactants, known as quaternary alkylammonium salts, are the most commonly used organic compounds for the preparation of organoclays (Yariv & Cross, 2002). For example, kaolinite modified with hexadecyltrimethylammonium bromide, has been used to remove significant quantities of nitrates, arsenate and chromates from aqueous solutions (Li & Bowman et al., 2001), while montmorillonite, kaolinite or palygorskite modified with octadecyltrimethylammonium bromide has been used as an efficient sorbent of various pesticides (linuron, atrazine and metalaxyl) in a sandy soil (Rodríguez-Cruz et al., 2007). However, cationic surfactants, such as hexadecyltrimethylammonium bromide and octadecyltrimethylammonium bromide can be environmentally hazardous; they are toxic to soil microbially mediated processes (dehydrogenase and nitrification) and earthworms (Sarkar et al., 2013).

The aim of the present study is to develop clay mineral and humic acid composite materials and to characterise their possible applications.

MATERIALS AND METHODS

Materials
Three types of industrially produced clay minerals were used – kaolinite (*Kaolin heavy*, Sigma – Aldrich Chemie GmbH), montmorillonite (*Montmorillonite K10,* Sigma – Aldrich Chemie GmbH) and bentonite (*Bentonite pure*, AppliChem Panreac GmbH) – as well as three types of humic substances – technical humic acid from lignite (Sigma – Aldrich Chemie GmbH), technical K humate from lignite (Czech Republic) and humic substances from raised bog peat (Latvia).

Characterisation of materials
FTIR. In order to characterise changes of functional groups, infrared spectra were taken for modified and unmodified clay samples. 10 mg of clay sample was mixed with 200 mg of KBr, 30 mg of the obtained powder was pressed into a tablet. Fourier Transform Infrared Spectrophotometer *Shimadzu IR- Tracer* 100 was used with following settings – wave number 4000–400 cm^{-1}; resolution 2 cm^{-1}; the number of scans 20.

SEM. SEM was performed on *Hitachi S-4800* Scanning Electron Microscope with 3.0 kV voltage. *Image J* programme was used for data processing.

Sorption experiments

Batch system was used to conduct sorption experiments. Three types of humic substances and 0.1 M NaOH were used for preparation of humic substances stock solutions with varied concentrations (5, 10, 25, 50, 100, 200, 500, 1,000 mg L^{-1}). 0.3 g of clay minerals were weighed in a glass vessel and 50 mL of humic substances concentrate was added. Vessels were subsequently shaken for 24 hours at room temperature at 150 rpm with orbital shaker *BioSan PSU U-20*. Suspensions were afterwards filtered into 50 mL plastic test tubes and then the concentrations of filtrates were measured with *Shimadzu UV Spectrophotometer UV-1800* at the 410 nm wavelenght.

The concentration after sorption was calculated using the equation of the calibration graph and the following formula:

$$C = (A + b_0) \div b_1, \tag{1}$$

where C – the concentration after sorption, mg L^{-1}; A – absorption; b_0 – the y-intercept; b_1 – the coefficient of slope. The sorbed amount was calculated with the following formula:

$$q_e = (C_1 - C_2) \times V \div m, \tag{2}$$

where q_e – the sorbed weight, mg g^{-1}; C_1 – the concentration before sorption, mg L^{-1}; C_2 – the concentration after sorption, mg L^{-1}; V – the volume of added solution, mL; m – the weight of clay minerals, g.

Sorption of chlorpromazine hydrochloride

Standard solutions preparation. Stock solution of reference standard was prepared by dissolving accurate weighed sample of a compound in 50 mM ammonium acetate solution at a concentration of 10,000 mg mL^{-1}. Working standard solutions (5.0–550 µg mL^{-1}) containing chlorpromazine hydrochloride ($\geq$ 98% (TLC) Sigma-Aldrich) was prepared by diluting the stock solutions. A sample of 2.0 µl was injected with an autosampler. The straight-line regression was not forced to a zero intercept. Linear least squares regression of the peak areas as a function of the concentrations was performed to determine the correlation coefficients ($R^2 > 0.9995$). The equation parameters (slope and intercept) of standard curve were used to obtain the concentration values (y = 20495x+23; y – peak area, mV·s; x – conc., µg mL^{-1}). The precision of the method was assessed by triplicate analysis of standard solutions at eight concentrations (5.0, 10.0, 50.0, 100.0, 200.0, 300.0, 400.0 and 550.0).

UPLC analysis of chlorpromazine. Chromatography of chlorpromazine compounds in clay samples was carried out using the methods of Larsimon et al (1998) and Takahashi (1980) with slight modification. Acidified (5 mM CH$_3$COONH$_4$) clay (100 mg) extract was filtered through an nylon syringe filter with 0.22 µm pore size (Membrane Solutions, Plano, TX, USA) straight to 1.5 mL glass vials and right away analyzed using the UPLC system. The chromatographic separation was carried out using the *Waters Acquity UPLC H-class* consisting of a ultra high-pressure gradient unit (*Quaternary Solvent Manager*), an auto injector (*FTN*), a column oven (*CHA*), and a fluorescence detector (*FLR*). Chromatographic data was collected via *Waters Empower*

chromatography software. Chromatography was carried out at 30 °C using a Acquity UPLC HSS CYANO column (1.7 μm, 2.1 × 450 mm) and a mobile phase consisting of acetonitrile and 50 mM CH_3COONH_4 (9:1 v/v) running a constant flow-rate of 0.50 mL min^{-1}. The total separation time was 3.5 min. The identification and quantification of chlorpromazine was estimated using a fluorescence detector at an excitation wavelength of 280 nm and emission wavelength of 450 nm.

Sorption of chlorpromazine on clay samples. The concentrate of chlorpromazine hydrochloride was obtained by dissolving 0.3 g of chlorpromazine hydrochloride in 500 mL 0.1% ammonia acetate. 0.1 g of each obtained type of sorbent as well as each type of raw clay minerals was weighed and 20 mL of chlorpromazine concentrate was added. The samples were shaken in *Biosan PSU U-20 (Latvia)* shaker for 24 hours in room temperature. The samples were subsequently filtered with paper filter and 0.45 μm membrane filter and analysed in the UPLC system.

RESULTS AND DISCUSSION

Characterisation of the materials

FTIR. In order to characterize the changes of obtained clay – humic acid sorbents' functional groups, FTIR spectra were taken and the differences between raw and modified clays were analysed. All of the modified samples apart from bentonite modified with technical K humate (Figs 1, 2, 3) had peaks at wave number 2,850–2,950 cm^{-1}, that canbe assigned to C-H aliphatic stretch. Common peaks were observed that can be assigned to clay mineral structure, such as peak at the wavenumber 3,620 cm^{-1} (approximately) that refers to hydroxylgroups between tetrahedral and octahedral sheets. Samples had peaks at the wavenumbers 3,653 cm^{-1} and 3,669 cm^{-1} that can be assigned to Si-O-Si and O-H stretch. The samples of bentonite and kaolinite had a peak at the wavelenght interval 950–800 cm^{-1} that refers to O-H bend and tri-valent central atoms in octahedral sheets. Bentonite samples had a peak in the wavelenght interval 1,400–1,300 cm^{-1} that can be assigned to Si-O stretch and bend as well as O-H bend. Kaolinite samples had a peak in the wavelenght interval 695–698 cm^{-1} that can be assigned to O-H bend and two-valent central atoms.
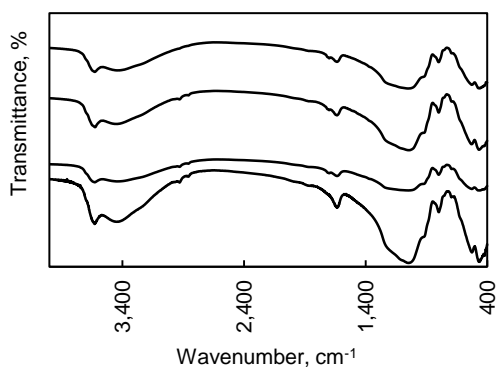
Figure 1. Montmorillonite FTIR spectra (from top to bottom: Mt_A – modified with technical humic acid; Mt_CH – modified with technical K humate; Mt – raw montmorillonite; Mt_HS – modified with raised bog peat humic substances).
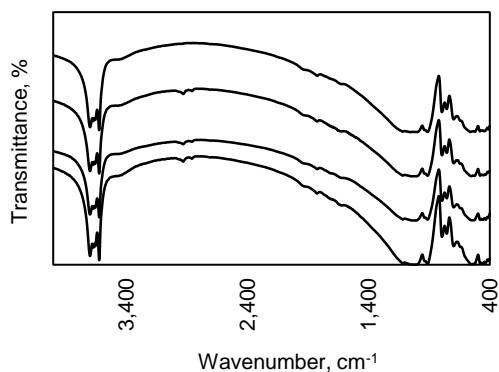
Figure 2. Kaolinite IR spectra (from top to bottom: K_A – modified with technical humic acid; K_CH – modified with technical K humate; K – raw kaolinite; K_HS – modified with raised bog peat humic substances).
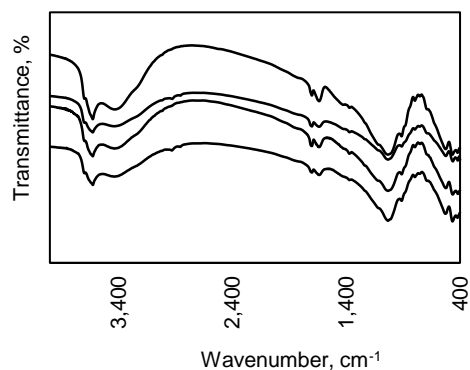
Figure 3. Bentonite IR spectra (from top to bottom: Bt_A – modified with technical humic acid; Bt_CH – modified with technical K humate; Bt – raw bentonite; Bt_HS – modified with raised bog humic substances).

SEM. SEM images can be seen in Fig. 4. Montmorillonite had an irregular surface both pre – (Fig. 4, a) and post (Fig. 4, b, c, d) modification. No significant changes in morphology were noted.
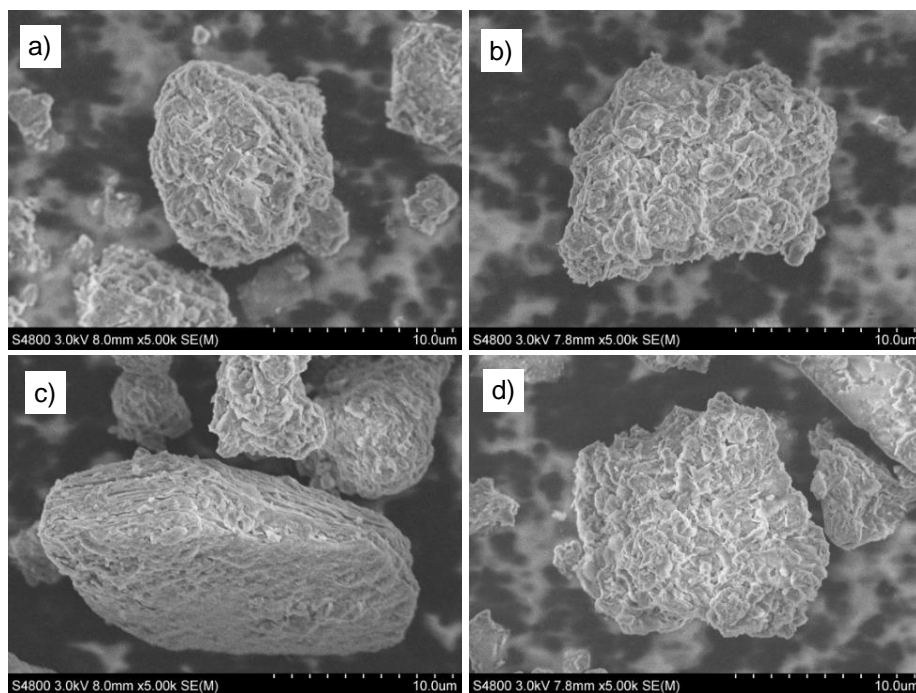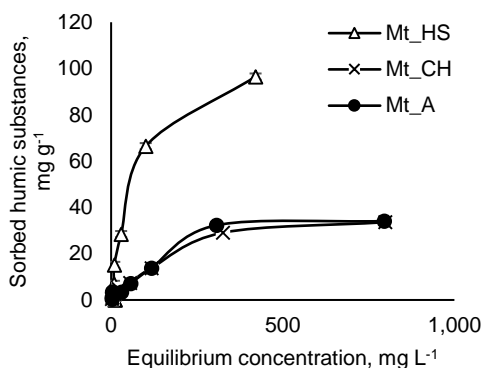

Figure 4. SEM images of a) raw montmorillonite; b) montmorillonite modified with high bog peat humic substances; c) montmorillonite modified with technical humic acid; d) montmorillonite modified with technical K humate.

Sorption experiments

In order to obtain the optimal conditions of clay minerals and humic substances composite materials synthesis, the initial concentration of humic substances was varied while maintaining other sorption parameters, e.g., the sorption time, pH value, the weight of clay minerals sample.

Comparing the isotherms of the sorbent motmorillonite, it can be seen that the highest sorption capacity by a significant margin was attained modifying with raised bog peat humic substances (96.5 mg g^{-1}), but the sorption capacities of the remaining sorbates where almost the same – 34.1 mg g^{-1} with technical humic acid as a sorbate and 33.6 mg g^{-1} with technical K humate as a sorbate (Fig. 5).
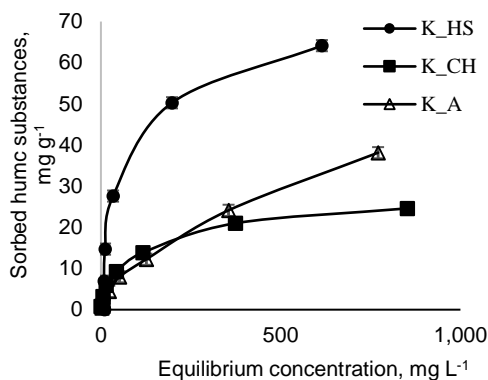

Figure 5. The sorption isotherms of montmorillonite samples (Mt_HS – modified with raised bog peat humic substances; Mt_CH – modified with technical K humate; Mt_A – modified with technical humic acid).
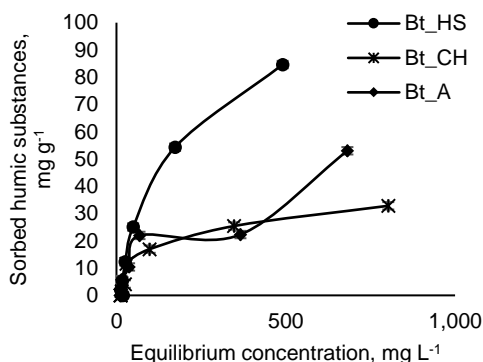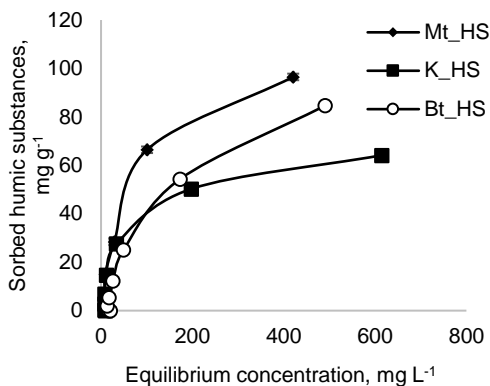
Figure 6. The sorption isotherms of bentonite samples (Bt_HS – modified with raised bog peat humic substances; Bt_CH – modified with technical K humate; Bt_A – modified with technical humic acid).

Similar results were obtained using bentonite as a sorbent – the raised bog peat humic substances sorption capacity was higher by a significant margin (84.6 mg g^{-1}) (Fig. 6). By contrast, the sorption capacities of remaining samples varied significantly – the sorption capacity of technical humic acid was 53.0 mg g^{-1}, and the lowest sorption capacity of bentonite was observed when K humate (32.8 mg g^{-1}) was used. Similarly, modifying kaolinite with raised bog peat humic substances, the highest sorption capacity was obtained (64.1 mg g^{-1}) (Fig. 7). The sorption capacity of kaolinite modified with technical humic acid was 38.1 mg g^{-1}, but kaolinite modified with technical K humate had the lowest sorption capacity (24.6 mg g^{-1}). Comparing the results of chosen sorbates, it can be concluded that the highest sorption capacity was found when raised bog peat humic substances were used as a sorbate.

Comparing isotherms of a common sorbate – raised bog peat humic substances – it can be concluded that montmorillonite had the highest sorption capacity (96.5 mg g^{-1}) followed by bentonite (84.6 mg g^{-1}). The lowest sorption capacity was found when kaolinite was used (64.1 mg g^{-1}) (Fig. 8).

Figure 7. The sorption isotherms of kaolinite samples (K_HS – modified with raised bog peat humic substances; K_CH – modified with technical K humate; K_A – modified with technical humic acid).

Figure 8. The sorption isotherms of sorbents modified with raised bog peat humic substances (Mt_HS – montmorillonite; K_HS – kaolinite; Bt_HS – bentonite).

A similar order can be seen when clay minerals where modified with technical K humate, although the sorption capacity of bentonite was almost the same as that of montmorillonite (32.8 mg g^{-1} and 33.6 mg g^{-1}, respectively) (Fig. 9). Kaolinite modified with technical K humate had the lowest sorption capacity (24.6 mg g^{-1}). The results differed modifying clay minerals with technical humic acid – bentonite had the highest sorption capacity (52.9 mg g^{-1}) (Fig. 10). The sorption capacity of kaolinite was 38.13 mg g^{-1}. Montmorillonite had the lowest sorption capacity (34.07 mg g^{-1}), although modified with raised bog peat humic substances or technical K humate it had the highest sorption capacity
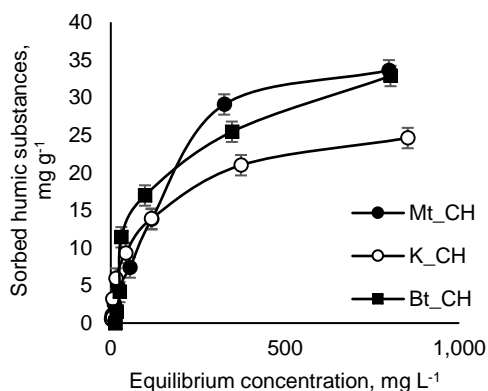
Figure 9. The sorption isotherms of sorbents modified with technical K humate (Mt_CH – montmorillonite; K_CH – kaolinite; Bt_CH – bentonite).
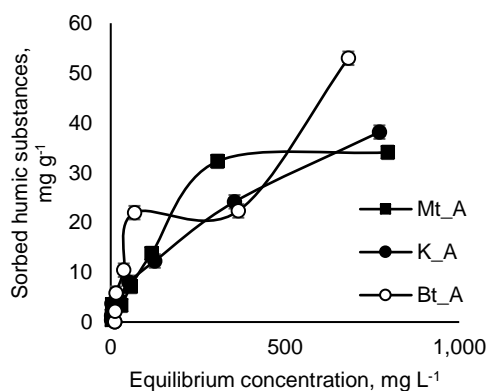
Figure 10. The sorption isotherms of sorbents modified with technical humic acid (Mt_A – montmorillonite; K_A – kaolinite; Bt_A – bentonite).

Chotzen et al. (2016) observed that kaolinite had higher sorption capacity that montmorillonite in the natural pH of the respective clay minerals, and it was argumented to be because of kaolinite's low natural pH. In acidic pHs, higher adsorbtion of humic substances can be achieved (Derakhshani & Naghizadeh, 2018). For this study an acidified montmorillonite was used and an identical pH was set, therefore the sorption capacity of montmorillonite in this study was higher than that of kaolinite. In comparison, while adjusting the humic acid solution to pH 7, Zhang et al. (2012) observed higher sorption capacity for smectite than kaolinite.

Sorption of chlorpromazine hydrochloride

Sorption experiments were done by adding 20 mL of chlorpromazine hydrochloride to 1 g of clay minerals and subsequently shaking the samples for 24 hours in room temperature on *Biosan* shaker. The filtrates were filtered through 45 μm membrane filter and analysed in UPLC system.

The sorption capacity of chlorpromazine by various samples is shown in Table 1. Modified bentonite samples had the highest sorption capacity of chlorpromazine (over 99%). The sorption capacity of montmorillonite samples were in the range of 73.48–93.21%. Kaolinite samples had the lowest sorption capacity (21.-12%–59.05%), because of its lower cation exchange capacity and surface layer (Schulze, 2005; Zhu et al., 2016).

Raw bentonite had the lowest sorption capacity of bentonite samples (99.44%), although the approximate difference with modified samples was only 0.5%. The results of modified bentonite samples were identical, therefore studies of higher inital concentration of chlorpromazine should be done. The results of lowest

Table 1. The sorption capacity of clay - humic acid composite materials (K – kaolinite; Mt – montmorillonite; Bt – bentonite; HS – raised bog peat humic substances; CH – technical K humate; A – technical humic acid)

Sample	Sorbed chlorpromazine amount, μg mL^{-1}	Sorbed chlorpromazine amount, %
Bt	596.67	99.4
Bt_CH	599.77	100.0
Bt_A	599.75	100.0
Bt_HS	599.82	100.0
K_A	155.18	25.8
K_HS	354.52	59.1
K_CH	141.18	23.5
K	127.18	21.1
Mt_A	559.29	93.2
Mt_HS	441.01	73.5
Mt_CH	546.18	91.0
Mt	517.92	86.3

sorption capacity were coherent with kaolinite samples – raw kaolinite had the lowest sorption capacity (21.12%). The highest sorption capacity of modified kaolinite samples by a significant margin was obtained with kaolinite modified with raised bog peat humic substances (59.05%). Kaolinite modified with technical humic acid and kaolinite modified with technical K humate showed a difference of only 2% (25.79% and 23.46%, respectively).

In contrast, montmorillonite modified with raised bog peat humic substances had the lowest sorption capacity of montmorillonite samples (73.48%). Montmorillonite modified with technical humic acid and modified with technical K humate had the highest sorption capacity (93.21% and 91.02%, respectively). The sorption capacity of raw montmorillonite was 86.13%.

To characterise the materials and their possible application comprehensively, X- ray diffraction (XRD) method will be used as well as sorption experiments depending on pH and sorption time.

CONCLUSIONS

The study of interaction of clay minerals and humic substances is of importance to understand the interaction of clay minerals and natural humic matter at the formation of soils. However clay-humic composites are prospective for development of sorbents for environmental technologies. In this study clay minerals were modified with three types of humic substances and tested for chlorpromazine sorption. Comparing the influence of clay minerals and humic substances on humic substances sorption, it can be concluded that the choice of humic substances affects the sorption capacity more. Modification of clay minerals mostly increased the sorption capacity of chlorpromazine. The highest sorption capacity of chlorpromazine was obtained by using montmorillonite and bentonite samples due to their higher surface area and sorption capacity. Although, in the case of bentonite further sorption experiments of chlorpromazine are needed.

REFERENCES

Derakhshani, E. & Naghizadeh, A. 2018. Optimization of humic acid removal by adsorption onto bentonite and montmorillonite nanoparticles. *Journal of Molecular Liquids* **259**, 76–81.

He, Z., Cheng, X., Kyzas, G.Z. & Fu, J. 2016. Pharmaceuticals pollution of aquaculture and its management in China. *Journal of Molecular Liquids* **223**, 781–789.

Jin, X., Zheng, M., Sarkar, B., Naidu, R. & Chen, Z. 2016. Characterization of bentonite modified with humic acid for the removal of Cu (II) and 2,4-dichlorophenol from aqueous solution. *Applied Clay Science* **134**, 89–94.

Larsimont, V., Meins J., Fieger-Büschges, H & Blum, H. 1998. Validated high-performance liquid chromatographic assay for the determination of promazine in human plasma Application to pharmacokinetic studies. *Journal of Chromatography B* **719**, 222–226.

Lee, S.M. & Tiwari, D. 2012. Organo and inorgano-organo-modified clays in the remediation of aqueous solutions: An overview, *Applied Clay Science* **59–60**, 84–102.

Li, Z. & Bowman, R.S. 2001. Retention of inorganic oxyanions by organo-kaolinite. *Water Research* **35**(16), 3771–3776.

Murray, H.H. 2007. *Applied clay mineralogy: Occurrences, processing and application of kaolins, bentonites, palygorskite-sepiolite, and common clays*. Elsevier, Amsterdam, 179 pp.

Ozola, R., Klavins, M. & Burlakovs, J. 2018. Clays, intercalated with organic substances for environmental technologies. *18th International Multidisciplinary Scientific GeoConference SGEM2018*. STEF92 Technology, Albena, pp. 197–202.

Rodríguez-Cruz, M.S., Sánchez-Martín, M.J., Andrade,s, M.S. & Sánchez-Camazano, M. 2007. Modification of clay barriers with a cationic surfactant to improve the retention of pesticides in soils, *Journal of Hazardous Materials* **139**(2), 363–372.

Sarkar, B., Megharaj, M., Shanmuganathan, D. & Naidu, R. 2013. Toxicity of organoclays to microbial processes and earthworm survival in soils. *Journal of Hazardous Materials* **261**, 793–800.

Schulze, D.G. 2005. Clay minerals. In: Hillel, D. (eds.) *Encyclopedia of Soils in the Environment*. Elsevier /Academic Press, Boston, 246–254 pp.

Takahashi, D.M. 1980. Rapid Determination of Chlorpromazine Hydrochloride and Two Oxidation Products in Various Pharmaceutical Samples Using High-Performance Liquid Chromatography and Fluorescence Detection. *Journal of Pharmaceutical Sciences* **69**(2), 184–187.

Zhang, L., Luo, L. & Zhang, S. 2012. Integrated investigations on the adsorption mechanisms of fulvic and humic acids on three clay minerals. *Colloids and Surfaces A: Physicochemical and Engineering Aspects* **406**, 84–90.

Zhang, L., Zhang, B., Wu, T., Sun, D. & Li., Y. 2015.Adsorption behavior and mechanism of chlorophenols onto organoclays in aqueous solution. *Colloids and Surfaces A: Physicochemical and Engineering Aspects* **484**, 118–129.

Zhu, R., Chen, Q., Zhou, Q., Xi, Y., Zhu, J. & He, H. 2016. Adsorbents based on montmorillonite for contaminant removal from water: A review. *Applied Clay Science* **123**, 239–258.

Wang, F., He, J., He, B., Zhu, X., Qiao, X. & Peng, L. 2018. Formation process and mechanism of humic acid-kaolin complex determined by carbamazepine sorption experiments and various characterization methods. *Journal of Environmental Sciences* **69**, 251–260.

Yariv, S. & Cross, H. (ed.) 2002. *Organo-Clay Complexes and Interactions*. Marcel Dekker, New York, 680 pp.

Work posture load evaluation in medium size metal processing enterprise in Latvia

H. Kalkis[1,2], Z. Roja[2], K. Bokse[2], S. Babris[3] and I. Roja[4]

[1]Riga Stradiņš University, Dzirciema street 16, LV-1007 Riga, Latvia
[2]University of Latvia, Aspazijas blvd. 5, LV-1050 Riga, Latvia
[3]BA School of Business and Finance, K. Valdemara 161, LV-1013 Riga, Latvia
[4]Riga 1st Hospital, Latvia, Bruninieku 5, LV-1001 Riga, Latvia
[*]Correspondence: henrijs.kalkis@gmail.com

Abstract. The aim of this study was to evaluate the exposure of individual workers to ergonomic risk factors associated with upper, lower extremities and trunk WRMSDs and to assess entire body posture for risk of WRMSDs. The company that produces finished metal products (ironing boards) was chosen for the research. Rapid Entire Body Assessment (REBA) was used to assess the entire body posture for risk of WRMSDs. Rapid Upper Limb Assessment (RULA) method was used for ironing boards employees to evaluate exposure of the neck, trunk, arms and legs in relation to physical load. Our study proved that employees are subjected to WRMSDs due to the load on certain body parts during the work: shoulder and neck area, lower back, legs and arms. Forced work postures are an essential risk factor at work. Assemblers and packers are subdued to high risk level, but inspectors – to medium risk level, which corresponds to evaluation with RULA and REBA methods.

Key words: ergonomics, RULA, REBA, work posture, physical load.

INTRODUCTION

In Latvia manufacturing industry, which employs approximately 14% of the total population, has been rapidly developing over the past 10 years. At the same time, the number of work-related musculoskeletal disorders (WRMSD) has increased. The literature analysis shows that employees in many industries, including manufacturing industry, are exposed to manual handling and forced labour positions. Forced labour positions are the most common ergonomic risk factor in this branch (Huisstede et al., 2006; Hoy, 2012).

Forced labour positions can be very different – standing, sitting, squatting, bending down, and stretching. They can be awkward or strained, particularly when performing precise tasks which require application of strength as well (Guidelines for Manual Handling at Workplace, 2018).

In such cases, the spinal column in the area of the neck and chest is bent, shoulders are slightly raised and expanded, which in a long-term period unfavourably affect health of the workers. Due to it, disability, sick leave, and early retirement are increasing (Keogh et al., 2000; Costa-Black et al., 2010). Performing assembling in metal-working

processes, moving of heavy loads is rather often associated with their holding. WRMSDs, such as lower back pain, neck pain, and pain in the lower and upper extremities are the most common health disorders among those employed in the industry (Muggleton et al., 1999; Leclerc et al., 2001; Costa &Vieira, 2010; Hoy et al., 2012). Many authors in their research have proved that in the origin of WRMSDs not only ergonomic risks, but also psycho-social risks at work are of essential significance, which include employee's present health condition, mood, worries about somatic symptoms (Vargas-Prada et al., 2013), sleep disturbances, perception of pain, their age, gender, stress, support at work and work/life imbalance (Okunribido & Wynn, 2010; Eatough et al., 2012).

Ergonomic assessment of Work-Related Musculoskeletal Disorders involves the evaluation of the risk of developing a range of disorders in muscles, nerves and joints, primarily in the upper and lower limbs and lower back, associated with occupational tasks.

The aim of this study was to evaluate the exposure of individual workers to ergonomic risk factors associated with the upper and lower extremities and trunk, and to assess entire body posture for the risk of WRMSDs. The company that produces finished metal products (ironing boards) was chosen for the research. The study was approved by the Human Ethics and Institutional Review Board of University of Latvia in 2018.

MATERIALS AND METHODS

The objective research involved 7 workers, all females, employed in assembly of ironing boards, 7 workers from packaging of ironing boards and 7- from inspection staff for ironing boards. All workers did not have acute musculoskeletal disorders, all agreed to participate in the survey and in research. Demographic factors are shown in Table 1.

Table 1. Demographic factors of the research groups: mean age and range, mean height, mean weight, mean body mass index (BMI), standard deviation (SD).

Profession/Length of service (years)	n	Mean age ± SD	Range	Mean height, cm ± SD	Mean weight, kg ± SD	Mean BMI, kg m^{-1} ± SD
Assembly of ironing boards workers	7					
0–5	3	36.0 ± 14.1	23–54	170.3 ± 2.5	73.0 ± 4.6	25.2 ± 2.3
6–15	3	41.7 ± 5.7		175.0 ± 7.9	82.7 ± 6.7	27.8 ± 4.0
> 16	1	54		178	87	27.5
Packaging of ironing boards workers	7					
0–5	4	32.0 ± 10.7	22–53	170.8 ± 8.6	76.5 ± 10.1	26.2 ± 1.5
6–15	1	53		168	81	28.7
> 16	2	41.5 ± 3.5		167.5 ± 3.5	72.5 ± 6.4	25.9 ± 3.4
Inspection staff for ironing boards	7					
0–5	3	50.3 ± 7.1	39–58	171.0 ± 3.6	73.0 ± 4.6	24.9 ± 0.5
6–15	2	47.0 ± 11.3		166.5 ± 3.5	75.0 ± 7.1	27.1 ± 3.7
> 16	2	52.0 ± 4.2		170 ± 2.8	81.5 ± 6.4	28.2 ± 1.3

Work cycles contains various operations for each chosen profession in the research. Hence such work operations were analysed due to the fact that management and workers of the company indicated main uncomfortable and painful postures, fatigue levels and load on various body parts in the long term in assembly, packaging and inspection operations. Duties of assemblers of ironing boards are related with assembling of boards. Within a shift workers lift and move the assembled boards averagely 150 times. One board weighs 7.8 kg. During the work mainly arms, legs and back receive the load. Operations analysed for workers in packaging of ironing boards were: to take ironing boards of different size and weight off the platform, put them on the table and attach markers to them. Within a shift 380 ironing boards are lifted with hands taking them from platforms and placing them onto the working table. The average weight of an ironing board is 7.8 kg, the lightest being 5.8 kg, but the heaviest – 9.8 kg. Lifting and placing of ironing boards require the load on the muscles of legs, back and arms. Ironing board inspection staff operations involved visual assessment of the quality of the packed ironing boards. Slightly bending forwards with stretched arms the worker has to turn round the ironing board whose average weight is 5.8–9.8 kg. The work process involves arms, legs and back.

The work postures of assemblers, packers and inspection staff are represented in the Fig. 1.

Figure 1. Assemblers, packers and inspection staff in the working process.

Survey of the employees was carried out with a specially worked out questionnaire in order to find out their opinion about ergonomic risks at work, work load, and work postures. The following questions were included in this questionnaire: age, length of service, height, weight, smoking status, musculoskeletal disorders after work, physical activity in the leisure time, supervisor's support at work, colleagues' support, and work intensity. Smoking status was determined by the question: 'do you smoke or have you ever smoked?' with the four response alternatives: no, never (0); yes, but not anymore (1); yes, occasionally (2) and yes, every day (3). Musculoskeletal disorders after work in neck, shoulders, back, arms and legs were evaluated by assessing pain/discomfort intensity after the work. Pain/discomfort intensity was classified by participants as - no pain/discomfort, mild pain/discomfort, moderate pain/discomfort or severe pain/discomfort.

About leisure-time and physical activities the participants reported which of the following activity levels corresponded best to their own level: inactive (e.g., reading, watching TV, movies); some physical activity (e.g., bicycling, walking,); regular activity (e.g., running, gymnastics).

In order to evaluate the body posture and physical load on body parts both sides the Rapid Entire Body Assessment (REBA) was used to assess the entire body posture for risk of WRMSDs, but the Rapid Upper Limb Assessment (RULA) method was used for ironing boards employees to evaluate exposure of the neck, trunk, arms and legs in relation to physical load.

The Rapid Upper Limb Assessment (RULA) was developed earlier by Mc Atamney and Corlett (McAtamney & Corlett, 1993). The RULA ergonomic assessment tool considers biomechanical and postural load requirements of job tasks/demands on the neck, trunk, and upper extremities. This tool requires no special equipment in providing a quick assessment of postures of the neck, trunk and upper limbs along with muscle function and the external loads experienced by the body. After the data for each region was collected and scored, tables on the form were then used to compile the risk factor variables, generating a single score that represented the level of musculoskeletal disorders risk as outlined below (see Table 2).

Table 2. The classification of risks according to RULA

RULA Score	Risk level		Action (including further assessment)
1–2	(0)	negligible risk	no action required
3–4	(1)	low risk	change may be needed
5–6	(2)	medium risk	further investigation, change soon
6+	(3)	high	implement change now
	(4)	very high risk	

REBA (Rapid Entire Body Assessment) was developed by Hignett and McAtamney (Hignett & McAtamney, 2000). REBA provides a quick and easy measure to assess a variety of working postures causing the risk of musculoskeletal disorders. It divides the body into sections to be coded independently, according to the movement planes and offers a scoring system for muscle activity throughout the entire body, stagnantly, dynamically, fast changing or in an unsteady way, and where manual handling may occur, which is referred to as a coupling score, as it is significant in the loads handling but may not always be using the hands. Postures of individual body parts are observed and postural scores increase when postures diverge from the neutral position. Group A includes trunk, neck, and legs, while group B includes upper and lower arms and wrists. Other items including the load handled, couplings with the load, and physical activity are specifically scored and then processed into a single combined risk score using a table provided. These scores are summed up to give one score for each observation, which can then be compared to tables stating the risk at five levels, leading to the necessity of actions.

REBA provides five action levels for estimating the risk level (Al Madani & Dababneh, 2016). These risk levels starting from 0 to 4 are corresponding to negligible, low, moderate, high and very high risk level respectively (see Table 3).

Table 3. The classification of risks according to REBA

Action level	REBA score	Risk level	Action (including further assessment)
0	1	(0) negligible	none necessary
1	2–3	(1) low	may be necessary
2	4–7	(2) medium	necessary
3	8–10	(3) high	necessary and soon
4	11–15	(4) very high	necessary and now

RESULTS AND DISCUSSION

The study involved 21 employees, all females, 16 of them having secondary education, but 5 – professional education. The younger employees recognised that they smoke averagely 10 cigarettes a day. They do it also during breaks. Fifteen of the employees were married, but 6 – single. None of the employees from the study do physical activities (swimming, gymnastics, etc.) after work. Only 57.1% of them recognised that they go to work by bicycle. As to feeling of pain/discomfort after work 66.7% of the employees pointed out that they felt pain/discomfort in the hands, legs and back, evaluating their level as moderate, but 33.3% of the employees of different age having length of service in the profession for 0–5 years, indicated that they did not feel pain/discomfort in individual parts of the body after work.

The acquired results assessing body postures with REBA method are shown in the Table 4.

Table 4. REBA method`s results, where count (n), standard deviation (SD)

Profession	n = 21	REBA score Mean ± SD	Risk level	Action
Assembly of ironing boards workers	7	4 = 8p 2 = 9p 1 = 7p 8.1 ± 0.7	3 high	necessary and soon
Packaging of ironing boards workers	7	3 = 9p 2 = 10p 2 = 10p 9.6 ± 0.5	3 high	necessary and soon
Inspection staff for ironing boards	7	5 = 6p 2 = 5 5.7 ± 0.5	2 medium	necessary

Assessing body conditions by REBA method it should be concluded that assemblers and packers are subdued to 3rd risk level, i.e. high risk level, but inspectors – to the medium risk.

Acquired results assessing the load of the upper parts of the body during work with RULA method are shown in the Table 5.

Table 5. RULA method`s results, where count (n), standard deviation (SD)

Profession	n = 21	RULA score Mean ± SD	Risk level	Action
Assembly of ironing boards workers	7	3 = 7p 2 = 6p 2 = 8p 7.0 ± 0.8	3 high	implement change now
Packaging of ironing boards workers	7	2 = 9p 3 = 8p 2 = 7p 8.0 ± 0.8	3 high	implement change now
Inspection staff for ironing boards	7	4 = 6p 3 = 5p 5.6 ± 0.5	2 medium	further investigation, change soon

Assessing work postures with RULA method, it should be concluded that assemblers and packers are subdued to high risk level, but inspectors – to medium risk level, which corresponds to evaluation with REBA method as well.

During the study it was observed that board assemblers use 5–10 seconds for one work operation. In this time the body takes posture bent at 10–25 degrees. The load goes to hands, legs and shoulder girdle. Within a shift the body is situated in this posture averagely for 40–45 minutes. As to board packers, during the work more load is received by the lower back and arms. During a work operation the lower back is bent at 10–25-degree angle from the vertical position. This lasts averagely for 10 seconds and within a shift it makes up 38–45 minutes. Assessing body postures in board inspectors it was found out that basically during the work the lower back, arms and shoulder girdle are loaded. The employees work in bent position (the inclination angle from the vertical is 10–25 degrees and the process lasts averagely 55–60 minutes per shift).

The results of our study correspond with those of the study on workers' postures in a car production enterprise, in which applying RULA and REBA method it was proved that the workers are under moderate to high risk of Work-related Musculoskeletal disorders (Qutubuddin et al., 2013). In other studies, for example, in the study of craftsmen's WRMSDs it is also pointed out that during the work employees' back, shoulder girdle, upper extremities and legs are loaded. It is promoted by work in forced postures, repeated and frequent body movements, age, length of service in the profession and psychosocial risks (Das et al., 2018). Our study proved that forced work postures are an essential risk factor at work and employees are subjected to WRMSDs due to the load on certain body parts during the work: shoulder and neck area, lower back, legs and arms. Main recommendations to reduce workload can be suggested by changing work tasks, meaning that the employee should work half a day at the assembling workplace and the other half, for example, at packaging workplace. It is currently being used partly already as workers are changing operations with ironing board packing and inspecting workplace, but in many these cases hard work is being replaced by hard work again. Hence additional measures are necessary. For example, workstations are recommended

to be adjustable, especially the work surface to worker`s height. Also different types of work chairs for changing work positions are recommended as well as the height of the shelf placement for all employees should be adjusted in order to assure comfortable reaching positions. During the rest breaks employees are recommended to perform muscle (lumbar, shoulder, neck) and stretching exercises to help avoid occupational diseases.

CONCLUSIONS

The chosen research methods proved that employees of an enterprise, related with the load and posture at work, are subjected to high and moderate risk according to RULA and REBA research methods. The study will be continued paying attention to psychosocial risks at work, including a bigger group in the study and use of objective research methods.

REFERENCES

Al Madani, D. & Dababneh, A. 2016. Rapid Entire Body Assessment: A Literature Review. *American Journal of Engineering and Applied Sciences* **9**(1), 107.118.

Costa-Black, K.M., Loisel, P., Anema, J.R. & Pransky, G. 2010. Back pain and work. *Best Pract Res Clin Rheumatol.* **24**(2), 227–40.

Da Costa, B.R. & Vieira, E.R. 2010. Risk factors for work-related musculoskeletal disorders: A systematic review of recent longitudinal studies. *Am J Ind Med.* **53**(3), 285–323.

Das, D., Kumar, A. & Sharma, M. 2018. A systematic review of work-related musculoskeletal disorders among handicraft workers. *International Journal of Occupational Safety and Ergonomics.* Published online: https://doi.org/10.1080/10803548.2018.1458487 Accessed 12.12.2018.

Eatough, E.M., Way, J.D. & Chang, C.H. 2012. Understanding the link between psychosocial work stressors and work-related musculoskeletal complaints. *Applied Ergonomics* **43**(3), 554–63.

Guidelines for Manual Handling at Workplace. 2018. Department of Occupational Safety and Health Ministry of Human Resources. Malaysia, 90 pp.
http://www.dosh.gov.my/index.php/en/competent-person-form/occupational-health/guidelines/ergonomic/2959-guidelines-for-manual-handling-at-workplace-2018/file Accessed 07.11.2018

Hignett, S. & McAtamney, L. 2000. Technical note Rapid Entire Body Assessment (REBA). *Applied Ergonomics* **31**. 201–205.

Hoy, D., Bain, C., Williams, G., March, L., Brooks, P., Blyth, F., Woolf, A., Vos, T. & Buchbinder, R.2012. A systematic review of the global prevalence of low back pain. *Arthritis Rheum.* **64**(6), 2028–37.

Huisstede, B.M., Bierma-Zeinstra, S.M., Koes, B.W. & Verhaar, J.A. 2006. Incidence and prevalence of upper-extremity musculoskeletal disorders. A systematic appraisal of the literature. *BMC Musculoskeletal Disorder* 7, 7.

Keogh, J.P., Gucer, P.W., Gordon, J.L. & Nuwayhid, I. 2000. Patterns and predictors of employer risk-reduction activities (ERRAs) in response to a work-related upper extremity cumulative trauma disorder (UECTD): reports from workers' compensation claimants. *Am J Ind Med.* **38**(5), 489–497.

Leclerc, A., Landre, M.F., Chastang, J.F., Niedhammer, I. & Roquelaure, Y. 2001. The Study group on Repetitive Work. Upper-limb disorders in repetitive work. *Scand J Work Environ Health* **27**, 268–78.

McAtamney, L. & Corlett, N.E. 1993. RULA: a survey method for the irvestigation of world-related upper limb disorders. *Applied Ergonomics* **24**(2), 91–99.

Muggleton, J.M., Allen, R. & Chappell, P.H. 1999. Hand and arm injuries associated with repetitive manual work in industry: a review of disorders, risk factors and preventive measures. *Ergonomics* **42**, 714–39.

Okunribido, O. & Wynn, T. 2010. Ageing and Work-Related Musculoskeletal Disorders: A Review of the Recent Literature. UK, *Health and Safety Executive*, 50 pp.

Qutubuddin, S.M., Hebbal, S.S. & Kumar, A.C.S. 2013 Ergonomic Risk Assessment using Postural Analysis Tools in a Bus Body Building Unit. Industrial Engineering Letters. www.iiste.org (online) Accessed 15.12.2018.

Urquhart, D.M, Kelsall, H.L. & Sim, M.R. 2012. Ergonomic design and training for preventing work-related musculoskeletal disorders of the upper limb and neck in adults. Cochrane Database Syst Rev. Aug. **8**, CD008570.
https://doi.org/10.1002/14651858.CD008570.pub2. Accessed 11.11.2018.

Vargas-Prada, S., Martínez, J.M., Coggon, D., Delclos, G., Benavides, F. G. & Serra, C. 2013. Health beliefs, low mood, and somatizing tendency: contribution to incidence and persistence of musculoskeletal pain with and without reported disability. *Scand J Work Environ Health*. **39**(6), 589–98.

Determining the influence of factors on retroreflective properties of traffic signs

M. Khrapova

[1]Czech University of Life Sciences Prague (CULS), Faculty of Engineering, Department of Vehicles and Ground Transport, Kamýcká 129, CZ165 00 Prague, Czech Republic
E-mail: khrapova@tf.czu.cz

Abstract. One of the distinguishing features of future autonomous cars is the ability to take into account and communicate with traffic infrastructure. Thereby detection and recognition of vertical traffic signing is an obvious requirement. Automatic recognition of traffic signs allows to check driver's reaction time, if it is necessary to react, and in that way to contribute to and increase the road safety. It is especially important in the darkness when the retroreflective sheeting materials on the traffic signs help to increase visibility. Unfortunately, environmental conditions around the traffic signs exert considerable influence on the sign's surface and alter their retroreflective properties. Many scientists explored different impacts on retroreflective properties of signs. Some impacts attracted more attention (such as detection distances and deterioration with age), some impacts were studied by several scientists only (such as dew and frost) and some factors were even omitted at all (e.g. the temperature during measurements of in-service signs). The paper is focused on the impact analysis of insufficiently explored factors influencing retroreflective properties of traffic sings. The findings of this research can support the development of further experimental research and could become a basis of reliable traffic signs usage on modern and smart roads.

Key words: autonomous cars, traffic safety, meteorological conditions, quality of signing.

List of abbreviations:

AC	artificially cleaned	ANOVA	analysis of variance
ADAS	advanced driver assistance systems	R_A	coefficient of retroreflection
AHR	after heavy rain	TSDR	traffic sign detection and recognition
AMR	after moderate rain	WR	without rain

INTRODUCTION

Every year, about 1.35 million people die as a result of traffic accidents that ranks to the eighth leading cause of death worldwide (Global status report on road safety, 2018). According to statistics, the main reason for the traffic accidents is a human factor (Rumar & Elsenaar, 2004). In order to eliminate the risk of traffic accidents due to drivers' negligence, ADAS was developed (Hechri et al., 2015). One of the main components of this system is TSDR that offers vital information to drivers about road restrictions in real time. However, the complexity of the surrounding environment and

the scenes around the traffic signs cause difficulties in road signs recognition (Toth, 2012).

Motorists of the Federal Republic of Germany conducted the experiment focused on the usage of TSDR technology in various car brands. Experimental results display that the maximal rate of successful recognition of road signs is 92% (Autoweb, 2011). The study showed that the TSDR system loses its sensitivity in the darkness, although it is especially required to enhance the road safety. The results were explained by declining brightness of the traffic signs.

The brightness of the traffic sign, according to its visibility in the darkness (Allen & Straub, 1956; Molino et al., 2013), is provided by a retroreflective sheeting of the sign, which reflects the light directly back to its source (Sivak & Olson, 1983; Federal Highway Administration, 2009; Kutz, 2011). The R_A is the conventional measure for this special kind of reflection in the case of retroreflective traffic signs (RS 101 Reflection, 2004). Since the first retroreflective sheetings were discovered and applied to the traffic signs, many types of research have been carried out with these materials.

Before the establishment of minimal retroreflective levels for retroreflective signs (Federal Highway Administration, 2007), a major part of the research studies were conducted to determine it (Black et al., 1992; Goodspeed & Mercier, 1993; Bildstein, 2001; Hawkins & Carlson, 2001; Carlson & Hawkins, 2003; Austin & Schultz, 2009). Later on, the mandated standards for 'adequate visibility' of the traffic signs (Austin & Schultz, 2009) were determined and most of the studies were focused on evaluating compliance of in-service traffic signs with mandated standards (Ellison, 2008; Ré et al., 2011a; Evans, 2012; Hummer et al., 2013). As a part of these researches, a greater number of variable factors were recorded during measurements in different combinations. These variables or some of their combinations are e.g.: characteristics of the sheeting type, headlight-beam pattern, vehicle types, sign position, roadway geometry, characteristics of drivers face direction/orientation, mount height, roadway type, form and severity of the sign's deterioration, geographic location, environmental factors (Kirk et al., 2001; Schoettle et al., 2001; Hildebrand, 2003; Carlson & Lupes, 2007; Austin & Schultz, 2009; Carlson et al., 2011; Khalilikhah & Heaslip, 2016).

According to the accomplished detailed literature review, it is possible to conclude that the common feature of all studies is a lack of the input data description that does not directly relate to the factors under the study. For example, the majority of the studies do not provide data about temperature and air relative humidity (except (Ré et al., 2011b)) during the experiment. However, according to the standards (EN 12899-1 Fixed, vertical road traffic signs, 2007; ASTM D4956 Standard Specification for Retroreflective Sheeting for Traffic Control, 2017), these tests should be carried out at the specified temperature and relative humidity to determine the R_A value. Precisely the determination of the degree of influence of air temperature and relative humidity on the retroreflection is one of the objectives of this work. This is especially important for the TSDR system that operates in real time and 'reads' the signs with the instantaneous value of R_A.

Weather conditions such as rain, drizzle, fog, dew, hoarfrost impair the 'instantaneous' visibility of the traffic signs by changing the refraction and scattering of the light beams and rendering less bright signs (Woltman, 1965). Despite the fact that these factors often lead to a significant number of accidents (Shahabi et al., n.d.; Abdel-Aty et al., 2010; Unified transport vector map, 2017), there are only four works devoted to the study of the influence of these factors on traffic signs retroflexion. The

results of the three of them were based on the subjective assessment of the participants. Munehiro et al. (2005) have made a conclusion that fog during the night does not have as great negative effect as that in the daytime. However, 'the subjective visibility values of targets under the night-time cloudy condition were worse than those under the daytime dense fog condition'. According to De Waard et al. (2005), for 9% of the participants, fog or dew was a reason of worse legibility of the signs. Hutchinson & Pullen (1978) have rated relative effects of dew and frost on target values of different types of retroreflective materials for sign's legend and background. And only E. Hildebrand (Hildebrand, 2003; Hildebrand & Bergin, 2004) has made conclusions in his works based on the measurement of R_A value. According to Hildebrand (2003), frost reduces the retroreflective level of the in-service traffic signs on average by 79%, dew – on average by 60%. The type of retroreflective material and its colour has a significant influence on the degree of degradation of the retroreflective values under dew and frost conditions.

Another degrading factor of the traffic sign optical properties is the dirtiness on its surface (Department for Transport, 2013). However, this factor to some extent loses its degree of importance, as the material's quality improvement provides new properties to it that eliminates the influence of the dirt. For example, Woltman (1982) has shown that the existence of the dirt on the surface of traffic signs reduces its reflective ability by 50%. Twenty years later, Wolshon et al. (2002) found that the average increase in retroreflectivity was about 33% after the signs had been washed. Ten years later, Jackson et al. (2013) determined that dirt reduces retroreflectivity of the signs by about 10%.

The purpose of this work is to study the 'instantaneous' factors affecting retroreflection of the signs and to determine the degree of their influence for improving detection and recognition systems of traffic signs.

MATERIALS AND METHODS

This research is divided into two parts: the first part of the study contains determination of the influence degree of dew, frost, drizzle and dirt; the second part describes identification of the correlation between retroreflectivity of a traffic sign and measurement conditions (air temperature and relative humidity). The first part includes data collection of in-service signs, during the second part measurements were carried out in the laboratory.

Study locations and test samples
The number of all tested samples of retroreflective films is represented in Table 1, that were divided according to their technology, class and study location. The classification depends on the mandated minimum R_A values which increases with the class number (EN 12899-1 Fixed, vertical road traffic signs, 2007).

In-service. The study encompassed 82 in-service traffic signs, located in Prague 6 or Horoměřice in the Czech Republic. Since 96% of all types of road signs in this country contain white and/or red elements on them (TP 65 Principles for traffic signs on communications, 2013), all selected signs also contain elements of these colours. Date of manufacture of road signs ranged from 2005 till 2017. All measurements were conducted during 2018.

<u>Laboratory</u>. Ten types of retroreflecting samples were chosen for studying the properties of sign's retroreflection in the laboratory. According to (EN 12899-1 Fixed, vertical road traffic signs, 2007; EAD 120001-00-0106 Microprismatic retro-reflective sheetings, 2016), for each type of microprismatic film 3 samples were created, for films with glass bead technology – 2. Microprismatic test samples were 20cm by 20 cm, glass bead – 10 cm by 10 cm. In addition, the measurement included a sample for calibration of the reflectometer, that had already been mounted by the device manufacturer on the front plate of the adapter.

Table 1. Summary of surveyed retroreflective sheeting according to its type and study location

Technology*	Class*	Number of samples	
		in-service	laboratoy
Microprismatic	RA1	4	6
	RA2	7	3
	RA3	8	12
Glass Bead	RA1	54	6
	RA2	9	

* – according to EN 12899-1 (EN 12899-1 Fixed, vertical road traffic signs, 2007).

Instrumentation

The retroreflectometer Zehntner ZRS 6060 was used for all measurements; this equipment allows to determine R_A in accordance with the European standard EN 12899–1 (EN 12899-1 Fixed, vertical road traffic signs, 2007), for illumination angle 5° and tree observation angles – 0.2°, 0.33°, 1°. Also, each measurement contains information about the colour of the sample, ambient temperature, relative humidity, GPS coordinates.

Methodology of measurement

The measuring principle with the retroreflectometer to get R_A value was the same for all measurements (except measurement of calibration standard). The first step is the calibration of the device using a calibration standard that is mounted on 'calibration side'. Than front plate is mounted on the 'measuring side'. The second stage is direct measurement when the instrument is planted on the surface of the traffic sign and the trigger is pulled. The measurement values are shown beside each observation on the display. Using the handheld retroreflectometer, three readings of each sign colour were collected.

Also, all for the first-time used samples for the research in the laboratory were measured. These R_A values for the first time used in-service signs were obtained from the manufacturer of the specified traffic signs. All inputs data were set according to EN 12899-1 (EN 12899-1 Fixed, vertical road traffic signs, 2007).

The difference in data collection consisted in a variety of data collection time for each specific factor affecting the retroreflection.

<u>Dirtiness.</u> The term 'dirty traffic sign' does not include the definition of the degree of contamination of the sign. Since there is no maintenance program for cleaning traffic signs, the only way of removing contamination is the influence of the atmospheric phenomenon, such as rain. Rain supposedly should sufficiently clear the sign. In order to verify the veracity of this statement, R_A values were measured for different types of retroreflective sheeting under the conditions WR, AMR and AHR.

The measurements of in-service traffic signs were carried out in March, the signs were not washed. Last precipitation (light rain) was fixed 16 days before measurements.

Next measurements were conducted in June and 3 days after a heavy rain (the intensity of rainfall was higher than 10 mm per hour) when the examples were dried. Then measurements were carried out two months later, after 3 days of moderate rain (the intensity of rainfall was between 2.5–10 mm per hour). For comparison all signs were washed by water (AC) and R_A values were measured after.

Dew, frost, drizzle. The measurement of retroreflection was conducted in the presence of dew, hoarfrost on the surface of the sign and during light drizzle from October till December. The traffic signs with a cover of frost were measured in December.

Temperature and relative humidity. In the laboratory, the test samples were measured in the range of ambient temperature -3–$25\,°C$, and the range of relative humidity of air 25%–100%. The measurement of the calibration standard was carried out when the front plate of the retroreflectometer was mounted on the 'calibration side'. Total **1,400 measurements were conducted** in the same range of temperature and relative humidity as laboratory test samples.

Data analysis

The data analysis software 'MappingTools' was used to export measured data and generate measuring reports. For statistical analysis, the 'STATISTICA' software was used, which allows to carry out a statistical analysis for comparison measured R_A values in different conditions.

Dirtiness, dew, frost, drizzle. A one-way repeated measures *ANOVA* was used to determine whether there is no difference between traffic signs with the impact of different types of precipitation or different level of dirtiness on the signs surface, at the significance level of 0.05. This test was used because three or more impacts were studied for the same test's samples. The *t-test* for dependent samples was used only if there were not sufficient number of measurements for each type of impact. For both tests, the null and alternative hypotheses were defined as follows:

H_0: no difference in means of R_A values between few data sets.

H_1: the average value of the R_A between few data sets is significantly different.

The null hypothesis for the performed tests can be rejected if the obtained *P*-value is lower than 0.05. In order to control the family-wise error rate for this case and to figure out which impact has considerable influence on the R_A, the *Tukey's* honestly significant difference post hoc test was carried out at the significance level of 0.05. The homogeneity of groups is controlled by the same test.

The average of R_A values was also obtained from *Tukey's* post hoc test but only meaningful difference between them will be discussed in this paper. The difference between groups is presented in percentage for the illustrating results in better way of perception.

Temperature and relative humidity. The one sample *t-test* was conducted in order to identify if the R_A values significantly changes with the changes in air temperature and relative humidity. As a constant for comparison were used R_A values that were measured by a manufacturer of sheeting in compliance with the standard according to the procedure described in the standard (EN 12899-1 Fixed, vertical road traffic signs, 2007) and they are assumed as true mean. The test was carried out at the significance level of 0.05 with the following null and alternative hypotheses:

H_0: the difference between the true mean and the average measured value is equal to zero.

H_1: the difference between the true mean and the average measured value is not equal to zero.

The null hypothesis for the tests is rejected if the obtained P-value is lower than 0.05.

In order to determine the influence of two independent variables such as air temperature and relative humidity on the dependent variable as the R_A, the multiple linear regression analysis at the significance level of 0.05 was carried out.

RESULTS AND DISCUSSION

Making traffic signs retroreflective is one of the ways to increase their brightness and reduce the number of traffic accidents in the darkness. Compliance with the necessary minimum of the retroreflective level is especially important in the context of detecting and recognizing traffic signs by autonomous cars. However, in the existing procedure for determining the level of retroreflection, there are several shortcomings that make an objective assessment difficult especially for in-service signs under field conditions. These disadvantages are such measurement conditions when the sign should be dried and cleaned, the measurements are conducted only at certain ranges of ambient temperature and relative humidity.

Dirtiness
The number of measurements was sufficient to perform static analysis using a one-way repeated measures *ANOVA*. The results of the tests were P-values that are shown in the Table 2. The P-values of red microprismatic RA1 and RA3 sheeting are higher than 0.05. That means that dirtiness does not have significant influence on the retroreflection. But this statement cannot be considered as a final conclusion since this analysis does not take into account an elevation of traffic signs and traffic intensity that have influence on the level of dirtiness of the sign (Khalilikhah & Heaslip, 2016).

Table 2. The results of a one-way repeated measures *ANOVA* and *Tukey's* post hoc test that are presented as P-values under pairs of conditions WR, AMR, AHR, AC

Technology	Class	Colour	*ANOVA*	*Tukey's* WR vs AMR	WR vs AHR	WR vs AC	AMR vs AHR	AMR vs AC	AHR vs AC
Microprismatic	RA1	red	0.099						
		white	**0.026**	0.188	0.076	**0.021**	0.869	0.322	0.684
	RA2	white	**0.048**	0.830	0.453	**0.039**	0.781	0.118	0.283
	RA3	red	0.078						
		white	**0.010**	0.052	0.058	**0.007**	0.989	0.557	0.518
Glass Bead	RA1	red	**0.00***	**0.00***	**0.00***	**0.00***	0.260	**0.007**	0.411
		white	**0.00***	**0.001**	**0.00***	**0.00***	**0.009**	**0.002**	0.955
	RA2	red	**0.00***	**0.001**	**0.001**	**0.00***	0.989	0.700	0.675
		white	**0.00***	**0.00***	**0.00***	**0.00***	0.060	**0.001**	0.350

* – values lesser than three decimal places after decimal point were neglected.

As shown in the Table 2, the presence of dirt has influence on all types of glass bead sheeting and white microprismatic RA1 and RA3 sheeting. For those sheeting's data sets the *Tukey's* post hoc test was carried out in order to find the pairs of groups where the mean difference is statistically significant. The results of this significant difference between pairs are also presented in the Table 2. According to the obtained *P*-values, there are significant differences between unwashed and artificially washed traffic signs (pair 'WR vs AC'). For all types of glass bead sheeting the rainfall intensity is a decisive factor since there is a significant difference between pairs 'WR-AMR', 'WR-AHR' (Table 2). For microprismatic sheeting the presence of precipitation is not so important because even after a heavy rain the R_A values do not significantly increase.

The largest difference in average values (between WR and AC) is observed for red microprismatic RA3 – 64%, the smallest for red glass bead RA2 – 8%. The difference in mean between AHR and AMR varies within 9%, except red microprismatic RA3 for which the difference is 14%.

It is worth noting, that almost all types of sheeting, even under the condition WR, met the standards (EN 12899-1 Fixed, vertical road traffic signs, 2007), their retroreflection coefficient significantly exceeded the minimum level. But 71% of the signs with the glass bead RA2 sheeting were under the minimum retroreflective level and increased above it only AHR or cleaning.

Precipitation on the surface of the sign

Dew and frost, which directly form water droplets (or even hoarfrost) on the traffic surface of the sign and minute water droplets that occurred during drizzle, were attributed to precipitation on the surface of the sign. It should be noted these types of precipitation differ not only in the phase of water but also in the size of the droplets that arise. For example, during the dew, larger drops were observed on the surface than during the drizzle. Fig. 1 shows the dew and hoarfrost on the surface of the sign that were observed during measurements.
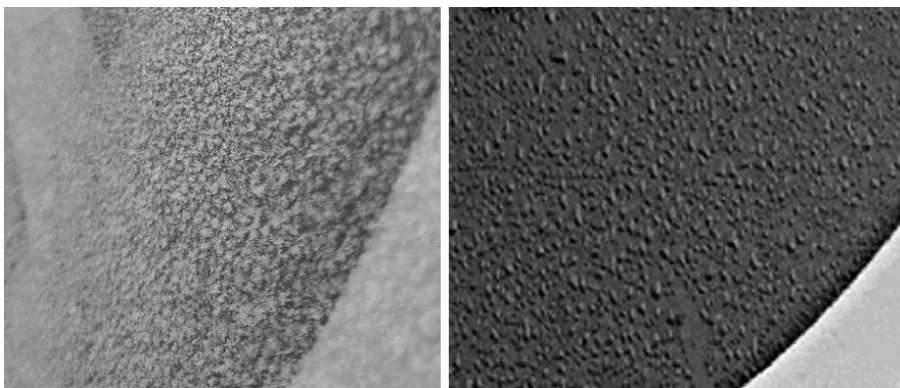
Figure 1. The presence of hoarfrost (left) and dew (right) on the surface of traffic sign.

In contrast to the previous series of measurements, during the study of these factors, the necessary number of measurements was not collected for all types of materials. For microprismatic RA2 and glass bead RA2, the effect of frost was only studied.

The measured data was analysed by one-way repeated measures *ANOVA*. The retroreflectivity of the signs with a different kind of precipitation on its surface were alternately compared with each other. The test results were *P*-values and they are presented in the Table 3. Almost all *P*-values did not exceed 0.05 (except red glass bead RA1 sheeting), which indicates significant differences between data sets. For red glass bead RA1 the presence of water droplets does not significantly impair the level of retroreflection as for microprismatic sheeting. The negligible difference for the red glass bead RA1 sheeting can be explained by the low required minimum R_A values, that means that even high difference in the R_A values is not statistically significant.

Table 3. The results of a one-way repeated measures *ANOVA* and *Tukey's* post hoc test that are presented as *P*-values under pairs of different type of precipitation on the sign's surface

Technology	Class	Colour	*ANOVA*	*Tukey's* AC vs dew	AC vs fog	AC vs frost	dew vs fog	dew vs frost	Fog vs frost
Microprismatic	RA1	red	**0.001**	**0.004**	**0.036**	**0.002**	**0.036**	0.886	**0.013**
		white	**0.010**	**0.037**	0.659	**0.015**	0.247	0.951	0.109
	RA3	red	**0.047**	0.670	0.524	**0.031**	0.965	0.186	0.249
		white	**0.011**	0.194	0.296	**0.006**	0.994	0.208	0.145
Glass Bead	RA1	white	**0.00***	0.078	0.069	**0.00***	0.988	0.114	0.124
		red	0.088						

* – values lesser than three decimal places after decimal point were neglected.

As seen in the Table 3, both for microprismatic and glass bead sheeting the difference between clean signs and signs with the hoarfrost on the surface of the signs is significant, the influence of other type of precipitation is not observed except microprismatic RA1 sheeting. For this type of material dew, fog and frost decrease the retroreflection properties.

The *t-test* for dependent samples was used to compare the difference in R_A values between two groups, AC and in the presence of hoarfrost, for microprismatic RA2 (white) and glass bead RA2 (white and red). The results of three tests show the significant difference between these two groups because all *P*-values were less than 0.05.

From the average R_A values, it was found that hoarfrost on the surface of the signs decreases the retroreflective properties more than 76%. Moreover 93% of traffic signs in the condition of frost do not meet the standards because R_A values are significantly below the minimum retroreflective levels. Very interesting discoveries were made, particularly that the dew has a worse effect on the retroreflectivity of the signs, especially for microprismatic sheeting material. The presence of dew on microprismatic RA1 reduces the retroreflectivity by about 61%, under the minimum level.

Temperature and relative humidity

During the measurement of R_A values of the same type of sheeting it was found that the values vary if the temperature or relative humidity changes. The assumption was made that retroreflection is influenced, among other factors, by temperature and humidity during measurements with a handled retroreflectometer. To test the assumptions, a series of measurements with different temperatures and humidity

were carried out. The measurements were analyzed using one sample *t*-test and as a result, *P*-values were obtained that are shown in Table 4. As shown in Table 4, the *P*-values are higher than 0.05, that the retroreflectivity of samples 3–5 and 7 does not change with temperature and relative humidity. For other samples, the difference is significant, especially for sample number 10.

Table 4. The results of the one sample *t-test* for measured signs by sheeting type and colour that was compared with values measured by manufactures

Technology	Manufacturer	Class	Colour	Sample sheeting number	P-value
Microprismatic	3M	RA1	white	1	0.022
			red	2	0.017
		RA2	white	3	**0.063**
		RA3	fluorescent	4	**0.086**
			red	5	**0.131**
			white	6	0.027
			red	7	**0.052**
Glass Bead	Avery Oralite	RA1	white	8	0.024
			white	9	0.025
			red	10	0.001

In order to assess the accuracy of the measurements, excluding all factors except the ambient temperature of the relative humidity, 1,400 measurements of the calibration standard were carried out. The multiple linear regression analysis was used to find the level of influence of each factor. As a result of the analysis, the coefficients for linear equation was obtained (Eq. 1) with the coefficient of determination equal to 0.917.

$$R_A = 228.793 + 0.792 \cdot T + 0.141 \cdot \varphi \qquad (1)$$

where R_A – the coefficient of retroreflection; T – temperature; φ – relative humidity.

The correctness of the model was tested by substituting the temperature and humidity specified by the standard (EN 12899-1 Fixed, vertical road traffic signs, 2007; $23 \pm 3°, 50 \pm 5\%$). The results corresponded to the retroreflection coefficient specified in the manufacturer's calibration standard.

CONCLUSIONS

The goal of this paper was to assess factors as dirtiness, precipitation, drizzle and dew occurring on the surfaces of traffic signs and if they can cause a significant deterioration in the retroreflection level, and, accordingly, impair visibility of the traffic signs. Based on the series of measurements and subsequent statistical analysis, it was found that the presence of any type of precipitation on the surfaces of signs significantly impairs its retroreflective properties. This is particularly relevant in the presence of hoarfrost when the retroreflective level for all types of sheeting material decreases by more than 76% and in most cases falls under the minimum level. The effect of dew and drizzle is also significant, though to a lesser extent. It is possible to conclude that the level of deterioration of retroreflection is largely related to the size of the water droplets formed on the surface of the sign. The large size of the droplets leads to a large distortion of the light reflection angles and the level of retroreflection falls.

The negative effect of dirt on the sign's surface was also confirmed during the statistical analysis. It was observed that red microprismatic RA3 sheeting material is more sensitive to purification, AHR, the retroreflection level may increase up to 64%. Despite the fact that in the Czech Republic there is no maintenance program for cleaning signs, the susceptibility of signs to 'natural' cleaning should be taken into account, since the distribution of the number of precipitations during the year is uneven and the direction of the raindrops could affect cleaning effect. In winter, when the amount of precipitation is the smallest (snow cannot be taken into account), it is still worth cleaning the sign manually, because according to the measurements, the retroreflection coefficient of glass bead RA2 sheeting is below the established minimum level. After a heavy rain, the level of retroreflection is set up above the minimum.

According to the results of the survey carried out and statistical analysis, the influence of ambient temperature and relative humidity on the traffic sign's retroreflective properties has been identified. Moreover, the dependence on ambient temperature during measurement is more apparent and that was demonstrated in the equations created on the basis of 1,400 measurements of the calibration standard. For example, a change in temperature of 25 °C leads to a 10% change in the retroreflective level. However, it was found that retroreflection does not always depend on the changes in temperature and humidity e.g. for sheeting with a high level of retroreflection, such as microprismatic R2/R3, significant changes in the measured values have not been observed. It proves necessity of the next future research to obtain true and verified information about sheeting properties.

The revealed dependence could not only explain the difference in the results of the previous studies but also, along with other established dependencies, may help to improve the recognition of traffic signs by adjusting the computational processes for different pairs of temperatures and humidity, with or without precipitation on the sign. And it could also serve as an impetus for cleaning signs not only in the Czech Republic but in every country where these procedures are not usual during the winter season.

REFERENCES

Abdel-Aty, M.A., Oloufa, H., Hassan, M., Ahmed, C., Siddiqui, A.E. & Huang, H. 2010. Developing an early detection system for reduced visibility. *FDOT Report*, 61–62.

Allen, T.M. & Straub, A.L. 1956. Sign brightness and legibility. *Highway Research Board bulletin* **127**, 1–14.

ASTM D4956 Standard Specification for Retroreflective Sheeting for Traffic Control. 2017.

Austin, R.L. & Schultz, R.J. 2009. *Guide To Retroreflection Safety Principles And Retrorereflective Measurements*. RoadVista, San Diego.

Autoweb. 2011. *https://www.autoweb.cz/systemy– rozlisujici– znacky– ktery– funguje– nejlepe/*. Accessed 31.1.2018 (In Czech).

Bildstein, A.F. 2001. The effect of environmental illumination on traffic sign conspicuity and retroreflectivity. Retrieved from *https://www.researchgate.net/publication/35252762*.

Black, K.L., McGee, H.W. & Hussain, S.F. 1992. *Implementation strategies for sign retroreflectivity standards*. Transportation Research Board, Virginia, 43 pp.

Carlson, P.J. & Hawkins, H.G. 2003. *Updated minimum retroreflectivity levels for traffic signs*. (No. FHWA– RD– 03– 081).

Carlson, P.J. & Lupes, M.S. 2007. *Methods for Maintaining Traffic Sign Retroreflectivity*. Federal Highway Administration, McLean, VA, 47 pp.

Carlson, P.J., Higgins, L. & Re, J. 2011. *Research and recommendations for a statewide sign retroreflectivity maintenance program*. Austin, Texas, 108 pp.

Department for Transport. 2013. *Traffic signs manual*.

EAD 120001– 00– 0106 Microprismatic retro– reflective sheetings. 2016.

Ellison, J.W. 2008. Tapping into the power of a traffic sign inventory to meet the new retroreflectivity requirements. In *ITE 2008 Annual Meeting and ExhibitInstitute of Transportation Engineers*.

EN 12899– 1. Fixed, vertical road traffic signs. 2007.

Evans, T.L. 2012. Development of Assessment Strategies For Sign Retroreflectivity. Utah State University.

Federal Highway Administration. 2007. *The Manual on Uniform Traffic Control Devices*. Department of Transportation, Washington, 95 pp.

Federal Highway Administration. 2009. *The Manual on Uniform Traffic Control Devices*. Department of Transportation, Washington, 816 pp.

Global status report on road safety. 2018. World Health Organization, Geneva.

Goodspeed, C.H. & Mercier, C.R. 1993. *Nighttime Sign Visibility Performance. Unpublished Draft Final Report*. Federal Highway Administration, Washington.

Hawkins, J.H. & Carlson, P.J. 2001. Sign retroreflectivity: Comparing results of nighttime visual inspections with application of minimum retroreflectivity values. *Transportation Research Record: Journal of the Transportation Research Board* **1754**, 11–20.

Hechri, A., Hmida, R. & Mtibaa, A. 2015. Robust road lanes and traffic signs recognition for driver assistance system. *International Journal of Computational Science and Engineering* **10**(1), 202.

Hildebrand, E. 2003. Reductions in Traffic Sign Retroreflectivity Caused by Frost and Dew. *Transportation Research Record: Journal of the Transportation Research Board* **1844**(1), 79–84.

Hildebrand, E. & Bergin, T. 2004. Traffic sign retroreflectivity and the canadian environment. In *CITE Conference*. Moncton, 24 pp.

Hummer, J.E., Harris, E.A. & Rasdorf, W. 2013. Simulation– Based Evaluation of Traffic Sign Retroreflectivity Maintenance Practices. *Journal of Transportation Engineering– Asce* **139**(6), 556–564.

Hutchinson, J.W. & Pullen, T.A. 1978. Performance of signs under dew and frost conditions. *Transportation research record* **681**, 16–20.

Jackson, N.M., Carlson, P.J., Ye, F. & Jackson, G.R. 2013. *Use of high intensity reflective sheeting in lieu of external lighting of overhead roadway signs.* Dept. of Transportation, Florida.

Khalilikhah, M. & Heaslip, K. 2016. Analysis of factors temporarily impacting traffic sign readability. *International Journal of Transportation Science and Technology* **5**(2), 60–67.

Kirk, A.R., Hunt, E.A. & Brooks, E.W. 2001. *Factors affecting sign retroreflectivity*. Oregon.

Kutz, M. 2011. Highway sign visibility. In *Handbook of Transportation Engineering, Volume II: Applications and Technologies, Second Edition*. McGraw Hill Professional, Access Engineering.

Molino, J.A., Kennedy, J.F., Beuse, P.A., Davis, W. & Andersen, C. 2013. *Daytime Color Appearance of Retroreflective Traffic Control Sign Materials*. Federal Highway Administration, McLean, VA, 63 pp.

Munehiro, K., Tokunaga, R., Asano, M. & Hagiwara, T. 2005. Part 3: Signing and Marking Materials: Effect of Time and Foggy Conditions on Subjective Visibility: Evaluation of Retroreflective Traffic Control Devices. *Transportation Research Record: Journal of the Transportation Research Board* **1911**, 84–104.

Ré, J., Miles, J. & Carlson, P. 2011a. Analysis of In– Service Traffic Sign Retroreflectivity and Deterioration Rates in Texas. *Transportation Research Record: Journal of the Transportation Research Board* **2258**, 88–94.

Ré, J.M., Miles, J.D. & Carlson, P.J. 2011b. Analysis of In– Service Traffic Sign Retroreflectivity and Deterioration Rates in Texas. *Transportation Research Record: Journal of the Transportation Research Board* **2258**(1), 88–94.

RS 101 Reflection. 2004.

Rumar, K. & Elsenaar, P. 2004. *Road safety manual: recommendations from the World Road Association*. Route2 Market, Switzerland.

Schoettle, B., Sivak, M. & Flannagan, M.J. 2001. *High– beam and low– beam headlighting patterns in the U.S. and Europe at the turn of the millennium*. SAE Technical Paper, 29 pp.

Shahabi, M., Hlaing, A., Martinelli, D.R. & Unnikrishnan, A. n.d. *Fog Detection for Interstate and State Highways*. West Virginia University Morgantown, 71 pp.

Sivak, M. & Olson, P.L. 1983. *Optimal and Replacement Luminances of Traffic Signs: A Review of Applied Legibility Research*. (No. UMTRI– 83– 43 Final Rpt.).

Toth, Š. 2012. Difficulties of Traffic Sign Recognition. In *The 7– th winter school of mathematics applied to ICT*. Sachticky.

TP 65 Principles for traffic signs on communications. 2013. (In Czech)

Unified transport vector map. 2017. *http://www.jdvm.cz/*. Accessed 8.12.2017.

De Waard, D., Brookhuis, K. & Mesken, J. 2005. Evaluation of legibility of not properly reflecting signs. *International Journal of Industrial Ergonomics* **35**(7), 645–651.

Wolshon, B., Swargam, J. & Degeyter, R. 2002. Analysis and Predictive Modeling of Road Sign Retroreflectivity Performance. In *16th Biennial Symposium on Visibility and Simulation*.

Woltman, H. 1982. Use of retroreflectors in the improvement of nighttime highway visibility. *Color Research & Application* **7**(3), 247–251.

Woltman, H.L. 1965. A Study of Dew and Frost Formation on Retro– Reflectors. *Highway Research Record* **70**, 63–66.

Half-cell potential mapping for corrosion risk evaluation of prestressed concrete ribbed panels from agricultural building after 20 years of service

M. Kiviste[1,*], V. Tamme[2], L. Linnus[1] and R. Halgma[1]

[1]Estonian University of Life Sciences, Institute of Forestry and Rural Engineering, Chair of Rural Building and Water Management, F.R. Kreutzwaldi 5, EE51006 Tartu, Estonia
[2]Estonian University of Life Sciences, Institute of Forestry and Rural Engineering, Chair of Forest Management Planning and Wood Processing Technologies, F.R. Kreutzwaldi 5, EE51006 Tartu, Estonia
*Correspondence: mihkel.kiviste@emu.ee

Abstract. Corrosion of steel is a significant problem in prestressed concrete structures as it decreases structural capacity and performance. In this research the 20-year-old prestressed concrete ribbed ceiling panels (of type PNS-12) with dimensions of 6 m (length) by 1.5 m (width) from an existing Estonian agricultural building (pigsty) are studied. The objective is to evaluate the corrosion risk of steel reinforcement of ribbed panels by means of a indirect (non-destructive) method and compare the results with a direct method.

The methodology consists of a) non-destructive measurements of half-cell potential and b) comparision with actual condition of steel reinforcement after concrete removal (demolition). Non-destructive measurements were performed on the 10 longitudinal ribs of 5 ribbed panels, respectively. Steel half-cell potential maps were developed based on 900 measurement points recorded by half-cell (Great Dane).

After destructive tests the ribbed panels including their longitudinal ribs were demolished and the concrete was carefully removed. The position and condition of steel details was photographed (direct method), which enabled the comparison with potential maps (indirect method).

The results demonstrated that in general, half-cell potential maps give a rather good indication on the condition of corroding steel rebars with respect to intact details. Also, half-cell potential maps were found relatively useful in estimating the corrosion risk in the studied precast ribbed panels.

Key words: half-cell, potential mapping, corrosion risk, ribbed panels.

INTRODUCTION

Corrosion of steel is a significant problem in reinforced concrete structures as it decreases structural capacity and performance. The decrease of structural capacity is due to the reduction of bond strength between steel bar and concrete and the reduction of steel cross section. The decrease of performance is due to the cracking of concrete cover and the increase of deflection.

During recent decades the expense of repair and rehabilitation of existing reinforced concrete structures has increased due to corrosion deterioration, which can also be considered as significant economic problem. It is estimated that approximately
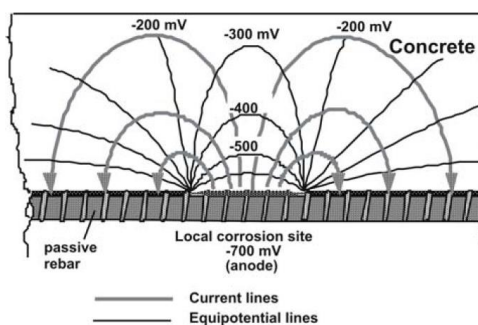
50% of the expenditure in the construction industry is spent on repair, rehabilitation and maintenance of existing reinforced concrete structures (Long et al., 2001).

A half-cell is a section of metal in a solution of its own ions (such as copper in copper sulphate, silver in silver chloride etc.). If it is connected to another metal in a solution of its own ions (such as iron in ferrous hydroxide, $Fe(OH)_2$) there will be a potential difference between the two "half-cells". It is a simplified battery or an electrical single cell. It will generate a voltage because of the different positions of the two metals in the electrochemical series and due to the difference in the solutions (Broomfield 2007).

Half-cell potential mapping has provided a very useful, non-destructive method to locate areas of corrosion for monitoring and condition assessment of reinforced concrete structures as well as in determining the effectiveness of repair work (Schiegg, 1995; Bertolini et al., 2004). As an early-warning system, corrosion is detected long before it becomes visible at the concrete surface. Based on potential mapping, destructive and laboratory analysis (e.g. concrete cores) and corrosion-rate measurements can be performed more rationally (SIA, 2006). In addition, the amount of concrete removal in repair works can be minimized because the corrosion sites can be located. Today potential mapping is the most widely recognized and standardised non-destructive method for assessing the corrosion state of rebars in concrete structures. In addition to the Americal Standard (C876 -15) and RILEM recommendation (RILEM TC 154-EMC, 2003), several national guidelines (e.g. Concrete Society TR60 2004 in UK, SIA 2006 in Switzerland) describe the use and interpretation of half-cell potential measurements.

Corrosion of steel in concrete follows the well-established electrochemical mechanism of corrosion of a metal in an electrolyte (Page & Treadaway, 1982; RILEM TC 60 CSC, 1988). Corrosion of a metal implies separate anodic and cathodic processes occurring simultaneously on the same metal surface. At the anodes, iron dissolves and iron ions diffuse into the concrete, leaving behind electrons. At the cathodic sites, the iron ions combine with water and oxygen to form an expansive corrosion product, i.e., rust. Corrosion is controlled by how easily the iron ions can move through the concrete from the anodes to the cathodes and it depends on the availability of oxygen and moisture at the cathodes.

The corrosion potential E_{corr} (half-cell rebar /concrete) is measured as a potential difference (or voltage) against a reference electrode (half-cell). The numerical value of the measured potential potential difference between the steel in concrete and the reference electrode will depend on the type of the reference electrode used and on thecorrosion condition of the

Figure 1. Schematic view of the electric field and current flow in an active / passive macrocell on steel in concrete (RILEM TC 154-EMC, 2003).

steel in concrete. In addition, half-cell potential of steel in concrete cannot be measured directly at the interface concrete / rebar due to the presence of the concrete cover (Fig. 1), the potentials are thus influenced by iR drop in the cover, by macrocell current and possibly by junction potentials (RILEM TC 60 CSC, 1988).

Depending on the spatial distribution of anodic and cathodic reactions on the surface of the steel and the conductivity of the medium, two types of corrosion (uniform and macro-cell or localized corrosion) can take place. Half-cell potential measurements allow the location to be determined of areas of corroding rebars (anodic processes) being the most negative zones in a potential field. However, the interpretation of the half-call readings is not straightforward because the concrete cover and its resistivity influence the readings at the concrete surfaces (Bertolini et al., 2004), represented in the discussion section of the current paper.

In Estonian industrial and agricultural buildings there exist a lot of precast concrete load-bearing structures, which were manufactured in the 1970's and 80's during the mass-industrialization and production of reinforced and prestressed concrete structures. By now, due to corrosion deterioration, many of these structures are near to reaching their designed service life. In this research the 20-year-old prestressed concrete ribbed ceiling panels with dimensions of 6 m (length) by 1.5 m (width) from an existing agricultural building (pigsty) are studied. The objective of this study is to evaluate the corrosion risk of steel rebars in ribbed panels by means of indirect (non-destructive) methods and compare the results with a direct method.

MATERIALS AND METHODS

Five 20 years old prestressed concrete ribbed ceiling panels of type PNS-12 from an existing agricultural building (pigsty) are the subject of the current study. The top view, longitudinal and transverse section of a ribbed panel PNS-12 is shown in Fig. 2. The prestressing and reinforcing steel rebars of a ribbed panel PNS-12 are shown in Fig. 3.
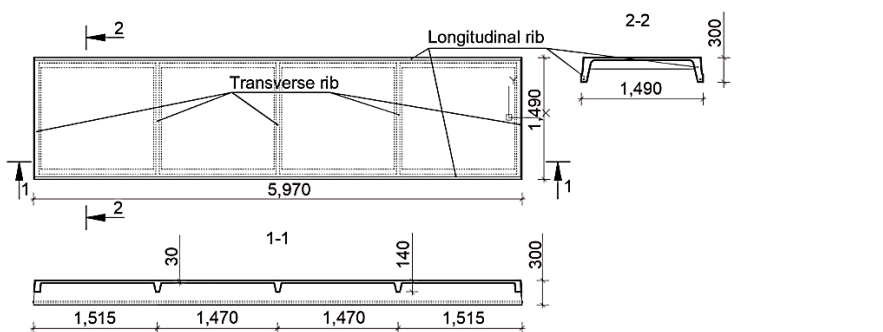
Figure 2. Top view, longitudinal and transverse section of a ribbed panel PNS-12 (PK-01-111, 1961 *Dimensions are in mm.*
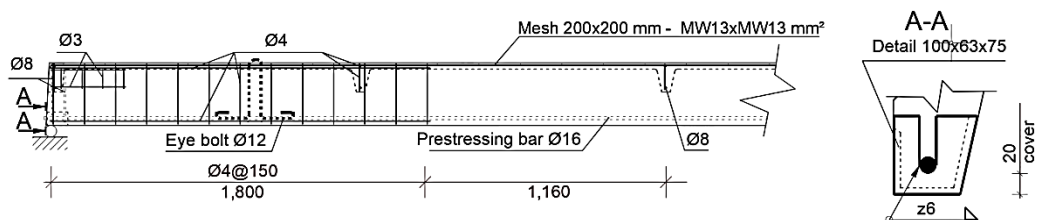
Figure 3. Reinforcement and anchorage of the ribbed panel PNS-12 (PK-01-111, 1961). *Dimensions are in mm.*

The study methodology in general consists of a) non-destructive measurements by half-cell potential of a longitudinal rib (of a ribbed panel PNS-12) and b) comparision with actual condition of steel rebars after removal of concrete (demolition of longitudinal ribs of ribbed panels PNS-12).
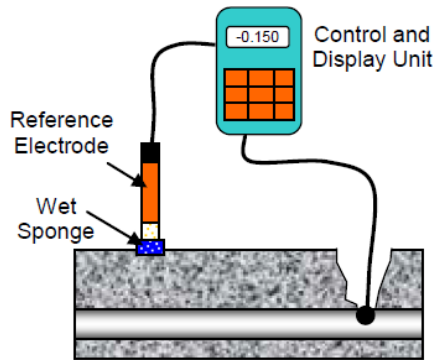
The procedure for measuring half-cell potentials is presented as follows (Fig. 4).

A sound electrical connection is made to the rebar, namely prestressing bar ø16mm in the current study. An external reference electrode is placed on a wet sponge on the concrete surface and potential readings are taken with a high impedance voltmeter (> 10 MΩ) on a regular grid on the free concrete surface. Good electrolytic contact is essential to get stable readings, the point of measurement should be clean and wetted with a water-soaked sponge on the surface.

The mapping of the corrosion

Figure 4. Principle and main components of half-cell potential measurements: reference electrode, high impedance voltmeter, connection to the rebar.

potential of steel was performed with a German Instruments GD-2000 Mini Great Dane system (Fig. 5) The Mini Great Dane measures the surface potentials relative to an Ag/AgCl/1M KCl reference electrode and the electrical resistance of the cover concrete between the electrode and the reinforcement. The indicated potential, E_{corr}, is in terms of a Cu/CuSO$_4$ electrode (CSE), which are -110 mV lower in value than for the Ag/AgCl/1M KCl electrode.

Half-cell potential measurements were performed on the 10 longitudinal ribs of 5 ribbed panels, respectively. Four horizontal and 30 vertical gridlines were marked in each longitudinal rib, with measuring points formed at the crossing of the gridlines. In this way, 30 (horizontally) x 4 (vertically) grid of 120 measurement points per longitudinal rib was formed. Altogether 120 (measurement points per longitudinal rib) x 2 (ribs) x 5 (ribbed panels) = 1,200 measurement points were recorded for steel potential.

Figure 5. The Great Dane corrosion mapping system.

Representation of half-cell potential data was performed by developing colour plots of the measurement points (potential maps).

After the non-destructive tests, the ribbed panels including their longitudinal ribs were demolished and concrete was carefully removed. The actual position and condition of the steel (main prestressing bar, reinforcing wire meshes (acting for shear) and eye

bolt (for lifting ribbed panels)) was photographed (direct method), which enabled the comparison with the potential map (indirect non-destructive method).

RESULTS AND DISCUSSION

Half-cell potential measurements allow the location to be determined of areas of corroding rebars, being the most negative zones in a potential field, but not showing the corrosion rate. The interpretation of the potential readings is not straightforward because the concrete cover and its resistivity in addition to the corrosion potential of the steel influence the readings at the concrete surface. The resistivity itself varies with temperature, with concrete moisture and chloride content or carbonation (Bertolini et al. 2004).

According to atmospherically exposed reinforced concrete the potential of passive steel is between +170 and -80 mV derived for the Ag/AgCl/1M KCl electrode (SSE) as applied in the current study (+ 50 to -200 mV CSE). If corrosion is ongoing the potential becomes more negative: chloride-induced pitting corrosion typically results in values from -280 to -580 mV SSE (-400 to -700 mV CSE), corrosion due to carbonation usually results in values from -80 to 380 mV SSE (-200 to -500 mV CSE), strongly depending on the presence of moisture (Bertolini et al. 2004).

The ASTM C876-91 provides one possibility for interpretation of half-cell potential readings (Table 1). This interpretation was devised empirically from chloride-induced corrosion of cast in place bridge decks in the USA, thus not fully applicable to the current study.

Table 1. ASTM C876-91 criteria for corrosion of steel in concrete for Ag/AgCl/1M KCl standard reference electrode

Silver/silver chloride/ 1.0M KCl	Corrosion condition
> - 100 mV	Low (10%) risk of corrosion
- 100 to -250 mV	Uncertain corrosion risk
< - 250 mV	High (> 90%) risk of corrosion
< - 400 mV	Severe corrosion (or low oxygen/water saturation)

The results from Halgma & Linnus, 2007 show that uniform corrosion was detected in some of the steel prestressing bars during visual inspection. In some ribbed panels the prestressing bars were found to be non-corroded referring to passive steel. No signs of chloride-induced localised (or pitting) corrosion were detected during visual inspection.

The results of half-cell potential measurements are shown in Table 2. Also, average concrete carbonation and cover depth data are presented as background information in Table 2. As the areas of corroding rebars are the most negative, the minimum potential values are considered as important. Also, the maximum values are given in Table 2 to indicate the range of potential measurements.

The carbonation depth versus cover depth ratio in Table 2 indicates that at least one third of the cover (Fig. 3) of all studied ribbed panels PNS-12 is carbonated. According to theory of steel corrosion in concrete, the active corrosion starts, in the presence of moisture, when the concrete cover is fully carbonated. In two cases (P8 longitudinal rib D-C and P12/A-B, respectively) almost the full cover is carbonated in average. The

corresponding minimum potentials (-210 mV in P8/D-C and -225 mV in P12/A-B), however, correspond to an uncertain corrosion risk in Table 2.
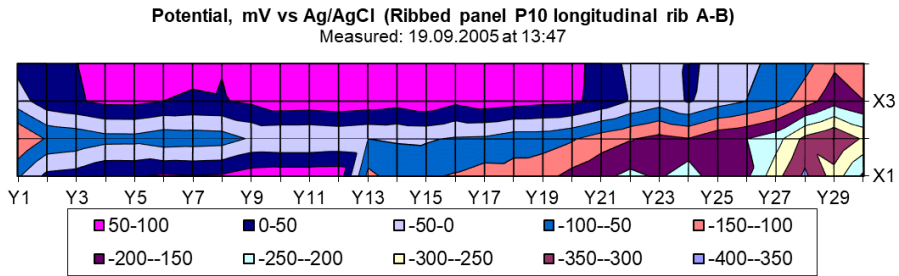
Table 2. Results of half-cell potential, carbonation and cover depth measurements at the studied longitudinal ribs of ribbed panels. Values in bold indicate significant results, which are further discussed in the text

Ribbed panel / Longitudinal rib	Potential, mV vs. Ag/AgCl		Average concrete carbonation/ cover depth, mm
	min	max	
P7/A-B	-121	121	7.0 / 23.6
P7/ D-C	-216	55	7.4 / 24.2
P8/A-B	-218	-1	**27.0 / 24.4**
P8/ D-C	-210	95	*22.3 / 24.3*
P9/A-B	-166	70	8.4 / 25.0
P9/ D-C	**-297**	4	8.4 / 24.2
P10/A-B	**-361**	98	9.9 / 25.6
P10/D-C	-160	46	9.4 / 27.7
P11/A-B	-91	47	8.1 / 24.3
P11/D-C	-228	130	9.1 / 24.6
P12/A-B	-225	11	*14.4 / 18.1*
P12/D-C	-151	1	9.1 / 21.3

In one case (P8 longitudinal rib A-B, marked as bold in Table 2) the cover is fully carbonated on average (average carbonation depth is more than average cover depth). The corresponding minimum potential (-218 mV in P8/A-B), also corresponds to uncertain corrosion risk in Table 2. It should be noted that carbonation depth measurement locations did not correspond to the half-cell potential grid in ribbed panels, because it was not possible to perform the carbonation measurements at the exactly same location. The carbonation depth was measured in 10 locations per one concrete core, drilled from the longitudinal rib. Five cores were drilled from each longitudinal rib of a ribbed panel. Therefore, each average carbonation depth value, in Table 2, is based on 50 measurements.

The largest negative potentials were found in ribbed panel longitudinal rib A-B (P10/A-B) and P9/D-C (-361 and -297 mV versus Ag/AgCl/KCl reference electrode, respectively in Table 2)). According to ASTM C876-91 criteria, both of these values exceed the high (>90%) risk of corrosion condition (< -250 mV versus Ag/AgCl/KCl reference electrode). However, only approximately one third of the cover was carbonated in both of those cases (9.9/25.6 for P10/A-B and 8.4/24.2 for P9/D-C in Table 2), indicating that the corrosion should not have yet started.

The half-cell potential map of P10/A-B shows the most negative potentials in the lower right corner of the Fig. 6. The position and condition of steel details of P10/A-B was also photographed (direct method, in Fig. 7), which enabled the comparison with half-cell potential map (indirect, non-destructive method). Fig. 7 shows that that the steel prestressing bar (initial ø16 mm in Fig. 3), reinforcements (ø3 and 4 mm), eye bolt (ø12 mm) and other details of P10/A-B had relatively large visually distinguishable corrosion deterioration. It should be mentioned that large negative potential readings of half-cell have also other causes such as water saturation and pressure of galvanised components.

Potential, mV vs Ag/AgCl (Ribbed panel P10 longitudinal rib A-B)
Measured: 19.09.2005 at 13:47

Legend: 50-100 | 0-50 | -50-0 | -100--50 | -150--100 | -200--150 | -250--200 | -300--250 | -350--300 | -400--350
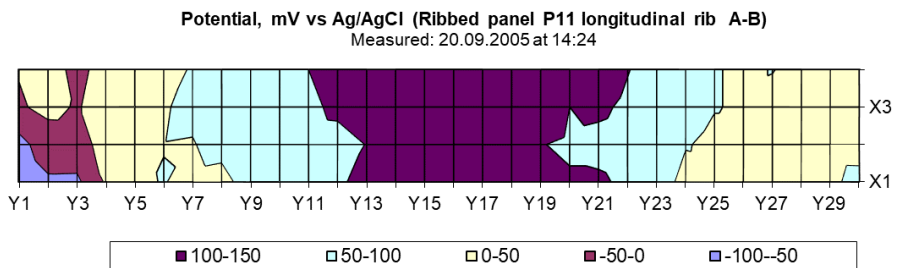
Figure 6. Half-cell potential map of the longitudinal rib with the largest negative potential (P10/A-B).

Figure 7. Photograph of the steel prestressing bar, reinforcements and eye bolt details of the longitudinal rib A-B of ribbed panel P10 (P10/A-B) after demolition.

For comparison purposes the half-cell potential map of the ribbed panel with the smallest negative potential difference (P11/A-B) was chosen (Fig.8). The position and condition of steel details of P11/A-B was also photographed (Fig. 9)

Potential, mV vs Ag/AgCl (Ribbed panel P11 longitudinal rib A-B)
Measured: 20.09.2005 at 14:24

Legend: 100-150 | 50-100 | 0-50 | -50-0 | -100--50

Figure 8. Half-cell potential map of the longitudinal rib with the lowest negative potential (P11/A-B).

Figure 9. Photograph of the steel prestressing bar, reinforcements and eye bolt details of the longitudinal rib A-B of ribbed panel P11 (P11/A-B) after demolition.

Fig. 9 shows that the steel prestressing bar (initial ø16 mm in Fig. 3), reinforcements (ø3 and 4 mm) and eye bolt (ø12 mm) of P11/A-B details are relatively intact in visual observation. This corresponds rather well with the half-cell potential map (Fig. 8) of the same member (P11/A-b). Therefore, good correlation between half-cell measurements and visual observation was found in the current study.

CONCLUSIONS

Half-cell potential mapping offers a possibility to quantitatively evaluate the corrosion risk in the studied precast concrete structures (ribbed panels PNS-12) with a non-destructive technique, which is a major step forward in comparison with visual inspection.

Despite the difficulties in interpreting the half-cell potential maps reported in the literature, the proposed ASTM criteria correlated well with the results of the current study. However, the most severe corrosion conditions according to ASTM criteria were not recorded in the current study. This should be addressed in the further research.

The current study also confirmed that half-cell only indicates a risk of corrosion, not the rate, so it is common for areas to be discovered with negative potentials and no corrosion.

REFERENCES

ASTM C876-15. 2015. Standard Test Method for Corrosion Potentials of Uncoated Reinforcing Steel in Concrete. ASTM International, West Conshohocken, PA, 2015, 8 pp. www.astm.org

Bertolini, L., Elsener, B., Pedeferri, P. & Polder, R. 2004. Corrosion of Steel in Concrete. Prevention, Diagnosis, Repair. Wiley-VCH Verlag GmbH & Co. KGaA. Weinheim.

Broomfield, J.P. 2007. *Corrosion of Steel in Concrete. Understanding, investigation and Repair*. 2nd Edition E & FN Spon, London, pp. 294.

Concrete Society Technical Report No. 60. 2004. Electrochemical Tests for Reinforcement Corrosion, Part 4: Half-cell potential surveys. The Concrete Society. Riverside House, 4 Meadows Business Park, Blackwater, Camberley, GU17 9AB, UK. www.concrete.org.uk

Halgma, R & Linnus, L. 2007. Determination of some properties of concrete and reinforcement of prestressed ribbed panels. *Master thesis*. Estonian University of Life Sciences, Tartu, pp. 75.

Long, A.E, Henderson, G.D. & Montgomery, F.R. 2001. Why assess the properties of near-surface concrete? *Construction and Building Materials* **15**(2-3), 65–79.

Page, C.L. & Treadaway, K.WJ. 1982. Aspects of electrochemistry of steel in concrete. *Nature* **297**, 109–115.

PK-01-111. 1961. Prestressed concrete ceiling ribbed panels of dimensions 1.5 by 6m. Work drawings). Moscow, Central institute of typical projects, 20 p. (in Russian). (Крупнопанельные железобетонные предварительно напряженные плиты покрытий размером 1,5x6 м. Рабочие чертежи).

RILEM TC 60 CSC. 1988. Corrosion of Steel in Concrete ed. P. Schiessl, Chapman and Hall, London.

RILEM TC 154-EMC recommendations. 2003. Electrochemical techniques for measuring metallic corrosion. Half-cell potential measurements - Potential mapping on reinforced concrete structures. In Elsener, B., Andrade C., Gulikers, Polder, R., Raupach, M. 2003. Recommendation on half-cell potential measurements. *Materials and Structures* **36**, 461–471

Schiegg, Y. 1995. Half-cell potential measurements – an important tool for the evaluation of RC Structures (in German). (Potentialmessung - ein wesentliches Instrument für die Beurteilung von Bauwerken) *SIA Documentation D 0126. Swiss Association of Engineers and Architects, Zürich,* **87** pp.

SIA 2006. 1997. Guideline for half-cell potential measurement (In German). (Richtlinie zur Potentialfeldmessung). SIA Documentation 2006. *Swiss Association of Engineers and Architects*, Zürich, 48 pp.

Research on influence of cyclic degradation process on changes of structural adhesive bonds mechanical properties

V. Kolář[1,*], M. Tichý[1], M. Müller[1], P. Valášek[1] and A. Rudawska[2]

[1]Czech University of Life Sciences, Faculty of Engineering, Department of Material Science and Manufacturing Technology, Faculty of Engineering, Kamýcká 129, CZ165 21 Prague, Czech Republic
[2]Lublin University of Technology, Department of Production Engineering, Mechanical Engineering Faculty, Nadbystrzycka 36, PL20 618 Lublin, Poland
*Correspondence: vkolar@tf.czu.cz

Abstract. The paper deals with an influence of a cyclic degradation process on changes of a shear tensile strength of single lap-shear adhesive bonds and their elongation according to ČSN EN ISO 9142. Five one-component structural adhesives used in a construction of car body works were used within the research. The degradation of adhesive bonds is a significant factor which influences a quality and a service life of adhesive bonds exposed to environment. A main requirement in production companies is not only reaching satisfactory initial mechanical properties but namely ensuring a reliability and a safety of adhesive bonds during their usage.

These reasons show a great importance of adhesive bonds tests either directly in the operating environment or by a simulation of operating conditions in laboratories. The degradation process of adhesive bonds worsens mechanical properties of not only the bond itself but also of the bonded material. This process is progressing and it is usually permanent and irreversible. It is a change of mechanical and physical properties which can endanger a safety and a reliability of parts, prospectively of the whole equipment. It can leads up to a complete failure of its function in the extreme case. A temperature, a moisture, a direct contact with water and chemicals or an atmospheric corrosion belong among the most serious degradation agents. It is important to take into regard time of the processes influence at the same time which can act either independently or concurrently when their effects grow stronger.

From that reason the adhesive bonds were exposed to the cyclic degradation process according to the standard ČSN EN ISO 9142. Subsequently, the adhesive bonds mechanical properties were tested on universal testing machine and by means of SEM analysis (TESCAN MIRA 3).

Results of mechanical tests proved a fall of the shear tensile strength of single lap-shear adhesive bonds after 42 cycles of the degradation process of 12.8 to 21.7%. The bond strength fall was gradual and it showed a linear trend at some adhesives. Other adhesives showed a significant fall after the exposition to the degradation process after which the strength fall stabilized.

Key words: shear tensile strength, elongation, temperature, moisture, SEM, automotive, ageing process.

INTRODUCTION

The main advantages of adhesive bonding in comparison with other joining are better load distribution, reducing stress concentrations, increasing fatigue resistance,

corrosion resistance, weight savings and the ability to join different materials. In these reasons are adhesive bonding technics used in the automotive, aerospace, electronic industries (Baldan, 2004; Crocombe et al., 2006).

The disadvantages of adhesive bonds are various resistance at combination of aggressive environment and mechanical loading. The main conditions of aggressive environment are moisture and variable temperature. The various temperature can influence mechanical strength of adhesive bonds. The heat degradation on epoxy adhesive affect also elongation and strain at strength on shear test (Goda et al., 2010; Bar-Cohen, 2014).

There is a require for development on adhesive bonds and adhesive able to resist high and low temperature conditions. This requirement is for structural adhesives challenging because they are mostly polymer-based, which has a relatively low resistance to high temperature. However, there is a combination of adhesives in the chemistry development which allow the adhesive bonding in extreme temperature, e.g. vulcanizing silicones, high-temperature epoxies and ceramic-based adhesives (Marques et al., 2015; Qin et al., 2018; Yang et al., 2019).

The subject of this paper is an influence of a cyclic degradation process on changes of a shear tensile strength of single lap-shear adhesive bonds and their elongation. In general is known that mechanical properties deteriorate during degradation process but the exactly value is not established. For these reason was the degradation process followed in this research. In the research were examined a structural adhesive used in in a construction of car body works. The adhesive bonds of car body are exposed to wide span of temperature condition. A temperature, a moisture, a direct contact with water and chemicals or an atmospheric corrosion belong among the most serious degradation agents. For these reasons is degradation of adhesive bonds a significant factor which influences a quality and a service life of adhesive bonds exposed to environment. A main requirement for automotive production is not only reaching satisfactory initial mechanical properties but namely ensuring a reliability and a safety of adhesive bonds during their usage (Müller et al., 2014; Müller and Valášek, 2014; Sousa et al., 2018).

Temperature variations are the most important environmental factors which influence the tensility of adhesive bonds. Degradation effect is caused by exposure to extreme temperatures on the adhesive and the adherends. The thermal cycles also caused the eventually difference between the coefficients of thermal expansion of the adherends and the adhesive. This process between adhesive and adherend can caused creating the micro-cracks at the interfaces of adhesive layer or even delamination of adhesive bond (Marques et al., 2015).

In the research was used cyclic degradation process to simulate exposition of a car body in a real environment condition. Car body is exposed to increasing a decreasing temperature cycles in long time span. For these reasons are also important the time of exposition of adhesive bonds. It is needed to take into regard time of the processes influence at the same time which can act either independently or concurrently when their effects grow stronger. All these parameters of exposition influence mechanical properties of not only adhesive bonds itself but also of the bonded material. This process is progressing, and it is usually permanent and irreversible. The changes of mechanical and physical properties can a safety and a reliability of parts, prospectively of the whole equipment. This can lead up to a complete failure of its function in the extreme case.

The aim of this research is to study influence of cyclic degradation process on mechanical properties of single lap-shear structural adhesive bonds.

MATERIALS AND METHODS

Single lap-shear bonds were created by five one-component structural adhesive with filler. The filler is supply in adhesive from manufacture of one component adhesive. For research were tested type of adhesive Betamate 1496F, Betamate 5103-3, Betamate 1440G, Betamate 1040 and Sika Power 492 (E) used in car body construction (Table 1.). These adhesives were chosen because they are commonly used in automotive.

Table 1. The tested one component adhesive with designation for research, product name and standard curing

Designation for research	Product name of adhesive	Standard curing
A	Betamate 1496F	180 °C/30 min
B	Betamate 5103-3	180 °C/30 min
C	Betamate 1440G	180 °C/30 min
D	Betamate 1040	180 °C/30 min
E	Sika Power 492	< 220°C

Adherend for bonds was used carbon steel S235J0 of thickness 1.5 ± 0.1 mm and dimensions 100 x 25 mm. The bonded surface of adherend was sandblasted by Garnet MESH 80 (ČSN ISO 8501-1) and degreased by an acetone (ČSN EN 13887). The roughness of sandblasted surface was measured on $R_a = 1.76 \pm 0.18$ μm, R_z 11.22 ± 0.84 μm by portable profilometer Mitutoyo Surftest 301. The overlap length of bonds was 12.5 ± 0.25 mm.

The cyclic degradation process was performed in a laboratory programmable chamber MKF240 (ISO 483) of the firm Binder (Fig. 1) according to the standard ČSN EN ISO 9142 (Adhesives - Guide to the selection of standard laboratory ageing conditions for testing bonded joints) in the cycles D from the standard. The single lap-shear bonds were exposed in degradation cycle, which contains two phases. The bonds in first phases was exposed to the increased temperature 70 ± 2 °C and the relative moisture 90% for the time 16 hours, subsequently a gradual cooling to the temperature -40 ± 3 °C and staying 3 hours at this temperature. The bonds in second phases were exposed again to the increased temperature 70 ± 2 °C

Figure 1. The laboratory programmable chamber MKF240 of the firm Binder.

at the relatively moisture 50% for 16 hours and staying for the 5 hours at this temperature. The quantity of degradation cycles were split in 14, 28 and 42 cycles.

After cyclic degradation process were single lap-shear bonds loaded to analyse their mechanical properties. Mechanical properties of single lap-shear bonds were measured

on universal testing machine LabTest 5.50ST at loading speed 2 mm·min^{-1} with evaluation software Test&Motion. As mechanical properties were studied shear tensile strength and elongation according to ČSN EN 1465.

The disruptions of single lap-shear bonds were examined according to ČSN ISO 10365. The interaction of one-component structural adhesive was followed up by scanning electron microscope TESCAN MIRA 3 GMX (SEM) in nitrogen vacuum with acceleration voltage (HV) of 10 kV at a distance approx. 15.5 mm.

The measured values were processed by statistical analysis *Anova F-test* (Analysis of Variance). The difference between values was compared by p-values. The null hypothesis H_0 for no statistically significant difference on median values was set to *p > 0.05*.

RESULTS AND DISCUSSION

On Fig. 2 is apparently, that increasing number of cycles influence decreasing shear tensile strength of the adhesive bond. The tensile lap shear strength meet the materials lists of adhesives in 0 cycles of degradation process. The largest decrease of shear tensile strength occurred at 42 cycles for all tested adhesive. The largest decrease of shear tensile strength between 0 and 42 cycles has occurred on adhesive C and up to 22.4%. The least decrease shear tensile strength between 0 and 42 cycles has occurred on adhesive B and up to 12.8%. The largest shear tensile strength was 20.92 ± 0.63 MPa at 42 cycles on adhesive E and contrariwise the least strength was 17.13 ± 1.07 MPa on adhesive B. From Fig. 2 is there noticeable linear decrease of shear tensile strength according to number of degradation cycles on some type of adhesives. The largest linear accordance is on adhesive D with reliability value $R^2 = 0.97$. This value shows Table 2, there are listed reliability values (R^2) and trend equation (τ) of adhesives.
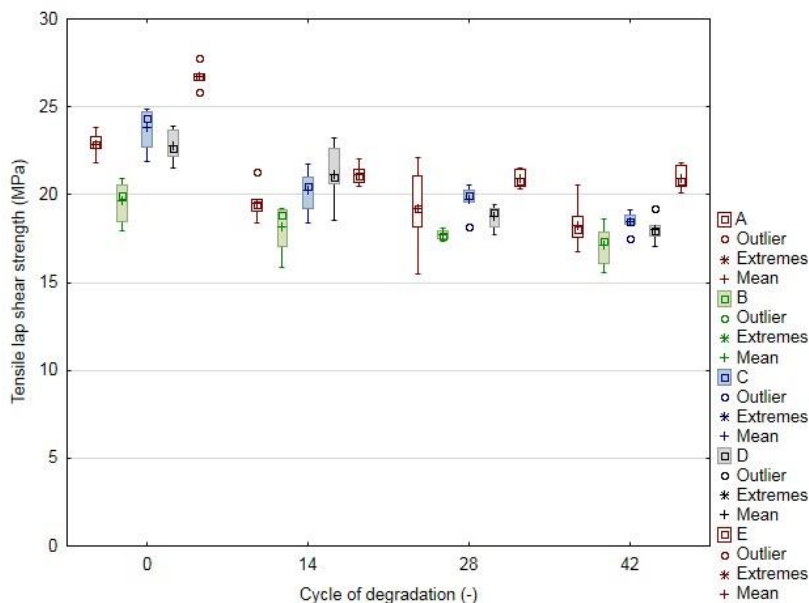
Figure 2. Accordance of degradation cycles on shear tensile strength of adhesive bond.

Table 2. The reliability values R2, trend equation τ and *p–parameter* of statistical test *ANOVA* for accordance of degradation cycles on shear tensile strength of adhesive bond

Adhesive	Reliability value R^2	Trend equation τ (NC – number of cycle)	p - parameter
A	0.83	$\tau_A = -0.1009NC + 22.093$	0.0002
B	0.92	$\tau_B = -0.0571NC + 19.354$	0.0046
C	0.87	$\tau_C = -0.1176NC + 23.023$	0.0000
D	0.97	$\tau_D = -0.1990NC + 22.673$	0.0000
E	0.63	$\tau_E = -0.1264NC + 25.074$	0.0000

The statistical testing of influence of degradation cycles on shear tensile strength at significance level *0.05* confirm, that there is statistical inhomogeneous group, i.e. there is significant difference between measured values (*p < 0.05*). Hypothesis H_0 was rejected and was confirm the number of degradation cycles on shear tensile strength of adhesive bonds.
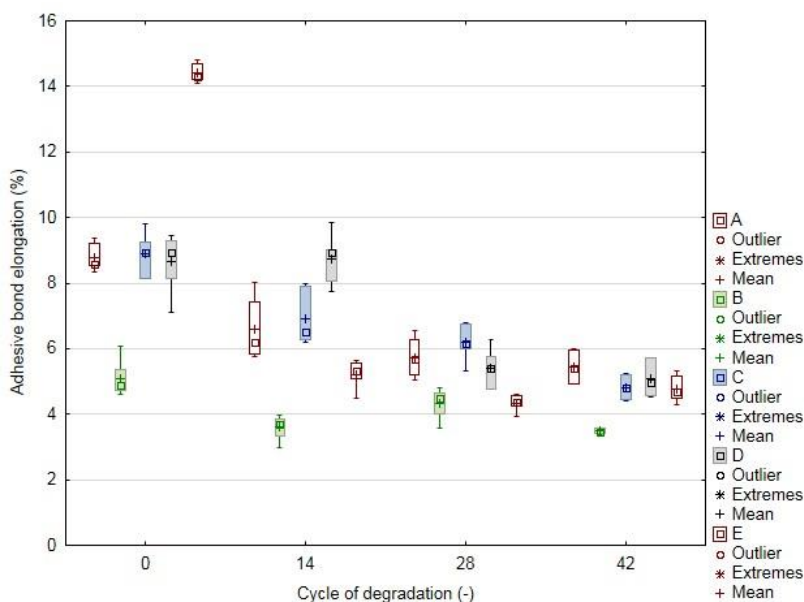

Figure 3. Accordance of degradation cycles on adhesive bond elongation of adhesive bond.

On Fig. 3 is apparently, that elongation decrease with increasing number of degradation cycles. The adhesive bond elongation meet the materials lists of adhesives in 0 cycles of degradation process. This effect is given by lower tensility of tested adhesive after degradation process. The results show, that the largest elongation 5.43 ± 0.47% happens at 42 cycles on adhesive A. The least elongation 3.48 ± 0.42% was on adhesive B. On adhesive D was elongation increased up to 1.25% at 14 degradation cycles against no degradation exposition adhesive bonds and elongation increase up to 0.1% at 42 degradation cycles on adhesive E. The largest elongation happens at all tested adhesive between 0 and 14 degradation cycles and on average 13.02 ± 5.23%. Between other degradation cycles was average elongation 3.28 ± 2.85%.

The significant decrease of elongation up to 21% happened on adhesive E between 0 and 14 degradation cycles. This was caused by influence of degradation process, i.e. adhesive lose own tensility. On Fig. 3 is apparently, that elongation decrease in accordance to degradation cycles was linear on some type of adhesive. The largest linear accordance between degradation cycles was on adhesive C with reliability value $R^2 = 0.97$. This value shows Table 3, there are listed reliability values (R^2) and trend equation (ε) of adhesives.

Table 3. The reliability values R^2, trend equation ε and *p–parameter* of statistical test *ANOVA* for accordance of degradation cycles on elongation of adhesive bond

Adhesive	Reliability value R^2	Trend equation ε (NC – number of cycle)	p - parameter
A	0.86	$\varepsilon_A = -0.0775NC + 8.2565$	0.0000
B	0.50	$\varepsilon_B = -0.0292NC + 4.7390$	0.0000
C	0.97	$\varepsilon_C = -0.0918NC + 8.6298$	0.0000
D	0.82	$\varepsilon_D = -1.0050NC + 9.0778$	0.0000
E	0.63	$\varepsilon_E = -0.2124NC + 11.644$	0.0000

The statistical testing of influence of degradation cycles on adhesive bond elongation at significance level *0.05* confirm, that there is statistical inhomogeneous group, i.e. there is significant difference between measured values ($p < 0.05$). Hypothesis H_0 was rejected and was confirm the number of degradation cycles on adhesive bond elongation of adhesive bonds.

Tested adhesive points out the failure type SCF (special cohesive failure – ISO 10365) on steel bonded surface. Exposition process of degradation cycles did not change the type of fracture surface.
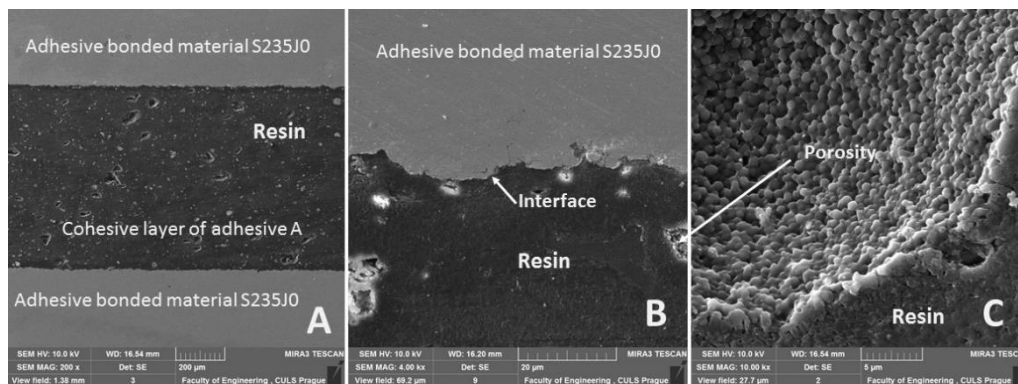
Figure 4. SEM images of cut through of adhesive bond A (SE detector, 10 kV): A: cut through of adhesive bond (MAG 200 x), B: adhesive layer interaction and bonded material (MAG 4000 x), C: porosity inside of adhesive layer (MAG 10000 x).

On the Fig. 4. and Fig. 5. is apparently sample of cut through on adhesive A and D. The figures present the adhesive layer and its interaction with bonded material. The Fig. 4, A. and Fig. 5, A. present overall view on cut through of adhesive layer. The Fig. 4, B and Fig. 5, B. show good interaction between adhesive and bonded material, i.

e. good wettability of adhesive and bonded material. From Fig. 5, B. is evident good interaction between resin and filler (filler in adhesive is supply in adhesive from manufacture of one component adhesive). The adhesive contains higher part of porosity, which is presented on Fig. 4, B and 4, C.
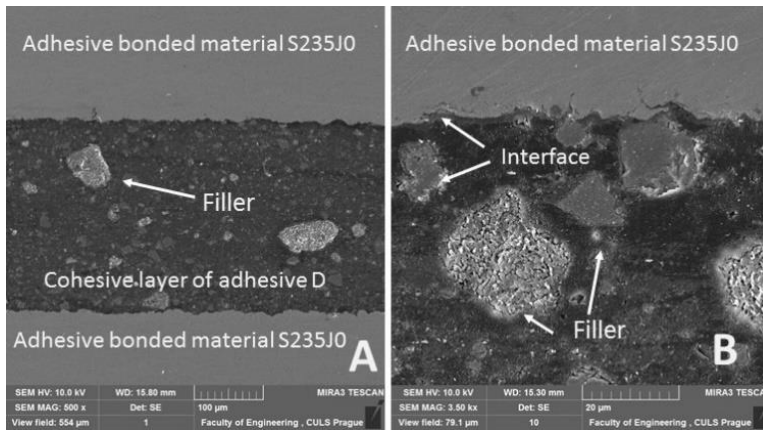
Figure 5. SEM images of cut through of adhesive bond A (SE detector, 10 kV): A: cut through of adhesive bond – one component epoxide containing filler (MAG 500 x), B: adhesive layer interaction, bonded material and filler (MAG 3500 x).

The research results of other authors confirm negative influence of different environment or mediums on quality of adhesive bond (Court et al., 2001; Doyle & Pethrick, 2009).

CONCLUSIONS

Results of mechanical tests proved a fall of the shear tensile strength of single lap-shear adhesive bonds after 42 cycles of the degradation process of 12.8 to 21.7%. The bond strength fall was gradual, and it showed a linear trend at some adhesives. Other adhesives showed a significant fall after the exposition to the degradation process after which the strength fall stabilized. The results classify the selected adhesives and their practical usage in degradation environment. The results also give the possibility to calculate the lifetime by the trend equation τ and ε.

The above conclusion from research results of on influence of cyclic degradation process on changes of structural adhesive bonds mechanical properties:

- In accordance on increasing number of degradation cycles decrease shear tensile strength of adhesive bond.
- The largest shear tensile strength 20.92 ± 0.63 MPa at 42 degradation cycles on adhesive E.
- The least shear tensile strength 17.13 ± 1.07 MPa at 42 degradation cycles on adhesive B.
- The influence of degradation cycles in accordance to shear tensile strength on adhesive bond was confirm at significance level 0.05, i.e. hypothesis H_0 was rejected ($p < 0.05$).

- In accordance on increasing number of degradation cycles decrease elongation of adhesive bond, which is cause lower tensility of tested adhesive.
- The largest average elongation $13.02 \pm 5.23\%$ between 0 and 14 degradation cycles.
- The influence of degradation cycles in accordance to elongation on adhesive bond was confirm at significance level *0.05*, i.e. hypothesis H_0 was rejected ($p < 0.05$).
- Exposition process of degradation cycles did not change the type of fracture surface.

REFERENCES

Baldan, A. 2004. Adhesively-bonded joints in metallic alloys, polymers and composite materials: Mechanical and environmental durability performance. *Journal of Materials Science* **39**(15), 4729–4797.

Bar-Cohen, Y. 2014. *High Temperature Materials and Mechanisms*. CRC Press.

Court, R.S., Sutcliffe, M.P.F. & Tavakoli, S.M. 2001. Ageing of adhesively bonded joints—fracture and failure analysis using video imaging techniques. *International Journal of Adhesion and Adhesives* **21**(6), 455–463.

Crocombe, A.D., Hua, Y.X., Loh, W.K., Wahab, M.A., & Ashcroft, I.A. 2006. Predicting the residual strength for environmentally degraded adhesive lap joints. *International Journal of Adhesion and Adhesives* **26**(5), 325–336.

ČSN EN 1465. 2009. Adhesives - Determination of tensile lap-shear strength of bonded assemblies. Prague: Czech Standards Institute (in Prague).

ČSN ISO 10365. 1995. Adhesives - Designation of main failure patterns. Prague: Czech Standards Institute (in Prague).

ČSN ISO 8501-1. 1998. Preparation of steel substrates before application of paints and related products. Visual assessment of surface cleanliness. Part 1: Rust grades and preparation grades of uncoated steel substrates and of steel substrates after overall removal of previous coatings. Prague: Czech Standards Institute (in Prague).

ČSN ISO 9142. 2004. Adhesives - Guide to the selection of standard laboratory ageing conditions for testing bonded joints. Prague: Czech Standards Institute (in Prague).

ČSN EN 13887. 2003. Structural adhesives. Guidelines for surface preparation of metals and plastics prior to adhesive bonding. Prague: Czech Standards Institute (in Prague).

Doyle, G. & Pethrick, R.A. 2009. Environmental effects on the ageing of epoxy adhesive joints. *International Journal of Adhesion and Adhesives* **29**(1), 77–90.

ISO 483. 2005. Plastics - Small enclosures for conditioning and testing using aqueous solutions to maintain the humidity at a constant value. Geneva: International Organization for Standardization (in Geneva).

Goda, Y., Sawa, T., Himuro, K. & Yamamoto, K. 2010. Impact Strength Degradation of Adhesive Joints Under Heat and Moisture Environmental Conditions. In *Volume 9: Mechanics of Solids, Structures and Fluids* (pp. 29–36). ASME.

Marques, E.A.S., da Silva, L.F.M., Banea, M.D. & Carbas, R.J.C. 2015. Adhesive Joints for Low- and High-Temperature Use: An Overview. *The Journal of Adhesion* **91**(7), 556–585.

Müller, M., Ružbarský, J. & Valášek, P. 2014. Degradation Process in Area of Connecting Metal Sheets by Adhesive Bonding Technology in Agrocomplex. *Applied Mechanics and Materials* **616**, 52–60.

Müller, M. & Valášek, P. 2014. Influence of Environment Temperature on Strength of Quick-Setting Adhesives Based on Cyanoacrylates. *Advanced Materials Research* **1030–1032**, 272–275.

Qin, G., Na, J., Mu, W., Tan, W., Yang, J. & Ren, J. 2018. Effect of continuous high temperature exposure on the adhesive strength of epoxy adhesive, CFRP and adhesively bonded CFRP-aluminum alloy joints. *Composites Part B: Engineering* **154**, 43–55.

Sousa, J.M., Correia, J.R., Firmo, J.P., Cabral-Fonseca, S. & Gonilha, J.2018. Effects of thermal cycles on adhesively bonded joints between pultruded GFRP adherends. *Composite Structures* **202**, 518–529.

Yang, Y., Silva, M.A.G., Biscaia, H. & Chastre, C. 2019. Bond durability of CFRP laminates-to-steel joints subjected to freeze-thaw. *Composite Structures* **212**, 243–258.

Analysis of operating parameters of hybrid vehicle under real traffic condition

M. Kotek[*], M. Krumbholc and V. Hartová

Czech University of Life Science Prague, Faculty of Engineering, Department of Vehicles and Ground Transport, Kamýcká 129, CZ16500 Prague, Czech Republic
[*]Correspondence: kotekm@oikt.czu.cz

Abstract. Nowadays, protecting the environment and reducing harmful emissions is an increasingly discussed topic. One way to reduce vehicle emissions, especially for individual car traffic, is to use a hybrid drive. The advantages of the electric drive and the classic combustion engine are used here. By combining both types of drive, a synergetic effect is achieved, where both drives can be used in optimal operating mode.

The aim of the experiment was to demonstrate the benefit of a hybrid vehicle in real driving. The operating parameters of the Lexus LX400h hybrid vehicle was compared to a conventional low-class vehicle Škoda Fábia 1.2 HTP with a classic SI engine. The experiment took place on a route including typical urban, extra-urban and motorway traffic condition. During experiment, the engine operating parameters and CO, CO_2, HC and NO_X emissions were measured.

The results show that the emission production and fuel consumption of the hybrid vehicle are significantly lower in urban traffic condition than the vehicle with classic internal combustion engine. On the contrary, in motorway conditions, the hybrid vehicle must use both drives, as higher performance is required to overcome higher driving resistances and therefore achieves higher fuel consumption and higher emissions than a conventional vehicle.

Key words: fuel consumption, emission production, urban traffic, energy recuperation.

INTRODUCTION

The reduction of transport-generated energy consumption and consequent emission production are currently a problem of global interest. Hybrid electric vehicles (HEVs) are considered as one promising technological solution for limiting transport-generated energy consumption and emission production. HEVs can be categorised with respect to the level of electric power integration in the powertrain system and the engine-electric motor coupling strategy. HEVs may be classified as either parallel or series in powertrain configuration. Parallel HEVs may be simultaneously powered by the engine and electric motor. In a series HEV, the drive system is solely powered by the electric motor that draws its power from the on-board battery unit which is charged by the vehicle engine (Adly et al., 2006; Fontaras et al., 2008).

There also exist configurations that combine the characteristics of both series and parallel powertrain. What basically characterises all HEVs regardless of their powertrain architecture is reduced engine capacity, compared to the equivalent conventional model,

engine shut-off capability and the ability of regenerative braking. Based on the level hybridisation HEVs can be characterised as presented in Table 1 (Fontaras et al., 2008).

Table 1. Type of hybrid electric vehicles

Vehicle operation	Conventional vehicle	Belt/muscle/ micro hybrid	Mild hybrid	Full hybrid	Plug-in hybrid
Engine shut-off	Yes	Yes	Yes	Yes	Yes
Regenerative braking		Yes	Yes	Yes	Yes
Smaller IC engine compared to conventional			Yes	Yes	Yes
Electric drive				Yes	Yes
Electric grid battery recharge					Yes

Currently, the number of HEVs in the market remains limited, but this picture will change in the years to come as HEVs are expected to pave the way for cleaner technologies transport (Fontaras et al., 2008).

Study comparing HEVs and conventional cars was carried out with the aim to prove benefits of HEVs under legislated driving cycle conditions (e.g. New European Driving Cycle, NEDC) or real world conditions (simulation driving cycles ARTEMIS). The Artemis measuring protocol called according to the project Assessment and Reliability of Transport Emission Models and Inventory Systems (ARTEMIS), which was a scientific programme funded by the European Commission aiming at the development of a harmonised emission model. It is important to note that the simulation essentially works in a reverse direction to what happens in the real world – that is, the drive cycle is the input to the vehicle model, and the required changes to the vehicle speed are calculated based on the drive cycle (Manzie et al., 2007).

A driving cycle is composed of a unique profile of stops, starts, constant speed, accelerations and decelerations and is typically characterized by an overall time-weighted average speed (Frey & Unal, 2000). Different driving cycles (e.g. see above) are used to represent driving under different conditions. Dynamometer tests typically suffer from well-known shortcomings associated with non-representativeness of actual driving conditions (Frey & Unal, 2000). For example, many tests under-represent short-term events that causes high emissions even for a properly functioning vehicle, such as high accelerations. Driver behaviour can affect the duration of both cold starts and of events leading to high-emissions enrichment operation, which in turn have substantial effects on emissions regardless of the total number of vehicle miles travelled.

Results of dynamometer measurements conducted on a Prius II and a Honda Civic IMA using both the European legislated driving cycle (New European Driving Cycle, NEDC) and real-world simulation driving cycles (Artemis) indicate that in most cases both vehicles present improved energy efficiency and pollutant emissions compared to conventional cars. The fuel economy benefit of the two HEVs peaked under urban driving conditions where reductions of 60% and 40% were observed, respectively. Over higher speeds the difference in fuel economy was lower, reaching that of conventional diesel at 95 (km h^{-1}). The effect of ambient temperature on fuel consumption was also quantified. It is concluded that urban operation benefits the most of hybrid technology, leading to important fuel savings and urban air quality improvement (Fontaras et al., 2008).

From the above laboratory experiments, it is clear that HEV vehicles have the potential to reduce the production of harmful emissions, especially in urban traffic condition. The aim of this article is to demonstrate the benefit of a hybrid vehicle in real traffic condition and to analyse the production of harmful exhaust gases and fuel consumption of HEV and conventional vehicle (ICEV - internal combustion engine vehicle) in different real traffic conditions. In the experiment as a representantive of HEV vehilce Lexus LX400H was choosen. As a ICEV vehicle has been selected Skoda Fabia 1.2 HTP as a typical representative of one of the most used lower-class cars in the Czech Republic typically designed for operating in urban traffic condition. Despite the obvious technical differences between these two vehicles, there is a presumption that significantly larger and heavier HEV can achieve better operating parameters than small ICEVs in urban traffic condition.

MATERIALS AND METHODS

Measurement of harmful emission production of driven vehicles under ordinary urban and suburban traffic conditions was carried out with the aim to assess an ecological benefit of hybrid vehicles' use. The only condition of driving was that driver's behaviour had to be complying with the instantaneous traffic situation i.e. high non-casual accelerations or braking etc. was forbidden.

The measurement was carried out with the hybrid vehicle LEXUS LX400H (see Table 2) and conventional car equipped with a combustion engine i.e. Skoda Fabia 1.2 HTP, spark ignition (other details are in Table 3). Both cars were equipped with PEMS analyzer, GPS and OBD diagnostic system.

A mobile PEMS on-board emission analyser VMK was used to measure emissions. The analyser uses non-dispersive infrared (NDIR) method to detect CO, CO_2, and HC emissions and electrochemical cell to O_2 and NO_X emissions. Data was recorded with 1 Hz frequency on memory card. The analyser was equipped with GPS system Garmin GPS-18x-5Hz to record vehicle's position and speed. The technical data of analyser are summarized in Table 4.

Table 2. Technical parameters of Lexus LX400H

Engine	Hybrid
Power	200 kW (272 hp)
Voltage	650 V
Combustion engine	
Volume	3,311 ccm
Power	155 kW (211 hp) under 5,600 rpm
Torque	288 Nm under 4,400 rpm
Front electro-engine	
Power	123 kW under 4,500 rpm
Torque	333 Nm under 0–1,500 rpm
The highest revolutions	12,400 rpm
Voltage	650 V
Rear electro-engine	
Power	50 kW under 4,610–5,120 rpm
Torque	130 Nm under 0–610 rpm
The highest revolutions	10,752 rpm
Voltage	650 V
Accumulator	
30 8-cells modules (240 cells with 12V)	
Type	Nikl-metal hydrid
Power	45 kW (61 hp)
Capacity	65 Ah
Gearshift box	
Drive	Elec. driven all wheels
Torque distribution f/r box	Front el. + V6 / rear el. E-CVT

Table 3. Technical parameters of measured vehicles

COMBUSTION ENGINE	LEXUS LX400H	FABIA 1.2 HTP
Design	spark ignition, atmospheric	spark ignition, atmospheric
Number of cylinders	6, in V, 24 valves	3, row, 6 valves
Volume of cylinders	3,311 ccm	1,198 ccm
Power	155 kW	40 kW
	under 5,600 rpm	under 4,750 rpm
Torque	288 Nm	106 Nm
	under 4,400 rpm	under 3,000 rpm
EU limit	EU4	EU4
Year of manufacture	2005	2003
CAR BODY		
Service weight	2,000 kg	1,055 kg
Total weight	2,505 kg	1,570 kg
DRIVE PERFORMANCE		
Max. speed	200 km h^{-1}	150 km h^{-1}
Acceleration 0-100 km h^{-1}	7.6 s	18.5 s
Fuel consumption	9.1 / 7.6 / 8.1	7.8 / 4.8 / 5.9
	(liter·100 km^{-1})	(liter·100 km^{-1})

Table 4. Technical parameters of mobile emission analyser

Measured values	Measurement range	Resolution	Accuracy
CO	0...10% Vol.	0.001% Vol.	0…0.67%: 0.02% absolute, 0.67%…10%: 3% of measured value
CO_2	0...16% Vol.	0.01% Vol.	0…10%: 0.3% absolute, 10…16%: 3% m.v.
HC	0...20,000 ppm	1 ppm	10 ppm or 5% m.v.
NO_X	0...5,000 ppm	1 ppm	0…1,000 ppm: 25 ppm, 1,000…4,000 ppm: 4% m.v.
O_2	0...22% Vol.	0.1% Vol.	0…3%: 0,1% 3…21%: 3%

Vehicle operating data from the engine control unit via the OBD interface were recorded using car diagnostic system VAG–COM. The fuel consumption was evaluated by a flow meter WF007 fitted to the fuel system of the car. The technical parameters of the flowmeter is shown in Table 5.

Routes (or tracks see Fig. 1) of drives were selected with the aim that they should consist of three different sections. The first section was a typical urban drive influenced by ordinary traffic conditions (congestions, signal lights etc.). The second section was oriented out from the city. Its origin was placed on a parking lot next to last underground station and the destination

Table 5. Technical parameters of flow–meter WF007

Parameter	Value
Measuring principle	Oval gear
Sensing principle	Hall Sensor
Flow range	0.005–1.5 L min^{-1}
Pulses output	1,800 pulses L^{-1}
Viscosity	0–2,000 mPas
Accuracy	± 0.5%

in a suburb municipality in app. 15 km distance. This section is taken as semi-urban conditions. The last section was proposed prevailingly on motorways around Prague and this route performs as extra urban conditions. The road test uncertainty has been minimized by repetition of measurement. With respect to time-consuming of experiment, the measurement was repeated five times on each track.
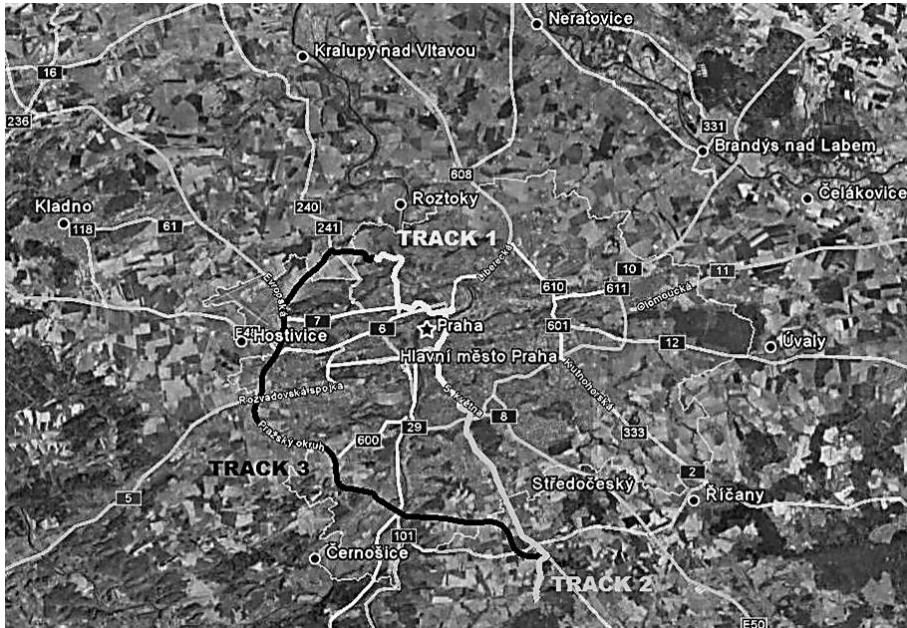
**Figure 1.** Single routes (Tracks1−3) of measurement (map source Google Earth).

RESULTS AND DISCUSSION

Table 6 summarizes the basic results describing each test car routes in terms of distance, average speed and selected operating parameters of tested cars. As is evident from Table 6, Track 1 represents typical urban traffic conditions with frequent stops and accelerations with low average speed of 30 km h^{-1}. Track 2 represents semi-urban traffic conditions with slightly higher average speed. The last test route Track 3 with average speed of 77 km h^{-1} represents motorway traffic conditions.

Table 6. Results of selected operating parameters on tracks

	TRACK 1	TRACK 2	TRACK 3
Distance (km)	16.4	15.1	41.3
Average speed (km h^{-1})	30 ± 8.6	36 ± 5.6	77 ± 4.2
LEXUS LX400H			
Averag fuel consumption (L 100 km^{-1})	10.9 ± 2.1	8.7 ± 1.6	10.9 ± 1.8
Fraction of engine in operation (%)	37 ± 8.8	41 ± 2.6	80 ± 2.1
CO_2 production (g km^{-1})	256 ± 35	204 ± 15	255 ± 12
SKODA FABIA 1.2 HTP			
Average fuel consumption (L 100 km^{-1})	12.2 ± 2.5	9.1 ± 2	7.1 ± 1.2
CO_2 production (g km^{-1})	284 ± 29	215 ± 18	165 ± 10

Results in Table 6 assess also a total CO_2 emission production and fuel consumption of conventional vehicle and HEV on specified sections of road. Measurement was carried out with HEV Lexus and conventional car equipped with a combustion engine i.e. Skoda Fabia 1.2 HTP, spark ignition (other details are in Table 3). This vehicle has been selected as a typical representative of one of the most used lower-class cars in the Czech Republic typically designed for operating in urban traffic conditions. It necessary to underline that the comparison of these vehicles is radically different in vehicles' parameters. Vehicles have different combustion engines, design, service weights and powertrains. It is necessary to compare results even with single technical parameters of both referred vehicles. Yet, in a certain type of traffic conditions, a significantly larger hybrid vehicle achieves better operating results.

In case of HEV, the percentage part of combustion engine's operational time is very important information. From Table 6 is evident that the Lexus combustion engine is more than half of operational time switched off under city and semi-urban conditions - the lower is vehicle's average speed the more is used its electromotor. Under motorway conditions it possible to see the significant increase of emission production. These higher speeds bring the requirement for higher percentage part of combustion engine power and it is evident when the electromotor is not able to provide the adequate power the combustion engine is more than 80% of time in operation. Similar results were obtained from several studies. The fuel savings (and emission production as well) of hybrid cars are more obvious under urban conditions due to their ability to reduce engine operation time under low efficiency conditions (Huang et al., 2019).
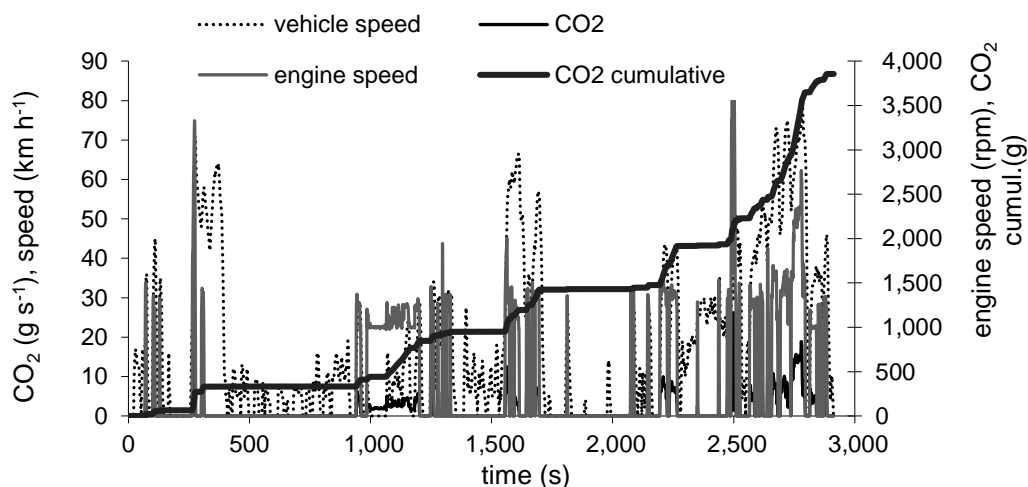
Figure 2. LEXUS LX400H under congestion conditions (Track 1).

Fig. 2 shows obtained and processed quantities of measurement on Track 1 under city congestion conditions. These values prove positive role of hybrid vehicles under urban traffic conditions. The decision making criterion used to decrease harmful emission production is fulfilment of conditions when combustion engine not used during operation. The first assumption of proper hybrid car's function is sufficiently charged accumulators. In case that accumulators are discharged (charge level less than 55%) the

combustion engine takes the role as a generator of electric power and charges accumulators as possible to see Fig. 2 in time app t = 1,000 s - i.e. vehicle stands, and combustion engine is in a operation. The second important assumption is the requirement for instantaneous power. This requirement is affected by acceleration quantities under the city conditions (time period to reach the vehicle's required speed). Especially required speed changes (increments) are rather low under these congestion conditions and the required power for these increments is normally covered by an electromotor only. It is evident (see Fig. 2) mainly in time t = 400–900 s when vehicle stopped or during a low speed increase (combustion engine is not in operation i.e. revolutions are equal to zero). In case of higher requirement for the instantaneous power both as a combustion engine as an electromotor are in operation simultaneously. Revolutions of the combustion engine are controlled in a relation to required power quantity. During accumulator charging the combustion engine was used in operation with 1,000 rpm, during drive the most often used range 1,400–2,400 rpm or exceptionally during the full acceleration 4,500 rpm. It possible to suppose that hybrid car's producer adjusted control of these combustion engine's operational revolutions with the aim to minimise a harmful emission production and fuel consumption. In case of a braking the combustion engine is not in operation, the electromotor shifts automatically into generator mode and accumulators are charged immediately.

The car Škoda Fabia 1.2 HTP has absolutely different trend in an emission production. The emission production (see Fig. 3) is significantly higher under city conditions in comparison with the semi-urban and motorway conditions. It is caused that this conventional vehicle with combustion engine is prevailingly operated on idle revolutions, i.e. in ineffective way, especially under congestion conditions (Grote et al., 2016).
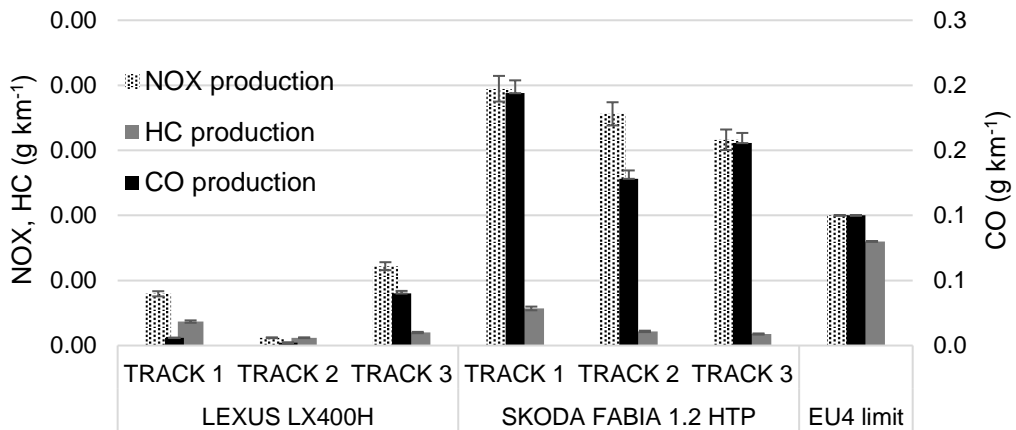
Figure 3. Result of emission on individual routes.

Further disadvantage of the conventional car during frequently repeated accelerating periods is its higher harmful emission production. (Brundell-Freij & Ericsson, 2005). This production is caused by transient modes of engine that prefers the requirement for instantaneous power at the expense of fuel mixture quality control which causes the decrease of catalyser's effectiveness (Fontaras et al., 2017). As can be seen from Fig. 3, Škoda Fabia produced significantly higher emissions than a hybrid vehicle, even exceeding the CO and NO_X emission limits for EURO-IV vehicles. This is a fairly common situation when in real driving condition the limits are exceeded. The NEDC driving cycle test (related to setting the EURO-IV limits) disregards various real-world conditions such as real weight (number of passengers), use of air conditioning, individual gear shifting, cold starts, operation at higher accelerations and congestion, etc. (Fontaras & Dilara, 2012) and examines only a small operating range of the engine (Pelkmans & Debal, 2006). However as is can be seen from Fig. 3., the Lexus vehicle did not exceed the limits set in all emission components. The benefits of HEV are obvious, but they depend on many factors, such as (temperature, air conditioning, ambient temperature, traffic situation, etc.) to be taken into account (Fontaras et al., 2008; Alvarez et al., 2012; Sonchal et al., 2012).

CONCLUSIONS

This study focused the real-driving fuel consumption and pollutant emissions performance of HEVs and conventional vehicle under real traffic condition. From the experiments carried out, the HEV benefits are particularly evident in urban traffic. Hybrid cars can cover inefficient combustion engine modes by means of an electric motor. The experiments carried out show that in urban and semi-urban traffic HEV can reach up to 60% save of combustion engine operating time, which leads to minimize of harmful exhaust gas production. Furthermore, it has been shown that in real operation the same results as in laboratory testing are often not achieved. Škoda Fabia in real-traffic condition exceeded the EURO-4 limits, while HEV fulfilled these limits. Appropriate use of advantageous HEV operating modes is needed to minimize fuel consumption and emission. This is one of the ways to meet the stringent emission limits for newly manufactured vehicles.

REFERENCES

Alvarez, R. & Weilenmann, M. 2012. Effect of low ambient temperature on fuel consumption and pollutant and CO2 emissions of hybrid electric vehicles in real-world conditions. *Fuel* **97**, 119–124. DOI: 10.1016/j.fuel.2012.01.022. ISSN 00162361

Brundell-Freij, K. & Ericsson, E. 2005. Influence of street characteristics, driver category and car performance on urban driving patterns. Transportation Research Part D: *Transport and Environment* **10**(3), 213–229. DOI: 10.1016/j.trd.2005.01.001. ISSN 13619209

Fontaras, G. & Dilara, P. 2012. The evolution of European passenger car characteristics 2000–2010 and its effects on real-world CO_2 emissions and CO_2 reduction policy. *Energy Policy* **49**, 719–730. DOI: 10.1016/j.enpol.2012.07.021. ISSN 03014215

Fontaras, G., Pistikopoulos, P. & Samaras, Z. 2008. Experimental evaluation of hybrid vehicle fuel economy and pollutant emissions over real-world simulation driving cycles. *Atmospheric Environment* **42**(18), 4023–4035. DOI: 10.1016/j.atmosenv.2008.01.053. ISSN 13522310

Fontaras, G., Zacharof, N-G. & Ciuffo, B. 2017. Fuel consumption and CO2 emissions from passenger cars in Europe – Laboratory versus real-world emissions. *Progress in Energy and Combustion Science* **60**, 97–131. DOI: 10.1016/j.pecs.2016.12.004. ISSN 03601285

Frey, Ch.H. & Unal, A. 2000. Use of On-Board Tailpipe Emissions Measurements for Development of Mobile Source Emission Factors, 2000 Proceedings of conference, Session 9b – Mobile Sources, *http://www.epa.gov/ttnchie1/conference/ei11/index.html.* Accessed 22.1.2019

Grote, M., Williams, I., Preston, J. & Kemp, S. 2016. Including congestion effects in urban road traffic CO2 emissions modelling: Do Local Government Authorities have the right options?. *Transportation Research Part D: Transport and Environment* **43**, 95–106. DOI: 10.1016/j.trd.2015.12.010. ISSN 13619209

Huang, Y., Surawski, N., Organ, B., Zhou, J, Tang, H.H. & Chan, F.C. 2019. Fuel consumption and emissions performance under real driving: Comparison between hybrid and conventional vehicles. *Science of The Total Environment* **659**, 275–282. DOI: 10.1016/j.scitotenv.2018.12.349. ISSN 00489697

Manzie, Ch., Watson, H. & Halgamuge, S. 2007. Fuel economy improvements for urban driving: Hybrid vs. intelligent vehicles. T*ransportation Research Part C: Emerging Technologies* **15**(1), 1–16. DOI: 10.1016/j.trc.2006.11.003. ISSN 0968090X

Pelkmans, L. & Debal, P.2006. Comparison of on-road emissions with emissions measured on chassis dynamometer test cycles. *Transportation Research Part D: Transport and Environment* **11**(4). 233–241. DOI: 10.1016/j.trd.2006.04.001. ISSN 13619209

Sonchal, Ch.P., Gajankush, J., Kulkarni A.V. & Pawar, S. 2012. Energy Efficient Hydraulic Power Assisted Steering System (E 2 HPAS). DOI: 10.4271/2012-01-0976

Periodic polynomial regression analysis of urban driving characteristics

J. Kreicbergs and A. Grislis[*]

Riga Technical University, Faculty of Mechanical Engineering, Transport and Aeronautics, Department of Automotive Engineering, 1 Kalku Str., LV1658 Riga, Latvia
[*]Correspondence: juris.kreicbergs@rtu.lv

Abstract. Urban driving characteristics with a focus on energy consumption have been tested in Riga on three main city streets with inflexible coordinated traffic lights control. The aim of this article is to investigate periodic polynomial regression analysis method to analyse car urban driving parameters' change during weekday twenty-four hours to assess the influence of vehicle technologies on energy consumption in city driving, to map the energy demand on Riga city main street sections and to evaluate the traffic lights control on flow energetic characteristics. The tests have been done using GPS and OBD data loggers on a test car repetitively driven along a pre-planned route at around-the-clock hours. A regression analysis using periodic polynomials was developed and applied to evaluate the traffic flow characteristics with a given time shift. It was concluded that using polynomial regression function, the polynomial order has to be at least seven although a visual conformation of good regression line to the measured data has to be checked especially with lower orders. To evaluate the traffic conditions at a given 20 minutes to one hour shift the application of regression function is limited for the periods with fast changing traffic flow, especially after the end of rush hours when the usability of regression line for the given data has to be checked individually for tested street sections.

Key words: city driving, energy consumption, traffic flow.

INTRODUCTION

Energy consumption reduction has been an important issue for many industries. As shown by IEA (2018) passenger cars in IEA countries use above one fifth of the total energy. As classified by Fontaras (2017) the car energy consumption in urban traffic depends on vehicle technologies, environmental and traffic conditions and vehicle drivers actions. Modern vehicle technologies are focused first on safety, environment and performance, in many ways increasing energy requirements of the vehicle while certain technologies contribute to energy savings and it is important to understand the scope of usability of the technologies.

The research of vehicle energy consumption on three major Riga city streets was performed to assess the influence of vehicle characteristics and technologies on energy consumption in city driving, to map the energy demand on street sections and to evaluate the traffic lights control on flow energetic characteristics.

With the highly limited budget for the research, the traffic flow rate was measured by analysing the opposite traffic flow from the videos captured during the tests.

According to the test plan the cars return to the same street sections in the opposite direction after 10 to 11 km meaning the difference in time from 20 minutes to one hour. To evaluate the traffic flow at the time of test, it was decided to find regression lines that may allow to evaluate the traffic rate at least within the given time shift.

Traffic flow as a function of time of the day characteristics are documented by many researchers and are shown in Traffic Engineering textbooks like by Mannering et al. (2009), Garber & Hoel (2010), Roess et al. (2011) etc. Usually there are peaks for the morning and evening rush hours, calm traffic during the night and different transition periods between the peaks. The best regression line can be found if the functional relationship is exactly known. There is no one regression line that fits all the circumstances because traffic flow parameters depend on many factors, but it is clear that the function has to allow at least two peaks at it has its range of definition within 24 hours and it has to be periodic by this meaning that the end and the start of the day is a continuous process.

Periodic functions can be well analysed by Fourier series, but since most of the data processing was done in MS Excel, the closest built trendline fitting the data was polynomial. The function range does not have negative values and is limited by 24 hours, having value of 1 in MS Excel, therefore a truly periodic function is not needed, and the function has to give values in a single period only. Every new series in a Fourier transform allow the number of peaks doubled while every next order of polynomial adds just one extreme therefore it was decided to analyse polynomial regression lines where by setting certain limits the values and the first derivatives at the ends of the period may be equalized. As noted by Cobanovic et al. (2006) periodic regression is seldom included in syllabus of statistical course therefore there was made decision to make an exercise by finding the regression polynomial model for the performed urban driving tests. The found regression lines are not tested for other research data but well served for the analysis of the acquired data and may be extended to other driving characteristics data spread without essential time gaps along 24 hours of the day.

MATERIALS AND METHODS

Driving tests

The data have been taken from multiple driving tests performed in Riga city that have been described by Kreicbergs et al. (2018). The tests analysed in this paper were done with 2004 production year Opel Zafira with a 1.6i-16V petrol engine, driving more than 1000 km and 45 hours along a pre-planned route in the Riga city having extensive street sections with inflexibly coordinated traffic lights, by this enhancing repeatability of tests due to the time shifts between the traffic lights remaining constant for the whole duration of the tests. The route included three street sections that were driven along in both directions with a length between 2.3 and 2.8 km and having an inflexible traffic lights green wave (GW) in one direction and quite restricted traffic control against the green wave (AGW) in the other direction. The 25 km route was covered 41 times.

Fuel rate and car speed have been recorded by Auterra DashDyno SPD OBD logger. Car speed and GPS position were recorded by GPS logger RaceLogic DriftBox with a 10 Hz recording frequency. GPS speed data have been used for OBD speed calibration and for data synchronization, GPS position was used to split the driving route into sections allocated to the street grid.

Distance covered has been calculated from car speed data and logging timing data, then compared to car odometer recordings and distances calculated from GPS data. Fuel consumption FC in litres per 100 km calculated from the fuel rate and car speed. Traction energy consumption TW calculated from traction force and distance covered. The traction force is a sum of rolling resistance, air drag, grade force and inertia force, each calculated from car technical characteristics, car coast-down procedure and city streets vertical geometry data.

Periodical regression analysis
To perform the regression analysis of city driving parameter change during 24 hour period, up to eleventh degree of univariate polynomial equations n were tested:

$$P(x) = \sum_{i=0}^{n}(a_i \cdot x^i) \tag{1}$$

where x – time of the day, expressed as MS Excel value from 0 to 1 in a 24 hour period; a_i – variable at the i index of a data-set; N; n – degree of the polynomial.

To ensure the continuity of the regression polynomial, to get a polynomial with equalized endpoints, the values and the first derivative of the regression polynomial at midnight or any other time of the day have to be identical:

$$P(0) = P(1) \tag{2}$$

$$\dot{P}(0) = \dot{P}(1) \tag{3}$$

Solving Eq. 2:

$$a_1 = -\sum_{i=2}^{n} a_i, \tag{4}$$

and solving Eq. 3:

$$a_2 = -0.5 \cdot \sum_{i=3}^{n}(i \cdot a_i), \tag{5}$$

from Eqs 4 and 5 re-calculating a_1:

$$a_1 = \sum_{i=3}^{n}((0.5i - 1) \cdot a_i), \tag{6}$$

transforming the Eq. (1) to:

$$P(x) = a_0 + \sum_{i=3}^{n}(a_i \cdot (x^i - 0.5 \cdot i \cdot x^2 + (0.5 \cdot i - 1) \cdot x)). \tag{7}$$

The least-squares method finds values of each a_i by minimizing the sum S of squared residuals:

$$S = \sum_{j=1}^{m}\left[y_j - a_0 - \sum_{i=3}^{n}\langle a_i \cdot (x_j^i - 0.5 \cdot i \cdot x_j^2 + \lfloor 0.5 \cdot i - 1 \rfloor \cdot x_j)\rangle\right]^2, \tag{8}$$

where m – number of measurements; y_j – value of the j_{th} measurement.

There are n-1 sought parameters a_i and n-1 partial differential equations:

$$\begin{cases} \dfrac{\partial S}{\partial a_0} = -2 \cdot \sum_{j=1}^{m} \left[y_j - a_0 - \sum_{i=3}^{n} \langle a_i \cdot (x_j^i - 0.5 \cdot i \cdot x_j^2 + \lfloor 0.5 \cdot i - 1 \rfloor \cdot x_j) \rangle \right] \\ \dfrac{\partial S}{\partial a_k} = -2 \cdot \sum_{j=1}^{m} \left[\begin{aligned} &\left\{ y_j - a_0 - \sum_{i=3}^{n} \langle a_i \cdot (x_j^i - 0.5 \cdot i \cdot x_j^2 + (0.5 \cdot i - 1) \cdot x_j) \rangle \right\} \cdot \\ &(x_j^k - 0.5 \cdot k \cdot x_j^2 + (0.5 \cdot k - 1) \cdot x_j) \end{aligned} \right] \end{cases}, \quad (9)$$

where k – parameter a index; k values are from 3 to n.

Equating each differential equation to 0, solving the system of equations can be done by solving a matrix equation:

$$A = X^{-1} \cdot Y, \tag{10}$$

where $X =$

$$\begin{bmatrix} m & \sum_{j=1}^{m} P(3) & \sum_{j=1}^{m} P(4) & \cdots & \sum_{j=1}^{m} P(i) \\ \sum_{j=1}^{m} P(3) & \sum_{j=1}^{m}(P(3) \cdot P(3)) & \sum_{j=1}^{m}(P(4) \cdot P(3)) & \cdots & \sum_{j=1}^{m}(P(i) \cdot P(3)) \\ \sum_{j=1}^{m} P(4) & \sum_{j=1}^{m}(P(3) \cdot P(4)) & \sum_{j=1}^{m}(P(4) \cdot P(4)) & \cdots & \sum_{j=1}^{m}(P(i) \cdot P(4)) \\ \vdots & \vdots & \vdots & \ddots & \vdots \\ \sum_{j=1}^{m} P(k) & \sum_{j=1}^{m}(P(3) \cdot P(k)) & \sum_{j=1}^{m}(P(4) \cdot P(k)) & \cdots & \sum_{j=1}^{m}(P(i) \cdot P(k)) \end{bmatrix}; (11)$$

$$A = \begin{bmatrix} a_0 \\ a_3 \\ a_4 \\ \vdots \\ a_k \end{bmatrix}; \quad Y = \begin{bmatrix} \sum_{j=1}^{m} y_j \\ \sum_{j=1}^{m}(y_j \cdot P(3)) \\ \sum_{j=1}^{m}(y_j \cdot P(4)) \\ \vdots \\ \sum_{j=1}^{m}(y_j \cdot P(k)) \end{bmatrix} \tag{12}$$

where $P(r) = x_j^r - 0.5 \cdot r \cdot x_j^2 + (0.5 \cdot r - 1) \cdot x_j$.

Matrix calculations were done by means of MS Excel using VBA code to find regression polynomials with degrees from 3 to 10 for fuel consumption, average speed, traction energy consumption, braking energy, stoppage time and fuel consumption both for polynomial regression and polynomial regression with equalized endpoints. In total 75 sets of measurement data have been analysed.

To find an optimal polynomial degree for city driving parameters when analysed against the time of the day for each regression polynomial coefficients of determination R^2 and R^2 adjusted have been calculated and put in MS Excel charts for comparison. For R^2 adjusted the degree of freedom for polynomial is equal to the degree of the polynomial, for the polynomial with equalized endpoints the degree of freedom is n-2, since a_1 and a_2 are calculated from other polynomial constants (4) and (5). Besides the

numerical evaluation of R^2 values, visual comparison of regression lines was done to see how well the regression lines fit the data.

RESULTS AND DISCUSSION

The driving tests were planned to be spread during all 24 hours of the day, but due to higher variations in traffic intensity in the evenings, slightly more tests were done in the evenings. Regression function may be influenced by gaps between the measurement points therefore the plan was to avoid essential time gaps between measurements even when no essential traffic condition changes were expected.

Comparison of PR and PRE regression lines

In the case with dense data during all hours there is no essential difference between the polynomial regression (PR) and polynomial regression with equalized endpoints (PRE). Traction energy consumption TW per 100 km on street sections where coordinated traffic lights ensure green wave is shown on Fig. 1. The difference in R^2 values between PR and PRE is close to 0.01.
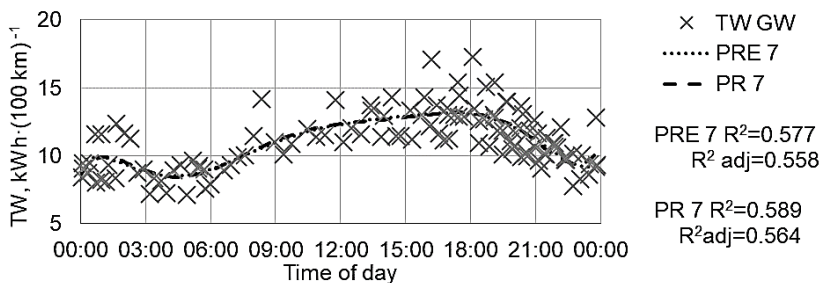
Figure 1. Car traction energy consumption on the test streets in the direction of the traffic lights green wave.

To visually see the difference in regression lines, the same graph is shown on Fig. 2 without data points and with smaller axis units. There is 1.5 kWh 100 km^{-1} or slightly above 10% difference in energy consumption regression line for PR just before and just after the midnight.
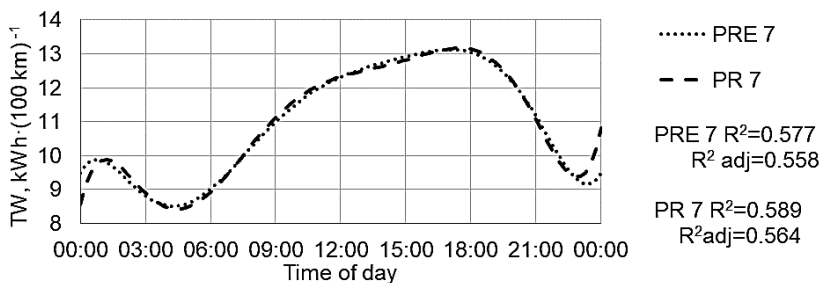
Figure 2. Car traction energy consumption regression lines on the test streets in the direction of the traffic lights green wave; PRE 7 – 7th order polynomial regression line with equalised endpoints, PR 7 – without equalised endpoints.

In certain cases, especially with less data around midnight like in Fig. 3, where fuel consumption FC is given for Čaka Street only in the direction of the green wave, the difference in R^2 values between PR and PRE is still quite small, but the fuel consumption for PR just before the midnight is more than double of the value just after the midnight. There is quite a small variance between regression lines where there is a small time gap in the dataset, but for the rest of the time PR and PRE lines are really close.
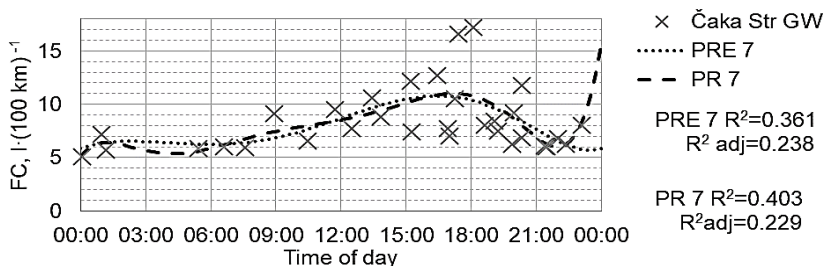
Figure 3. Car fuel consumption regression lines in the direction of the traffic lights green wave; PRE 7 – 7th order polynomial regression line with equalised endpoints; PR 7 – without equalised endpoints.

To find an optimal degree of polynomial for describing the change of various driving characteristics the PRE lines were calculated and plotted for polynomial orders from 3 to 10.

Optimal degree of the polynomial for driving characteristics
To evaluate the PRE regression lines the Excel VBA code also calculated R^2 and R^2 adjusted values for each line and for every characteristic a graph was plotted. The R^2 values for traction work on the test streets in both directions and for a total route are shown on Fig. 4. Different R^2 values for various streets do not describe how good the PRE line fits the data. The more the parameter changes during the day, the higher is R^2 value. It can be seen that for different street sections the increase of R^2 with the polynomial order is different, for some sections the values are close to the maximum already at 4 while for others quite noticeable increase is up to the polynomial order of 10, meaning that there is no equally good regression model for all datasets.
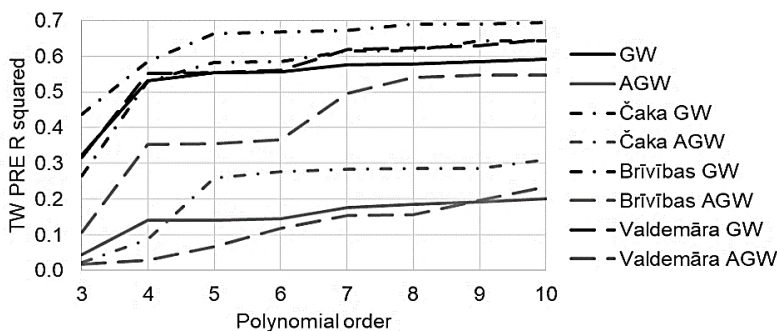
Figure 4. R squared values for traction work 3rd to 10th order polynomial regression lines on test streets; GW – in the direction of green wave; AGW – in the direction against the green wave.

The adjusted R^2 values shown along the R^2 value for fuel consumption data on Fig. 5 the growth up to 9th polynomial order for fuel consumption data on Valdemāra Street against the green wave direction while for some street sections the order of 6 seems using excessive polynomial degrees.
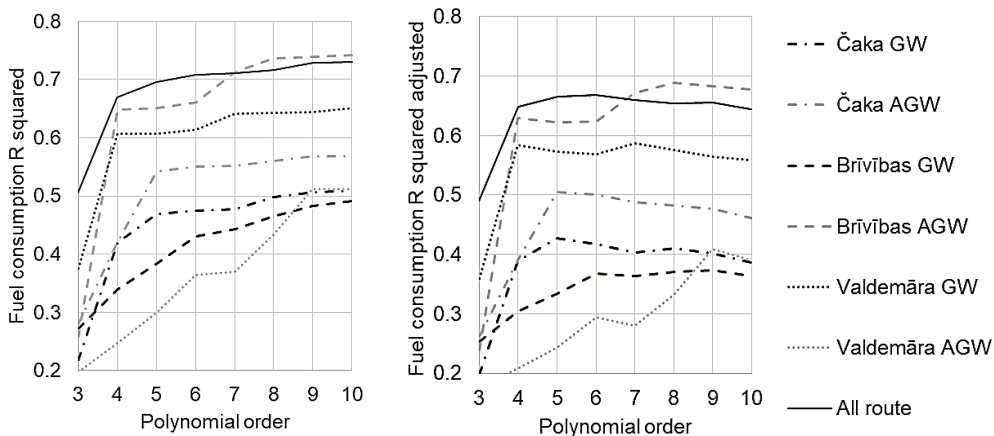
Figure 5. R squared and R squared adjusted values for fuel consumption 3rd to 10th order polynomial regression lines on test streets; GW – in the direction of green wave; AGW – in the direction against the green wave.

The visual inspection of regression lines were performed for all datasets. The PRE lines for traction work per 100 km for polynomial orders from 3 to 10 for GW direction leading out of the city for all three streets analysed are shown on Fig. 6. For the ease of analysis every next polynomial order line is shifted up by 1 kWh per 100 km. PRE line 3 depends on a_3 coefficient only, therefore the line is very simple and the corresponding R^2 value is essentially lower than for higher orders of polynomial.
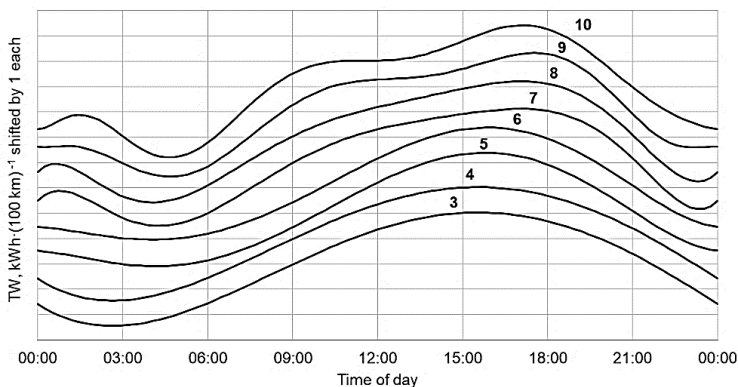
Figure 6. Polynomial regression lines with equalised endpoints for traction work per 100 km for polynomial orders from 3 to 10 in the direction of green wave.

From the shape of the regression line several periods for the traffic conditions can be found. All streets investigated have bus and trolleybus lines, therefore the lowest

energy demand is while there is almost no public transport on streets between 2 am and 5 am. This period can be well seen from line 7. There can be seen only a minor peak for the morning traffic on lines 9 and 10 because the GW direction leads out of the city and the tests are done in the city centre while the traffic jams in the mornings are mostly on the approach to the centre. The highest energy demand is around 6 pm when people return from the work home and gradually diminishes up to 11 pm.

In the direction against the green wave towards the city centre shown on Fig. 7 there is higher morning peak detected from line 7 and due to multiple stops during the night time, the low peak is smaller and again can be observed from line 7.
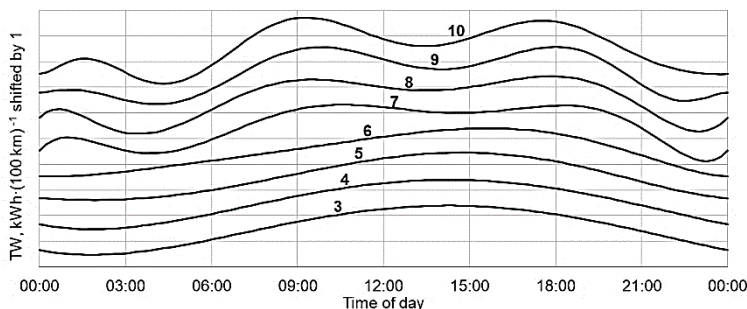
Figure 7. Polynomial regression lines with equalised endpoints for traction work per 100 km for polynomial orders from 3 to 10 in the direction against the green wave.

When comparing the regression lines against the data on certain occasions it can be seen that for certain times of day the line does not describe well the process. On Fig. 8 where the average speed on Brīvības street in the direction of green wave is calculated, it can be seen that just before 7 pm the speeds have reached the minimum and then in a short time jumped up for some 20 km per hour indicating that the traffic flow is instable and a special attention has to be devoted to evaluating the traffic flow at this time period. Since one of the goals for this particular regression analysis is to find traffic flow characteristics above 10 km from the actual measurement, between 6 pm and 8 pm the speeds cannot be evaluated from the regression line only.
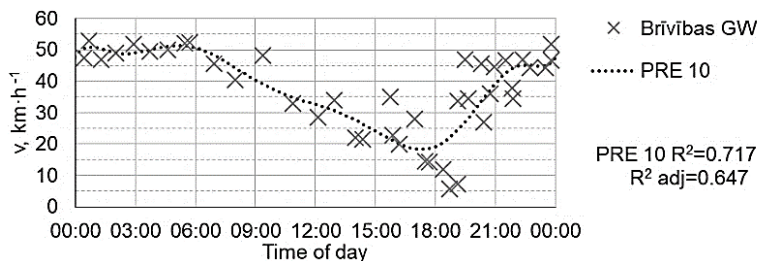
Figure 8. Average speed on Brīvības Street in the direction of green wave with 10th order polynomial regression line with equalised endpoints.

The same speed graph on the same street but against the direction of the green wave shown on Fig. 9 is much more stable without steep changes and the regression calculation would give a sensible result.

The regression analysis described cannot be extended to any traffic parameters analysis but is really helpful for the goals stated.
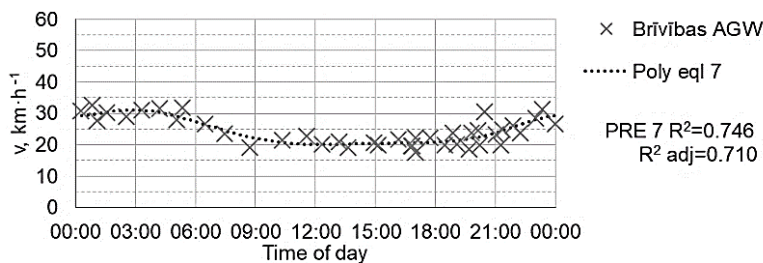
Figure 9. Average speed on Brīvības Street in the direction against the green wave with 7th order polynomial regression line with equalised endpoints.

CONCLUSIONS

The periodic polynomial regression analysis is not a regular textbook statistical analysis case while it is an enjoyable exercise to solve the equations with setting limits for function and the first derivative values to get a usable periodic function regression model.

The periodic polynomial regression function can be used for road traffic parameter change as a function of the time of the day analysis. The polynomial order has to be at least 7 although a visual conformation of good regression line to the measured data has to be checked especially for the lower polynomial orders.

The regression polynomials obtained can be used for the rate of flow estimates by measuring the oncoming traffic on most of the street sections analysed for most of the time, but due to high variance in traffic flow at certain conditions, any regression line would not be applicable for certain short time periods.

REFERENCES

International Energy Agency (IEA) 2018. Key world energy statistics. 40 pp.

Fontaras, G., Zacharof, N.G. & Ciuffo, B. 2017. Fuel consumption and CO2 emissions from passenger cars in Europe Laboratory versus real-world emissions. *Progress in Energy and Combustion Science* **60**, 97–131.

Mannering, F.L., Washburn, S.S. & Kilareski, W.P. 2009. *Principles of Highway Engineering and Traffic Analysis.* Wiley, USA, 398 pp.

Garber, N.J. & Hoel, L.A. 2010. *Traffic and Highway Engineering.* Cengage Learning, Stamford CT, 1229 pp.

Roess, R.P., Prassas, E.S. & McShane, W.R. 2011. *Traffic Engineering.* Pearson, Upper Saddle River NJ, 744 pp.

Cobanovic, K., Lozanov-Crvenkovic, Z. & Nikolic-Doric, E. 2006. Periodic regression. *International Association for Statistical Education Conference Proceedings* **7**, 1–4.

Kreicbergs, J., Gailis, M. & Grislis, A. 2018, Urban Real Driving Analysis with and without Coordinated Traffic Lights Control. In*: Transport Means 2018: Proceedings of the 22nd International Scientific Conference. Part 1, Lithuania, Trakai, 3-5 October, 2018.* Kaunas University of Technology, Kaunas, pp. 157–161.

Analysis of operation parameters of electric and gasoline vehicle in real driving

M. Krumbholc[*] and M. Kotek

Czech University of Life Science Prague, Faculty of Engineering, Department of Vehicles and Ground Transport, Kamýcká 129, CZ16500 Prague, Czech Republic
[*]Correspondence: krumbholc@tf.czu.cz

Abstract. The reduction of transport-generated energy consumption and consequent emission production are currently a problem of global interest. Electric vehicles (EVs) are considered as one promising technological solution for limiting transport-generated energy consumption and emission production, but theirs operating parameters are strongly influenced by immediately operating conditions and it is often very problematic to prove or disprove benefits of EVs in real operation.

The aim of this paper is to present comparison of operating parameters of the full-electric vehicle VW e-UP! with identical vehicle Skoda Citigo with gasoline engine in real driving. Both vehicles were tested together in several different areas of the Czech Republic. The experiment was focused on analysis of energy (fuel) consumption and production of exhaust gases (CO, CO_2, NO_X). VAG-COM diagnostics system was used for sensing engine operating parameters, GPS coordinate were measured by Garmin GPS-18x, vehicle Skoda Citigo was equipped by the PEMS analyzer VMK for RDE emission sensing (CO, CO_2, HC, NO_X). The results bring a real comparison between the electric vehicle and the vehicle with gasoline engine in terms of fuel consumption and emissions production.

Key words: real driving emissions, vehicle range, fuel consumption, recuperation.

INTRODUCTION

Transport, especially individual car transport, is one of the main factors of air pollution and greenhouse gas emissions in urban areas. This trend has provoked European regulations to place a great emphasis on the decarbonisation of the transport sector (Directive 98/69/EC 1998), resulting in an increased production of pure electric, hybrid, and plug-in hybrid electric vehicles. Electric vehicles (EVs) are considered as environmentally friendly, but they always depend on the power source of electricity for charging. The promotion of EVs make sense only if it is ensured that a major share of electricity they use is generated from renewable sources, because the final goal is not just to increase the number of EVs but to reduce emissions (Ajanovic & Haas, 2016). Some results indicate EVs may prove to be dirtier than conventional vehicle with combustion engine in certain areas of usage (Manjunath & Gross, 2017).

EV can contribute to sustainable road transport (Huang et al., 2019). However, the limited range represents a significant disadvantage of EV compared to vehicle powered by internal combustion engine (ICEV - internal combustion engine vehicle). This disadvantage can discourage potential customers (Egbue & Long, 2012; Dimitropoulos

et al., 2013) or lead them to purchase high-range EV, which are not cost-effective and even the most sustainable solution due to the environmental impact (McManus, 2012; Neubauer et al., 2012).

There are many factors that influence the potential environmental benefits of EVs (Li et al., 2017). Therefore it is necessary to verify the operating parameters of the electric vehicle in real operation (under real traffic conditions) and to compare the achieved results with the identical conventional vehicle. The aim of this paper is to compare the operating parameters (energy or fuel consumption, indirect and direct production of harmful exhaust gases) of the full-electric vehicle VW e-up! and the vehicle with gasoline engine together operated in two significantly different geographic areas of the Czech Republic. The results follow previous research, which was focused primarily on the operating parameters of the electric vehicle (Marcev & Kotek, 2018).

MATERIALS AND METHODS

The electric vehicle VW e-up! and Skoda CitiGo (Fig. 1) were used for this experiment. The e-up! is the electric version of Volkswagen up! city car identical to the Skoda CitiGo. It is powered by a 60 kW electric motor which is powered by a

Figure 1. Volkswagen e-up! and Skoda CitiGo.

18.7 kWh lithium-ion battery pack integrated in the floor. Detailed technical parameters are shown in Table 1.
Second vehicle Skoda Citigo is a small car from Škoda Auto producer equipped by small-volume 3 cylinder petrol engine. Other technical parameters are summarized in Table 1.

Table 1. Technical parameters of VW e-up! and Skoda CitiGo

	VW E-Up!	Skoda CitiGo
ENGINE		
Design	synchronous AC electric motor with permanent magnets	3 cylinder, spark ignition, atmospheric
Power	60 kW	55 kW at 5,000 rpm
Torque	210 Nm at 0 rpm	95 Nm at 3,000–4,300 rpm
Fuel system	electric plug-in	Multi-point gasoline injection
BATTERY		
Type	li-ion 323 V	
Capacity	18.7 kWh	
Number of cells	17 modules, 12 cells per module	
Weight	230 kg	
CAR BODY		
Service weight	1,185 kg	929 kg
Manufacture year	2016	2016
DRIVE PERFORMANCE		
Max. speed	130 km h^{-1}	160 km h^{-1}
Acceleration 0–100 km h^{-1}	12.4 s	13.2 s
Fuel consumption	11.7 kWh 100 km^{-1}	4.7 L 100 km^{-1}
Tank range	150 km	750 km

The vehicle operating data of both vehicles from the engine control unit were recorded via the OBD interface. Car diagnostic system VAG–COM was used for communication and record operating data from the OBD (engine speed, vehicle speed, voltage and current of the electric motor and battery, battery charge status).

The position and immediate speed and GPS coordinate were measured by Garmin GPS 18x USB with 1 Hz frequency.

A mobile PEMS on-board emission analyser VMK was used to measure emissions of Skoda CitiGo. The analyser uses non-dispersive infrared (NDIR) method to detect CO and CO_2 emissions and electrochemical cell to O_2 and NO_X emissions. Data was recorded with 1 Hz frequency on memory card. The technical data of analyser are summarized in Table 2.

Table 2. Technical parameters of mobile emission analyser

Measured values	Measurement range	Resolution	Accuracy
CO	0...10 % Vol.	0.001 % Vol.	0…0.67%: 0.02% absolute, 0.67%…10%: 3% of measured value
CO_2	0...16 % Vol.	0.01 % Vol.	0…10%: 0.3% absolute, 10…16%: 3% m.v.
HC	0...20,000 ppm	1 ppm	10 ppm or 5% m.v.
NO_X	0...5,000 ppm	1 ppm	0…1,000 ppm: 25 ppm, 1,000…4,000 ppm: 4% m.v.
O_2	0...22 % Vol.	0.1 % Vol.	0…3%: 0.1%, 3…21%: 3%

The measurement was carried out on the two significantly different geographic areas of the Czech Republic (see Fig. 2). In both areas, extensive questionnaire surveys were conducted to identify the most frequent transport destinations of the population. In both locations there is a well-available fast-charging station within a distance of 20 km.
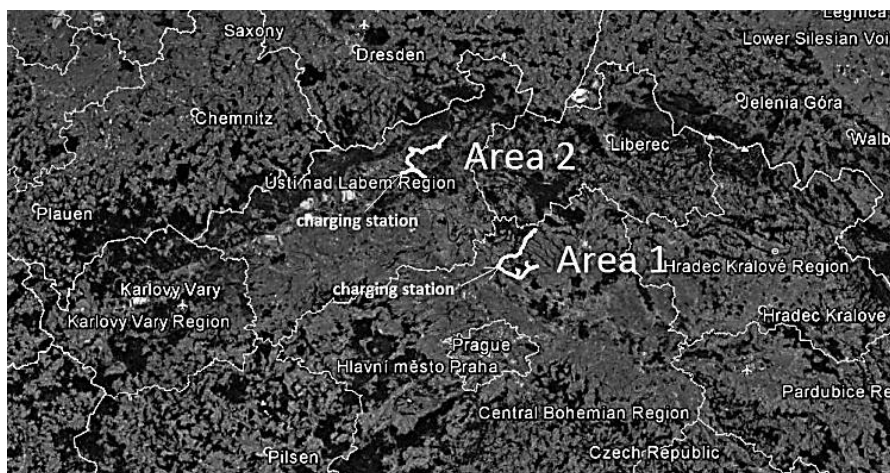
Figure 2. The map of tested areas with charging stations.

The first tested area was the lowland area in the vicinity of municipality Mělník which seems to be ideal for the use of an electric vehicle due to the appropriate terrain's properties. The first area is shown on the Fig. 3.

Figure 3. The map of area 1 – Mělník.

The second area (Fig. 4) was a hilly area near the municipality of Ústí nad Labem with frequent and very sharp altitude changes, which seems to be a very problematic altitude profile for an electric vehicle use because of on the first look this profile require much more power to overcome driving resistances, especially the gradient resistance.
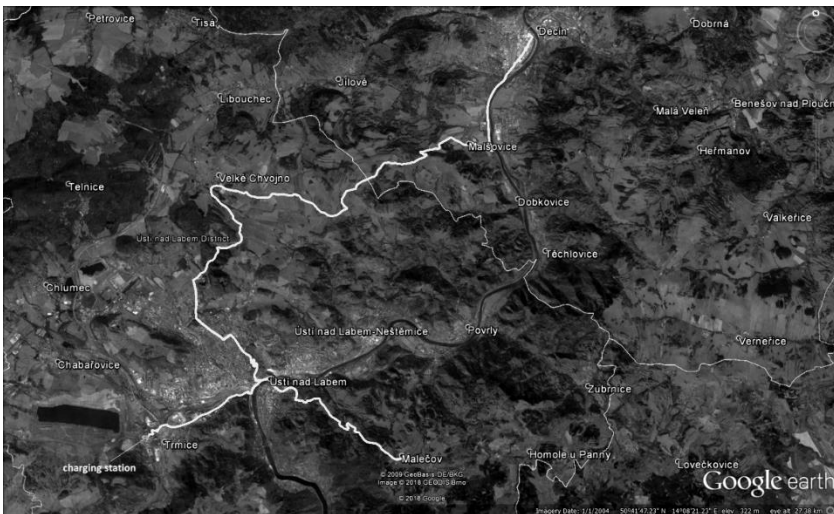
Figure 4. The map of area 2 – Ústí nad Labem.

The altitude road profile of both tested area is shown on Fig. 5. Table 3 provides brief description of both areas with regard to time and track length spent with drive to uphill, downhill and along plane.
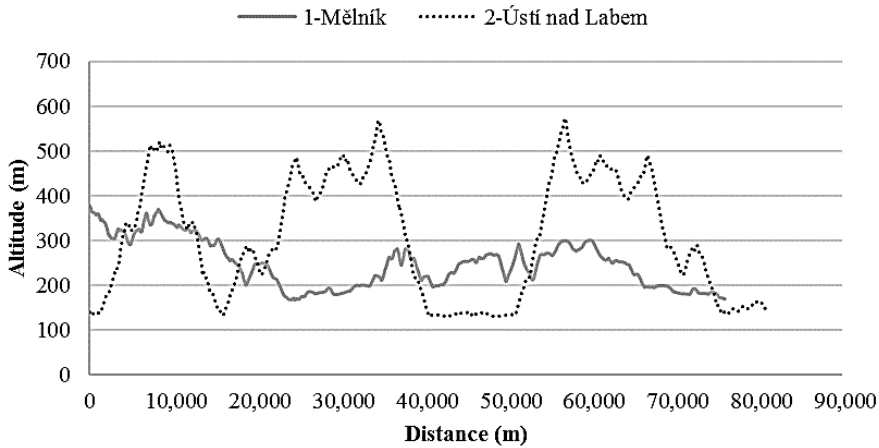
Figure 5. Altitude profile of tested areas.

The experimental drives were conducted during weekdays at the time of morning and afternoon rush hour on 19–21 September 2017. The road test uncertainty has been minimized by repetition of measurement. With respect to time-consuming of experiment, the measurement was repeated five times on each track. The method floating car data (FCD) were used in the experiment. It means that the driver kept calm driving style and the drive is influenced by the immediate traffic situation. Both vehicles drove just behind to ensure identical traffic conditions for the operation of both vehicles. During the experiment, the outdoor temperature was around 12 °C, windless, partly cloudy, dry roads. In the vehicle the internal temperature was set to 20 °C and no additional electrical appliances were switched on.

Table 3. Tracks characteristics

	1 – Mělník	2 – Ústí n.L.
total track length (km)	75.92	80.77
total travel time (s)	6,187 ± 167	7,239 ± 278
avg. speed (km h^{-1})	44 ± 2.3	40±3
abs. elevation difference (m)	210	442
PLANE		
track length (km)	10.92	6.58
ASCENT		
track length (km)	28.99	37.62
ascent (m)	0.796	1,953
avg. ascent (%)	2.75	5.19
DESCENT		
track length (km)	36.01	36.57
descent (m)	1,004	1,943
avg. descent (%)	2.79	5.31

For the purpose of comparing both cars in terms of emission production it is necessary to know the emission factors in the production of electricity. For the Czech Republic, emission factors for 2018 (see Table 4) are known according to the so-called energy mix taking into account the representation of different types of power plants (ČEZ, 2018).

The individual emission components were calculated according to the following formula:

$$emission \left(\frac{g}{km}\right) = energy\ consumption \left(\frac{kWh}{km}\right) \cdot emission\ factor(\frac{g}{kWh}) \qquad (1)$$

1093

RESULTS AND DISCUSSION

Table 5 summarizes the resulting operating parameter values of both tested vehicles. Both vehicles achieved a higher average consumption in location 2, where both had a similar increase in fuel consumption by approximately 10%. The geographically more demanding locality 2 was thus reflected by the same increase in consumption and there is no obvious benefit of any of the drive types. The same trend can be observed for CO_2 production, but in terms of the absolute value the EV achieved a 40% decrease in CO_2 production. This may be due both to the higher energy efficiency of electricity production but also to the fact that EVs can use of recuperation (Li et al., 2017).

Indirect exhaust emissions of EV are directly affected by the power source and the relevant emission factor reflecting the current energy mix for the area or country. The emission factors used - see Table 4 and the following calculation according to formula (1) are based on the energy mix of the Czech Republic for 2018. Similar emission factors for CO_2 are described (Jochen et al., 2015), when the Czech Republic ranks among the EU countries with a higher utilization of coal power plants, corresponding to a higher emission factor than the EU average (0.43 g kWh^{-1}). In the case of NO_X production, the same emission factor was also observed (Weiss et al., 2019) in Germany since 2010, when there was a similar share of coal-fired power plants as in the Czech Republic.

Table 4. Emission factors for electricity production in the Czech Republic (ČEZ, 2018)

NO_X	CO	CO_2
G kWh^{-1}	g kWh^{-1}	g kWh^{-1}
0.441	0.0698	581

Table 5. Resulting values of the operating parameters of the tested vehicles

Vehicle	Location	Consumption 100 km^{-1}	CO_2 g km^{-1}	CO mg km^{-1}	NO_X mg km^{-1}
Skoda CitiGo	1-Mělník	4.15 ± 0.15 L	100 ± 4	150 ± 10	9.54 ± 0.12
	2-Ústí	4.61 ± 0.22 L	108 ± 6	816 ± 84	24.11 ± 0.31
VW E-Up!	1-Mělník	10.23 ± 0.52 kWh	59.4 ± 2.1	7.15 ± 0.15	45.1 ± 2.3
	2-Ústí	11.28 ± 0.61 kWh	65.5 ± 2.4	7.87 ± 0.17	49.8 ± 2.9

In terms of CO emissions, there was a significant impact of locality 2 on CO production of the Skoda CitiGo, where there was approximately 5 times higher, while CO production of VW e-Up increased by only 10%. This may be caused, in particular, by the transition modes of the internal combustion engine where the stoichiometric fuel ratio cannot be maintained and thus the efficiency of the catalyst is considerably reduced. Therefore, the EV achieves negligible CO values compared to the classic vehicle.

The opposite situation is evident in the NO_X production, where from the point of view of the absolute value, the classic vehicle achieved the significantly better results (50%–80% decrease). However, the influence of the locality on the increase in NO_X emissions is significant again at the classic vehicle because of strong influence of transient operation modes of combustion engine.

CONCLUSIONS

The production of harmful emissions from EVs is strongly dependent on the source of electricity, that is, on the type of power plant and its primary source of energy. The advantages of electric vehicles are mainly the independence of emission production due to transient operation modes, which are often occur in real traffic condition where maximum emissions are achieved especially at the classical combustion engines. As the results show, ICEV has achieved 5 times higher CO emissions and 2.5 times higher NO emissions in more demanding terrain, while for EV only a slight increase up to 10 percent has occurred. Power production can be considered as stationary regimes where very good measures can be taken to eliminate harmful emissions. From the point of view of the absolute value of produced exhaust emission, the EV achieved 40% decrease in CO_2 production, 95% decrease in CO emission and up to 4 times increase in NO_X production.

Another advantage is that emissions can be produced outside human settlements, and emissions from electricity generation may not directly affect to people, but, of course, the impact of these emissions in the environment (eg acid rain) should be taken into account.

EV does not produce harmful emissions at the point of driving, but it should be noted that it produces indirect emissions depending on how the electrical energy is produced, and also it is necessary takes into account the whole lifecycle of an electric vehicle from production to disposal.

REFERENCES

Ajanovic, A. & Haas, R. 2016. Dissemination of electric vehicles in urban areas: Major factors for success. *Energy* **115**, 1451–1458. DOI: 10.1016/j.energy.2016.05.040. ISSN 03605442.

ČEZ a.s. Emission factors for the purposes of energy audit and energy assessment, 2018, https://www.cez.cz/*cs/udrzitelny-rozvoj/zivotni-prostredi/emisni-faktory-pro-ucely-zpracovani-energetickeho-auditu-a-energetickeho-posudku.html* Accessed 18.12.2018 (in Czech).

Dimitropoulos, A.,Rietveld, P. & Van Ommeren, J.N. 2013. Consumer valuation of changes in driving range: A meta-analysis. Transportation Research Part A: Policy and Practice **55**, 27–45.

Egbue, O. & Long, S. 2012. Barriers to widespread adoption of electric vehicles: an analysis of consumer attitudes and perceptions. *Energy Policy* **48**, 717–729.

Huang, Y., Surawski, N., Organ, B., Zhou, J., Tang, H.H. & Chan, F.C. 2019. Fuel consumption and emissions performance under real driving: Comparison between hybrid and conventional vehicles. *Science of The Total Environment* **659**, 275–282. DOI: 10.1016/j.scitotenv.2018.12.349. ISSN 00489697

Jochem, P., Babrowski, S. & Fichtner, W. 2015. Assessing CO2 emissions of electric vehicles in Germany in 2030. *Transportation Research Part A: Policy and Practice* **78**, 68–83. DOI: 10.1016/j.tra.2015.05.007

Li, W., Long, R., Chen, H. & Geng, J. 2017. A review of factors influencing consumer intentions to adopt battery electric vehicles. *Renewable and Sustainable Energy Reviews* **78**, 318–328. DOI: 10.1016/j.rser.2017.04.076. ISSN 13640321

Manjunath, A. & Gross, G. 2017. Towards a meaningful metric for the quantification of GHG emissions of electric vehicles (EVs). *Energy Policy* **102**, 423–429. DOI: 10.1016/j.enpol.2016.12.003. ISSN 03014215

Marčev, D. & Kotek, M. 2018. Influence of the road profile in different geographical areas of the Czech Republic to the operational parameters of the electric vehicle. *Agronomy Research* **16**, 1025–1031. DOI: 10.15159/ar.18.071

McManus, M.C. 2012. Environmental consequences of the use of batteries in low carbon systems: the impact of battery production. *Applied Energy* **93**, 288–295.

Neubauer, J., Broker, A. & Wood, E. 2012. Sensitivity of battery electric vehicle economics to drive patterns, vehicle range, and charge strategies. *Journal of Power Sources* **209**, 269–277.

Weiss, M., Zerfass, A. & Helmers, E. 2019. Fully electric and plug-in hybrid cars - An analysis of learning rates, user costs, and costs for mitigating CO2 and air pollutant emissions. *Journal of Cleaner Production* **212**, 1478–1489. DOI: 10.1016/j.jclepro.2018.12.019

Hygrothermal analysis of masonry wall with wool glass interior insulation

K. Leiten, P. Kirotar and M. Kiviste

Estonian University of Life and Science, Institute of Forestry and Rural Engineering, Kreutzwaldi 5, EE51014 Tartu Estonia
*Correspondence: kadri.keskkyla@mail.ee

Abstract. When the external appearance of the building is fixed due to heritage requirements the interior thermal insulation is the only possible solution for thermal upgrade of the building envelope. Applying internal insulation to existing buildings is known to pose a challenge in relation to hygrothermal risks, as this can lead to high relative humidity levels, condensation and ultimately, mould growth and decay. The case study building is under historical preservation and therefore this is not allowed to be insulated from outside. The paper describes the hygrothermal assessment of applying internal glass wool insulation and vapour barrier in masonry wall with air gap. In addition to the calculations the condition investigation was also performed. Data loggers measuring temperature and RH were applied during the period of 31.01.2013–16.02.2013. The conclusions were based to theoretical calculations (case study and DIN 4108-3) and practical measurement results based on the data logger values obtained. The calculations showed that glass wool and vapour barrier insulated system were in risk on condensation but the condensed water dries out during summer time. Due to the fact that logger measurements were recorded during the time when inside plastering was still in progress the relative humidity in the room was very high. As a result of calculations it is possible to build this type of wall effectively, but in this case it was not the most reliable way because of ongoing interior fitting.

Key words: interior insulation, hygrothermal performance, energy efficiency.

INTRODUCTION

Construction is the largest energy consumption industrial sector in the world (Transition to …, 2013). Energy consumption of building sector is increasing constantly because people build more and want to live and work in energetically balanced houses. The building stock in Estonia and in EU as well, is characterised by a quite big number of old buildings needed to be retrofitted to change the energy use more efficient. EU has been worked out several roadmaps for obtaining these goals: like renovating heating systems, using more state of art lightning and home machinery, to insulate buildings envelopes and so on (Transition to …, 2013).

Among buildings additional insulation are needed in two main groups: old buildings under heritage protection and with all the restrictions connected with renovation; all other insufficiently insulated buildings. Internal insulation is obvious for this first group of houses.

Accoding to EU comments 40% of total energy is used for heating and cooling of buildings, so if we insulate houses properly the savings could be quite remarkable. In this article only the possibilities for internal insulation were investigated. Many researches have been shown that internally insulated walls (Harrestrup & Svendsen, 2015; Nielsenet al., 2012; Fantucci et al., 2017) will fulfil the requirements set to thermal conductance and moisture condensation of the envelope. Still there are many risks needed to avoid: mould growing, condensation, frost damage, decay of wooden beams ends, so there are a lot of different wall structures which need the special insulating solutions. This is essential to insulate buildings in the cold climate but this must be done correctly from the hygrothermal behaviour point of view (Rasmussen, 2011).

So a lot of different insulation solutions has been investigated by researchers. The wooden beam ends on the brick wall might be a problem because of high relative humidity causes the decay. The next research show how important is airtight sealing of timber beams embedded into the wall (Vereecken & Roels, 2017). In some studies were declared that even the content of the brick is important to take into account (T. de Mets et al., 2017), and was proven that critical saturation point of tested clay bricks differs greatly if calculations have been made by ASTM for instance. The critical saturation degree of bricks also varied between UCC (Upper Canada Collage historical bricks the value is 0.25) and Canada brick (0.87) (Straube et al., 2010).

Mold growth in cold climate has been investigated in several works and found to be a problem. Condensation risks were handled and stated that internal insulation in masonry wall poses great risks related to interstitial condensation (Fantucci et al., 2017). The thaw-freeze cycles could be a problem too. So this will be better if the moisture will not intrude to the bearing brick structure at all. And again it is needed to mention that to work out correct internal insulation solutions is really challenging, because there are so many different structures i.e. different proper insulation solutions needed (Biseniece et al., 2017; Hansen et al., 2017).

Several systems of internal thermal insulation are worked out in Germany and in other western countries and many 'how to do' work lists have been produced by enterprises like Gutex, King-Span, Basf SE, Multipor and so on. In Estonia however exactly the same systems can't be applied due to different climate conditions. The investigation done in Estonia in 2013 show that the airtight vapour proof material inside gave the lowest relative humidity values in point where the condensation is the most critical. The main problem using PIR material was developing mould growth. Also it was seen that the need to use dry method decreases the relative humidity values (Klõšenko et al., 2013).

The diffusion tight synthetic foams that can hinder the vapour diffusion from indoor space perform well when there is no unintended leakage therefore a good workmanship and a perfect tightness are required during the implementation and operating stages. The most reliable way to build such tight system is to use glass-foam. It is lightweight, high-strength, moisture and fire proof low thermal conductivity but very expensive. It still remains vapour tight even when small piercing is done in surface. Less expensive way is to use other synthetic foams like polyurethane board with foil cover Kingspan SPU Sauna (Rakenna & Remontoi, 2012). The cons in these system is, that you have to seal the whole envelope to make one tight system therefore the relative humidity and ventilation has to be controlled. These systems limit the inward drying potential, leading to the moisture increase in the underlying massive masonry.

The chosen solution was cost effective, dry stud method, using glass-wool covered with OSB board and varnish it with 3 layers of bitumen mastic was supposed to make it vapour tight.

MATERIALS AND METHODS

Case study building

The case study building is situated in Estonia Tartu Veski Street 13. It was designed by architect Reinhold Guleke. In 1893 the construction was completed and taken into use by student corporation Livonia. Originally the building was one-storied and rectangular shaped. In 1958 the second story was built (National Registry of Cultural Monuments). In 1997 the building (Fig. 1) was listed as 'Cultural monument building' and therefore became under strict preservation regime (Regulation of Cultural Ministry no 12 published 20.03.1997). In 2010 the building was privatised and renovation works began. The renovated house is presented in Fig. 2.

Figure 1. Veski 13 before renovation.

Figure 2. Veski 13 after renovation.

The thickness of the masonry wall of the first wall is 600 mm and the thickness of the wall of the second floor is 450 mm and consists layers from inside to out: clay brick masonry wall 130 mm, non-ventilated air gap 50 mm, clay brick masonry wall 270 mm. Wall parts where originally were windows are thinner and there the outer clay brick masonry is only 130 mm thick and the case study was made in this part of the wall (northern side of the house) our case study was made and the calculated U-value of that wall part was U = 1.45 W m^{-2} K^{-1}.

Applied materials

The aim was to build interiorly insulated wall according to Estonian suggestions for thermal conductance. In the regulation of 'Methodology for calculating the energy performance of buildings' the U-value is not determined (Regulation of Minister of Economic Affairs and Communications no 63 'Methodology for calculating the energy performance of buildings' published 01.01.2019). On the inner side of the inner clay brick masonry wall glasswool ISOVER KL-37 200 mm between wooden frame (cross section of b = 50 mm, h = 200 mm, cc 600 mm) was applied. The wooden frame was covered from inside with OBS 3 (OSB-oriented standard board, d = 15 mm). The OSB-board was varnished with three layers bitumen mastic ICOPAL Water Renovator

Dysperbit DN. To make window frames vapour-retardant the window surroundings were sealed with tape and varnished with ICOPAL. On the mastic layer wooden laths (b = 25 mm, h = 50 mm, cc 600 mm) were placed for air gap and covered with wooden siding (d=25 mm) and lime mortar (d=25 mm). U value of this case study wall was U = 0.15 W m^{-2} K^{-1}.

Applied devices and sensors

The measuring devices were actually applied on 07.01.2013 and taken away on 28.02.2013. Values were measured during the period of time 31.01.2013–16.02.2013 and calculated as arithmetic averages. By this time the interior insulation work of the test wall was completed except the interior lime plastering. There were three humidity absorbers on site to remove excessive relative humidity but the level of humidity was still high.

To install the devices into the wall we had to open it from inside as shown in Fig. 3. Afterwards the perimeter of excluded piece of OSB-board was sealed with silicone as seen in Fig. 4.

Figure 3. Applying sensors between layers.

Figure 4. Sealing the opening with silicone.

The temperature inside/outside was measured using sensors on the wall TMC1-HD/TMC6-HD and connected to data logger HOBO U12. Relative humidity was measured inside with HOBO U12 and ambient air values were taken from the archive of Tartu weather service (Estonian Weather Service 2013). The TMC-HD sensors measurement range is -40 °C to 100 °C. HOBO U12 has temperature range of -20 °C to 70 °C (accuracy ± 0.35 °C from 0 °C to 50 °C) and RH 5% - 95% (accuracy ± 2.5% from 10% to 90%).

Between installed layers temperature and relative humidity was

Lime plaster	20 mm
Clay bricks	130 mm
Air gap	50 mm
Clay bricks	130 mm
ISOVER KL-37	200 mm
OSB 3	15 mm
Bituumenmastic	3 mm
Air gap	25 mm
Wood siding	25 mm
Lime plaster	25 mm
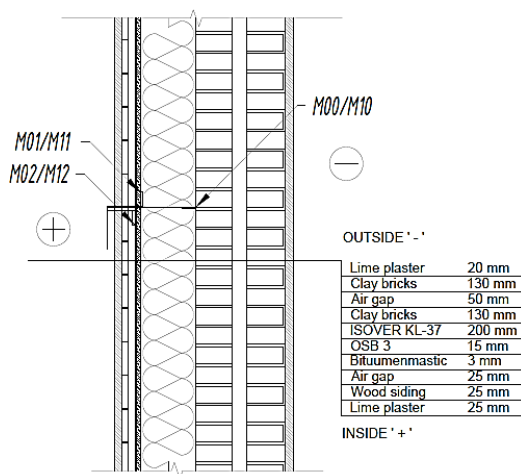
Figure 5. The cross-section of the insulated wall and installed sensors between layers.

measured in three points with capacitive humidity sensor FHA 646 R connected to Almemo® 2890-9 data logger. Sensors operative range is -30 to +100 °C, 5 to 98% RH (accuracy ± 2% RH in the range < 90%)

The sensor M00/M10 measuring temperature/relative humidity was applied between the wool and clay brick masonry wall, M01/M11 was placed between wool and OSB board, M02/M12 was placed on the interior side of bitumen mastic (facing the air gap). The cross-section of the wall and applied sensors are presented in Fig. 5.

Methodology

The study was carried out by two methods: simulation of hygrothermal behaviour using Glaser method based on: 1) measured values and 2) DIN 4108-3. Glaser method is a simplified procedure, based on pure diffusion moisture transport in one dimensional steady-state condition. It ignores some issues, such as moisture and heat accumulation in materials and built-in moisture, the dependence of material properties on humidity and temperature, the capillary transport of liquid water and the rising damp or wind driven rain.

Data saving interval was one hour. Calculations were done on three different bases. 1) During the time period of 31.01.2013–16.02.2013 the outside average temperature was -0.5 °C and inside +14 °C. The average relative humidity was outside 89. 9% and inside 64.7%. 2) Calculation done on the coldest day on 20.01.2013 when the ambient temperature was -28 °C. Interior temperature was +10 °C. The values of the relative humidity were accordingly 75% and 55%. 3) Calculations based on DIN 4108-3: outside temperature -10 °C, RH 80%; inside +20 °C RH 50%; period of time 2,160 h. Drying period conditions according to DIN: outside +12 °C, RH 70%; inside +12 °C, RH 70%; point of condensation +12 °C, RH 100%, time of period 2,160 h.

RESULTS AND DISCUSSION

Values measured during the period of time 31.01.2013 – 16.02.2013 were calculated as arithmetic averages. Measured values of temperature and relative humidity inside/outside in points M00/M10; M01/M11; M02/M12 are presented in Fig. 6 and Fig. 7. Until 18.02.2013 all the devices were working properly. Afterwards were some periods when some of the devices were out of order.

The relative humidity between layers depended correlatively on the inside relative humidity. There was no correlation with outside relative humidity.

The fact that relative humidity in point M11 was correlated to the inside relative humidity show that using the bitumen mastic was risky and it was not suitable vapour retarder as assumed in calculations.

In Fig. 7 the relative humidity in the point M11 was about 20% lower comparing to RH in the point M12. It leads to acknowledgment that bitumen mastic is working because only OSB board can't make such a big difference in relative humidity values.

The temperature line in Fig 6 show us that whole masonry wall was frozen throughout measuring period. The sensor, M00, between insulation layer and masonry wall show also mainly zero degrees in the measuring period and the relative humidity sensor M10 at the same place indicated that during the measuring period the RH was above 80% as seen in Fig. 7. These numbers refer to a great risk of decay and destruction of the wall caused by moisture and freezing. As the temperature remains more constant

there will not be many freeze-thaw cycles. In further studies it has to be found out how and if the layer of ice between insulation and masonry will protect the masonry from saturation. Also it would be interesting to know how far the saturation extends in masonry brick and whether the bricks get saturated in any point.
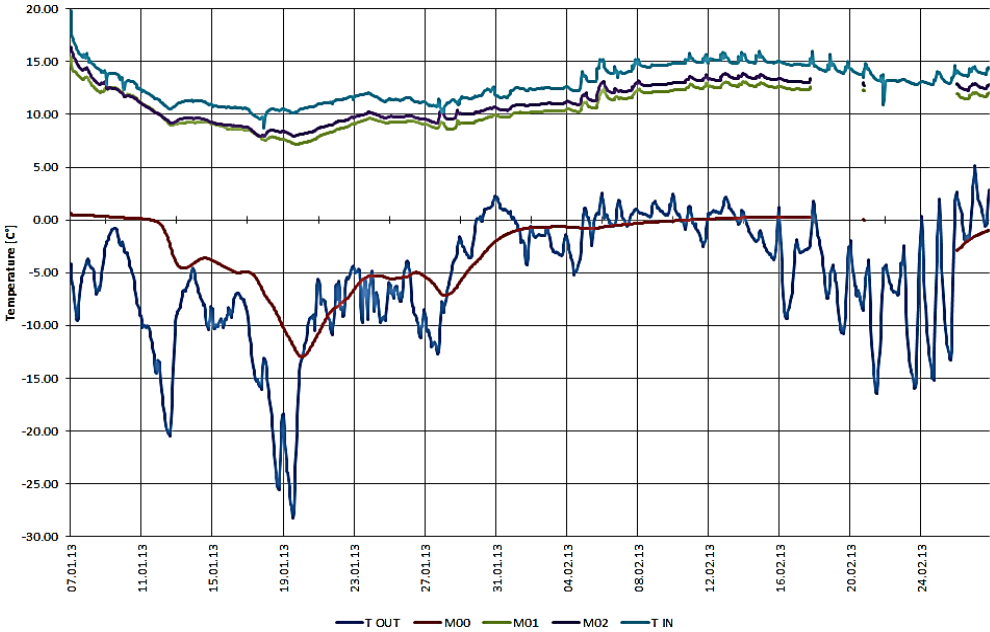

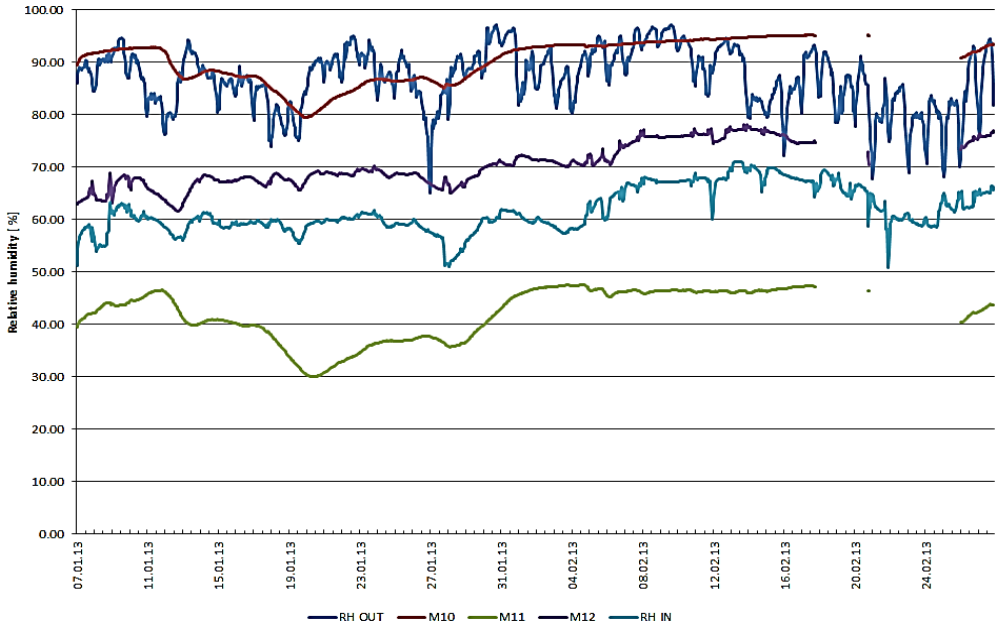**Figure 6.** Measured temperature values: inside, in points M00, M01, M02 and outside.

Figure 7. Measured relative humidity values: inside, in points M10, M11, M12 and outside.

It is really important to make on site tests to see if the moisture will dry out during the summer time and how strong is the correlation between exterior RH and in point M10. It would also be worth to investigate does the masonry wall`s air gap ventilation affects the evaporation.

Differences between measured and calculated temperature and relative humidity values during the period 31.01.2013–16.02.2013 are shown in Table 1 and Table 2.

Table 1. Differences between average measured and calculated temperature values

31.01.2013–16.02.2013	Temperature				
	OUTSIDE	M00	M01	M02	INSIDE
	°C	°C	°C	°C	°C
Average measured values	-0.49	-0.43	11.57	12.28	13.95
Calculated	-0.50	0.73	12.70	13.00	14.00

Table 2. Differences between average measured and calculated relative humidity values

31.01.2013–16.02.2013	Relative humidity				
	OUTSIDE	M10	M11	M12	INSIDE
	%	%	%	%	%
Average measured values	89.93	93.63	46.20	73.95	64.67
Calculated	89.90	106.50	47.70	62.2	64.70

Based on the measurements the average value of the relative humidity in point M10 was higher than 90%. The temperature in point M00 was constantly below zero. Calculations show high risk of condensation and mould growth and condensed water amount was 0.06 kg m^{-2} but according to DIN it dries out during the summer time.

During extreme winter conditions when the measured outside temperature was -28 °C the differences between calculated and measured values turned out huge (Table 3 and Table 4).

Table 3. Differences between average measured and calculated temperature values

Extreme period 20.01.13	Temperature				
	OUTSIDE	M00	M01	M02	INSIDE
	°C	°C	°C	°C	°C
Average measured values	-28.21	-11.85	7.26	7.98	10.14
Calculated	-28.00	-24.78	6.60	7.37	10.00

Table 4. Differences between average measured and calculated relative humidity values

Extreme period 20.01.13	Relative humidity				
	OUTSIDE	M10	M11	M12	INSIDE
	%	%	%	%	%
Average measured values	75.00	80.38	31.85	65.65	55.48
Calculated	75.00	363.00	39.60	45.90	55.00

The most extreme differences between measurements and calculation results were in point M00/M10 that was between masonry and insulation layers. It might be that the sensor was covered with ice and therefore did not give the proper temperature and relative humidity values. Even though when calculations done by DIN give condensed

water amount during 24 h to be 0.024 kg m^{-2} and amount of dried out water in 24 h to be 0.017 kg m^{-2}, it is possible to predict based on calculations that the water dries out during 2160 h. As climate is always unpredictable it is impossible to know how many times extreme minus degrees during winter will be. As we have not measured the saturation of clay bricks it may occur that the clay bricks will be demolished in one winter.

The third calculations were done according to DIN 4108-3 (2017) and results are presented in Table 5.

Table 5. Calculations according to DIN

Temperature		OUT	-10	°C				
		IN	20	°C				
Relative humidity		OUT	80	%				
		IN	50	%				
Vapour saturation pressure		OUT	259.7	Pa				
		IN	2337	Pa				
Vapour pressure		OUT	207.76	Pa				
		IN	1168.5	Pa				
Layer		Thickness	Thermal conductivity	Thermal resistance	Temperatuuid	Vapur pressure	Vapour saturation pressure	Relative humidity
Materjal		d ; [m]	λ [W/m-K]	R [m²-K/W]	[°C]	e [Pa]	E [Pa]	RH [%]
					-10	207.76	259.70	80.0
Outerior surface				0.04	-9.82	207.76	264.13	78.7
Lime plaster	Layer 1	0.02	1	0.02	-9.73	261.70	266.29	98.3
Clay brick	Layer 2	0.13	0.81	0.16	-8.99	378.59	284.15	133.2
Air gap	Layer 3	0.05	0.28	0.18	-8.17	382.23	305.31	125.2
Clay brick	Layer 4	0.13	0.81	0.16	-7.44	499.11	325.56	153.3
Glasswool Isover KL	Layer 5	0.2	0.037	5.41	17.32	526.08	1977.67	26.6
OSB 3	Layer 6	0.015	0.13	0.12	17.85	566.54	2044.57	27.7
Bithumen mastic	Layer 7	0.003	0.17	0.02	17.93	971.13	2054.98	47.3
Air gap	Layer 8	0.025	0.28	0.09	18.34	972.95	2108.34	46.1
Wood siding	Layer 9	0.025	0.12	0.21	19.29	1141.53	2237.58	51.0
Lime plaster	Layer 10	0.025	1	0.03	19.40	1168.50	2253.55	51.9
Interior surface				0.13	20.00	1168.50	2337.00	50.0
		R$_T$ (m²-K)/W		6.55				
		U W/(m²-K)		0.15				

The temperature and relative humidity were inside +20 °C and 50% and outside -10 °C and 80%. The basic values given in DIN 4108-3 (2017) are marked with green colour in Table 5. According to DIN calculations whole masonry part of the wall will freeze and the water will condense in three points as seen in Table 5. The abnormal calculated relative humidity values are represented in blue colour. The amount of condensed water is 0.051 kg m^{-2}. According to DIN 4108-3 (2017) it will dry out.

As the calculations made according to DIN 4108-3 (2017) are simplified and don't take into account may aspects of hygrothermal behaviour, it is not safe to use it to predict how interior insulation will perform. There exists a lot of complex programs like WUFI, DELPHIN, COMSOL that enable us to predict more adecvately how the interiorly insulated wall will perform more adequately (Knarud & Geving, 2017) than used Glaser method.

CONCLUSION

The one dimensional calculations made according to DIN 4108-3 allowed to conclude that it is safe to build such an interiorly insulated stud wall. Calculations show that condensed water will dry out during the evaporation period. The measured values confirmed that the material technical data were correct but a layer of ice was discovered on devices removal in point M02/M12 between the layers. Without further investigations to build this type of interiorly insulated wall is not suggested.

As vapour-proof systems are proven to be reliable, but the most problematic point is how to generate the totally vapour proof layer. There is no study for a wall with interior vapour-retardant insulation is covered with hydrophilic water absorbent material minimizing onsite piercing and avoiding piercing during period on building life cycle.

REFERENCES

Biseniece, E., Žogla, G., Kamenders, A., Purvinš, R., Kašs, K., Vanaga, R. & Blumberga, A. 2017. Thermal performance of internally insulated historic brick building in cold climate: a long term case study. *Energy and Buildings* **152**, 577–586.

Bjarlov, S.P., Finken, G.R. & Odgaard, T. 2015. Retrofit with Interior Insukation on Solid Masonry Walls in Cool Temperate Climates – An Evaluation of the influence of interior Insulation Materials on Moisture Condition in the Building Envelope. *Energy Procedia* **78**, 1461–1466.

DIN 4108-3:2017-09 Thermal protection and energy economy in buildings - Part 3: Protection against moisture subject to climate conditions - Requirements and directions for design and construction p. 70 (in German).

Estonian Weather Service 2013. *http://www.ilmateenistus.ee/ilm/ilmavaatlused/vaatlusandmed/* (assessed in 2013, in Estonian).

Fantucci, S., Isaia, F., Serra, V. & Dutto, M. 2017. Insulating coat to prevent mould growth in thermal bridges. *Energy Procedia* **34**, 414–422.

Hansen, T.K., Bjarlov, S.P., Peuhkuri, R.H. & Harrestrup, M. 2017. Long term in situ measurements of hygrothermal conditions at critical points in four cases of internally insulated historic solid masonry walls. *Energy and Buildings* **172**, 235–248.

Harrestrup, M. & Svendsen, S. 2015. Full-scale test of an old heritage multi-storey building undergoing retrofitting with focus on internal insulation and moisture. *Building and Environment* **85**, 123–133.

Klõšenko, P., Arumägi, E. & Kalamees, T. 2013. „Interreg IVB Baltic Sea Region Project $Co_2olBricks$ - Climate Change, Cultural Heritage & Energy Efficient Monuments", scientific work pp. 1–26 (in Estonian).

Knarud, J.I. & Geving, S. 2017. Comparative study of hygrothermal simulations of masonry wall. *Energy Procedia* **132**, 771–776.

Mets de, T., Tilmans, A. & Loncour, X. 2017. Hygrothermal assessment of internal insulation systems of brick walls through numerical simulation and fullscale laboratory testing. Energy Procedia, 11-th Nordic Symposium on Building Physics, NSB2017, Trondheim, Norway, pp. 753–758.

National Registry of Cultural Monuments.
https://register.muinas.ee/public.php?menuID=monument (assessed in 2013, in Estonian).

Nielsen, A., Møller, E.B., Rasmussen, T.V. & Hansen, E.J. de Place. 2012. Use of sensitivity analysis to evaluate hygrothermal conditions in solid brick walls with interior insulation. *In Proceedings of the 5th IBPC, Kyoto, Japan,* pp. 377–384.

Rakenna & Remontoi. 2012. Asennusvideo: saunan eristäminen
https://www.rakentaja.fi/tv/vid1472saunan_eristaminen.aspx (assessed 2013, in Finnish).

Rasmussen, T.V. 2011. Retrofitting Listed Buildings: Measures, Savings and Requirements. *The Open Construction and Building Technology Journal*, **5**, pp. 174–181.

Regulation of Cultural Ministry no 12 list of 'Cultural monument building' published 20.03.1997. *https://www.riigiteataja.ee/akt/25290* (assessed in 2013, in Estonian).

Regulation of Minister of Economic Affairs and Communications no 63 'Methodology for calculating the energy performance of buildings' published 01.01.2019. *https://www.riigiteataja.ee/en/eli/ee/MKM/reg/520102014002/consolide* (assessed in january 2019, in Estonian).

Straube, J., Schumacher, C. & Mensiga, P. 2010. Assessing the Freeze-Thaw Resistance of Clay Brick for Interior Insulation Retrofit Projects, Building Science Press, CP 1013.

Transition to Sustainable Building, Strategies and Opportunities to 2050. OECD/International Energy Agency 2013.

Vereecken, E. & Roels, S. 2017. Wooden beam ends in combination with internal insulation: the importance of an airtight sealing. *Energy Procedia* **132**, 664–669.

Contamination of transmission and hydraulic oils in agricultural tractors and proposal of by-pass filtration system

R. Majdan[*], R. Abrahám, D. Uhrinová and J. Nosian

Slovak University of Agriculture in Nitra, Faculty of Engineering, Department of transport and handling, Tr. A. Hlinku 2, SK949 76 Nitra, Slovak Republic
[*]Correspondence: radoslav.majdan@gmail.com

Abstract. Tractors use various types of lubricating oils in transmission and hydraulic system. Oils are contaminated by different ways depending on the work of the lubricated system. There are general requirements on the cleanliness level of the oil in the tractor transmission and hydraulic system according to the standard DIN 51524. According to all that, this paper presents research conducted by two tractors. The tractor John Deere 8100 used only its own implements (ploughs, trailers etc.) and it was operated in compliance with user manual. In this tractor, the oil cleanliness level met the standard DIN 51524 because reached the stage 7 (NAS 1638). The tractor Zetor Forterra 124 41 contained extremely contaminated oil, it reached stage > 12 (NAS 1638), due to the non-standard operation which was opposite to the user manual. Both ways of tractor operation are typical for farmers activity in the Slovak Republic, depending on the tractor type and style of agricultural production at most. The second part of this paper is aimed at the proposal of by-pass filtration system to eliminate the oil contamination. The by-pass filtration system is the second stage of the oil filtration in the tractor, whereas the first one means standard tractor filter. Function of the system was tested according to the decrease of chemical elements concentration characterising the oil contamination and visual method based on filter and its change after operating of tested tractor. There was evaluated the decrease of concentration of Fe (41.6%), Cu (28.7%) and Si (20.5%) after by-pass filtration system was running under operational conditions. It can be concluded that the by-pass filtration system was proposed correctly and it is suitable for tractors operation.

Key words: tractor oil, tractor maintenance, elimination of the oil contamination ~~elimination~~, quality of lubricants.

INTRODUCTION

Tribotechnical diagnostics is mainly aimed at qualitative changes of the oil properties and wear processes happened in machines. In this case, diagnostic parameters are obtained by means of the oil analysis. Changes of the oil technical state is the most common because of the chemical oxidation processes and contaminates presence. There are two sources of the hydraulic and transmission oil contamination (Fig. 1):

− external sources, as the dust and various liquids as the water from environment, the fuel for combustion, degraded oils from tractor implements (ploughs, seeders, trailers etc.), antifreezes from leakage of cooler etc.,

– internal sources (contamination coming from inside of the lubricated system), as wear processes of the machine (wear particles) and oil degradation processes (sludge, acids, etc.).

Fig. 1 shows the main sources of the oil contamination and contaminant types of the tractor hydraulic and transmission system. The external sources contaminate the oil from environment, the tractor implements and the tractor operation. Old, degraded and oxidized oils can contaminate the tractor oil if old and unknown implements (ploughs, trailers etc.) are connected to the tractor external hydraulic system. Lubricated systems are not ideally sealed, so certain amount of the dust and water can get to the oil. The tractor implement can be very significant source of the oil contamination if various tractors use the same implement. By using of incorrect type of the oil to refill or change the oil fill, the tractor operation can contaminate the oil.

The tribotechnical diagnostics evaluates the technical state of machines based on the oil contamination coming from the wear process. In this case, adhesive, abrasive, erosion, and cavitation wear processes produce the contamination. The tribotechnical laboratories utilise the various techniques to detect failures of lubricated systems and lubricant degradation.

Hnilicová et al. (2016) presents, that hydraulic oil is subjected to the constant process of changes. Dust, water and wear particles constantly contaminate the oil systems. High operating temperature and contact with oxygen reduces its lifetime. The tribotechnical diagnostics uses several analytical methods to assess the degree of hydraulic oil degradation, thus its lubricating power and monitor the state of mechanical systems of the machines. Wang et al. (2016) presents, that the failure resulting from hydraulic oil contamination is the main mode in the case of the piston pumps. Thus, it had been established a life prediction model for aviation hydraulic piston pumps.

Wear particles have typical shape and size, depending on the type of wear process (adhesive, abrasive, erosive or cavitation). Metal wear particles are very dangerous for machines because they lead to the next wear processes if filters do not remove them and circulate in the system. All hard and insoluble particles (regardless of their origin) with larger size than is the clearance between moving parts are very dangerous, because they do not flow in the oil film and can stick in. To analyse the size, concentration, and origin of the wear particles, the following methods of the tribotechnical diagnostics can be used:
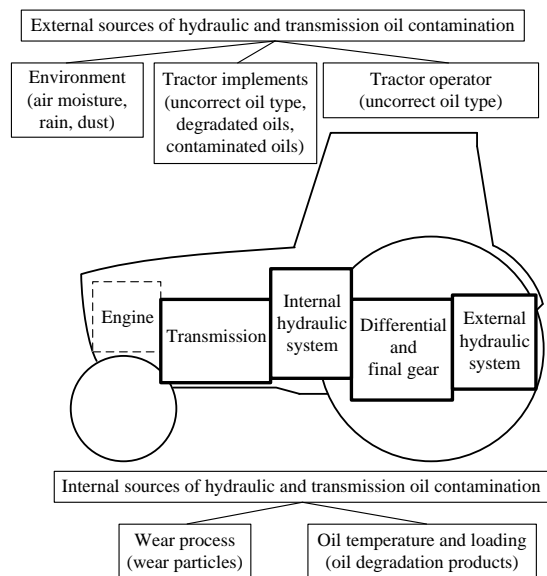
Figure 1. Internal and external sources of the oil contamination in hydraulic and transmission system of the tractor.

- Analytical ferrography, which uses strong magnetic field to separate particles from the oil sample. Non-ferromagnetic particles are separated while flow in the oil sample between ferromagnetic particles. Microscope allows observing shape, size and colour of the particles and states the particle origin by visual method. Tulík et al. (2014), Turis & Kučera (2016) and Tkáč et al. (2017) present evaluation of the contaminant particles in various hydraulic oils using the analytical ferrography.
- Direct reading ferrography (DR-ferrography), which measures amount of ferrous metals in the oil sample. Particles are classified into two groups. Particles larger than 15 µm (denoted DL) and particles smaller than 15 µm (denoted DS). The larger particles (DL) are produced by normal wear process and the smaller particles (DS) are produced by abnormal wear process.
- Filtration analysis, which separates contaminative particles from the oil sample using the paper filter disk. To separate the contaminative particles, the vacuum filtration unit is used. The particles on filter patch are evaluated by microscope. Comparing to the microscopic evaluation with reference photographs, the rapid assessment of the fluid contamination (cleanliness class classification by ISO 4406 or NAS 1638) can be made. This method can be also used for gravimetric analysis to determine the oil contamination.
- Gravimetric analysis, which quantifies the total mass of the particles from specific volume of the oil (mg dm^3). The gravimetric analysis cannot indicate the size of the particles. To state the distribution of the particle size, a particle counter is needed.
- Particle size distribution, which uses the particle counters to classify the contaminative particles according to their size. The particle distribution is expressed by one of the following standards:
  - ISO 4406-1999, which uses three figures (X_1/X_2/X_3) representing the level of the contamination grades for particles larger than 4 µm (X_1), 6 µm (X_2) and 14 µm (X_3). Rusnák et al. (2013), Kučera et al. (2015) and Kučera et al. (2016) present evaluation of the oil contamination according to the standard ISO 4406-1999.
  - NAS 1638, which applies one figure corresponding with the maximum allowed amount of the particles (i.e. worst-case) for the size range 5–15 µm, 15–25 µm, 25–50 µm, 50–100 µm and < 100 µm.
  - SAE AS 4059 (ISO11171), which uses six letters A, B, C, D, E and F representing the size of the particles (> 4 µm, > 6 µm, > 14 µm, > 21 µm, > 38 µm and > 70 µm) and number (X) representing the level of the contamination grade.
  - GOST 17216-2001, which uses one figure expressing the maximum level of the contaminative particles for the size range 5–10 µm, 10–25 µm, 25–50 µm, 50–100 µm and < 100 µm.
- Spectral analysis, which uses the principle of the spectroscopy to detect and quantify the chemical elements in the oil sample. If add back up energy to the oil sample, the chemical elements start to emit the spectrum with specific wavelengths. The spectral analysis involves various methods with different principles of chemical elements excitation f. e. the inductively coupled plasma spectrometry (ICP), the proton-induced X-ray emission (PIXE) or the rotating disc electrode optical emission spectroscopy (RDEOES). The spectral analysis is very precision

method specifying the concentration of the solid particles on the basis of the chemical elements concentration mainly for the smaller particles. Using the ICP spectrometry, Kosiba et al. (2013) and Tulík et al. (2017) monitored the solid particles in biodegradable oils. Research about RDEOES spectrometry is presented by Quazi & Khatavkar (2015).

All types of the oil contamination negatively affect machines and oils. In the extreme, the oil contaminants accelerate the wear process of very precision components of the machine. The solid particles generate other particles due to the abrasive were process. Metal particles and water are very harmful for oil oxidation stability and additives. Ecological oils are very sensitive to degradation. To apply the biodegradable oils, many researchers (Tóth et al., (2014a), Tóth et al., (2014b), Dobeš (2006) and Kučera et al., (2014)) require the highest possible oil cleanliness level to ensure the protection against degradation of the oil in machines. Machinery working in ~~an~~ agricultural sector is characterized by contact with primary food products and all elements of environment (Tkáč et al., 2014).

Therefore, it is necessary to research all factors affecting application of the ecological oils and also ensures reliable tractor operation. This paper presents the proposal of the by-pass filtration system and publish the observed results of the cleanliness level of the oils in the tractors hydraulic and transmission systems operating under standard and non-standard operation mode.

MATERIALS AND METHODS

Characteristics of monitored tractors and oils
The tractors were selected on the basis of cleanliness level of the universal transmission and hydraulic oils to present the difference between low and high level of the oil contamination. Regarding sources of the oil contamination (Fig. 1) of the tractor John Deere 8100 and Zetor Forterra 124 41 were selected.

The tractor Zetor Forterra 124 41 represents tractors which are often used on the small farms in the Slovak Republic because they are easy reparable and small farmers can repair it with reachable and relatively cheap spare parts. This tractor is an example of the simple construction of manual transmission and hydraulic system with external gear pump. The small farmers do not own all implements such as ploughs, trailers, seeders etc. so they can share them. Various tractors operate with various equipments because their simple construction allows it. So, the oil is often contaminated with degraded oils from the different tractors. These tractors do not immediately get out of order, but wear process of every lubricated part is accelerated and produces next solid particles. Zetor Forterra tractor uses the PP 90 (Slovnaft, Slovak Republic) gear oil type (Dynamax, 2017) in the hydraulic and transmission system. This gear oil is cheaper alternative for prescribed universal tractor transmission oil.

Tractor John Deere 8100 represents tractors which use the modern technical innovations and so its construction is more complicated and sensitive to operational conditions. It is equipped with automatic transmission and its hydraulic system is powered by removable piston pump. Both these main parts are very sensitive to the oil contamination and therefore the tractors owner has to pay attention to operate the tractor only with its own implements and use the same oil type and quality as is used in the tractor. We can assume that this lubricated system is producing only minimal amount of

the solid particles due to normal operational wear process. Prescribed universal tractor transmission oil Shell Donax 5W30 (Shell, Netherlands) type was used in this tractor.

Therefore, we can consider that the mode of the tractor operation mostly affects the oil contamination. The tractors were classified into the two groups as follows:

−   Standardly operated tractor. The tractor John Deere 8100 was operated in compliance with the user manual. This tractor was using only its own implements with correct oil type and with the same cleanliness level as is in the tractor oil fill. The tractor operator took care about the prescribed volume of the oil fill and refilled the oil loss with the correct oil type. This tractor was garaged to protect it against the water. Authorized tractor service realised the change of the oil fill and periodical maintenance.

−   Non-standardly operated tractor. The tractor Zetor Forterra 124 41 was not operated in compliance with the user manual. The tractor was using various implements with degraded oil fill. The oil change and refilling were not realised in authorized tractor service but on the farm and the tractor operator used only the universal tools. The tractor operator used the cheapest oil type and not the prescribed one. The tractor was yearly parked in the space without protection against the water and atmosphere moisture.

Considering operation of the tractor hydraulic system at normal pressure (< 25 MPa), standard DIN 51524 requires the minimum cleanliness classes 7, 8 according to the NAS 1638. The tractors classification mentioned above, reflects the minimum recommended cleanliness level (Table 1) in case of the tractor operated standardly and maximum level 12 in case of the tractor operated non-standardly.

Table 1. Required cleanliness classes for hydraulic systems (Casey, 2004)

Type of hydraulic system	Minimum recommended cleanliness level NAS 1638
Silt sensitive	4
Servo mechanisms	5
High pressure (25 to 40 MPa)	6
Normal pressure (10 to 25 MPa)	7
Medium pressure (5 to 15 MPa)	9
Low pressure (< 5 MPa)	10
Large clearance	12

Evaluation of the oils properties

This paper is aimed at the oil contamination in transmission and hydraulic system of the two tractors and at suggestion of the design of the by – pass filtration system improving the oil cleanliness level. Following base physical properties of the oils were evaluated in accredited laboratory Wearcheck (Hungary):

−   kinematic viscosity at 40 °C and 100 °C,
−   viscosity index,
−   water content (Carl Fisher).

The same laboratory evaluated the oil contamination on the basis of the chemical elements content (Fe, Cu, Si, Al, Pb, Sn and Cr) in the oil samples according to the ICP spectrometry.

Besides the oil sample evaluation in laboratory Wearcheck, the FT-IR spectroscopy was realized in accredited tribotechnical laboratory Intertribodia (Slovak Republic) to state the oxidation stability, additive depletion and water content.

Proposal of by – pass filtration system for tractors

The by-pass filtration system was installed in the tractor Zetor Forterra 124 41 operated with the oil type PP 90. The system was tested at 1,889 engine hours of tractor operation. The prescribed oil change interval is 2,000 engine hours. The volume of the oil fill in the transmission and hydraulic system is 56 dm^3.

The filtration system uses the internal hydraulic system of the tractor. The hydraulic pump supplies the filtration system with universal oil from the transmission. After filtration, the oil returns to the transmission through T-fitting and hydraulic return line. This system uses the filter body FT-B68 with filter element FT-V68 (Filtration technology, Czech Republic). The main parameters of the filter body and the filter element are listed in Table 2. The by-pass filtration system is the second stage of the oil filtration. The first stage is operational oil filtration with 20 μm filter ability (standard oil filters in tractor).

Function of the by-pass filtration system was evaluated according to the decrease of the chemical elements content (Fe, Cu and Si) characterising significant oil contamination. The chemical elements (Cr, Pb, Al and Sn) characterized non-significant oil contamination because concentration before the oil filtration reached non-significant value. Using the ICP spectrometry (Wearcheck, Hungary), the chemical elements concentration in the oil was measured.

Table 2. The main parameters of the filter body and the filter element

Parameter	Unit	Value
Nominal flow rate	dm^3 min^{-1}	1.8
Nominal filter ability of the filter element	μm	1
Volume of the oil fill	dm^3	50–300
Oil viscosity	cSt	9–220
Operation pressure	MPa	0.2–0.4
Weight	kg	4.5

The decrease of the chemical elements content characterising the oil contamination was calculated by formula (Majdan et al., 2016):

$$\Delta_C = \frac{C_{BF} - C_{AF}}{C_{BF}} \cdot 100 \qquad (1)$$

where Δ_C – decrease of chemical elements content characterising the oil contamination, %; C_{BF} – chemical elements content before the oil filtration, mg kg^{-1}; C_{AF} – chemical elements content after the oil filtration, mg kg^{-1}.

The oil circulation number states, how often the oil fill circulates in the unit for time (Mang, 2014). The oil circulation number is calculated as follows:

$$o = \frac{Q_f}{V}, \text{ s}^{-1} \qquad (2)$$

where o – oil circulation number, s^{-1}; Q_f – flow rate dm^3 s^{-1}; V – volume if the oil fill in the tractor, dm^3.

Using the oil circulation number, we can state how many times the oil flew through the filter element during the tractor operation with by-pass filtration system. The count of the oil circulation through the filtration system is calculated as follows:

$$C = o t_o \qquad (3)$$

where C – count of the oil circulation -; o – oil circulation number, s^{-1}; t_o – tractor operation, s.

If the oil flows through the by-pass filtration system, the filter element has to be dirty when it is removed from the filter body. Therefore, the function of the oil filtration system was also visually checked after tractor testing in operation.

RESULTS AND DISCUSSION

Impact of the tractor operation mode on the universal oil

Before discussing the oil contamination, the tractor operation and its impact on the oil contamination should be characterised.

Agricultural tractors can be classified into the two groups on the basis of tractor operation in practice. The first group includes the tractors operated standardly, with standard oil care. The owner of the tractor pays attention to the cleanliness during the routine maintenance, checks the oil level, stuffs the oil leaks, and mainly connects only its own implements with the right type of the clean oil.

Regarding to the standard tractor operation mentioned above, it had been selected the tractor John Deere 8100 with Shell Donax 5W30 universal oil type. The contamination (Fig. 2) and the physical properties (Table 1) hint the excellent technical condition of the oil after 1,900 running hours (prescribed oil change was after 2,000 running hours). This way of the tractor operation allows eliminating of the abnormal wear process and risk of the catastrophic failure. Concretely, this tractor was operating almost 13,000 running hours without any problems mentioned above.
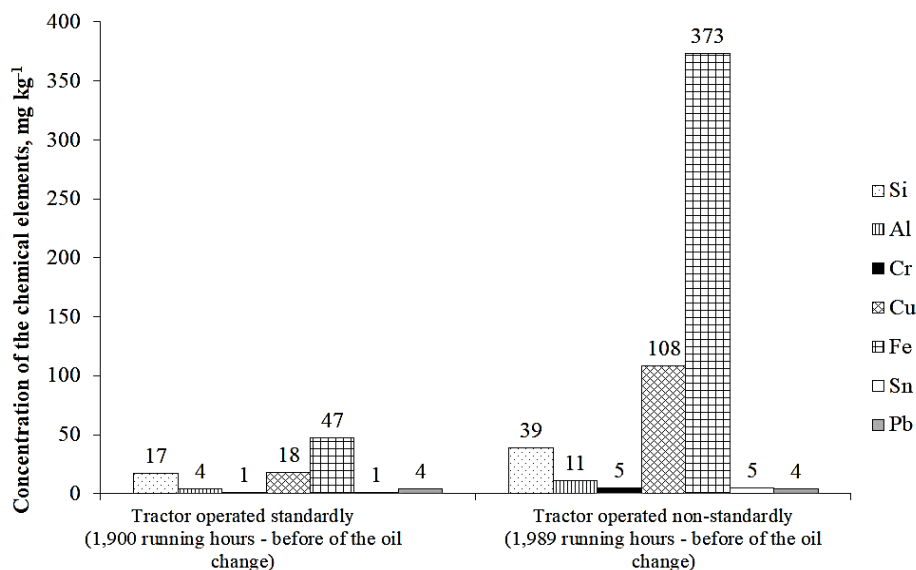
Figure 2. The oil contamination of the tractors operated standardly and non-standardly.

The tractor Zetor Forterra 124 41 with the oil PP 90 was selected as the example of the tractors operated non-standardly. The oil was strongly contaminated which extreme content of the iron (373 mg kg^{-1}) and copper (108 mg kg^{-1}) as demonstrated in Fig. 2. This level of the oil contamination does not allow reliable operation of the tractors for a long time. In this tractor, the low–quality oil was used instead of the required universal oil. Aleš (2009) observed the same oil type (PP 90) in the tractor Zetor 121 45 with the

same transmission and hydraulic system. In this tractor, the kinematic viscosity did not exceed the limits. Aleš (2009) also confirms the fact, that the higher particle contamination of this oil type could indicate the lower ability to form the boundary lubricating film. This confirms the fact, that the right tractor operation mode significantly influences the cleanliness level and quality of the oil. Considering the tractor operated non-standardly, that means with different and unknown implements (trailers, ploughs, etc.), or with old and degraded oils of unknown types which are mixed with tractor oil fill, all this means higher oil contamination.

The tractor operated non-standardly (in this case Zetor Forterra 124 41) was operated incorrectly in comparison with the tractor operated standardly (in this case John Deere 8100) which was used only with its own implement and with the same oil as was used in the tractor. On the other hand, simply construction and manual transmission of the tractor Zetor Forterra 124 41 made it less sensitive to the oil contamination compared with the tractor John Deere 8100 with power shift automatic transmission requiring higher oil cleanliness level. Kosiba et al. (2016) evaluated the oil contamination of the universal oil Shell Spirax S4 in hydraulic and transmission system of the tractor John Deere 5720.This tractor is also equipped with automatic transmission and it is very sensitive to the oil contamination. Therefore, the owner of this tractor pays high attention to the oil cleanliness level. During the tractor operation, the content of iron (49.63 mg kg^{-1}), copper (20.47 mg kg^{-1}) and aluminium (3.41 mg kg^{-1}) reached values similar to the tractor John Deere 8100.

The physical properties of the oils in the tractors operated standardly and non-standardly are represented by kinematic viscosities at 40 °C and 100 °C, viscosity index and water content (Table 1). Jánošová et al., 2016 presents that hydraulic system is sensitive to the viscosity of the oil. The viscosity influences oil's ability to flow through the hydraulic system, therefore affects pressure required to push the oil and make the necessary flow.

The oil samples of the new oil and used oil were analysed to state the changes in the oil properties. In the case of the tractor operated standardly (John Deere 8100), the values of the kinematic viscosity at 40 °C reached 7.3% and at 100 °C it reached 4.2%. Both values did not exceed the limit value 10%. Therefore, this oil was only minimally degraded during the operation in the tractor operated standardly. The value of the kinematic viscosity at 40 °C reached 27.9% and at 100 °C it reached 19.8% in the case of the tractor operated non-standardly (Table 3). Therefore, the values of the kinematic viscosity exceed the limit value 10%.

Table 3. Properties of the oils in tractors operated standardly and non-standardly

Parameter	Unit	Tractor operated standardly		Tractor operated non-standardly	
Type of oil		Shell Donax 5W30		PP 90	
Tractor operation	Running hour	0 (new oil)	1,900	0 (new oil)	1,989
Kinematic viscosity at 40 °C	mm^2 s^{-1}	38	41	172	124
Kinematic viscosity at 100 °C	mm^2 s^{-1}	7.1	6.8	15.6	12.5
Viscosity index	-	151	123	92	91
Water content	ppm	N*	N*	N*	N*

* Non-measurable value (Wearcheck laboratory).

The results of Eissa, Mohammed, Abd-Allah, and El-Sheltawy (2013) show that water content considerably affects the most of the oil properties. In the case of the both tractors, the non-measurable value of the water content (Table 3) is typical for the most of tractors because the transmission and hydraulic system is well protected against the water from the environment. Liquefied water from the ambient air represents only the negligible amount regarding the high-volume of the oil fill.

The tractor operated non-standardly contained the highly contaminated oil. Fig. 3 shows the layer of the contaminants which covers the filter patch. Dark colour of the filter patch expresses that the white filter paper is completely covered by contaminants. We can observe a lot of very small particles of the dark colour which create the layer on the filter paper and originate from the old and contaminated oil fills from the tractor implements. The left figure shows the larger particles from the wear process. The right figure shows the typical colourless transparent particles of silicium from the dust. The oil also contains two types of the small yellow particles. The transparent yellow particle is typical for varnish which originates from oxidative or thermal oil degradation. Shiny and non-transparent yellow particles can originate from the wear process of the single parts of the tractor components made of copper alloys (brass or bronze).
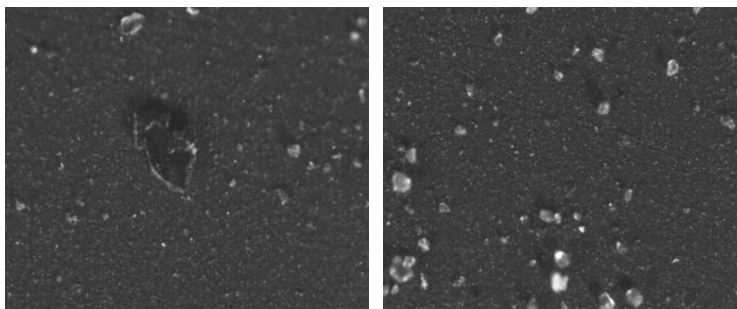
Figure 3. The filter patch of the oil PP 90 from the tractor operated non-standardly.

Fig. 4 shows the filer patch of the oil from the tractor operated standardly. Left and right figures show the white background of the filter paper which separated only the low amount of the oil contaminants because the cleanliness level of this oil is very high. Small dark particles of overheated steel can be observed. These particles are typical for common wear process and can originate from the high pressure contact in the roller bearings or teeth of gear wheels.
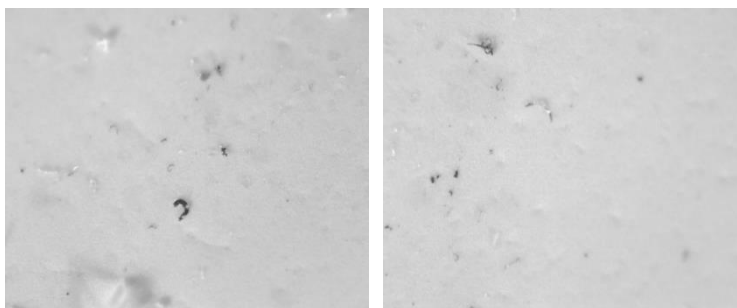
Figure 4. The filter patch of the oil Shell Donax 5W30 from the tractor operated standardly.

Comparing Figs 3 and 4, it is possible to observe the high cleanliness level of the oil from the tractor operated standardly and high contamination level of the oil from the tractor operated non-standardly.

The NAS 1638 class is usually reported as the number representing the maximum allowed particle counts (i.e. worst case) for designated size ranges of the particles. The cleanliness level according to the standard NAS 1638 reached the class 7 in the case of the oil in the tractor operated standardly and the class > 12 for tractor operated non-standardly, Table 4. These results show the high level of the oil contamination in the case of the tractor operated non-standardly in comparison to the typical level of the oil contamination in the case of the tractor operated standardly.

Table 4. The cleanliness level and the count of the particles (NAS 1638) of the oils of the tractors operated standardly and non-standardly

	NAS 1638 class	Maximum contamination limit (particles per 100 mL of the oil)				
Size range		5–15 µm	15–25	25–50	50–100	< 100
Unit			µm	µm	µm	µm
Tractor operated standardly	7	32,000	5,700	1,012	180	32
Tractor operated non-standardly	12	1,024,000	182,400	32,400	5,760	1,024

Aleš et al. (2015) presents that the failures of the machines are caused by variety of external and internal effects and processes that cause ultimately interruption of the operation. These factors have resulted in changes of properties of the machines parts and these changes are the first cause of technical failures. Fig. 3 shows solid particles from wear process as internal effect that does not cause the interruption of the operation because it is normal wear process in the case of tractor operated standardly. The more dangerous is the oil contamination from the old and degraded oil fills in the old equipment (the external effect) which were connected to the tractor operated non-standardly. This high oil contamination can lead to the ultimate interruption of the tractor operation by the reason of abnormal wear process.

The effect of oxidation is that the oil becomes acidic and the oil viscosity increases. The increase of the viscosity may be masked by other factors such as other oil type dilution. The characteristic spectral region for the oil oxidation is about 1,720 cm^{-1}. The spectrum changes of the new oil (0 running hours) and of the used oil were observed in this region in the case of the oil PP 90 type, Fig. 5. Table 2 do not show the typical increase of the oil viscosity if the oil is oxidized on the contrary, the oil viscosity decreased. This fact confirms our assumption that the oil was contaminated with the oil fills from the unknown tractor implements.

The next increase in absorbance was observed in the spectral region of the nitration formation (the characteristic of infrared absorbances of nitration formation was found out between 1,180 and 1,120 cm^{-1}). Various oxides of sulphur and water react together to form sulphuric acid. This acid is neutralized by a basic reserve in the additive package of the oil and normally results in formation of metallic sulphates. Sulphur is the typical component of the crude oil and it is also used as additive. The new oil PP 90 contains relatively high concentration of the sulphur (12,203 mg kg^{-1}) compare with the oil Shell Donax 5W30 with lower concentration of the sulphur (5,050 mg kg^{-1}). In case of this oil type, decrease of sulphur (in region between 1,180 and 1,120 cm^{-1}) is observed probably

due to the sulphur additives depletion (Fig. 5). Kržan & Vižintin (2003) also measured the sulphur concentration in tested oils to state the additive depletion. These authors presented that the lower concentration of the sulphur mentions the higher quality of the base oil because it needs lower additive concentration. In our case, the low quality of the oil PP 90 contains the higher sulphur concentration than oil with higher quality Shell Donax 5W30.
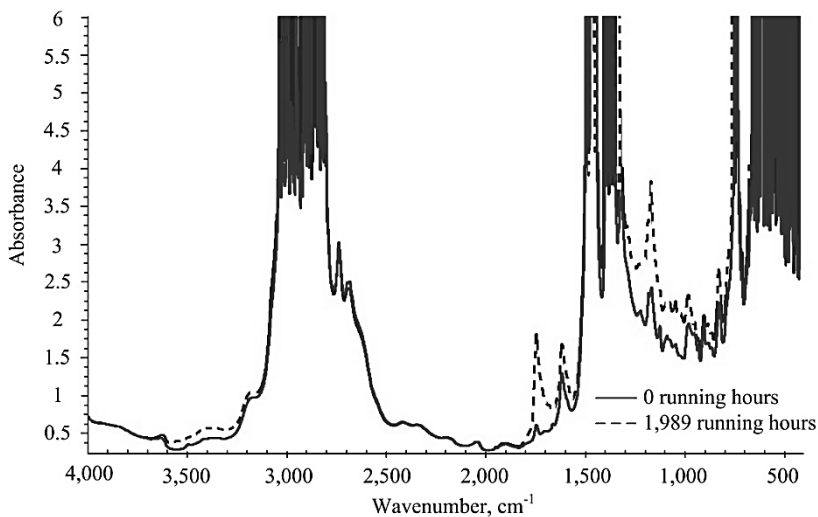
Figure 5. FT-IR spectrum of the oil PP 90.
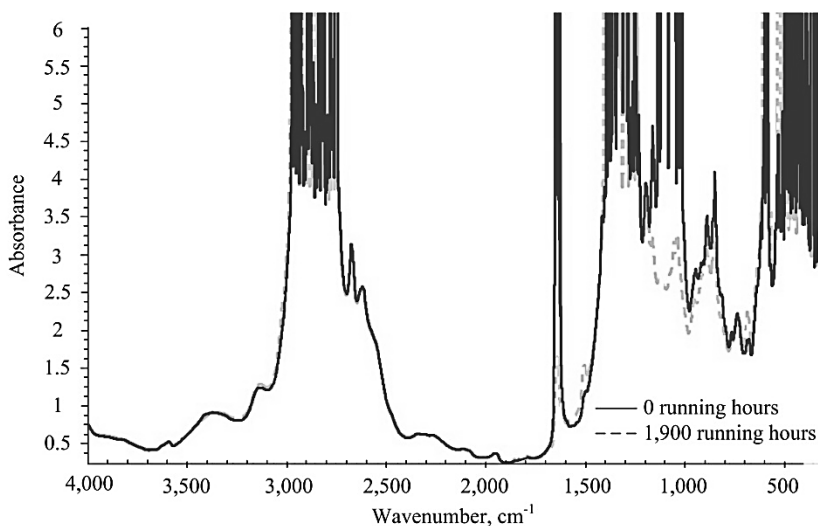
Figure 6. FT-IR spectrum of the oil Shell Donax 5W 30.

The water content is an interesting parameter because the Wearcheck laboratory state non-measurable value of the water content in all oil samples according to the Carl Fisher method, whereas the FT-IR spectrum shows absorbance increase in the typical

1117

spectral region for water (between 3,500 and 3,100 cm^{-1}). FT-IR is very precise method to state the water content because it is very strong absorber of infrared radiation. Water appears in the region, where the few other compounds that appear in petroleum oils will have significant absorbencies. This difference probably results in the oil sampling errors due to the poor oil sample homogeneity by the reason of high contamination level.

Absorbance decreases in the spectrum region between 1,500 and 1,700 cm^{-1} illustrates the common degradation process of the oil Shell Donax 5 W 30 (Fig. 6). It characterises the moderate level of the ester additives depletion.

By-pass filtration system in the tractor Zetor Forterra 124 41

The second part of this contribution is oriented on the design of the by-pass filtration system to improve the cleanliness level of the universal tractor oil (Fig. 7).
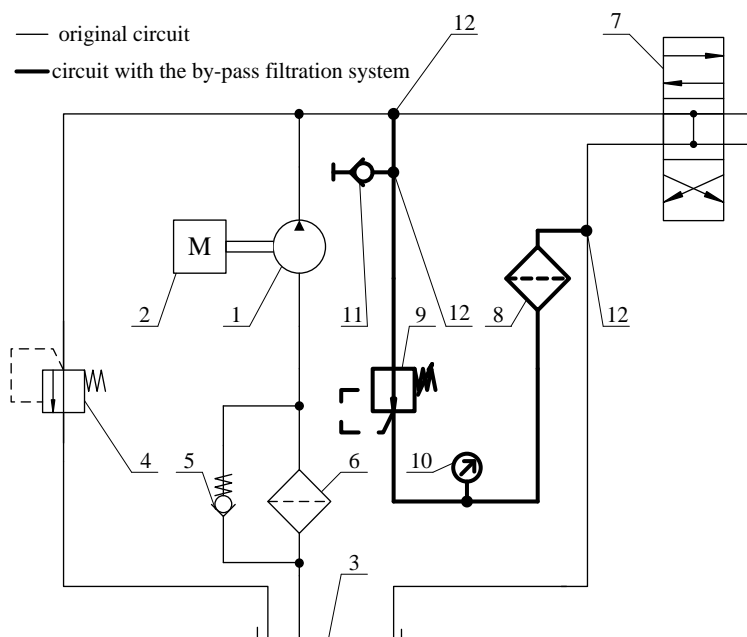
Figure 7. Tractor hydraulic circuit with the by-pass filtration system: 1 – hydraulic pump; 2 – combustion engine; 3 – oil fill of the tractor transmission; 4 – pressure relief valve; 5 – one direction valve; 6 – operational filter; 7 – directional control valve; 8 – by-pass filter; 9 – pressure-reducing valve; 10 – pressure gauge; 11 – minimess type valve; 12 – T-fitting.

There was used the oil circulation in the hydraulic system. The hydraulic pump (1) sucks the oil from the transmission system (3) through the operational filter (6). The one direction valve (5) allows the oil to flow when the operational filter is strongly contaminated. The pressure relief valve (4) limits the maximum pressure of the tractor hydraulic system. Components of the by-pass filtration system are marked by thick lines. The pressure and return lines were disconnected and the T-fittings were mounted to the tractor hydraulic system. The oil flows through the by-pass filter because the hydraulic pump generates the pressure indicated by the pressure gauge (10). Using the minimess

type valve (11), the oil samples were taken to evaluate the function of the filtration system.

Regarding the tractor oil fill (56 dm^3), the size of the by-pass filter body with element (1µm nominal filter ability) were proposed. In the case of the larger by-pass filter system, it could allow to filter the oil faster. On the other hand, it is more expensive and the next size complicates its placement in the tractor. Therefore, this proposal takes into account the oil filtration time, the price, and the size of the filter body. The by-pass filter system was placed in the cab behind the engine on the tractor chassis. This place is appropriate because it is easily to check and maintain the filter, Fig. 8, a).
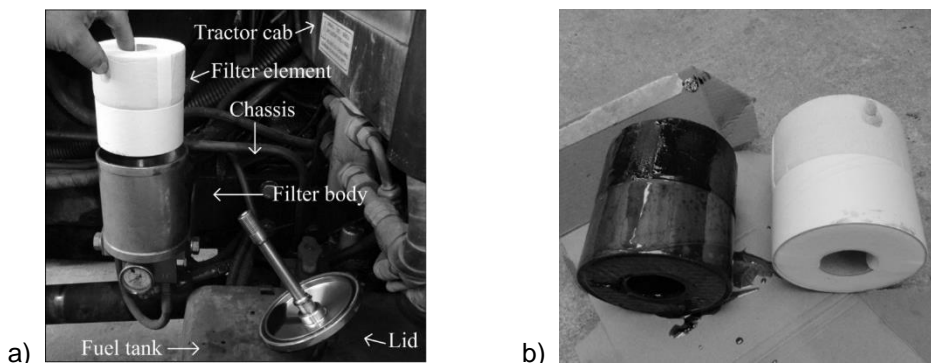
Figure 8. The change of the filter element after the tractor testing operation with the by-pass filtration system: a) placement of the filter body in the cab-behind-engine; b) the new and the used filter element.

The by-pass filtration system was tested under the real operation conditions of the tractor. Considering the oil fill volume (56 dm^3) and the flow rate (0.5 dm^3 min^{-1}) through the by-pass filtration system, the oil circulation number $o = 0.0089$ was calculated according to the Eq. (2). The count of the oil circulations through the filtration system $c = 107$ was calculated according to the Eq. (3) during 201 running hours of the tractor operation with the oil filtration system.

Pošta (2010) and Pošta et al. (2016) presents, that problems with hydraulic pressure fluids and oils are caused by their contamination and aging, which leads to the wear of the precise components. The important solution of this problem appears the external purification in addition to the operational filter. The additional filtration system reaches the higher filtration ability comparing to the operational filter. The results of this research present the improvement of the oil cleanliness level using the by-pass filtration system with the higher filtration ability (1µm) compare to the operational filters (20 µm).

Schmitz & Lennartz (2006) and Phillips & Staniewsky (2016) noticed, that the filtration surface can be saturated after the several hundred running hours and the filtration system does not effectively clean the oil. This problem can also negatively affects the filter efficiency of the by-pass filtration system in the case of the non-standardly operated tractors. Firstly, the extreme oil contamination (Fig. 2) must be solved by elimination of the contamination sources (Fig. 1). Considering the normal oil contamination in the case of the tractors standardly operated, the problem mention above is not important and the by-pass filtration system as the second stage of the oil filtration

(the operational filter is the first stage of the oil filtration) can improve the reliability and durability of the tractor.

Majdan et al. (2016) presented the filtration system for the hydraulic and transmission oil in agricultural tractors using the external filtration device. This solution does not filter the oil during common operation of the tractor. On the other hand, the by-pass filtration system allows to clean the oil immediately after the tractor starting.

The decrease of the chemical elements characterising the oil contamination according to the ICP spectrometry is the main parameter to evaluate the function of the by-pass filtration system and it was calculated according to the Eq. (1). All dangerous chemical elements were classified into the two groups namely significant (Fe, Cu and Si) (Table 5) and non-significant (Al, Cr, Sn and Pb) (Table 6) oil contaminants, considering their concentration in the oil. Concentration of Fe decreased to 41.6% during the test operation of the tractor with the by-pass filtration system. The significant decrease occurred also in the case of Cu (28.7%) and Si (20.5%). The decrease of the chemical elements concentration was also observed in the case of Al, Cr, Sn and Pb, but low concentration makes it non-significant.

Table 5. The content of the chemical elements characterising the significant oil contamination

Chemical element	Unit	Before the by-pass filtration (1,889 running hours)	After the by-pass filtration (2,100 running hours)	Difference, %
Fe		373	218	41.6
Cu	mg kg^{-1}	108	77	28.7
Si		39	31	20.5

Table 6. The content of the chemical elements characterising the non-significant oil contamination

Chemical element	Unit	Before the by-pass filtration (1,889 running hours)	After the by-pass filtration (2,100 running hours)
Al		11	7
Cr	Mg kg^{-1}	5	3
Sn		5	5
Pb		4	3

It was also visually checked the function of the oil filtration system. Fig. 8 shows the change of the filter elements after the tractor operation with the by-pass filtration system. The dark colour of the used filter elements shows that the oil was flowing through the filtration system.

Considering the decrease of the chemical elements characterising the oil contamination and visual checking of the filter elements after the testing operation, it could be stated that the filtration system is functional and suitable for exploitation in the tractor hydraulic system.

CONCLUSIONS

The oil cleanliness level affects the wear processes, oil degradations, and durability of the all machines. The hard operation conditions affect the oil contamination in the tractor hydraulic and transmission system. The paper presents the oil cleanliness level in compliance with the standard DIN 51524 in the case of the tractor operated standardly

and the strongly contaminated oil in the case of the tractor operated non-standardly. The results confirmed the fact, that the tractor operation mode in compliance with the user manual significantly and positively affect the oil cleanliness level. On the other hand, the usage of the tractor in conflict with the user manual (usage of the unknown implement, incorrect oil type used in tractor, tractor parking without protection against the environment etc.) causes the strong oil contamination.

The by-pass filtration system was proposed and applied to improve the oil cleanliness level. It was used as the a second stage of the oil filtration while the operational filter is the first one. Concentration of iron (373 mg kg^{-1}), cooper (108 mg kg^{-1}) and silicium (39 mg kg^{-1}) showed the decrease as follow 41.6% (Fe), 28.7% (Cu) and 20.5% (Si) after the tractor testing operation with the by-pass filtration system. The decrease in of the chemical elements characterising the oil contamination and the visual checking of the filter elements after the testing operation affirmed the right function of the by-pass filtration system in the tractor.

REFERENCES

Aleš, Z. 2009. Field experience with transmission oil EP Gear Synth 150. *Research in Agricultural Engineering* **55**, 18–23.

Aleš, Z., Pexa, M., Pavlů, J., Kucera, M. & Čedík, J. 2015. Analysis of wear particles morphology of machine parts based on aluminium. Manufacturing Technology **15**, 664–670.

Casey, B. 2004. How to define and achieve hydraulic fluid cleanliness. Machinery lubrication **3**, 12–16.

Dobeš, P. 2006. Long term operational tests of agricultural tractor using environmentally acceptable lubricants. In *15th International Colloquium Tribology – Automotive and Industrial Lubrication*, Technische Akademie Esslingen, Ostfildern, Germany, pp. 151–151.

Eissa, A.S., Mohammed, N.I., Abd-Allah, R.I. & El-Sheltawy, S.T. 2013. Characterization of used and fresh hydraulic oils of heavy machinery plants. Petroleum science and technology 31, 625–632.

Hnilicová, M., Kučera, M. & Pavlů, J. 2016. Analysis of hydraulic oil in handling lines Baljer & Zembrod using the methods of tribotechnical diagnostics. *Key engineering materials* **669**, 451–458.

Jánošová, M., Petrović, A., Vozárová, V., Hujo, Ľ., Csillag, J. & Malínek, M. 2016. Analysis of the physico-chemical properties of the hydraulic fluids in order to modify change intervals. In *MendelNet* 2016, Mendel university in Brno, Brno, Czech Republic, pp. 858–863.

Kosiba, J., Črňák, Š., Glos, J., Jablonický, J., Vozárová, V., Petrović, A. & Csillag, J. 2016. Monitoring oil degradation during operating tests. *Agronomy Research* **14**, 1626–1634.

Kosiba, J., Tkáč, Z., Hujo, Ľ., Tulík, J., Ševčík, P., Šinský, V. & Rašo, M. 2013. Effect of ecological energy carriers on flow characteristics of tractor hydraulic pump. *Journal of central european agriculture online* **14**, 1415–1425.

Kržan, B. & Vižintin, J. 2003. Tribological properties of an environmentally adopted universal tractor transmission oil based on vegetable oil. *Tribology International* **36**, 827–833.

Kučera, M., Aleš, Z. & Pexa, M. 2016. Detection and characterization of wear particles of universal tractor oil using a particles size analyser. *Agronomy research* **14**, 1351–1360.

Kučera, M., Aleš, Z., Pavlů, J. & Hnilicová, M. 2015. Applying of automatic laser particle counter as technique to morphology assessment and distribution of wear particles during lifetime of transmission oils. *Key engineering materials* **669**, 417–425.

Kučera, M., Bujna, M., Korenková, M. & Haas, P. 2014. Possibilities of using ecological fluid in agriculture. *Advanced Materials Research* **1059**, 61–66.

Majdan, R., Tkáč, Z., Abrahám, R., Szabó, M., Halenár, M., Rášo, M. & Ševčík, P. 2016. Proposal for filtration system for biodegradable lubricants in agricultural tractors. *Agronomy research* **14**, 1395–1405.

Mang, T. 2014. *Encyclopedia of Lubricants and Lubrication.* Springer-Verlag Heidelberg, Berlin, 2403 pp.

Phillips, W.D. & Staniewski, J.W.G. 2016. The origin, measurement and control of fine particles in non-aqueous hydraulic fluids and their effect on fluid and system performance. *Lubrication science* **28**, 43–64.

Pošta, J. 2010. External purification of hydraulic and machine oils. In 4th International conference, *TAE 2010: Trends in agricultural engineering*, Prague, Czech Republic, pp. 488–492.

Pošta, J., Peterka, B., Aleš, Z., Pexa, M., Pavlů, J. & Vutman, H. 2016. Lubricity of thermo-oxidized engine oils. *MM Science journal* **11**, 1214–1217.

Quazi, T.Z. & Khatavkar, S. 2015. Engine wear analysis by rotating disc electrode optical emission spectroscopy (RDEOES). *International journal on recent technologies in mechanical and automobile engineering* **2**, 21–24.

Rusnák, J., Kadnár, M., Tóth, F. & Kročko, M. 2013. Possibilities of using the ecological oil Arnica S 46 in agricultural engineering. Journal of central european agriculture **14**, 1444–1455.

Schmitz, S. & Lennartz, R. 2006. Filtration of lubrication oil in railway applications. In Spring technical *conference of the ASME internal combustion engine division*, Aachen, Germany, pp. 761–768.

Turis, J. & Kučera, M. 2016. Analysis of oil charge – Instrument of the production line wear regime prediction. *Key engineering materials* **669**, 467–476.

Tkáč, Z., Hujo, Ľ., Tulík, J., Kosiba, J., Uhrinová, D. & Šinský, V. 2014. Greening of agricultural and forestry tractors. *Acta universitatis agriculturae et silviculturae mendelianae brunensis* **62**, 1135–1139.

Tkáč, Z., Čorňák, Š., Cviklovič, V., Kosiba, J., Glos, J., Jablonický, J. & Bernát, R. 2017. Research of biodegradable fluid impacts on operation of tractor hydraulic system. *Acta technologica agriculturae* **20**, 42–45.

Tóth, F., Rusnák, J., Kadnár, M. & Čavojský, P. 2014a. Effect of selected ecological lubricants on the wear of defined sliding bearing. *Acta technologica agriculturae* **17**, 13–16.

Tóth, F., Rusnák, J., Kadnár, M. & Váliková, V. 2014b. Study of tribological properties of chosen types of environmentally friendly oils in combined friction conditions. *Journal of central european agriculture* **15**, 185–192.

Tulík, J., Kosiba, J., Stančík, B. & Štulajter, I. 2014. Pollution analysis of new synthetic biodegradable fluid during durability test of hydrostatic pump. *Acta technologica agriculturae* **17**, 24–28.

Tulík, J., Hujo, Ľ., Kosiba, J., Jablonický, J. & Jánošová, M. 2017. Evaluation of new biodegradable fluid on the basis of accelerated durability test, FTIR and ICP spectroscopy. *Research in agricultural engineering* **63**, 1–9.

Wang, X., Lin, S. & Wang, S. 2016. Remaining useful life prediction model based on contaminant sensitivity for aviation hydraulic piston pump. In *International conference on aircraft utility systems*. Beijing, People's Republic of China, pp. 266–272.

Use of qualimetry method in production labour estimation

D. Maksimov[1,*], H. Kalkis[2], Y. Perevoschikov[1] and Z. Roja[3]

[1]Institute of Economics and Management, Udmurt State University, 1, Universitetskaya Str, bld. 4, RU426034 Izhevsk, Russia
[2]Faculty of European Studies, Riga Stradins University, Dzirciema street 16, LV 1007 Riga, Latvia
[3]University of Latvia, Raina blvd. 19, LV-1586 Riga, Latvia
*Correspondence: maksim.dan.gen@gmail.com

Abstract. Every work process of production organization involves employees and employer interaction with each other by "agreement". Such agreement is contracted based on the implementation of concrete types of work processes in particular workplaces. The general the total number of workplaces are continuous interaction areas of people to transform substance, energy and information. The solution of the assigned tasks requires the methodology for designing product quality, analyzing market consumer needs, forecasting potential prices and detecting effectiveness in order to present the strategic objectives in digital values. This study is part of a larger investigation which involves principles of economic metrology and qualimetry of work. The purpose of the research is to demonstrate use of qualimetry in the production organization, based on experience of several years in many industry organisations by focusing on engineering.

Key words: work, qualimetry, ergonomics, quantitative, manufacturing.

INTRODUCTION

The problem of estimating the complexity of the product manufacturing without a detailed design of the technological manufacture process is relevant. Many contemporary inventions have significantly transformed the meaning of manufacturing. Today there are new concepts in manufacturing, such as LEAN management, the theory of constraints, statistical process control, ergonomics and design etc. In order to reach high quality and efficiency in products and operations, many production solutions are implemented in creative ways. Therefore, methods of qualimetry analysis are also necessary to combine economic interests, in particular, labor costs, material costs, costs of electrical energy with engineering parameters, which are calculated based on the theory and methods of qualimetry (Hendrick, 2003).

There is a certain mathematical expression $y = f(x_1, x_2, ... x_3)$. Then the function y should be the price, and x is the parameters of the products that one wants to do. But if one puts just a detail, then under the word 'detail' all the parameters are merged that are included in the algorithm for performing calculations of economic parameters - the economic indicators of this detail. If one do not take these engineering parameters, then, therefore, it can only conditionally call the economic character in the form of an analogy,

that is, those that have already been (Nazarov & Krushnyak, 2006). The detail is this, so the price will be the same, but it is not a scientific method, it is a method of expert evaluation (Freivalds & Niebel, 2009). Use of known methods for estimating labor intensity (Zandin, 2002; Genkin, 2005; Caragnano & Lavatelli, 2012) requires a huge amount of time. The research results presented in this article are gained and considered over a long period of time and involves the application of the qualimetry theory that can improve the technical and economic planning of production in engineering operations.

The theory of qualimetry got its start in the 60s of the 20th century regarding the works of Azgaldov (1968), Raikhman (1970), Glichev (1983), Syskov and others. Qualimetry originated as a science due to the great experience accumulated by mankind in assessing product quality. It relies on experimental and statistical research methods.

On the basis of the qualimetry method, the following studies were carried out: foundry production (Kalinkina, 1984; Kalinkina & Perevoshchikov, 2018), instrument-making (Nekrasov, 1985), determination of labor input (Kudryavtsev, 1993), packages (Lebedenko, 2003; Lebedenko Perevoshchikov & Perevoshchikov, 2018), industrial production (Mukhina, 1997; Khilchenko, 2013), small business operations (Maksimov, 2009), and clothing industry (Yeremeyeva, 2004; Pevoshchikov, Bobkov & Nemirovchenko, 2005), water qualimetry (Rozental & Averbukh, 2013). In the United States it is called benchmarking (Allmon et al., 2000). However, in author`s opinion, the used methodology reveals much more precisely the interrelation of the function of engineering parameters with economic rather than recommendations made in benchmarking.
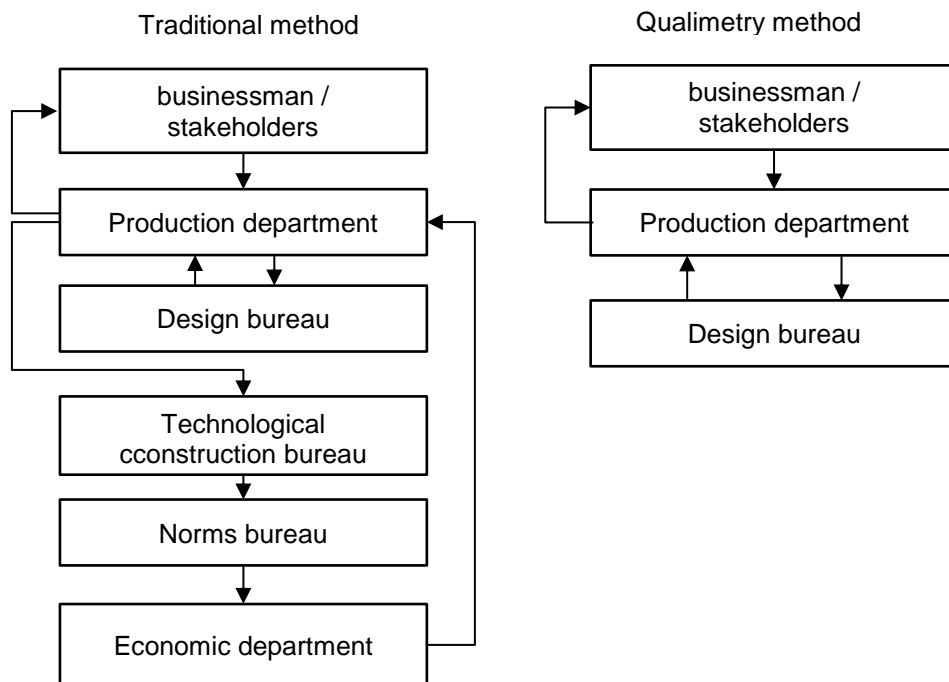
Figure 1. Diagram of order execution.

Qualimetry method of preparing documents for the product production can significantly reduce the duration of the creating the design and estimate necessary documentation. For the application of the qualimetry method, it is important to create a system of norms and standards that helps calculating production costs and the predicted price for the product manufacturing in real organizational and technical conditions.

Based on the developed technique, a new algorithm was presented, which can be seen in Fig. 1.

Fig. 1. (Yeremeeva, 2004) shows order flow of two patterns: traditional and qualimetry method. The comparison shows that qualimetry method allows to reduce the time of order passing between departments and is less complex as traditional method procedure. It involves only direct interaction between production department and design bureau and relation to stakeholders or business decision makers.

MATERIALS AND METHODS

As a research methodology, a qualimetry approach is applied. Qualimetry is a method for determining integrated and integral quality indicators. The development of qualimetry indicator starts with presentation of fulfilled certain conditions to the object of qualimetry analysis in accordance with the provision of the methodology.

In the qualimetry approach, the base part is selected, which determines the quality of the machinery in quantitative terms. The selected base part is adopted by the expert standard for the quantitative analysis of other parts in the field of research. Further the parameters are calculated, that are called the quality parameters of the parts. The qualimetry parameters of the part include: the complexity of the geometric shape, the mass of the part, the material of the part, the roughness parameter, the features of technological operations.

The qualimetry method is based on a statistical study of the labor intensity dependencies in manufacturing process. Technical characteristics of the product requires a large amount of design documentation to be created. In this paper, the main part of the price calculation will be considered – this is the definition of the labor intensity in manufacturing process. In contemporary age of computer technology development, this problem is not so relevant. There exists a development software for the calculation automation. In this paper, it will be briefly considered the modification of the method to determine the complexity. The methodology of qualimetry indicators for determining labor intensity reflects such parameters of parts as constructive-technological features, dimensions and mass. The identification of significant factors of labor-intensiveness required the processing of many technological charts, maps of the manufacturing process. Having analysed a large amount of information, it was found that the amount of complexity of the production parts is significantly affected by:
-    mass of the workpiece;
-    complexity of the geometric shape of the part;
-    material use factor;
-    type and weight of the workpiece;
-    parameters of the surface roughness of the part;
-    material details;
-    the number of parts in the batch;
-    the complexity of assembling parts into assembly units;

- features of technological operations.

Authors decomposes the assembly unit into separate parts and defined qualimetry indicators for each part. The overall qualimetry index of parts manufactured using metal-cutting equipment is defined as

$$K_O = K_{GH} \cdot К_m \cdot K_M \cdot K_R \cdot K_{TF} \qquad (1)$$

where K_{GH} – the qualimetry index of the complexity of the geometric shape (configuration complexity qualimetry) of the part; K_m – qualimetry indicator of the mass of the part (mass qualimetry); K_M – qualimetry index of the material of the part (material qualimetry); K_R – qualimetry index of the surface roughness of the part (qualimetry of the roughness); K_{TF} – a qualimetry indicator of technological features of the part (qualimetry of technological features).

Hence it can be pointed out description factors and their parametric values that form a qualitative set of properties:

1. Length, width and thickness (expressed in mm)

2. The geometric shape of the part according to the Classifier of the unified system for design documentation (ESKD, 1986). Classification code was applied.

3. The volume of the part in space (expressed in cm^3)

4. Determine the composition of the substance in the details, choosing the brand of material in the list of names placed in the classifiers of engineering materials (the conditional expression of the brand of material was used)

5. Calculate the mass of the part (expressed in kg)

6. Number of dimensions affixed to the drawing was substituted, which uniquely form the spatial image of the part (expressed in the number of dimensions reduced to linear dimensions).

7. Select from the total number of sizes, the dimensions affixed to the internal cavities, holes, grooves (expressed in the number of sizes, reduced to linear dimensions).

8. Determine the symmetry coefficient of the part`s geometric shape by calculating accordingly to the drawing and the volume part (ILM, 1988). Or in accordance with the six-digit code using an approximate method (HAN, 1988).

9. Determine the qualimetry measure of the detail's complexity.

$$K_{GH} = ln\,I \cdot e^{\frac{I_{id}}{I} - \alpha} \qquad (2)$$

10. We determine the qualimetry mass index of the part K_m, depending on the mass of the part found in item 5.

11. We determine the qualimetry index of the material of the part, based on the information obtained in item 4.

12. Considers the requirements of accuracy and surface roughness of the part, subjected to processing (Ra) and determine the quality indicator of the part

$$K_R = R_a{}^{-0,347} \qquad (3)$$

13. We calculate the qualimetry indicator of the technological features of the part.

$$K_{TF} = e^{\Sigma d_i} \qquad (4)$$

14. We determine the general qualimetry parameter on the basis in formula 1. We enter the values into the special technical part`s economic map and determine the labor intensity of the part manufacturing using a special technique (currently being processed).

15. We save the received indicators.

Determine the labor intensity of creating parts (LIQ, 1988)

$$T = (K_o \cdot T_q \cdot \sum_{i=1}^{m} p_i + \sum_{j=1}^{l} \Delta T) \cdot K_n \qquad (5)$$

where K_o – a general qualimetry indicator, kvsht (kkg); T_q – normative labor intensity, standard hour; p_i - the normative ratio of the complexity of the types of technological operations performed; i – the number of technological operations performed; K_n – correction factor for the number of parts in the party; ΔT is the laboriousness of operations, which are additionally introduced in comparison with the foreseen technological operations in accordance with this methodology; j – the number of technological operations introduced additionally as compared with the stipulated technological operations.

RESULTS AND DISCUSSION

Based on the results obtained, a database is being created for qualimetry parameters and derived time rate. These indicators can be linked to the workplace that result as indicator of the ergonomic passport in the workplace (Maksimov & Kalkis, 2018).

They will be the basis for determining the various costs and results of labor in a given workplace and will not depend on a particular person.

The calculation of the technical and economic indicators of the product production at the design engineering stage is carried out both manually and automatically using the Kompas-3D CAD system.

In this paper we describe the sequential stage of the calculation of parameters. Kompas-3D was used as the CAD system for creating drawings and 3D models. There is a methodology developed by authors for qualimetry analysis and calculation of qualimetry indicators of engineering products, developed and tested in practice in the manual documentation of both the drawings themselves and their analysis (Perevoshchikov, 2015; Maksimov & Kalkis, 2018). Currently, there is an integrated automated system for performing graphic drawing, which included engineering calculations, isolation and generalization of information and economic-qualimetry analysis and justification of production efficiency indicators.

Figure 2. Drawing details of the washer.

A software (Ermilov, V.V. & Perevoshchikov, 2018a, 2018b) was used to automate the calculation of qualimetry parameters. When using this method, it is necessary to remember that it needs to be adapted to the specific organizational and technical conditions of the enterprise. To represent the work of the algorithm, authors present a

sequential calculation of the necessary parameters. We calculate the qualitative parameters of the parts and the complexity of manufacturing on a specific example.

As one example, consider detailed drawing 'Washer' (Fig. 2).

According to the classifier ESKD determine the code details: 758491. To calculate the general qualimetry index of the part (formula 1), it is necessary to determine such parameters:

- -qualimetry indicator of geometric shape;
- -qualimetry mass index details;
- -qualimetry indicator of the material details;
- -qualimetry surface roughness indicator;
- -qualimetry indicator of technological features.

1. Qualimetry indicator of geometric shape:

The number of common dimensions I = 12, including internal dimensions I_{id} = 7. Symmetry α = 0.83.

$$K_{GS} = ln\,I \cdot e^{\frac{I_{id}}{I} - \alpha} = ln\,15 \cdot e^{\frac{7}{12} - 0,83} = 1.832$$

2. Qualimetry mass index details

Weight of details: m=0.007 kg

$$K_m = 0.23 + 0{,}111 \cdot ln(m \cdot 1000) = 0.23 + 0.111 \cdot ln(0.007 \cdot 1000) = 0.446$$

3. Qualimetry indicator of the material details K_M=0,85.

4. Qualimetry surface roughness indicator

$$K_R = R_a{}^{-0,347} = 10^{-0,347} = 0.45$$

5. Qualimetry indicator of technological features K_{TF}=1.03.

6. Determine the total qualimetry indicator (formula 1)

$$K_O = 1.832 \cdot 0.446 \cdot 0{,}85 \cdot 0.45 \cdot 1.03 = 0.322$$

7. Calculate the utilization of the material indicator

$$K_{mq} = 0.007^{0.08} \cdot \left(\frac{1}{0.39} - 1\right)^{0.28} \cdot e^{0.2 \cdot (0.007 - 1)} \cdot 0.322 = 0.201$$

The obtained data is saved in the drawing and in the database. The qualimetry indicator details are represented in Table 1.

Table 1. Qualimetry indicators details

Code	α	I	I_{id}	K_m	K_{GS}	K_M	K_R	K_{TF}	K_O	K_{mq}
758491	0.89	12	7	0.446	1.832	0.85	0.45	1.03	0.322	0.201

Gained data on project labor intensity id summarized in Table 2.

For a more detailed disclosure of the methodology, authors define and compare the complexity of the manufacture of two products (Tables 3 & 4). Products have the same design but are released in different time periods.

Table 2. Project labor intensity

Name of technological processing	Labor intensity	
	Part	Time, working hours
Cutting	0.08	0.1262
Turning	0.51	0.8047
Finishing	0.001	0.0016
Drilling	0.15	0.2367
Project labor intensity	0.741	1.1692

Table 3. Summary sheet of indicators of labor intensity of manufacturing parts of the product 'Manual meat grinder GOST 4025-95'

No	Item designation	Part name	Code	Project labor intensity, working hours
1	G95.715511.001	Bolt 1	715511	0.610
2	G95.715521.002	Bolt 2	715521	2.674
3	G95.714633.003	Worm	714633	1.338
4	G95.753111.006	Nut 1	753111	0.555
5	G95.753151.007	Nut 2	753151	0.373
6	G95.713467.009	Body	713467	0.991
7	G95.712363.010	Cover	712363	1.406
8	G95.753436.011	Receiving knife	753436	6.299
9	G95.711144.014	Receiving grate	711144	7.201
10	G95.743111.015	Handle	743111	0.397
11	G95.711321.016	Pivot	711321	1.114
12	G95.758491.017	Washer	758491	1.169
13				24.127

Table 4. Summary sheet of indicators of labor intensity of manufacturing parts of the product 'Manual meat grinder GOST 4025-73'

No	Item designation	Part name	Code	Project labor intensity, working hours
1	G73.715521.101	Bolt	715521	3.835
2	G73.731467.105	Body	731467	1.180
3	G73.743111.110	Handle	743111	1.317
4	G73.712363.106	Cover	712363	2.477
5	G73.711144.109	Receiving grate	711144	12.454
6	G73.741684.108	Gasket	741684	0.000
7	G73.753436.107	Receiving knife	753436	8.406
8	G73.711321.113	Pivot 1	711321	1.518
9	G73.751742.111	Pivot 2	751742	3.888
10	G73.741314.115	Washer	741314	0.632
11	G73.714633.102	Worm	714633	1.874
12	G73.713111.112	Key (spline)	713111	0.179
13				37.76

Based on the findings, it can be concluded that the labor intensity of manufacturing identical products is different. This is influenced by the modified form of the product, the material of the product, as well as design features. The obtained results may be used in the future to determine the value of the product. It is also possible to use as a base of newly created similar products and individual elements of products - parts.

CONCLUSIONS

The qualimetry in production organization was demonstrated with the following solutions: the structure and content of automated planning systems based on the example of individual products was developed that involved the qualimetry method. Projects were made with specific products on automated systems based on the ideas of the standardized notion of qualimetry. The obtained results allow to bind the possibilities of the workplace

from the quantitative and qualitative sides. The main indicators of the performed work can be categorized as follows: a) a techno-economic map for the specific enterprise; b) the cost of parts production in a specific period that is in accordance with the technological capabilities of the enterprise. Hence the automation will allow a significant reduction in the qualimety analysis of machinery parts as well as it will provide simple analysis that will allow to determine the influence of individual technical characteristics of the product during the manufacturing process.

REFERENCES

Allmon, E., Haas, C.T., Borcherding, J.D. & Goodrum, P.M. 2000. US construction labor productivity trends, 1970-1998. *Journal of construction engineering and management-asce.* **126**(2), 97–104.

Azgaldov, G.G., Glichev, A.V. & Panov, V.P. 1968. *What is quality?* Ekonomika, 135 pp. (in Russian).

Caragnano, G. & Lavatelli, I. 2012. ERGO-MTM model: an integrated approach to set working times based upon standardized working performance and controlled biomechanical load. In: *18th World congress on Ergonomics-Designing a sustainable future*, IEA, Work pp. 4422–4427.

Ermilov, V.V. & Perevoshchikov, Yu.S. 2018a. *Economic metrology and qualimetry of labor: Automated system for calculating the qualimetric characteristics of machine parts based on CAD Compass 3D. (Part 1 and 2 of the topic 1.4.10. Development of the concept of qualimetric analysis for areas of economic activity).* Vol. 5. Udmurt University Publishing Center, Izhevsk, 194 pp. (In Russia).

Ermilov, V.V. & Perevoshchikov, Yu.S. 2018b. *Economic metrology and qualimetry of labor: Automated system for qualimetry analysis of the complexity of a product according to its kinematic scheme based on the method of analogues. (Sections 3 of topic 1.4.10. Development of the concept of qualimetric analysis for areas of economic activity)* Vol. 6. Udmurt University Publishing Center, Izhevsk, 194 pp. (In Russian).

ESKD. 1986. *Classifier ESKD. Classes 71, 72, 73, 74, 75, 76*. Publishing House of Standards, Moscow, 1986. (in Russian).

Freivalds, A. & Niebel, B. 2009. *Niebel`s Methods, Standards & Work Design*, 12th Ed. New York: Mc-Graw Hill, 736 pp.

Genkin, B.M. 2005. *Economics and sociology of labour*. Norma, Moscow, 402 pp. (in Russia).

Glicev, A.V., Rabinovich, G.O. & Primakov, M.M. 1983. *Applied questions of qualimetry.* Izdatelstvo Standartov, Moscow, 136 pp. (in Russian).

Hendrick, H.W. 2003. Determining the Cost-benefits of Ergonomics Projects and Factors that Lead to their Success. *Applied Ergonomics* **34**, 419–427.

HAN. 1988. *Handbook of values of symmetry of the geometric shape of parts of the general engineering application*. UdSU, Izhevsk, 139 pp. (in Russian).

ILM. 1988. *Industry leading material. Calculation of the complexity of the design of parts and assembly units*. UdSU, Izhevsk, 100 pp. (in Russian).

Kalinkina, G.E. & Perevoschikov, Y.S. 2018. *Economic metrology and qualimetry of labor: Qualimetric method for calculating and planning the production capacity of casting shops (sand casting) in mechanical engineering. Vol.3* UdSU, Izhevsk, 166 pp. (in Russian).

Kalinkina, G.E. 1984. *Improving the capacity planning of foundry shops:* dissertation ... candidate of economic sciences. Sverdlovsk, 184 pp. (in Russian).

Khilchenko, L.V. 2013. *Planning of the production activity of a machine-tool enterprise on the basis of an aggregated approach*: dissertation ... Candidate of Economic Sciences. Tyumen, 143 pp. (in Russian).

Kudryavtsev, G.M. 1993. *Forecasting the complexity of the design and manufacture of new mechanical engineering products*: abstract ... candidate of economic sciences, Izhevsk, 18 pp. (in Russian).

Lebedenko, T.A., Perevoshchikov, Yu.S. & Sergeev, G.A. 2018. *Economic metrology and qualimetry of labor: Qualimetric standards for organizing the production of products (large forgings)*. Vol. 2. Udmurt University Publishing Center, Izhevsk, 144 pp. (in Russian).

Lebedenko, T.A. 2003. *Labor input of products in system of an economic substantiation of enterprise activity of the enterprise*: the dissertation ... Candidate of economic sciences. Izhevsk, 184 pp. (in Russian).

Maksimov, D.G. 2009. *Standard tools in system of intrafirm planning at small enterprises*: the dissertation ... A Cand.Econ.Sci . Izhevsk, 188 pp.

Maksimov, D.G. & Kalkis, H. 2018 Ergonomic modelling parameters and the influence of ergonomics on planning workplaces. *Agronomy Research* **16**(4), 1762–1770.

Nazarov, N.G. & Krushnyak, N.T. 2006 What is measured in qualimetry? *Measurement techniques* **49**(3), 238–243.

LIQ. 1988. *The method of enlarged calculation of labor intensity on the basis of qualimetric analysis, obtained by machining in workshops and industries operating in conditions of full cost accounting. Industry Guidance*. UdSU, Izhevsk 50 pp. (in Russian).

Mukhina, I.A. 1997. *The place and role of the reproduction of labor in the economy of labor*: dissertation ... Candidate of Economic Sciences: Izhevsk, 190 pp. (in Russian).

Nekrasov, V.I. 1985. *The study of the effectiveness of the creation of instrument making at the design stage Cand.Diss.* Sverdlovsk. 262 pp. (in Russian).

Perevoshchikov, Yu.S., Bobkov, V.N. & Nemirovchenko, N.M. 2005. *Quarimetry economics of an enterprise (clothing industry)*. VZUZH, Moscow, 570 pp. (in Russian).

Perevoshchikov, Yu.S. 2015. *Economic metrology. Labor qualimetry.* VZUZH, Moscow, 504 pp. (in Russian).

Rozental, O.M. & Averbukh, A.I. 2013 Introduction to water qualimetry. *Water resources* **40**(4), 447–461.

Raikhman, E.P. & Azgaldov, G.G. 1970. Interrelationship between metrology and qualimetry (A contribution to discussion). *Measurement Techniques.* 13(1) pp. 143–146.

Yeremeeva, E.A. 2004. *A qualimetry method for determining labor costs in the manufacture of garments:* the dissertation ... Candidate of economic sciences. Izhevsk, 221 pp. (In Russian).

Zandin, B. 2002. MOST *Work Measurement Systems.* 3rd Editio. CRC Press. 552 pp.

Linear pressing of coconut copra meal (*Cocos nucifera* L.) under different temperatures

Č. Mizera[1,*], D. Herák[2], P. Hrabě[3] and T. Saller[4]

[1,2,4]Czech University of Life Sciences Prague, Faculty of Engineering, Department of Mechanical Engineering, Kamýcká 129, CZ165 21 Praha 6 Suchdol, Czech Republic
[3]Czech University of Life Sciences Prague, Faculty of Engineering, Department of Material Science and Manufacturing Technology, Kamýcká 129, CZ165 21 Praha 6 Suchdol, Czech Republic
[*]Correspondence: mizera@tf.czu.cz

Abstract. Pressing of vegetable oils plays an important role in the food processing. This study described the compression behaviour of copra (*Cocos nucifera L.*) using the universal compression testing machine and vessel diameter of 60 mm with a plunger. The influence of heat treatment on oil recovery efficiency and specific mechanical energy were determined. Compression tests at the rate of 1 mm s^{-1} under five different temperatures 20, 40, 60, 80 and 100 °C were performed. The measuring range of force was between 0 kN and 50 kN. It has been found that the amount of obtained oil increased and specific mechanical energy decreased with increased temperature. Measured data were analysed by computer software Mathcad 14 (MathCAD 14, PTC Software, Needham, MA, USA). Mathematical model describing the mechanical behaviour of bulk copra under compression loading was represented.

Key words: coconut oil, compression loading, compressive force, specific mechanical energy.

INTRODUCTION

Coconut (*Cocos nucifera L.*) is the fruit of a tree that grows in tropical areas and is commonly used for oil production. It consists of three layers: mesocarp, endocarp and solid endosperm, which is also referred to as coconut meat (Heathcock & Chapman, 1983). Endosperm is approximately 1–2 cm thick, white and fleshy edible part of the fruit. Dried and crushed material is known as copra, which is used to obtain oil.

Coconut oil is used in the food industry and exhibits good digestibility (Che Man & Marina, 2006). Two methods are used to obtain coconut oil, dry processing and wet processing. The wet process is to extract oil directly from coconut milk. Various ways of obtaining oil have been studied by many authors (Rosenthal et al., 1996; Seow & Gwee, 1997; Chen & Diosady, 2003) This methods eliminates the use of solvents which reduce the cost and energy requirements (Mariana et al., 2009). The disadvantage of this method is in the low oil recovery efficiency, therefore, it is unsuitable for commercial applications (Rosenthal, Pyle & Niranjan, 1996). The most common way of processing is the dry oil extraction process. Dried, ground copra is pressed by screw press or hydraulic press to obtain coconut oil. The vegetable oils obtained by mechanical pressing

are characterized by high quality and can be used for special applications (Willems et al., 2008).

To design a suitable pressing technology with minimum input power it is necessary to know the mechanical behavior of copra under compression loading. The available literature on the mechanical behaviour of copra shows the need for further research to address the effect of temperature on amount of oil obtained and energy requirements. The relationship between the compressive force and deformation of bulk copra needs to be transformed to the deformation characteristics used in nonlinear environments that are in screw presses. Therefore, the aim of this study was to describe the linear pressing of bulk copra under different temperatures and to determine the mathematical model describing the pressing behaviour.

MATERIALS AND METHODS

Sample

Dried, clean and ground copra from coconut (*Cocos nucifera L.*) obtained from North Sumatra, Indonesia was used in this experiment. The moisture content $M_c = 5.6 \pm 0.6\%$ (w.b.) of sample was determined using the standard oven method, ASAE method (ASAE S410.1 DEC97, ASAE, 1998). The procedure was that the initial mass of the sample before and after oven drying was weighed. For measuring of mass of each sample m_s (g) an electronic balance (Kern 440–35, Kern & Sohn GmbH, Balingen, Germany) was used. The oil content of copra $O_c = 65.5 \pm 3.2\%$ was determined using the Soxhlet apparatus. For Soxhlet extraction 10 g of find ground copra was extracted with petroleum in a Soxhlet apparatus for 6 h at 60 °C.

Compression test

To determine the relationship between the pressing force and deformation, the compressive device (Labortech, MPTest 5.050, Czech Republic) was used to record the course of deformation function. The amount of 100 g of copra was filled into a pressing vessel of diameter 60 mm and pressing height 100 mm. The pressing vessel was equipped with a heating element for change of temperature. Compression tests at the rate of 1 mm s^{-1} under five different temperatures 20, 40, 60, 80 and 100 °C were performed. For each temperature, the material was preheated in the oven (MEMMERT GmbH + Co. KG, Germany) for 15 minutes. The material temperature was checked using a thermometer (Comet System, C0111, Czech Republic). The measuring range of force was between 0 kN and 50 kN, which represents the normal pressure range commonly used for natural materials. The experiment was repeated five times for each temperature. The schema of pressing vessel is shown in the Fig. 1.

The volume energy is the area under the compressive force – deformation curve and was calculated using Eq. 1 (Kabutey et al., 2015).

$$E_x = \sum_{n=0}^{n=i-1}\left[\left(\frac{F_{n+1} + F_n}{2}\right) \cdot \left(X_{n+1} - X_n\right)\right] \tag{1}$$

where E_x – deformation energy, J; F_{n+1} and F_n – values of compressive force, N; X_{n+1} and X_n – values of deformation, m.

The specific mechanical energy was calculated as the ratio of mechanical energy and total oil yield.
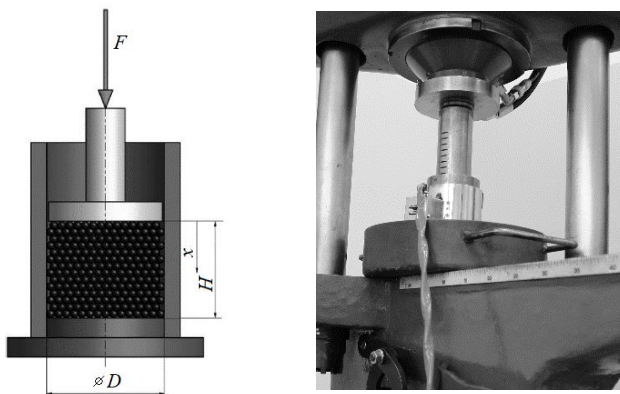
Figure 1. Scheme of pressing vessel diameter D of 60 mm with plunger (Herák et al., 2013) and compression test.

Processing of measured data

The measured amounts of compressive force and deformation of copra for different temperatures were analysed with computer program Mathcad 14 (MathCAD 14, PTC Software, Needham, MA, USA), (Pritchard, 1998) uses Levenberg-Marquardt algorithm for data fitting (Marquardt, 1963). The determined model of curves was statisticaly verified by using ANOVA.

RESULTS AND DISCUSSION

Measured data of individual pressing curve for different temperatures of pressed material are shown in Fig. 2. Dependency between compressive force and deformation for temperatures 40, 60, 80 and 100 °C was fitted by tangent curve equations (Eq. (2)) and the coefficients are presented in Table 1.

$$F(x) = G_0 \times \tan(G_1 \times x) \qquad (2)$$

where $F(x)$ – compressive force, N; G_0, G_1 – force coefficients of mechanical behaviour, N; x – deformation of bulk copra, mm.

From statistical analysis ANOVA (Table 1) follows, that measured amounts of compressive force at diferent temperatures and results from the tangent curve (Eq. 2) were statistically significant at significance level 0.05, that is, the values of F_{crit} (critical value comparing a pair of models) were higher than the F_{rat} values (value of the F – test) and values of P_{value} (significance level at which it can be rejected the hypothesis of equality of models) (Table 1) were higher than 0.05 which is also confirmed by very high coefficients of determination R^2.

Table 1. Determined coefficients of deformation characteristics of pressing vessel for bulk copra and their statistical analysis

Temperature (°C)	G_0 (N)	G_1 (N)	F_{rat} (-)	F_{crit} (-)	P_{value} (-)	R^2 (-)
40-100	$3.281 \cdot 10^3$	0.024	$9.462 \cdot 10^{-3}$	4.301	0.923	0.897

The authors Herák et al., 2013 used a tangent curve to describe the mechanical behavior of oilseeds under compression loading.
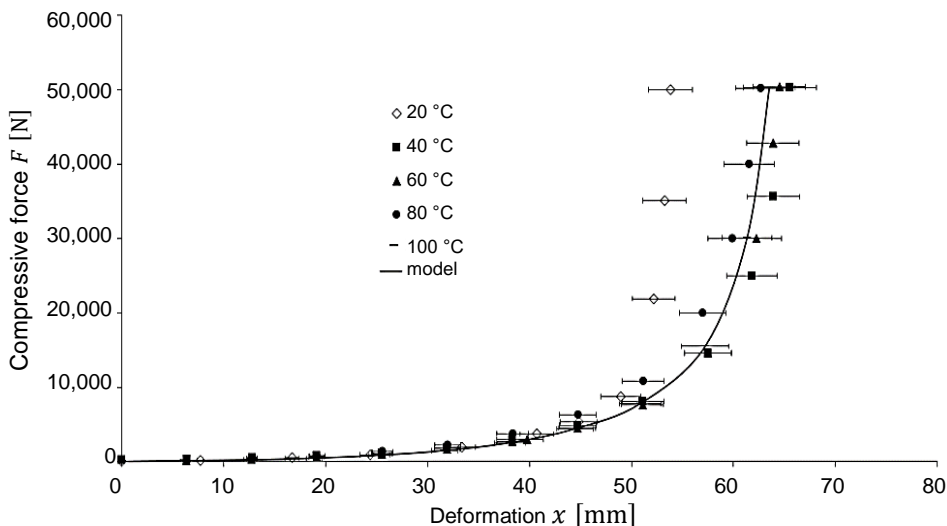
Figure 2. Measured amounts of mechanical characteristic of copra under different temperatures with displayed amounts of coefficients of variation.

Fig. 3 shows the dependence between oil recovery efficiency and temperature of pressed copra. From the Fig. 3 is evident, that with increasing temperature also increases the quantity of obtained oil.
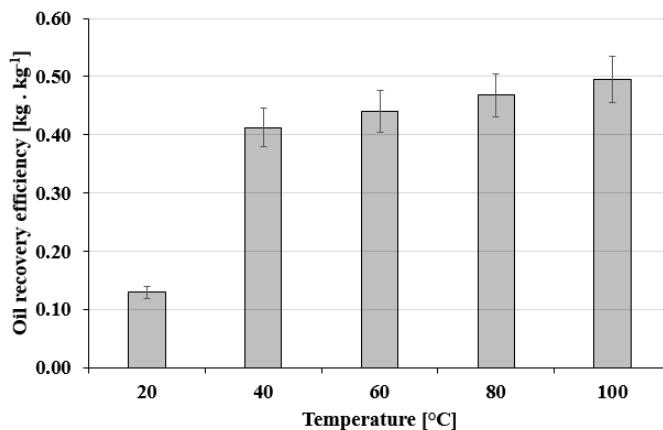
Figure 3. The effect of temperature of coconut copra on oil obtained ratio.

Fig. 4 shows the correlation of specific energy input versus temperature of copra. It is also evident that specific energy decreases as the temperature increases. This is also confirmed by the authors Kabutey et al., 2017. They examined the influence of temperature on mechanical energy by linear pressing of rapeseeds. Copra reaches lower values of specific mechanical energy compared to oil seeds (Mizera et al., 2017).
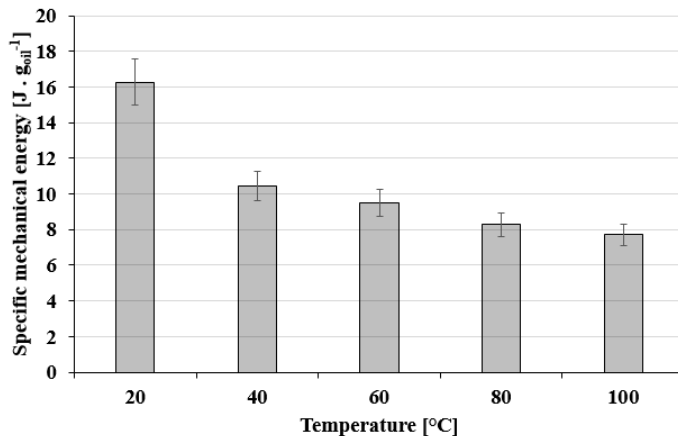
Figure 4. Dependence between temperature and mechanical energy for obtaining one gram of coconut oil.

By pressing at 20 °C was obtained 11.4 g of coconut oil (of the total weight of 88 g). When the temperature increased to 40 °C, an oil gain of 36.3 g was obtained. It can be seen from the individual figures that the greatest difference occurs when the temperature reaches 40 °C. When increasing the temperature above 40 °C there is a linear increase in oil recovery efficiency and even decrease in specific mechanical energy.

CONCLUSIONS

In this study, the compression behaviour of bulk coconut copra was examined at different heat treatment temperatures. A general equation describing the mechanical behaviour of bulk copra under compression loading was determined by tangent curve equation. The results showed that the optimal temperature for copra pressing is about 40 °C. When the temperature is raised to 40 °C, specific mechanical energy for one gram of oil reduced from 16.3 J g_{oil}^{-1} to 10.4 J g_{oil}^{-1} and oil recovery efficiency increased from 0.13 to 0.41 (kg kg^{-1}), compared to room temperature. Future studies should focus on analysing different pressing speed, pressing diameter and physical properties of the copra material as well as temperature influence on oil quality.

REFERENCES

ASAE S410.1 DEC97. 1998. Moisture measurement of peanut. In: ASAE standards, 45th edition. 560–561.

Che Man, Y.B. & Marina, A.M. 2006. Medium chain triacylglycerol. In F. Shahidi (Ed.), Nutraceutical and specialty lipids and their coproducts (pp. 27–56). Boca Raton: Taylor & Francis Group.

Chen, B.K. C. & Diosady, L.L. 2003. Enzymatic aqueous processing of coconuts. *International Journal of Applied Science and Engineering* **1**, 55–61.

Heathcock, J.F. & Chapman, J.A. 1983. The Structure of Fresh Desiccated Coconut. *Food Microtructure* **2**, 81–90.

Herak, D., Kabutey, A., Divisova, M. & Simanjuntag, S. 2013. Mathematical model of mechanical behaviour of Jatropha curcas L. seeds under compression loading. *Biosystems Engineering* **114**, 279–288.

Kabutey, A., Herak, D., Choteborsky, R., Sigalingging, R. & Mizera, C. 2015. Effect of compression speed on energy requirement and oil yield of Jatropha curcas L. bulk seeds under linear compression. *Biosystems Engineering* **136**, 8–13.

Kabutey, A., Herak, D., Choteborsky, R. & Dajbych, O., Sigalingging, R. & Akangbe, O.L. 2017. Compression behaviour of bulk rapeseed: Effects of heat treatment, force, and speed. *International Journal of Food Properties* **20**, 654–662.

Marina, A.M., Che Man, Y.B. & Amin, I. 2009. Virgin coconut oil: emerging functional food oil. *Trends in Food Science & Technology* **20**, 481–487.

Marquardt, D.W. 1963. An Algorithm for Least-Squares Estimation of Nonlinear Parameters. *Journal of the Society for Industrial and Applied Mathematics* **11**, 431–441.

Mizera, C., Herak, D., Hrabě, P., Aleš, Z. & Pavlu, J. 2017. Mechanical behaviour of selected bulk oilseeds under compression loading. *IOP Conference Series: Materials Science and Engineering. 1st Nommensen International Conference on Technology and Engineering*. Medan, Indonesia.

Pritchard, P.J. 1998. Mathcad: A tool for engineering problem solving. McGraw-Hill Science Engineering, New York, 336 pp.

Rosenthal, A., Pyle, D.L. & Niranjan, K. 1996. Aqueous and enzymatic processes for edible oil extraction. *Enzyme and Microbial Technology* **19**, 402–420.

Seow, C.C. & Gwee, C.N. 1997. Coconut milk: chemistry and technology. *International Journal of Food Science and Technology* **32**, 189–201.

Willems, P., Kuipers, N.J.M. & de Haan, A. 2008. Hydraulic pressingof oilseeds: experimental determination and modeling of yield andpressing rates. *Journal of Food Engineering* **89**, 8–16.

Management of parts and components for units and assemblies in mechanical engineering industry and its impact on the environment

V. Mitrofanovs[*], I. Boiko and Ē. Geriņš

Riga Technical University, Institute of Mechanical Engineering, Viskalu 36A,
LV-1006 Riga, Latvia
[*]Correspondence: v.mitrofanovs@meistars.lv

Abstract. Most of the service centers operating in the repair and maintenance of machines and mechanisms apply warehouse management systems based on event prediction, which ensures inventory replenishment based on the initial diagnosis of the units. Such methodology is enforced measure, since the components and assemblies, even from the same manufacturer, having similar functions, design and connecting components have their own engineering numbers and part numbers for ordering. Unfortunately, this method is relevant only with perfect logistics and minimal time factor. If these criteria cannot be fulfilled, the maintenance and repair time increases, especially at a distance from logistic centers.
By reducing lost sales and quick customer satisfaction, own warehouse stocks based on statistical data increases. Unfortunately, none of the modern methods gives a 100% result and eventually leads to overstocking and formation of deadstock. On the other hands more and more components are made from composite materials, complex alloys, permanent joints are being used. But due to ineffective management the significant part of expensive components is became needless. The aim of this research is to develop an algorithm allowing to optimise the logistics chain and reduce the inventory and deadstock, reduce disposal of used and obsolete units and assemblies, resulting in significantly lower consumption of natural resources, energy and reduced negative impact of waste on the environment. Our research shows that in various fields of science there are being developed methodologies, which would solve the described tasks by combining those methodologies in a single algorithm.

Key words: management of parts and components, impact on the environment, parts algorithm.

INTRODUCTION

In general, in the repair and maintenance of machines and mechanisms there are being applied event prediction-based warehouse management systems, which ensures inventory replenishment based on the initial diagnosis of the units. Unfortunately, this method is relevant only with perfect logistics and minimal time factor. If these criteria cannot be fulfilled, the maintenance and repair time increases, especially at a distance from logistic centers. On the other hand, none of the modern methods gives a 100% result and eventually leads to overstocking and formation of deadstock.

There are known some research in the field of spare parts management with the goal to minimize the downtime of the capital assets needs, because the capital assets are

essential to the operational processes of the companies involved. Thus in (Driessen et al., 2014) the focus of the research is on the responsibility of a Maintenance Logistics Organization (MLO) to minimize maintenance delay due to unavailability of required spare parts. This framework can be used to increase the efficiency, consistency and sustainability of decisions on how to plan and control the spare parts supply chain. Nevertheless, authors point out, that the proposed framework in which the connection between these decisions is outlined, will need refinement and alterations for every particular organization.

In other research (Geertjes, 2014) focus is on the process of replenishing spare parts inventories and on the study the ordering decisions made by planners. During the study author finds 31 potential factors causing interventions in spare parts planning, which were categorized to five different processes concerning spare part planning and control, in order to allocate the factors to concrete process owners. After analysis of the empirical data achieved from 3 companies author concludes, that the planning systems should be modified in such a way that interventions and reason for interventions are stored. In this way, the efficiency of the implemented improvements can be determined and ordering decisions can be easier monitored in the future. Additionally, author proposes to develop a feedback mechanism to learn from own past decisions (take into account human factor) and to study the exact impact of intervening. Thus, the ready methodology has not yet elaborated.

A system approach to repairable stocking and expediting in a fluctuating demand environment is used in (Arts, 2013). As a result, a general framework for maintenance spare parts planning and control of spare part supply chain have elaborated, which outlines the decision functions at strategic, tactical, and operational level and also describes the interactions and (hierarchical) relations between these decisions and provides an outline of how these decisions can be decomposed. But proposed framework still needs to be elaborated in details for using in industry.

It is clear that the impact of the management of parts and components in industry have strong influence on the environmental issues. Companies around the world are challenged to manage the opportunities and risks of developing successful products in increasingly competitive and regulated markets (HIS, 2011): in today's stressed economic climate, technology continues to advance at an increasing pace and supply chains are expanding globally, while regulations and consumers drive demand for green products. So, industry needs simple and reliable methodology as a simple algorithm for management of parts and components for units and assemblies.

Nowadays, writing an algorithm to be executed by modern computers and setting multitasking between them is a reality. However, unfortunately, today 'Artificial Intelligence' is not capable of inventing and developing an algorithm for itself. Hence it is possible and necessary to set milestones to create a route to the desired goal. Knowledge, education and regular improvement of both complemented with modern tools and technologies allow to come up with solutions to extraordinary tasks.

The aim of this research is to develop an algorithm allowing to optimise the logistics chain and reduce the inventory and deadstock, reduce disposal of used and obsolete units and assemblies, resulting in significantly lower consumption of natural resources, energy and reduced negative impact of waste on the environment. Our research shows that in various fields of science there are being developed methodologies,

which would solve the described tasks by combining those methodologies in a single algorithm.

Let us review the path of components from the task of design to their disposal step by step.

METHODS

Any component manufacturer aims to provide consumers with necessary volume of products that meet technical requirements during operation in a timely manner (Fig. 1).

The parameter of the required production volume of a component is obtained considering several main factors:

1. production volume of assembly units in which the component is used;

2. operation period of the component and operation period of the assembly unit;

3. correction factor, which is based on unforeseen replacement of the component ($k_{fm} > 1$);

4. correction factor, which is based on the probability of the component being produced by a competitor ($k_{ks} \leq 1$).
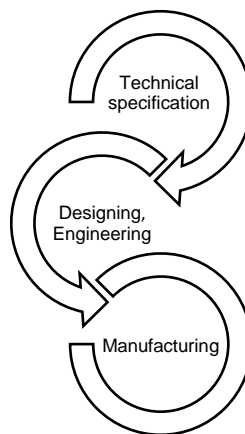
Figure 1. PLC from manufacturer.

It is a kind of puzzle, which analysts of the manufacturers strive to put together. In our opinion, the most effective is **RCM Methodology** (Fig. 2) (SKF, 2008), which is widely spread among manufacturers.

Unconditional requirements for components are environmentally friendly production process and eco-friendly operation. Most of the service centers operating in the repair and maintenance of machines and mechanisms apply warehouse management systems based on event prediction, which ensures inventory replenishment based on the initial diagnosis of the units (Fig. 3).

Reason					
A	C	B	A	A	A
B	D	C	B	A	A
C	D	C	C	B	A
D	D	D	C	C	B
E	D	D	D	D	C
	5	4	3	2	1
Probability					

Figure 2. RCM Methodology.

Such methodology is enforced measure, since the components and assemblies, even from the same manufacturer, having similar functions, design and connecting components have their own engineering numbers and part numbers for ordering. Unfortunately, this method is relevant only with perfect logistics and minimal time factor. If these criteria cannot be fulfilled, the maintenance and repair time increases, especially at a distance from logistic centers (Serov, 2005).

At the heart of stock planning of most distribution centers are:

- ABC analysis (method that allows to classify resources according to the level of their importance)
- XYZ analysis (allows to classify resources of the company depending on the character of their consumption and accuracy of predicting changes in their consumption within specific timeframe)
- VEN analysis (Vital Essential Non-essential) – direct segmentation of the 'need' of the product range

Figure 3. PLC from distributer.

- RFM analysis (Fastest Medium Rare) – product range analysis based on the frequency of hits/taking)
- SWOT analysis (strategical planning method, which consists of identifying the factors of the internal and external environment of the organization and dividing them into four categories):
  - ➢ Strengths,
  - ➢ Weaknesses,
  - ➢ Opportunities,
  - ➢ Threats.

Currently, telematics systems are being developed and implemented, which are able to inform about the need to replace one or another component in a specific period of time. This is certainly a positive factor for reducing the extent of error when storing spare parts (Driessen, 2014).

Reliability Centered Maintenance (Fig. 4) allows to anticipate equipment failures based on the data on previously consumed spare parts and the readings of telematics systems (Defense Acquisition University, 2018). The diagram shows the methodology proposed by the world's largest component manufacturer ZF.

Using unique spare parts for assembly units of the same type leads to a general increase in the volume of undemanded or damaged before the moment of operation homogenous spare parts.

More and more components are being made from composite materials, complex alloys and permanent joints are being used more often. Scientific centers and universities in different countries are developing disposal methods for used components (Fig. 5) (Bakran, 2000).

Figure 4. ZF Reliability Centered Maintenance.

Below are graphs of our research on Fast Moving Parts of filtering group products.

In addition to that we should understand that **Pareto Principle** 80%, 15% and 5% is used as a basis. Nevertheless, any inaccuracy or unpredictable event leads to lost sales or to overstocking and the formation of deadstock.

Creating the models of the supply chain and applying the maximum number of methods allow to approach more accurate rate of the possible consumption (Defense Acquisition University, 2018). Unfortunately, none of the modern methods ensures a 100% result (Fig. 6). Based on the data collected we have calculated and created graphs using various event processing methods. As can be seen on the graphs all of the methods have certain error.
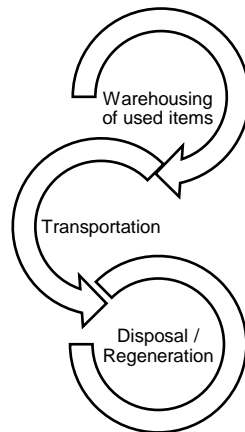
Figure 5. PLC from recycler.
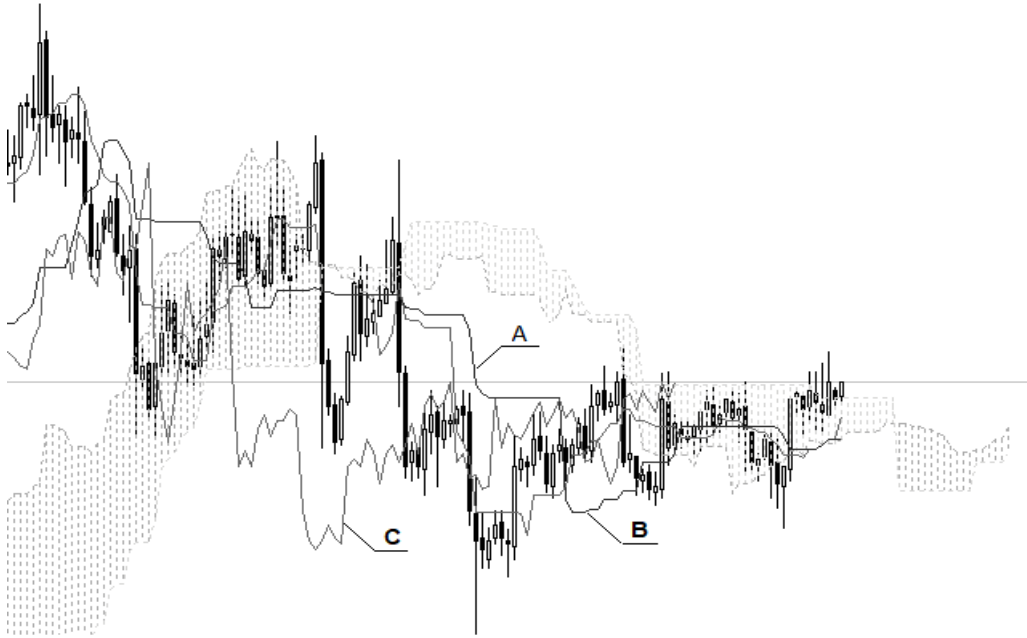
Figure 6. Combined graph of the required storage volume with the use of various methods: A) Curve of the real state of the warehouse; B) Curve of the average expected consumption amount; C) Curve of the real consumption.

a)   b)   c)

Figure 7. Steel housing (a), plastic housing (b) and steel housing with aluminum valve (c).

We have carried out the study of various types of filtering elements (Fig. 7) and in addition to that we have obtained technical specifications from a number of manufacturers based on which was found that at least half of the materials do not perform the function of the main working component directly, but serve only as a unique constructive element (Fig. 8 and Fig. 9).

Our research reveals the gap in the supply chain for setting up the design task of components and assemblies in the full life cycle of materials.

Please note that currently there are tasks:

- for manufacturer to develop a product that meets technical requirements of the life cycle during operation period;

- for distributor to provide information to manufacturer about the predicted volume of the required products;
- for recycling organizations to develop a methodology for the disposal of products in the post-operational period (Bakran, 2000).
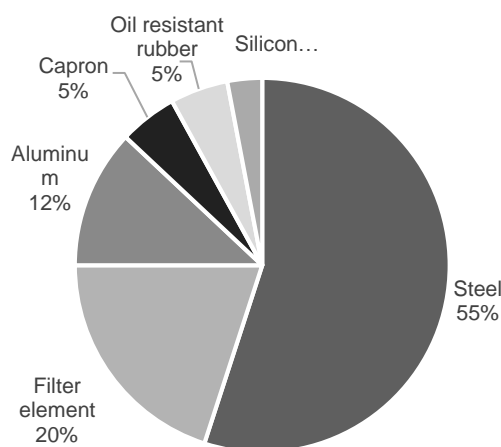
Figure 8. Steel housing.
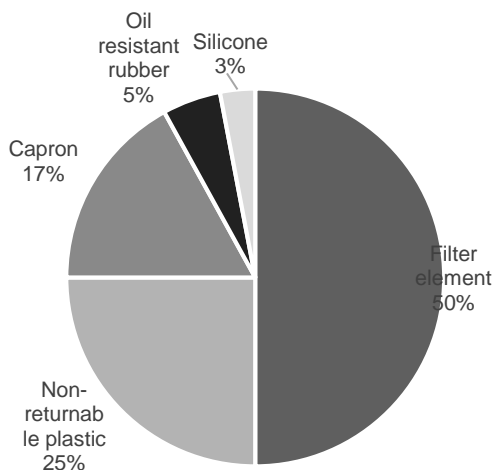
Figure 9. Plastic housing.

RESULTS AND DISCUSSION

We believe that the task in the design of products should be set more comprehensively: from the very beginning of production to the methodology of recycling and disposal of products, as well as methods of applying or dismantling the components that were not included in operation.

We are exploring the possibilities of patent law on the opportunities of applying the standards and unification to already existing assemblies.

Standardization and unification of a number of products will allow to significantly reduce the disposal of undemanded spare parts.

Rules for using the materials for spare parts, particularly for frequent wear and tear items, should be further elaborated in more detail.

Within further research we consider possible scenarios for solving the tasks describe above and possibilities of introducing these solutions into production, which would save logistics time, reduce inventory, deadstock, disposal of used and obsolete assembly units and components. The solution of each task will significantly reduce the consumption of natural resources, energy and negative impact of disposal on the environment.

CONCLUSIONS

A key thesis in our work is to introduce changes into the product life cycle by taking into account the influence of all factors on setting up the technical specifications for product design and implementing the ECO solutions being developed by us (Fig. 10).
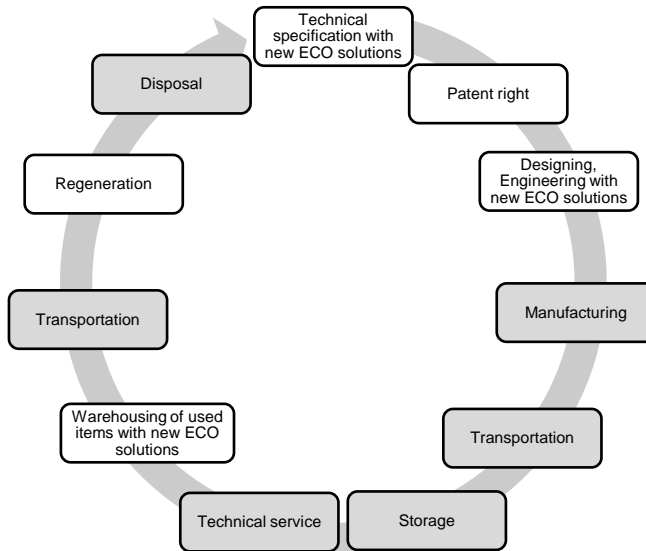
Figure 10. New vision of Product life-cycle.

REFERENCES

Arts, J.J. 2013. Spare Parts Planning and Control for Maintenance Operations, 217 pp.

Bakran, M.-M. 2000. Maschinenbau Energie und Umwelt, Universität Bayreuth, 75 pp.

Defense Acquisition University Reliability Centered Maintenance (RCM), 2005-2018.

Driessen, M.A., Arts, J.J., van Houtum, G.J., Rustenberg, W.D. & Huisman. B. 2014. *Maintenance Spare Parts Planning and Control: A framework for control and agenda for future research*, 30 pp.

Geertjes, F. 2014. *A first step towards fully automated spare parts planning systems An empirical study on ordering behaviour*, 74 pp.

IHS Parts Management Solutions: Information Resources and Tools for the Life of Your Products, 2011.

Serov, I.A. 2005. *Stochastic simulation of a logistics chain 'production - storage-distribution'*, 438 pp. (in Russian)

SKF GmbH Optimierung des Instandhaltungsaufwands mit Methode: Reliability Centered Maintenance (RCM), 2008.

Improving the quality of critical tractor parts through the dynamic stabilisation of the manufacturing process in regard to CNC machines

J. Olt[1,*], V. Maksarov[2] and A. Efimov[2]

[1]Estonian University of Life Sciences, Chair of Biosystems Engineering, Kreutzwaldi 56, EE51006 Tartu, Estonia
[2]Saint-Petersburg Mining University, Department of Mechanical Engineering, 2, 21st Line, St Petersburg RU199106, Russia
*Correspondence: jyri.olt@emu.ee

Abstract. This article focuses on the evaluation of a rod improvement which is considered in detail below. The rod in question is part of an hydraulic cylinder manufacturing process which takes place on CNC machines. The need for ensuring a process improvement in this area arose because the rod often breaks down under operational conditions. It was found that the cause of this is a finishing operation in the existing production process. The effect of charging which occurred during the grinding process brings about the embedding of abrasive particles into the workpiece surface layer. Therefore, at the running-in stage, the mating surfaces on the rod and the system being used to seal the rings both experience intense wear in their contact areas, with this being caused by abrasive microparticles which serves to reduce the performance characteristics of the part in question. However, even if we dispense with the grinding process, ensuring the necessary roughness of $R_a = 0.63$ μm at the machining stage alone will present problems of their own for a number of reasons. First and foremost is the connection with the phenomenon that results in an auto-oscillation processes which is generated by the manufacturing system, as well as the formation of flow chips during machining on CNC machines. In this regard, in order to avoid any negative factors creeping into the process, we propose that a new approach be taken in achieving the necessary surface roughness, one which is based on the suppression of the auto-oscillation process during machining by means of creating a selective metastable structure. At the machining stage, any inhomogeneous structure in the local chip formation area will be destroyed, thereby suppressing the auto-oscillation process and reducing the surface roughness. Eventually, the proposed method will allows the grinding operation to be dispensed with entirely from the manufacturing process.

Key words: production process, local laser impact, metastable structure, machining process system, chip formation, auto-oscillation processes, surface roughness.

INTRODUCTION

At present in mechanical engineering special attention is being given to the tractor industry. The reason for such interest is primarily the high demand for specialised machinery in road and civil construction, in mineral resource-mining enterprises, and also in agriculture. Great demand for special-purpose machinery, as well as the resultant need for spare parts, compels tractor plants to increase their production rates, and this is

impossible to accomplish without modernising existing production facilities. For this purpose, the large-scale integration of up-to-date flexible machining cells which are based on the use of CNC machines is presently underway. Such an approach allows output levels to be increased and also the necessary quality parameters to be ensured.

Besides this, as with all machine factories, there are manufacturing problems that can be connected to CNC machines which exist in relation to a wide scope of high-precision tractor parts. For example, the critical part - the rod (C63-3405121 - see Fig. 1) which is part of the C63-3405115 steering linkage hydraulic cylinder for MTZ-2522 tractors - is not an exception in this respect.
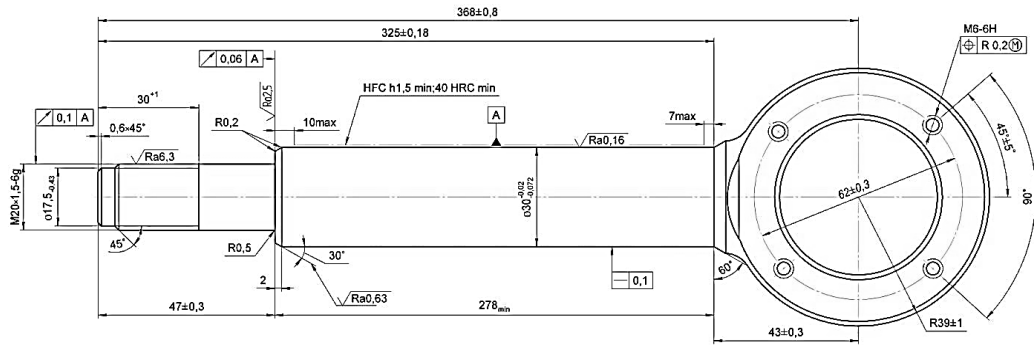
Figure 1. A diagram of rod C63-3405121, part of an hydraulic cylinder.

This item was not chosen at random. The highest single figure in relation to operational failures (about 70%) is caused by this part. Operational failures are caused by breakdowns in the rod sealing system which result in an hydraulic power cylinder seal failure. The loss of the seal is directly connected to rod surface preparation at the manufacturing stage, in spite of the fact that this item must meet strict requirements regarding surface roughness and precision of form (Efimov et al., 2017, Maksarov et al., 2018; Olt et al., 2018).

Firstly, the situation is made more complicated when the surface finish manufacturing parameters that are obtained during the process of precision rod fabrication on CNC machines do not meet the specified standards due to a number of reasons. One of these is metal ductility, which results in the following circumstances: the winding of flow chips on the manufacturing machinery parts; malfunctions in the automatic system which measures the machined part and monitors the state of the cutting tool's levels of wear; and scratching on the machined part's surface and an increase in roughness indicators. Besides all of this, the plastic properties of the metals have a specific impact on the closed *machining process system* (MPS), increasing the amplitude of the auto-oscillation process due to periodic changes in the cutting force and the ambiguity of those changes, increased contact friction between the chip and the cutting tool, and also chip adhesion to the cutting edge (Weitz & Maksarov, 2000). Such physical processes bring about an increase in amplitude and frequency dynamic characteristics, both of which serve to result in the catastrophic wear of the cutting tools, along with surface finish deterioration and a deviation in workpiece form precision (Elyasberg, 1993).

Secondly, the finishing-off which involves a round grinding operation brings about a charging effect which involves surface saturation with abrasive microparticles. In the next stage (thermodiffusion chromising) chromium atoms will not diffuse completely into a metal

surface which includes embedded abrasive particles. Such a form of surface manufacture will have the following consequences: in the normal operational process, incomplete chromium diffusion will facilitate the destruction of the protective chromium layer, resulting in heavy wear on the rod sealing system against the surface that has been charged with an abrasive. As a result of the loss of the seal on the power hydraulic cylinder, dust and dirt microparticles will get onto the rod's rubbing surfaces and also onto the bore, resulting in corrosion on the surfaces and mechanical damage to both areas. All of these negative impacts will eventually result in economic losses being suffered thanks to machine downtime that is caused by the removal and reinstallation of a defective power hydraulic cylinder. As a result, in order to solve the problems that have been described above, we have to take a closer look at the aspects involved in the machining process that takes place on CNC machines (Madissoo & Olt, 2011; Stephenson & Agapiou, 2016).

MATERIALS AND METHODS

One possible way of solving the problems that have been outlined above is the dynamic stabilisation of the machining process through the 'workpiece' subsystem (Madissoo et al., 2012). The authors have developed a method which consists of two consecutive stages that will accomplish this objective. The objective of the first stage is to create a metastable structure on the in-process workpiece surface. Since, at present, hydraulic cylinder rods are made of 45-grade steel (Fig. 2), it is possible to create a non-equilibrium structure that is different from the base metal primarily by using local high-energy laser irradiation (Grigoriants, 1989; Sufiiarov et al., 2017; Olt et al., 2018). A 5 kW continuous-wave ytterbium fibre optics laser is used for this purpose.
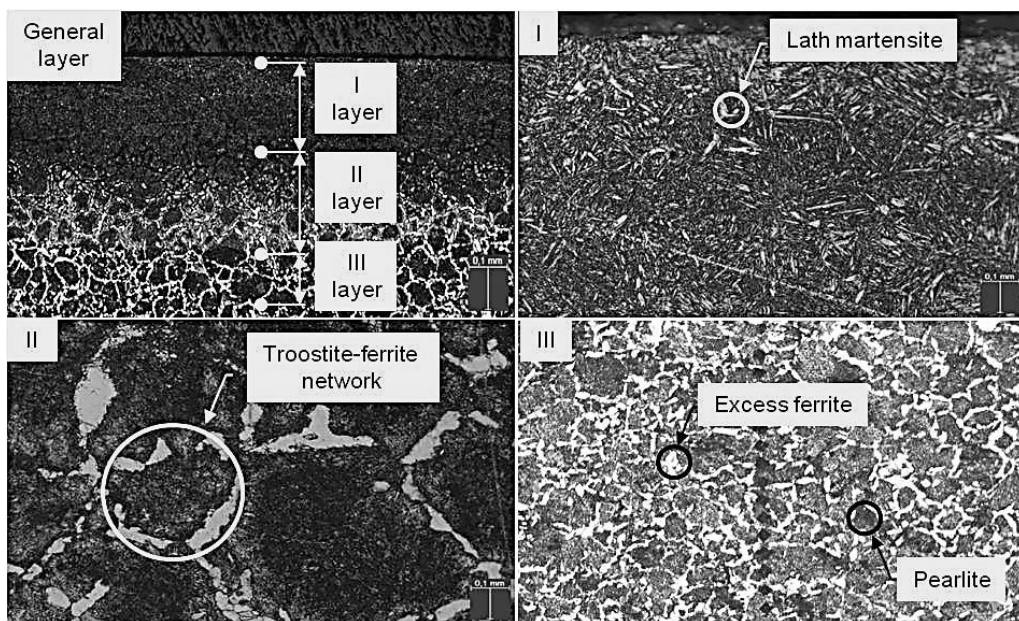
Figure 2. Fabricated metastable structure with (I) being the martensite-structured zone, (II) being the tempered zone (the troostite-ferrite network), and (III) being the initial metal zone.

The energy generated by this process was sufficient to concentrate a threshold radiation power density of $E = 10^4$ W cm^{-2} in a laser beam with a diameter of $d_s = 4$ mm. The initial metal structure that is under consideration consists of two phases: perlite and pro eutectoid ferrite (see (III) in Fig. 2). When laser radiation is applied to the surface of 45-grade carbon steel, a local area of the near-surface workpiece layer experiences ultra-fast heating of approximately 10^3 to $10^4\,°$C s^{-1} to the temperature point of iron/carbon A_{c1} phase transfer. Ultra-fast heating facilitates a shift of the critical point A_{c1} into a higher temperature range with values of approximately 50–200 °C (Grigoriants et al., 2006). Following this, favourable conditions arise for the simultaneous occurrence of two processes under the influence of the emerging temperature and pressure: the transformation of the ferrite/cementite mixture into austenite, and the transformation of pro-eutectoid ferrite into austenite. A subsequent flash heat ensures the diffusion rearrangement of pro-eutectoid ferrite volume-centred cubic lattice into austenite face-centred cubic lattice. Whereupon the recrystallisation process may lack time in which it can end at the iron/carbon GS diagram line, causing a shift of the A_{c3} critical point. Upon the completion of structural transformations, carbon homogenisation takes place. This is completed above the point A_{c3} within the $T_S \rightarrow T_L$ temperature range. This ensures ultra-fast cooling deep into the metal at the rate of $V_c = 400$–600 °C s^{-1}, thereby bringing about a diffusionless martensite transformation in a local area of the metal (see (I) in Fig. 2). A tempered structure takes place closer to the border with the initial metal (see (II) in Fig. 2). Therefore, high-rate cooling brings about an increase in phase hardening, with recovery and recrystallisation processes both slowing down, and austenitic phase defects being inherited more fully. This brings about the crushing of blocks $D = 0.33$–$0.57\ 10^5$ cm, an increase in dislocation density levels $\rho_d = 9\ 10^{-10}$ cm^2, and an increase in crystal lattice stresses. As a result, the structure that took shape during this process is over-defective and is also prone to brittle failure when compared to the initial structure.

This fact is confirmed by residual stress tests on the resulting metastable structure which were carried out using a STRESSVISION scanner. The map of residual longitudinal strains on the metastable structure surface is shown in Fig. 3.
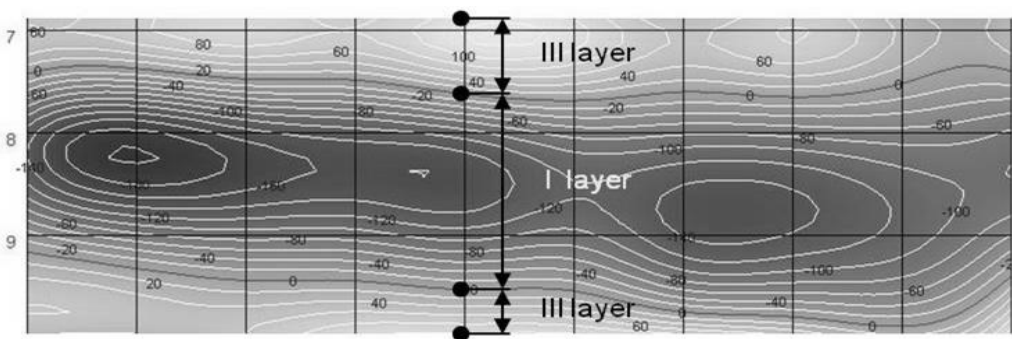
Figure 3. A map of residual strains after local metastable structure-shaping on a workpiece surface under laser impact: $P = 2.5$ kW; $V_l = 2000$ mm min^{-1}; $d_s = 4$ mm.

It has been established that, in zone I, the metastable structure experiences residual compression stresses which are caused by martensite transformation, accompanied by an increase in volume during cooling. Compressive stresses that are equal to -180 MPa

take shape closer to the centre of the laser-impacted area. As heat flow advances towards the initial material, compressive stresses drop to -100 MPa. A further advance towards the borders of transitional zone III demonstrates that compressive stresses drop to between -10 MPa and -80 MPa. As compressive stresses move away from the border of zone III, they reach a zero value and change smoothly to tensile stresses that amount to between 20 MPa to 80 MPa. The closer to the initial point - the non-impacted metal - the greater become the tensile stresses, with them reaching a value of 100 MPa. The above results give evidence of a significant inhomogeneity in terms of residual stress distribution in the local area of the irradiated workpiece surface.

Apart from residual stresses, an important parameter is the depth of the created metastable structure that was determined using the COMSOL Multiphysics 5.1 software environment. This software simulated the depth distribution of temperature patterns caused by a laser impact on metal (Fig. 4). A medium-temperature tempering takes place in the area in which the temperature reaches about 350 °C. As is known, structural changes do not occur at temperatures below the above values; therefore, this is the border of the metastable zone - this being its depth.
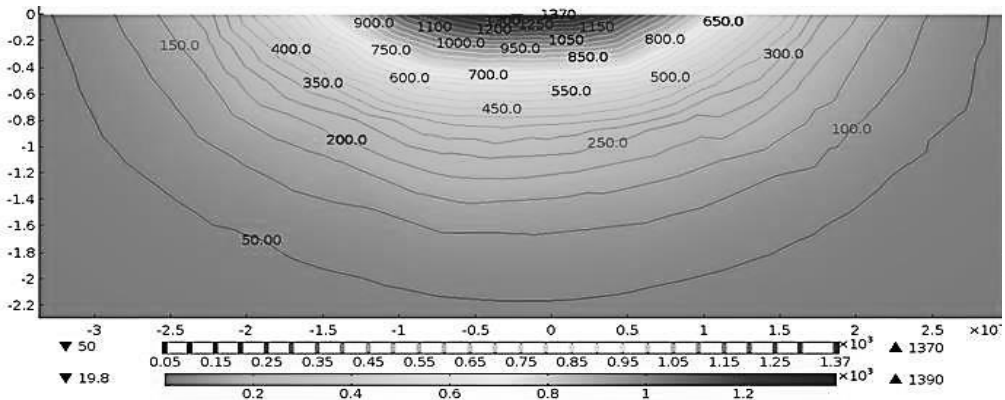
Figure 4. The simulated distribution of temperature patterns under the impact of local laser irradiation where exposure parameters are as follows: $P = 2.5$ kW; $V_l = 2,000$ mm min^{-1}; $d_s = 4$ mm. The exposure depth amounted to $t_g' = 0$. mm.

The results obtained from the computer simulation were confirmed by measuring the in-depth microhardness of the created metastable structure. A dependency between geometric parameters in the altered structure and laser impact characteristics was established by means of comparative analysis (Tabl 1).

Table 1. The influence of irradiation power on impact depth and width for 45-grade steel

No	Spot diameter d_s, mm	Irradiation power P, kW	Machining rate V_l, mm min^{-1}	Gradient structure depth t_g, mm	Calculated gradient structure depth t_g', mm
1	4	2.5	2,000	0.68	0.7
2	4	2.0	2,000	0.34	0.38
3	4	1.5	2,000	0.17	0.15

The task of the second stage was to carry out experimental tests on the machining of a workpiece with a local metastable structure. All of the experimental studies which aimed at the identification of the auto-oscillation process were carried out on an EMCO Concept TURN 250 lathe. A Prüftechnik VIBXPERT vibrodiagnostic instrument was connected to a cutting tool through vibration sensors that were installed in the directions of the tangential cutting force P_z and radial cutting force P_y. Laser impact modes for creating a metastable structure were chosen according to Table 1: with mode 1 for rough machining, mode 2 for semi-finish machining, and mode 3 for final machining. The results of the experimental studies are presented in oscillograms (Fig. 5, a, b, c).

a)

b)

c)
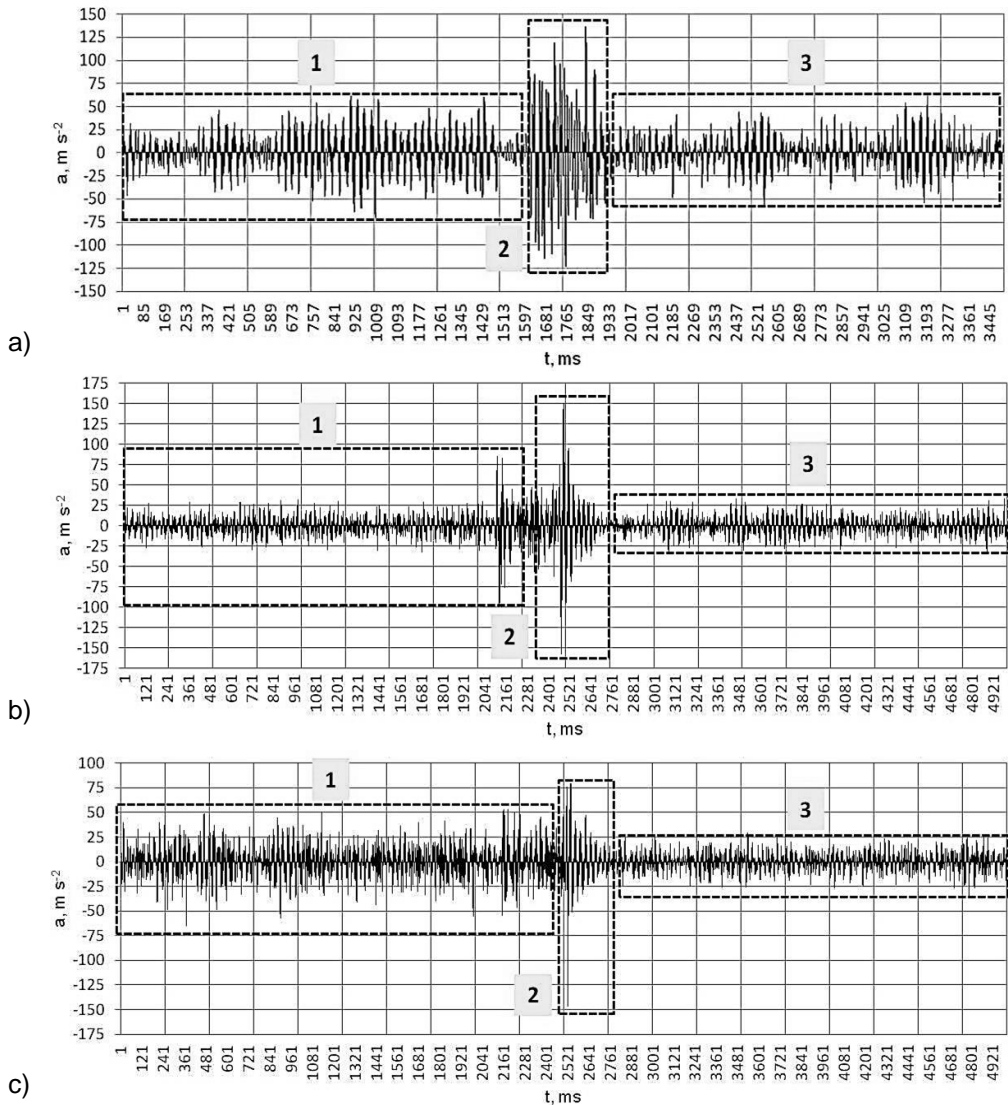
Figure 5. Oscillograms of vibration accelerations during the process of machining a workpiece with a local metastable structure where: *a* is rough machining: $V = 70$ m min^{-1}, $S = 0.35$ mm rev^{-1}, $t = 0.68$ mm; *b* is semi-finish machining: $V = 120$ m min^{-1}, $S = 0.15$ mm rev^{-1}, $t = 0.35$ mm; *c* is finish machining: $V = 160$ m min^{-1}, $S = 0.1$ mm rev^{-1}, and $t = 0.2$mm.

The oscillograms that were obtained are interpreted as follows: as a tool enters the workpiece, an auto-oscillation process arises which is accompanied by an increase in amplitude. This process is marked out as section **1**. When the tool reaches a local metastable zone in which a martensite structure is predominant, a crack is instantly initiated, causing a brittle failure. Then, at the moment of time $t = 1.597$ ms for rough machining, $t = 2.401$ ms for semi-finish machining, and $t = 2.501$ ms for final machining, the 'tool' process subsystem experiences acceleration until the crack encounters the initial ferrite/perlite structure. Such a structure is subject to a ductile failure mechanism that slows down the advance of the crack. Its further development brings about a fully-fledged rupture and the separation of a chip segment from the surface that is being machined. This effect forces the manufacturing system to unlock for between 200–400 ms and causes section **2** to execute free-damped oscillations, thereby dissipating the amplitude of the auto-oscillations that have been established during this period. In other words, this method allows for a short period of time a friction bond to break that has been effected through chip formation between the 'tool' and the 'workpiece' subsystems, allowing the energy in the auto-oscillation process to dissipate where it has been accumulated in the manufacturing system. Subsequent machining is within the range of the auto-oscillation process amplitudes, in section **3**.

RESULTS AND DISCUSSION

After carrying out dynamic tests that were connected with the machining of the 'rod' part that was preliminarily subjected to local laser action, microgeometric surface characteristics were evaluated. At present, the stylus method is the most precise one available for measuring surface roughness. This surface assessment method was implemented with the help of a Surftest SJ-210 profilometer. Experimental information that could be gathered is presented in the form of the profilograms of machined surfaces of the 'rod' part, following three machining operations in the following modes: finishing operation: $V = 160$ m min^{-1}, $S = 0.1$ mm rev^{-1}, $t = 0.2$ mm (Fig. 6, a, b); semi-finishing operation: $V = 120$ m min^{-1}, $S = 0.15$ mm rev^{-1}, $t = 0.35$ mm (Fig. 6, c, d); rough operation: $V = 70$ m min^{-1}, $S = 0.35$ mm rev^{-1}, and $t = 0.68$ mm (Fig. 6, e, f).

After the experimental tests have been concluded, a tendency is clearly discerned in the profilograms towards a reduction in microgeometric surface characteristics when using the preliminary local laser action method.

CONCLUSIONS

As the authors of this paper have been able to sum up, it is safe to say that the proposed method for ensuring machining-process dynamic stabilisation through the creation of a metastable structure in the 'workpiece' subsystem surface layer allows for a successful reduction in the auto-oscillation processes level by as much as 30%. Reducing amplitude dynamic characteristics during machining allowed, in turn, surface quality characteristics to be improved by as much as 42% and for roughness values to be achieved that were established by the manufacturing process specifications: $R_a = 0.63$ μm. As a result, it turns out that it is possible to dispense with the finishing grinding

operation in the existing manufacturing process. It should be noted that the problem of flow chips segmentation has also been solved.

a) With local laser action: $R_a = 0.57$ μm   b) Without local laser action: $R_a = 1.373$ μm

c) With local laser action: $R_a = 1.61$ μm   d) Without local laser action: $R_a = 1.912$ μm

e) With local laser action: $R_a = 3.123$ μm   f) Without local laser action: $R_a = 4.893$ μm
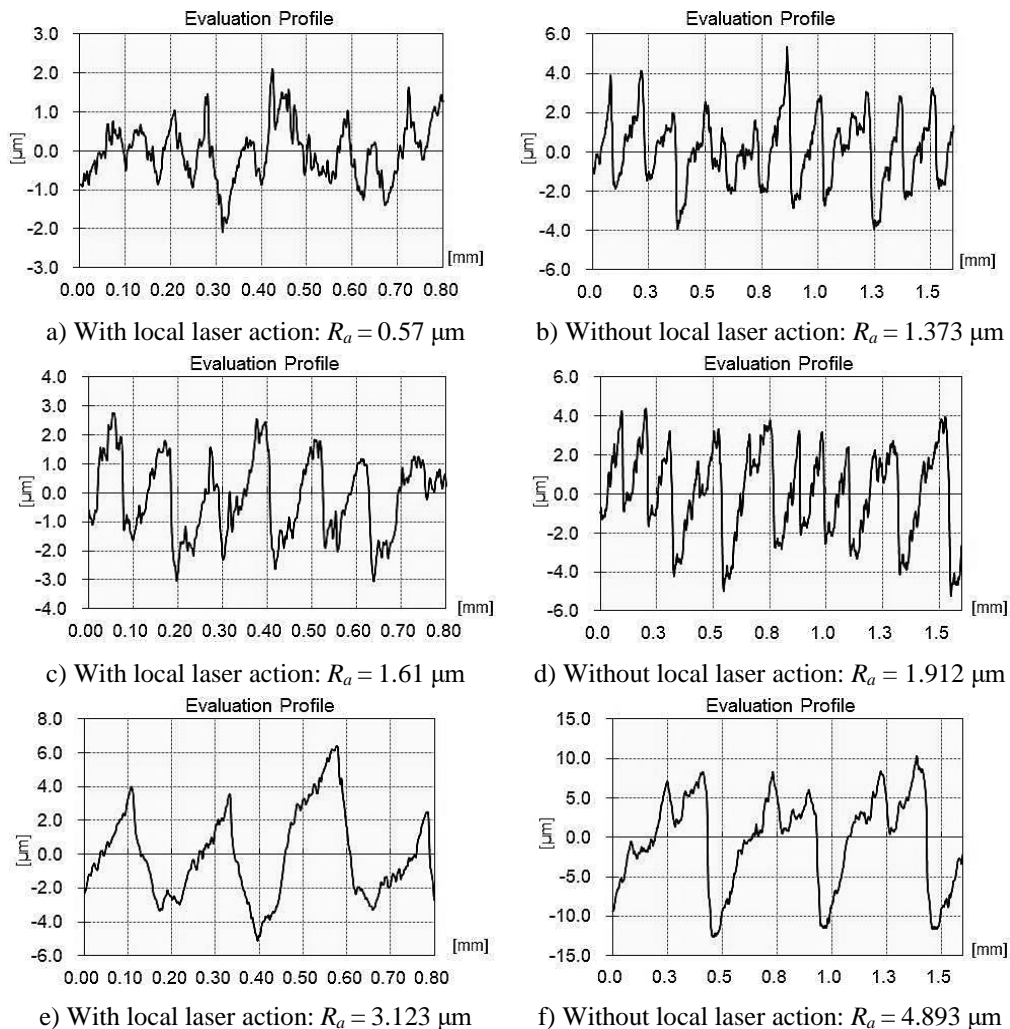
Figure 6. Surface roughness profilograms after machining with and without the utilisation of local laser action.

REFERENCES

Efimov, A., Maksarov, V. & Vjushin, R. 2017. Technological control of surface layer roughness on the basis of modeling of transients. *Metalworking*, **2**, 39–45. (in Russian).

Elyasberg, M.E. 1993. Self – Excited Machine – Tool Chatter. Theory and practice, St. Petersburg, OKBS, 180 pp. (in Russian).

Grigoriants, A.G., Shiganov, I.N. & Misjurs, A.I. 2006. *Technological processes of laser processing*. Tutorial, Moscow, MSTU named after N.E. Bauman, 664 pp. (in Russian).

Grigoriants, A.G. 1989. *Fundamentals of laser processing of materials*. Moscow, Mechanical Engineering, 304 pp. (in Russian).

Madissoo, M., Olt, J. 2011. Dynamic modeling of the cutting process. *Annals of DAAAM and Proceedings of the 22nd International DAAAM Symposium*, **22**, 1203-1204; Vienna; Austria.

Madissoo, M., Maksarov, V., Arak, M., Olt, J. 2012. Dynamic Modeling of the Cutting Process, Chapter 18 in DAAAM International Annals & Proceeding 2012, 213-224, B. Katalnic (Ed.), Published by DAAAM International, ISBN 978-3-901509-86-5, ISSN 1726-9679, Vienna, Austria, DOI: 10.2507/daaam.scibook.2012.18.

Maksarov, V.V., Krasnyy, V.A., Viushin, R.V. 2018. Simulation of dynamic processes when machining transition surfaces of stepped shafts, , IOP Conference Series: Materials Science and Engineering, 327(2), Article number 022047, DOI: 10.1088/1757-899X/327/2/022047

Olt, J., Maksarov, V.V., Efimov, A. 2018. Impacts of gradient structure on the dynamic characteristics of machining process system, Proceedings of the 29th DAAAM International Symposium, B. Katalinic (Ed.), Published by DAAAM International, ISBN 978-3-902734-20-4, ISSN 1726-9679, Vienna, Austria, 0190-0196,
DOI: 10.2507/29th.daaam.proceedings.027.

Stephenson, D.A., Agapiou, J.S. 2016. *Metal cutting theory and practice.* Third edition, CRC Press, 931 p. ISBN: 978-146658754-0; 978-146658753-3

Sufiiarov, V.S., Popovich, A.A., Borisov, E.V., Polozov, I.A., Masaylo, D.V., Orlov, A.V, 2017. The effect of layer thickness at selective laser melting. *Procedia Engineering* **174**, 126-134. DOI: 10.1016/j.proeng.2017.01.179.

Weitz, W.L. & Maksarov, V.V. 2000. *Dynamics and control of process of chip formation with cutting edge machining*. Monograph, St. Petersburg, SZPI, 160 pp. (in Russian)

Usage of grid support inverter on long distribution grid lines

V. Osadčuks[*], A. Pecka and A. Galiņš

Latvia University of Life Sciences and Technologies, Faculty of Engineering, Institute of Energetics, Čakstes blvd. 5, LV-3001 Jelgava, Latvia
[*]Correspondence: vtl@tvnet.lv

Abstract. The paper focuses on the evaluation of new possibilities to improve voltage quality in remote branches of 230 V grid. Decrease of power electronic costs may potentially make battery-backed inverters a viable alternative to the costly reconstruction of 230 V distribution grid connections, which are of poor quality or cannot match changing load requirements, extending power transmission lines or adding boost transformers. The object of the current study is a household-type consumer with 20 A single-phase connection to distribution line with a distance of 2 km to a 20 kV transformer station. The calculated resistance of the power line is 2.8 ohms. The load profile was captured during 5 days in summer and 10 days in winter and was used to calculate the capacity of the grid support equipment. Measurements indicated, that in the worst case 2% of time the voltage was below 10% of nominal and 8% of time – below 5% of it. This is outside of the regulatory limits of EU and national regulations. The experimental setup for a voltage quality improvement system was based on an OutBack Power Radian series grid inverter with 7 kW output power. Battery consisting of 12 V 120 Ah VRLA accumulators wired in 48 V system was used. The inverter was configured to work in grid support mode using battery power when the consumer's active load increased above 1.2 kW. Results showed improvement in voltage quality over the full consumer load range. The total efficiency of the grid support system was 89%. The use of DC bus and batteries allows easy incorporation of renewable energy sources, thus giving the opportunity to scale power and battery capacity of the system. An Additional benefit of using a battery-backed inverter in grid support mode is that consumer can temporarily use more power that is allowed by grid due to its capacity constraints.

Key words: distribution grid, load, voltage quality, inverter efficiency.

INTRODUCTION

Installation of accumulator backed inverters at loads along with 1 kV lines and voltage boosters are one of the possible solutions for improving the quality of electrical energy parameters on long distribution lines. Moreover, an inverter-accumulator based system also serves as a starting point for renewable resource integration. Viability of this approach is further governed by the decrease of power electronic costs (Everts et al., 2010). Besides the technical aspect, which implies compensation of losses in distribution lines there is also an economical aspect. When the high load is necessary only temporarily, it is reasonable to limit grid connection capacity to decrease installation and maintenance costs and use accumulated energy or local resources generated from renewables. In addition, the presence of even limited power grid can improve the

stability of local renewable energy generators (Allik & Annuk, 2017). Also, the ongoing extensive introduction of electric vehicles can affect the stability of the grid itself during peak load hours (Dharmakeerthi et al., 2014; Lillebo et al., 2018). Local microgeneration could solve this problem too (Meyer&Wang, 2018).

The aim of this study was to evaluate technical outcomes of using a grid supporting inverter on long distribution lines with low-quality voltage on the load side.

MATERIALS AND METHODS

The object of the current study is a household-type consumer with 20 A single-phase connection to distribution line with distance 2 km to 20/0.4 kV 100 kVA transformer station. The transformer feeds additional 4 consumer branches connected before object under study, which is placed at the end of the line, AMKA 3x35+50 cable is used for the connection.

In order to evaluate possibilities of voltage quality improvement using existing cable connection and to avoid its reconstruction, grid interactive OutBack Power Radian series inverter GS7048E with 7 kW output power was used. Choice of this inverter was justified by various grid operation options as well as a built-in optional possibility to connect local renewable energy based sources and back-up generator.

The inverter was configured to operate in grid support mode, which implies grid voltage pass-through until a given load power is reached. When it is reached, the inverter begins to augment grid output using energy from batteries. Thus power taken from the grid is restricted to configured value and voltage drop in distribution line is also limited. When the load power drops, grid capacity is used to recharge batteries. Besides of grid support mode additional modes like grid-tie, microgeneration and UPS are available, but those were not covered in the scope of this study. Battery setup consisted of two series with four 12 V VRLA (ABT TM12-535W) accumulators in series forming a 48 V 240 Ah battery bank. It should also be noted, that when operating GS7048E in grid support mode power is passed-through the inverter, therefore fast transients and flickering in the grid may remain on the load side. Installation of inverter was performed according to connection schematics in Fig. 1.

Voltage relay QS1 is controlling relays QK1 and QK2 used to disable inverter, if there is no grid input to be sure, that only grid-support functionality is tested. The input is protected by a C16 breaker (S1). Three-phase model was already installed at the consumer and was not changed during tests. Fig. 1 also shows the location of the voltage and current sensor probes, signals from which are described in detail in Table 1.

Fig. 2 shows the overall setup after the installation of the inverter. Power distribution and control devices are in separate compartments from the batteries. The compartment with the energy meter is not shown here. A dedicated earthing circuit was installed for all components of the setup.

Measurements of electrical energy quality were performed both before and after installation of the grid support inverter. Prior measurements were performed in two periods: in summer July 5-10, 2017 (120 hours) and in winter February 2-10, 2018 (250 hours). The average hourly temperature for July was +10 to +22 °C and -4 to -6 °C for February. The measurements after adding the grid support inverter were performed from September 24 to October 7, 2018 (370 hours).
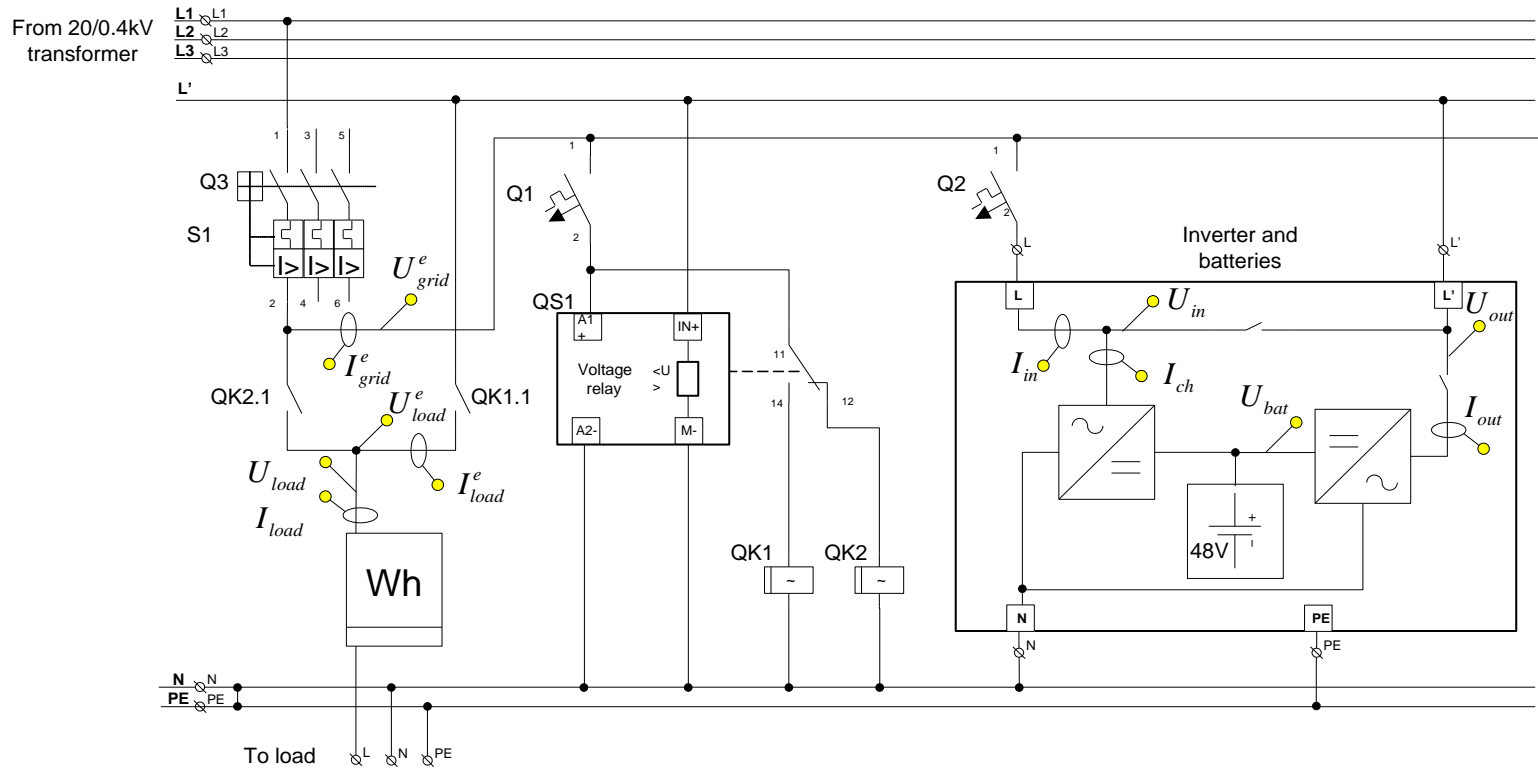
Figure 1. Inverter connection and measurement points.

Advangid GridLink data logger was used at the client's load side right before the energy meter in both measurement periods and it's data was used to compare the voltage characteristics before and after the installation of the inverter. Whereas ELSPEC G-4500 logger measured the voltage quality both before and after inverter only on the last period of the investigation. Additional battery charging related data was acquired by using an OutBack Power Radian system controller Mate3.

The studied object is a typical household, and it was not possible to have a controlled load graph, so there could be some differences in load power graphs between measurement periods, but they were partly mitigated by statistical data.

Figure 2. Inverter and batteries in their compartments.

Table 1. Summary of measured signals and calculated variables

Signal	Unit	Source (instrument or calculation)	Measure step, s	Description
U^e_{grid}	V	ELSPEC G-4500	1	Grid voltage
I^e_{grid}	A		1	Grid current
P^e_{grid}	W		1	Grid power (grid probes)
U^e_{load}	V		1	Load voltage
I^e_{load}	A		1	Load current
P^e_{load}	W		1	Load real power (load probes)
U_{load}	V	Advangid GridLink	5	Load voltage
I_{load}	A		5	Load current
U_{in}	V	Outback Mate3	1	Inverter input voltage
I_{in}	A		1	Inverter input current
I_{ch}	A		1	Charger input current (at 230 V side)
U_{bat}	V		1	Batery voltage
U_{out}	V		1	Inverter output voltage
I_{out}	A		1	Inverter output current
S_{load}	W	$S_{load}=U_{load} \cdot I_{load}$	-	Load apparent power
E_{grid}	kWh	$E_{grid} = \dfrac{\sum P_{grid}}{7.2 \cdot 10^5}$	-	Energy taken from grid
E_{load}	Wh	$E_{load} = \dfrac{\sum P_{load}}{7.2 \cdot 10^5}$	-	Energy supplied to load
P_{ch}	kW	$P_{ch}=U_{in} \cdot I_{ch}$	-	Battery charging power (at 230 V side)
P_{disch}	kW	$P_{disch}=U_{out} \cdot I_{out}$	-	Battery discharging power (at 230 V side)
E_{ch}	kWh	$E_{ch} = \dfrac{\sum P_{ch}}{7.2 \cdot 10^5}$	-	Total charging energy
E_{disch}	kWh	$E_{disch} = \dfrac{\sum P_{disch}}{7.2 \cdot 10^5}$	-	Total discharging energy

The measured signals are summarized in Table 1. For all AC signals, the average RMS values were recorded in each measurement step. The measurement interval of 5 s (limited by Advangid GridLink) was used for all instruments and data was merged in a single table by the timestamp of each instrument. Due to 5 s power to energy conversion coefficient in calculations was $7.2 \cdot 10^{-5}$.

Data processing was performed using R statistics software (R Core Team, 2017). Obtained data from prior measurements without a grid support inverter was used to calculate necessary energy for compensating grid to bring voltage to a client within defined minimum limits according to (LVS EN 50160, 2010). The standard states, that the 10 min mean RMS voltage at a client-side should be within -15% to +10% limits of nominal 230 V at all times and should not exceed ±10% limits no more than 95% of weekly measurements.

The compensated energy for the current object was calculated from the measurement data as losses in the distribution lines knowing it's resistance and assuming only a resistive load (1). The distribution line resistance was obtained from an UI scatter plot using linear regression.

$$E_{\text{comp}(1)} = \frac{T_m \sum P_{\text{comp}}}{7.2 \cdot 10^5} = \frac{T_m \sum I^2_{\text{load}<\text{Umin}} R_{\text{line}}}{7.2 \cdot 10^5}, \text{kWh} \qquad (1)$$

where T_m – measurement period, s; P_{comp} – compensation power, W; $I_{load<Umin}$ – load current, when the voltage is below limit in the measurement data, A; R_{line} – distribution line resistance, Ω.

This is the precise compensation scenario when the inverter for compensating voltage fluctuations can follow all voltage changes and respond accordingly. Additionally compensation energy was calculated for a scenario, when the inverter starts to augment the grid only when the load current exceeds a given value (2).

$$E_{\text{comp}(2)} = \frac{T_m \sum P_{\text{comp}}}{7.2 \cdot 10^5} = \frac{T_m \sum (I_{\text{load}>\text{I}'} - I') U_{\text{load}}}{7.2 \cdot 10^5}, \text{kWh} \qquad (2)$$

where I' – current limit to be taken from grid, A.

RESULTS AND DISCUSSION

Measurement results without a grid support inverter are summarized in Figs 3, 4 and Table 2. The current grid connection does not meet LVS EN 50160 as -15% is violated in July measurements, but -10% limit is reached in 2.09 % of measurements in July and 0.32 – in February. Additionally, calculations were performed for more strict 7% and 5% tolerances.

Unconformity to standard is minimal, however, the UI scatter plot shows, that the voltage drop due to distribution line resistance will result in voltages out of limits with load currents between 15 and 20 A almost at all times. Therefore this could lead to more severe unconformities to standard on higher load scenarios. Moreover low distribution line capacity results in voltage fluctuations when there is small or no load due to load changes in other line branches. This can be seen as horizontal lines at currents approximately 3.5, 5 and 10 A. Such voltage changes could be introduced by constant power loads (e.g. switching PSUs).
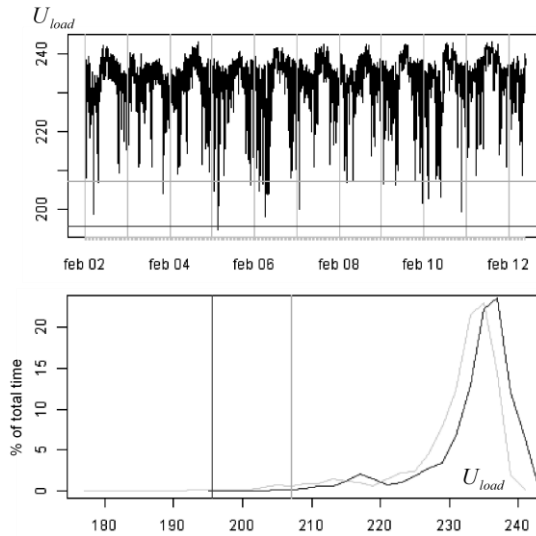
Figure 3. Load voltage time series (February 2018) and histogram (light gray – July 2017, dark gray – February 2018) of measurements without grid support inverter, dark gray vertical line – 15% tolerance, light gray vertical line – 10% tolerance.
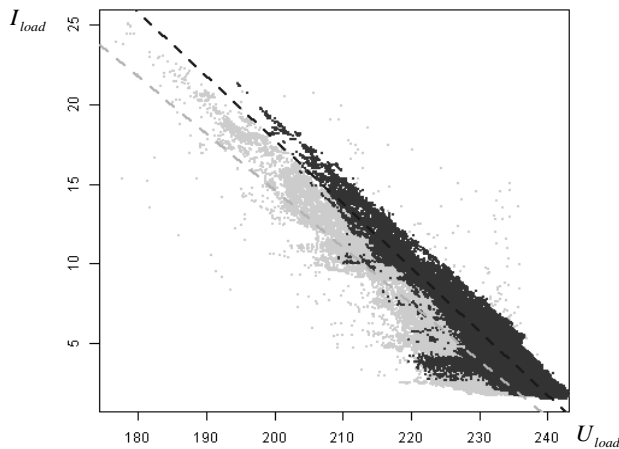
Figure 4. Voltage drop depending on current: light gray – July 2017, dark gray – February 2018.

Line resistance was calculated by adding linear regression lines to the UI scatter plot. For July it was 2.8 Ω, for February – 2.5 Ω. The average temperature difference between the measurement periods was 20 ºC, which was the main source of resistance difference as the temperature coefficient of copper is 0.393% per °C. The theoretical calculations using this temperature coefficient taking winter's 2.5 Ω as 100% will give 2.7 Ω in summer, which is 0.1 Ω less than the data obtained from measurement statistics shows. As it can be seen from Table 2, the resistance increase results in a increase of compensation energy $E_{comp(1)}$ necessary to keep the load side voltage within limits. Interesting to note, that seasonal effect has significant impact on necessary compensation energy. In winter $E_{comp(1)}$ is decreased by 42% for -5% limit and more than 90% for -15% limit.

1160

In the case of the current limiting scenario (Table 3, 5 A row is highlighted as actual inverter setting in grid support test) the tendency is the same: when increasing the current limit from the grid, thus decrease the necessary hourly average compensation energy and in winter the conditions for energy requirements are smaller.

However at smaller current limits from the grid (increased need to compensate energy) the situation is the opposite. This could be explained by current measurement errors at smaller loads and by differences in load scenarios between winter and summer.

Table 2. Allowable load voltage *Uload* variation, percent of time, when the limit is exceeded and calculated energy necessary to compensate voltage variations during all period *Ecomp*(1) and hourly average *Ecomp*(1)avg

K_{Utol}, %	U_{min}, V	U_{max}, V	K_{U-}, %	K_{U+}, %	$E_{comp(1)}$, kWh	$E_{comp(1)}^{avg}$, kWh
July 5–10, 2017 (120 hours)						
5	218.5	241.5	7.92	0.00	3.942	0.033
7	213.9	246.1	5.43	0.00	3.152	0.026
10	207.0	253.0	2.09	0.00	1.666	0.014
15	195.5	264.5	0.29	0.00	0.357	0.003
February 2–10, 2018 (250 hours)						
5	218.5	241.5	5.19	1.34	5.123	0.020
7	213.9	246.1	1.65	0.00	2.192	0.009
10	207.0	253.0	0.32	0.00	0.594	0.002
15	195.5	264.5	0.00	0.00	0.008	0.000

Nevertheless, this can serve as an additional argument for the successful use of photovoltaic microgeneration for voltage loss compensation in distribution grids. As in Northern Europe, the conditions available to produce energy between seasons vary around yearly average from -95% in winter to 110% in summer (Šúri et al., 2007).

The measurement results with a grid support inverter installed are presented in Figs 5 and 6. The inverter was configured to operate in a grid support mode with a current limit from grid 5 A. The value was chosen graphically from the UI scatter plot (Fig. 4) for a nominal voltage of 230 V.

Table 3. Compensation energy calculation results for grid current limiting scenario during all period $E_{comp(2)}$ and hourly average $E_{comp(2)}^{avg}$

Grid limiting current I', A	July 5-10, 2017 (120 hours)		February 2-10, 2018 (250 hours)	
	$E_{comp(2)}$, kWh	$E_{comp(2)}^{avg}$, kWh	$E_{comp(2)}$, kWh	$E_{comp(2)}^{avg}$, kWh
3	27.589	0.230	82.046	0.328
5	**15.995**	**0.133**	**38.659**	**0.155**
7	9.964	0.083	20.739	0.083
10	3.911	0.033	7.058	0.028

It can be clearly seen from the time series and voltage histogram, that -15% and -10% limits are met in this case (Fig. 5). The UI scatter plot (Fig. 6) in its turn shows a non-linear behavior as the voltage drop on the distribution line is mitigated by the inverter.
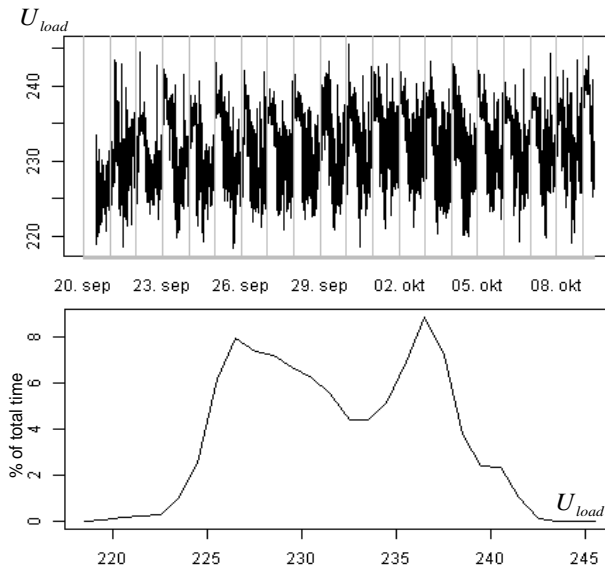
Figure 5. Load voltage time series and histogram of measurements after installation of grid support inverter.
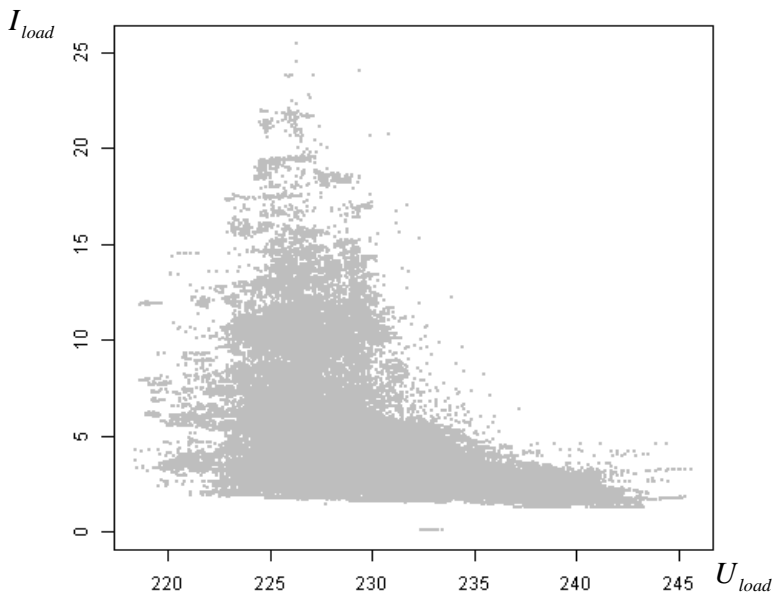
Figure 6. Voltage drop depending on current after installation of the grid support inverter.

The dynamics of energy drawn from grid and fed to the load as well as energy used to charge the battery and the energy taken from the battery during the measurement period are given in Fig. 7. The overall efficiency of the system was calculated from total energies (E_{load}/E_{grid}) and was 89%. It is affected by the inverter efficiency, the battery and it's charger's efficiency. The battery efficiency (E_{dich}/E_{ch}) was 63%. As the battery is

the main source of power loss (affected by discharge rate and depth, age and temperature), the total system efficiency will increase if the battery usage is minimized.
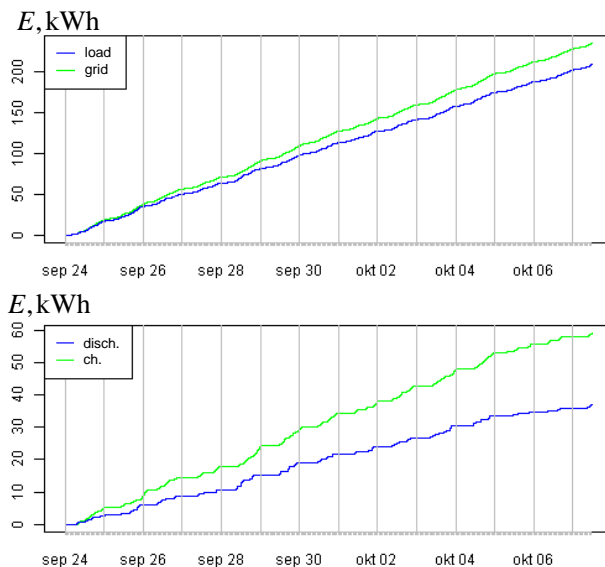
Figure 7. Cumulative charts of energy taken from the grid and supplied to the load (top) and battery charge and discharge energy (bottom).

The total energy taken from the batteries during the 370 hour test period was 36.81 kWh. It resulted in an hourly average of 0.099 kWh of grid compensation energy. It was smaller than the theoretically calculated hourly average of 0.133 kWh in summer conditions (see Table 3).

CONCLUSIONS

Adding a grid support inverter resulted in voltage levels above the -5% limit of nominal voltage in all measurements in an 370 hour period, which fully meets the standard requirements.

The overall efficiency of the GS7048E grid support inverter was 89 %, but the efficiency of the batteries was 63 %.

A grid support inverter can be used from a technical point of view on long distribution lines to increase the available power and from an economical point of view to decrease the necessary grid connection current, when high power consumers are used only occasionally.

The decrease of losses in the winter season due to changes of ambient temperature can serve as an additional factor for the successful use of photovoltaic microgeneration for voltage loss compensation in distribution grids. In Northern Europe, the conditions for PV output between seasons can vary significantly, but the necessary grid support energy to keep the voltage within limits for typical a household consumer in winter's negative temperatures can be significantly smaller.

Further research at this point can be conducted in two main directions: reliability of the system in winter conditions and use of short-term storage technologies (e.g. supercapacitor banks) to extend the lifespan of chemical batteries.

REFERENCES

Allik, A. & Annuk, A. 2017. Transient processes in small scale autonomous photovoltaic and wind power systems. In *2017 IEEE 6th International Conference on Renewable Energy Research and Applications (ICRERA)* (pp. 159–163). https://doi.org/10.1109/ICRERA.2017.8191259

Dharmakeerthi, C. H., Mithulananthan, N. & Saha, T.K. (2014). Impact of electric vehicle fast charging on power system voltage stability. *International Journal of Electrical Power and Energy Systems*. https://doi.org/10.1016/j.ijepes.2013.12.005

Everts, J., Das, J., Van den Keybus, J., Germain, M. & Driesen, J. 2010. GaN-Based Power Transistors for Future Power Electronic Converters. In *Proceedings of the IEEE Benelux Young Researchers Symposium on Smart Sustainable Power Delivery (YRS 2010), 29-30 March, Leuven, Belgium*.

Lillebo, M., Zaferanlouei, S., Zecchino, A. & Farahmand, H. 2018. Impact of Large-Scale EV Integration and Fast Chargers in a Norwegian LV Grid. In *7th International Conference on Renewable Power Generation*. https://doi.org/10.1016/j.obhdp.2006.08.003

LVS EN 50160 Voltage characteristics of public voltage distribution grid. 2010.

Meyer, D. & Wang, J. 2018. Integrating ultra-fast charging stations within the power grids of smart cities: a review. *IET Smart Grid*, **1**(1), 3–10. https://doi.org/10.1049/iet-stg.2018.0006

R Core Team. 2017. R: A Language and Environment for Statistical Computing. Vienna, Austria. Retrieved from https://www.r-project.org/

Šúri, M., Huld, T. A., Dunlop, E.D. & Ossenbrink, H.A. 2007. Potential of solar electricity generation in the European Union member states and candidate countries. *Solar Energy*. https://doi.org/10.1016/j.solener.2006.12.007

Exhaust particle number of a non-road diesel engine fuelled by methyl esters with different fatty acid compositions

T. Ovaska[*], S. Niemi, K. Sirviö and O. Nilsson

University of Vaasa, School of Technology and Innovations, P.O. Box 700, FI-65101 Vaasa, Finland
[*]Correspondence: teemu.ovaska@univaasa.fi

Abstract. The main aim of this study was to find out how methyl esters with different fatty acid compositions affect the exhaust particle numbers. Along with fossil diesel fuel oil (DFO) and renewable diesel (HVO), a high-speed non-road diesel engine was fuelled by rapeseed (RME) and soybean (SME) methyl esters. Particle numbers within the size range of 5.6–560 nm were measured by means of an engine exhaust particle sizer (EEPS). The exhaust smoke, gaseous emissions and the basic engine performance were also determined. During the measurements, the 4-cylinder, turbocharged, intercooled engine was run according to the non-road steady cycle. Methyl esters reduced particles within the size range of 70 to 200 nm. For RME and SME, both positive and significant correlations were found between the sum of the particle numbers detected above the size category of 23 nm and methyl palmitate (C16:0), methyl stearate (C18:0) and methyl linoleate (C18:2) contents at 10% load at rated speed. In terms of nitrogen oxide (NO_x) and hydrocarbon (HC) emissions, HVO was beneficial while carbon monoxide (CO) emission was the lowest with DFO. The level in smoke emission was negligible.

Key words: diesel engine, particle number, methyl ester, fatty acid composition.

INTRODUCTION

The European Parliament and of the Council promoted the use of energy from renewable sources by setting the renewable energy directive in 2009. For the transport sector, the sub-target of the directive was that 10% of the fuels are from renewable sources by 2020 (Directive 2009/28/EC). In order to meet this target, the Fatty Acid Methyl Esters (FAME) has been widely used in EU as a blending component with fossil diesel fuel oil (DFO) during the past 10 years. Furthermore, the use of FAME in cultivation, transportation and distribution machineries is seen as an option for the improvement of the life cycle based greenhouse gas (GHG) balances of FAME (Jungmeier et al., 2016).

Diesel engine exhaust particles form the size distribution with two distinctive particle modes; accumulation mode and nucleation mode. The particle mean diameters in nucleation mode are under 50 nm, whereas the mean diameter range in accumulation mode is 50–500 nm (Kittelson, 1998; Rönkkö et al., 2006; Rönkkö et al., 2007; Filippo & Maricq, 2008; Lähde et al., 2010). Nucleation mode includes the particles which are believed to form during dilution when the exhaust gas gets mix up with the ambient air. Accumulation mode is thought to consist mainly of the agglomerated carbon soot

particles which result from the incomplete burning of either the fuel or the lubricating oil remnants inside the cylinder (Kittelson et al., 1999; Rönkkö et al., 2007; Nousiainen et al., 2013). Soot formation can be enhanced by improving soot oxidation (Wang et al., 2016b).

FAME fuels contain fatty acids with different lengths of molecule chains. As the molecule chain shortens, relative amount of oxygen increase in the chain. Soot oxidation improves (Pinzi et al., 2013; Barrientos et al., 2015). Moreover, the different fatty acids have divergent number of carbon–carbon double bonds in the chemical structure of FAME. Saturated fatty acids do not have double bonds while unsaturated have one or more. The less the fraction of unsaturated fatty acids the lower the soot precursors resulted from FAME fuel combustion (Zhu et al., 2016; Wang et al., 2016b).

Schönborn et al. (2009) studied the combustion behaviour of pure individual fatty acid alcohol ester molecules in a single-cylinder research engine. As a one result, particulate mass was detected to increase as the length of ester molecule was increased. They gave reason for the increased mass by means of particle numbers. Unsaturated fatty ester molecules produced more particles in the diameter range of about 40 and 200 nm compared to diesel fuel. In the study of Pinzi et al. (2013), particulate mass was increased as chain length of methyl ester was increased.

This paper presents how methyl esters with different fatty acid compositions affected the exhaust particle numbers. Along with fossil diesel fuel oil (DFO) and renewable diesel (HVO), a high-speed non-road diesel engine was fuelled by rapeseed (RME) and soybean (SME) methyl esters. Alongside the exhaust gas particle number and size distributions, the exhaust smoke, gaseous emissions and basic engine performance were determined. The high-speed off-road diesel engine was driven according to the non-road steady cycle (NRSC). During the experiments, no parameter optimization was applied with the studied fuels.

MATERIALS AND METHODS

The experimental measurements were performed by the University of Vaasa at the engine laboratory of the Technobothnia Research Centre in Vaasa, Finland.

Engine

The 4-cylinder test engine was a turbocharged, intercooled (air-to-water) off-road diesel engine, equipped with a common-rail fuel injection system. The engine had no exhaust gas after treatment. The main engine specification is given in Table 1.

Table 1. Main engine specification

Engine	AGCO POWER 44 AWI
Cylinder number	4
Bore (mm)	108
Stroke (mm)	120
Swept volume (dm^3)	4.4
Rated speed (rpm)	2,200
Rated power (kW)	101
Maximum torque with rated speed (Nm)	455*
Maximum torque with 1,500 rpm (Nm)	583*

*conformable to measured torques obtained with DFO fuel.

Fuels

The effects of rapeseed methyl ester (RME), soybean methyl ester (SME), and hydrotreated vegetable oil (HVO) on the exhaust gas particles were investigated along

with commercial low-sulphur diesel fuel oil (DFO). The fuel specifications are in Table 2. RME and SME fulfilled the requirements of EN14214 standard. DFO was used as the reference fuel, completely fulfilling the fuel standard EN590. For DFO, the lower heating value (MJ L^{-1}) was based on the information received from the fuel supplier. The unit conversion from MJ l^{-1} to MJ kg^{-1} was calculated. The lower heating values of RME, SME and HVO were computed based on the elementary analyses of fuels (Mollenhauer & Schreiner, 2010).

Table 2. Fuel specifications

Parameter	Method	DFO	RME	SME	HVO	Unit
Cetane number	ASTM D6890	-	53.5	47.3	74.7	-
Density (15 °C)	EN ISO 12185	834	883	885	779	kg m^{-3}
Sulfur content	EN ISO 20846	3.6	-	-	< 1	mg kg^{-1}
	ASTM D7039	-	< 2	3	-	mg kg^{-1}
Carbon content	ASTM D5291	-	77.4	77.0	84.2	wt.-%
Hydrogen content	ASTM D5291	-	12.2	11.9	15.1	w.t-%
Nitrogen content	ASTM D5291	-	< 0.2	< 0.2	-	wt.-%
Water content	EN ISO 12937	-	132	353	19	mg kg^{-1}
Kin. viscosity (40 °C)	Fuel supplier's info	-	4.5	4.1	2.9	mm^2 s^{-1}
Lower heating value	Fuel supplier's info	36.0*	-	-	-	MJ L^{-1}
	By calculating	43.2	37.7	37.2	43.8	MJ kg^{-1}

*(Teboil, 2019).

Any parameter optimization was not made with the studied fuels. The engine lubricant was the development product of the supplier. The fatty acid composition of RME and SME were analysed, Table 3.

Analytical instruments
The particles from a size range of 5.6 to 560 nm were recorded by using the engine exhaust particle sizer (EEPS). The adopted measurement instruments for gaseous emissions and air mass flow rate are also listed in Table 4.

Before the measurements, the analysers were calibrated manually once a day according to the instructions of the instrument manufacturers. For the EEPS, the sample flow rate was adjusted at 5.0 L min^{-1}, and the 'SOOT' inversion was applied in the data processing (Wang et al., 2016a). The arrangement of the test bench and measurement devices is seen in Fig. 1.

Table 3. Fatty acid compositions for RME and SME

Methyl ester	RME %	SME %
10:0	< 0.1	-
12:0	-	0.1
14:0	< 0.1	0.1
16:0	4.5	11.2
16:1 cis	0.4	0.1
17:0	< 0.1	0.1
17:1	0.2	0.1
18:0	1.6	4.4
18:1 cis	61	21.8
18:2 konj.	-	< 0.1
18:2 n-6 cis	19.3	52.9
18:3 n-3 cis (ALA)	9.9	7.6
20:0	0.6	0.3
20:1	1.3	0.2
20:2 n-6 cis	0.1	0.1
22:0	0.3	0.3
22:1 n-9 cis	0.3	0.1
24:0	0.1	0.1
24:1	0.2	-
Saturated fatty acids total	7.1	16.7
Monounsaturated fatty acids total	63.3	22.3
Polyunsaturated fatty acids total	29.3	60.5
Iodine number	113.8	130.8

Table 4. Measuring equipment for gaseous emissions and intake air

Parameter	Device	Technology
Particle number and size distribution	TSI EEPS 3090	spectrometer
Hydrocarbons	J.U.M. VE7	HFID
Smoke	AVL 415 S	optical filter
NO_x, CO, CO_2, O_2	TSI CA-6203 CA-CALC	electrochemical
NO_x, λ	WDO UniNO$_x$ sensors	ZrO_2-based multilayer
O_2	Siemens Oxymat 61	paramagnetic
Air mass flow rate	ABB Sensyflow P	thermal mass

During the measurements, the exhaust gas sample was diluted at two stages in order to decrease the particle concentration of the sample for the EEPS. The sample was first diluted with ambient air by means of the porous tube diluter (PTD, Ntziachristos et al., 2004). Then, the sample was led through the secondary dilution, which was performed with Dekati ejector diluter. The total dilution ratio of exhaust sample was determined by simultaneously measuring CO_2 concentration before and after the dilution stages. The particle sampling system was provided by Tampere University. This study was a part of the larger measurement campaigns and emission data acquirement. In the studies of Karjalainen et al. (2014) and Alanen et al. (2017), the above-mentioned dilution devices were also used upstream of the EEPS. However, a thermodenuder was not employed in this study (An et al., 2007).
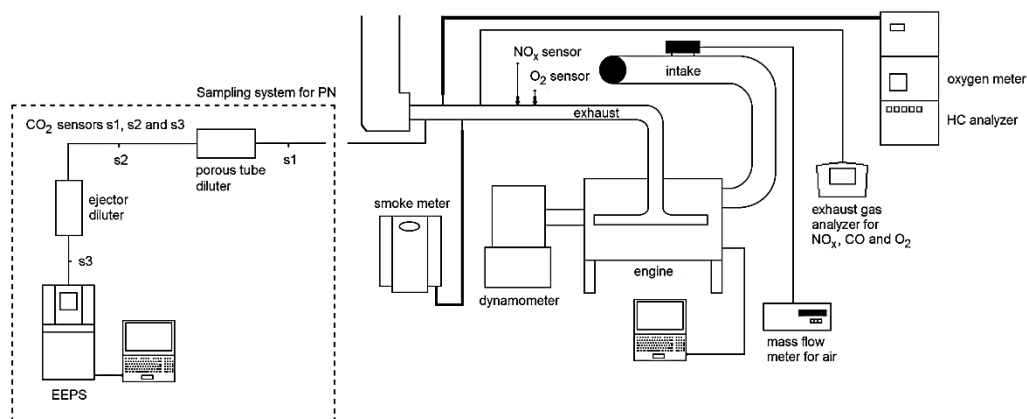
Figure 1. Experimental set-up.

The particle number (PN) was recorded consecutively three times. Each recording was one-minute long. The averaging interval of 2 seconds was used when the data was stored. The uncertainty of the PN measurement was approximated by calculating the standard deviation of the PN averages, taken from each one-minute recording.

Total particle numbers (TPN, from 5.6 to 560 nm) were calculated from the PN recordings by adding up the PN concentrations indicated in the size bins of the EEPS spectrometer during the one averaging interval. For the presented results of this paper, the average of PN sums was calculated. Moreover, the averages of the normalized PN concentrations ($dN/d\log D_p$) were calculated from each bin in order to illustrate the particle size distributions.

Based on the measured CO_2 concentrations before and after the dilution stages, the dilution ratios were calculated both for the porous type diluter (DR_{PTD}) as in (1) and for the ejector diluter ($DR_{ejector}$) as in (2). Then, the total dilution ratio (DR_{tot}) was calculated as in (3).

$$DR_{PTD} = \frac{(CO_2)_{s1} - (CO_2)_{bg}}{(CO_2)_{s2} - (CO_2)_{bg}} \qquad (1)$$

$(CO_2)_{s1}$ and $(CO_2)_{s2}$ are the CO_2 concentrations of raw exhaust and diluted exhaust after first dilution stage, respectively. $(CO_2)_{bg}$ is the ambient CO_2 concentration.

$$DR_{ejector} = \frac{(CO_2)_{s2} - (CO_2)_{bg}}{(CO_2)_{s3} - (CO_2)_{bg}} \qquad (2)$$

$(CO_2)_{s3}$ is the CO_2 concentration after the dilution stages before the EEPS.

$$DR_{tot} = DR_{PTD} \cdot DR_{ejector} \qquad (3)$$

The calculated TPN averages and the averages of the normalized PN concentrations were multiplied by the DR_{tot} of the exhaust sample in order to present the corresponding concentrations in the raw exhaust.

However, no consistent conclusions could be drawn concerning the particle numbers under the size category of 20 nm due to the following reasons. Firstly, mobility particle size spectrometers, as EEPS, have been found to be best for the measurement of the particle numbers within the size range of 20–200 nm (Wiedensohler et al., 2012). Outside this size range, the elevated uncertainties may exist as described by Wiedensohler et al. (2018). Secondly, the nucleation mode formation has been reported to be sensitive not only to the engine parameters (Lähde et al., 2011), fuel and lubricating oil characteristics (Vaaraslahti et al., 2005), and exhaust after-treatment (Maricq et al., 2002), but also to dilution conditions such as dilution ratio, temperature and relative humidity of the dilution air (Mathis et al., 2004). On the other hand, Rönkkö et al. (2007) reported that its formation was insensitive to the fuel sulphur content, dilution air temperature, and relative humidity of ambient air.

The recorded particle numbers below 23 nm were omitted due to the two reasons. The first reason was the uncertainties related to the complex nature of nucleation mode PN and the PN measurement by means of EEPS under the size category of 20 nm. The second reason was the PN legislation which limits the particle number from the size of 23 nm on. Thus, the calculated TPN was divided into two categories depending on how many of the particles out of the average TPN were below or above the size category of 23 nm.

The authors of this paper believe the nucleation mode formation could be avoided if a thermodenuder is employed during the PN measurement (An et al., 2007). According to Vaaraslahti et al. (2004), the nucleation mode evaporates completely when an exhaust sample is heated enough.

The recorded smoke value was the average of three consecutively measured smoke numbers.

The sensor data were collected and the engine control parameters were followed via engine management software, provided by the engine manufacturer. By using the software, the temperatures of cooling water, intake air and exhaust gas plus the pressures of the intake air and exhaust gas were recorded.

Based on the measured hydrocarbon (HC), nitrogen oxides (NO_x) and carbon monoxide (CO) concentrations, the brake specific emissions of HC, NO_x and CO were calculated according to the ISO 8178 standard.

Experimental matrix and running procedure

The measurements were conducted according to the test cycle C1 of the ISO 8178-4 standard, known as the non-road steady cycle (NRSC) (ISO 8178-4:2017, 2017). The rated speed of the engine was 2,200 rpm and the intermediate speed was chosen to be 1,500 rpm. At full load, the maximum torque was 410 nm at rated speed and 525 nm at intermediate speed. The test engine was installed in a test bed and loaded by means of an eddy-current dynamometer of model Horiba WT300.

Each day before the measurements, the intake air temperature was adjusted at 50 °C downstream the charge air cooler when the engine was run at full load at rated speed. The temperature was controlled manually by regulating cooling water flow to the heat exchanger. After this initial adjustment, the temperature was allowed to change with engine load and speed. The engine was then run according to the NRSC cycle for the measurements.

Before the recordings at each load point, it was waited that the engine had stabilized, the criteria being that the temperatures of coolant water, intake air and exhaust were stable. The length of the measurement period was not tied to a certain time apart from the particle mass collection.

All measurement values were recorded once at each load point of the cycle. The particle number and size distribution were recorded continuously at each load point. For each fuel, the engine warm up and measurements were performed in an exactly similar way.

The original target was to keep the engine injection parameters constant for all fuels. Due to the lower heating values, the injection rate had, however, to be raised at full loads when the engine was run with the methyl esters. Pre-, main, and post-injections were used for the fuel injection. The upper limits of the total injection rates were changed in the electronic control unit of the engine by means of the WinEEM4 program.

The control system enabled the shift of injection quantity within the entire full load (ultimate torque) curve, Fig. 2. For RME and SME, the required increases in the injection rates were from 95 mg to 100 mg at 1,400 rpm and at 1,500 rpm. With these increases, a proper shape of the injection rate curve could be maintained. For all fuels, the position of the limited injection was also moved from 2,200 rpm to 2,250 rpm.

Fig. 3, a and 3, b show the shares of the pre-, main, and post-injection rates at the load points of the NRSC cycle. For the methyl
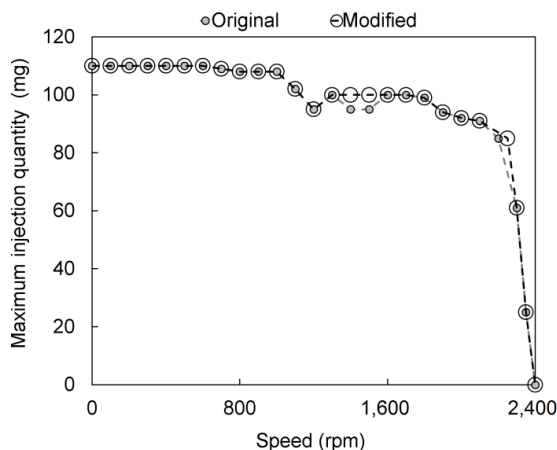
Figure 2. Upper limits of total injection rates at engine operation area.

esters, the main injection rates were higher than for DFO or HVO since the lower heating value of the esters were lower than those of DFO and HVO.
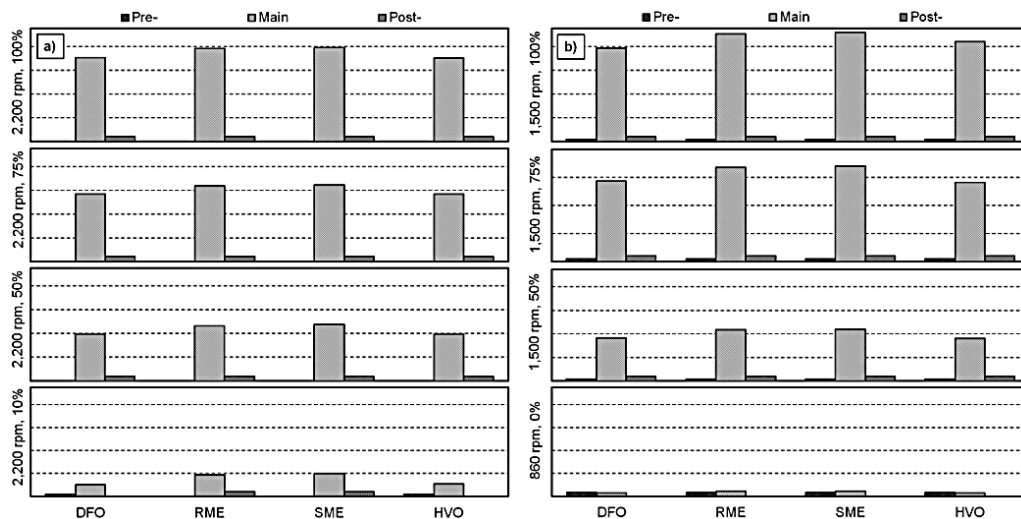
Figure 3. The shares of the pre-, main, and post-injection rates a) at 2,200 rpm and b) at 1,500 rpm and at idle.

RESULTS AND DISCUSSION

Particle size distributions

Due to the uncertainties related to the particle number measurement under the size category of 20 nm and the legislative limitation of PN from the size of 23 nm on, Figs. 4–6 illustrate the detected size distributions between 23 nm and 560 nm. Irrespective of fuel, the detected particles larger than 200 nm accounted for less than 1% of the particles larger than 23 nm in this study. Below, the distributions are examined more thoroughly at certain loads.

Fig. 4 shows the particle size distributions at 75% load at rated speed. Considering the particles

Figure 4. Exhaust particle size distributions from 23 to 560 nm at 75% load at rated speed for different fuels.

above the size category of 23 nm, the detected distributions were quite similar for, on one hand, the methyl esters and, on the other hand, for DFO and HVO. The methyl esters produced less particles above 40 nm compared to DFO and HVO.

For 10% load, the size distributions from 23 to 560 nm are illustrated in Fig. 5. Now, the lowest PN was recorded with HVO and the highest with the methyl esters within the entire size range. The esters emitted considerably higher particle numbers than HVO and DFO.

At idle (Fig. 6), HVO emitted the lowest while the methyl esters the highest PN below the size of 70 nm. The change in order of the fuels was detected above 100 nm. With the methyl esters, the lowest PN was detected from the size of 100 nm on. HVO was particularly favourable within the range of, say, below 50 nm.

Figure 5. Exhaust particle size distributions from 23 to 560 nm at 10% load at rated speed for different fuels.

The physical properties of the liquid fuel tend to control fuel spray characteristics while the fuel composition determines the pathways of chemical reactions during combustion (Eastwood, 2008). Besides the fuel sulphur content, particle formation is also influenced by other fuel characteristics such as the fuel density (Szybist et al., 2007; Bach et al., 2009), viscosity (Mathis et al., 2005; Tsolakis, 2006), cetane number (Li et al., 2014; Alrefaai et al., 2018), and the water content of fuel (Samec et al., 2002).

The current test fuels were practically free of sulphur. Therefore, the effects of sulphur could be assumed as negligible although lube oil contained sulphur. The lube oil consumption is, however, so small that the effects of sulphur compounds were assessed negligible.

Fuel density, viscosity, and compressibility determine the start of injection. After the injection has started, an increased cetane number leads to a shortened ignition delay plus advanced combustion. (Kegl et al., 2013). Higher fuel density and viscosity lead to an advanced

Figure 6. Exhaust particle size distributions from 23 to 560 nm at idle for different fuels.

start of injection. This may be followed by incomplete combustion due to poor fuel atomization. Thus, the soot emission will increase (Nabi et al., 2012).

However, the higher the water concentration in the fuel jet, the more heat is needed to vaporize the water bound by fuel. The heat absorption by water vaporization lowers the surrounding intake air temperature in the engine cylinder. As a consequence, the ignition delay period extends and thus, combustion period shortens (Samec et al., 2002;

Armas et al., 2005). This lowers the peak temperatures in combustion region due to an increase in specific heat of the air-fuel mixture around the propagating flame across the cylinder (Bedford et al., 2000). Furthermore, the vaporization of water releases oxygen which promotes soot oxidation. In this study, however, the water content of both methyl esters was low, and for DFO and HVO, negligible.

At several loads, however, the methyl esters reduced the PN within the size range of 100 to 300 nm most likely due to oxygen bounded in mono-alkyl-ester molecules (Yang et al., 2007; Lapuerta et al., 2008). More complete combustion was enabled and more effective soot oxidation was promoted during the methyl ester usage compared with DFO or HVO.

Earlier studies have also reported how FAMEs, either as neat or as blending components, had a similar decreasing effect on the number of accumulation mode particles (Jung et al., 2006; Heikkilä et al., 2009; Rounce et al., 2012). Moreover, in the study of Hellier et al. (2019), waste date pit methyl ester led to the reduced PN within the size range of 100 to 200 nm compared to fossil diesel. However, they did not detect the corresponding PN reduction with RME or SME.

Above the particle size of 23 nm at 10% load at rated speed and under 70 nm at low idle, HVO showed the most favourable PN results. This was assumed to be caused by the low sulphur content when compared to DFO, and the high cetane number when compared to the methyl esters.

Share and number of particles above 23 nm

Table 5 shows the calculated percentage shares of the particles above the size of 23 nm. At several loads, the share of the particles above 23 nm was below 10%. Irrespective of fuel, the shares greater than 10% were detected at 10% load at rated speed, and at half load at intermediate speed. Furthermore, the share of the particles above 23 nm was above 10% with HVO at full load at rated speed, with DFO at 75% load at intermediate speed, and with RME and SME at idle.

Table 5. The share of particles larger than 23 nm out of the TPN for all fuels at different loads

Speed	Rated				Intermediate			Idle
Load (%)	100	75	50	10	100	75	50	0
PN > 23 nm (%)								
DFO	4.7	5.9	5.8	20	2.5	16	52	2.8
RME	6.9	2.2	6.3	75	2.6	1.9	46	15
SME	1.5	0.9	1.4	83	1.1	0.5	45	11
HVO	16	3.0	2.8	12	1.0	2.9	48	9.4

Fig. 7 presents the sum of detected PN above 23 nm at rated speed. At full load, DFO emitted the lowest PN sum whereas HVO the highest. From 75% to 10% load, HVO emitted the lowest PN sum. The highest PN sum was then detected with either of the methyl esters.

At full load at intermediate speed, DFO emitted the lowest PN sum whereas RME the highest, Fig. 8. But at 75% load, the PN sum was the lowest with SME and the highest with DFO. The sum of detected PN above 23 nm was not varied as much at half load as at the other loads.
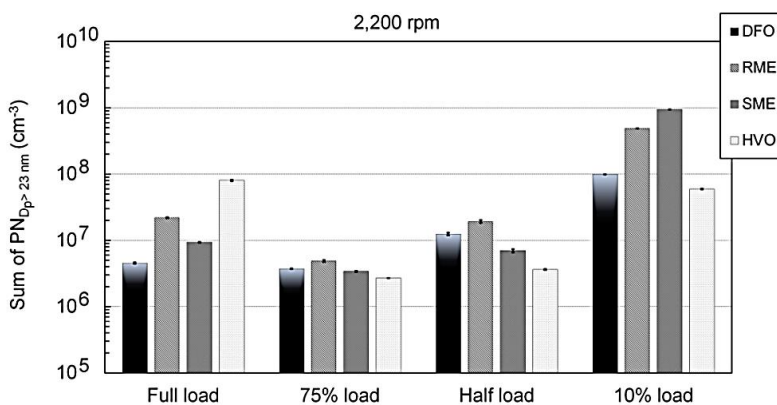
Figure 7. Sum of detected PN above 23 nm at rated speed.
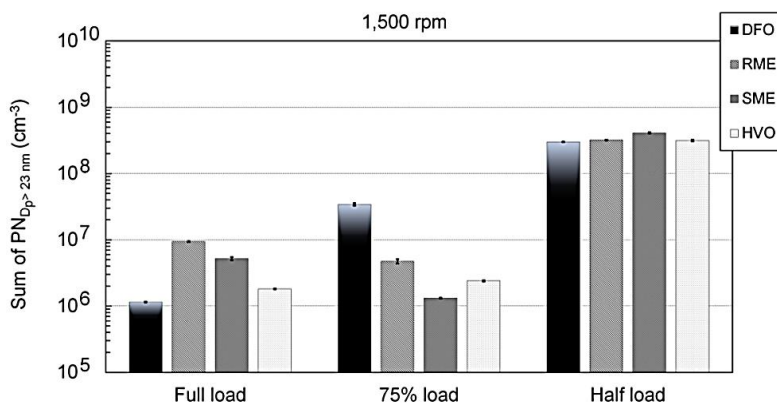
Figure 8. Sum of detected PN above 23 nm at intermediate speed.

For DFO, RME and SME, the sums of detected PN of above 23 nm were compared with the fatty acid compositions of RME and SME. DFO was selected for the comparison, as it did not contain fatty acids. Pearson correlations were calculated in order to find out measures of the strengths of relationships between the percentage shares of fatty acids and the sum of detected PN of above 23 nm. All analysed fatty acids, presented in Table 3, were considered. Moreover, the statistical significance of the correlation was assessed by using the Student's *t-test* under the null hypothesis. Significant correlations were only found between the shares of methyl palmitate (C16:0), methyl stearate (C18:0), methyl linoleate (C18:2), the saturated and the polyunsaturated fatty acids and the sum of detected PN of above 23 nm at 10% load at rated speed, Fig. 9. In this study, significant correlations did not exist at the other load points.

In general, the higher share of C16:0, C18:0, C18:2, the saturated and the polyunsaturated fatty acids, the more particles were detected above the size category of 23 nm. All correlations were both positive and significant at the confidence level of 93%. For the presented interdependences, the values of squared correlation factors were between 0.99–1.0. The calculated significance levels (*p*-values) were between

1174

0.019–0.069. The least squares method was used to the illustrated linear fittings between the data points, Fig. 9.
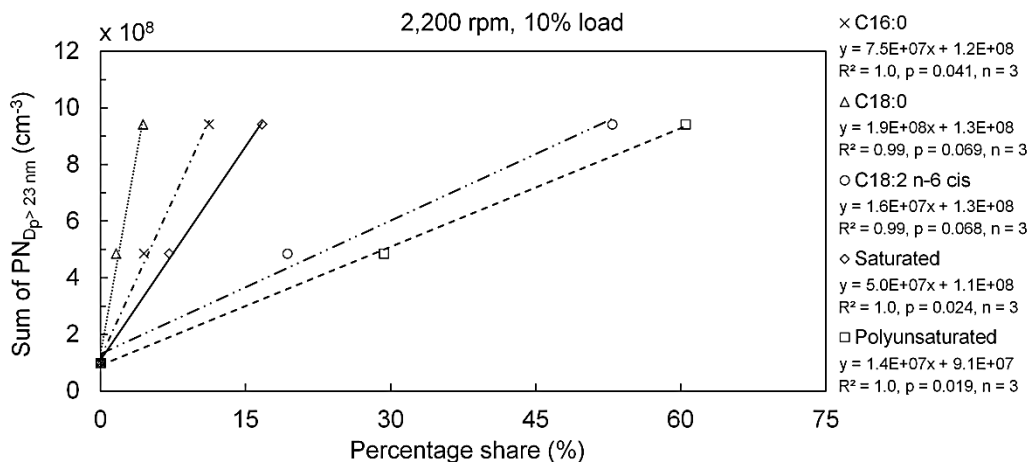
Figure 9. Sum of detected PN above 23 nm of DFO, RME and SME versus the percentage shares of C16:0, C18:0, C18:2), the saturated and the polyunsaturated fatty acids at 10% load at rated speed.

Bünger et al. (2016) found a very strong correlation between polyunsaturated fatty acids and particle mass. They fuelled a heavy-duty diesel engine with four different vegetable oils made from coconut, linseed, palm tree, and rapeseed.

Gaseous emissions and smoke

Generally, HVO was beneficial in terms of hydrocarbon (HC) and nitrogen oxide (NO_x) emissions, Table 6. Carbon monoxide (CO) emission was the lowest with DFO. The combined HC emission varied between 0.13–0.52 g kWh^{-1}. The smallest emissions, calculated all along the whole cycle, were created when HVO was used. The greatest emissions were emitted by SME.

Table 6. Cycle-weighted brake specific emissions of HC, NO_x and CO and smoke number ranges from lowest to highest within the NRSC cycle with different fuels

	HC (g kWh^{-1})	NO_x (g kWh^{-1})	CO (g kWh^{-1})	Smoke (FSN)
DFO	0.19	8.8	0.61	0.006–0.062
RME	0.38	10.0	1.55	0.005–0.012
SME	0.52	10.0	2.05	0.006–0.019
HVO	0.13	8.4	1.34	0.011–0.032

In the study of Niemi et al. (2016), the experimental setup was exactly the same when only the HC measurement is considered. For comparison, the cycle-weighted brake specific emission of HC was then 0.18 g. kWh^{-1} when DFO was used as fuel.

The less unburned HC available after fuel combustion, the smaller the likelihood that gaseous HC species affect the nanoparticle growth by condensation during the exhaust gas dilution and cooling processes (Kittelson, 1998; Khalek et al., 2000; Northrop et al., 2011).

Combined NO$_x$ emissions varied between 8.6–10. g kWh^{-1}. The smallest NO$_x$ emissions were created when HVO was used. The greatest NO$_x$ emissions were emitted by RME. The difference between RME and SME was negligible. The combined CO emission varied between 0.61–2.04 g kWh^{-1}. The greatest emissions were produced by SME.

The level in smoke emission was negligible. If the test engine were a part of a typical agricultural powertrain instead of the laboratory use, it would have been equipped with an SCR catalyst. Therefore, the test engine had been tuned to the high NO$_x$, which caused, most likely, a decreasing effect on smoke.

Performance

The fuel conversion efficiency of the engine is presented in Figs 10 and 11 for the studied fuels at the speeds of 2,200 rpm and 1,500 rpm. The efficiencies were almost equal with the fuels.
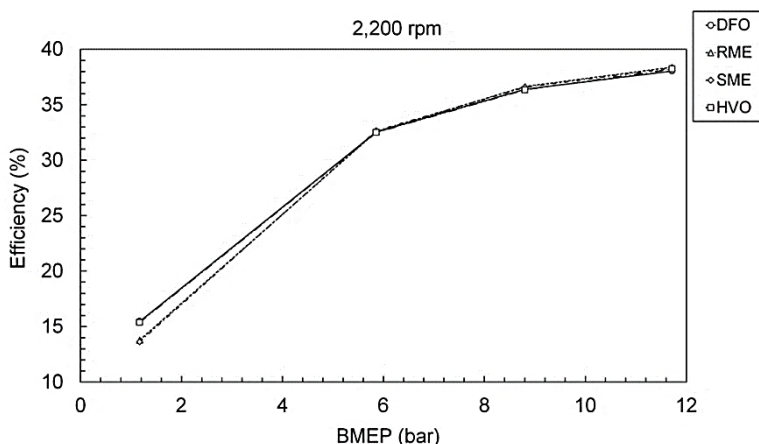
Figure 10. Engine efficiency against engine load at 2,200 rpm with the studied fuels.
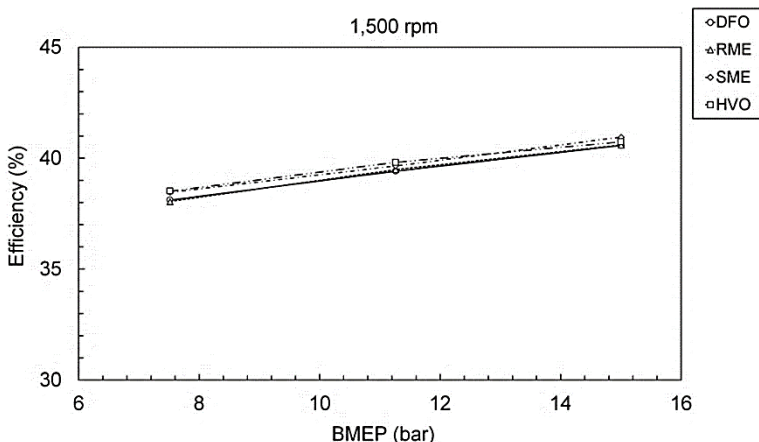
Figure 11. Engine efficiency against engine load at 1,500 rpm with the studied fuels.

CONCLUSIONS

This study focused on the determination of particle number emissions of a high-speed non-road diesel engine. The engine was driven with three bio-based fuels, RME, SME and HVO. DFO formed the baseline fuel. Based on the obtained results, the following conclusions could be drawn:

- Except at 10% load at rated speed, DFO or HVO produced the lowest particle numbers under the size of 30 nm.
- Except at 10% load at rated speed and at half load at intermediate speed, the methyl esters reduced the particle numbers within the size range of 100 to 300 nm most likely due to oxygen bounded in mono-alkyl-ester molecules.
- HVO emitted the least particles above the particle size of 23 nm at 10% load at rated speed and under 70 nm at low idle; this was assumed to be caused by the low sulphur content when compared to DFO, and the high cetane number when compared to the methyl esters.
- In case of RME and SME, both positive and significant correlations were found between the sum of the particle numbers detected above the size category of 23 nm and methyl palmitate (C16:0), methyl stearate (C18:0) and methyl linoleate (C18:2) contents at 10% load at rated speed.
- HVO was beneficial in terms of nitrogen oxide (NO_x) and hydrocarbon (HC) emissions.
- Carbon monoxide (CO) emission was the lowest with DFO.
- The level in smoke emission was negligible.

REFERENCES

Alanen, J., Simonen, P., Saarikoski, S., Timonen, H., Kangasniemi, O., Saukko, E. & Keskinen, J. 2017. Comparison of primary and secondary particle formation from natural gas engine exhaust and of their volatility characteristics. *Atmos. Chem. Phys.* **17**(14), 8739–8755.

Alrefaai, M.M., Peña, G.D.G., Raj, A., Stephen, S., Anjana, T. & Dindi, A. 2018. Impact of dicyclopentadiene addition to diesel on cetane number, sooting propensity, and soot characteristics. *Fuel* **216**, 110–120.

An, W.J., Pathak, R.K., Lee, B.H. & Pandis, S.N. 2007. Aerosol volatility measurement using an improved thermodenuder: Application to secondary organic aerosol. *J. Aerosol Sci.* **38**(3), 305–314.

Armas, O., Ballesteros, R., Martos, F.J. & Agudelo, J.R. 2005. Characterization of light duty diesel engine pollutant emissions using water-emulsified fuel. *Fuel* **84**(7–8), 1011–1018.

Bach, F., Tschöke, H. & Simon, H. 2009. Influence of Alternative Fuels on Diesel Engine Aftertreatment. In: 7th International Colloquium Fuels - mineral oil based and alternative fuels 14–15th January, Ostfildern, Germany.

Barrientos, E.J., Maricq, M.M., Boehman, A.L. & Anderson, J.E. 2015. Impact of ester structures on the soot characteristics and soot oxidative reactivity of biodiesel. *SAE Tech. Pap.* 2015-01-1080.

Bedford, F., Rutland, C., Dittrich, P., Raab, A. & Wirbeleit, F. 2000. Effects of direct water injection on DI diesel engine combustion. *SAE Tech. Pap.* 2000-01-2938.

Bünger, J., Bünger, J.F., Krahl, J., Munack, A., Schröder, O., Brüning, T., Hallier, E. & Westphal, G.A. 2016. Combusting vegetable oils in diesel engines: the impact of unsaturated fatty acids on particle emissions and mutagenic effects of the exhaust. *Arch. toxicol.* **90**(6), 1471–1479.

Eastwood, P. 2008. Particulate Emissions from Vehicles. Chichester: John Wiley & Sons Ltd. 494 p. ISBN 978-0-470-72455-2.

Filippo, A.D. & Maricq, M.M. 2008. Diesel nucleation mode particles: Semivolatile or solid?. *Environ. Sci. Technol.* **42**(21), 7957–7962.

Heikkilä, J., Virtanen, A., Rönkkö, T., Keskinen, J., Aakko-Saksa, P. & Murtonen, T. 2009. Nanoparticle emissions from a heavy-duty engine running on alternative diesel fuels. *Environ. Sci. Technol.* **43**(24), 9501–9506.

Hellier, P., Jamil, F., Zaglis-Tyraskis, E., Ala'a, H., Al Haj, L. & Ladommatos, N. 2019. Combustion and emissions characteristics of date pit methyl ester in a single cylinder direct injection diesel engine. *Fuel* **243**, 162–171.

ISO 8178-4:2017. 2017. Reciprocating internal combustion engines. Exhaust emission measurement. Part 4: Steady-state and transient test cycles for different engine applications. 237 pp.

Karjalainen, P., Pirjola, L., Heikkilä, J., Lähde, T., Tzamkiozis, T., Ntziachristos, L., Keskinen, J. & Rönkkö, T. 2014. Exhaust particles of modern gasoline vehicles: A laboratory and an on-road study. *Atmos. Environ.* **97**, 262–270.

Kegl, B., Kegl, M. & Pehan, S. 2013. Green diesel engine. Biodiesel usage in diesel engines. London: Springer-Verlag. 263 p. ISBN 978-1-4471-5324-5.

Khalek, I.A., Kittelson, D.B. & Brear, F. 2000. Nanoparticle growth during dilution and cooling of diesel exhaust: Experimental investigation and theoretical assessment. *SAE Tech. Pap.* 2000-01-0515.

Kittelson, D.B. 1998. Engines and nanoparticles: a review. *J. Aerosol Sci.* **29**(5–6), 575–588.

Kittelson, D.B., Arnold, M. & Watts, W.F. 1999. Review of diesel particulate matter sampling methods: Final Report. University of Minnesota, Minneapolis, MN, 63.

Jung, H., Kittelson, D.B. & Zachariah, M.R. 2006. Characteristics of SME biodiesel-fueled diesel particle emissions and the kinetics of oxidation. *Environ. Sci. Technol.* **40**(16), 4949–4955.

Jungmeier, G., Pucker, J., Ernst, M., Haselbacher, P., Lesschen, J.P., Kraft, A., Schulzke, T. & van Loo, E.N. 2016. Improving the sustainability of fatty acid methyl esters (Fame–biodiesel)–assessment of options for industry and agriculture. In: The 24th European Biomass Conference and Exhibition, 6–9 June 2016, Amsterdam, The Netherlands.

Lapuerta, M., Armas, O. & Rodriguez-Fernandez, J. 2008. Effect of biodiesel fuels on diesel engine emissions. *Progr. Energy Combust. Sci.* **34**(2), 198–223.

Li, R., Wang, Z., Ni, P., Zhao, Y., Li, M. & Li, L. 2014. Effects of cetane number improvers on the performance of diesel engine fuelled with methanol/biodiesel blend. *Fuel* **128**, 180–187.

Lähde, T., Rönkkö, T., Happonen, M., Söderström, C., Virtanen, A., Solla, A., Kytö, M., Rothe, D. & Keskinen, J. 2011. Effect of fuel injection pressure on a heavy-duty diesel engine nonvolatile particle emission. *Environ. Sci. Technol.* **45**(6), 2504–2509.

Lähde, T., Rönkkö, T., Virtanen, A., Solla, A., Kytö, M., Söderström, C. & Keskinen, J. 2010. Dependence between nonvolatile nucleation mode particle and soot number concentrations in an EGR equipped heavy-duty diesel engine exhaust. Environ. Sci. Technol. 44(8), 3175–3180.

Maricq, M.M., Chase, R.E., Xu, N. & Laing, P.M. 2002. The effects of the catalytic converter and fuel sulfur level on motor vehicle particulate matter emissions: light duty diesel vehicles. *Environ. Sci. Technol.* **36**(2), 283–289.

Mathis, U., Mohr, M., Kaegi, R., Bertola, A. & Boulouchos, K. 2005. Influence of diesel engine combustion parameters on primary soot particle diameter. *Environ. Sci. Technol.* **39**(6), 1887–1892.

Mathis, U., Ristimaki, J., Mohr, M., Keskinen, J., Ntziachristos, L., Samaras, Z. & Mikkanen, P. 2004. Sampling conditions for the measurement of nucleation mode particles in the exhaust of a diesel vehicle. *Aerosol Sci. Technol.* **38**(12), 1149–1160.

Mollenhauer, K. & Schreiner, K. 2010. History and fundamental principles of the diesel engine. In: K. Mollenhauer & H. Tschöke (Eds.), Handbook of diesel engines, pp. 3–30. Heidelberg, Berlin: Springer-Verlag. ISBN 978-3-540-89082-9.

Nabi, M.N., Brown, R.J., Ristovski, Z. & Hustad, J.E. 2012. A comparative study of the number and mass of fine particles emitted with diesel fuel and marine gas oil (MGO). *Atmos. Environ.* **57**, 22–28.

Niemi, S., Vauhkonen, V., Mannonen, S., Ovaska, T., Nilsson, O., Sirviö, K., Heikkilä, S. & Kiijärvi, J. 2016. Effects of wood-based renewable diesel fuel blends on the performance and emissions of a non-road diesel engine. *Fuel* **186**, 1–10.

Northrop, W.F., Madathil, P.V., Bohac, S.V., Assanis, D.N. 2011. Condensational Growth of Particulate Matter from Partially Premixed Low Temperature Combustion of Biodiesel in a Compression Ignition Engine. *Aerosol Sci. Technol.* **45**, 26–36.

Nousiainen, P., Niemi, S., Rönkkö, T., Karjalainen, P., Keskinen, J., Kuuluvainen, H., Pirjola, L. & Saveljeff, H. 2013. Effect of injection parameters on exhaust gaseous and nucleation mode particle emissions of a Tier 4i nonroad diesel engine. *SAE Tech. Pap.* 2013-01-2575.

Ntziachristos, L., Giechaskiel, B., Pistikopoulos, P., Samaras, Z., Mathis, U., Mohr, M., Ristimäki, J., Keskinen, J., Mikkanen, P., Casati, R., Scheer, V. & Vogt, R. 2004. Performance evaluation of a novel sampling and measurement system for exhaust particle characterization. *SAE Tech. Pap.* 2004-01-1439.

Pinzi, S., Rounce, P., Herreros, J.M., Tsolakis, A. & Dorado, M.P. 2013. The effect of biodiesel fatty acid composition on combustion and diesel engine exhaust emissions. Fuel 104, 170–182.

Rounce, P., Tsolakis, A. & York, A.P.E. 2012. Speciation of particulate matter and hydrocarbon emissions from biodiesel combustion and its reduction by aftertreatment. Fuel **96**, 90–99.

Rönkkö, T., Virtanen, A., Vaaraslahti, K., Keskinen, J., Pirjola, L. & Lappi, M. 2006. Effect of dilution conditions and driving parameters on nucleation mode particles in diesel exhaust: Laboratory and on-road study. *Atmos. Environ.* **40**(16), 2893–2901.

Rönkkö, T., Virtanen, A., Kannosto, J., Keskinen, J., Lappi, M. & Pirjola, L. 2007. Nucleation mode particles with a nonvolatile core in the exhaust of a heavy duty diesel vehicle. *Environ. Sci. Technol.* **41**(18), 6384–6389.

Samec, N., Kegl, B. & Dibble, R.W. 2002. Numerical and experimental study of water/oil emulsified fuel combustion in a diesel engine. *Fuel* **81**(16), 2035–2044.

Schönborn, A., Ladommatos, N., Williams, J., Allan, R. & Rogerson, J. 2009. The influence of molecular structure of fatty acid monoalkyl esters on diesel combustion. *Combustion and flame* **156**(7), 1396–1412.

Teboil. 2019. Product data - summer quality. Helsinki. Available from: https://www.teboil.fi/globalassets/tuotetiedotteet/motor_lammitys-kl_2019.pdf.

Tsolakis, A. 2006. Effects on particle size distribution from the diesel engine operating on RME-biodiesel with EGR. *Energy & Fuels* **20**(4), 1418–1424.

Szybist, J.P., Song, J., Alam, M. & Boehman, A.L. 2007. Biodiesel combustion, emissions and emission control. *Fuel Process. Technol.* **88**(7), 679–691.

Vaaraslahti, K., Virtanen, A., Ristimäki, J. & Keskinen, J. 2004. Nucleation mode formation in heavy-duty diesel exhaust with and without a particulate filter. *Environ. Sci. Technol.* **38**(18), 4884–4890.

Vaaraslahti, K., Keskinen, J., Giechaskiel, B., Solla, A., Murtonen, T. & Vesala, H. 2005. Effect of lubricant on the formation of heavy-duty diesel exhaust nanoparticles. *Environ. Sci. Technol.* **39**(21), 8497–8504.

Wang, X., Grose, M.A., Caldow, R., Osmondson, B.L., Swanson, J.J., Chow, J.C., Watson, J.G., Kittelson, D.B., Li, Y., Xue, J., Jung, H. & Hu, S. 2016a. Improvement of Engine Exhaust Particle Sizer (EEPS) Size Distribution Measurement – II. Engine Exhaust Particles. *J. Aerosol Sci.* **92**, 83–94.

Wang, Z., Li, L., Wang, J. & Reitz, R.D. 2016b. Effect of biodiesel saturation on soot formation in diesel engines. *Fuel* **175**, 240–248.

Wiedensohler, A., Birmili, W., Nowak, A., Sonntag, A., Weinhold, K., Merkel, M., Wehner, B., Tuch, T., Pfeifer, S., Fiebig, M., Fjäraa, A.M., Asmi, E., Sellegri, K., Depuy, R.,Venzac, H., Villani, P., Laj, P., Aalto, P., Ogren, J.A., Swietlicki, E., Williams, P., Roldin, P., Quincey, P., Hüglin, C., Fierz-Schmidhauser, R., Gysel, M., Weingartner, E., Riccobono, F., Santos, S., Grüning, C., Faloon, K., Beddows, D., Harrison, R., Monahan, C., Jennings, S.G., O'Dowd, C.D., Marinoni, A., Horn, H.-G., Keck, L., Jiang, J., Scheckman, J., Mcmurry, P.H., Deng, Z., Zhao, C.S., Moerman, M., Henzing, B., De Leeuw, G., Löschau, G., Bastian, S. 2012. Mobility particle size spectrometers: harmonization of technical standards and data structure to facilitate high quality long-term observations of atmospheric particle number size distributions. *Atmos. Meas. Tech.* **5**, 657–685.

Wiedensohler, A., Wiesner, A., Weinhold, K., Birmili, W., Hermann, M., Merkel, M., Müller, T., Pfeifer, S., Schmidt, A., Tuch, T., Velarde, F., Quincey, P., Seeger, S. & Nowak, A. 2018. Mobility particle size spectrometers: Calibration procedures and measurement uncertainties. *Aerosol Sci. Technol.* **52**(2), 146–164.

Zhu, L., Cheung, C.S. & Huang, Z. 2016. A comparison of particulate emission for rapeseed oil methyl ester, palm oil methyl ester and soybean oil methyl ester in perspective of their fatty ester composition. *Appl. Therm. Eng.* **94**, 249–255.

Yang, H.H., Chien, S.M., Lo, M.Y., Lan, J.C. W., Lu, W.C. & Ku, Y.Y. 2007. Effects of biodiesel on emissions of regulated air pollutants and polycyclic aromatic hydrocarbons under engine durability testing. *Atmos. Environ.* **41**(34), 7232–7240.

Effective control and battery charging system of an island PV power plant

V. Papez[1] and S. Papezova[2,*]

[1]Czech Technical University in Prague, Faculty of Electrical Engineering, Department of Electrotechnology, Technicka 2, CZ166 27 Pague 6, Czech Republic
[2]Czech University of Life Sciences in Prague, Faculty of Engineering, Department of Electrical Engineering and Automation, Kamycka 129, CZ165 21 Prague 6 - Suchdol, Czech Republic
[*]Correspondence: papezovas@tf.czu.cz

Abstract. The paper presents a new concept of an autonomous PV power plant regulatory system with LiFePO$_4$ batteries, which was functionally verified. The hardware system is significantly simpler and more operationally reliable. It also shows higher efficiency and lower acquisition costs than conventional commercial systems. The proposed control system was optimized for charging a multi-cell battery by PV electric energy. The system automatically maximizes the power supplied by the photovoltaic source and minimizes the power loss caused by balancing the individual cell charging processes. The problem of charge balancing is solved without the balancers. Battery cells are recharged from the separate converters supplying the PV power. The converters are controlled to observe a LiFePO$_4$ battery charging mode while controlling the photovoltaic generator (PVG) load resistance based on an MPP monitoring. PVG power is not supplied to the charged cells, which are in this way protected from overcharging. The entire PVG power is fed to the cells to be charged. The transmission from the converters is controlled in order not to exceed the voltage and current limits at the terminals and to minimize the actual voltage deviation from the control voltage at the PVG output. The control voltage is generated as an MPP voltage approximation according to the load character-istics and the actual PVG operating conditions.

Key words: LiFePO$_4$ battery, autonomous PV power plant regulatory system, MPP tracking.

INTRODUCTION

An autonomous PV power source must be equipped with a battery that is capable of covering the power supply requirements in case the PVG is not sufficiently illuminated. The battery is recharging in case of sufficient PVG irradiation and if its power is greater than the power consumed by the appliances.

Charging the battery by a direct interconnection with the PVG is possible only in special cases, i.e., an optimum working voltage of the photovoltaic generator must be slightly higher than the battery charging voltage. Since the battery cells connected in series will charge unevenly, they must be resistant to overcharge (e.g., NiCd batteries with a liquid elecrolyte).

Therefore, currently used modern systems are designed to maximize the power supplied from the PVG and to prevent overloading the battery cells in a wide range of operating voltages and currents (Glavin & Hurley, 2007; BMS123, 2019). A block diagram of the charge control is shown in Fig. 1.
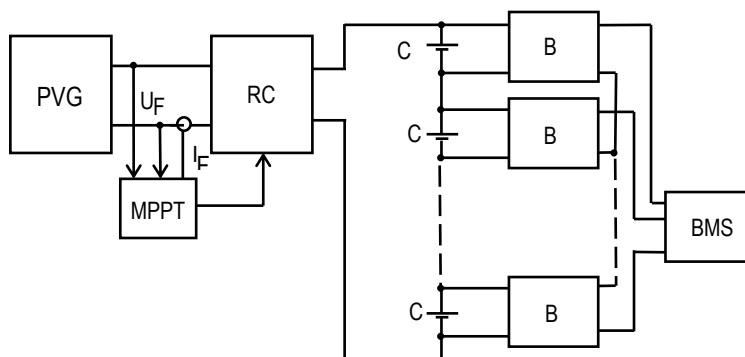
Figure 1. Block diagram of the charge control.

The PVG and C battery cells are interconnected via an regulated converter (RC) that transforms the power supplied from the PVG to its input at a certain voltage. The output power is then consumed at a different voltage, corresponding to the battery charge. Voltage and current levels at a PVG output are controlled by the Maximum Power Point Tracker (MPPT), so that the PVG delivers maximum power under actual operating conditions. The current I_{MP} and voltage U_{MP} corresponding to the MPP, when the PVG supplies the highest electric power, are found on the actual load characteristic, see Fig. 2.
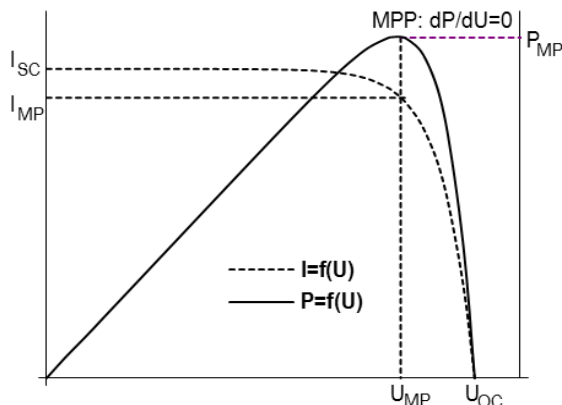
Figure 2. Power and current characteristics of the photovoltaic generator.

If the operating conditions change, the course of the PVG load characteristic changes as well. The current supplied from the PVG is approximately directly proportional to its irradiation. A PVG open-circuit voltage U_{OC} depends decisively on the temperature. As the temperature rises, it decreases by approximately 2.1 mV K^{-1}.

The MPPT is currently implemented as a control computer. Its input parameters are the values of output voltage and PVG current, or other potential values. Its output signal sets the voltage or current transmission of the controllable RC so that the actual values of its input voltage U_C and current I_C are as close as possible to the U_{MP} voltage and current I_{MP} in the maximum PVG power point.

The voltage and current levels in the output circuit of the controllable RC converter are controlled automatically according to the actual charging voltage of the battery so that the converter supplies the required power. Balancers B are connected to the individual cells, which are usually connected to the Battery Management System (BMS), as well. The BMS ensures the compliance with the permissible operating conditions of each battery cell.

MATERIALS AND METHODS

Electrical output power P supplied by the panel can be expressed as (1), (Papez & Papezova, 2016). The point, when the panel supplies a maximum power (P_{MP}) could be determined by finding the function extreme (1) according to Eq. (2).

$$P = U\,I = \left[\frac{NnkT}{e} \ln\left(\frac{I_{ph} + I_o - I}{I_o} \right) - IR_s \right] I, \tag{1}$$

where I – output current of the solar panel (A); I_{ph} – photovoltaic current of the solar panel (A); I_o – equivalent diode saturation current; R_s – equivalent series resistance of the solar panel (Ω); N – number of cells in series in the solar panel; n – equivalent diode ideality factor; k – Boltzman constant ($k = 1.381 \times 10^{-23}$ J.K^{-1}); e – electronic charge ($e = 1.602 \times 10^{-19}$ C); T – cell temperature (K); U – output voltage of the solar panel (V).

$$\frac{\partial P}{\partial I} = \left[\frac{NnkT}{e} \ln\left(\frac{I_{ph} + I_o - I}{I_o} \right) - IR_s \right] - I\left[R_s + \frac{NnkT}{e(I_{ph} + I_o - I)} \right] = 0. \tag{2}$$

However, Eq. (2) is not suitable to search for MPP, as the equation neglects further dependence of solar panel parameters on the operating conditions that, in practice, significantly influence the MPP position.

Consequently, at present are used the techniques that determine the actual values of the solar panel parameters determining MPP (Abderezak et al., 2018):
A. Numerical calculation of the derivative of the observed power function is the basis of the Perturb and Observe change evaluation method (P&O). Gradually is reached the state in which the calculated derivative value approaches the zero value and which corresponds to the maximum delivered power.
A. The method of Incremental Conductance (INC) is based on a numerical calculation of conductivity and incremental conductivity at PVG terminals that are each other compared. In that way, a state, in which the calculated conductivity and incremental conductivity values are equivalent and which corresponds to the maximum delivered power is gradually found.
B. A constant voltage method (CV) is based on the fact that for standard monocrystalline photovoltaic panels holds the approximate ratio between the voltage at the MPP point and the U_{OC} voltage of the open-circuit photovoltaic panel, which is approximated according to the PVG output voltage if the load is disconnected.

C. A short-current pulse method (SCP) is based on the fact that for standard monocrystalline photovoltaic panels holds the approximate proportion between the current at the MPP point and a short-circuit current of the photovoltaic panel I_{SC}, which is approximately determined according to the PVG output current during a short circuit at its terminals.

The battery management system ensures the balancing of the charging processes of individual battery cells. In practice, if the battery is constructed as an inter-connection of non-identical cells in series, its simple control according to the total battery voltage leads to the cell damage. The lowest-capacity cells are deeply dis-charged. They are not fully charged because the battery charging process is terminated when high capacity cells start to be overcharged. Moreover, in the cyclic operation, insufficiently charged cells discharge more deeply in the succeeding cycles and the differences increase. Similarly, the lower charge efficiency of the cell appears. The cell is later charged, and if it is not fully charged, it is discharged earlier and the whole process leads in a deep discharge of the cell and further decrease in its charge efficiency.

The problem is solved by balancing the cells. An electronic circuit is connected in parallel to each cell. If the terminal voltage of the cell reaches the selected value during charging, the circuit consumes the charging current from the cell and stabilizes the terminal voltage at the selected value. Battery charging is complete when the voltage of all cells reaches this selected value and all cells are fully charged.

Balancers are, in the simplest case, passive voltage stabilizers with a I-V characteristic of an ideal Zener diode with a knee voltage corresponding to the voltage of a fully charged cell. At this voltage, after charging the cell, the balancer consumes the charging current, i.e., it prevents the cell from overcharging and dissipates the power.

The maximum dissipated power of the balancer must correspond to the maximum charging power that can be supplied to the cell. The maximum dissipated power of all balancers must correspond to the maximum power that can be supplied to the battery terminals.

When charging the last cell of the battery with n unequal discharged cells, the balancers dissipate *(n-1)/n* of the input power.

Significant decrease of power dissipation can be achieved by using active balancers. Active balancers are controllable bi-directional converters allowing draining the charging power from the cell terminals to the auxiliary bus after full charging. In case the electrical power is available on the auxiliary bus, it is distributed by other active balancers to the terminals of so far uncharged cells. In principle, the whole supplied power can be losslessly utilized during the entire charging process, and the battery can be charged in a shorter time.

The disadvantage of the described BMS in photovoltaic systems is their considerable HW and SW complexity. In the systems with passive balancers, complications lie also in their cooling, as their waste heat may cause a significant battery overheating.

In active balancing systems is used a DC/DC PWM converter chain, whose maximum transmitting power is greater than the double of the maximum PVG power. This makes the construction of the charging system more expensive and reduces its reliability. Computer-controlled systems can be very unreliable due to a complicated SW and possible malware attack, particularly if they are connected to a PC and allow a remote administration via the Internet.

DESIGN AND IMPLEMENTATION OF THE SYSTEM

The new control system uses separate converters for the power transmission from a photovoltaic generator to individual cells. They simultaneously provide both charge power transmission and cell balancing during charging. The block diagram of the system is shown in Fig. 3. The input ports of the converters are connected in parallel and are supplied from the PVG output. As to the load optimization of the PVG, all converters are controlled according to the control voltage. It approximates the voltage U_{MP}, which is generated by a special circuit according to the temperature of PVG panels and their irradiation following the Model-based MPPT algorithms. (Hohm & Ropp, 2003).
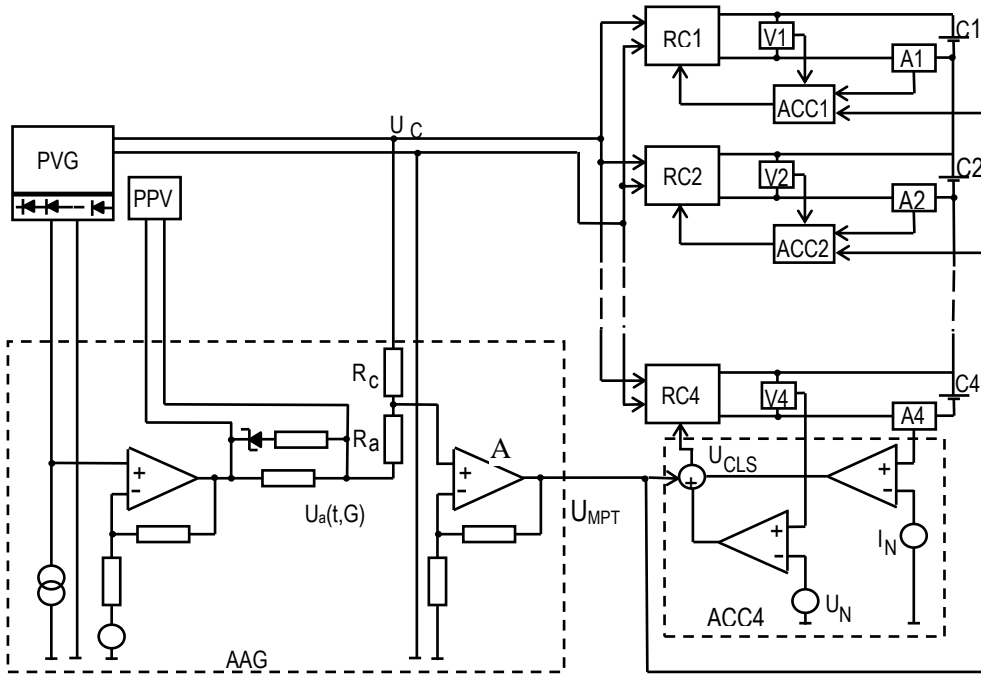
Figure 3. The block diagram of the realised system.

The control of the individual converters is further corrected according to the charging voltage and current of the connected cell such that the terminal cell voltage does not exceed the level corresponding to the full charge and that the maximum selected charging current is not exceeded.

The control is based on an analogue principle with analogue control signals and on the basis of physical principles in a controlled device without their digital simulation.

The system depicted in Fig. 3 comprises a PV generator (PVG) and a recharge-able battery consisting of three cells C1, C2, C3, C4. Each cell of the charged battery has its own control converter RC1, RC2, RC3, RC4, whose power inputs are interconnected in parallel and connected to the PVG output. The power outputs of the control converters are connected via voltage sensors V1, V2, V3, V4 and current sensors A1, A2, A3, A4 to the cells of the charged battery. The control port of each control converter is connected to its own analogue control circuit ACC1, ACC2, ACC3, ACC4. The control circuits

provide the charging process balancing of individual cells by correcting the common control signal MPT according to the actual values of the converter output voltage and current.

The MPPT controlling voltage corresponding to the model function (3) is generated in the implemented system by a non-linear analogue circuit in the analogue approximation generator (AAG).

The voltage U_a approximating U_{MP} is determined according to the working temperature t and the irradiation level G of the photovoltaic generator, according to the model function (Wolf, 2013).

$$U_a(t,G) = U_0(1 - \alpha t) + \beta \log(1 + G/\gamma) \tag{3}$$

where U_a (t, G) – an approximate voltage for temperature t and solar flux density G; U_0 – a reference voltage; α – a temperature coefficient of an approximate voltage and β, γ – constants.

The temperature-dependent voltage component U_a (t, G) is generated according to the voltage drop on the chain of silicon diodes which are placed in a heat contact with photovoltaic generator panels. The voltage drop across the diode chain shows principally the same temperature dependence as the U_{OC} voltage of the photovoltaic generator panels. After processing the voltage by a DC voltage amplifier with an adjustable reference level and gain, the output voltage of this amplifier in a wide range of temperatures is a very accurate image of the voltage U_{OC} of the PVG panels at a low level of irradiation.

The voltage dependence U_{OC} on the level of irradiation is compensated by the introduction of another correction component of the control voltage. This voltage is generated according to the current supplied by a small pilot PPV panel with a rated voltage of several V and current of several mA, located along with the PVG panels.

The correction component of the control voltage arises as a voltage drop on the non-linear resistive load, whose I-V characteristic approximates the logarithmic function of the voltage component U_a (t, G), which is dependent on irradiation. Since the total load impedance of the pilot panel is selected as low, the current supplied to the non-linear load is proportional to the panel irradiation, and the voltage drop corresponds to the PVG panel voltage U_{OC} dependence on the level of the irradiation.

The common MPT control signal for all controllable converters is generated by the charger control circuit according to the actual deviation U_{MP} from U_C voltage value at the RC input.

The approximate voltage U_a (t, G) is further compared by an analogue summator to the input voltage of the controllable U_c converters and according to their instantaneous values, a common U_{MPT} control signal is generated (4), where: A – amplifier gain.

$$U_{MPT} = -A \frac{R_c U_a(t,G) + R_a U_c}{R_a + R_c} \tag{4}$$

The control loop signal (CLS) of each converter, reducing its power transmission, is generated as a weighted sum of the MPT signal and the signals representing the deviations of the actual values of the cell charge voltage and current from the selected levels (5).

$$U_{CLS} = U_{MPT} + \delta(U_C - U_N) + \sigma(I_C - I_N) \tag{5}$$

1186

where U_{CLS} – the control voltage of the cell converter; U_{MPT} – the voltage of the control signal MPT; U_C, I_C – the actual cell charge voltage and the current of the converter; U_N, I_N – the rated values of the cell charge and current; δ, σ – the constants.

RESULTS AND DISCUSSION

The technical solution aims to realize a simple, cheap and reliable device for charging batteries from a photovoltaic source. The power transmission from the PVG to the individual cell terminals is provided by a set of controllable low-power converters, whose number corresponds to the number of battery cells. However, the cost of the system does not differ so much from the cost of the converter with the rated power corresponding to the rated power of the system, since the cost of the commercially produced converters is approximately proportional to the rated power.

Compared to a conventional digital control system, it enables achieving both higher reliability and time response to the change of input values, and the construction simplification.

The photovoltaic system for charging LiFePO$_4$ batteries was implemented and tested during the summer 2018. The block diagram of the charging system is shown in Fig. 4. A photovoltaic generator was constructed as two in-parallel connected SUNRISE SR-M536100 panels (SR Module, 2019), having a firm position with a south orientation and a 45° slope. The battery was composed of four cells Winston-Battery WB-LYP100AHA (Winston-Battery, 2019).
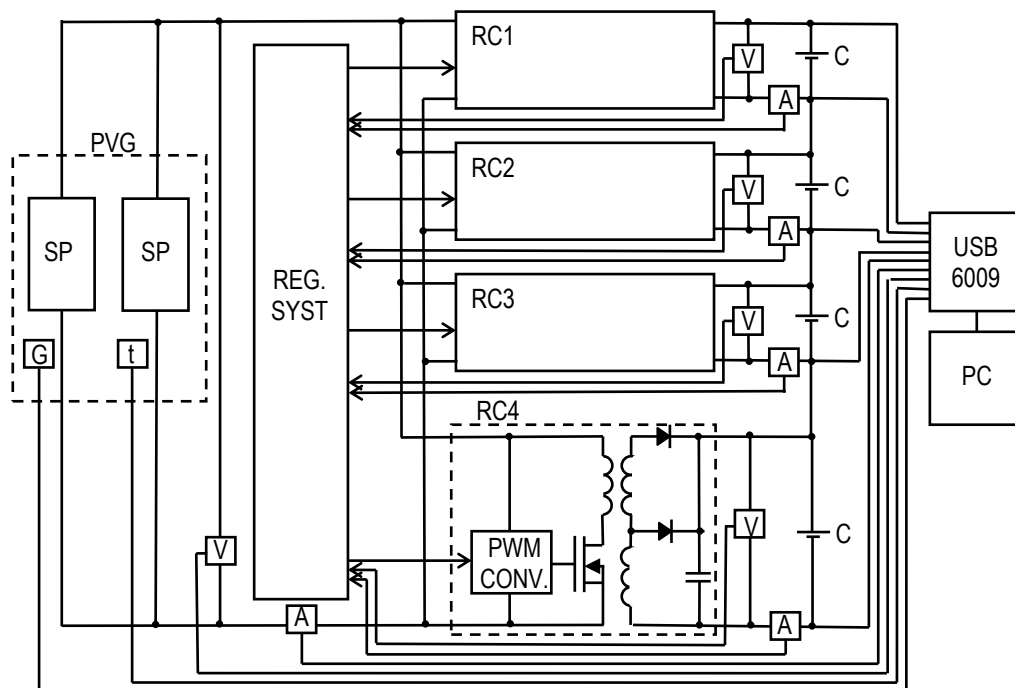
Figure 4. The block diagram of the charging system.

Control converters were realized by adapted simple single-switch PWM DC/DC converters with a maximum output of 50 W, an input voltage of 15–30 V and an output voltage of 4 V. Actual power transmitted by the converters was controlled by the described control system. The operating state of the system was monitored by a computer system. The NI 6009 USB measuring card was used to enter the monitored voltages. Terminal voltages of battery cells, output voltage, current, temperature and PVG irradiation were scanned. Labview SW was used for data procession on a PC.

A typical course of the basic operating values of the charger in charging during the day time is shown in Fig. 5. Although the solar flux density reached a maximum of 970 Wm^{-2}, its course during the day was decisively influenced by the cloudiness. During the day it was calm, so the maximum temperature of the panels reached up to 50 °C. The power, greater than 25% of the rated power, was supplied by PVG only from 9:00 to 13:45.
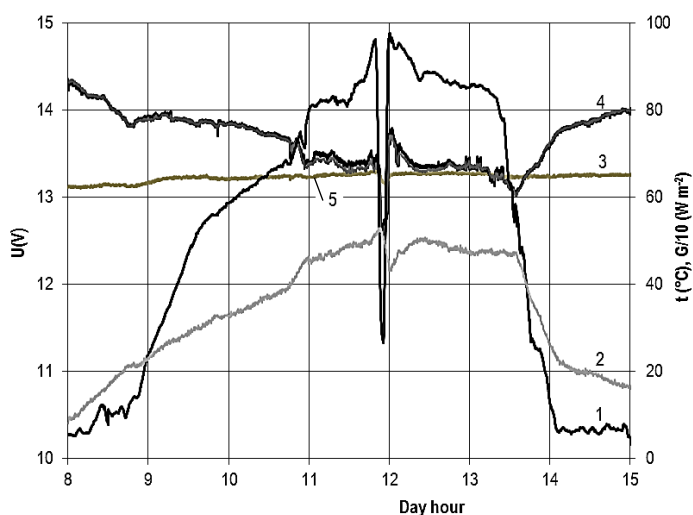
Figure 5. Course of PVG irradiation (curve 1), panel temperatures (2), battery terminal voltage (3), approximate voltage (4) and PVG output voltage (5) during the day time.

The function of the control system is illustrated by the courses of the approximate voltage $U_a(t,G)$ and output voltage of a photovoltaic generator U_c. The control loops of the converters ensure a good match of the voltage U_c with the approximate voltage $U_a(t,G)$. A maximum deviation at the highest transmitted power reaches approximately 1%.

The charging process of the battery is illustrated by the increase in its terminal voltage U_{bat} during charging, but regarding the variable value of the charging current, the indicated course is distorted due to the internal resistance of the battery.

Fig. 6 illustrates the comparison of the courses of the actual output power of the photovoltaic generator with the generator power calculated according to the solar flux density during the day time. The calculation was performed using the approximation by a direct proportion with regard to the PVG rated power of 200 W at the solar flux density of 1,000 Wm^{-2}.

The maximum actual power deviation from the calculated value is 6–8%. The decrease in actual power is caused by the increase in PVG operating temperature at high solar flux density levels, which was not considered in the calculation.
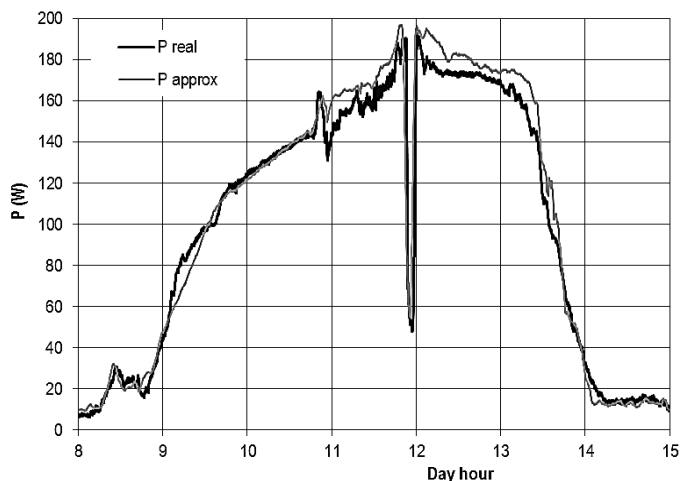
Figure 6. Comparison of the approximated and measured PVG output power courses during the day time.

The real dependence of the charging system power on the intensity of the solar flux density is shown in Fig. 7. The dependence corresponds to the direct proportion when considering the 96–97 W rated power of the panels
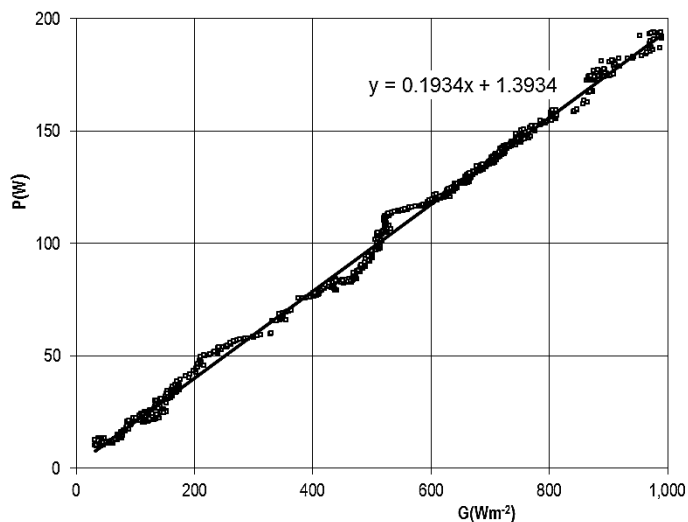
Figure 7. Dependence of the measured power of the charging system on the solar flux density and its approximation characteristic.

CONCLUSIONS

The control system automatically ensures the operation of the photovoltaic generator in the close proximity to the MPP. The charging processes of the individual battery cells are simultaneously balanced, i.e., the individual cells are protected against overcharging. The control system works exclusively in an analogue mode and does not comprise a computer, which significantly reduces its acquisition costs. By an individual control of the charging processes of the battery cells, there is no need to use cell balancers. This further simplifies the construction of the system, reduces its power losses and increases its reliability compared to the commercial computer-controlled systems.

REFERENCES

Abderezak, L., Sera D., Guerrero J., Mathe L. & Bouzid A. 2018.Discrete Model-Predictive-Control-Based Maximum Power Point Tracking for PV Systems: Overview and Evaluation. *IEEE Transactions on Power Electronics* **8**, 7273–7287.

BMS123, https://files.i4wifi.cz/inc/_doc/attach/StoItem/4493/User-Manual-BMS123-Smart.pdf, Accessed 2.1.2019.

Glavin, M. & Hurley, W. 2007. Battery Management System for Solar Energy Applications. In: *Proceedings of the 41st International Universities Power Engineering Conference. IEEE*, Newcastle, pp. 79–83.

Hohm, D.P. & Ropp, M.E. 2003.Comparative Study of Maximum Power Point Tracking Algorithms. *Progress in Photovoltaics: Research and Applications* **11**, 47–62.

Papez, V. & Papezova, S. 2016. Optimization of a solar power station by $LiFePO_4$ accumulators *Agronomy Research* **14**, 1200–1211.

SR Module sr-m536100. https://www.environmental-expert.com/downloads/monocrystalline-modules-sr-m536100-336374. Accessed 2.1.2019.

Winston-Battery WB-LYP100AHA. http://en.winston-battery.com/index.php/products/power-battery/item/wb-lyp100aha?category_id=176.Accessed 2.1.2019.

Wolf, P. 2013. Modeling of PV cells and panels in conditions of non-uniform radiation and emperature. *Doctoral Thesis*. České vysoké učení technické v Praze, Praha, 151 pp. (in Czech).

Analysis of plant materials pre-treated by steam explosion technology for their usability as insulating materials

T. Schnabel[1,*], H. Huber[1], A. Petutschnigg[1,2] and A. Jäger[3]

[1]Salzburg University of Applied Sciences. Department of Forest Products Technology & Timber Constructions. Marktstraße 136a, AT5431 Kuchl, Austria
[2]BOKU University of Natural Resources and Life Sciences, Konrad Lorenz-Straße 24, AT3430 Tulln, Austria
[3]University of Applied Sciences Upper Austria, Faculty of Engineering, Department of Bio & Environmental Technology, Stelzhamerstr. 23, AT4600 Wels, Austria
[*]Correspondence: thomas.schnabel@fh-salzburg.ac.at

Abstract Raw materials of annual plants fibres are not easily usable for industrial production applications. Pre-treatment of the annual plant fibres is necessary to increase the homogeneity of the material and to improve the material properties. This study deals with the influence of steam explosion treatment on the quality of annual plant fibres used as insulating material.

Maize and wheat straw were selected for production of insulating panels. To clarify the changes within the structure of the plants due to the pre-treatment process material analysis was carried out using FT-IR spectroscopy and raster electron microscope. Furthermore, the bulk density and the thermal conductivity were analysed as important values for insulating materials.

The results showed that the pre-treatment process homogenizes the materials and the processes could be used for the production of bulk insulation.

Key words: thermal-hydro treatment, thermal conductivity, maize straw, miscanthus.

INTRODUCTION

Crops material used as insulating material has a long tradition. Buildings with straw bales are energy efficient, durable and attractive (Ashour et al., 2001). Beside these advantages also considerable drawbacks like the thickness of the building wall and the anisotropic material properties exist for many applications. Pre-treatments of these plant fibres have potential to increase their homogeneity and to improve the material properties (Nagl et al., 2015a, b). In this study, the effect of steam explosion treatment of different straw material for insulating material was examined.

The steam explosion treatment modifies the chemical composition, the sorption behaviour and the mechanical properties of wheat straw fibres (Han et al., 2009). A degradation of lignin and hemicellulose (polyose) was determined. The structural changes due to the steam explosion treatment were analysed by Han et al. (2010). They concluded that higher steam temperatures and longer retention times results in more homogeneous fibre materials. Moreover, the opportunity of glue less fibreboards made from steam exploded *Miscanthus sinensis* was analysed by Velásquez et al. (2002). It

could be shown that the mechanical properties have increased due to the treatment process.

However, the insulation properties of steam pressurized straw materials have not been analysed in detail. This study deals with possible applications of treated plant materials for the application of bulk insulating material.

MATERIALS AND METHODS

Straw Materials

Straw of maize (*Zea mays* L.) and miscanthus (*Miscanthus sinensis Giganteus*) was used for the analysis of insulating properties. The air-dried materials were shredded by using a customary shredder system for the further process.

Steam Explosion Process

The straw was treated under steam explosion conditions using a pilot plant of the Upper Austria University of Applied Sciences. The pilot plant was detailed described by Eisenhuber et al. (2013). Steam temperature was 200 °C and the retention time was 20 minutes. Each batch of about 900 g of straw was put inside the steam chamber. The treated straw was dried to a moisture content between 6 and 12%.

Determination of the particle size distribution

The particle size distribution was analysed according to the DIN CEN/TS 15149-2 (2010). The vibratory sieve shaker AS 200 digit from Retsch was applied. For all materials the time for vibration was 15 min with an amplitude of 50. The weight for each sieve was used to calculate the percentage of the different particle sizes.

Determination of the bulk density

The bulk density of the various materials was determined according to the ÖNORM EN 15103 (2009).

Analysis of thermal conductivity

The thermal conductivity was measured according to EN 12667 (2001) using the lambda-meter EP500 of the Lambda Measurement Technologies Corporation. All various material was stored at 20 °C temperature and 65% relative humidity. The bulk densities in the measuring field of 25 x 25 x 2 cm³ for the measurement were varying depending on the material properties and due to the requirements of the standard used (e.g. completely material filling of the test area). The thermal conductivity measurements were taken at three temperatures, at 10°, 25° and 40 °C, respectively.

FT-IR Spectroscopy

For the FT-IR measurements each raw material was milled with a cutting mill (Retsch) to pass a mesh of 500 µm and the fractions between 250 and 63 µm were separated with a sieving apparatus (Retsch). The spectra of the milled materials were recorded between 4,000 and 600 cm^{-1} with 32 scans at a resolution of 4 cm^{-1} using a Frontier FT-IR spectrometer (PerkinElmer) equipped with a Miracle diamond ATR accessory with a 1.8 mm round crystal surface. The average of three spectra was baseline-corrected and used for the further analysis.

RESULTS AND DISCUSSION

Chemical and structural changes in materials

The chemical changes of the different materials due to the stream explosion process were analysed by using FT-IR spectroscopy (Fig. 1).
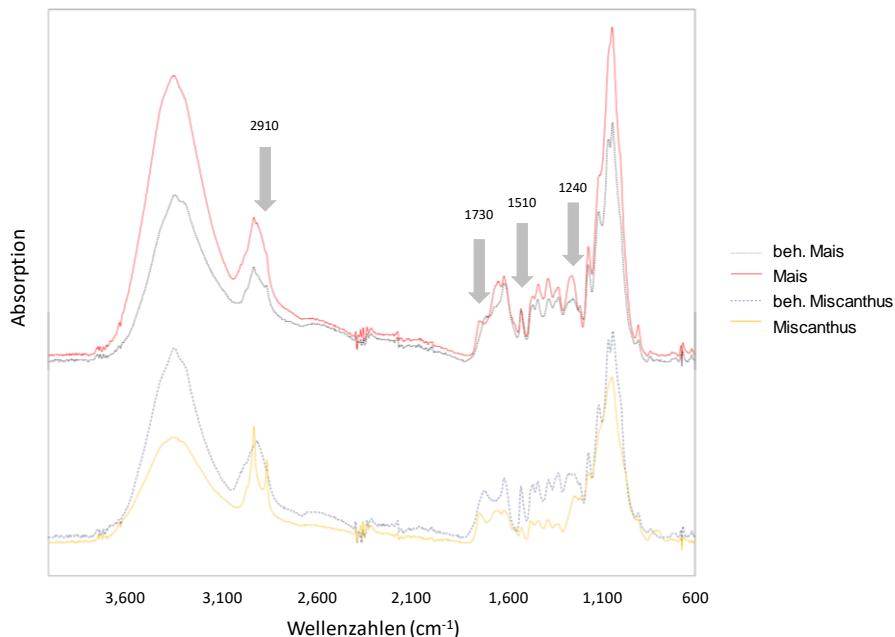
**Figure 1.** FT-IR spectra of treated and untreated maize as well as miscanthus, respectively.

The chemical changes of the plant components due to the steam explosion occurred mainly in holocelluloses and in lignin (Han et al., 2010a, b). This was also the first impression of the chemical changes caused by steamed pressurized treatments. A difference between the IR spectra of treated and untreated miscanthus and maize samples were observed at the wavenumbers in the area about 2910 cm^{-1}. The peaks obtained at 2,930 cm^{-1} and 2,890 cm^{-1} are an indication of stretching vibration form CH, CH$_2$ and CH$_3$ (Pretsch et al., 2010). These functional groups are corresponding with the wax on the raw materials. Miscanthus samples showed a clear form of the two bands. After the steam pressurised treatments, the heights of the flanks were decreased and clear form of the peaks cannot be observed anymore. The peak at around 1,730 cm^{-1} is an initiation of carbonyl groups or COOH-groups, which may correspond with the hemicellulose and fatty acids of the natural wax. At around 1,510 cm^{-1} a peak can be observed, which are corresponding to the aromatic molecules (Pretsch et al., 2010). This peak can be increased due to the treatment based on the exploration process of the miscanthus materials. The band around 1,240 cm^{-1} was confirmed to the stretching vibration of C = O and COOH groups of aromatic compounds and hemicellulose. Based on these results, it can be assumed that the hemicellulose was degraded due to the steam explosion process. Besides the chemical modification the changes in structure are important for the application for the use as insulating materials.

Fig. 2 shows the raw material of maize before and after the steam explosion process at the macro and micro levels. A high portion of leaves can be determined in Fig. 2, a, whereas the material from the stem is negligible. It can be observed that this process frayed out the cell complex of the lignocellulosic materials. However, the after the drying process some conglomerates of the material could be seen for maize and miscanthus, respectively.
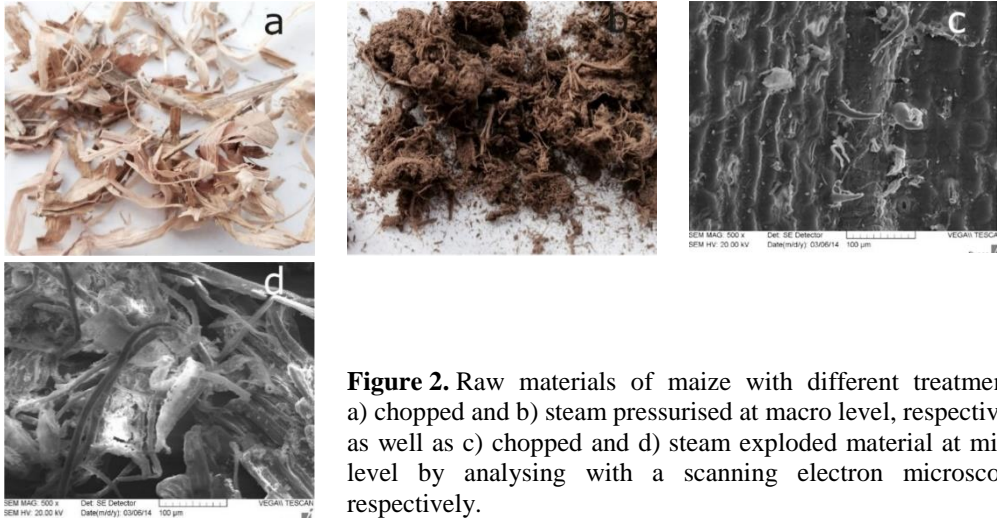

Figure 2. Raw materials of maize with different treatments: a) chopped and b) steam pressurised at macro level, respectively as well as c) chopped and d) steam exploded material at micro level by analysing with a scanning electron microscope, respectively.

The steam explosion influences on the material on fibre and fibrils levels were shown in Fig. 3 for miscanthus materials. Some intact parts of the miscanthus stem can be observed in Fig. 3, b. The retention time of the steam explosion process was too short for defibrating these big particles. Nevertheless, the wax surface of the various straw species was also destroyed due to the steam explosion process, which is in line with the results from the FT-IR spectroscopy. The analysis at the macro level depicted that the particle size distributions between the natural and untreated materials are different.
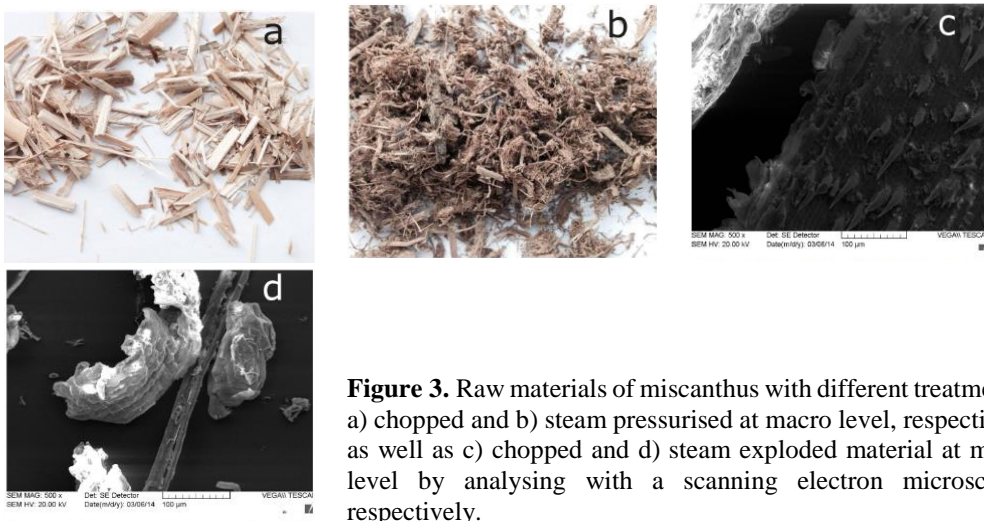
Figure 3. Raw materials of miscanthus with different treatments: a) chopped and b) steam pressurised at macro level, respectively as well as c) chopped and d) steam exploded material at micro level by analysing with a scanning electron microscope, respectively.

The results of the shift in particle size distribution of the raw material and different treatments are shown in Fig. 4. The portion of material fractions below 250 µm were almost zero for the chopped raw materials. By contrast the treated materials show an amount of 8%. Most of this fraction is dust and cannot be used for the development of insulating materials as well as this material is lost for the insulation material. However, this fraction has a high impact on the bulk density. In the range between 250 µm and below 1.0 mm the amount of particles was also lower for the chopped samples than for the steam pressurised samples.
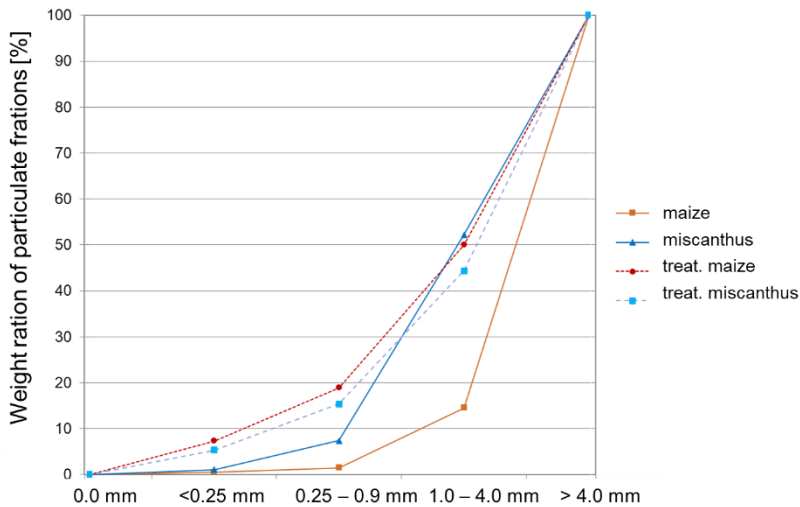
Figure 4. Particle size distribution regarding the different raw materials and treatments.

The sieve results for the particle fraction between 1.0 and 4.0 mm depict that the relative amount of copped miscanthus, steam treated maize and miscanthus have a range of 29 to 45%. Only the chopped maize samples have very low portion in this class, which the relative amount laid around 13%. This behaviour can be explained by the structure of the chopped maize straw. The samples from the maize had a higher portion of leaves than stem material, whereas the miscanthus samples presented a high amount of stem material (cf. Figs 2, a and 3, a). The relative amounts of the sieve fraction larger than 4 mm particle size showed different results. The values from the copped maize material showed the highest amount about 86%, which is followed by the steam pressurised miscanthus samples with 56% and treated maize material with 50%. The lowest values presented the chopped miscanthus materials with 48% of the relative portion.

Physical changes in materials properties

Table 1 shows that the bulk densities of the raw materials and stream pressurised materials are different. Due to the treatment the bulk density of the maize samples increased. This phenomenon results due to a relative high amount of dust in the materials compared to the untreated maize material (c.f. Fig. 4). For the miscanthus material a contrary change can be observed. The bulk density decreases due to the effect of the steam explosion process through the increase of material fraction in the range between 1.0 to 4.0 mm.

Table 1. Overview of different material properties of chopped and stream pressurised materials at 200 °C

Crops	Temperature (°C)	Retention time (min.)	Bulk density (kg m^{-3})	Moisture content# (%)
Maize	0	0	48.6	9.5
Maize	200	20	82.7	6.1
Miscanthus	0	0	137.6	10.1
Miscanthus	200	20	93.4	5.7

material storage at 23 °C temperature and 50% relative humidity.

Measurements of the thermal conductivity of chopped and steam treated maize showed that there is only a small difference between both materials, as bulk densities are very similar (Table 2). Separating the raw materials into different fractions show different results of the thermal conductivity. The larger the particle size the higher are the values of the thermal conductivity. The measurement area can compactly fill in with small particles. This phenomenon can be seen if the bulk density in the measurement area is compared. Higher densities represented higher amount of material and less air inside the measurement field.

Table 2. Results from the thermal conductivity measurements of maize samples at 10 °C temperature

Crops	Temperature (°C)	Retention time (min.)	Particle size (mm)	Bulk density (kg m^{-3})	Thermal conductivity (W (mK)$^{-1}$)
Maize	0	0	org.#	98.0	0.04600
Maize	200	20	org.#	100.8	0.04573
Maize	200	20	> 4	80.0	0.04626
Maize	200	20	< 4–2	86.2	0.04661
Maize	200	20	< 2–1	94.1	0.04362
Maize	200	20	< 1–0.25	106.6	0.04277

original material samples without fractionation.

Table 3. Results from the thermal conductivity measurements of miscanthus samples at 10 °C temperature

Crops	Temperature (°C)	Retention time (min.)	Particle size (mm)	Bulk density (kg m^{-3})	Thermal conductivity (W (mK)$^{-1}$)
Miscanthus	0	0	org.#	151.9	0.05147
Miscanthus	200	20	org.#	120.0	0.04726
Miscanthus	200	20	org. #	100.3	0.04546
Miscanthus	200	20	< 4–2	98.1	0.04725
Miscanthus	200	20	< 2–1	79.1	0.04484
Miscanthus	200	20	< 1–0.25	96.0	0.04286

original material samples without fractionation.

Table 3 shows the thermal conductivity of the miscanthus samples. However, the high bulk density in the measurement area of chopped miscanthus material of 151.9 kg m^{-3}, which could not obtain with the steam pressurised materials. The results

show that treated material samples have a lower thermal conductivity compared to the chopped miscanthus material. At a bulk density of 100.3 kg m^{-3} a thermal conductivity value of 0.04546 (W (mK)$^{-1}$ was determined and this value was lower than the measured value from the treated miscanthus materials with 120.0 kg m^{-3} bulk density. The low values in thermal conductivity and bulk densities are affected from the low moisture content of the steam pressurised material samples.

Measurements of the thermal conductivity of the fractionated treated materials showed a clear trend. With decreasing particle size, the values of thermal conductivity are getting lower to 0.04286 (W (mK)$^{-1}$). However, this behaviour is not related with the bulk density as measuring with the maize material. Thermal conductivity measurements with larger particle size than 4 mm could not be conducted due to the insufficient coverage of the test area.

CONCLUSIONS

Steam explosion treatment were used to defibrillate the straw materials of maize and miscanthus. These particles and fibres were analysed for the applicability as insulating material (e.g. bulk insulation). Within the limitation of this study, the main conclusion can be drawn as follows:

- The chemical composition of treated material is changing.
- The particle size of the steam pressurised samples decreases compared to the reference samples due to destroying of natural fibre composite.
- Lower material moisture contents were measured for the treated samples.
- The use of steam pressurised materials has positive effects on the bulk densities and thermal conductivity by using fractionated materials.

According to these results the possible application of steam pressurised materials as bulk insulating material is shown. These findings provide a basis for help in transfer from laboratory to industrial conditions for consumer applications.

Conflict of Interest Statement
The authors declare that they have no conflict of interest.

REFERENCES

Ashoura, T., Georg, H. & Wu., W. 2011. Performance of straw bale wall: A case of study. *Energy Build*. **43**, 1960–1967.
DIN CEN/TS 15149-2. 2010. *Solid biofuels - Determination of particle size distribution (Feste Biobrennstoffe -Bestimmung der Partikelgrößenverteilung).* Beuth Verlag GmbH. Berlin. (in German).
EN 12667. 2001. *Determination of the thermal resistance with the panel and heat flow panel measuring device.* European Committee for Standardization (CEN), Brussels.
Eisenhuber, K., Krennhuber, K., Steinmüller, V. & Jäger, A. 2013.Comparison of different pre-treatment methods for separating hemicellulose from straw during lignocellulose bioethanol production *Energy Procedia* **40**, 172–181

Han, G., Cheng, W., Deng, J., Dai, C., Zhang, S., Bicho, P. & Wu, Q. 2009. Effect of pressurized steam treatment on selected properties of wheat straws. *Ind. Crops. Prod.* **30**, 48–53.

Han, G., Deng, J., Zhang, S., Bicho, P. & Wu, Q. 2010. Effect of steam explosion treatment on characteristics of wheat straw. *Ind. Crops. Prod.* **31**, 28–33.

Nagl, K., Barbu, M.-C., Schnabel, T., Petutschnigg, A., Jäger, A. & Huber, H. 2015a. Use of annual and perennial plants for dimensionally stable insulation panels. *Pro Ligno* **11**, 181–186.

Nagl, K., Jäger, A., Huber, H., Barbu, M.-C., Petutschnigg, A. & Schnabel, T. 2015b. The use of crops as raw material for insulation materials. *Holztechnologie* **56**, 19–23 (in German).

Pretsch, E., Bühlmann, P. & Badertscher, M. 2010. *Structure determination of organic compounds (Spektroskopische Daten zur Strukturaufklärung organischer Verbindungen).* Springer-Verlag. Berlin Heidelberg (in German).

ÖNORM EN 15103. 2009. *Solid biofuels - Determination of bulk density (Feste Biobrennstoffe-Bestimmung der Schüttdichte).* Austrian Standards. Vienna, (in German).

Velásquez, J.A., Ferrando, F. & Salvadó, J. 2002. Binderless fibreboard from steam exploded Miscanthus sinensis: The effect of a grinding process. *Holz Roh. Werkst* **60**, 297–302.

Hydrogen production using waste aluminium dross: from industrial waste to next-generation fuel

K.K. Singh[*], A. Meshram, D. Gautam and A. Jain

Indian Institute of Technology, Banaras Hindu University, Department of Metallurgical Engineering, IN221005 Varanasi India
[*]Correspondence: kksingh.met@iitbhu.ac.in

Abstract. This article describes the production of hydrogen from white aluminium dross, an industrial waste generated in the aluminium smelter plants. Hydrogen is generated by metal-water reaction between aluminium and water in presence of alkalis like sodium hydroxide and potassium hydroxide. Aluminium dross is described as a heterogeneous material with its major constituents being metallic aluminium, alumina and other salt fluxes like NaCl and KCl. Utilizing the metallic aluminium content entrapped in the matrix of alumina for the metal-water reaction has been the driving force for the waste recycling and simultaneous hydrogen production. Bulk aluminium dross was crushed and downsized. The finer fraction of the powdered aluminium dross is used for the experiments. The effects of dross in the alkaline solution, temperature of the solution and the time of the reaction were studied to understand the generation of hydrogen. The alkaline solution breaks the protective layer of alumina and exposes the entrapped aluminium content to water, thereby commencing the hydrogen liberation.

Key words: aluminium dross, hydrogen, waste management, recycling.

INTRODUCTION

The development of the next-generation fuels is very crucial to match the demands of the world. Fuel consumption per capital has increased radically in the present day and it is projected to rise as the technological advancement takes place. The growth in industrial and transport sector simply necessitates the research in the field of fuel and energy.

In this scene of technological rush, hydrogen comes into the picture. Hydrogen is an important fuel and source of energy. Compared to the conventional fuels, the combustion of hydrogen gives rise to water vapour, whereas other fuels tend to release carbon dioxide and carbon monoxides. The gross calorific value of hydrogen is nearly 39.4 kWh kg^{-1} compared to gasoline (12.89 kWh kg^{-1}). The value of hydrogen increases readily as the conventional fuels are limited resources and the prices of these fuels are increasing with the passing day.

The production of hydrogen is usually carried out by coal gasification and water electrolysis. These methods are the conventional processes that have been optimized and studied thoroughly to improve the output of the hydrogen. These processes include the utilization of external fuels and energies to release the gas. Recently, the focus has

shifted to developing newer and better methods to produce hydrogen. One of the processes is the exploitation of metal-water reaction.

It is well known that when metal comes in contact with water, the formation of metal oxide and hydroxide takes place. This is accompanied with the release of hydrogen gas. The rate of gas evolution varies with the metal and the metal-water reaction rate. When highly reactive metals are employed for the hydrogen evolution, the chances of explosion are greater and it becomes very unsafe. Using aluminium for the purpose of metal-water reaction has always attracted the researchers. The two main reasons for this are: 1. Aluminium-water reaction is aggressive enough to produce sufficient amount of hydrogen. Theoretically, nearly 1.2 L of hydrogen can be generated from 1 g of aluminium. Also, the reaction with aluminium is controllable. The chances of explosion are reduced as the reactivity of aluminium is far less than sodium and other reactive metals. 2. The abundance of aluminium is fairly higher than any other metal.

Using aluminium as a raw material for hydrogen generation has been studied (Uehara et al., 2002). When fresh surface of metallic aluminium comes in contact with water, the generation of hydrogen takes place rapidly. The production of fresh surface takes place when the metal is machined and chipped. Just as the layer of aluminium is produced, the reaction for hydrogen generation increases.

The researcher fraternity has conducted many experiments and a large variety of opinions are already developed regarding the production of hydrogen using aluminium. Directly applying aluminium to produce hydrogen is expensive. To solve this problem, aluminium dross can be successfully used to supply for the metallic aluminium essential for aluminium-water reaction. Aluminium dross is a by-product waste generated in the aluminium industries. During the melting and remelting of aluminium ingots, the formation of aluminium dross takes place when molten aluminium comes in contact with atmospheric oxygen. This semisolid oxide layer is removed during the taping of molten metal. When this skimmed product is allowed to cool to room temperature, it becomes very rigid. This resultant product is aluminium dross.

There are mainly three types of aluminium dross: white dross, black dross and salt cakes. White dross is the dross generated during the primary processing of aluminium at primary aluminium smelter units. This type of dross has higher metallic aluminium content, hence the white colour. Black dross is produced in the secondary aluminium smelter units. It has relatively lower amount of metallic aluminium with greater percentage of aluminium oxide and salt fluxes. Salt cakes are generated after aluminium is extracted from white dross. These cakes essentially have higher amount of salts in it, with lower amount of oxides and metallic aluminium (Meshram & Singh, 2018).

As the amount of metallic aluminium is greater in white aluminium dross, the utilization of white aluminium dross for generation of hydrogen is a good alternative to pure aluminium. The major challenge associated with the utilization of aluminium dross is its lower tendency of reaction. It is well known that aluminium has a thin layer of alumina over it, which acts as a protective shield. This layer simply hinders all contact with the metallic content within the oxide layer. This oxide protection is removed when the water is turned alkaline or acidic. Since aluminium and alumina react with acids and alkalis, the protective layer gets damaged and metallic aluminium therein gets exposed for further reactions (Meshram & Singh, 2017).

Hydrogen production using aluminium dross as a raw material has been studied by researchers around the world (David & Kopac, 2012). The fine powder of aluminium

dross has been subjected to high energy ball milling to reduce the particle size to a range of few micrometres. Due to the great drop in the size of the particles, the specific surface area of the particles increases rapidly. This leads to greater exposure of surface to water and greater tendency of hydrogen evolution. It must be noted here that the water used for the reaction was tap water and no use of alkaline solution was carried out. The virtue of small particle size and larger specific surface area leads to the hydrogen evolution. The major disadvantage of this process is the use of high energy ball milling. This is a highly energy intensive process and the amount of sample prepared for the experiment is very less. The commercial applications of this process are quite not possible due to the economic reasons.

The use of alkaline solutions for aluminium-water reactions has not been thoroughly studied. Taking the raw material as white aluminium dross, the generation of hydrogen is a great opportunity to explore and establish another method to efficiently produce hydrogen. The present research deals with the generation of hydrogen using alkaline solutions and the recycling of white aluminium dross.

MATERIALS AND METHODS

As received aluminium dross is crushed and downsized to achieve fine powders. Since metallic content of white aluminium dross is quite high compared to black dross, the coarser fraction of the downsized dross is separated. The coarser fraction of white aluminium dross has a greater amount of aluminium in it because the metal drops tend to accumulate and agglomerate in the molten state. The finer fraction has a greater amount of oxide matrix that binds the metallic aluminium in it. Due to the greater specific area of finer fraction, it is used in the aluminium-water reaction.

The temperature of the water is increased using a hot plate with magnetic stirrer. Separately, aluminium dross fine powder is crushed with sodium hydroxide and potassium hydroxide pellets to make a homogeneous mixture using mortar and pestle. The weight of aluminium dross in the mixture is increased, keeping the amount of alkali constant. The objective is to study the variation in the amount of gas generated with change in amount of dross fed for the reaction and change in temperature.

The aluminium-water reaction takes place in a 100 mL conical flask. When aluminium dross-alkali mixture is added to the distilled water at the reaction temperature, a sudden surge of gas is observed. Care is to be taken that the evolution of gas doesn't take place before the mixture is added to water. The generation of hydrogen is possible even before that as the atmospheric water vapour can interfere severely, due to the hygroscopic nature of alkalis. It is important to make sure that just as the mixture comes in contact with water, the conical flask is sealed with a rubber cork fitted with a pipe. This arrangement will help in the transfer of the gas generated in the conical flask. This gas is collected and measured in an inverted measuring cylinder filled with water placed in a water bath.

The amount of gas collected is measured in a fixed period of time (15 minutes) and simultaneously the rate of gas evolution is determined. When the rate of gas evolution drops down to less than 5 mL minute^{-1}, the reaction is stopped and the final reading is measured. The final liquor obtained is filtered and the solution is separated from the residual solid. In all of the experiments, the weight of the dross has been varied from

1 to 3 g, while the weight of the alkali (NaOH and KOH) was kept constant at 1 g. This led to the variation of the weight ratios employed for the experiments.

Fig. 1 shows the schematic representation of the experimental procedure to efficiently produce hydrogen. The characterization of the dross has been done using the X-ray diffraction facility. Rigaku Tabletop Miniflex 600, Dtex Ultra with copper target has been used for this characterization. The XRD pattern has been illustrated in the Fig. 1,b.
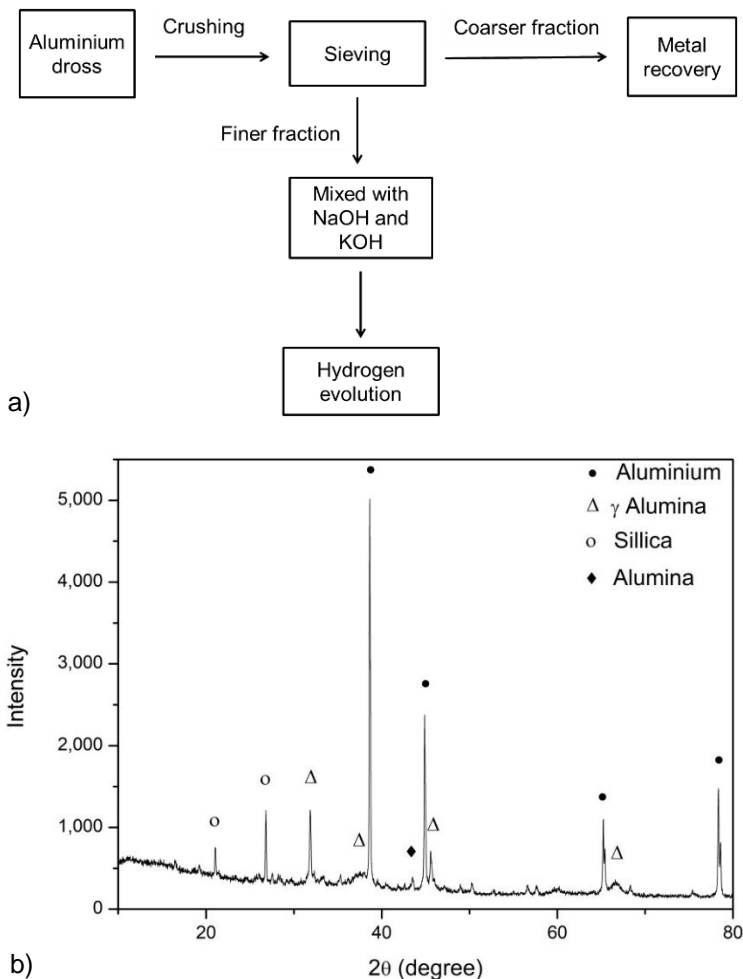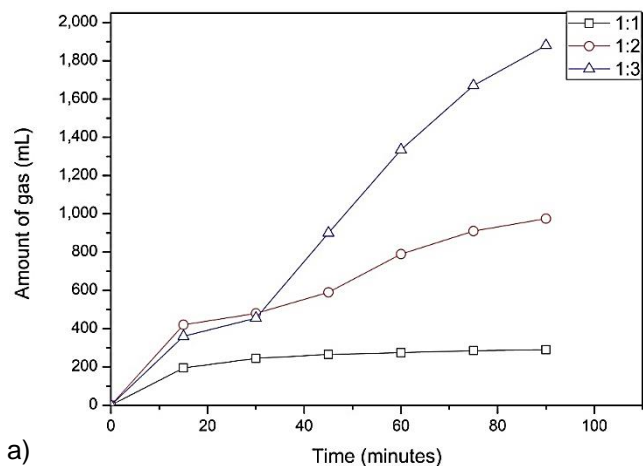

Figure 1. a) Schematic diagram illustrating the procedure for hydrogen gas evolution using aluminium dross is shown; b) X–ray diffraction pattern for powdered aluminium dross.

RESULTS AND DISCUSSION

The evolution of hydrogen gas is shown in Fig. 2 and Fig. 3. It can be seen from the graphs that the overall rate of gas evolution was initially high and then it became very less, thereby resulting in the stability of the overall gas production. The same trend is observed in both the alkalis used for the metal-water reaction.
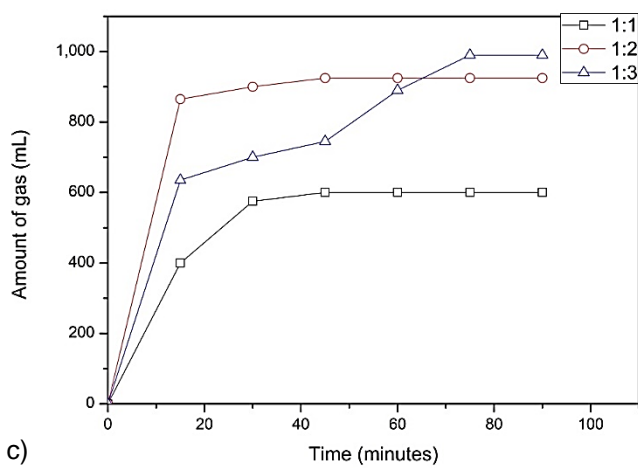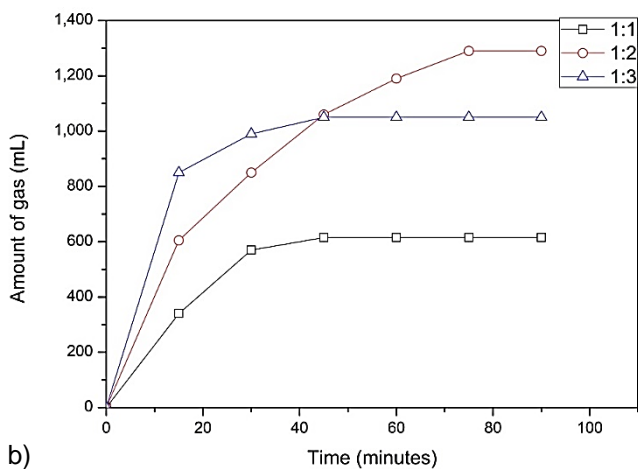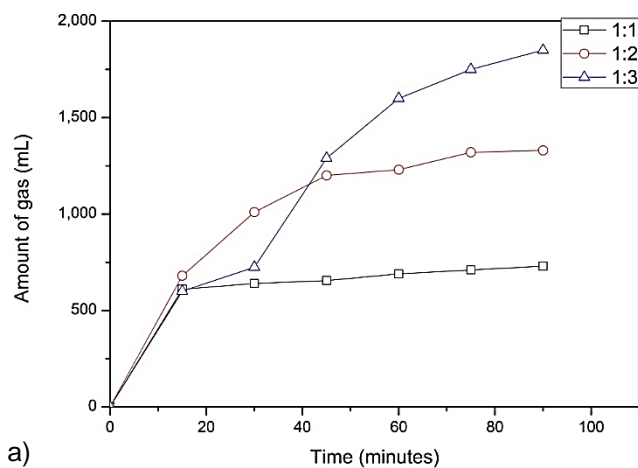
Figure 2. Gas evolution with the variation of temperature and weight ratios of NaOH:Dross is shown: a) reaction temperature is 40 °C; b) 50 °C and c) 60 °C.
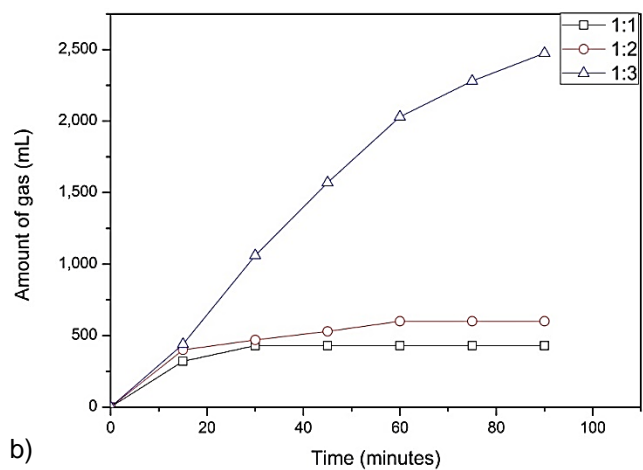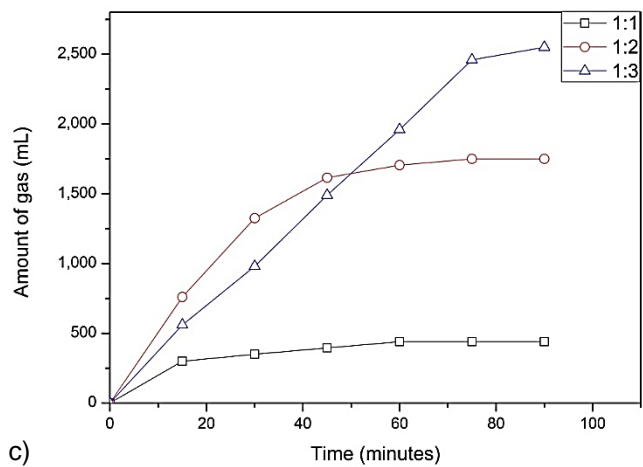
Figure 3. Gas evolution with the variation of temperature and weight ratios of KOH:Dross is shown: a) reaction temperature is 40 °C, b) 50 °C and c) 60 °C.

From the X-ray diffraction pattern analysis of the aluminium dross fines, it has been found that the major phases present in it are aluminium, alumina Al_2O_3, silica SiO_2 and γ alumina. With the presence of these phases, the heterogeneity of the raw material is clearly vivid. When aluminium dross is subjected to metal-water reaction under the presence of alkalis, the chances of reactions other than hydrogen production can take place. It is likely that these reactions interfere in the overall gas outcome.

Some of the reactions that contribute to the gas evolution are as under (Meshram et al., 2019):

$$2Al + 2NaOH + 6\,H_2O \rightarrow 2NaAl(OH)_4 + 3H_2 \qquad (1)$$

$$NaAl(OH)_4 \rightarrow Al(OH)_3 + NaOH \qquad (2)$$

$$2NaOH + Al_2O_3 + 3H_2O \rightarrow 2NaAl(OH)_4 \qquad (3)$$

It can be seen that when metallic aluminium reacts with sodium hydroxide and water, sodium aluminate forms with the evolution of hydrogen. However, when the same reactions take place with alumina, the hydrogen evolution is not observed. Also, it is observed that sodium aluminate decomposes into aluminium hydroxide and sodium hydroxide. Similar reactions take place in case of potassium hydroxide as well. The aluminate formed in this case, however, is relatively more stable than its sodium counterpart. Potassium aluminate does not dissociate into aluminium hydroxide and potassium hydroxide (Birnin-Yauri & Aliyu, 2014).

$$Al_2O_3 + 2KOH + 3H_2O \rightarrow 2KAl(OH)_4 \qquad (4)$$

$$2Al + 2KOH + 6H_2O \rightarrow 2KAl(OH)_4 + 3H_2 \qquad (5)$$
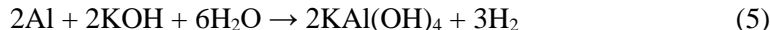
From Fig. 2, it is observed that the gas evolution is faster at the beginning. If the gas evolved at the beginning is not properly measured, or there are experimental errors during the trails, there is a fair chance that the overall amount of gas measured will have severe discrepancies. Just as the solid mixture of the dross and alkali comes in contact with the hot distilled water, the evolution of hydrogen takes place rapidly. It is this rate of gas evolution that needs to be measured properly.

At lower temperature (40 °C), the hydrogen evolution reaction is relatively slower. Also with lower amount of dross available for the reaction, the overall amount of gas generated is less, compared to higher ratios of dross and alkali. The trend is quite the same at higher temperatures (50 °C and 60 °C). Weight ratios 1:2 and 1:3 show greater evolution of hydrogen gas. This is merely due to the higher amount of aluminium available for the metal-water reaction. The temperature variation and the amount of aluminium in the system direct the gas generation.

Fig. 3 illustrates the gas evolution with potassium hydroxide mixture. It can be seen that the gas evolution has the similar trend as that of sodium hydroxide mixture. 1:1 weight ratio has least amount of gas evolution and rate of gas generation. 1:2 and 1:3 weight ratios perform better. The overall amount of gas increases with increase in the reaction temperature.

Comparing Fig. 2 with Fig. 3, it can be clearly observed that though the rate of gas evolution is initially less with potassium hydroxide mixtures, the amount of gas evolution is quite high at the climax of the reactions for a fixed period of time. While on the other hand, the initial surge of hydrogen is very large for sodium hydroxide. The

reaction rate reduces after nearly 30 minutes and thus the overall amount of gas produced becomes less. These trends in variation are mainly due to the side reactions taking place in the system.

CONCLUSIONS

This research presents a method of effectively producing hydrogen using aluminium-water reactions. Aluminium dross fine powder has been used for this purpose. With this method, hydrogen generation is coupled with industrial waste utilization. The waste metallic content sealed within the dross is utilized by the metal-water reaction. Employing alkalis (NaOH and KOH) for the reaction leads to great rise in the gas evolution.

It has been found that the potassium hydroxide solid mixture performs well with higher reaction temperatures, whereas the rate of gas evolution is very high for sodium hydroxide mixtures. The increase in the amount of dross in the mixture increases the overall amount of hydrogen produced, as the amount of aluminium available for the reaction increases.

Therefore, this research illustrates an alternative process to produce hydrogen with aluminium dross recycling. A complete circle is observed when industrial waste is linked with next-generation fuel.

REFERENCES

Birnin-Yauri, A.U. & Aliyu, M. 2014. Synthesis and Analysis of Potassium Aluminium Sulphate (Alum) from Waste Aluminium *Can. Int. J. Adv. Res. Chem. Sci.* **1**, 1–6.

David, E. & Kopac, J. 2012. Hydrolysis of aluminum dross material to achieve zero hazardous waste. *J. Hazard. Mater.* **209–210**, 501–509. https://doi.org/10.1016/j.jhazmat.2012.01.064

Meshram, A., Jain, A., Gautam, D. & Singh, K.K. 2019. Synthesis and characterization of tamarugite from aluminium dross: *Part I. J. Environ. Manage* **232**, 978–984. https://doi.org/10.1016/j.jenvman.2018.12.019

Meshram, A. & Singh, K.K. 2018. Recovery of valuable products from hazardous aluminum dross: A review. Resour. *Conserv. Recycl.* **130**, 95–108. https://doi.org/10.1016/j.resconrec.2017.11.026

Meshram, A. & Singh, K.K. 2017. *Generation of hydrogen-gas from aluminum dross, in: European Metallurgical Conference 2017*. Leipzig, Germany, pp. 1451–1460.

Uehara, K., Takeshita, H. & Kotaka, H. 2002. Hydrogen gas generation in the wet cutting of aluminum and its alloys. *Hournal Mater. Process. Technol.* **127**, 174–177.

Behavior of B20 fuels in arctic conditions

K. Sirviö[*], S. Niemi, R. Help, S. Heikkilä and E. Hiltunen

University of Vaasa, School of Technology and Innovations, PL 700, FIN-65101 Vaasa, Finland
[*]Correspondence: katriina.sirvio@univaasa.fi

Abstract. Several renewable and sustainable liquid fuel alternatives are needed for different compression-ignition (CI) engine applications to reduce greenhouse gas (GHG) emissions and to ensure proper primary energy sources for the engines. One of the shortcomings of several bio oils and first generation biodiesels has been their cold properties. Still, the need for alternative fuels is also present in arctic areas where the storing of the fuels may become problematic. The main aim of the current study was to determine how the storage related properties of fuel blends change if the fuels first freeze and then melt again. The samples were analyzed three times: as fresh, and after the first and second freezing-melting phase transitions.

The share of renewables within the blends was 20 vol-%. Rapeseed methyl ester (RME) and animal-fat based methyl ester (AFME) were blended with LFO in a ratio of 80 vol-% of LFO and 20-vol% of RME or AFME.

The investigated and compared properties were the FAME content of the neat FAMEs, and kinematic viscosity, density, oxidation stability index, and acid number of the blends. Cold filter plugging point was measured for AFME and its blend. According to the results, the quality of the FAMEs and their blends did not change significantly during the freezing over. The freezing-melting phase transition seems, thus, not to be as big a threat to the fuel quality as the high temperatures are. According to the results of this study, the studied fuels were feasible after the freezing-melting phase transition.

Key words: alternative fuels, fuel blends, storage conditions, arctic conditions, fuel stability, medium-speed engines.

INTRODUCTION

The 2030 EU climate & energy framework sets three key targets. The first one is to cut greenhouse gas emissions at least 40% from the level of 1990. The second target is to have at least a 27% share for renewables in energy consumption by 2030. The third one is to reach at least a 27% improvement in the energy efficiency (European Commission, 2017). All these actions are needed to delay the climate change. In marine industry, the need for cleaner fuels is the most urgent. The emission legislation in maritime is becoming stricter, first the limits of oxides of nitrogen, but now even the sulphur and particulate matter limits. For the EU inland waterways, the pollutant emissions must already be strongly reduced, also including the particulate number emissions. According to Third IMO GHG Study made in 2014, international shipping accounts for approximately 2.6% and 2.4% of CO_2 and GHGs on a CO_2e basis,

respectively (IMO, 2014). Additionally, shipping is one of the most important sources of black carbon in the Arctic sea areas (Quinn et al., 2011).

The development of the emissions legislation directs the transfer from fossil fuels to more sustainable alternative fuels. Many ship operators cannot yet meet the new regulations. The possibilities they have to meet the limitations is installing exhaust after treatment equipment or switching to low-sulphur diesel or residual, or to alternative fuels. Most of the latters are able to reduce engine emissions below the mandated limits. Many of them can be used in engines without engine modification. The commercial choice of the alternative, renewable fuels is, though, at the moment quite narrow. The share of renewables in transport is at present approximately 2.6% worldwide (REN21, 2017). For these reasons, the alternative fuel industry has grown dramatically for both liquid and gaseous fuels (McGill et al., 2013).

For compression-ignition (CI) engine applications, one reasonable solution is to use various blends of renewable and fossil liquid fuels until the availability of renewable fuels reaches the sufficient extent. Biodiesels, FAMEs, have been studied for long time and apparently, despite of the problems they may have, they are still of a great interest. Now, 95% of biodiesels are produced from edible vegetable oils, as RME (rapeseed methyl ester) in this study. The use of edible oils is problematic because it causes environmental problems, increases the edible oil prices and consumes food resources. Waste, recycled and non-edible oils would be much better options as raw materials. Waste animal-fat based biodiesel, AFME, also studied in the present study, forms a more favorable alternative. Nevertheless, the share of non-edible oils is minor, only 2% of total biodiesel production (Sajjadi et al., 2016). Waste animal-fats are still becoming more common feedstock as raw material for biofuel production. Veal and beef tallow, lard, chicken and goose fat have been successfully studied as raw materials for esterification process (Sander et al, 2018). Fur farming is one of the industries which produce animal fat as a residue and waste. The quantity of animal-fat based biodiesel manufactured as a by-product in fur farming is marginal but still it can have a notable regional impact on the energy efficiency and power production.

To be able to promote the transit from conventional fossil fuels to renewable alternatives, a large amount of additional research is required about various alternative fuels and in particular about their blends with conventional fuels. A lot of novel information has to be gathered about the blend properties through several fuel analyses.

Arctic conditions make extra problems in terms of alternative fuels and their handling. The saturated acids in FAMEs, present mainly in animal fat based methyl esters, cause them to solidify at low temperatures (Golimowski et al., 2017). This leads to blockages in filters or makes it even impossible to pump the fuel. For this reason, storing and using of biodiesels, at wintertime in arctic regions may be difficult. Fuel tank or store is usually placed outside. Biodiesels are not recommended to store for long time. The storage stability of fuels is threatened by contact with air, sunlight, metals and high temperature conditions (Agarwal & Khurana, 2013). Apparently, the effect of freezing-melting transitions on the fuel properties is not studied earlier. In case fuels are stored, and they solidify, it is important to know if they still are of good quality.

The main aim of the current study was to determine how the storage related properties of the B20 blends made of LFO and RME or AFME change if the fuels freeze. The samples were analyzed three times: as fresh, and after the first and second freezing-

melting phase transitions. The reference sample of each fuel was also analyzed. It was stored at dark at 20°C for 4 weeks.

The investigated and compared properties were the FAME content (for the neat FAMEs), and kinematic viscosity, density, oxidation stability index and acid number of the blends. The cold filter plugging point was measured for the AFME and its blend without reference sample.

MATERIALS AND METHODS

Fuels

Rapeseed methyl ester (RME) was a product of ASG Analytik-Service Gesellschaft mbH, Germany. As antioxidant, it contained 1,000 mg kg^{-1} of butylated hydroxytoluene (BHT) and it was delivered to the University of Vaasa (UV) in January, 2017. RME fulfilled the requirements of Standard EN 14214:2012 (EN 14214, 2012).

Animal-fat based methyl ester (AFME) was Feora Ecofuel, a product of Ab Feora which is located in Uusikaarlepyy, Finland. No antioxidant was added. AFME was delivered to the UV in October 2017.

Light fuel oil (LFO) was a product of Neste, Finland. It was low-sulphur (7.2 mg kg^{-1}) fuel, which fulfilled the requirements of Standard EN590 (EN 590, 2013). LFO was delivered to the UV in April 2017.

Methods

The samples were analyzed as fresh, and after the first and second freezing-melting phase transitions. The reference samples were stored at 20 °C, in dark, and measured after 4 weeks of storage. The temperature of the freezer was -26 °C. The investigated and compared properties were the FAME content for the neat FAMEs, and kinematic viscosity, density, oxidation stability index and acid number of the blends. Below, the analysis methods of the properties are described.

The oxidation stability index was measured by a Biodiesel Rancimat 873 instrument. The method is described in Standards EN 14112 (neat FAMEs) and EN 15751 (FAME blends) (EN 14112, 2003; EN 15751, 2014).

The acid number was analyzed by a titrator Metrohm Titrando 888. The measurement was produced according to Standard EN 14104 (EN 14104, 2003). The acid number was measured for fresh samples and after the first freezing-melting phase transition, as well as for the reference sample.

The kinematic viscosity and density were measured by a Stabinger SVM 3000 rotational viscometer (Anton Paar, 2012).

The ester content was measured by a Perkin Elmer gas chromatograph Clarus 580. The method is described in Standard EN 14103 (EN 14103, 2003).

The cold filter plugging point was measured using the method described in Standard EN116 (EN116, 2015). The cold filter plugging point was measured only for AFME sand its blend and after the first freezing-melting phase transition. The reference sample was not analyzed neither.

The relative standard deviations were the following: ester content < 1%, kinematic viscosity < 1%, oxidation stability 4.5%, acid number 7.9% and density < 1%. The relative standard deviation of CFPP measurement was not known.

RESULTS AND DISCUSSION

During the process, the neat AFME was frozen ice over. The LFO-AFME was frozen stiff but not ice over. The neat RME was also frozen ice over. RME-LFO was frozen stiff and two phases were distinguished.
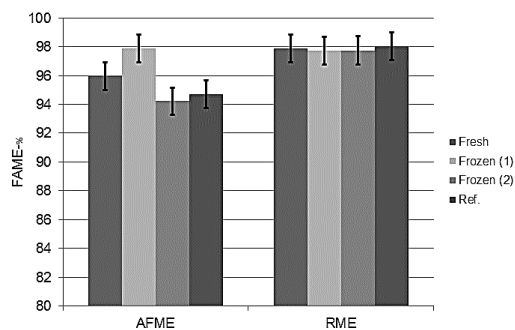
The results of the properties of neat animal-fat based methyl ester and its blend with LFO are presented in Table 1, Fig. 1 and Fig. 2. The results of the properties of neat rapeseed methyl ester and its blend with LFO are presented in Table 2, Fig. 1 and Fig. 3.

Table 1. Results of the properties of neat animal-fat based methyl ester and its blend with LFO

Sample	Kinematic viscosity, mm² s⁻¹ (40 °C)	Density, kg m⁻³ (15 °C)	OSI, h	Acid number, mgKOH g⁻¹	FAME content, % (m m⁻¹)	CFPP, °C
AFME-LFO						
Fresh	3.82	843	16	0.08		-4
Frozen (1)	3.83	843	16	0.07		-4
Frozen (2)	3.83	844	17	-		
Reference sample	3.82	844	20	0.08		
AFME						
Fresh	4.44	879	5.4	0.21	96.0	2
Frozen (1)	4.44	879	4.9	0.22	97.9	2
Frozen (2)	4.44	879	4.9	-	94.2	
Reference sample	4.43	879	5.2	0.23	94.7	

The FAME content of AFME, presented in Table 1 and Fig. 1, seemed to increase, from 96.0 m-% to 97.9 m-%, after the first freezing-melting phase transition. This increase is though within the error limits. After the second freezing-melting phase transition the result decreased to 94.2 m-% which is rather close to the result of reference sample, 94.7 m-%. The FAME content of RME, presented in Table 2 and Fig. 1, stayed rather constant during the experiment, for fresh sample it was 97.9 m-% and after both freezing-melting phase transition it was 97.7 m-%. The reference sample showed 98.0 m-%. The FAME content of AFME decreased after the second freezing-melting phase transition but the same was also observed in the reference sample. The trans-esterification reaction is known to be reversible (Fereidooni et al., 2018) and freezing-melting phase transition did not cause the reaction to go backwards.

Figure 1. FAME contents of AFME and RME.

The cold filter plugging point was measured only for the AFME and its blends (Table 2). CFPP was recorded as fresh, and after the first freezing-melting phase transition. For the neat AFME and AFME-LFO, the results were the same in both measurements. The result of AFME was 2 °C. AFME-LFO resulted in -4 °C.

Table 2. Results of the properties of neat rapeseed methyl ester and its blend with LFO

Sample	Kinematic viscosity, mm^2 s^{-1} (40 °C)	Density, kg m^{-3} (15 °C)	OSI, h	Acid number, mgKOH g^{-1}	FAME content, % (m m^{-1})
RME-LFO					
Fresh	3.85	844	21	0.13	
Frozen (1)	3.84	844	25	0.13	
Frozen (2)	3.84	844	25	-	
Reference sample	3.84	844	20	0.13	
RME					
Fresh	4.53	883	10	0.51	97.9
Frozen (1)	4.53	883	9.9	0.51	97.7
Frozen (2)	4.54	883	9.7	-	97.7
Reference sample	4.54	883	9.6	0.51	98.0

For fresh RME and RME-LFO, the CFPP had been measured in earlier studies and it was -14 °C and -29 °C, respectively. The difference in fatty acid contents explains the difference of the CFPPs between AFME and RME. High contents of saturated acids (C14:0, C16:0, C18:0) result in higher CFPP values while a high content of unsaturated fatty acids (C18:1, C18:2, C18:3) leads to lower CFPP values (Golimowski et al., 2017). Based on the earlier measurements, the content of saturated acids of AFME (C14:0, C16:0, C18:0, together 27.3%) was much higher than that for RME (6.2%). At the same time, the content of the unsaturated acids of RME (C18:1, C18:2, C18:3, in total 90.2%) was significantly higher than it was for the AFME (58.9%). The CFPP behavior of RME and its B20 blend in freezing-melting phase transition should thus be studied more detailed as it was done for AFME and its blend.

The kinematic viscosity, density and acid number of AFME and its blend stayed nearly constant during the experiment which can be seen in Table 1 and Fig. 2. The kinematic viscosity of AFME remained constant at 4.44 while the viscosity of blend was approximately 3.83 mm^2 s^{-1}. The density of AFME was 879 and of the blend 843 kg m^{-3}. The acid number was measured after the first freezing-melting phase transition but not after the second one. The acid number of AFME was 0.23 mg KOH g^{-1} and the acid number of blend 0.07 mg KOH g^{-1}. The reference samples resulted in slightly higher acid numbers compared to frozen samples. This increase is though within the error limits. The higher acid number of the reference sample may demonstrate that the freezing-melting phase transition did not promote acidification. As the acid number describes the corrosive potential of biodiesel (Xie et al., 2017), the lifetimes of fuel tanks and vehicle engines is reduced by time. According to the results of this study, the corrosive effect was not accelerated by freezing-melting phase transition. All the measured values were within a feasible range for instance for medium-speed engines.

The oxidation stability index (OSI) results of AFME and AFME blend are presented in Table 1 and Fig. 2. OSI was low for neat AFME, approximately 5 h, but for the LFO-AFME blend, it varied from 16 to 17 h. The OSI results for the reference samples were slightly higher than for the fresh samples, being 20 h. The measurements were carried out exactly the same way but there might still be chance for some unexpected issue which has caused the difference as the OSI result should not increase during the storage. Still, freezing over did not reduce the oxidation stability of the blend but. The oxidation stability of neat AFME needs improving for instance by antioxidant

addition. Antioxidants butylated hydroxytoluene (BHT) or butylated hydroxyanisole (BHA) are said to be effective in hindering the oxidation process of animal fat based methyl esters (Varatharajan & Pushparani, 2018).
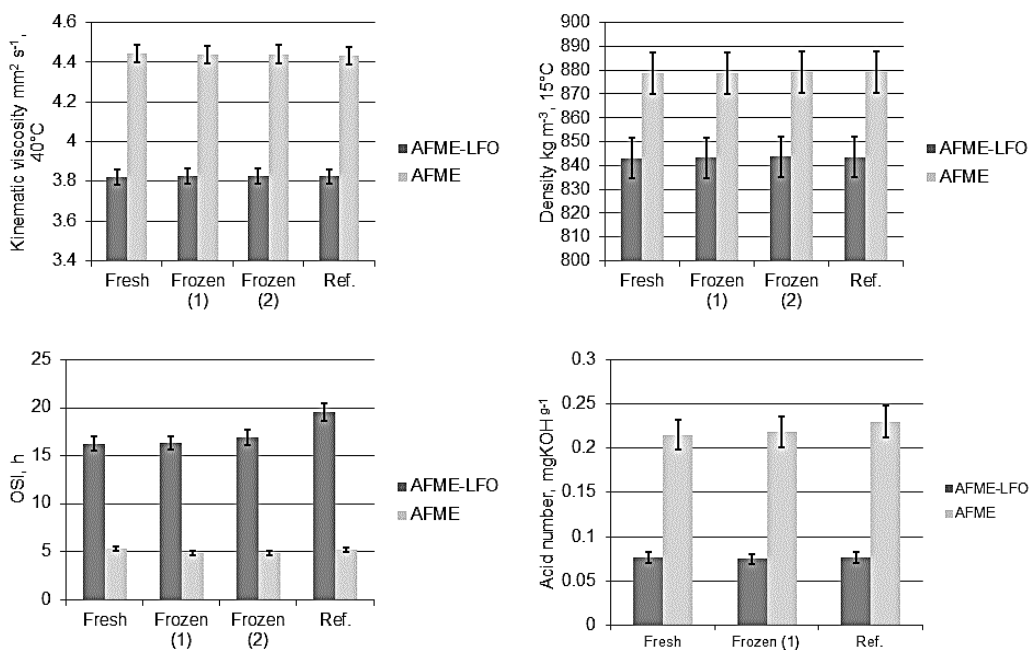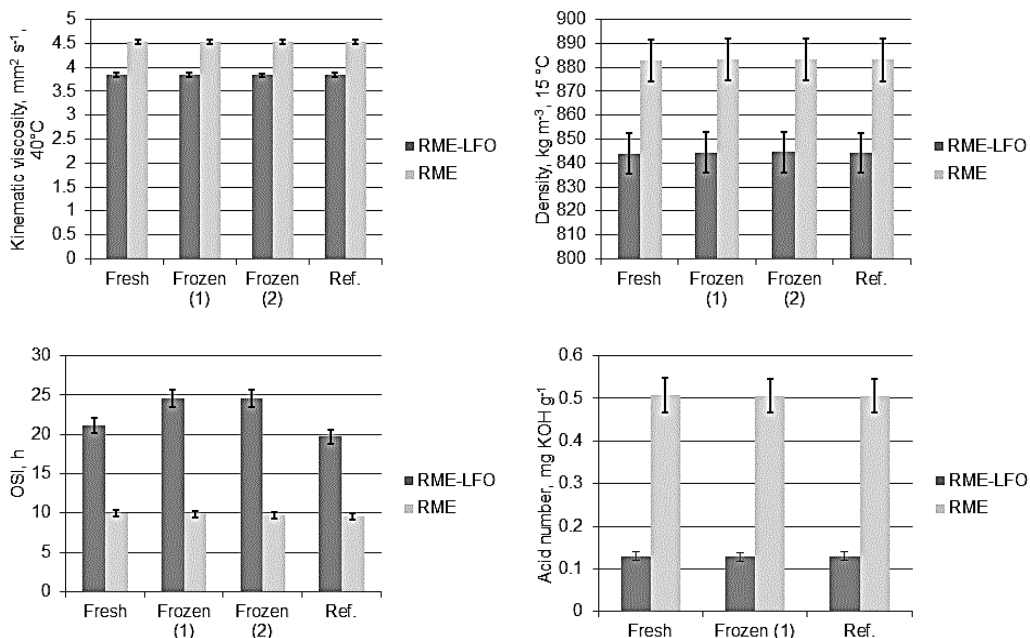

Figure 2. Kinematic viscosities, densities, oxidation stability indexes and acid numbers of AFME and its blend.

The kinematic viscosity, density and acid number of RME and its blend did not vary significantly during the experiment, in other words, freezing over did not reduce the quality of the fuels, which can be seen in Table 2 and Fig. 3. The kinematic viscosity of RME was 4.54 mm^2 s^{-1} and for the blend 3.84 mm^2 s^{-1}. The densities of the samples were 883 kg m^3 for RME and 844 kg m^{-3} for blend. The acid number was measured after the first freezing-melting phase transition but not after the second one. The acid number of RME was 0.51 mg KOH g^{-1} and acid number of RME-LFO blend was 0.13 mg KOH g^{-1}. As for the AFME blend, freezing-melting phase transition did not accelerate the corrosive effect in case of RME and its blend. The acid number of neat RME was though rather high, at its highest 0.51 mg KOH g^{-1}. This might slightly increase the corrosive potential of RME. FAME that is used for fuel blending should fulfill the requirements set in Standard EN 14214. This was not the case for this RME, as according to the mentioned standard, the acid number should not exceed 0.50 mg KOH g^{-1} (EN 14214, 2014).

The OSI results of RME and RME blend are also presented in Table 2 and Fig. 3. OSI of the neat RME remained approximately constant at 10 h. The OSI of RME-LFO blend seemed to increase from 21 h to 25 h after freezing over. The result of the reference sample was only 20 h. Still, similarly to AFME and its blend; freezing over did not reduce the oxidation stability of the RME blend. Altogether, all measured properties of the RME blend were at a proper level and this fuel was still, after freezing-melting

transition, feasible for engines. However, the acid number of neat RME was quite high and it may weaken the corrosion tolerance of the tanks and engine parts.

Figure 3. Kinematic viscosities, densities, oxidation stability indexes and acid numbers of RME and its blend.

Dunn (2008) studied the effect of temperature on the oil stability index (h) of biodiesel and found that the higher the temperature, the faster the decrease in oxidation stability (Dunn, 2008). Dwivedi & Sharma (2016) also stated the same, biodiesels are thermally unstable and the temperature increase decreases the oxidation stability (Dwivedi & Sharma, 2016). Compared to the found effects of high temperatures on the fuel stability, it seems that freezing is not as detrimental to the fuel quality as the high temperatures.

CONCLUSIONS

The main aim of the current study was to determine the feasibility and properties of neat RME and AFME and their B20 blends for arctic conditions by analyzing how the properties change if the fuels freeze.

The properties of the samples were analysed three times: as fresh, and after the first and second freezing-melting phase transitions. Rapeseed methyl ester (RME) and animal-fat based methyl ester (AFME) were blended with LFO in a ratio of 80 vol-% of LFO and 20-vol% of RME or AFME. The investigated and compared properties were the FAME content (for the neat FAMEs), and kinematic viscosity, density, oxidation stability index and acid number for the blends. The cold filter plugging point was analysed for AFME and its blend.

According to the results of the study, the following conclusions could be drawn:

- The quality of the FAMEs and their blends did not change significantly during the freezing over. The freezing-melting phase transition seems not to be as detrimental to the fuel quality as the high temperatures are. The studied fuels were feasible after the freezing-melting phase transition.
- The freezing-melting phase transition did not cause the reversible transesterification reaction of FAMEs to go backwards.
- AFME and its blend seemed to be feasible options for medium-speed engines in arctic conditions. The oxidation stability of neat AFME must, however, be improved, e.g., by adding suitable antioxidant.
- RME-LFO blend seemed to be feasible for medium-speed engines even in arctic conditions but the RME should fulfill the requirements set for FAMEs. Neat RME had a slightly high acid number which increases the risk for corrosion.

REFERENCES

Agarwal, A.K. & Khurana, D. 2013. Long-term storage oxidation stability of Karanja biodiesel with the use of antioxidants. *Fuel Processing Technology,* **106**, 447–452.

Anton Paar. 2012. SVM 3000 Stabinger Viscometer –brochure.

ASTM D7042-16e3, 2016. *Standard Test Method for Dynamic Viscosity and Density of Liquids by Stabinger Viscometer (and the Calculation of Kinematic Viscosity)*, ASTM International.

Dunn, R.O. 2008. Effect of temperature on the oil stability index (OSI) of biodiesel. *Energy Fuels* **22**(1), 657–662.

Dwivedi, G. & Sharma, M.P. 2016. Investigation of Oxidation stability of Pongamia Biodiesel and its blends with diesel. *Egyptian Journal of Petroleum* **25**(1), 15–20.

EN 116:2015. 2015. *Diesel and domestic heating fuels. Determination of cold filter plugging point. Stepwise cooling bath method*, Finnish Petroleum and Biofuels Association.

EN 14103:2003. 2003. *Fat and oil derivatives. Fatty Acid Methyl Esters (FAME). Determination of ester and linolenic acid methyl ester contents*. Finnish Standards Association SFS.

EN 14104:2003. 2003. *Fat and oil derivatives. Fatty acid methyl esters (FAME). Determination of acid value*. Finnish Standards Association SFS.

EN 14112. 2003. *Fat and oil derivatives. Fatty acid methyl esters (FAME). Determination of oxidation stability (accelerated oxidation test).* Finnish Standards Association SFS.

EN 14214:2012+A1:2014. 2014. *Liquid petroleum products - Fatty acid methyl esters (FAME) for use in diesel engines and heating applications - Requirements and test method.* Finnish Petroleum and Biofuels Association.

EN 15751:2014. 2014. *Automotive fuels. Fatty acid methyl ester (FAME) fuel and blends with diesel fuel. Determination of oxidation stability by accelerated oxidation method.* Finnish Petroleum Federation.

European Commission. 2017. 2030 climate & energy framework. *https://ec.europa.eu/clima/policies/strategies/2030_en*, accessed: 25.10.2018.

Fereidooni, L., Tahvildari, K., Mehrpooya, M. 2018. Trans-esterification of waste cooking oil with methanol by electrolysis process using KOH. *Renewable Energy* **116, A**, 183–193.

Golimowski, W., Berger, W.A., Pasyniuk, P., Rzeznik, Czechlowski, M., Koniuszy, A. 2017. Biofuel parameter dependence on waste fats' fatty acids profile. *Fuel* **197**, 482–487.

International Maritime Organization. Third IMO GHG Study. 2014. *http://www.imo.org/en/OurWork/Environment/PollutionPrevention/AirPollution/Pages/Greenhouse-Gas-Studies-2014.aspx*, accessed 23.10.2018.

McGill, R., Remley, W., Winther, K. 2013. *Alternative Fuels for Marine Applications. Annex 41.* A Report from the IEA Advanced Motor Fuels Implementing Agreement, p. 108.

Quinn, P.K., Stohl, A., Arneth, A., Berntsen, T., Burkhart, J.F., Christensen, J., Flanner, M., Kupiainen, K., Lihavainen, H., Shepherd, M., Shevchenko, V., Skov, H. & Vestreng, V. 2011. *The Impact of Black Carbon on Artic Climate. AMAP Technical Report No. 4*, p. 74.

Sajjadi, B., Raman, A.A.A., Arandiyan, H. 2016. A comprehensive review on properties of edible and non-edible vegetable oil-based biodiesel: Composition, specifications and prediction models. *Renewable and Sustainable Energy Reviews* **63**, 62–92.

Sander, A. Košćak, M.A., Kosir, D., Milosavljević, N., Vuković, J.P. & Magić, L. 2018. The influence of animal fat type and purification conditions on biodiesel quality. *Renewable Energy* **118**,752–760.

SFS-EN 590:2013. *Automotive fuels. Diesel. Requirements and test methods.* Finnish Petroleum and Biofuels Association; 2013.

SFS-EN 15751:2014. 2014. *Automotive fuels. Fatty acid methyl ester (FAME) fuel and blends with diesel fuel. Determination of oxidation stability by accelerated oxidation method,* Finnish Petroleum and Biofuels Association.

REN21. 2017. *Renewables 2017 Global Status Report*. ISBN 978-3-9818107-6-9. Pages 302.

Varatharajan, K. & Pushparani, D.S. 2018. Screening of antioxidant additives for biodiesel fuels. *Renewable and sustainable energy reviews* **82**(3), 2017–2028.

Xie, W.-Q., Gong, Y.-X. & Yu, K.-X. 2017. A rapid method for the quantitative analysis of total acid number in biodiesel based on headspace GC technique. *Fuel* **201**, 236–240.

Management of wastewater from landfill of inorganic fiberglass

K. Tihomirova[1,2,*], V. Denisova[1], K. Golovko[1], O. Kirilina–Gutmane[2],
L. Mezule[1] and T. Juhna[1]

[1]Riga Technical University, Faculty of Civil Engineering, Research Centre for Civil
Engineering, Water Research Laboratory, Kipsalas 6a–263, LV–1048 Riga, Latvia
[2]The Institute of Food Safety, Animal Health and Environment 'BIOR' Elemental
analysis division, Lejupes street 3, LV–1076 Riga, Latvia
*Correspondence: kristina.tihomirova@rtu.lv

Abstract. Sustainability is one of the key factors in smart environment management and include
the reduction of environment footprint. The waste and wastewater management plans are aimed
on actions to reduce the amount of waste and environmental pollution. This includes collection
of waste, logistics, storage, processing or valorisation and also treatment. The aim of this research
was to evaluate environmental pollution risk and to demonstrate one of the wastewater
management schemes to reduce the pollution level.
Evaluation of the better management scheme was performed in one of the landfills in Latvia,
where fiberglass waste and other inorganic waste is stored. Onsite evaluation results demonstrated
the need to develop a better wastewater management scheme of inorganic fiberglass landfill.
After that, laboratory–scale experiments for conventional coagulation and biodegradation tests
have been performed for efficient management.

Key words: landfill leachate, fiberglass, wastewater management, wastewater treatment,
environmental pollution.

INTRODUCTION

Over the recent years, people have become aware that environment is a
comprehensive resource that requires smart management. This has led to an increased
need for sustainable energy management, steady energy supply, reduced energy
consumption and search of new renewable energy sources (Coaffee, 2008). In the
meantime the security policy has been focused on terrorist hazards and natural disasters
(Collier et al., 2013), resource recovery and reduction of wastes.

Efficient waste management is one of the priorities in EU use of resources and is
described in Waste Avoidance and Resource Recovery Act from 2001, Waste Avoidance
and Resource Recovery Amendment (Container Deposit Scheme) Act 2016 No. 57 and
Waste Avoidance and Resource Recovery (WARR) Strategy updated every five years.
In 1992 the Convention on the Protection of the Marine Environment of the Baltic Sea
Area (Helsinki Convention) was signed to reduce the inflows of nutrients and hazardous
substances, as well as to promote a cleaner future of the Baltic Sea. The document was
adopted by HELCOM in 1993 (Fuller, 2013). The international convention encompasses
various measures for prevention and elimination of pollution of the Baltic Sea. Due to

high anthropogenic activities, increase in the level of the nutrients (nitrogen and phosphorus) in the Baltic Sea catchment area, eutrophication process occurs faster than expected (Ærtebjerg et al., 2003). The waste and wastewater management descriptions are aimed on actions to reduce the amount of waste and environmental pollution generated by households and industry, resource recovery including re–use, recycling, reprocessing and also better waste and wastewater management procedure. This includes collection of waste, logistics, storage, processing or valorisation and also treatment.

Although glass can be repeatedly recycled with no loss of quality, there are still large volumes of glass ending up in the landfill. Glass recycling rates in European Union nations are the world's highest, averaging 73% (FEVE News Corner, 2017), but in other countries glass recycling rate is less significant, for example in the US (34%) and Singapore 20%. One major barrier to conventional recycling is the need to separate glasses into its various types (Heiriyanto et al., 2018), e.g., fiberglass, cullet, container glass, mirrors and other metal–coated products. Thus, the formation of highly pollutant leachate by water infiltration through waste deposits is inevitable. The control of a landfill site and effective appropriate treatment has a high–priority importance for the present and future environmental conditions.

The most popular method to reduce the pollution from landfill leachates is reverse osmosis (RO). RO systems were developed in 1950 in USA for water desalination. These systems use a semipermeable membrane to remove ions, molecules and larger particles from solution (Busch et al 2010; Šír et al., 2012). These are effective, but have several disadvantages, for example, become clogged often and produce a limited amount of water per day. The RO filter system management is quite expensive and it is predicted that the amount of global landfill wastewaters will increase in the future; therefore, it is necessary to apply cost effective and alternative wastewater treatment methods such as coagulation and biofiltration. Certainly, advantages and disadvantages depend on the untreated water quality and requirements for treated water quality before it can be released into the environment.

The aim of this research was to evaluate environmental pollution risk and to demonstrate one of the wastewater management schemes to reduce pollution level with cost effective approaches like coagulation and biofiltration. The proposed technological approach was tested on wastes from a landfill where fiberglass and inorganic material is traditionally deposited.

MATERIALS AND METHODS

Sample collection

Wastewater samples (storm water after the direct contact with fiberglass waste) were collected from a landfill in Latvia in plastic carboys (50 mL^{-2} L) stored in a refrigerator (2 °C to 5 °C) after transport and analysed within 24 h for their chemical characteristics.

After field inspection there were six types (Table 1) of fiberglass solid wastes, based on the difference on its structure, hardness and thickness. All types were collected in plastic bags and stored at room temperature (RT) before experiments.

Table 1. Description of fiberglass samples

Sample	Picture of fiberglass	Description
1.		White, hard, dense, long threads with glass capsules
2.		Yellow, hard, dense, long threads
3.		Light yellow, soft fibre, short threads
4.		Yellow, hard, dense, long threads, similar to glass with fluffy surface
5.		Natural white, soft fibre, short threads
6.		Light white, hard, dense, very long threads, similar to fabric yarn

Experimental setup

In this study, the management scheme for wastewater from landfill of inorganic fiberglass was developed via: field inspection, sampling on the field, contaminant migration tests, coagulation tests, biodegradation tests, development of recommendations for waste management on the landfill.

Contaminants migration tests

To determine the contact time required to extract the maximum amount of contamination from the fiberglass samples and its migration into the water phase 200 g of fiberglass samples were soaked in 2 L of water (10% w v^{-1}) and kept for 24 hours at dark (RT = 21 ± 2 °C) in reservoirs with headspace. Six type of collected fiberglass were used to determine the amount of contamination from different type of fiberglass samples. Subsamples were taken for analysis after 48 h (Table 2).

To prepare average artificial wastewater fiberglass sample were homogenised trough the mixing in equal amount fiberglass, an average sample were soaked in tap water (10% w v^{-1}) and kept for 24 hours.

Coagulation or Jar tests

Standard Jar tests (Phipps & Bird PB–900 Six Paddle) were used to investigate the removal of the organic matter. Aliquots (2 L) of sample were dosed with 3 stock solutions of coagulant (aluminium sulphate, iron chloride, bentonite). Samples were refrigerated prior to coagulation Jar testing, which was undertaken at room temperature (21 °C) and involved a 1 min rapid mix at 313 rpm, a 30 min slow mix at 41 rpm and 1 h sedimentation period. The pH was adjusted before the coagulation using concentrated hydrochloric acid and 10 M sodium hydroxide. At the end of the sedimentation period subsamples were taken for analysis (Table 2).

Biodegradation tests

The biodegradation kinetic tests were performed by the manometric methods (Jouanneau et al., 2014) for BOD determination using the OxiTop® IS 12 system (WTW, Germany). The samples were incubated for 5 days at 20 ± 1 °C (incubator) in 510 mL nominal volume brown bottles closed tightly with the OxiTop® measuring head and placed at the stirring platform. The results were expressed as mg O_2 L^{-1} and this allowed to investigate the BOD removal efficiency.

Analysis of wastewater samples

All analyses were conducted according to the standard methods (Table 2).

Total organic carbon (TOC) measurements were performed with Primacs MCS TOC analyser (Scalar, Netherland) based on high temperature and acidification of sample and by the difference of the total carbon and inorganic carbon measurement. Each sample was tested in duplicate and the mean values were calculated (CV ≤ 2%).

Table 2. Water quality analytical methods

Parameter	Reference
Total Organic Carbon	LVS EN 1484:2000
Chemical Oxygen Demand	LVS ISO 6060:1989
Biological Oxygen Demand	LVS EN 1899–2:1998
Total Nitrogen	LVS EN ISO 11905–1:1998
Total Phosphorus	LVS 6878:2005 (part 7)
Metals	LVS ISO 17294–2:2016
pH	LVS EN ISO 10523:2012
Dissolved oxygen	LVS EN ISO 5814:2013
Turbidity	LVS EN ISO 7027–2002
Conductivity	LVS EN 27888:1993
Elements	LVS EN ISO 17294–2:2016

Total organic carbon (TOC)measurements were performed with Primacs MCS TOC analyser (Scalar, Netherland) based on high temperature and acidification of

sample and by the difference of the total carbon and inorganic carbon measurement. Each sample was tested in duplicate and the mean values were calculated (CV ≤ 2%).

Determination of concentration of Total Nitrogen (TN) and Total Phosphorus (TP) were performed with UV–Vis spectrophotometer M501 (Camspec, UK) after sample mineralisation.

Electrical conductivity (EC), pH, RedOx potential and dissolved oxygen were determined using Multi 340i SET B (WTW, Germany).

Turbidity was measured using the turbidimeter HACH 2100 P (HACH, USA).

Elements (boron (B), sodium (Na) and zinc (Zn)) concentrations were determined by Agilent 7700x ICP–MS (Inductively Coupled Plasma Mass Spectrometer, USA) using Nitric acid (69.0%, Trace Select) to preserve the samples.

Z–potential was determined using Zetasizer Nano ZS90 (Malvern, UK). The samples were taken for measurements of Z–potential at different pH level. Each sample was analysed at least 15 times and the arithmetic mean and standard deviation was calculated. Measurements were made at 20 °C. Analysis of control solutions was performed with each series of samples to evaluate the accuracy of the results.

Several repetitions of each sample ($n = 3$) were analysed to check the reproducibility of each method.

RESULTS AND DISCUSSION

In this study, the management scheme for wastewater from landfill of inorganic fiberglass was developed thought various laboratory scale tests.

Field inspection

Landfill under study can be divided into old organic and intermediate inorganic wastes sectors. If the organic waste sector is fully managed, thus inorganic wastes are located on a field without drainage and treatment system.

About 80% of wastes in inorganic sector are fiberglass, and other 20% form rubber tires, plastic, metal, textile and organic wastes, including wood.

Sampling on the field was performed in 3 sampling points. Sample points can be characterised as water ditches or pits on different landfill sites, where storm water after contact with wastes on landfill was collected. Results of the analysis of wastewater samples collected on the field showed that pollution risk is high (Table 3).

Table 3. Results of chemical characterization of samples from the field

	1.	2.	3.
pH	10.2 ± 0.1	9.2 ± 0.1	8.84 ± 0.1
EC, $\mu S\ cm^{-1}$	$2,100 \pm 21$	$2,030 \pm 40$	$1,783 \pm 35$
COD, mg L^{-1}	$2,580 \pm 258$	153 ± 13	200 ± 19
BOD$_5$, mg L^{-1}	$1,491 \pm 218$	40 ± 3	12 ± 1
TN, mg L^{-1}	149 ± 12	5.41 ± 0.43	17.7 ± 1.8
TP, mg L^{-1}	10.6 ± 0.5	0.24 ± 0.02	9.62 ± 0.98
B, mg L^{-1}	102 ± 10	46 ± 3	199 ± 16
Na, mg L^{-1}	$13,452 \pm 1,345$	397 ± 27	$2,694 \pm 215$

COD maximum was $2,580 \pm 258$ mg L^{-1}, BOD$_5$ $1,491 \pm 218$ mg L^{-1}, total nitrogen 149 ± 12 mg L^{-1} and total phosphorus 10.6 ± 0.5 mg L^{-1}. Due to the fact that main industries using the landfill are linked with glass and fiberglass production, boron and

sodium concentrations were evaluated primarily (EPA Report 815–R–08–012, 2008). Presence of high amount of boron was determined 102 ± 10 mg L^{-1}. With respect to the industry specifics (fiberglass processing), presence of elevated concentrations of other metals (especially Ni and Cr) might be regarded as an environmental risk a problem (Modin et al., 2011). According to the results, less than half of the organic substances are biodegradable (Table 3), indicating the need to combine various treatment methods, e.g. biological treatment with coagulation or other physicochemical methods.

The wastewater formed at the landfill can be compared with industrial wastewater that has strict management requirements. Difference between the results can be explained with the following remarks after field inspection: (I) the waste is located on an area without drainage system; (II) therefore, the collection of a representative sample was difficult. According to Brennan et al. (2017) inorganic waste on landfills are more biodegradable during the first 10 years.

After that, laboratory–scale experiments with collected fiberglass solid wastes for conventional coagulation and biodegradation tests have been performed.

Migration tests

The goal of the migration tests was to evaluate the pollution level from various fibreglass waste types. The results showed that the migration of contamination occurred already after 15 minutes, the peak was reached after 3 h and did not change significantly during the next 48 h. A tap water was used as a blank sample and a correction was made to calculate the contamination level for analysis (Table 4).

Table 4. Results of chemical characterization of samples after 24 h of contact time of fiberglass and water ($n = 1$)

Sample[*]	pH	EC, µS cm^{-1}	NTU	TOC, mg L^{-1}	B, mg L^{-1}	Na, mg L^{-1}	Zn, mg L^{-1}
Blank	7.39	451	0.88	7.4	0.003	9.60	0.025
1.	10.98	649	143	34.5	0.006	152.00	5.320
2.	6.94	514	61.2	25.8	0.243	10.30	0.077
3.	7.55	535	6.60	23.6	0.373	10.50	0.050
4.	7.55	504	16.9	26.7	0.101	9.76	0.033
5.	11.97	1,620	299	79.5	0.032	730.00	7.430
6.	7.56	544	16.7	25.6	0.584	20.40	0.214

[*]Sample identification according to Table 1.

Results of samples after 24 h contact of fiberglass and water showed that pH increased in the water and reached 10.98 and 11.97 in samples No. 1 and 5 after 24 h contact time. Turbidity level increased up to 143 and 299 NTU, respectively. The conductivity level increased to 1,620 µS cm^{-1} only in the solutions with sample No. 5. As a result of the migration process, a solution containing several elements is obtained (Table 4). Higher concentrations of boron were found in samples No. 6 (0.584 mg L^{-1}), 3 (0.373 mg L^{-1}) and 2 (0.243 mg L^{-1}), sodium – in sample No. 5 (20.40 mg L^{-1}), and zinc – in sample No. 5 (7.430 mg L^{-1}) and 1 (5.320 mg L^{-1}). According to results, there are two samples that have significant influence on the environment (No. 1 and 5). If it is not possible to sort the waste, homogenisation (e.g. mixing in equal amount) of all fiberglass waste is recommended for the treatment plant to obtain average leached wastewater from the field.

To determine the stability of the fiberglass solutions, measurements of Z–potential at different pH level were performed for average artificial wastewater solutions (Fig. 1).
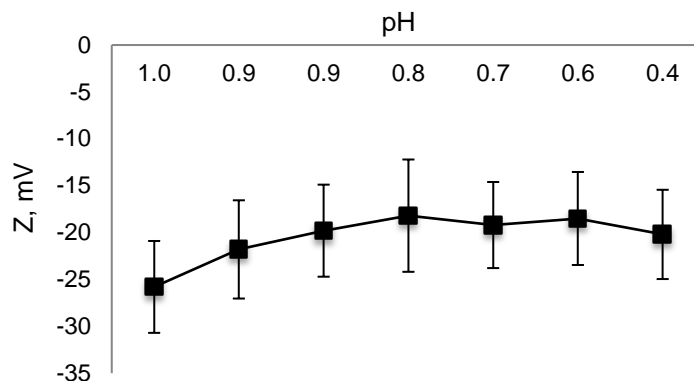
Figure 1. Changes of Z–potential in solution at different pH level.

Usually pH has a significant effect on Z–potential and indicates that coagulation process is active and agglomeration of contaminants and coagulant is performed. The results showed that the Z–potential ranged from -20.2 to -25.8 mV with pH of 3.99 to 10.02. This means that the solution contains a suspension whose balance does not change with changing environmental conditions, thus the optimisation of coagulation to increase efficiency by using the pH control is impossible.

Coagulation tests
To evaluate the potential of coagulation for removal of the fiberglass pollution, three coagulants were tested on average artificial wastewater solutions: aluminium sulphate; iron chloride and bentonite.

The results with aluminium sulphate showed that pH of the solution decreased from 5.17 to 4.45, but the EC of the solution increased from 686 to 828 μS cm^{-1} with an increase in coagulant dose from 35 mg Al L^{-1} to 60 mg Al L^{-1}, respectively. TOC removal was not effective (24%). The boron concentration in the initial solution was 3.50 ± 0.35 mg L^{-1} and ranged from 2.90 ± 0.29 to 2.83 ± 0.28 mg L^{-1} in samples after coagulation. Z–potential in the initial solution was -17.50 ± 5.08 mV and increased to 1.27 ± 4.33 mV with alum dose of 35 mg Al L^{-1} and reached a maximum of 5.81 ± 3.03 mV at alum dose of 60 mg Al L^{-1}. The maximum removal of TOC concentration was only 30% after coagulation with alum dose 35 mg Al L^{-1} and pH 5. After coagulation with 55 mg Al L^{-1} coagulant doses, the maximum turbidity reduction (2.59 NTU) was observed (Fig. 2). No changes in element concentrations at different coagulant doses and pH level were observed.

Similar tendency was observed with iron coagulant. The pH decreased from 9.55 to 6.48 and the EC of the solutions increased from 685 to 1,030 μS cm^{-1} with increase in coagulant dose from 35 mg Fe L^{-1} to 60 mg Fe L^{-1}. TOC removal was not effective (only 20%). Removal of elements was not observed. Z–potential ranged from -7.72 ± 5.72 mV in the initial solution to 2.75 ± 5.28 mV and 2.28 ± 3.92 mV at various Fe doses. The lowest turbidity was obtained at a coagulant dose of 60 mg Fe L^{-1} (4.68 NTU) and the same dose at pH 5 (8.91 NTU) (Fig. 2).

Bentonite was chosen as natural and low cost coagulant. It demonstrated the maximum reduction of turbidity (97%) and TOC (71%) at the dose of 1,050 mg L^{-1} and pH 5 (Fig. 2). Unfortunately, element concentrations in solutions before and after coagulation did not change (including coagulation with aluminium and iron) or slightly increased boron by 0.4% and sodium by 20% after coagulation with bentonite. This observation can be explained by the fact that bentonite coagulants are clays containing natural hydrated aluminium silicates, in which some magnesium and iron atoms replace aluminium and silicon atoms. Due to the inefficient coagulation process, overall concentration of elements in wastewater sample and added coagulant solutions can increase. At the same time bentonite coagulant showed significantly higher efficiency on the removal of organic and colloidal particles.
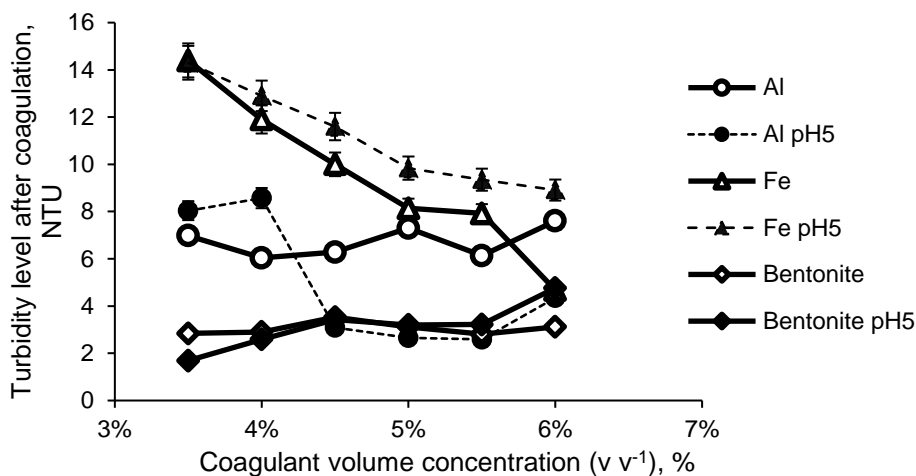
Figure 2. Changes of turbidity level during the coagulation process with alum, iron and bentonite coagulants (to compare process efficiency the volume concentration of coagulants was used in this graph).

Approximately 90% of hydrophobic contaminants can be removed by coagulation (Hu et al., 2016; Bu et al., 2019) due to the solubility (hydrophobic is less soluble) and stronger interaction with metal coagulant (hydrophobic fractions form stable metal – organic complex) (Sharp et al., 2006; Ghernaout, 2014). Wastewater formed after fiberglass contact with water contains high concentrations of organic matter, metals and elements. Main component of fiberglass is the silicon that form complex compounds with metals, resulting in low efficiency of surface discharge (e.g. coagulation).

Biodegradation tests

The aim of the experiments was to estimate the degradation rate of BOD in pre–treated wastewater samples. BOD kinetic tests were performed with an untreated and 6 pre–treated samples after coagulation: (1) IN (pH 10.63); (2) 35 mg Al L^{-1} (pH 6.75); (3) 35 mg Al L^{-1} (pH 5.40); (4) 35 mg Fe L^{-1} (pH 9.37); (5) 35 mg Fe L^{-1} (pH 5.20); (6) 1,050 mg of Bentonite L^{-1} (pH 10.35); (7) 1,050 mg of Bentonite L^{-1} (pH 5.42).

Fig. 3 shows the removal efficiencies after pre–treatment with three different coagulant types at the best pH level.
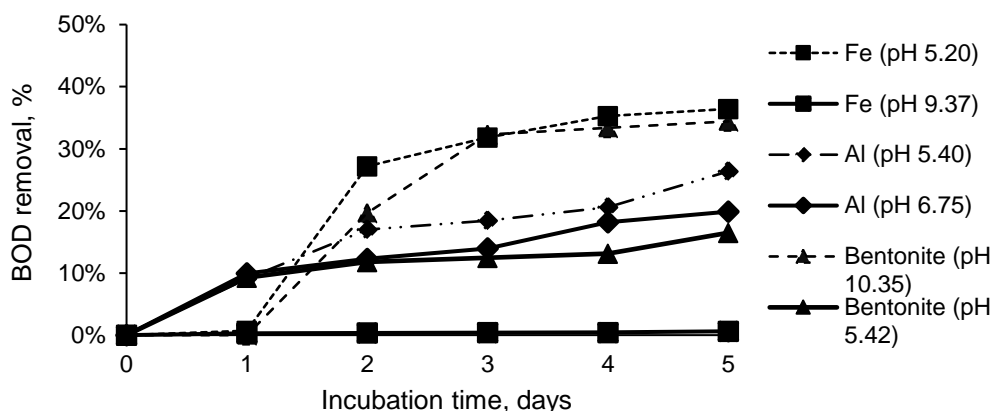
Figure 3. BOD removal through 5 incubation days for pre–treated samples after coagulation.

After the pre–treatment, among three coagulants, iron chloride at pH 5.20 showed the highest removal of BOD – 36%, the concentration reduced from 131 mg L^{-1} to 83 mg L^{-1}. Similar result was observed with the bentonite coagulant at pH 10.35, 34% BOD removal was achieved. The aluminium sulphate coagulant showed the lowest BOD removal efficiency – 26%. The average BOD removal after coagulation process can be estimated at about 30% (not effective).

The results showed that the COD value in the initial (IN) fiberglass solution was 635 ± 64 mg L^{-1} and the biodegradable fraction was only 20%. In the pre–treated samples after coagulation, the COD concentration decreased to 346 mg L^{-1} with 35 mg Al L^{-1}, 279 mg L^{-1} – with 35 mg Fe L^{-1} and 299 mg L^{-1} – with 1,050 mg Bentonite L^{-1}. The biodegradable fraction was 31%, 30% and 38% respectively.

The efficiency of biological treatment depends on the type of substrate (hydrophobicity/hydrophilicity, concentration of contaminants), the age of landfill and continuous biological activity (Costa et al., 2019). BOD can be calculated from the decrease of the dissolved oxygen concentration that is proportional to the initial biodegradable substrate concentration. (Pitman et al., 2015). Biological treatment processes usually remove about 70–90% of BOD (Peng, 2017), thus, increasing water stability. To avoid bacterial regrowth after wastewater treatment, the threshold value for the BOD_5 is set to ≤ 25 mg L^{-1}, however, the effluent limit values for WWTPs with pollution load less than 2,000 population equivalent (PE) are not regulated by these requirements (Council Directive 91/271/EEC, 1991).

Taking into account the maximum process efficiencies, obtained during the laboratory tests, it can be concluded that by coagulation about 40% of organic compounds and 90% of colloidal particles can be removed. Element concentrations were not significantly affected.

Table 5. Efficiency of used methods

Coagulant	Coagulation stage	Biological treatment	Total efficiency of contaminant removal, %
Alum	46%	31%	77%
Iron	56%	30%	86%
Bentonite	53%	38%	91%

Approximately 30% of organic contaminants can be removed by biodegradation (Table 5).

Existing rules (Council Directive 91/271/EEC, 1991) set that the BOD and COD should be reduced by 50–70% and 50–75%, respectively (for pollution load 200–2,000 PE). Laboratory experiments have shown that combination of chemical coagulation and biological purification can reduce organic matter and turbidity according to the rule requirements (Table 5). However, these methods were not effective to reduce metals concentration and boron. Therefore, further purification with activated carbon or biosorption technologies can be recommended.

CONCLUSIONS

Management scheme, developed during this study is based on the field survey and laboratory scale tests and include two main steps:

1) Provide a waste sorting process and suitable drainage system for landfills that provide collection of one type wastewater in the receiving chamber (avoiding different consistency of wastewater mixing). The volume of the receiving chamber should provide well homogenisation of wastewater contaminants in this volume.

2) Plan for two–stage treatment: coagulation/sedimentation with bentonite and biological treatment (aerobic). The dose of coagulant (bentonite) is about 1,000 mg L^{-1} without changing the pH of the water. Both active sludge reactors and biofilter can be used for biological purification, but effective separation of phosphorus and nitrogen must be ensured.

To provide efficient separation of metals and other specific chemicals, e.g., boron, post–treatment with filtration system (ex. activated carbon or biosorbent) are necessary.

REFERENCES

Ærtebjerg, G., Andersen, J.H. & Hansen, O.S. 2003. *Nutrients and Eutrophication in Danish Marine Waters*. A Challenge for Science and Management. National Environmental Research Institute. 126 pp.

Brennan, R., Clifford, E., Morrison, L., Healy, M.G. & Devroedt, C. 2017. Treatment of landfill leachate in municipal wastewater treatment plants and impacts on effluent ammonium concentrations. *Journal of Enviromental Management* **188**, 64–72.

Bu, F., Gao, B., Yue, Q., Shen, X. & Wang, W. 2019. Characterization of dissolved organic matter and membrane fouling in coagulation-ultrafiltration process treating micro-polluted surface water. *Journal of Enviromental Sciences* **75**, 318–324.

Busch, J., Ahrens, L., Sturm, R. & Ebinghaus, R. 2010. Polyfluoroalkyl compounds in landfill leachates. *Enviromental Pollution* **158**(5), 1467–1471.

Coaffee, J. 2008. Risk, resilience, and environmentally sustainable cities. *Energy Policy* 36, 4633–4638.

Collier, M.J., Nedovic-Budic, Z., Aerts, J., Connop, S., Foley, D., Foley, K., Newport, D., McQuaid, S., Slaev, A. & Verburg, P. 2013. Transitioning to resilience and sustainability in urban communities. *Cities* **32**(1), S21–S28.

Costa, A.M., Alfaia, R.G.S.M. & Campos, J.C. 2019. Landfill leachate treatment in Brazil – An overview. *Journal of Enviromental Management* **232**, 110–116.

Council Directive 91/271/EEC of 21 May 1991 concerning urban wastewater treatment.

EPA Report 815-R-08-012. Regulatory Determinations Support Document for Selected Contaminants from the Second Drinking Water Contaminant Candidate List (CCL 2). Part II: CCL 2 Contaminants Undergoing Regulatory Determination. (2008).

FEVE News Corner (accessed in 10.05.2017). Glass recycling hits 73% in the EU. Retrieved from FEVE: http://feve.org/glass-recycling-hits-73-eu/

Fuller, B.S. 2013. T*he Precautionary Principle in Marine Environmental Law*, 320 pp. https://doi.org/10.4324/9780203765715

Ghernaout, D. 2014. The hydrophilic/hydrophobic ratio vs. dissolved organics removal by coagulation – A review. *Journal of King Saud University - Science* **26**(3), 169–180.

Heiriyanto, Pahlevani, F. & Sahajwalla, V. 2018. From waste glass to building materials – An innovative sustainable solution for waste glass. *Journal of Cleaner Production* 191, 192–206.

Hu, H., Ding, L., Geng, J., Huang, H., Xu, K. & Ren, H. 2016. Effect of coagulation on dissolved organic nitrogen (DON) bioavailability in municipal wastewater effluents. *Journal of Enviromental Chemical Engineering* **4**(2), 2536–2544.

Jouanneau, S., Recoules, L., Durand, M.J., Boukabache, A., Picot, V., Primault, Y., Lakel, A., Sengelin, M., Barillon, B. & Thouand, G. 2014. Methods for assessing biochemical oxygen demand (BOD): a review. *Water Research* **49**, 62–82.

LVS 6878:2005 (part 7). Water quality. Determination of phosphorus. Ammonium molybdate spectrometric method.

LVS EN 1484:2000. Water analysis. Guidelines for the determination of total organic carbon (TOC) and dissolved organic carbon (DOC).

LVS EN 1899–2:1998. Water quality. Determination of biochemical oxygen demand after n days (BODn). Part 2: Method for undiluted samples (modified ISO 5815:1989).

LVS EN 27888:1993. Water Quality. Determination of Electrical Conductivity.

LVS EN ISO 10523:2012. Water quality. Determination of pH.

LVS EN ISO 11905–1:1998. Water quality. Determination of nitrogen. Part 1: Method using oxidative digestion with peroxodisulfate.

LVS EN ISO 5814:2013. Water quality. Determination of dissolved oxygen. Electrochemical probe method.

LVS EN ISO 7027–2002. Water quality. Determination of turbidity. Part 1: Quantitative methods.

LVS ISO 17294–2:2016. Water quality. Application of inductively coupled plasma mass spectrometry (ICP-MS). Part 2: Determination of selected elements including uranium isotopes.

LVS ISO 6060:1989. Water quality. Determination of the chemical oxygen demand.

Modin, H., Persson, K.M., Andersson, A. & van Praagh, M. 2011. Removal of metals from landfill leachate by sorption to activated carbon, bone meal and iron fines. *Journal of Hazardous Materials* **189**(3), 749–754.

Peng, Y. 2017. Perspectives on technology for landfill leachate treatment. *Arabian Journal of Chemistry* **10**(2), S2567–S2574.

Pitman, K., Raud, M. & Kikas, T. 2015. Biochemical oxygen demand sensor arrays. *Agronomy Research* **13**(2), 382–395.

Sharp, E.L., Jarvis, P., Parsons, S.A. & Jefferson, B. 2006. Impact of fractional character on the coagulation of NOM. *Colloids and Surfaces A: Physicochemical and Engineering Aspects* **286**(1–3), 104–111.

Šír, M., Podhola, M., Patočka, T., Honzajková, Z., Kocurek, P., Kubal, M. & Kuraš, M. 2012. The effect of humic acids on the reverse osmosis treatment of hazardous landfill leachate. *Journal of Hazardous Materials* **207–208**, 86–90.

Analysis of non-stationary flow interaction with simple form objects

I. Tipans, J. Viba, M. Irbe and S.K. Vutukuru[*]

Riga Technical University, Faculty of Mechanical Engineering, Transport and Aeronautics, Department of Theoretical Mechanics and Strength of Materials, Viskalu Street 36A, LV – 1006, Riga, Latvia
[*]Correspondence: vshravankoundinya1989@gmail.com

Abstract. The paper is devoted to the analysis of a non-stationary rigid body interaction in a fluid flow. Initially, an approximate method for determining the forces due to fluid interaction with the rigid body is offered. For this purpose, the plane movement of a mechanical system with an infinite DOF (degrees of freedom) is reduced to 5 DOF motion: 3 DOF for the body and 2 DOF for the areas of compression and vacuum in fluid flow. Differential equations of non-stationary motion are formed by the laws of classical mechanics. The use of an approximate method has been quantified by computer modelling. The average difference in results was found to be small (< 5%). The analysis of the fluid (air) interaction is carried out for a rigid body of two simple geometries - flat plate and diamond. The results obtained are used to refine the parameters of the proposed approximate method that is addressed in the present study for fluid interaction with the non-stationary rigid body. Theoretical results obtained in the final section are used in the analysis of the movement of prismatic bodies in order to obtain energy from the fluid flow.

Key words: degree of freedom, energy, fluid interaction, mathematical modelling, flow parameters, rigid body.

INTRODUCTION

Analysis of fluid interaction with a rigid body is a challenging task; unfortunately, this interaction phenomenon is not extensively investigated. The subject of the study is the determination of fluid interactions with a rigid body in non-stationary motion by using a mathematical model according to classical mechanics. Existing computational fluid dynamic methods are based on deforming and moving mesh techniques that fail when the mesh deformation is severe, which requires frequent re-meshing, time-consuming and is computationally expensive (Crank, 1984; Finlayson, 1992). The present article is the first of its kind, as no research article in this field in the past was based on a mathematical model that is simple, easy to understand for the study of non–stationary rigid body flow interactions. The only disadvantage of the proposed model is that the model does not consider the viscous effect of the fluid.

In order to understand the importance of mathematical modelling technique, we refer to scientific works that involve mathematical modelling for the case of stationary rigid body fluid interaction. For the case when relative velocity vectors are constant, the

motion is well researched and described (Sears, 2011). It follows that only the velocity of relative motion, the density of the fluid, the area perpendicular to the velocity and the experimental drag coefficient are necessary to determine the reduced interaction of fluid force (Hoerner, 1965). (1)

$$\overline{F}^{(F)} = \frac{D \cdot v^2 \cdot \rho \cdot A}{2} \left(\frac{-\bar{v}}{|\bar{v}|} \right) \tag{1}$$

where $\overline{F}^{(F)}$ – interaction force; D – drag coefficient; $\bar{v}$ – flow velocity; ρ – air density; A – object frontal area.

Non-stationary interaction tasks between the continuous medium (fluid flow) and the rigid body motion has complex interaction (Hossenfelder, 2018). In that case, non-stationary interaction can only be solved numerically with space-time programming methods (Beal & Viroli, 2015). A practical model of space-time function applications was used and theoretical and empirical results were presented (Beal et al., 2013).

In the present article, a new method for describing the interaction of non – stationary rigid body, fluid flow in engineering tasks is presented. The numerical validation of the new method was carried out with the help of a two-dimensional continuous flow model for two body shapes, i.e., diamond and rectangular prisms. As a result, it will be shown that engineering calculations do not require a step by step space–time calculation to find coefficient D in formula (1). Instead of the formula (1), a new non-stationary flow interaction formula will be obtained, which will include the object shape, state, and flow rate direction parameters.

MATERIALS AND METHODS

New mathematical model
To simplify calculations for analysis, optimization and synthesis tasks, our work offers a mathematical model without considering the viscous effects of a fluid. For that, the interaction fluid is divided into two spaces: one space on the pressure side and the other on the vacuum side.

The essence of the model is described for flat plate body (Fig. 1) and for the diamond-shaped rigid body (Fig. 2) respectively. On the pressure side, the theorem of change in linear momentum in the differential form is applied (Goldstein et al., 2015) and (Meriam et al., 2015).

Accordingly, it can be expressed as:

$$dm \cdot v \cdot cos(\beta) = dN \cdot dt; \tag{2}$$

$$dm = v \cdot cos(\beta) \cdot dt \cdot dL \cdot B \cdot \rho, \tag{3}$$

where dm – mass of the elementary volume of the flow, having velocity v against the inclined surface; β – theangle between the flow and the surface at the normal point of impact; dN – the impact force in the direction of the normal surface of the elementary area; t – time; dL – the elementary length of the surface; B – the width of the object, which is constant in the case of a two dimensional task, ρ – density.
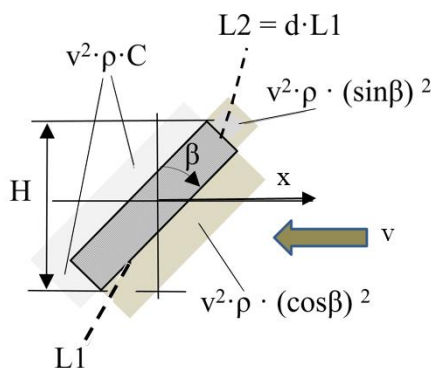
Figure 1. Pressure distribution for rectangle cross section flat plate body.
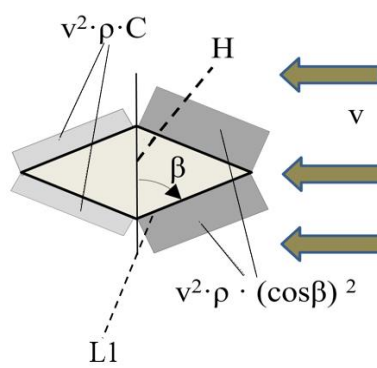
Figure 2. Pressure distribution for the diamond body.

By integration of equation (2) additional pressure in the flow direction for the edges $L1$, $L2$ for flat plate and diamond can be calculated. Pressure distribution for each of edges $L1$, $L2$ for the here given bodies shown in Fig. 1 and Fig. 2. as (4), (5):

$$v^2 \cdot \rho \cdot (cos\beta)^2 \qquad (4)$$

or

$$v^2 \cdot \rho \cdot (sin\,\beta)^2. \qquad (5)$$

In the proposed new model, at the vacuum side along the edge just behind the body, it is recommended to be taken as constant pressure $\Delta p2$, proportional to the density ρ multiplied by the flow velocity v square in the following form (6):

$$\Delta p2 = v^2 \cdot \rho \cdot C, \qquad (6)$$

where: C– constant, to be found out experimentally or by computer modelling.
Thus it is possible to find the total force in the direction of the flow for the rigid body.

As an approximation, the rectangle body will get force Fxr as given in Eq. (7), and for the diamond-shaped rigid body Fxd, along the direction of flow as given by the Eq. (8).

$$Fxr = -\mathrm{H} \cdot B \cdot v^2 \cdot \rho \cdot \left[C + \frac{cos(\beta)^3 + d \cdot sin(\beta)^3}{cos(\beta) + d \cdot sin(\beta)} \right]; \qquad (7)$$

$$Fxd = -\mathrm{H} \cdot B \cdot v^2 \cdot \rho \cdot [C + (cos\beta)^2], \qquad (8)$$

where d – the ratio of edges $L2/L1$; B – body width; H - section height, perpendicular to the flow (Fig. 1., Fig. 2.). β – the angle between the flow and the surface at the normal point of impact; ρ – density of the fluid.

From the obtained correlations (7) and (8) it can be shown that an approximate analytical method can be applied in the scope of identification of fluid and body interactions problems. The validation is required for the application of the proposed method, which was performed by using computer simulations discussed in the following section.

2D diamond shaped body transient analysis

From the analysis and modelling graphs obtained, it can be concluded that on the pressure side, the interaction forces quickly reach a stable state. In contrast, on the suction, vacuum side, the flow settled after a certain period of time (Fig. 3). Therefore, the parameters of this body – stationary flow interaction could be used for approximate calculations. It was found that the interaction forces changed with time so an average value is taken (Table 1) at a velocity of 10 m.sec^{-1}.
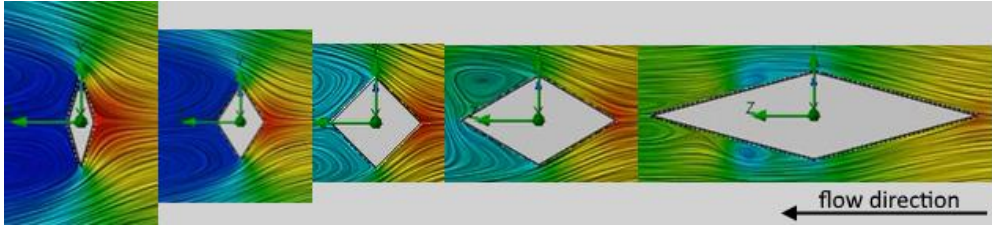
Figure 3. Stream lines and pressure distribution for the diamond body.

Table 1. Average interaction force and average interaction coefficient

β(degrees)	Name	Unit	Averaged value
15	Force (Fxde)	[N]	0.19587
	Interaction coefficient (Dex)		1.440817
30	Force(Fxde)	[N]	0.176314
	Interaction coefficient(Dex)		1.296965
45	Force (Fxde)	[N]	0.164733
	Interaction coefficient(Dex)		1.21177
60	Force(Fxde)	[N]	0.157237
	Interaction coefficient(Dex)		1.156635
75	Force(Fxde)	[N]	0.073616
	Interaction coefficient(Dex)		0.541519

Accordingly, from Table 1. interaction coefficient C was identified: D – theoretical interaction coefficient (9), Dex – calculated interaction coefficient((10), (Table 1) and approximated D_p – interaction coefficient as fifth degree polynomial function (11):

$$D = C + (cos\,\beta)^2; \tag{9}$$

$$Dex = \frac{Fxde}{Av^2\rho}; \tag{10}$$

$$D_p = 1.5 + 3.7266\beta^3 - 1.5249\beta^4 - 0.10135\beta^5 - 2.8129\beta^2 + 0.2823\beta, \tag{11}$$

where *Fxde* – interaction force for diamond plate along the flow direction (Table 1). From Eqs (9) and (10) it follows that $C = 0.5$ when $\beta = 0$.
Therefore, the following approximation formula is recommended for the interaction coefficient in case of the diamond shaped body (12):

$$D = 0.5 + (cos\,\beta)^2. \tag{12}$$

Similarly, in this work modelling results for a rectangle flat plate were approximated and compared to the approximate formula (7). In a similar procedure like

in diamond plate, it was found that the coefficient C is about 0.5, similar to (12). The estimation of the accuracy of the approximate formula (7) and (8) for diamond-shaped and rectangular objects at $C = 0.5$ is depicted in Fig. 4. and Fig. 5. The difference is not large and the percentage average value is less than 5%.
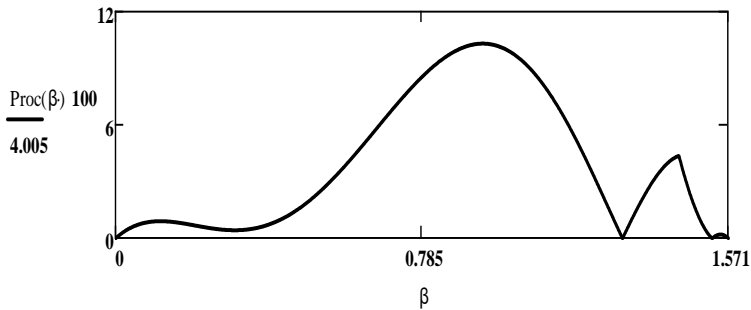
Figure 4. *β* radians against percentage difference. The accuracy of the approximate formula (8) for diamond plate when C = 0.5, expressed as a percentage. The mean value is about 4%.
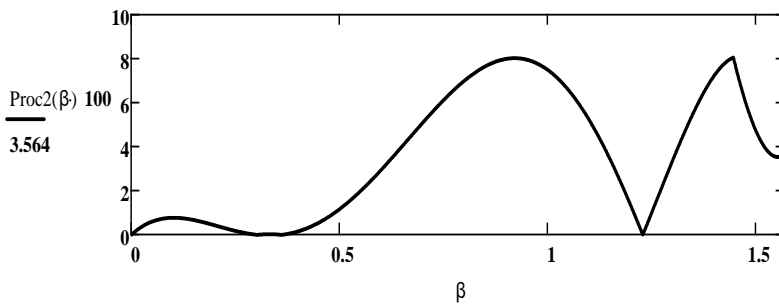
Figure 5. *β* radians against percentage difference. The accuracy of the approximate formula (7) for rectangle plate when C = 0.5, expressed as a percentage. The mean value is about 3,6%.

Based on analysis from Fig. 4. and Fig. 5. the proposed new method can be applied to engineering calculations with sufficient accuracy (less than 5%), excluding work-based calculations with space-time programs. In the subsequent section as an example, the calculation for a thin flat plate showing the effectiveness of applying the new method to generate energy from airflow is discussed.

RESULTS AND DISCUSSION

Theory and modelling for moving plate
The thin plate (d ~ 0, Fig. 1.) two dimensional (2D) analysis model in the translation motion is shown in Fig. 6. Model includes linear spring with stiffness c and linear damping with proportionality coefficient b. According to the approximation theory, taken into account relative interaction velocity Vr:

$$Vr = (V + v), \qquad (13)$$

where V – fluid velocity; v – plate velocity along x axis.
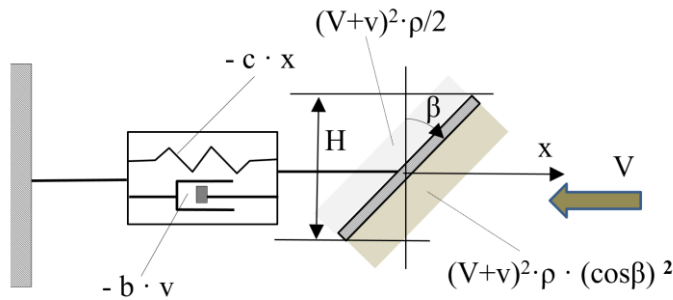Differential equation of plate motion along x axis will be (14):

1231

$$m\ddot{x} = -cx - b\dot{x} - A\rho[0.5 + (\cos\beta)^2](V + \dot{x})^2 \frac{V+\dot{x}}{|V+\dot{x}|}, \qquad (14)$$

where A – surface area of the plate; ρ – density; β – plate angle against flow.
The renewable energy is represented as the damping force $-b\dot{x}$ (). Accordingly, power P will be (15):

$$P = b(\dot{x})^2. \qquad (15)$$

Accordingly the average power Pa will be (16):

$$Pa = \frac{\int_0^t b(\dot{x})^2 \cdot dt}{t}. \qquad (16)$$

Figure 6. Model for obtaining renewable energy from fluid.

Analysis of equation (14) allows to conclude that there are five possibilities to analyse the efficiency of the given system. They are: two parameters (c, b) of a system and three time or phase coordinates control actions (β, V and A).

Some equation modelling results are shown in (Figs 7–10). Comments are given under all graphs. For all results presented in graphs, systems parameters are:

$A = 0.004$ m^2; $V = 10$ m s^{-1}; $\rho = 1.25$ kg m^{-3}. Average power, Pa is calculated as a percentage of maximal power $Pmax$, when $Pmax$ is taken as a function of flow velocity (17):

$$P\,max = bV^2 \cdot \frac{V}{3}. \qquad (17)$$

Angle β time control modelling results are shown in (Figs 7–10), for $\beta = \frac{\pi}{2.5}\sin(7t)$
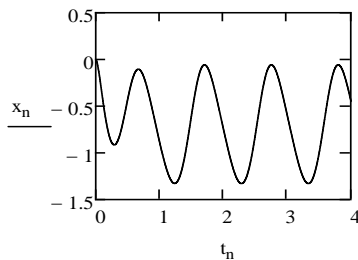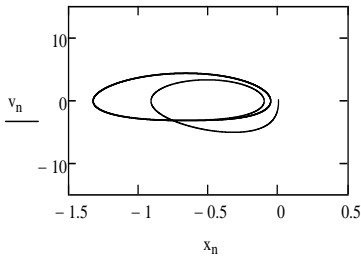
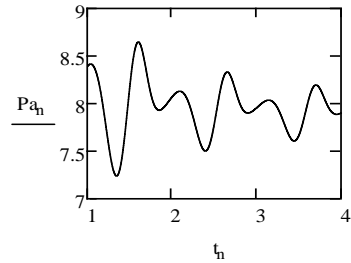

Figure 7. Displacement x as time t function.
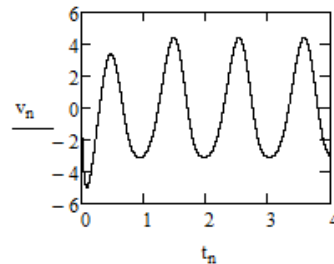
Figure 8. Plate centre velocity v as time t function.
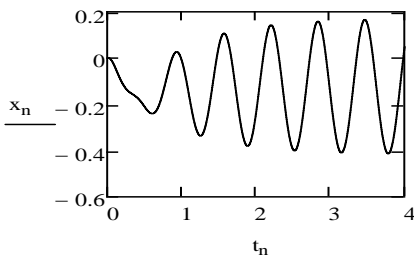
Figure 9. Motion in phase plane $v = v(x)$.

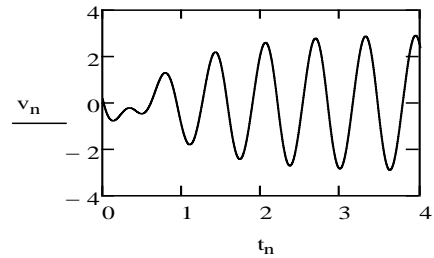**Figure 10.** Average power Pa of generator force bv.

Motion modelling (Figs 7–10) in a case of varying the angle of the plate to the flow (angle β as a mono harmonic function of time $\beta = \frac{\pi}{2.5} sin(7t)$) show the following:

- motion occurs very quickly, practically within two, three back and forth oscillating cycles;

- it is possible to synthesize the optimal parameters of the system (i.e. stiffness, area, frequency, amplitude), which would provide the maximum power for the given limits;

- additional optimum angle controls can be obtained such as bi – harmonics $\beta = \frac{\pi}{2.5}[sin(7t) + 2 sin(14t)]$, poly-harmonics.
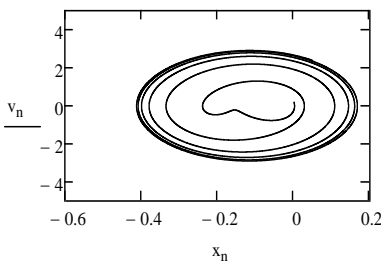
Fluid flow velocity V control modelling results are shown in (Figs 11–14). By function: $V = V0 \cdot (2 - 0.5 sin(10t))$, were $V0 = 10\ m\ s^{-1}$.
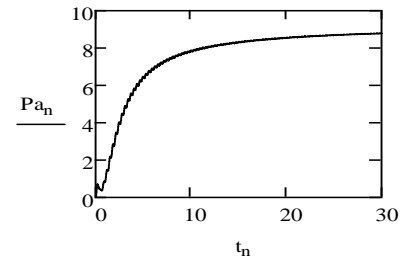

Figure 11. Displacement x as time t function.

Figure 12. Plate centre velocity v as time t function.

Figure 13. Motion in phase plane $v = v(x)$.

Figure 14. Average power Pa of generator force bv.

1233

Results of the mathematical modelling in the case of changing the flow velocity as harmonic time function (Figs 11–14) shows the following:

- a new opportunity to generate energy, changing the flow rate harmonically is discovered.

- opportunity to use new forms of control for flow such as harmonic, bi-harmonic, pulse is open. The summary of results of the present work is as follows:

1. In the present paper a new approximated method was developed for calculating flow and rigid body interaction according to classical mechanics.

2. The essence of the method is based on the evidence of numerical and analytical modelling that the interaction can be split separately on the sides of the additional pressure and then on the suction, vacuum.

3. The most interesting is the interaction of the suction side which was almost constant, depending only on the fluid flow rate.

4. The average difference in the results as obtained is found to be less than 5%.

CONCLUSIONS

The article provides new knowledge through mathematical modelling for the analysis of fluid and rigid body interactions. The proposed analytical method being mathematical is highly advantageous as can be easily understood. Some important conclusions that can be drawn from the resent work are as follows:

1. The developed method allows performing the tasks of analysis, optimization and synthesis in a simplified way in the interaction of objects with fluids.

1. For specific tasks, there is no need to use large space - time computing programs for solving engineering problems.

2. Further, the proposed mathematical model can be extended for calculations of flying or diving robot systems as well as in the extraction of energy from the fluid flow.

3. In future studies, it would be advisable to observe the effect of flow viscosity on the accuracy of the developed method.

REFERENCES

Crank, J. 1984, *Free and Moving Boundary Problems*. Oxford University Press, 425pp.

Finlayson, B.A. 1992. *Numerical Methods for Problems with Moving Fronts*. Ravenna Park, WA, Ravenna Park Publishing, 605pp.

Sears, W.R. 2011. *Introduction to Theoretical Aerodynamics and Hydrodynamics*. American Institute of Aeronautics and Astronautics, Reston, VA, 203 pp.

Hoerner, S.F. 1965. *Fluid-Dynamic Drag*. Published by the Author, Bakersfield, CA,. 456 pp.

Hossenfelder, S. 2018. *https://iai.tv/articles/is-space-time-fluid-auid-897*.

Beal, J. & Viroli, M. 2015. Space–time programming. *Phil. Trans. R. Soc. A 373: 20140220.*

Beal, J., Usbeck, K. & Benyo, B. 2013.On the Evaluation of Space-Time Functions. *The Computer Journal.* **56**(12),1500–1517.

Goldstein, H., Poole, C. & Safko, J. 2015. *Classical Mechanics*. Third Edition, Wesley, 625pp.

Meriam, J. L., Kraige, L.G. & Bolton, J.N. 2015. *Engineering Mechanics: Dynamics*, 8th Edition, Wiley, 736 pp.

Reduction of moisture and thermal conductivity of wet walls by special plaster

M. Topol[1,*], P. Kic[1] and P. Neuberger[2]

[1]Czech University of Life Sciences Prague, Faculty of Engineering, Department of Technological Equipment of Buildings, Kamýcká 129, CZ165 21 Prague, Czech Republic
[2]Czech University of Life Sciences Prague, Faculty of Engineering, Department of Mechanical Engineering, Kamýcká 129, CZ165 21 Prague, Czech Republic
*Correspondence: TopolMilan@seznam.cz

Abstract. This paper is focused on the problems of moisture reduction in old buildings. Wet walls are very common problem of old buildings, but it can appears also in new buildings as well. The moisture in the wall influence the insulation quality; bigger heat losses continuously cause problems of worse heat balance, higher consumption of energy for heating and it can result in not sufficient indoor conditions in such a room or building. Old rural residential buildings and also agricultural buildings for housing of animals, storage of different materials, workshops etc. could be repaired and reconstructed by the used of some special methods. The application of special plaster can reduce the walls moisture as well as improve the thermal properties of the buildings by reduction of thermal conductivity. This paper includes the results of laboratory experiments focused on research of plaster properties (temperature, moisture and thermal conductivity) and tests provided in the real building. Different measuring principles, enabling mutual comparison of results were used for this research. The measurement results showed a significant effect of high wall moisture on the heat losses. Differences between the walls improved by new tested plaster and old untreated walls are discussed in this paper. Obtained results from this measurements and findings may be useful for further research in this issue as well as for the practical solutions for similar problems in many old buildings.

Key words: heat losses, measurement, natural material, rural buildings.

INTRODUCTION

In this time, there are more and more modern houses and buildings in our towns and villages. Also, there are still many old houses, which have problems with wet walls and heat losses. Wet walls and heat losses are very common problem, which can make difficulties for residents of old houses such as health problems because of mould, bad thermal conditions and higher energy consumption. It can result in not sufficient indoor conditions in such a room or building.

There are many reasons of creation of wet walls. It can be because of ruined or no hydro isolation, condensation of water steam in the interior of buildings, heavy rains, rising water from foundations of the house etc. The moisture in the wall influence the insulation quality of construction and static and physical properties, these problems can result even in the breakdown of the wall (Franzoni, 2018).

As has already been said, one of the main problems in old buildings is bad thermal conditions, which relate with thermal comfort. Thermal comfort is the state of mind, which expresses satisfaction with the thermal environment and it is an important aspect of the building design process (van Hoof et al., 2010).

Thermal comfort is important because modern people spend most of the day indoors. Air temperature and air humidity have main influence on people feelings in building environment. It is the reason why it is so important to control these two parameters in all types of buildings.

The application of insulation materials can reduce the walls moisture, improve the thermal properties of the buildings and also indoor environmental conditions. There is very important which type of insulation is used. As in some cases, bad choice of insulation can lead to worse situation than before insulation installation and the use of external insulation sometimes can lead to closing of moisture in the construction.

It is important to know structure of the wall and reasons of problems, e.g. what causes the high amount of moisture in walls. Then can be decided, which methods for insulation will be chosen, e.g. interior or exterior, which type of material, thickness etc.

There are many types of insulation materials in the market. One of new type of insulation materials is a special plaster with thermal insulation properties. These plasters often have natural composition and interesting properties and they can replace some synthetic insulation materials in the future. As the people often prefer natural products instead of synthetic materials, which have bigger negative impact on environment. Synthetic materials often consume more energy for their production, resulting in higher CO_2 emissions that contribute to global warming due to an increasing greenhouse effect (Zach et al., 2013; Pargana et al., 2014; Bakatovich, et al., 2018).

The one of the most important parameters of thermal-technical properties of materials is a thermal conductivity. It is used mainly in civil engineering and obviously coefficient of thermal conductivity λ is used in practice. Its real value is a function of several internal and external variables such as e.g. moisture, temperature, density, porosity, chemical and mineralogical composition and phase composition etc. (Muizniece et al., 2015; Kocova & Kic, 2016; Pleiksnis et al., 2016; Týbl & Kic, 2016; Valasek et al., 2016).

Another important parameter is an overall heat transfer coefficient U. This parameter relates to the whole multi-layer wall, not only individual materials as in the case of a coefficient of thermal conductivity. Overall heat transfer coefficient is the heat flow that passes through a unit area of a complex component or inhomogeneous material due to a temperature gradient equal to 1 K. Thermal resistance is connected with overall heat transfer coefficient, its value equals to the inverse value of overall heat transfer coefficient (Schiavoni et al., 2016).

The aim of this research is to measure properties of thermal insulation and moisture-protective plaster Manto Plate (MP), which was created in Turkey (Izozek Insulation, 2012).

The results of these measurements are evaluated and compared with data which are presented by producer or other authors. Then applicability of this plaster for purpose presented by producer can be evaluated. Differences between the walls improved by new tested plaster and old untreated walls will be also discussed in this paper.

MATERIALS AND METHODS

This paper includes the results of two types of experiments. There were carried out laboratory experiments and measurements to find out properties of plaster MP such as temperature, moisture and thermal conductivity and tests provided in the real building to find out influence of the MP to properties of walls and indoor environment in the house.

Two samples of tested material were prepared for laboratory experiments. The first sample was a brick, on which 1 cm layer of MP plaster was applied. A second sample was cast into the aluminium form of shape 200 x 80 x 40 mm only from the pure MP material.

Surface temperature and moisture were measured on both samples. The purpose of these measurements were to study the properties of MP and effect of MP on moisture and temperature of the brick on which it is applied.

Partially stiff and hardened MP material sample was removed from the form and thermal conductivity was measured. Temperature and humidity of air were registered inside the laboratory each 15 minutes.

The measurements in the real building were carried out in an old family house, with the aim to test the quality of MP plaster used inside the rooms as an insulating material. Photos and schematic drawings (layout) of the house with the marks showing the measured rooms are presented on the Figs 1, 2 and 3. Areas and volumes of all measured rooms are shown in the Table 1.

Figure 1. Family house from the north, measured walls are marked.

Figure 2. Family house from the south, measured walls are marked.

During the measurement there were not all rooms insulated by MP. To compare the quality of MP plaster four rooms were chosen. Two rooms covered by MP and other two which were not insulated by this plaster.

Measurement was made in winter time in December to use big temperature difference between inside and outside.

The house consists of two parts. The older one was built in the 19th century. In that time, it was only one floor house with three rooms. The new part was built during the reconstruction in 1986. Ground floor was enlarged, and second floor was built within the reconstruction. The measurements were carried out in newer part of the house.

All perimeter walls, which were used for measurement purposes, have the same structure and same width. Information about particular layers are shown in Table 1. The

walls are built from Autoclaved aerated concrete (AAC), also called Plyosilicate blocks. The first layer on interior part of walls is stucco plaster and MP is the second one. The exterior surface of walls is covered by stucco plaster and Brizolit, which is scratched facade plaster.

According to the figures the living room is No.1. It is situated on the ground floor. There is installed fireplace, which has very positive influence on the local temperature. The room is insulated by plaster MP. Wall which was used for measurement purposes is oriented to the north.

Kids room (No.2) is situated on the first floor of the family house. This room is also insulated by MP and measured wall is also oriented to the north.

The room (No.3) is the hall which connects ground floor and the first floor of the house. The hall is directly connected with room No.1, where is the fireplace. There is staircase. The room is not insulated by any special insulating material. The measured wall is oriented to the south.

Table 1. Structure of walls and coefficient of thermal conductivity of each layer

Layer	Thickness (mm)	Coef. of thermal conductivity (W m^{-1} K^{-1})
Plaster Manto Plate	10	0.055
Stucco plaster (interior)	10	0.99
ACC (Plyosilicate blocks)	500	0.205
Stucco plaster (exterior)	15	0.99
Brizolit (facade plaster)	10	1.1
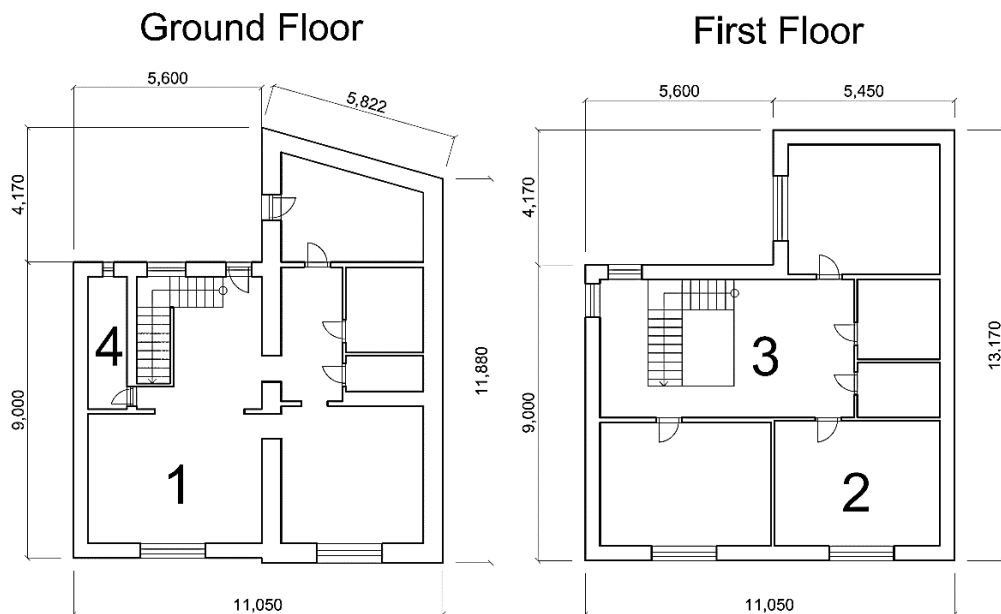
Figure 3. Layout of the house, where measured rooms are märked.

Room No.4 is the chamber. This room is not heated. There is not used any insulating material and measured wall is oriented to the south.

Data about the rooms which were used for the measurement such as area and volumes are given in Table 2.

Based on the measured data in the family house, principal parameters which are internal and external surface heat transfer coefficient, internal and external thermal resistance of walls, total thermal resistance of construction and overall heat transfer coefficient, are calculated according to the following formulas (1) to (8).

Table 2. Areas and volumes of measured rooms

Room number	Area (m^2)	Volume (m^3)
No. 1	21.44	60.032
No.2	19.82	55.496
No.3	24.87	69.636
No.4	4.92	13.776

$$\Delta t = t_{si} - t_{se} \tag{1}$$

where Δt – temperature difference of the wall (K); t_{si} – internal surface temperature of the wall (°C); t_{se} – External surface temperature of the wall (°C)

$$h_{si} = \frac{q}{t_{ai} - t_{si}} \tag{2}$$

where h_{si} – heat transfer coefficient of internal surface (W m^{-2} K^{-1}); q – heat flux (W m^{-2}); t_{ai} – internal air temperature by the wall (°C); t_{si} – internal surface temperature of the wall (°C)

$$h_{se} = \frac{q}{t_{ae} - t_{se}} \tag{3}$$

where h_{se} – heat transfer coefficient of external surface (W m^{-2} K^{-1}); q – heat flux (W m^{-2}); t_{ae} – external air temperature by the wall (°C); t_{se} – external surface temperature of the wall (°C)

$$R_i = \frac{1}{h_{si}} \tag{4}$$

where R_i – internal thermal resistance (m^2 K W^{-1}); h_{si} – heat transfer coefficient of internal surface (W m^{-2} K^{-1})

$$R_e = \frac{1}{h_{se}} \tag{5}$$

where R_e – external thermal resistance (m^2 K W^{-1}); h_{se} – heat transfer coefficient of external surface (W m^{-2} K^{-1})

$$R = \sum \frac{d_i}{\lambda_i} \tag{6}$$

where R – thermal resistance of the wall (m^2 K W^{-1}); d_i – thickness of layer (m); λ_i – coefficient of thermal conductivity of the layer (W m^{-1} K^{-1})

$$R_T = R_i + R + R_e \tag{7}$$

where R_T – total thermal resistance of the wall (m^2 K W^{-1}); R_i – internal resistance of heat transfer (m^2 K W^{-1}); R – Thermal resistance of the wall (m^2 K W^{-1}); R_e – external resistance of heat transfer (m^2 K W^{-1})

$$U = \frac{1}{R_T} \tag{8}$$

where U – overall heat transfer coefficient (W m^{-2} K^{-1}); R_T – external resistance of heat transfer (m^2 K W^{-1})

Plaster MP is a moisture-protective plaster consisting of 80% perlite, 10% pumice stone, 10% inorganic binders and binders based on water, cellulose and glass fibres. It

consists only of natural and recycling materials and does not contain any carcinogenic substances.

Plaster MP, thanks to its main components, perlite and pumice, is a porous and breathable material. No kind of diluent is used in, after mixing it is immediately ready to apply. Application of the material can be done indoors or outdoors, even on wet walls.

Before the application, the plaster must be mixed by electric stirrer or drilling machine with a stirrer. Stirring takes about 2 minutes at 700 rpm. As longer the mixing is, as the plaster is thinner. It is not diluted with water.

No anchors or adhesives are not needed for application. It is applied by spraying or steel trowel. The thickness of plaster MP layer on the inside surface of walls is 1 cm. It can be used for up to 6 hours after mixing. Not fixed material does not harden and can be used after a long time. The drying time is influenced by ambient temperature and by ventilation, at a temperature in the range of 20 to 30 °C, the material deposited in the 1 cm layer is dried for approximately 48 hours. To create 1 m^2 of 1 cm thick layer is needed about 7 kg of material.

The thermal conductivity was measured by the instrument Isomet 2104 (Applied Precision Ltd, Bratislava). According to the physical properties of the tested material the surface sensor was used in this research. To improve the adhesion of the probe to the measured material, the contact surfaces were painted with thin layer silicone grease. The calibration was provided by the constant stored in the sensors memory. The permissible measurement error of thermal conductivity is 5% of reading + 0.003 W m^{-1} K^{-1}. The instrument was powered from AC during the measurement. The measured values were stored in the internal instrument memory and transferred via RS-232 interface to the PC after the measurement.

Air temperatures and relative humidity inside and outside the building were measured by data loggers ZTH65 with registration at intervals of 15 minutes during two cold winter days (long-time measurement). Parameters of ZTH65 are: temperature operative range –30 to +70 °C with accuracy ± 0.4 °C and operative range of relative humidity 5 – 95% with accuracy ± 2.5%. The same sensor was used for measurement in the laboratory during the tests of MP.

The surface temperatures in some specific places of tested walls were measured by special surface sensor S 106 9R (NiCr-Ni, with adapter G017R) connected to the instrument THERM 2253-2 (Ahlborn GmbH, Germany) for contact temperature measurement. This instrument was used also with sensor for air temperature measurement AMR TK 127 10R. This instrument and sensors can be used in operative range from –100 to +1,370 °C, with display resolution 0.1 °C and with accuracy ± 1% from the measured value.

There was used for the indirect measurement of wall moisture capacitive sensor FH A696–MF with operative range of mineral construction materials from 0 to 20% with accuracy 0.1%. The sensor was connected to the data logger ALMEMO 2690–8 (Ahlborn GmbH, Germany).

The heat flux density were measured by special heat flux sensor FQA018C (Ahlborn GmbH, Germany) which has dimensions 120 x 120 x 1.5 mm. It is made from epoxy resin with the resistance to 80°C and calibration constant 9.69 W m^{-2} mV^{-1} and relative measurement uncertainty 5%.

RESULTS AND DISCUSSION

Main parameters measured in family house which are heat flux q, interior air temperature near the wall t_{ai}, internal surface temperature of the wall t_{si}, external surface temperature of the wall t_{se}, exterior air temperature by the wall t_{ae}, moisture of the wall (interior) r_i, moisture of the wall (exterior) r_e, relative air humidity in the room φ_i, average air temperature t_i in the room and dew point temperature t_{dp} are given in the Table 3. The data are the mean values ± SD (standard deviation).

Table 3. Measured data in the family house

Parameter	Room No.1	Room No.2	Room No.3	Room No.4
q ± SD (W m^{-2})	25.49 ± 1.5	25.80 ± 0.9	39.81 ± 2.0	27.65 ± 1.6
t_{ai} ± SD (°C)	25.10 ± 0.7	19.62 ± 0.6	23.7 ± 0.73	15.97 ± 1.1
t_{si} ± SD (°C)	21.51 ± 0.3	16.74 ± 0.3	20.05 ± 0.7	12.28 ± 0.5
t_{se} ± SD (°C)	-0.59 ± 0.3	-0.81 ± 0.2	-0.33 ± 0.1	-0.27 ± 0.1
t_{ae} ± SD (°C)	-1.38 ± 0.2	-1.47 ± 0.1	-0.91 ± 0.2	-1.46 ± 0.1
r_i ± SD (°C)	3.60 ± 0.2	1.89 ± 0.2	3.91 ± 0.3	4.31 ± 0.2
r_e ± SD (°C)	4.79 ± 0.27	4.87 ± 0.3	4.63 ± 0.5	4.68 ± 0.4
φ_i ± SD (°C)	37.24 ± 1.9	60.72 ± 2.5	48.74 ± 1.9	52.19 ± 1.5
t_i ± SD (°C)	25.61 ± 0.9	18.46 ± 0.3	20.95 ± 0.6	15.97 ± 0.3
t_{dp} ± SD (°C)	9.90 ± 0.6	10.71 ± 0.6	9.74 ± 0.5	6.16 ± 0.6

q – heat flux; t_{ai} – interior air temperature by the wall; t_{si} – internal surface temperature of the wall; t_{se} – external surface temperature of the wall; t_{ae} – exterior air temperature by the wall; r_i – moisture of the wall (interior); r_e – moisture of the wall (exterior); ϕ_i – relative air humidity in the room; t_i – average air temperature in the room; t_{dp} – dew point temperature.

SD – Standard deviation.

The air temperature t_i in the room No. 1 is the highest from all measured rooms, its value is 25.61 ± 0.9 °C. On the other side the air relative humidity φ_i is the lowest one (37.24 ± 1.9%). The reason of this situation that fireplace is installed there. The humidity in the room No.2 is the highest from all measured rooms (60.72 ± 2.5%). The reason is that there is a large number of plants, which are there during the winter season. Local temperature in the room No.3 is the second highest (20.95 ± 0.6 °C), because this room is directly connected with room No.1. The room No. 4 is not heated, because of it there is the lowest temperature among measured rooms, 15.97 ± 0.3 °C.

Walls which are insulated by the plaster MP (rooms No.1 and No.2), have lower surface moisture r_i than the walls which are not insulated by this plaster (room No.3 and No.4). The lowest value of internal surface moisture was in the room No.2, it was 1.89 ± 0.2% and the highest one was in the room No.4 it was 4.31 ± 0.2%. Exterior surface moisture r_{se} of walls insulated by MP plaster is higher than moisture of walls without insulation. But the difference is very small, and it is probably not caused by the internal plaster, but it is influenced by the walls orientation. The walls insulated by MP plaster are oriented to the north and not insulated walls to the south. The values of the heat flux q were in the rooms No.1, No.2 and No.4 very similar, they were in the range of 25.49 ± 1.5 to 27.65 ± 1.6 W m^{-2}. At the same time the highest value was measured in the room No. 3 (39.81 ± 2.0 W m^{-2})

Table 4 shows data which are calculated from the measured data shown in the Tables 1 and 3.

Table 4. Calculated data of family house

| Parameter	Room No. 1	Room No. 2	Room No. 3	Room No. 4
Δt (K)	22.10	17.55	20.38	12.55
h_{si} (W m^{-2} K^{-1})	7.30	8.78	10.91	8.47
h_{se} (W m^{-2} K^{-1})	32.27	31.02	68.64	26.26
R (m^2 K W^{-1})	2.66	2.66	2.47	2.47
R_i (m^2 K W^{-1})	0.14	0.11	0.09	0.12
R_e (m^2 K W^{-1})	0.031	0.032	0.015	0.038
R_T (m^2 K W^{-1})	2.83	2.81	2.58	2.63
U (W m^{-2} K^{-1})	0.35	0.35	0.39	0.38

Δt – temperature difference of the wall; h_{si} – heat transfer coefficient of internal surface; h_{se} – heat transfer coefficient of external surface; R – thermal resistance of wall; R_i – internal thermal resistance; R_e – external thermal resistance; R_T – total thermal resistance of construction; U - overall heat transfer coefficient.

The highest temperature difference Δt between internal and external surfaces of the wall were in the rooms 1 and 3. These rooms had the warmest evironment of all measured rooms, in the room No.1 it was 22.10 K and 20.38 K in No.3. The lowest value of heat transfer coefficient h_{si} of internal surface was in room No.1 (7.30 W m^{-2} K^{-1}) and the highest in the room No.3 (10.91 W m^{-2} K^{-1}). Different situation in the case of external value of this coefficient h_{se}, where the lowest value was in the room No.4 (26.26 W m^{-2} K^{-1}) and second in the room No.2 (31.02 W m^{-2} K^{-1}). On the other side highest value of external surface coefficient of heat transfer was measured in the room No.3 (68.64 W m^{-2} K^{-1}). Total thermal resistance of construction R_T and overall heat transfer coefficient U had better results in cases of rooms, where the plaster MP was used. In the room No.1 $U = 0.35$ W m^{-2} K^{-1} and $R_T = 0.35$ m^2 K W^{-1}, in the room No.2 $U = 0.35$ W m^{-2} K^{-1} and and $R_T = 0.35$ m^2 K W^{-1}, values are in these cases very similar.
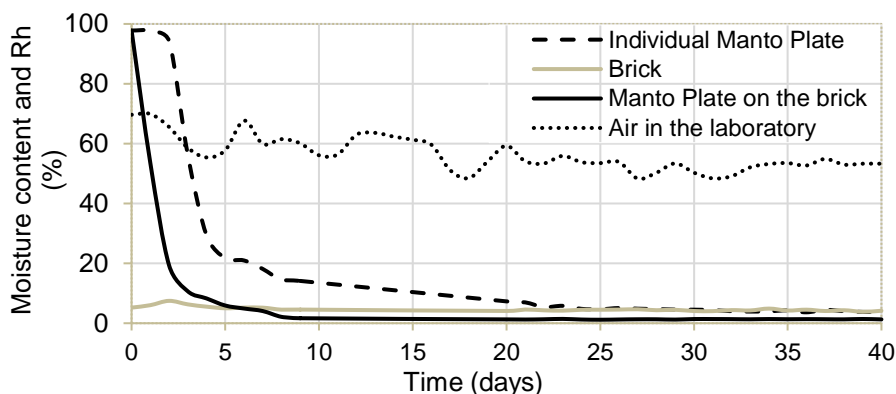
Figure 4. Measured data in the laboratory – moisture content of samples and relative humidity of air Rh during 40 days.

The graphs in the Fig. 4 show changes of moisture of samples during 40 days. It shows that moisture of both samples was the same on the beginning of measurement, it was about 97%. The moisture in the brick was very stable. The moisture of MP plaster layer on the brick decreased faster than individual sample of the MP. The relative humidity of air in laboratory was in range of approximately 50 to 65%. The air humidity had not big influence to moisture of the samples.

The graph in Fig. 5 shows change of moisture content of measured samples within first 10 days. It follows that the moisture content of layer of the plaster on the brick decreased faster than individual sample of plaster. From graph it is clear that moisture content of the brick was not influenced by the layer of the plaster. The sixth day of measurement the moisture content of layer of MP and the brick had same value. From this day the moisture of the layer had the lowest value among all samples.
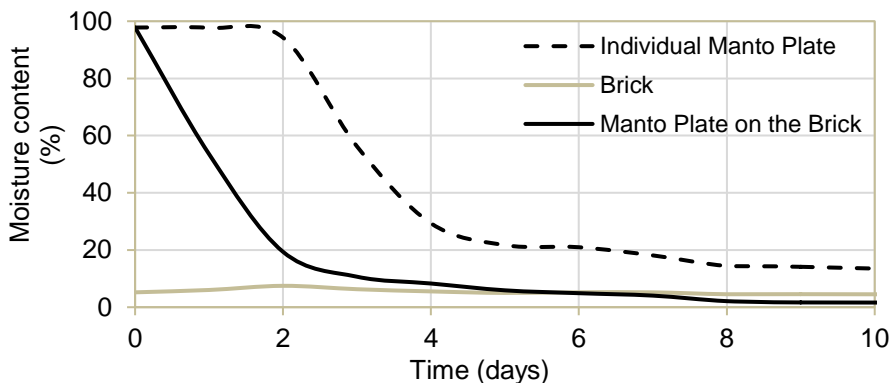
Figure 5. Measured data in the laboratory – the moisture content of samples during the first 10 days.

The graph in Fig. 6 shows the values of moisture content of the brick and individual sample of MP was very similar in the last 10 days of measurement. Value of layer of MP was very stable, there were only small fluctuations.
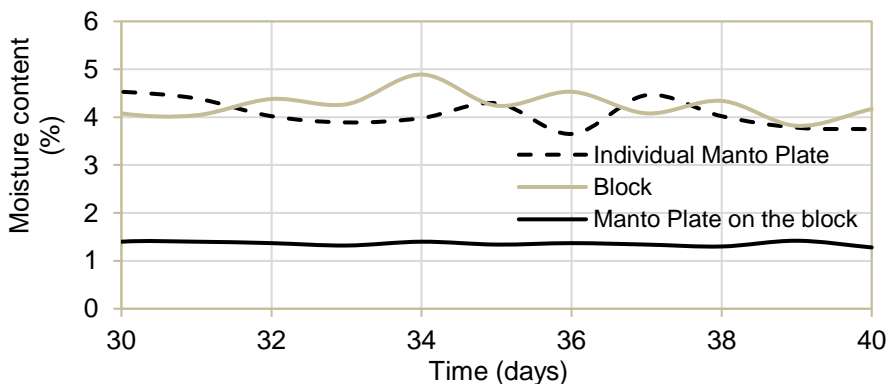
Figure 6. Measured data in the laboratory – the moisture content of samples during the last 10 days.

There was only a small difference between the temperatures of measured samples in the laboratory presented in the Table 5. Temperatures of samples were influenced by the air temperature in the laboratory. Small differences between the temperatures during the beginning of measurement were caused by the changes of materials moisture.

The influence of moisture content of the plaster measured on the individual MP sample on the coefficient of thermal conductivity is obvious from the Table 6. The lower the moisture content is, the smaller the coefficient of thermal conductivity is, and better thermal insulation properties of the material are.

Table 5. Measured data in the laboratory – the temperature and standard deviation (SD) of samples and air temperature in the laboratory

Sample	Temperature ± SD (°C)
Individual Manto Plate	20.19 ± 0.74
Brick	20.71 ± 0.51
Manto Plate on the brick	21.07 ± 0.90
Temperature in the laboratory	20.33 ± 0.38

The result is that the walls covered by MP have better thermal insulation properties than those that have not yet been insulated by any insulating material. The MP plaster also has a positive effect on the surface moisture of the walls. The surface moisture of the walls insulated by MP was lower than that of the other walls that were not insulated by the MP layer.

The measured value of the thermal conductivity coefficient differed from that stated by the manufacturer. The manufacturer presents the thermal conductivity value of 0.05 W m^{-1} K^{-1}. The value of this coefficient measured in the Thermal Measurement Laboratory at

Table 6. Moisture content and coefficient of thermal conductivity of the plaster MP

Moisture of the plaster Manto Plate (%)	Coefficient of thermal conductivity (W m^{-1} K^{-1})
91.78	0.38
18.22	0.29
11.03	0.18
8.15	0.19
4.95	0.12
4.88	0.12
4.15	0.11
3.89	0.11

University of Salford in Manchester is 0.05547 W m^{-1} K^{-1} (Thermal conductivity of Manto Plate heat insulation plaster and render, 2014).

During the laboratory measurement, the lowest coefficient of thermal conductivity 0.11 W m^{-1} K^{-1} was measured, so the result is different from the value measured at University of Salford about 0.05453 W m^{-1} K^{-1}. The reason of different results can be caused by different measuring methods. The measurement methods presented in this paper is based on the dynamic principle measurement using the instrument Isomet 2104, which needs more massive and thicker sample of tested material. Another reason of different results can be caused by different temperature and humidity of surrounding environment.

CONCLUSIONS

The results of the measurement in the reconstructed old building in this research confirm that the plaster MP has suitable thermal properties and can be successfully applied for improvement of the walls inside the old buildings. The surface moisture of the walls the rooms in which the plaster was used was lower than moisture in the rooms without MP plaster. It influenced positively also the relative humidity of air inside the rooms during the measurement.

The layer of MP plaster improved also the thermal insulation of the rooms. The overall heat transfer coefficient, which expresses the thermal properties of the construction, was lower in the isolated rooms than in rooms that have not yet been insulated by MP.

The measurements in the laboratory have shown that the moisture of MP plaster influences the coefficient of thermal conductivity significantly. The lower the moisture content is, the smaller the coefficient of thermal conductivity is, and better thermal insulation properties of the material are.

It can be said that MP plaster is a good alternative for people who want to use natural materials that has the lower environmental impact than synthetic materials. It can be used for old and for new buildings as well.

REFERENCES

Bakatovich, A., Davydenko, N. & Gaspar, F. 2018. Thermal insulating plates produced on the basis of vegetable agricultural waste. In: *Energy and Buildings* **180**, 72–82.

van Hoof, J., Mazej, M. & Hensen, J.L.M. 2010. Thermal comfort: research and practice. In: *Frontiers in Bioscience* **15**, 765–788.

Franzoni, E. State-of-the-art on methods for reducing rising damp in masonry. *Journal of Cultural Heritage* **31**, S3–S9.

Izozek Insulation. *http://www.izozek.com*. Accessed 2012.

Kocova, D. & Kic, P. 2016. Technical and economic aspects of thermal insulation of buildings. In: *15th International Scientific Conference Engineering for Rural Development*. Latvia University of Agriculture, Jelgava, 50–55.

Muizniece, I, Vilcane, L. & Blumberga, D. 2015. Laboratory research of granulated heat insulation material from coniferous forestry residue. *Agronomy Research* **13**, 690–699.

Pargana, N., Pinheiro, M.D., Silvestre, J.S. & de Brito, J. 2014. Comparative environmental life cycle assessment of thermal insulation materials of buildings. In: *Energy and Buildings* **82**, 466–481.

Pleiksnis, S., Skujans, J., Visockis, E. & Pulkis, K. 2016. Increasing fire proofness of sapropel and hemp shive insulation material. In: *15th International Scientific Conference Engineering for Rural Development*. Latvia University of Agriculture, Jelgava, 403–408.

Schiavoni, S., D′Alessandro, F., Bianchi, F. & Asdrubali, F. 2016. Insulation materials for the building sector: A review and comparative analysis. In: *Renewable and Sustainable Energy Reviews* **62**, 988–1011.

Thermal conductivity of Manto Plate heat insulation plaster and render. *https://www.sazus.cz/images/docs/certifikaty/0-EN.jpg*. Accessed 25.9.2014

Týbl, J. & Kic, P. 2016. Thermal properties and reduction of energy consumption of buildings. *Agronomy Research* **14**, 1222–1231.

Valasek, P., Chocholous, P. & Muller, M. 2016. Mechanical properties of thermal insulating sandwich materials. In: *15th International Scientific Conference Engineering for Rural Development*. Latvia University of Agriculture, Jelgava, 324–328.

Zach, J., Hroudová, J., Brožovský, J., Krejza, Z. & Gailius, A. 2013. Development of thermal insulating materials on natural base for thermal insulation systems. In: *Procedia Engineering* **57**, 1288–1294

Thermal analysis of asynchronous machines under intermittent loading

Z. Vondrášek, V. Ryženko[*], M. Linda

Czech University of Life Sciences Prague, Faculty of Engineering, Kamýcká 129, CZ165 21 Prague, Czech Republic
[*]Correspondence: ryzhenko@tf.czu.cz

Abstract. The operation of electric machines is accompanied by losses which are mostly converted to heat. The heat needs to be dissipated from the machine. With a properly dimensioned motor, the arising heat is balanced with dissipated one. After the motor is started at ambient temperature, all functional parts of the machine are gradually warmed until stabilized. Any overloading of the machine leads to stabilization at temperatures higher than expected by the designers. High temperatures in the machine could cause a crash by damaging an insulation. In case of machines with permanent magnets, the temperature affects their magnetic properties and can leads to demagnetization at the Curie temperature. Therefore, the measuring of temperature is so important for verifying the allowed warming of the motor. Contact and noncontact methods could be used for temperature measuring. Thermal warming and temperature distribution in an electric machine can be also determined by theoretical calculations based, for example, on the finite element method. This method is used by a number of computer software such as Ansys. The article deals with generation and propagation of heat in electric motors and with measuring of warming characteristics with a variable value of a load factor for intermittent periodic loading of asynchronous machine. The loading is carried out by the dynamometer. The temperature measurement is implemented by temperature sensors which are located on the stator winding of the asynchronous motor and are in operation for the whole time the motor is loaded.

Key words: electric machine, loading, losses, load factor, warming.

INTRODUCTION

Asynchronous motors are among the most common nowadays, due to fact that they are the simplest, and at the same time the most reliable motors without the need for frequent maintenance. During operation, heat caused by friction or electricity conduction is generated throughout various parts of the asynchronous motor. This heat then gradually expands (from its place of origin) towards the surface of the motor, where it is being leaked into ambient (Staton & Šušnjić, 2009). Not all the heat however is dispersed and part of it remains inside of the motor.

Material out of which the motor is constructed plays a major role. Just like any other object, asynchronous motors have their own exponential curve of heating and cooling. Slow application of load to the motor gradually increases its temperature to the point of reaching the maximal steady warm-up value. As the motor speeds up during start-up sequence from zero to nominal values, it consumes a notably greater amount of

electricity than during normal operation. In a matter of seconds, the temperature of rotor and stator winding increases considerably. This is caused by the fact that during this short amount of time the surrounding iron did not manage to increase its temperature high enough to be able to conduct and radiate the heat. Therefore it is imperative to take into consideration the amount of time the motor needs to start up, during which the thermal protection should not be triggered. The heat transfer in the asynchronous motor under no-load and different cooling conditions is discussed by Gedzurs (2014).

Higher operating temperatures shorten lifespan of individual parts as well as the entire motor. Reasons of exceeding motor's operating temperatures could be high frequency of power-ups, locked rotor or failure of power supply phase etc. This is why the thermal protection of motors should be constructed in a way to protect all of its sensible components from high temperatures for which the machine and its components are not dimensioned (Pawlus et al., 2017). The different modes of motor operation (overload, locked rotor, too frequent or prolonged acceleration etc.) are discussed for example in Venkataraman et al. (2005).

At the same time, the motor must not be disconnected during spool-up or spool-down sequence. Cooling system that removes generated heat, which consequently lowers the stress caused by high temperatures is therefore one of the most important parts of the motor, directly prolonging its overall lifespan (Staton et al., 2005). Cooling systems can be divided into three types: natural cooling, self-cooling and artificial cooling. Natural cooling is characterized by the motor conducting thermal energy to space (convection) without the use of a ventilator or coolant. Self-cooling motors have a ventilator unit placed on their operating shaft which brings cool air from the surrounding area to the motor. Artificial cooling consist of a ventilator that is completely independent of the motor's operating shaft and, as a result, the motor is still being cooled even if in idle state.

In diagnostics, temperature is one of the most important values, and has to be taken into consideration during revisions and inspections of electrical motors. With the help of temperature it is possible to determine whether the motor works according to its requirements and parameters, or if there has been a malfunction. High temperature can cause damage to the motor's isolation, which may result in its failure (Kosmodamianskii et al., 2011). Magnetic properties of motors with permanent magnets can be affected by high temperatures. Reaching Curie's temperature may cause their demagnetization. Taking measurements of electric motors under applied load plays an important role in their electromagnetic dimensioning. This is to check the correctness of previous design and the motor's properties under special conditions.

MATERIALS AND METHODS

The load factor z is defined as a ratio of the loading duration t_z to the period $T = t_z + t_0$ (see Fig. 1). As a loading device was used the 1DS541N dynamometer manufactured by MEZ Vsetin. Its schedule power is 18 kW for generator mode and 14.7 kW for motor mode. It allows measurement at a maximum rotational speed of 8,000 rpm and a torque peak of 80 Nm. It is a DC machine with a swinging stator. The forces applied on the swinging stator during the machine's operation are transmitted to a force meter with scale. The force meter is calibrated in torque units. The power

supply of the DC machine is realized by a Ward-Leonard rotary converter, type 1DP642-4. The converter consists of asynchronous and DC machines. It is designed as a mono-block.
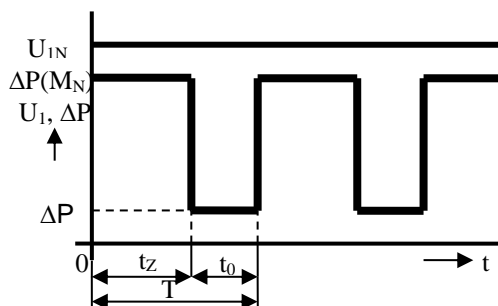
The asynchronous motor has a power of 22 kW, 1455 rpm and is connected to a three-phase distribution network 3x380 V, 50 Hz. It starts as a motor using the Y / Δ switch. It can work both as a motor and as a generator. The DC machine has a power output of 16.5 kW, 1500 rpm. Its rotor circuit parameters are 230 V, 71.7 A, the excitation circuit voltage is up to 220 V.

Figure 1. Time diagram of intermittent load of asynchronous motor at constant terminal voltage $U_1 = U_{1N}$. T [min] – motor load cycle time; t_z [min] – motor running time with defined loading; t_0 [min] – motor idle running time; $\Delta P(M)$ [W] – total losses of asynchronous motor at defined load; ΔP_0 [W] – overall losses of asynchronous motor during idle operation; M_N – motor load under nominal current I_{1N}.

After starting the dynamometer and the asynchronous motor the nominal values of the motor voltage were set. The asynchronous motor was connected via a clutch to a dynamometer. For temperature measurements we used 4 K type thermocouples with low time constant in order to capture the rapid temperature change with sufficient accuracy.

In the motor stator winding, three thermocouples have been attached to points 1−3, which are located at different places in order to display temperature differences of the motor components. Thermocouple number 4 was used to measure an ambient air temperature. These thermocouples are composed of NiCr (+) and NiAl (-). The thermocouple outputs were connected via the connectors to the Agilent 34972A Data Acquisition / Switch Unit via the Agilent 34902A 16-Channel Multiplexer.
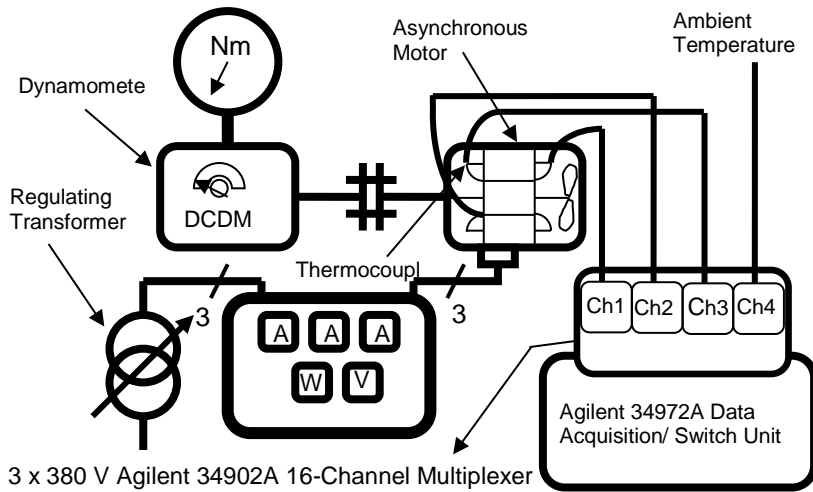
The circuit was connected according to the wiring diagram, see Fig. 2. Temperature recording was done automatically in 2s − intervals and measured data was automatically saved on the Flash storage device. The resulting temperature values were graphically plotted as temperature characteristics $\theta = f(t)$.

For measuring of heating of the asynchronous motor during its operation, it is necessary to know its main operation modes. Standard ČSN EN 60034-1 distinguishes between 10 modes of operation according to international classification. With respect to the given limitations of carrying out the test, two representative loading modes were selected. The first one is continuous operation of the motor at its nominal load, marked as S1.

Figure 2. Measuring scheme.

    The tested device is 4AP100L-2 induction motor with performance 3 kW. The load was applied using the 1DS541N dynamometer. The motor was started and the voltage set to the nominal value of 380 V (line-to-line). Subsequently, the dynamometer was activated and the load torque set to 8 Nm; during such a load the motor consumes the current around the nominal value of 6.2 A. The asynchronous motor is designed to run with such continuous load value. The test was run for 50 minutes in order to determine the limit operating temperature of selected winding parts – namely at the front end winding, near the front shield at the fan (sensor 1), at the rear shield at the outlet of the winding from groove (near the shaft; sensor 2) and at the rear end winding (sensor 3). During the measurement however, the normalized ambient temperature of 40 °C was not maintained. To simplify the theory, the motor is replaced by a homogeneous body with the same temperature in all parts. In our case, this assumption does not apply on the whole motor, but to the parts of the winding whose heating is monitored. For the physical description of the thermal processes of the motor, it is necessary to define the following quantities according to Petrbok et al. (1985):

m [kg] - weight of a monitored part;

c [J K^{-1} kg^{-1}] – the specific heat capacity of the material of the parts;

α [W m^{-2} K^{-1}] – heat transfer coefficient;

S [m^2] – surface of the monitored part;

ϑ [°C] – temperature of the monitored part;

ϑ_0 [°C] – ambient temperature;

ΔP [W] – power dissipation in the defined part.

From these quantities the thermal time constant τ_{th} is derived as:

$$\tau_{th} = \frac{m \cdot c}{\alpha \cdot S} \qquad (1)$$

Warming:

$$\Delta \vartheta = \vartheta - \vartheta_o \qquad (2)$$

In each monitored part of the motor the power dissipation is converted to the heat according to the equation:

$$dQ_\Delta = \Delta P \cdot dt \qquad (3)$$

This heat is partually move through the surface of the monitored part into the environment:

$$dQ_{konv} = \alpha \cdot S \cdot (\vartheta - \vartheta_o) \cdot dt, \qquad (4)$$

and partially increase the temperature of the mentioned above part according to:

$$dQ_{th} = m \cdot c \cdot d\vartheta \qquad (5)$$

The energy balance of the monitored part is described by the differential equation:

$$dQ_\Delta = dQ_{konv} + dQ_{th} \qquad (6)$$

$$\Delta P \cdot dt = \alpha \cdot S \cdot (\vartheta - \vartheta_o) \cdot dt + m \cdot c \cdot d\vartheta \qquad (7)$$

This differential equation is solved by separating of variables:

$$\Delta P \cdot dt - \alpha \cdot S \cdot (\vartheta - \vartheta_o) \cdot dt = m \cdot c \cdot d\vartheta \qquad (8)$$

The warming is given by the equation:

$$\{\Delta P - \alpha \cdot S \cdot (\vartheta - \vartheta_o)\} \cdot dt = m \cdot c \cdot d\vartheta \qquad (9)$$

At steady state ($t \to \infty$), the warming is

$$\Delta\vartheta = \Delta\vartheta_\infty = \frac{\Delta P}{\alpha \cdot S} \qquad (10)$$

The temperature of the monitored part varies continuously according to the next equation:

$$\Delta\vartheta = \frac{\Delta P}{\alpha \cdot S} - K \cdot e^{-\frac{t}{\tau_{th}}} \qquad (11)$$

The integrating constant K can be determined from the boundary conditions for t = 0, where the warming is $\Delta\vartheta = 0$.

Similar behavior of the monitored part can be expected during the cooling process. Differences occur in two cases. If the motor is disconnected during cooling from the source, there is no heat loss. In this case the motor stops and the cooling occurs only by natural convection and radiation. It is easier to determine the steady state as the motor temperature returns to the same level as its surroundings. A different situation applies for instances of intermittent load. During cooling, the motor is not disconnected from the power supply and it is running idle. This way the losses are reduced by the square of the consumed current. This is the second measured case of intermittent load motor load with different load factors according to ČSN EN 60034-1, marked as S6. The described operating mode is similar to the operation of machine tools. During the load, the generated losses cause the motor to heat up gradually, as with a constant load.

RESULTS AND DISCUSSION

The main aim of this research was to find the highest rate of motor heating during operation. Asynchronous motor has exponential dependence of the heating with time. The motor was loaded with torque of 8 Nm; hereby the motor consumed nominal current of 6.18 A. During the idle run, the average current was 2.77 A, i.e. 44.6% of the nominal

current. The losses in the winding decrease with the square of the current, here to about 20% of the original value. The motor was loaded in 10-minute cycles with different load factors from the initial state (disconnected from the power supply) when the motor temperature was the same as in its surroundings. The selected load factor levels were 20%, 40%, 60% and 80%. As was mentioned above, the normalized ambient temperature of 40 °C was not applied, but fluctuated, specifically between 24 and 27 °C.

In total, 7 cycles for each load factor value were performed. During the cyclic loading, saw-toothed course of the temperature was observed, as can be seen in the graphs in Figs. 3–6.
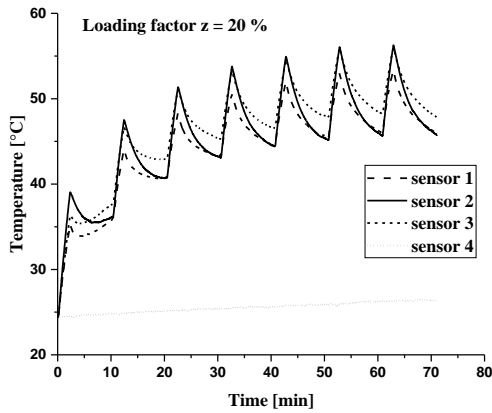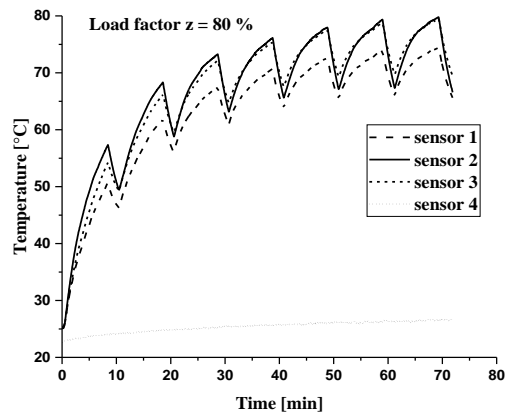

Figure 3. Time course of temperature of the observed asynchronous motor stator winding parts, and of the nearby air under 20% motor load factor.
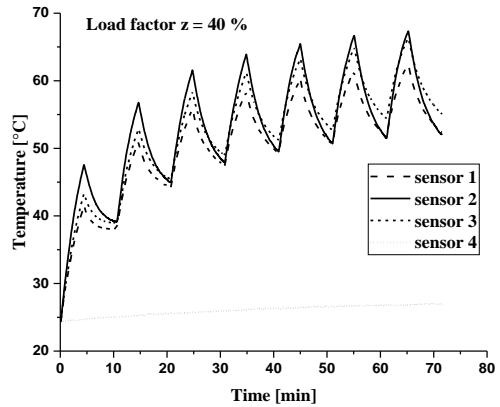
Figure 4. Time course of temperature of the observed asynchronous motor stator winding parts, and of the nearby air under 40% motor load factor.
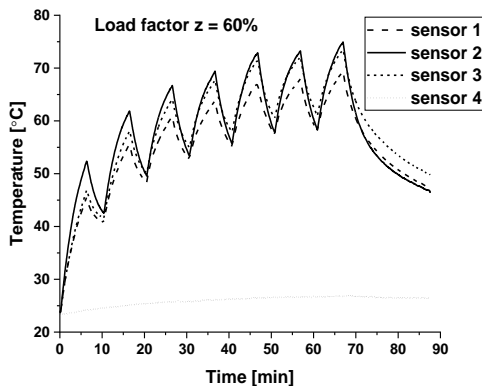
Figure 5. Time course of temperature of the observed asynchronous motor stator winding parts, and of the nearby air under 60% motor load factor and its cool-down during the motor idle running (after 66 min.).

Figure 6. Time course of temperature of the observed asynchronous motor stator winding parts, and of the nearby air under 80% motor load factor.

Basing on the temperature course, for each load factor value and for each temperature sensor, respective regression curves can be determined; the boundary points of the warming and cooling characteristics lie on this regression curve (see Fig. 7).

One of the objectives of the research was an idle running asynchronous motor heating test. The time course of temperature of the observed asynchronous motor stator winding parts, and of the nearby air during the motor's idle state after direct nominal voltage start-up (during 30 minutes) and its cool-down after power supply disconnection (during 30 minutes) can be seen in the graph in Fig. 8.
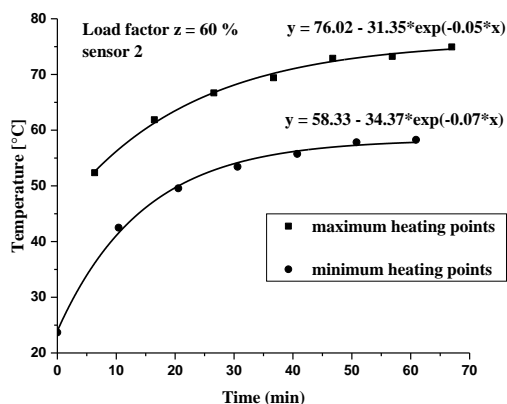

Figure 7. Envelope of individual maximal and minimal heating points (with approximate functions) of the asynchronous motor winding, measured by sensor 2 under 60% motor load factor.
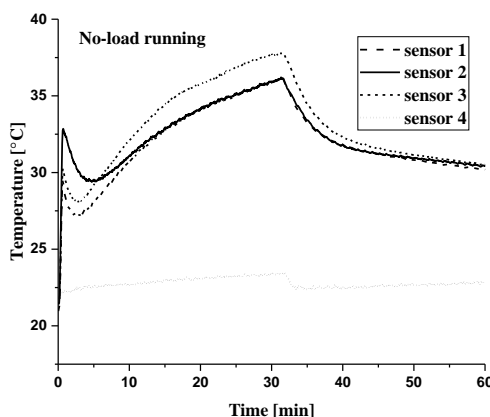
Figure 8. Time course of temperature during the motor's idle state after direct nominal voltage start-up and its cool-down after power supply disconnection (rotor stationary).

The start of the asynchronous motor was implemented by its direct connection to the power supply. It was also the current impulse in the stator winding that was transferred to the rotor winding. In spite of a short-term duration of the above-mentioned impulse, the rotor cage winding is likely to be heavily heated. The heat radiation from the cage winding affected the temperature of sensor 2 as did the motor running under load. The impact of the heat emission was greater than the heat dissipation from the stator winding to the cold ferromagnetic circuit. After the effect of the current impulse during the motor start finished, the originally hot parts cooled down as a result of the heat transfer to the cold ferromagnetic circuit. Subsequently, it was sensor 3 that recorded the highest temperatures on the rear winding face. The rear face of the winding can be cooled down only by air. As there was no air exchange with the environment, the heating of the rear winding face was faster than in the ferromagnetic circuit.

Fig. 9. shows the time course of temperature of the observed asynchronous motor stator winding parts, and of the nearby air under constant nominal motor load. The resulting maximal temperature at the end of the monitored running time was approximately 81 °C.
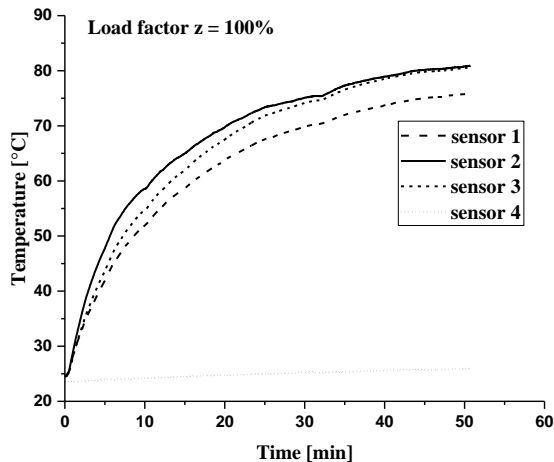
Figure 9. Time course of temperature of the observed asynchronous motor stator winding parts, and of the nearby air under constant nominal motor load.

CONCLUSIONS

As is apparent from the measurements, applying intermittent load on the asynchronous motor leads to lower heat stress of its electrical circuits. An important finding is the possibility of the use of insulation materials for achieving lower operating temperatures. When using more thermally resilient insulants of motor windings, and applying intermittent load, it is possible to securely overload the motor. It is important to take into consideration the increasing power losses with the second power of motor's current drawn. By comparing the changes in temperature of the individual motor winding segment, it was found that at the place of winding groove output located at the opposite side from the ventilator experiences the highest fluctuations in temperature. This is most apparent during motor load up to 60%.

Detected deviation from the expected high temperature fluctuations, at the front of the winding that faces away from the ventilator, is most likely caused by the fact that the winding conductors are not placed as close to each other. The thermal sensor therefore is not heated as intensively as it is in the place of winding output. Mentioned sensor is located at the side of the winding's air gap. It can be partially affected by heat radiating from the ring of the rotor's cage winding.

The rings and the outer parts of the rotor winding rods are according to O.Badran et al. (2012) the most heated components of the motor during its operation. In the case of the front part of the motor winding, at the side of the ventilator was temperature the lowest. This is caused by the presence of the ventilator, which intensively cools down the motor's surface, and therefore easily removes generated heat from this part of the motor.

Another finding indicates that in the case of 80% motor load, the maximal observed temperature of motor winding parts reach similar values as of motors running on maximal load. Possible structural savings are in this case negligible.

1253

REFERENCES

Badran, O., Sarhan, H. & Alomour, B. 2012. Thermal performance analysis of induction motor. *International Journal of Heat and Technology* **30**(1), 75–88.

ČSN EN 60034-1 ed.2 Rotating electrical machines - Part 1: Rating and performance. 2011.

Gedzurs, A. 2014. Heating of low-power induction motor under no-load mode and different cooling conditions. In: *Research for rural development 2014: annual 20th international scientific conference proceedings* **1**, Latvia University of Agriculture. Jelgava: LLU, pp. 219.-224.

Kosmodamianskii, A. S., Vorobiev, V. I. & Pugachev, A. A. 2011. The Temperature Effect on the Performance of a Traction Asynchronous Motor. *Elektrotekhnika* **8**, 50–54.

Pawlus, W., Khang, H.V. & Hansen, M.R. 2017. Temperature Rise Estimation of Induction Motor Drives Based on Loadability Curves to Facilitate Design of Electric Powertrains. *IEEE Transactions on Industrial Informatics* **13**(3), pp. 985–994.

Petrbok, K., Pokorný, K. & Klíma, J. 1985. Electrical Engineering and Electrification II. Czech University of Life Sciences, Prague, 108 pp (in Czech).

Staton, D., Boglietti, A. & Cavagnino, A. 2005. Solving the More Difficult Aspects of Electric Motor Thermal Analysis in Small and Medium Size Industrial Induction Motors. *IEEE Transactions on Energy Conversion* **20**(3), 620–628.

Staton, D. & Šušnjić, L. 2009. Induction Motors Thermal Analysis. *Strojarstvo* **51**(6), 623-631.

Venkataraman, B., Godsey, B., Premerlani, W., Shulman, E., Thakur, M. & Midence, R. 2005. Fundamentals of a Motor Thermal Model and its Applications in Motor Protection. In: *Proceeding of the 58th Annual Conference for Protective Relay Engineers*. College Station, TX, pp. 127–144.

INSTRUCTIONS TO AUTHORS

Papers must be in English (British spelling). English will be revised by a proofreader, but authors are strongly urged to have their manuscripts reviewed linguistically prior to submission. Contributions should be sent electronically. Papers are considered by referees before acceptance. The manuscript should follow the instructions below.

Structure: Title, Authors (initials & surname; an asterisk indicates the corresponding author), Authors' affiliation with postal address (each on a separate line) and e-mail of the corresponding author, Abstract (up to 250 words), Key words (not repeating words in the title), Introduction, Materials and methods, Results and discussion, Conclusions, Acknowledgements (optional), References.

Layout, page size and font
- Use preferably the latest version of **Microsoft Word**, doc., docx. format.
- Set page size to **ISO B5 (17.6 x 25 cm)**, all **margins at 2 cm**. All text, tables, and figures must fit within the text margins.
- Use single line spacing and **justify the text**. Do not use page numbering. Use **indent 0.8 cm** (do not use tab or spaces instead).
- Use font Times New Roman, point size for the title of article **14 (Bold)**, author's names 12, core text 11; Abstract, Key words, Acknowledgements, References, tables, and figure captions 10.
- Use *italics* for Latin biological names, mathematical variables and statistical terms.
- Use single ('…') instead of double quotation marks ("…").

Tables
- All tables must be referred to in the text (Table 1; Tables 1, 3; Tables 2–3).
- Use font Times New Roman, regular, 10 pt. Insert tables by Word's 'Insert' menu.
- Do not use vertical lines as dividers; only horizontal lines (1/2 pt) are allowed. Primary column and row headings should start with an initial capital.

Figures
- All figures must be referred to in the text (Fig. 1; Fig. 1 A; Figs 1, 3; Figs 1–3). Use only black and white or greyscale for figures. Avoid 3D charts, background shading, gridlines and excessive symbols. Use font **Arial, 10 pt** within the figures. Make sure that thickness of the lines is greater than 0.3 pt.
- Do not put caption in the frame of the figure.
- The preferred graphic format is Excel object; for diagrams and charts EPS; for half-tones please use TIFF. MS Office files are also acceptable. Please include these files in your submission.
- Check and double-check spelling in figures and graphs. Proof-readers may not be able to change mistakes in a different program.

References
- **Within the text**

In case of two authors, use '&', if more than two authors, provide first author 'et al.':

Smith & Jones (1996); (Smith & Jones, 1996);

Brown et al. (1997); (Brown et al., 1997)

When referring to more than one publication, arrange them by following keys: 1. year of publication (ascending), 2. alphabetical order for the same year of publication:

(Smith & Jones, 1996; Brown et al., 1997; Adams, 1998; Smith, 1998)

- **For whole books**

Name(s) and initials of the author(s). Year of publication. *Title of the book* (*in italics*). Publisher, place of publication, number of pages.

Shiyatov, S.G. 1986. *Dendrochronology of the upper timberline in the Urals*. Nauka, Moscow, 350 pp. (in Russian).

- **For articles in a journal**

Name(s) and initials of the author(s). Year of publication. Title of the article. *Abbreviated journal title* (*in italic*) volume (in bold), page numbers.

Titles of papers published in languages other than English, should be replaced by an English translation, with an explanatory note at the end, e.g., (in Russian, English abstr.).

Karube, I. & Tamiyra, M.Y. 1987. Biosensors for environmental control. *Pure Appl. Chem.* **59**, 545–554.
Frey, R. 1958. Zur Kenntnis der Diptera brachycera p.p. der Kapverdischen Inseln. *Commentat.Biol.* **18**(4), 1–61.
Danielyan, S.G. & Nabaldiyan, K.M. 1971. The causal agents of meloids in bees. *Veterinariya* **8**, 64–65 (in Russian).

- **For articles in collections:**

Name(s) and initials of the author(s). Year of publication. Title of the article. Name(s) and initials of the editor(s) (preceded by In:) *Title of the collection (in italics)*, publisher, place of publication, page numbers.

Yurtsev, B.A., Tolmachev, A.I. & Rebristaya, O.V. 1978. The floristic delimitation and subdivisions of the Arctic. In: Yurtsev, B. A. (ed.) *The Arctic Floristic Region*. Nauka, Leningrad, pp. 9–104 (in Russian).

- **For conference proceedings:**

Name(s) and initials of the author(s). Year of publication. Name(s) and initials of the editor(s) (preceded by In:) *Proceedings name (in italics)*, publisher, place of publishing, page numbers.

Ritchie, M.E. & Olff, H. 1999. Herbivore diversity and plant dynamics: compensatory and additive effects. In: Olff, H., Brown, V.K. & Drent R.H. (eds) *Herbivores between plants and predators. Proc. Int. Conf. The 38th Symposium of the British Ecological Society*, Blackwell Science, Oxford, UK, pp. 175–204.

....………

Please note
- Use '.' (not ',') for decimal point: 0.6 ± 0.2; Use ',' for thousands – 1,230.4;
- Use '–' (not '-') and without space: pp. 27–36, 1998–2000, 4–6 min, 3–5 kg
- With spaces: 5 h, 5 kg, 5 m, 5 °C, C : D = 0.6 ± 0.2; $p < 0.001$
- Without space: 55°, 5% (not 55 °, 5 %)
- Use 'kg ha^{-1}' (not 'kg/ha');
- Use degree sign ' ° ' : 5 °C (not 5 ^{O}C).

1256